

Probing the Correlated Spin-Dynamics of Ultracold Atoms: Magnetic and Polaronic Properties

Dissertation

zur Erlangung des Doktorgrades
an der Fakultät für Mathematik,
Informatik und Naturwissenschaften,
der Universität Hamburg,
Fachbereich Physik

vorgelegt von

Georgios Koutentakis

geboren am 13.05.1992 in Iraklion

Hamburg

2021

Gutachter/innen der Dissertation:	Herr Prof. Dr. Peter Schmelcher Herr Prof. Dr. Michael Potthoff
Zusammensetzung der Prüfungskommission:	Frau Prof. Dr. Daniela Pfannkuche Herr Prof. Dr. Peter Schmelcher Herr Prof. Dr. Michael Potthoff Herr Prof. Dr. Andreas Hemmerich Herr Dr. Tim Laarmann
Vorsitzende/r der Prüfungskommission:	Frau Prof. Dr. Daniela Pfannkuche
Datum der Disputation:	16.09.2021
Vorsitzender Fach-Promotionsausschusses PHYSIK:	Prof. Dr. Wolfgang Hansen
Leiter des Fachbereichs PHYSIK:	Prof. Dr. Michael Potthoff
Dekan der Fakultät MIN:	Prof. Dr. Heinrich Graener

To Alexandra

Zusammenfassung

Ultrakalte Quantengase bieten eine gut kontrollierbare und variable Plattform zur Untersuchung von Effekten, die von Quantenkorrelationen herrühren. Diese beiden Eigenschaften machen sie zu idealen Kandidaten für die Realisierung von Quantensimulatoren. Insbesondere bieten ultrakalte Atome den Rahmen für den Aufbau von Versuchsanordnungen, die theoretischen Modellen eng entsprechen, die zur Beschreibung der Quanten-Vielteilchendynamik vorgeschlagen wurden, die z. B. in korrelierten Materialien vorkommt. Ein wichtiges Merkmal der atomaren Ensembles ist die Möglichkeit, Aufbauten mit Spinor-Charakter zu realisieren. Ultrakalte Spinor-Atome ermöglichen die Untersuchung von Quantensystemen, die grundsätzlich auf dem Vorhandensein eines Spin-Freiheitsgrades beruhen, und die Implementierung hochgradig kontrollierbarer Sonden zur Verfolgung der Eigenschaften einer größeren Klasse von Quantensystemen inner- und außerhalb des Gleichgewichts. Diese beiden Grenzbereiche von ultrakalten Spinor-Atomen bilden die beiden Schwerpunkte unserer Studien. Zur Erforschung der Feinheiten der Dynamik von Spinor-Ensembles verwenden wir eine hochentwickelte *ab-initio*-Variationsmethode für die zeitliche Entwicklung der Vielkörper-Schrödinger-Gleichung, nämlich die Multi-Layer Multi-Configuration Time-Dependent Hartree Methode für atomare Mixturen oder ML-MCTDHX.

Der erste Teil dieser Arbeit erforscht den itineranten Ferromagnetismus in ultrakalten Atomen. Diese Form des Ferromagnetismus beeinflusst die magnetischen Eigenschaften von Metallen und ist einer der fundamentalsten Effekte, die durch den Spinorcharakter der Elektronen entstehen. Sein Auftreten wird üblicherweise mit starken kurzreichweitigen abstoßenden Wechselwirkungen zwischen Elektronen mit entgegengesetzten Spins assoziiert, die den kinetischen Energievorteil ihrer Paarung im gleichen Einteilchenzustand aufheben. In einem solchen Rahmen ist das Phänomen des Ferromagnetismus mit der Spinpolarisation des Ensembles verbunden. Unsere Studien konzentrieren sich genau auf die Entschlüsselung dieser Beziehung, indem wir die korrelierte Dynamik von eindimensionalen ultrakalten Systemen untersuchen, initialisiert in Konfigurationen, die als ferromagnetisch gelten. Insbesondere untersuchen wir die Stabilitätseigenschaften eines parabolisch gefangenen und spinpolarisierten Fermi-Gases weniger Teilchen, wenn es durch ein transversales inhomogenes Magnetfeld gestört wird. Wir zeigen, dass der spinpolarisierte Zustand, der als der Gleichgewichtszustand eines Ferromagneten im Limes starker Wechselwirkungen vorhergesagt wird, inhärent instabil ist. In ähnlicher Weise wird gezeigt, dass ein Doppeltopf-Aufbau, der in einer Domänenwand-Struktur aus Spin-Up- und Spin-Down-Atomen initialisiert wurde, sich zu einem Zustand mit mischbaren Spinkomponenten entwickelt, im Gegensatz zu den üblichen Ansichten über Ferromagnetismus, wo solche phasentrennten Zustände für moderate Abstoßungen stabil sind. Trotz der scheinbaren Abwesenheit ferromagnetischen Verhaltens bleiben in beiden Fällen die Spin-Spin-Korrelationen zwischen den Atomen während der dynamischen Entwicklung weitgehend ferromagnetisch, was auf einen anderen Mechanismus hinter der Stabilität der ferromagnetischen Ordnung auf der Ebene der Korrelationen zwischen den Teilchen hindeutet. Dieser Mechanis-

mus kann durch die Konkurrenz zwischen Spin-Spin-Wechselwirkungen ferromagnetischen und antiferromagnetischen Charakters beschrieben werden, die aus dem wechselwirkungsgetriebenen beziehungsweise kinetischen Spin-Austausch der Atome entstehen. Wir zeigen explizit die Existenz dieser Mechanismen und erfassen ihren Haupteinfluss auf die Zerfalldynamik der Spinpolarisation, indem wir ein geeignetes Spin-Ketten-Modell verwenden. Wichtig ist, dass durch dieses Zusammenspiel der Wechselwirkungen die Erzeugung von Quantenkorrelationen höherer Ordnung und von Verschränkung aufgedeckt wird. Unsere Ergebnisse liefern einen Ausgangspunkt für die Entwicklung einer Bottom-up-Charakterisierung des itineranten Ferromagnetismus, basierend auf der Konkurrenz zwischen den ferromagnetischen und antiferromagnetischen Korrelationen, die auf einer fundamentalen Ebene liegen als die bisher vorgeschlagenen energetischen Argumente.

Der zweite Teil dieser Arbeit befasst sich mit der Verwendung von Spinor-Fremdteilchen als Sonden für die Quantendynamik von Fermi- und Bose-Polaronen. Ein Polaron ist ein besonders wichtiges Quasiteilchen in den Materialwissenschaften mit einer Vielzahl von Anwendungen. Es besteht aus einer Fremdteilchen, die von der Wolke der Anregungen des Mediums, in dem es sich befindet, umhüllt wird. Diese zusammengesetzte Struktur bildet eine eigenständige Einheit mit stark veränderten Eigenschaften im Vergleich zu einer isolierten Fremdteilchen. Unsere Schlüsselbeiträge zu diesem Thema sind die Identifizierung eines wohldefinierten Fermi-Polarons für repulsiv wechselwirkenden eindimensional gefangenen fermionischen Ensembles und der dynamische Zerfall des Bose-Polarons im entsprechenden bosonischen Fall. Insbesondere zeigen wir, dass eine Fremdteilchen, eingebettet in ein eindimensionales Wenig-Körper-Fermi-Gas aus leichteren Atomen polaronische Eigenschaften annimmt, wie sie durch seine Energie, sein Residuum und seine Kohärenz angezeigt werden, im Gegensatz zum Rahmen der Anderson-Orthogonalitätskatastrophe. Weiter haben wir das Phänomen der zeitlichen Orthogonalitätskatastrophe in Bose-Polaronen aufgedeckt und charakterisiert. Insbesondere zeigen wir, dass nicht-perturbative nicht-lineare Prozesse die Lebensdauer von Bose-Polaronen für starke Wechselwirkungen zwischen dem Medium und dem Fremdteilchen begrenzen. Für die Erforschung dieses Effekts schlagen wir eine neue Generation von Experimenten vor, die auf zeitabhängigen spektroskopischen Techniken basieren, und analysieren sie theoretisch. Genauer gesagt, zeigen wir, dass die Ramsey-Spektroskopie in der Lage ist, den Zusammenbruch des Polaron-Bildes zu identifizieren. Ebenso ist die Pump-Probe-Spektroskopie dazu geeignet, die Lebensdauer des Bose-Polarons und die Tendenz des Medium-Fremdteilchen-Systems zur Eigenzustands-Thermalisierung zu erforschen. Darüber hinaus wurden schwer fassbare Eigenschaften von eindimensionalen Bose und Fermi-Polaronen identifiziert und quantifiziert, wie z. B. ihre Quasiteilchen-Residuen, ihre Energien und die effektiven Polaron-Polaron-Wechselwirkungen im Fall von mehrfachen Fremdteilchen. Unsere Ergebnisse verdeutlichen die Bedeutung nichtlinearer Prozesse für die adäquate Beschreibung der korrelierten Dynamik polaronischer Quasiteilchen und eröffnen unerforschte Wege für zukünftige Forschung.

Abstract

Ultracold quantum gases offer a well-controlled and tunable platform to examine effects stemming from quantum correlations. Both of these properties render them ideal candidates for realizing quantum simulators. In particular, ultracold atoms provide the framework for building up experimental setups corresponding closely to theoretical models proposed to describe the quantum many-body dynamics exhibited e.g. in correlated materials. An important feature of the atomic ensembles is the feasibility to realize setups of a spinor character. Spinor ultracold atoms enable the investigation of quantum systems relying fundamentally on the presence of a spin degree-of-freedom, and the implementation of highly tunable probes for tracking the in- and out-of-equilibrium properties of a wider class of quantum setups. These two frontiers of spinor ultracold atoms constitute the two focal points of our studies. To tackle the intricacies of the dynamics of spinor ensembles we employ a highly-advanced *ab initio* variational method for the time-evolution of the many-body Schrödinger equation, namely the Multi-Layer Multi-Configuration Time-Dependent Hartree Method for Atomic Mixtures or ML-MCTDHX.

The first part of this thesis explores itinerant ferromagnetism in ultracold atoms. This form of ferromagnetism affects the magnetic properties of metals and it is among the most fundamental effects emanating due to the spinor character of electrons. Its onset is commonly associated to strong short-range repulsive interactions between electrons with anti-aligned spins, that negate the kinetic energy benefit of their pairing in the same single-particle state. Within such frameworks, the phenomenon of ferromagnetism is connected to the spin-polarization of the ensemble. Our studies focus exactly on unraveling this latter relation, by studying the correlated dynamics of one-dimensional ultracold systems, initialized in configurations which are deemed as ferromagnetic. In particular, we study the stability properties of a parabolically confined few-body and spin-polarized Fermi gas when perturbed by a transverse inhomogeneous magnetic field. We reveal that the spin-polarized state, predicted to be the equilibrium state of a ferromagnet in the strong interacting limit, is inherently unstable. Similarly, a double-well setup initialized in a domain-wall structure of spin-up and spin-down atoms is shown to evolve to a state with miscible spin-components, in contrast to the usual views on ferromagnetism where such phase-separated states are stable for moderate repulsions. Nevertheless, despite the apparent absence of ferromagnetic behaviour, in both cases the spin-spin correlations among the atoms remain largely ferromagnetic throughout the dynamical evolution, hinting at the existence of a different mechanism behind the stability of ferromagnetic order on the level of interparticle correlations. This mechanism can be characterized by the competition between spin-spin interactions of ferromagnetic and antiferromagnetic character, which emerge from the interaction-driven and kinetic spin-exchange of the atoms, respectively. We explicitly demonstrate the existence of these mechanisms and capture their main influence in the decay dynamics of the spin-polarization, by employing an appropriate spin chain model. Importantly, due to this interplay of interactions the generation of higher order quan-

tum correlations and entanglement is revealed. Our findings provide a starting point for developing a bottom-up characterization of itinerant ferromagnetism based on the competition between the ferromagnetic and antiferromagnetic correlations, which lie at a more fundamental level than the energetic arguments proposed thus far.

The second part of this thesis regards the use of spinor impurities as probes of the quantum dynamics of Fermi and Bose polarons. A polaron is a particularly important quasi-particle in material science with a wide range of applications. It consists of an impurity dressed by the excitation cloud of its host. This composite structure forms a distinct entity, with severely altered properties, compared to an isolated impurity. Our key contributions in this topic are the identification of a well-defined Fermi polaron for repulsively interacting one-dimensional confined fermionic ensembles and the dynamical decay of the Bose polaron in the corresponding bosonic case. In particular, we show that an impurity embedded in an one-dimensional few-body Fermi gas of lighter atoms accumulates polaronic properties, as indicated by its energy, residue and coherence, in contrast to the framework of the Anderson orthogonality catastrophe. Furthermore, we have unveiled and characterized the phenomenon of temporal orthogonality catastrophe in Bose polarons. In particular, we show that non-perturbative non-linear processes limit the lifetime of Bose polarons for strong impurity-host repulsions. For the exploration of this effect we propose and theoretically analyze a new generation of experiments based on time-dependent spectroscopic techniques. More specifically, we demonstrate that Ramsey spectroscopy is able to identify the break down of the polaron picture. Similarly, pump-probe spectroscopy is adequate for exploring the lifetime of the Bose polaron and the tendency of the bath-impurity system towards eigenstate thermalization. In addition to the above, elusive properties of one-dimensional Bose and Fermi polarons were identified and quantified such as their quasi-particle residues, their energies and the effective polaron-polaron interactions in the case of multiple impurities. Our findings outline the importance non-linear processes for the adequate description of the correlated dynamics of polaronic quasiparticles and opens up several unexplored avenues of future research.

Contents

Preface	iii
1 Introduction	1
2 Theoretical Framework	9
2.1 Spinor and Pseudospinor condensates	9
2.1.1 Internal states of atomic systems and ultracold experiments . . .	9
2.1.2 Optical Trapping	13
2.1.3 Dimensional Reduction of 3D Hamiltonians	16
2.2 Magnetic properties of Spinor Fermi Gases	23
2.2.1 Stoner model of Ferromagnetism	23
2.2.2 Stoner model and beyond: Description of ferromagnetism in condensed matter settings	27
2.3 Stationary and magnetic properties of confined spin-1/2 Fermi gases in one-dimension	30
2.3.1 Hamiltonian and basic symmetries	31
2.3.2 Non-interacting many-body eigenspectrum	33
2.3.3 Magnetic properties of weakly interacting systems	36
2.3.4 Strongly interacting 1D spin-1/2 fermions	39
2.3.5 Spin-chain models for strongly interacting 1D systems	42
2.4 Bose and Fermi polarons	49
2.4.1 The Fröhlich Hamiltonian	49
2.4.2 Impurities in a weakly interacting Bose gas	52
2.4.3 The phase-diagram of Bose polarons	55
2.4.4 The effective potential	57
2.4.5 Non-linear effects in BECs and their relevance in polaron physics	58
2.4.6 Extension to Fermi polarons	60
2.5 Radiofrequency spectroscopy	61
2.5.1 Adiabatic and diabatic spin-dynamics and importance for spectroscopic applications	62
2.5.2 Injection and ejection spectroscopy	69
2.5.3 Ramsey spectroscopy	71
2.5.4 Pump-probe spectroscopy	74

CONTENTS

2.6	Many-Body Methodological Approach: ML-MCTDHX	75
2.6.1	Basic elements of the ML-MCTDHX approach	77
2.6.2	Limiting cases of the ML-MCTDHX approach and convergence .	82
2.6.3	Efficiency of ML-MCTDHX method for addressing the impurity problem	84
2.6.4	Advantages of spectroscopic simulations	85
3	Outline of scientific contributions	87
3.1	Itinerant ferromagnetism in 1D few-fermion gases	87
3.1.1	Dynamical stability of parabolically trapped spin-polarized fermions [K1]	88
3.1.2	Relation of ferromagnetism and phase separation [K2]	89
3.2	Spectroscopic properties of Bose and Fermi Polarons	92
3.2.1	Reverse radiofrequency spectroscopy of Fermi polarons in few- body ensembles [K3]	92
3.2.2	Ramsey spectroscopy of the Bose polaron and evidence towards an orthogonality catastrophe phenomenon [K4]	94
3.2.3	Multiple Bose polarons and their induced interactions [K5]	97
3.2.4	Pump-Probe spectroscopy of Bose polarons: lifetime and relax- ation of the quasiparticle structures [K6]	99
4	Scientific Contributions	103
4.1	Magnetic properties of 1D degenerate few-fermion gases	104
4.1.1	Probing ferromagnetic order in few-fermion correlated spin-flip dynamics	104
4.1.2	Interplay of phase separation and itinerant magnetism for corre- lated few fermions in a double-well	123
4.2	Spectroscopic properties of Bose and Fermi Polarons	147
4.2.1	Repulsive Fermi polarons and their induced interactions in binary mixtures of ultracold atoms	147
4.2.2	Quench Dynamics and Orthogonality Catastrophe of Bose Polarons	163
4.2.3	Many-body quantum dynamics and induced correlations of Bose polarons	178
4.2.4	Pump Probe Spectroscopy of Polarons and Evidence for Ther- malization	206
5	Conclusions and Outlook	223
	Acknowledgments	231

Preface

The present cumulative dissertation is based on the publications [K1–K6].

List of publication on which this dissertation is based:

- [K1] G. M. Koutentakis, S. I. Mistakidis, and P. Schmelcher, “Probing ferromagnetic order in few-fermion correlated spin-flip dynamics”, *New J. Phys.* **21**, 053005 (2019).
- [K2] G. M. Koutentakis, S. I. Mistakidis, and P. Schmelcher, “Interplay of phase separation and itinerant magnetism for correlated few fermions in a double-well”, *New J. Phys.* **22**, 063058 (2020).
- [K3] S. I. Mistakidis, G. C. Katsimiga, G. M. Koutentakis, and P. Schmelcher, “Repulsive Fermi polarons and their induced interactions in binary mixtures of ultracold atoms”, *New J. Phys.* **21**, 043032 (2019).
- [K4] S. I. Mistakidis, G. C. Katsimiga, G. M. Koutentakis, Th. Busch, and P. Schmelcher, “Quench Dynamics and Orthogonality Catastrophe of Bose Polarons”, *Phys. Rev. Lett.* **122**, 183001 (2019).
- [K5] S. I. Mistakidis, G. M. Koutentakis, G. C. Katsimiga, Th. Busch, and P. Schmelcher, “Many-body quantum dynamics and induced correlations of Bose polarons”, *New J. Phys.* **22**, 043007 (2020).
- [K6] S. I. Mistakidis, G. C. Katsimiga, G. M. Koutentakis, Th. Busch, and P. Schmelcher, “Pump-probe spectroscopy of Bose polarons: Dynamical formation and coherence”, *Phys. Rev. Research* **2**, 033380 (2020).

Note here that when referring to the above mentioned scientific contributions throughout the current thesis we will always use the reference index [K1–K6] provided above.

Thesis Outline

Chapter 1 provides a general overview into the field of spinor ultracold atom ensembles and embeds our work into the body of the corresponding scientific literature. Special emphasis is given on the particular questions that we aim at addressing within

this thesis. Chapter 2 focusses on the theoretical framework underlying our work. In particular, the state-of-the-art understanding regarding the properties of magnetic ultracold atom ensembles and polaron physics is outlined. Within this chapter we also provide our main theoretical tools that are employed in the works [K1–K6] in order to address the open questions established in chapter 1. Chapter 3 gives an overview over each one of our scientific contributions with special emphasis on the particular deficiency in the literature that is addressed, as well as, the corresponding conclusions and insights that are gained. Chapter 4 provides the scientific contributions [K1–K6] in their published form and finally, chapter 5 summarizes, provides the general conclusion of this thesis and mentions possible future avenues of study that are established in view of this thesis.

Personal contributions to the publications [K1–K6]

I have conducted the projects resulting in [K1, K2] in their entirety, including the definition of the particular research goals, the numerical calculations, the conceptualization and implementation of the employed approximate models and the writing of both manuscripts. Dr. Simeon I. Mistakidis has substantially contributed in optimizing of the presentation of our results. The projects [K3–K6] were all collaborative efforts with substantial contributions from Dr. Garyfalia C. Katsimiga, Dr. Simeon I. Mistakidis and myself. Namely, I have contributed the related numerical implementations regarding the analysis of the results and the numerical simulations were performed by Dr. Simeon I. Mistakidis and me in all these cases. All of the above mentioned authors contributed to the analysis and interpretation of the results and to the writing of the manuscripts. The research goals of the projects [K3, K6] was set by Dr. Garyfalia C. Katsimiga, Dr. Simeon I. Mistakidis and myself. The concepts of the works [K4, K5] stem from discussions of Prof. Dr. Peter Schmelcher and Prof. Dr. Thomas Busch. In all cases, the project progress was supervised on a regular basis by Prof. Dr. Peter Schmelcher.

Further list of publications:

- [F1] S. Mistakidis, G. Koutentakis, F. Grusdt, H. R. Sadeghpour, and P. Schmelcher, “Radiofrequency spectroscopy of one-dimensional trapped Bose polarons: crossover from the adiabatic to the diabatic regime”, *New J. Phys.* (in press).
- [F2] S. I. Mistakidis, F. Grusdt, G. M. Koutentakis, and P. Schmelcher, “Dissipative correlated dynamics of a moving impurity immersed in a Bose–Einstein condensate”, *New J. Phys.* **21**, 103026 (2019).
- [F3] G. C. Katsimiga, S. I. Mistakidis, G. M. Koutentakis, P. G. Kevrekidis, and P. Schmelcher, “Many-body dissipative flow of a confined scalar Bose-Einstein condensate driven by a Gaussian impurity”, *Phys. Rev. A* **98**, 013632 (2018).

FURTHER LIST OF PUBLICATIONS:

- [F4] S. I. Mistakidis, G. M. Koutentakis, and P. Schmelcher, “Bosonic quantum dynamics following a linear interaction quench in finite optical lattices of unit filling”, *Chem. Phys.* **509**, 106 (2018).
- [F5] G. C. Katsimiga, S. I. Mistakidis, G. M. Koutentakis, P. G. Kevrekidis, and P. Schmelcher, “Many-body quantum dynamics in the decay of bent dark solitons of Bose–Einstein condensates”, *New J. Phys.* **19**, 123012 (2017).
- [F6] L. Cao, V. Bolsinger, S. I. Mistakidis, G. M. Koutentakis, S. Krönke, J. M. Schurer, and P. Schmelcher, “A unified ab initio approach to the correlated quantum dynamics of ultracold fermionic and bosonic mixtures”, *J. Chem. Phys.* **147**, 044106 (2017).
- [F7] G. C. Katsimiga, G. M. Koutentakis, S. I. Mistakidis, P. G. Kevrekidis, and P. Schmelcher, “Dark–bright soliton dynamics beyond the mean-field approximation”, *New J. Phys.* **19**, 073004 (2017).
- [F8] G. M. Koutentakis, S. I. Mistakidis, and P. Schmelcher, “Quench-induced resonant tunneling mechanisms of bosons in an optical lattice with harmonic confinement”, *Phys. Rev. A* **95**, 013617 (2017).

FURTHER LIST OF PUBLICATIONS:

List of Abbreviations

Here we provide the list of abbreviations employed throughout this work.

Abbreviation	Meaning
1D	One-dimension or one-dimensional
BEC	Bose-Einstein condensate
MCTDH	Multi-configuration Time-Dependent Hartree method
MCTDHB	Multi-configuration Time-Dependent Hartree method for bosons
MCTDHF	Multi-configuration Time-Dependent Hartree method for fermions
ML-MCTDHX	Multi-configuration Time-Dependent Hartree method for atomic mixtures
SPEE	Single-particle eigenenergies
SPES	Single-particle eigenstates
tJU (model/Hamiltonian)	Tunnelling (t), spin-spin exchange Interaction (J), on-site interaction (U) (model/Hamiltonian)
XXZ (model/Hamiltonian)	Anisotropic Heisenberg (model/Hamiltonian)

Chapter 1

Introduction

Ever since the experimental realization of the first atomic Bose-Einstein Condensate (BEC) [1,2] ultracold atoms have been a fertile platform for comprehending the complex physics of many-body systems deep in the quantum regime. Advances in trapping and cooling techniques have allowed for the realization of elaborate physical scenarios, involving the controlled confinement of a single or multiple species [3–10] of atoms in different hyperfine [11–14] or electronic states [10, 15, 16]. In particular, atomic species of bosonic [6, 9, 11, 17–19] and fermionic character [8, 20, 21] or even mixtures thereof [3–5, 7, 10] can be generated and cooled all the way to quantum degeneracy, enabling not only the observation of bosonic [22, 23] and fermionic [22–24] superfluidity but also the study of the impact of different particle statistics on various quantum phenomena [22, 24]. Regarding their confinement, a large variety of external potentials including for instance, ring shaped [25–28] and box-like [29–32] geometries can be generated. Atomic ensembles in one or two spatial dimensions have been also realized [33–35] and intensively studied [23, 36], as well as, lattice potentials of various symmetries [37], with some exotic examples including the honeycomb [38–40] and the Lieb lattices [41]. This tunability of the external confinement allows for the study of several geometric effects enabling, among others, for the study of Luttinger-liquids [36, 42–47], Josephson junctions [48–51], bosonic [52–55] and fermionic [56–62] Hubbard models and even topological phenomena [63–76]. The above technological advances combined with the precise control of interatomic interactions with the aid of Fano-Feshbach resonances [77] lead to a new era of investigations as they allowed for the long sought after precise analog quantum simulation of condensed matter models [78–80] and further the generation and characterization of unexplored new quantum phases of matter [36, 81–86].

Out of this plethora of experimentally realizable setups we choose herein to unravel the physics of ultracold atoms involving spin degrees-of-freedom [14, 87, 88]. Understanding the physics emanating in spinor ensembles is paramount, both in terms of exploring their intrinsic phenomenology, as well as, exploiting their properties to realize novel probes for the ultracold dynamics [89–93]. On the one hand, the almost perfect isolation of ultracold atoms from environmental effects provides a simpler means to explore the effect of spin on their equilibrium properties and dynamics. On the other

INTRODUCTION

hand their well-controlled nature offers a platform for experimentally addressing the effects of theoretically proposed physical mechanisms to the dynamical and equilibrium properties of quantum matter. In this thesis we exploit the above mentioned benefits of ultracold atoms and apply them to two systems relevant for condensed matter physics. Regarding the inherent properties of spinor systems one of the most interesting topics constitutes the ferromagnetic properties of repulsive itinerant spin-1/2 Fermi gases [94–101]. In particular, the mechanism behind the emergence of ferromagnetism [102,103] in metals is conjectured to be related to the interplay of kinetic energy and interaction [104].

Since 2009, spinor degenerate Fermi gases have been used for the investigation of magnetic properties of interacting fermions. Early studies [94,96] have focussed on examining the validity of the Stoner instability [104]. The latter states that when the interaction energy of short-range repulsively interacting spin-1/2 fermions exceeds the kinetic energy contribution, the system becomes ferromagnetic in the sense that it develops a large spontaneous magnetization of the constituting spins. The concept of the Stoner instability superseded the model of Bloch ferromagnetism [105,106] relying on the long-range character of the Coulomb interaction, as it proved to be successful in identifying the common ferromagnetic metals of iron, nickel and cobalt [107]. However, even shortly after the conceptualization of this instability mechanism in 1930s, a large amount of issues regarding this description of itinerant ferromagnetism has emerged [108–112]. Nevertheless, the Stoner instability even to date is regarded as the proper way to qualitatively understand the phenomenon of metallic ferromagnetism [113,114].

The reliance of the Stoner instability on short-range interactions that naturally emerge in degenerate Fermi gas ultracold experiments, and the poorly understood intricacies it involves regarding its validity, rendered ultracold gases a promising venue for the exploration of ferromagnetism [94]. An important problem in the realization of repulsively interacting Fermi gases is that they constitute a metastable state [115–117], since for repulsive interactions the eigenspectrum of two- and three-dimensional Fermi gases features a shallow bound state [77]. Indeed, three-body recombination processes [118–121] lead to the formation of Feshbach molecules, resulting in unavoidable atom losses and reducing the lifetime of repulsive Fermi gases. Nevertheless, the Ketterle group in 2009 [94] claimed the identification of a ferromagnetic instability by identifying a maximum atom loss rate and size of the gas accompanied by a minimum kinetic energy when the interaction strength of a Fermi gas is suddenly increased (quenched) to the strong interaction regime. These observations thought to be related to a Stoner instability but importantly they lacked a direct probing of the spin-configuration of the system. In fact, later [95] it was realized that these features can be explained via a resonant enhancement of the two-body Feshbach molecule formation, which dominates the processes related to the Stoner instability for all interaction strengths. In a followup experiment [96] it was indeed found that the spin fluctuations experienced in this regime are not consistent with a ferromagnetic instability and it was verified that the formation rate of ferromagnetic domains is lower than the rate of creation of Feshbach molecules. Essentially, with this experiment [96] the results of Ref. [95]

were verified, leading to the temporary conclusion that the Stoner instability cannot be identified in ultracold atomic systems.

Research of ferromagnetic phenomena in degenerate ultracold Fermi gases has been reinvigorated, following the experiment of Ref. [97] which demonstrated that the phase separated state, where spin- \uparrow and spin- \downarrow atoms form a domain wall structure, is metastable [122]. The latter hinted that the ferromagnetic properties of ultracold Fermi gases can be identified indirectly by studying the decay dynamics of metastable states. This proposal was advanced further in recent studies involving pump-probe spectroscopy [100, 101]. These works explicated that the formation of microscopic sized ferromagnetic domains, possessing a size of the order of the interatomic separation, is faster than the molecular decay [100]. It was further suggested [101] that these ferromagnetic domains coexist with the Feshbach molecules in an inhomogeneous metastable state which can be characterized as a “quantum emulsion” of the two phases (see also [123, 124]). The claim of microscopically sized and emulsified ferromagnetic domains is supported by the selective spectroscopy of the atoms not paired in Feshbach molecules, which are found to possess properties similar to spin-polarized fermions [101]. Nevertheless, owing also to the complex character of such a possible emulsified state there is a large amount of open questions regarding the nature of the ferromagnetic properties emanating in ultracold quantum gases. The most crucial of these questions is whether the emergence of ferromagnetism can be solely attributed to the competition between the kinetic and interaction energy of fermionic spinor ensembles [113, 114], supporting then a physical mechanism in the spirit of the Stoner instability [104]. In this case, understanding, also, the role of different kinds of exchange interaction processes in the formation of ferromagnetic domains might be crucial in reconciling the Stoner framework with its numerous criticisms [108–112].

In this thesis we propose an alternative approach to tackle ferromagnetism in ultracold atom systems by invoking one-dimensional (1D) ensembles [125, 126]. One-dimensional ultracold fermions have the benefit that they do not feature a weakly bound Feshbach molecule state for effectively positive interactions [127]. As such, the repulsive Fermi gas is largely stable against three-body recombination [118–121]. In addition, it has been shown that the static properties and dynamics of 1D fermions, both in the strong (near infinite) [128–133] and weak (near zero) [134, 135] interaction regime, can be mapped to those referring to an appropriately chosen spin-chain model. The advantage of such spin-chain models is that they provide an ideal candidate for exposing the magnetic properties and microscopic mechanisms of itinerant systems. More specifically, the well-behaved nature of spin-chain models [107] allows us to perceive the intricate magnetic interactions of the itinerant systems that they approximately describe. Moreover, 1D fermions involve several intriguing unresolved questions regarding the role of the breaking of the $SU(2)$ symmetry, associated with the total spin of the Fermi gas, and the relation of magnetic properties to phase separation [130, 135–138] which we address within our studies. Particularly, our research reveals that the ferromagnetic correlations emanating in the 1D ensembles are not connected to the emergence of spin-polarization [K1] or phase separation [K2] among the

INTRODUCTION

spin-components, as proposed by the Stoner model. Instead, ferromagnetic properties emerge due to the competition of effective spin-spin interactions originating from interaction-driven [139–141] and kinetic [142] spin-exchange of the atoms respectively. Our findings motivate an altered framework for characterizing itinerant ferromagnetism, based on the interplay of ferromagnetic and antiferromagnetic spin-spin correlations, that generalizes the energetic arguments inherent in the Stoner model.

The importance of spinor atoms in ultracold setups is not exhausted by the involved dynamics and stationary properties of spinor gases. Indeed, the spin degree of freedom offered by one or several spinor impurities immersed in a more extensive atomic background allows for probing the structures and properties emanating in such composite systems. In particular, ultracold atoms enable the application of various spectroscopic techniques [143] such as injection [144], ejection [91, 116], Ramsey [145] and pump-probe [100, 101] spectroscopy, allowing for tracking a large class of observables that are otherwise difficult to measure. Spectroscopic studies provide information regarding the energy content of a quantum system both in the equilibrium case, as well as, during its dynamics. Notice that typically ultracold experiments employ absorption or fluorescence imaging [22] where such energy probes are difficult to obtain. In addition, spectroscopic tools enable the investigation of the overlap between distinct many-body states of a system [146]. Spinor impurities when combined with spectroscopic techniques provide ideal probes for the few-body or collective excitations of many-body systems, since the properties of the composite impurity-environment system can be mapped to the spin-state of the impurity [92, 147]. Therefore, understanding the properties of extensive quantum gases containing a small number of impurity atoms is a highly relevant application of spinor quantum gases and for this reason consists the second focal point of our work.

The concept of quasi-particles is a cornerstone of impurity physics. Quasi-particles refer to composite structures consisting of excitations and/or particles that collectively propagate, similarly to a new species of particle [148]. One of the first kinds of quasi-particles examined is the so-called polaron [149–152]. The original concept of a polaron emerges in condensed matter setups involving deformable crystal structures and itinerant electrons [153]. Such polarons emerge in several classes of technologically relevant materials such as polar semiconductors and ionic crystals [154], organic semiconductors [155–157] and even transition metal oxides [158, 159]. In these systems it was found that the motion of electrons leads to deformations of the crystal lattice, i.e the generation of phonons [153], giving rise to significant modifications of the conduction properties of the material [152]. In particular, the electrons in these materials are dressed by a cloud of phonons forming a quasi-particle, which is heavier and subsequently less mobile than the original electron [152], especially for strong electron-phonon couplings [151]. Besides the different effective mass compared to an electron, the polaron exhibits only partial coherence (due to the involved phononic excitations of the crystal) which is quantified by its residue/quasi-particle weight [152, 160]. Another intriguing aspect of polaron physics is the effective interactions between different polarons [161] which are mediated by their host. These interactions stem from the exchange of background ex-

citations among the different polarons and are always attractive, even though the bare particle-particle or particle-background interactions might be repulsive. The formation of two-body bound states of polarons referred to as bipolarons [162] is especially important in condensed matter setups as it has been proposed to explain phenomena such as the electric conductivity of polymers [163, 164] and the organic magnetoresistance [165]. Interestingly, a bipolaron theory for explaining the phenomenon of high-temperature superconductivity for a certain class of materials has been formulated [166–169], but to date it remains unclear whether this scenario is realizable [170, 171]. This original concept of a polaron has been generalized and extended to different setups, including for instance the small [172, 173], magnetic (or spin) [174] and the exciton polarons [175], adhering also to different disciplines of physics such as atomic [176] and even biophysics [177].

Despite the above mentioned widespread realizations of polaronic quasi-particles and the presence of several distinct classes of related theoretical models, the behavior of setups involving highly mobile impurities is far less explored [178], especially in the intermediate interaction range where the impurity is neither self-localized or weakly interacting with its environment. Ultracold settings allow the control of impurity mobility as both homonuclear [91, 144] and heteronuclear [116] atomic mixtures can be realized which, in addition, offer tunable interparticle interactions [127]. For these reasons recently there was an immense interest in realizing polarons with mixtures of ultracold atoms which probe this largely unexplored regime [179]. Moreover, except the scenario of a bosonic background (Bose polaron) [179, 180] as in the case of electron-phonon coupling, ultracold atoms also allow for a fermionic environment giving rise to the so-called Fermi polaron [117, 181]. It is worth mentioning here that the dimensionality of the background gas is also tunable by manipulating the external confinement [19, 34, 35]. To date both Bose [91, 182, 183] and Fermi [98, 116, 144, 145] polarons in three-dimensions have been realized experimentally and their equilibrium properties have been probed mainly via injection and ejection spectroscopy techniques. Additionally, there exists a realization of the Fermi polaron in two dimensions [184] and several aspects of the impurity problem in 1D have been explored both in the fermionic [185] and the bosonic case [9, 89]. These experimental advances sparked a renewed interest in theoretically describing the properties of those quasi-particles and in the development of existing and novel approaches for their study [186–189]. Importantly, the presence of polarons in an ultracold setting opens up also the possibility of dynamical studies. Indeed, the typical timescales for the dynamics of ultracold polarons lie on the ms regime [22, 23], rather than the fs timescale [107, 146] which is the characteristic one for condensed matter setups. As a result, the spatial and momentum distributions of the impurities are easily tractable experimentally.

Our work regarding polarons revolves around the study of the impurity problem in 1D by utilizing appropriate spectroscopic techniques tailored to directly capture the intricacies of these correlated systems while explicitly taking into account and thus exposing the effects caused by the existing parabolic confinement. In particular, it is well-known that 1D Fermi ensembles involve strong quantum fluctuations resulting

INTRODUCTION

to the phenomenon of the Anderson orthogonality catastrophe which occurs for any mass ratio between the impurities and their environment in the thermodynamic limit [190–192]. Indeed, it has been shown that a single impurity interacting with an 1D Fermi gas causes the macroscopic modification of the quantum state of the latter. Accordingly, the states of the Fermi-gas in the presence and absence of the impurity become orthogonal to each other as the particle number of the gas is increased or equivalently as the thermodynamic limit is approached [192]. This fact implies that the 1D Fermi polaron cannot occur in the thermodynamic limit. However, recent experiments showed that the physics in the limit of infinitely large systems can be well monitored even in the few-body regime evading such difficulties [185]. In our studies [K3] we demonstrate that impurities embedded in a few-body 1D Fermi gas accumulate polaronic properties such as a finite quasi-particle residue and well-defined interaction energy with their environment. In the case of multiple polarons, induced interactions acting among them are mediated by the excitation of their fermionic host. Quite remarkably, even in the case of strong repulsive impurity-bath interactions the 1D Fermi polaron appears to be long lived despite the predicted impossibility of its existence.

For Bose gases the situation is even more complicated. In the thermodynamic limit, the Anderson orthogonality catastrophe is even more severe as any microscopic deformation of the order parameter $\sim P$ of the BEC corresponds to a large reduction of the many-body overlap $\sim (1-P)^{N_c}$, where N_c is the number of condensed atoms. This is extremely relevant for the study of Bose polarons since non-perturbative mechanisms that modify the order parameter of an ultracold BEC are well-documented in the literature. First, it is known that a moving potential within a BEC can induce non-linear excitations [193–195] such as solitons [196–200] when the velocity that it traverses the Bose gas exceeds a critical one thus violating the Landau criterion for superfluidity [201]. In addition, phase separation is a prominent feature in binary ultracold bosonic mixtures [202–206]. In particular, relying on energetic arguments it can be proven that if the interspecies interactions exceed a threshold value set by the intraspecies ones, the miscible state of the two components is no-longer stable [207]. The dynamics during the manifestation of such an instability have been studied [208–210] demonstrating the pronounced deformation of the order parameters of the Bose gases which form filament-like structures in order to minimize the spatial overlap among the two species. Last but not least, a feature that is not considered within the condensed matter polaron models are the additional forces resulting from the density gradients of the environment to the impurity which inevitably occur when a parabolic confinement is employed [211, 212]. Indeed, one of our key findings is that the impurities in confined systems experience a total potential that is the sum of the external harmonic potential and an additional potential barrier stemming from their interactions with the density of the bath that crucially affects their properties [K4–K6]. The above lead to the emergence of intriguing phenomena such as the temporal orthogonality catastrophe [K4, K5] of Bose polarons, that signifies the breakdown of the polaron picture. This process occurs for strong impurity-bath interactions where the rapid expansion of the impurity density results in

the excitation of its host. Due to this process the Bose polaron becomes short lived [K6] and after its decay the system tends to an eigenstate thermalized state [213–216]. Our findings showcase the ability of time-resolved spectroscopic techniques to identify elusive features of the polaron physics, such as the induced polaron-polaron interactions [K5], and motivate the importance of excitation pathways associated for instance with the non-linear dynamics of BEC [196–200] for the adequate characterization of the Bose polaron.

Objectives of this thesis

In this thesis we aim to demonstrate that the *ab initio* study of the correlated dynamics of spinor systems provides valuable insights into the dynamics of correlated ultracold vapors. In particular, our objective is twofold. First the dynamics of spin-1/2 fermions is studied in order to obtain a deeper understanding of the magnetic mechanisms that emanate in these systems. Namely, we initialize the system into a state that is supposedly stable for sufficiently large repulsions within the framework of Stoner instability [104] and address the dynamical stability properties of this state embedded in a quantum environment. By tracking observables related to the magnetization and the spin-spin correlations of the system we are able to provide insights into

- Whether the standard framework of Stoner instability is adequate to describe the magnetic properties of spin-1/2 fermions in 1D.
- Whether novel spin-chain models applicable for weakly interacting systems are able to capture the decay dynamics of the initial state.
- Extend such models to capture the dynamics within the intermediate interaction regime and characterize the emerging magnetic order.

To achieve the above we further

- Analyze the constituting ingredients of such models and compare to accurate fully correlated calculations in order to extract the underlying magnetic mechanisms.
- Expose the involved magnetic mechanisms, and exhaustively characterize the many-body state of the spinor system, as well as, find their imprint on experimentally addressable quantities.
- Clarify the relation of phase separation and ferromagnetism which are inherently related in the Stoner model picture.

The analysis regarding the Bose and Fermi polarons by employing injection, Ramsey and pump-probe spectroscopy also proves quite fruitful [K3–K6]. In these works, we simulate different spectroscopic sequences to realize polaron states. The main observable employed in these works is the spectroscopic signal for different environment-impurity interaction strengths and different pump (dark) times for injection (Ramsey

INTRODUCTION

and pump-probe) spectroscopy. This choice facilitates a direct comparison with a corresponding experiment and demonstrates the direct access on the quasi-particle properties obtained within the ultracold environment. Our key findings are summarized below.

- We unravel the spectrum of Fermi and Bose polarons in the case of one or multiple quasiparticles.
- We identify the emergence of additional spectral features emerging due to the distinct excitation pathways of polaronic states and the involved two-impurity mechanisms.
- The Ramsey spectroscopy of Bose polarons reveals the phenomenon of “Temporal orthogonality catastrophe” associated with the fact that the many-body state of the impurities rapidly becomes almost orthogonal to the non-interacting one. During this sequence the contrast of the Ramsey spectrum tends to a zero value even for small dark times.
- By means of pump-probe spectroscopy, we characterize the energy redistribution occurring in the system during the temporal orthogonality catastrophe.
- We unveil spectral evidences for the tendency of the bath impurity system to reach an emergent eigenstate-thermalized state after the manifestation of a temporal orthogonality catastrophe.

Chapter 2

Theoretical Framework

2.1 Spinor and Pseudospinor condensates

2.1.1 Internal states of atomic systems and ultracold experiments

A. Atomic internal states and their scattering properties

Ultracold atoms constitute one of the most advantageous platforms for studying multi-component quantum fluids [217, 218]. Before commencing our presentation of the particular setups and physical phenomena addressed within this thesis it is instructive to present some basic features of ultracold multi-component ensembles and briefly review some of their history while exposing also their extraordinary level of control and tunability [37]. The first step in realizing a multi-component fluid is to identify which distinct components can be employed. Atoms possess a variety of different internal states [219, 220] that are experimentally addressable and accordingly mixtures of the latter can be utilized to realize a multi-component gas [11–14, 22]. However, most of these internal states are inherently unstable [219] and the thermal equilibration of the atomic motion during their lifetime is impossible. Naturally, this fact precludes their use in ultracold experiments. Notable examples constitute the low-lying electronically excited states. These possess a dipole allowed transition to the ground state leading to a fast spontaneous decay at a ns timescale [219]. Nevertheless, particular electronically excited states are relevant for ultracold applications. For instance, ^{174}Yb experiments have successfully produced relatively stable bosonic gases utilizing the metastable $(6s6p)^3P_2$ state [10] and even heteronuclear mixtures of Li and Yb including this electronically excited atomic species [15, 16]. In addition, ultracold atom experiments utilizing highly excited Rydberg states [221] embedded in a Bose gas of neutral atoms, are nowadays feasible [222]. Here a particularly striking example constitutes the realization of the Rydberg polaron [223, 224].

Within this thesis we are mostly concerned with the application of the different hyperfine states of the ground state manifold $^2S_{1/2}$ of alkali atoms as the individual components of our setup. The above mentioned hyperfine states possess an exceptionally large radiative lifetime (as far as isolated atoms are concerned) [219] which can

be neglected. In practice, their lifetime is limited by inelastic processes which involve two [19], three [118–121] or more [225, 226] colliding atoms. The kinetic energy of the reactants is altered due to the change of the particles’ internal states (hyperfine relaxation) [19] and/or due to the formation of diatomic molecules [77]. There are several known cases of individual hyperfine states and mixtures thereof that are relatively robust against two-body hyperfine relaxation collisions [14]. Examples consist the different m_F states of the $F = 1$ [17] and $F = 2$ [18] manifolds of ^{87}Rb . However, there are important counterexamples where the collisional relaxation is particularly pronounced. These include the $F = 2$ states of ^{23}Na [19] and the $F = 3$ [227] and $F = 4$ [228] states¹ of ^{133}Cs [230, 231]. Moreover, the molecule formation due to three-body collisions [118–121] is in general a rather slow process for the small atomic densities $\sim 10^{14} \text{ cm}^{-3}$ of ultracold atomic ensembles. However, there exist cases where such processes have made the experimental realization of particular setups challenging. A relevant example is the Bose-Einstein condensation of a ^{133}Cs in its absolute ground state, $F = 3$, $m_F = 3$ [232, 233]. Four [225, 226] or more body collision processes are even less relevant than three-body ones due to the low atomic densities and are almost always neglected². To date there is a plethora of multi-component mixtures of hyperfine states referring to atomic species having either bosonic [11, 17–19] or fermionic [20, 21] character and exhibiting large lifetimes with a negligible rate of inelastic processes. Except for those cases, heteronuclear mixtures involving distinct atomic species are possible [6, 8, 9], allowing among others for the experimental realization mixtures of atoms with different particle exchange statistics [3–5, 7, 10].

B. Trapping mechanisms

Another obstacle for experiments with multi-component and particularly spinor gases has been the underlying trapping mechanisms [22]. Spinor gases refer to n -component systems whose interactions possess an $\text{SU}(2)$ invariance so that they are formally equivalent to a gas of spin- $(2n+1)/2$ particles [22]. Originally, ultracold experiments utilized magnetic traps based on the Zeeman effect of the atoms within an inhomogeneous magnetic field. This trapping mechanism, however, introduces several hurdles for realizing spinor setups. First, not all hyperfine states can be trapped in magnetic traps. Indeed, creating a local maximum of magnetic field in a region where current is absent is impossible [237, 238]. As a consequence, only states that are low-field seekers, i.e. are attracted to magnetic field minimums can be trapped. This fact already precludes the realization of the simplest form of a spinor gas consisting of all the hyperfine states of a particular F manifold since the states with $m_f \geq 0$ are not low-field seekers. Additional detrimental factors arise from the different magnetic moment of the distinct hyperfine

¹Within these manifolds there are specific states that can be stabilized against collisional hyperfine relaxation provided that no other hyperfine state with the same value of F is occupied. These are the absolute ground state $F = 3$, $m_F = 3$ of ^{133}Cs [229] and the doubly polarized (stretched) state $F = 2$, $m_F = 2$ of ^{23}Na [19].

²A notable exception regards the study of Efimov physics [234–236], where four-body collision events are relevant

states resulting to unavoidable hyperfine state-dependent confinement potentials [22]. Notice also that atoms moving within a magnetic trap subjected to a time-dependent magnetic field in their frame of reference even if the latter is a stationary field in the lab frame. The magnetic field can, therefore, induce transitions between distinct hyperfine states that might not be able to be confined, leading to the decrease of the lifetime of the gas. All of these problems were overcome by the development of optical tweezers (at the era of early experiments they used to be referred to as far-off-resonant traps or FORT) [14, 17, 127] for the confinement of neutral polarizable atoms. An optical tweezer counteracts all the above-described drawbacks as it can be tuned to produce a confining potential that is equal to all hyperfine states. Optical traps similarly to magnetic traps also decrease the lifetime of the trapped atoms as the latter can scatter with the photons of the confining laser resulting to their heating [127]. However the rate of these scattering events can be substantially reduced via appropriately tuning the frequency of the applied radiation [219].

An additional benefit of the optical trapping is that it profoundly increases the tunability of atomic systems. In particular, optical tweezers allow for the realization of a variety of potentials by modulating the beam parameters or simply adding more laser fields [37]. In particular lattice structures [37], multi-well potentials [97, 239] and even rectangular box-like potentials [29–32] can be created with relative ease and these potentials can selectively be either hyperfine-state dependent [240–245] or not [14, 22] according to the experimental needs. Furthermore, even in the case of approximately harmonic confinement the shape of the trap can be either spherical, pancake-like or elongated along one spatial directions [33–35], allowing for the study of three-, two- and 1D systems respectively. Notice that this is not the case for magnetic traps where the potential is fixed by the geometry of the involved coils without a large room for variation [22]. A remarkable advantage of optical traps is that removing the need for magnetic confinement they allow for the use of magnetic and radio-frequency fields for the manipulation of the atomic states. Indeed, the Zeeman shift possesses important applications other than the confinement of atoms. For instance, the magnetic field can be utilized to manipulate the rates of spin-exchanging elastic collisions [246], for inducing hyperfine-state-dependent potentials [240–245] and for tuning the energy gaps between the involved hyperfine states [219, 247]. The latter except for the rather obvious application of enabling hyperfine-state selective coupling schemes via optical or radiofrequency fields also plays a crucial role for the control of interatomic interactions [21, 77, 248–250].

C. Interatomic interactions in ultracold ensembles

The control of interatomic interactions is a remarkable feature of ultracold atom experiments [21, 77, 248–250], as it renders them exceptional examples of quantum simulators [78–80]. Elastic collisions between neutral atoms yield two-body interactions of extremely short-range when compared to the confinement length scale of typical traps allowing them to be well-approximated as zero-range *s*-wave collisions [77]. Zero-range interactions constitute a common approximation employed in different fields of

THEORETICAL FRAMEWORK

theoretical physics [104] and therefore a setup that inherently features them is highly desirable. In particular considering the low kinetic energy of ultracold atoms their s -wave interactions for given hyperfine states are completely characterized by only one parameter, namely the scattering length [77]. Ultracold atom ensembles enable for the control of these scattering lengths via processes such as Fano-Feshbach resonances [15,21,77,90,251]. Fano-Feshbach resonances occur when the energy of a bound (molecular) state of a closed collision channel³ lies in the vicinity of the collision threshold of the entrance channel⁴. In this case even a small coupling among the involved hyperfine-states referring to the closed and entrance channels results in a sizable shift of the scattering length of their interactions [77]. Provided that the molecular state possesses a different magnetic moment than the atoms in the entrance channel its energy with respect to the threshold can be tuned via the Zeeman effect. This leads to the control of the scattering length of atoms via a magnetically-tuned Fano-Feshbach resonance. In systems with reduced dimension (i.e. referring effectively to one- or two- spatial dimensions) the interatomic interactions can also be tuned by modulating the confinement along the strongly confined direction [77, 248–250, 252–256]. In this case a two particle bound state referring to an excited state along the strongly confined axis (axes) can be tuned to resonance with the threshold of colliding particles referring to the ground state of strong confinement. This gives rise to the so-called Confinement induced resonance. It is noteworthy that these resonant effects are able to tune the scattering length over all values of both positive and negative scattering lengths [77, 248].

Let us also mention in passing that different kind of interactions are also implementable in ultracold gases. A large class of atoms have quite pronounced magnetic dipole-dipole interactions [257, 258], that cannot be properly accounted by zero-range scattering models, requiring their treatment as long-ranged ones. In addition, Fano-Feshbach resonances of higher partial waves such as p -wave ones [256, 259, 260] can be invoked although these typically suffer from large two- and three-body inelastic collision rates [261]. Finally, composite systems of ions embedded in a gas of neutral atoms have been realized which exhibit charge-induced electric dipole interactions [86, 262, 263]. Nevertheless, neutral atom ensembles possessing tunable s -wave interactions remain the workhorse of ultracold atom experiments and constitute our focus within this thesis. The remainder of this chapter deals with the basic properties of the optical trapping technique [14, 17, 127] that as mentioned above spearheaded the experiments of spinor and multi-component systems. Subsequently we provide the derivation of the effective 1D Hamiltonians employed within our studies [K1–K6] from the corresponding experimentally implementable three-dimensional ones.

³A closed channel refers to the energetically prohibited scattering process. In particular, it is characterized by the transition of the scattering atoms to different hyperfine-states as a result of their collision with their final total energy being larger than the initial one.

⁴The threshold energy of a scattering channel refers to the energy of the particles in the appropriate hyperfine states when they are found at an infinite separation.

2.1.2 Optical Trapping

The use of optical tweezers is a technique to confine neutral polarizable particles of size much smaller than the wavelength of optical electromagnetic fields [127, 264, 265]. Accordingly, this technique is not limited to atomic ensembles but it has found applications in the confinement of larger particles such as molecules [266, 267] or even μm -sized particles [268, 269]. The working principle of optical tweezers relies on the interaction of induced electric dipoles with an inhomogeneous classical electromagnetic field [219]. The Lorentz force exerted by an electromagnetic field to an electric dipole reads

$$\mathbf{F}_L = (\mathbf{d} \cdot \nabla) \mathbf{E} + \frac{d\mathbf{d}}{dt} \times \mathbf{B}, \quad (2.1)$$

where \mathbf{d} is the dipole moment of the particle and \mathbf{E} , \mathbf{B} denote the electric and magnetic fields. To proceed we further assume that the field interacts weakly enough with the polarizable particles so that their induced dipole moment can be expressed in the linear response approximation as $\mathbf{d}(t) = \text{Re}[\alpha(\omega)\mathbf{E}(t)]$. Here, $\alpha(\omega)$ is the polarizability of the medium. The polarizability, $\alpha(\omega)$, is dependent on the frequency of the applied electromagnetic field and possesses complex values accounting for the phase difference between the applied electromagnetic field and the induced dipole moment. By using the above mentioned assumption the force exerted to a polarizable particle reads

$$\mathbf{F}_L = \underbrace{\frac{1}{2} \nabla [\alpha(\omega) E^2]}_{\equiv \mathbf{F}_d} + \underbrace{\frac{\alpha(\omega)}{\varepsilon_0} \frac{d\mathbf{p}_{\text{em}}}{dt}}_{\equiv \mathbf{F}_{\text{sc}}}, \quad (2.2)$$

where $\mathbf{p}_{\text{em}} = \varepsilon_0 \mathbf{E} \times \mathbf{B}$ is the momentum density of the electromagnetic field and ε_0 is the vacuum electric permeability. The first term in Eq. (2.2) indicates that the electric-field acts as a time-dependent potential for the polarizable particles, while the second term indicates that additional forces stem from the variation of the momentum of the electromagnetic field in time. Let us now assume that the intensity of the external electromagnetic field is constant in time. Then the only variation in \mathbf{p}_{em} stems from the dipole radiation emitted by the confined particles due to its fluctuating dipole moment $\mathbf{d}(t)$. The emitted dipole radiation possesses a frequency equal to the oscillation frequency of the induced dipole moment and the confining electromagnetic field which due to the optical nature of the latter is of the order of several hundreds of THz [219]. Since massive particles such as atoms, molecules or nanodroplets are employed they are not able to follow this rapidly fluctuating force and as a consequence $\langle\langle \mathbf{F}_{\text{sc}} \rangle\rangle = \mathbf{0}$ for the relevant timescales of their motion [127]. Here $\langle\langle \rangle\rangle$ indicates the time-averaging over the rapid frequency of the electromagnetic field. Due to the vanishing contribution of $\langle\langle \mathbf{F}_{\text{sc}} \rangle\rangle$ the Lorentz force can be regarded as conservative, namely $\langle\langle \mathbf{F}_d \rangle\rangle = -\nabla U_d$ where the dipole potential reads

$$U_d(\mathbf{r}) = \langle\langle -\frac{1}{2} \alpha(\omega) E^2 \rangle\rangle = -\frac{\text{Re}[\alpha(\omega)]}{2\varepsilon_0 c} I(\mathbf{r}). \quad (2.3)$$

In the above expression the definition of the intensity $I(\mathbf{r}) = \varepsilon_0 c E_0^2(\mathbf{r})/2$ is employed, where E_0 is the amplitude of the electric field. Notice that \mathbf{F}_d produces work during

THEORETICAL FRAMEWORK

each particular oscillation of the electromagnetic field resulting in an increase of the energy of the particles. Assuming a thermal equilibrium state between the particles and the tweezer this energy has to be expelled by the emission of dipole radiation [127]. The corresponding scattering rate refers to the fraction of the average power produced by \mathbf{F}_d over the energy of a single trap photon reading

$$\Gamma_{\text{sc}}(\mathbf{r}) = \frac{1}{\hbar\omega} \left\langle \left\langle \frac{d}{dt} \left(\frac{1}{2} \alpha(\omega) E^2 \right) \right\rangle \right\rangle = \frac{\text{Im}[\alpha(\omega)]}{\hbar\epsilon_0 c} I(\mathbf{r}). \quad (2.4)$$

Atom-photon scattering is an undesirable effect since such a process imparts momentum to the scattered atoms leading to their heating. The resulting heating power is proportional to the recoil energy $E_R = (\hbar\omega)^2/(2mc^2)$, where m refers to the particle mass, and the scattering rate Γ_{sc} . The recoil energy E_R is the characteristic energy scale of photon-particle collisions referring to a value of $h \times \text{kHz}$ and being of the same order of magnitude as the achievable trap depths [127] stemming from Eq. (2.3). Therefore, there is a tradeoff between the realizable strength of the dipole potential U_d and the heating rate stemming from Γ_{sc} , which fundamentally depends on the polarization properties of the particles, $\alpha(\omega)$, a fact that we will briefly sketch below for Alkali atoms.

For a monochromatic source, such as an optical laser, the electric field is expressed as $\mathbf{E} = \text{Re}[\mathbf{E}_0(\mathbf{r})e^{i(\mathbf{k}\cdot\mathbf{r}+\omega t)}]$ and therefore the induced dipole moment reads

$$\mathbf{d}(t) = \mathbf{E}_0(\mathbf{R}) \{ \text{Re}[\alpha(\omega)] \cos(\omega t + \mathbf{k} \cdot \mathbf{R}) + \text{Im}[\alpha(\omega)] \sin(\omega t + \mathbf{k} \cdot \mathbf{R}) \}, \quad (2.5)$$

where \mathbf{R} is the center of mass position of the atom. Equation (2.5) allows us to gain insight into the interplay of the optical dipole potential amplitude U_d and the photon scattering rate Γ_{sc} . In particular, the optical potential is proportional to the amplitude of the in-phase dipole moment oscillations with respect to the electric field. Similarly the trap scattering rate is proportional to the corresponding out-of-phase oscillations. Lorentz has shown (strikingly enough before the advent of quantum theory) that the dipole moment oscillations of atoms can be approximated by a classical model of driven and damped oscillators [219]. Each oscillator corresponds to a distinct dipole allowed transition, with the frequency $\omega_{0,j}$ being given by the energy difference of the involved states, $|\Psi_0\rangle$ and $|\Psi_j\rangle$, possessing a value in the range of several hundreds of THz. The damping rate is given by the decay rate $\gamma_j/2$ of the excited state (or equivalently the natural linewidth of the transition) referring to several MHz. Finally, the driving amplitude for each transition is scaled via the oscillator amplitude, $\mathbf{f}_j = 2m\omega_{0,j}/(e\hbar)|\langle\Psi_j|\hat{\mathbf{d}}|\Psi_0\rangle|^2$, where $\langle\Psi_j|\hat{\mathbf{d}}|\Psi_0\rangle$ is the related dipole matrix element. Notice that $|\mathbf{f}_j| \sim 0.1 - 1$. This mapping to a classical oscillator model yields a dipole moment [219]

$$\mathbf{d}(t) = \text{Re} \left[\underbrace{\left(\sum_j \mathbf{f}_j \frac{e^2/m}{(\omega_{0,j}^2 - \omega^2) + i\gamma_j\omega} \right)}_{\equiv \alpha(\omega)} \cdot \mathbf{E}(t) \right], \quad (2.6)$$

while typically different dipole allowed transitions are separated by several THz, allowing each term in $\alpha(\omega)$ to be treated individually. Eq. (2.6) allows for the identification of three regimes of different behaviour. Focusing on a single transition, $|\Psi_0\rangle \leftrightarrow |\Psi_j\rangle$, the first refers to the large negative detuning regime i.e. $\omega - \omega_{0,j} \ll \gamma_j$ where the oscillations of the dipole moment are in-phase with the electric field and $\alpha(\omega) \approx \text{Re}[\alpha(\omega)] > 0$. The second regime corresponds to small detunings $\omega - \omega_{0,j} \approx \gamma_j$, where the dipole moment oscillations are out-of-phase with respect to the electric-field $\alpha(\omega) \approx \text{Im}[\alpha(\omega)]$. Finally, for large positive detunings in-phase oscillations are exhibited, however, the direction of the exhibited polarization is inverted with respect to the electric field, $\alpha(\omega) \approx \text{Re}[\alpha(\omega)] < 0$. The above imply that the regimes of large negative or positive detuning are the optimal ones for trapping atomic ensembles as within them the scattering rate $\Gamma_{\text{sc}} \propto \text{Im}[\alpha(\omega)]$ is minimized and therefore the system remains coherent for longer times [127]. Furthermore, this model reveals that red detuned laser beams create attractive potentials for the atoms while blue-detuned potentials result in repulsive potentials, see also Eq. (2.3). Notice that the above mentioned model is only valid in the regime of linear response, which implies that the intensity of the electromagnetic field is well below a frequency dependent threshold where saturation effects occur. In practice, this limitation is not constraining since as mentioned above large detunings are desirable, where such non-linear effects are heavily suppressed even for relatively strong lasers [127].

As it is evident from above, the confining potential of optical tweezers is determined by the electronic properties of atomic systems which are hardly affected by the specifics of the atomic hyperfine structure, especially when the far-detuned regime is considered [219]. In particular, it can be shown that for linearly polarized light the trapping potential experienced by all hyperfine states is equivalent [240, 245]. This allows for freely manipulating the spin of the atoms by addressing magnetic dipole transitions using radiofrequency and static magnetic fields without affecting their optically controlled confinement. The latter allows for the realization of Fano-Feshbach resonances [15, 21, 77, 90, 251] and the study of the magnetic properties of spinor and pseudospinor systems [14, 87, 88].

Recently, there is also an interest in circularly polarized optical tweezers which allow for the realization of hyperfine state dependent potentials [270, 271]. Recall that for alkali atoms the two energetically lowest dipole allowed transitions constitute the $n \ ^2S_{1/2} \leftrightarrow (n+1) \ ^2P_{1/2}$ and $n \ ^2S_{1/2} \leftrightarrow (n+1) \ ^2P_{3/2}$ ones that are referred to as D₁ and D₂ lines. By assuming an unresolved hyperfine structure for the excited state (a reasonable approximation for $|\omega - \omega_0| \gg \Gamma$) and linear Zeeman splitting among the different $|F, m_F\rangle$ states of $n \ ^2S_{1/2}$ a circularly polarized tweezer results in the hyperfine state dependent optical potential [127]

$$U_d(\mathbf{r}) = \frac{\pi c^2 \bar{\Gamma}}{2\bar{\omega}_0^3} \left(\frac{1 - s g_F m_F}{\omega - \omega_{0,D1}} + \frac{2 + s g_F m_F}{\omega - \omega_{0,D2}} \right) I(\mathbf{r}), \quad (2.7)$$

where $s = +1, -1$ indicates the chirality of the circularly polarized light, $\omega_{0,D1}, \omega_{0,D2}$, $\bar{\omega}_0 = (\omega_{0,D1} + \omega_{0,D2})/2$ refer to the resonance frequency of the D₁, D₂ lines and their

average respectively, $\bar{\Gamma} = (\Gamma_{D_1} + \Gamma_{D_2})/2$ is the average decay rate of the excited P states and g_F corresponds to the Landé factor. The behaviour of $U_d(\mathbf{r})$ is quite intriguing when the optical tweezer frequency lies in between the D_1 and D_2 lines, $\omega_{0,D_1} < \omega < \omega_{0,D_2}$. In this case the potential created by the D_1 line is repulsive (blue-detuned) while the corresponding one from the D_2 line is attractive (red-detuned). Then, the frequency of the confining laser can be tuned such that the contributions from the D_1 and D_2 lines cancel for a particular hyperfine $|F, m_F\rangle$ state which is accordingly unaffected by the optical tweezer [240,245]. This frequency is referred to as the tuneout frequency [242,244] and has found applications in recent optical lattice experiments to generate hyperfine-state dependent potentials [241,243].

2.1.3 Dimensional Reduction of 3D Hamiltonians

A. 1D spin-1/2 fermions

Suppose an ensemble of confined ultracold fermions in two different hyperfine states, denoted as \uparrow and \downarrow , thus constituting a pseudospin-1/2 system. Here, we will assume that the confinement is time-independent and that this ensemble is influenced by a possibly time-dependent field that couples the hyperfine states.

The *ab initio* Hamiltonian describing such a system consists of three parts $\hat{H} = \hat{H}_0 + \hat{H}_{SD} + \hat{H}_I$. The spin-independent contribution \hat{H}_0 up to an overall shift in energy reads

$$\hat{H}_0 = \int d^3r \sum_{\alpha \in \{\uparrow, \downarrow\}} \hat{\psi}_\alpha^\dagger(\mathbf{r}) \left(-\frac{\hbar^2}{2m} \nabla^2 + V_0(\mathbf{r}) \sigma_{\alpha\alpha}^z \right) \hat{\psi}_\alpha(\mathbf{r}), \quad (2.8)$$

where m is the mass of the atomic species and $\hat{\psi}_\alpha(\mathbf{r})$ corresponds to the spin- $\alpha \in \{\uparrow, \downarrow\}$ fermionic field operator, satisfying the appropriate anticommutation relations [107,146]. Namely, $\{\hat{\psi}_\alpha(\mathbf{r}), \hat{\psi}_{\alpha'}^\dagger(\mathbf{r}')\} = \delta_{\alpha\alpha'} \delta(\mathbf{r} - \mathbf{r}')$, $\{\hat{\psi}_\alpha(\mathbf{r}), \hat{\psi}_{\alpha'}(\mathbf{r}')\} = 0$ with $\sigma_{\alpha\alpha'}^z = (\delta_{\alpha\uparrow} - \delta_{\alpha\downarrow}) \delta_{\alpha\alpha'}$ being the spin- z Pauli matrix. $V_0(\mathbf{r})$ refers to the spin independent part of the confining potential. Such spin-independent confining potentials can be generated with the use of an optical dipole trap as discussed in Sec. 2.1.2. Usually, in this case the atomic ensemble occupies only the energetically lowest levels of the potential $V_0(\mathbf{r})$ and the approximation of harmonic confinement can be employed,

$$V_0^{\text{eff}}(\mathbf{r}) \approx V_0^{\text{eff}}(\mathbf{r}_0) + \frac{1}{2} \sum_{i,j=1}^3 \left. \frac{\partial^2 V_0}{\partial r_i \partial r_j} \right|_{\mathbf{r}=\mathbf{r}_0} (r_i - r_{i;0})(r_j - r_{j;0}). \quad (2.9)$$

Here $\mathbf{r}_0 = (r_{1;0}, r_{2;0}, r_{3;0})$ corresponds to the position of the global minimum of the *ab initio* potential, $V_0(\mathbf{r})$. For most experiments involving optical tweezers the approximate potential of Eq. (2.9) characterizes the system sufficiently well. However, it is noteworthy that many ultracold atom experiments utilize a non-parabolic potential (see e.g. [25–32]). For instance, in the case of optical lattice experiments a periodic potential is realized by employing retro-reflected optical dipole traps [37], where the precise form of the confining potential is important for the accurate description of the system.

The coupling of the hyperfine states by an electric or a magnetic field is also possible and it introduces a spin-dependent part in the Hamiltonian, namely

$$\hat{H}_{\text{SD}} = \int d^3r \sum_{\alpha, \beta \in \{\uparrow, \downarrow\}} \hat{\psi}_\alpha^\dagger(\mathbf{r}) \left[V_x(\mathbf{r}; t) \sigma_{\alpha\beta}^x + V_y(\mathbf{r}; t) \sigma_{\alpha\beta}^y + \left(V_z(\mathbf{r}; t) + \frac{B_{\text{eff}}}{2} \right) \sigma_{\alpha\beta}^z \right] \hat{\psi}_\beta(\mathbf{r}), \quad (2.10)$$

where $\sigma_{\alpha\beta}^i$, with $i \in \{x, y, z\}$ correspond to the Pauli matrices. $V_x(\mathbf{r}; t)$ refer to the components of the spin-dependent potential, which can also possess complex values. B_{eff} corresponds to the energy difference (Zeeman splitting) of the two hyperfine levels, generated by the application of a magnetic field along the z -axis [219]. Spin-dependent potentials can be created by the usage of magnetic fields if the magnetic moments of the hyperfine states \uparrow and \downarrow are sufficiently different [125] or by employing optical fields that yields a state dependent AC Stark shift [270, 271] (see also 2.1.2). Note, also, here that only two hyperfine levels are involved and consequently effects such as the quadratic Zeeman shift [219] only result to a non-linear dependence of the Zeeman splitting, B_{eff} , on the amplitude of the applied magnetic field.

Typically, the atomic interactions between different hyperfine states are short-ranged [77] and accordingly due to the Pauli exclusion principle we can neglect the interactions of the fermions in the same hyperfine state, since it holds that $\lim_{\mathbf{r} \rightarrow \mathbf{r}'} \hat{\psi}_\alpha^\dagger(\mathbf{r}) \hat{\psi}_\alpha^\dagger(\mathbf{r}') = \lim_{\mathbf{r} \rightarrow \mathbf{r}'} \hat{\psi}_\alpha(\mathbf{r}) \hat{\psi}_\alpha(\mathbf{r}') = 0$ for $\alpha \in \{\uparrow, \downarrow\}$. In this case the interaction term takes the form

$$\hat{H}_{\text{I}} = \int d^3r d^3r' \hat{\psi}_\uparrow^\dagger(\mathbf{r}) \hat{\psi}_\downarrow^\dagger(\mathbf{r}') U(\mathbf{r}, \mathbf{r}') \hat{\psi}_\downarrow(\mathbf{r}') \hat{\psi}_\uparrow(\mathbf{r}), \quad (2.11)$$

where $U(\mathbf{r}, \mathbf{r}')$ is the atomic scattering potential for the two involved hyperfine states. Due to the low-collisional energy exhibited in ultracold atoms we can safely neglect the p -wave or higher partial wave interactions [22, 23]. Within this limit, the s -wave scattering of the atoms can be characterized by a single parameter a_s being the s -wave scattering length. By taking also into account that the range of atomic interactions is much smaller than the length scale of the confinement we can replace $U(\mathbf{r}, \mathbf{r}')$ by a short-ranged pseudo-potential. Conventionally the zero-range regularized Dirac δ pseudo-potential is employed [77, 272]

$$U_{\text{p}}(\mathbf{r}, \mathbf{r}') = \frac{4\pi\hbar^2 a_s}{m} \delta(\mathbf{r} - \mathbf{r}') \frac{\partial}{\partial |\mathbf{r} - \mathbf{r}'|} (|\mathbf{r} - \mathbf{r}'| \bullet), \quad (2.12)$$

where the symbol \bullet indicates that the differentiation occurs after the multiplication of the wavefunction by the factor in the parentheses. The scattering length a_s can be tuned by employing a Fano-Feshbach resonance [15, 21, 77, 90, 251] between the two hyperfine levels. A well-known example of such a resonance is exhibited between the hyperfine states $|F = \frac{1}{2}, m_F = -\frac{1}{2}\rangle$ and $|F = \frac{1}{2}, m_F = \frac{1}{2}\rangle$ of ${}^6\text{Li}$ atoms for a magnetic field of 800G [90]. Note also that herein we employ an energy independent a_s an assumption that does not hold close to a narrow Fano-Feshbach resonance even on the ultracold regime due to finite effective-range corrections [77]. For our scope the choice of an energy independent a_s is reasonable as we either restrict ourselves to the case of

THEORETICAL FRAMEWORK

broad Fano-Feshbach resonances [K1, K2] or because the finite effective-range effects are negligible for the densities employed within our few-body setups [K3].

Before proceeding, it is helpful to elaborate on the spin-symmetries emanating in the system. First note that \hat{H}_0 and \hat{H}_I commute with the spin operators \hat{S}_z , $\hat{S}_\pm = \hat{S}_x \pm i\hat{S}_y$ and consequently also commute with the total spin operator $\hat{S}^2 = \hat{S}_+ \hat{S}_- + \hat{S}_z(\hat{S}_z - 1)$, where

$$\hat{S}_i = \frac{\hbar}{2} \int d^3r \sum_{\alpha, \beta = \{\uparrow, \downarrow\}} \hat{\psi}_\alpha^\dagger(\mathbf{r}) \sigma_{\alpha\beta}^i \hat{\psi}_\beta(\mathbf{r}), \quad (2.13)$$

with $i \in \{x, y, z\}$. The above imply that both \hat{H}_0 and \hat{H}_I are invariant under spin-rotations and hence the spin and spatial directions are not coupled. Indeed, as long as the terms of \hat{H}_{SD} are properly transformed the spin and spatial directions can be rotated independently from one another. Therefore, in the following while the same symbols $\{x, y, z\}$ will be used to denote both the spatial and the spin directions, they have to be understood as two independent frames or reference. Note here that the above are a consequence of the SU(2) invariance of the Hamiltonian terms Eq. (2.8) and (2.11) and consequently hold exclusively for spin-1/2 fermions and not to the bosonic pseudospinor case that is discussed later on.

The focus of this thesis is the study of the dynamics of 1D ensembles. In order to effectively reduce the dimensionality of the experimentally realizable 3D systems a strong confinement along the two transversal spatial directions has to be employed [22, 23, 273]. Such a confinement usually involves a tight parabolic trap along the two perpendicular directions,

$$V_0(\mathbf{r}) = V_{1D}(x) + \frac{1}{2}m\omega_\perp^2(y^2 + z^2), \quad (2.14)$$

where the x -axis has been selected as the direction of weak confinement without any loss of generality (see also the comments above). The frequency of the transverse confinement ω_\perp has to be selected such that the excited states of the harmonic trap along the y and z directions are not occupied. If that is the case, the 3D field operators can be expressed in terms of 1D ones as follows

$$\hat{\psi}_\alpha^\dagger(\mathbf{r}) = \sqrt{\frac{m\omega_\perp}{\pi\hbar}} e^{-\frac{m\omega_\perp}{2\hbar}(y^2+z^2)} \hat{\psi}_\alpha^\dagger(x). \quad (2.15)$$

Note here that the above condition is more difficult to be satisfied in the case of fermions rather than bosons due to the Pauli exclusion principle. Indeed, due to the fact that no two fermions with the same spin can occupy the same motional state of the potential $V_0(\mathbf{r})$, Eq. (2.15) only holds for $\omega_\perp \gg E_N/\hbar$. Here, E_N refers to the N -th energetically lowest single-particle eigenenergy (SPEE) of $V_{1D}(x)$ with N being the total number of particles.

By employing Eq. (2.15) the terms \hat{H}_0 and \hat{H}_{SD} of the 3D Hamiltonian can be reduced to 1D effective Hamiltonians by evaluating the corresponding integrals along

the transverse directions. The 1D effective Hamiltonian for \hat{H}_0 reads

$$\hat{H}_0 = \int dx \sum_{\alpha \in \{\uparrow, \downarrow\}} \hat{\psi}_\alpha^\dagger(x) \left(-\frac{\hbar^2}{2m} \frac{d^2}{dx^2} + V_{1D}(x) + \hbar\omega_\perp \right) \hat{\psi}_\alpha(x), \quad (2.16)$$

and the spin-dependent Hamiltonian \hat{H}_{SD} reads

$$\hat{H}_{SD} = \int dx \sum_{\alpha \in \{\uparrow, \downarrow\}} \hat{\psi}_\alpha^\dagger(x) \left(\tilde{V}_x(x; t) \sigma_{\alpha\beta}^x + \tilde{V}_y(x; t) \sigma_{\alpha\beta}^y + \left(\tilde{V}_z(x; t) + \frac{B_{\text{eff}}}{2} \right) \sigma_{\alpha\beta}^z \right) \hat{\psi}_\beta(x), \quad (2.17)$$

where $\tilde{V}_i(x; t) = \sqrt{\frac{m\omega_\perp}{\pi\hbar}} \int dydz e^{-\frac{m\omega_\perp}{2\hbar}(y^2+z^2)} V_i(\mathbf{r}; t)$, for $i \in \{x, y, z\}$. It is important to note here that the dimensional reduction relies on the fact that the spin dependent potentials are slowly-varying along the transverse directions, $\frac{\partial^2 V_i}{\partial y^2}, \frac{\partial^2 V_i}{\partial z^2} \ll m\omega_\perp^2$, in order to ensure the absence of spin-excitations along the strongly confined directions.

The dimensional reduction of \hat{H}_I is more complicated. In particular, if the transverse confinement length $a_\perp = \sqrt{\frac{\hbar}{m\omega_\perp}}$ defines a length scale of similar magnitude as a_s the phenomenon of the Confinement induced resonance is exhibited [77, 248–250, 252–256]. This implies that the actual coupling of the 1D interaction shifts away from the mean-field value $g_{1D}^{\text{MF}} = \frac{2\hbar^2 a_s}{ma_\perp^2}$ obtained by the evaluation of the y and z integrals appearing in Eq. (2.11). Detailed theoretical [248, 252–254] and experimental [249, 250] investigations reveal that the coupling strength of the 1D interaction g_{1D} possesses a simple analytic form $g_{1D} = g_{1D}^{\text{MF}} \left(1 - \frac{|\zeta(1/2)| a_s}{\sqrt{2} a_\perp}\right)^{-1}$ [248] and the effective 1D interaction Hamiltonian reduces to the simple form

$$\hat{H}_I = g_{1D} \int dx \hat{\psi}_\uparrow^\dagger(x) \hat{\psi}_\downarrow^\dagger(x) \hat{\psi}_\downarrow(x) \hat{\psi}_\uparrow(x). \quad (2.18)$$

B. 1D spin-1/2 bosons

Similarly to the fermionic case a pseudospin-1/2 bosonic system consists of two occupied hyperfine states of a bosonic element, e.g. ^{87}Rb . Notice that in contrast to spin-1/2 systems all of these systems are artificial due to the spin-statistics theorem, which dictates that bosons are characterized by an integer spin [146]. The dimensional reduction of the 3D Hamiltonian for bosons is completely analogous to the fermionic case. In particular, the terms \hat{H}_0 and \hat{H}_{SD} possess exactly the form of Eq. (2.16) and Eq. (2.17) respectively, when the fermionic field operators are substituted with bosonic ones. Recall that the bosonic field operators obey the commutation relations $[\hat{\psi}_\alpha(\mathbf{r}), \hat{\psi}_{\alpha'}^\dagger(\mathbf{r}')] = \delta_{\alpha\alpha'} \delta(\mathbf{r} - \mathbf{r}')$, $[\hat{\psi}_\alpha(\mathbf{r}), \hat{\psi}_{\alpha'}(\mathbf{r}')] = 0$ [146]. However, the interaction term in the bosonic case is slightly different since intracomponent interactions between bosons with the same spin are involved. Consequently the 1D interaction term reads

$$\hat{H}_I = \sum_{\alpha \in \{\uparrow, \downarrow\}} \frac{g_{\alpha\alpha}}{2} \int dx \hat{\psi}_\alpha^\dagger(x) \hat{\psi}_\alpha^\dagger(x) \hat{\psi}_\alpha(x) \hat{\psi}_\alpha(x) + g_{\uparrow\downarrow} \int dx \hat{\psi}_\uparrow^\dagger(x) \hat{\psi}_\downarrow^\dagger(x) \hat{\psi}_\downarrow(x) \hat{\psi}_\uparrow(x), \quad (2.19)$$

THEORETICAL FRAMEWORK

with $g_{\alpha\alpha'} = \frac{2\hbar^2 a_{\alpha\alpha'}}{ma_{\perp}^2} (1 - \frac{|\zeta(1/2)| a_{\alpha\alpha'}}{\sqrt{2} a_{\perp}})^{-1}$ and $a_{\alpha\alpha'}$ referring to the 3D scattering length of the corresponding channel. Notice here that in contrast to the interaction Hamiltonian for fermions, Eq. (2.18), the interaction Hamiltonian for bosons, Eq. (2.19), does not commute with the spin operator $\hat{S}^2 = \hat{S}_x^2 + \hat{S}_y^2 + \hat{S}_z^2$, except in the special case of $g_{\uparrow\uparrow} = g_{\downarrow\downarrow} = g_{\uparrow\downarrow}$ [87, 88]. Due to this property, the system of 1D spin-1/2 bosons does not possess an SU(2) rotation symmetry in spin space and it is therefore referred to as a pseudospinor gas.

C. Beyond spin-1/2 systems: spin-exchanging collision processes

An ultracold atomic gas can be regarded as a pseudospin-1/2 system if it consists of two distinct hyperfine states of the same atomic species. Spinor gases possess additionally an SU(2) invariance regarding rotations in the spin space spanned by the occupied hyperfine states [87, 88]. Therefore, a necessary condition for realizing a (pseudo)spin-1/2 system is that the population of all possible atomic states except for two can be neglected. Provided a spin-independent confinement and the absence of radiofrequency or optical pumping between the different hyperfine states an important consideration is whether the atomic interactions allow for such a condition to be met. As argued in Sec. 2.1A, transitions between distinct hyperfine states can be induced via inelastic collisions [19, 118–121, 225, 226], which accordingly have to be negligible for a spinor system, narrowing the choice of atomic species where such setups are realizable. However, elastic collisions should be also considered in order to infer the stability of setups with (pseudo)spin. Indeed, elastic spin-exchanging collisions within hyperfine state manifolds with $F > 1/2$ can lead to the redistribution of the atoms among the different m_F states [87, 88]. Accordingly, a poor choice of the correspondence between pseudospin and hyperfine states can lead to a small lifetime of the pseudospin-1/2 system. Below, we briefly examine the interaction properties of systems with $F > 1/2$ and discuss their relevance for realizing (pseudo)spin-1/2 systems.

The short-range s -wave elastic collisions emanating in ultracold atoms can be well-described within the delta pseudopotential approximation of Eq. (2.12) provided that inelastic collisions are negligible. We can utilize the conservation of angular momentum among the colliding particles to expand the resulting interaction Hamiltonian in terms of the different participating two-body collision channels [87, 88]. These two-body collision channels are characterized by the conserved angular momentum $\hat{\mathbf{F}}_t = \hat{\mathbf{F}}_1 + \hat{\mathbf{F}}_2$, where $\hat{\mathbf{F}}_1$ and $\hat{\mathbf{F}}_2$ refer to the sum of electronic and nuclear angular momenta of the colliding atoms. Expressed in terms of the above identified channels the interaction term reads

$$\hat{H}_I = \frac{1}{2} \sum_{F_t=0}^{2F} \frac{4\pi\hbar^2\alpha_F}{m} \sum_{m_{F_t}=-F_t}^{F_t} \int d^3r \hat{C}_{F_t m_{F_t}}^\dagger(\mathbf{r}) \hat{C}_{F_t m_{F_t}}(\mathbf{r}), \quad (2.20)$$

where the channel operators have the form

$$\hat{C}_{F_t m_{F_t}}(\mathbf{r}) = \sum_{m_F=-F}^F \sum_{m'_F=-F}^F \langle F_t, m_{F_t} | F, m_F; F, m'_F \rangle \hat{\psi}_{m_F}(\mathbf{r}) \hat{\psi}_{m'_F}(\mathbf{r}), \quad (2.21)$$

with $\langle JM | j_1, m_1; j_2 m_2 \rangle$ denoting the Clebsch-Gordan coefficients [219,247] and $\hat{\psi}_{m_F}(\mathbf{r})$ referring to the field operators of the $|F, m_F\rangle$ hyperfine state which obey the proper according to the spin-statistics theorem [146] commutation or anticommutation properties. Here the scattering lengths a_{F_t} are allowed to be channel dependent accounting for such variations of the actual atomic scattering potential. The particle exchange statistics plays a crucial role since the s -wave character of the interactions implies that the channels that are characterized by antisymmetric spatial two-body wavefunctions do not contribute to scattering. Accordingly, for fermionic particles the scattering lengths for all even-valued channels vanish, i.e. $a_{F_t=2n} = 0$ for $n = 0, 1, \dots$, while for bosons all odd-valued channels do not contribute to scattering, namely $a_{F_t=2n+1} = 0$ for $n = 0, 1, \dots$. Based on the above one can derive Eq. (2.18) from Eq. (2.20) by employing $F = 1/2$, indicating that fermionic systems involving the $|F = 1/2, m_F = \pm 1/2\rangle$ hyperfine states are of spinor character. In particular, it can be shown [87, 88] that $[\hat{H}_I, \hat{F}^2] = 0$ and accordingly all systems involving interactions of the form appearing in Eq. (2.20) possess SU(2) spin-rotational invariance independently of the specific value of F . In this sense, they constitute realizations of spin- F spinor systems. As mentioned above an important consequence of the SU(2) symmetry of a spin- $F > 1/2$ ensemble is the emergence of spin-exchanging interactions. Although the presence of such properties can be shown for arbitrary F , here we consider as a specific example a system of $F = 1$ bosons, a scenario which is relevant for ^{87}Rb experiments. The interaction part of Eq. (2.20) when expressed in terms of the corresponding field operators of the $|F = 1, m_F = 0, \pm 1\rangle$ states reads

$$\begin{aligned} \hat{H}_I = & \frac{2\pi\hbar^2}{m} \left[a_2(\hat{U}_{1,1} + \hat{U}_{-1,-1} + \hat{U}_{1,0} + \hat{U}_{-1,0}) + \frac{a_0 + 2a_2}{3} \hat{U}_{0,0} + \frac{2(a_0 - a_2)}{3} \hat{U}_{1,-1} \right. \\ & \left. + \frac{2(a_2 - a_0)}{3} \int d^3r (\hat{\psi}_0^\dagger(\mathbf{r}) \hat{\psi}_0^\dagger(\mathbf{r}) \hat{\psi}_1(\mathbf{r}) \hat{\psi}_{-1}(\mathbf{r}) + h.c.) \right], \end{aligned} \quad (2.22)$$

where $\hat{U}_{m_F, m'_F} = \int d^3r (\hat{\psi}_{m_F}^\dagger(\mathbf{r}) \hat{\psi}_{m'_F}^\dagger(\mathbf{r}) \hat{\psi}_{m'_F}(\mathbf{r}) \hat{\psi}_{m_F}(\mathbf{r}))$ is the interaction operator referring to the involved density-density interactions between the components m_F and m'_F while a_0, a_2 correspond to the scattering lengths of the $F_t = 0, F_t = 2$ scattering channels respectively. Eq. (2.22) makes obvious that if $a_2 \neq a_0$ due to the interference of the $F_t = 2$ and $F_t = 0$ scattering channels, it is possible that a scattering event involving a $m_F = 1$ and a $m_F = -1$ atom allows both of them to transit to the $m_F = 0$ state. Similarly, the inverse process with a pair of $m_F = 0$ atoms transiting to the $m_F = 1$ and $m_F = -1$ states is also possible. Therefore, the SU(2) symmetric interactions for $a_2 \neq a_0$ realize in this case elastic spin-exchanging collisions [87, 88]. Notice that this kind of a spin-exchanging collision preserves the expectation value $\langle \hat{F}_z \rangle$

THEORETICAL FRAMEWORK

of the ensemble but redistributes the particles between the different spin-states. Another important feature of Eq. (2.22) is that different weights correspond to different density-density interactions, e.g. the $m_F = 0$ atoms interact among themselves with strength $\frac{2\pi\hbar^2(a_0+2a_2)}{3m}$, while the $m_F = \pm 1$ possess interactions proportional to $\frac{2\pi\hbar^2 a_2}{m}$. Also, the intercomponent interactions possess different weights based on which m_F states are coupled. The above imply that the interaction energy stemming from Eq. (2.22) depends on the distribution of atoms among the different spin-states, resulting in density induced shifts of the energies of each particular spin state. Those density shifts can be utilized so that spin-exchange processes can be enhanced or suppressed via the coincidence or the discrepancy of energies corresponding to the different m_F components.

Indeed, spin-1 Bose gases possess a rich phase diagram in terms of the occupied m_F states which can be probed by manipulating the energies of the different hyperfine states via Zeeman shifts [87,88]. For higher spin bosonic or fermionic gases the phase diagram becomes even more interesting since more spin-states and more intricate couplings among them via spin-exchanging collisions are involved [87,88]. However, in the present effort we are mostly interested in spin-1/2 and pseudospin-1/2 systems immersed in an environment that consists either of the same or different atomic species. As a consequence, we intend to suppress as much as possible the effect of spin-exchanging collisions. Indeed, such a suppression can be achieved by exploiting the Zeeman shift of hyperfine states, for instance the experiment of Ref. [246] reports that the spin-exchanging collisions of a ^{87}Rb spin-1 condensate are essentially negligible for magnetic fields as low as 45.5 G.

The underlying physical mechanism regarding the suppression of spin exchanging collisions can be understood by the following energetic argument. The amplitude of the Zeeman energy shifts in Alkalis is of the order of $h \times \text{MHz/G}$, for instance in ^{87}Rb this amplitude is $\sim 0.7 h \times \text{MHz/G}$ [274]. In addition, quadratic Zeeman shifts, that lead to a non-equidistant distribution of m_F levels are important even for relatively weak magnetic fields. Using as an example ^{87}Rb Zeeman shifts possessing an amplitude of several $h \times \text{MHz}$ can be observed already for magnetic fields of ~ 10 G [274]. Typical ultracold atom experiments involve interaction energies of hundreds of $h \times \text{Hz}$ to a few $h \times \text{kHz}$ per particle [22–24] generating interaction energy shifts and spin-exchange processes characterized by an energy scale of the same order of magnitude. Therefore, a matching between the energies of different m_f states that allows for spin-exchange processes to occur can be achieved only for magnetic fields not exceeding a few Gauss. A similar argumentation can be employed for hyperfine manifolds possessing a different total-spin F and accordingly the coupling between different $|F, m_F\rangle$ states can be neglected for large magnetic fields. As a final comment note also that the typical energy difference between hyperfine levels possessing different F is of the order of several $h \times \text{GHz}$. In particular for ^{87}Rb the hyperfine splitting between the two lowest hyperfine manifolds $F = 1$ and $F = 2$ is $E_{F=2} - E_{F=1} \approx h \times 6.83 \text{ GHz}$ [274] and as such no particle exchange occurs among those different manifolds within the ultracold regime.

2.2 Magnetic properties of Spinor Fermi Gases

One of the main topics analyzed within our work is the properties of spin-1/2 externally confined ultracold fermions. Here our major motivation is to develop an in-depth understanding of the underlying magnetic mechanisms of those setups that might be transferable to condensed matter systems. The link between ultracold and condensed matter setups is provided by the Stoner model [104] which assumes zero-range interactions and small electron densities, where effects stemming from the lattice geometry can be ignored, consisting two adequate and feasible assumptions within the ultracold realm. As a consequence, it is of value to review the basic properties of the Stoner ferromagnetism and subsequently briefly discuss the successes and drawbacks of this model [107, 114] in describing itinerant ferromagnetism as understood within the condensed matter community.

2.2.1 Stoner model of Ferromagnetism

The Stoner model [104] constitutes the most widely accepted framework to qualitatively examine the phenomenon of ferromagnetism in systems consisting of itinerant electrons [107]. The Stoner model is established within the Hartree-Fock approximation [275, 276] and therefore is a mean-field theory. Within the Stoner model the electrons are assumed to interact with short-range interactions that can be well-treated within the framework of the zero-range pseudopotential defined in Eq. (2.12). Let us further assume, for simplicity, a vanishing overall confinement of the electrons, $V(\mathbf{r}) = 0$. In that case the Hamiltonian of the d -dimensional spin-1/2 Fermi gas reads [107]

$$\hat{H}_h - \mu\hat{N} = \sum_{\mathbf{k}\alpha\beta} \left[(\varepsilon_{\mathbf{k}} - \mu)\delta_{\alpha\beta} - \frac{B_{\mathbf{k}}}{2}\sigma_{\alpha\beta}^z \right] \hat{\psi}_{\mathbf{k}\alpha}^\dagger \hat{\psi}_{\mathbf{k}\beta} + \frac{g}{L^d} \sum_{\mathbf{k}\mathbf{k}'\mathbf{q}} \hat{\psi}_{\mathbf{k}+\mathbf{q}\uparrow}^\dagger \hat{\psi}_{\mathbf{k}'-\mathbf{q}\downarrow}^\dagger \hat{\psi}_{\mathbf{k}'\downarrow} \hat{\psi}_{\mathbf{k}\uparrow}, \quad (2.23)$$

where $\varepsilon_{\mathbf{k}} = \frac{\hbar^2 \mathbf{k}^2}{2m}$ is the non interacting dispersion relation, μ denotes the chemical potential, $B_{\mathbf{k}}$ is a spatially dependent magnetic field and L^d is the spatial extent (e.g. the volume for $d = 3$) of the system. Notice that in Eq. (2.23) the chemical potential contribution $\sim -\mu\hat{N}$ has been subtracted from the Hamiltonian, \hat{H}_h , since the equilibrium density matrix within the grand canonical ensemble reads $\hat{\rho}_{\text{eq}} = Z^{-1} \exp[-(\hat{H}_h - \mu\hat{N})/(k_B T)]$, where k_B and T are the Boltzmann constant and temperature respectively, while Z is the partition function ensuring the normalization of $\hat{\rho}_{\text{eq}}$ [146]. In addition, notice that \hat{H}_h has been expressed in momentum space where the non-interacting part is diagonal. This choice implies that the zero-range interaction potential in the configuration space $\sim \delta(\mathbf{r}_i - \mathbf{r}_j)$ has been transformed to a completely delocalized one in momentum space where all interaction terms are scaled by the same amplitude. To proceed the Hartree-Fock approximation is performed neglecting all two-body correlations, by demanding that the Wick theorem [146] holds, i.e.

$$\begin{aligned} \langle \Psi | \hat{\psi}_{\mathbf{k}'_1\alpha'_1}^\dagger \hat{\psi}_{\mathbf{k}'_2\alpha'_2}^\dagger \hat{\psi}_{\mathbf{k}_2\alpha_2} \hat{\psi}_{\mathbf{k}_1\alpha_1} | \Psi \rangle &= \langle \Psi | \hat{\psi}_{\mathbf{k}'_1\alpha'_1}^\dagger \hat{\psi}_{\mathbf{k}_1\alpha_1} | \Psi \rangle \langle \Psi | \hat{\psi}_{\mathbf{k}'_2\alpha'_2}^\dagger \hat{\psi}_{\mathbf{k}_2\alpha_2} | \Psi \rangle \\ &\quad - \langle \Psi | \hat{\psi}_{\mathbf{k}'_1\alpha'_1}^\dagger \hat{\psi}_{\mathbf{k}_2\alpha_2} | \Psi \rangle \langle \Psi | \hat{\psi}_{\mathbf{k}'_2\alpha'_2}^\dagger \hat{\psi}_{\mathbf{k}_1\alpha_1} | \Psi \rangle. \end{aligned} \quad (2.24)$$

THEORETICAL FRAMEWORK

Note that Eq. (2.24) is only applicable to the case of $g = 0$, as two-body correlations can possibly emanate in the interacting case. In addition, since we are interested in the ground state of the system the self-consistent assumption of a homogeneous density phase i.e. $\langle \Psi | \hat{\psi}_{\mathbf{k}\alpha}^\dagger \hat{\psi}_{\mathbf{k}'\beta} | \Psi \rangle = \delta_{\mathbf{k}\mathbf{k}'} \langle \Psi | \hat{\psi}_{\mathbf{k}\alpha}^\dagger \hat{\psi}_{\mathbf{k}\beta} | \Psi \rangle$ is employed [146]. The above mentioned assumptions can be incorporated self-consistently by the appropriate truncation of the Bogoliubov-Born-Green-Kirkwood-Yvon (BBGKY) equations [277–280], leading to the following approximation for the interaction term

$$\begin{aligned} \hat{H}_I \approx \hat{H}_I^{MF} = \frac{g}{L^d} & \left[\sum_{\mathbf{k}\mathbf{k}'} \langle \Psi | \hat{\psi}_{\mathbf{k}\uparrow}^\dagger \hat{\psi}_{\mathbf{k}\uparrow} | \Psi \rangle \hat{\psi}_{\mathbf{k}\downarrow}^\dagger \hat{\psi}_{\mathbf{k}\downarrow} + \sum_{\mathbf{k}\mathbf{k}'} \langle \Psi | \hat{\psi}_{\mathbf{k}\downarrow}^\dagger \hat{\psi}_{\mathbf{k}\downarrow} | \Psi \rangle \hat{\psi}_{\mathbf{k}\uparrow}^\dagger \hat{\psi}_{\mathbf{k}\uparrow} \right. \\ & - \sum_{\mathbf{k}\mathbf{k}'} \langle \Psi | \hat{\psi}_{\mathbf{k}\uparrow}^\dagger \hat{\psi}_{\mathbf{k}\downarrow} | \Psi \rangle \hat{\psi}_{\mathbf{k}\downarrow}^\dagger \hat{\psi}_{\mathbf{k}\uparrow} - \sum_{\mathbf{k}\mathbf{k}'} \langle \Psi | \hat{\psi}_{\mathbf{k}\downarrow}^\dagger \hat{\psi}_{\mathbf{k}\uparrow} | \Psi \rangle \hat{\psi}_{\mathbf{k}\uparrow}^\dagger \hat{\psi}_{\mathbf{k}\downarrow} \\ & - \sum_{\mathbf{k}\mathbf{k}'} \langle \Psi | \hat{\psi}_{\mathbf{k}\uparrow}^\dagger \hat{\psi}_{\mathbf{k}\uparrow} | \Psi \rangle \langle \Psi | \hat{\psi}_{\mathbf{k}\downarrow}^\dagger \hat{\psi}_{\mathbf{k}\downarrow} | \Psi \rangle \\ & \left. + \sum_{\mathbf{k}\mathbf{k}'} \langle \Psi | \hat{\psi}_{\mathbf{k}\uparrow}^\dagger \hat{\psi}_{\mathbf{k}\downarrow} | \Psi \rangle \langle \Psi | \hat{\psi}_{\mathbf{k}\downarrow}^\dagger \hat{\psi}_{\mathbf{k}\uparrow} | \Psi \rangle \right]. \end{aligned} \quad (2.25)$$

In order to reveal the magnetic order of the Hamiltonian it is instructive to define the so-called Stoner gap parameters

$$\begin{aligned} \Delta_x &= \frac{g}{L^d} \sum_{\mathbf{k}} \left(\langle \Psi | \hat{\psi}_{\mathbf{k}\uparrow}^\dagger \hat{\psi}_{\mathbf{k}\downarrow} | \Psi \rangle + \langle \Psi | \hat{\psi}_{\mathbf{k}\downarrow}^\dagger \hat{\psi}_{\mathbf{k}\uparrow} | \Psi \rangle \right), \\ \Delta_y &= \frac{-ig}{L^d} \sum_{\mathbf{k}} \left(\langle \Psi | \hat{\psi}_{\mathbf{k}\uparrow}^\dagger \hat{\psi}_{\mathbf{k}\downarrow} | \Psi \rangle - \langle \Psi | \hat{\psi}_{\mathbf{k}\downarrow}^\dagger \hat{\psi}_{\mathbf{k}\uparrow} | \Psi \rangle \right), \\ \Delta_z &= \frac{g}{L^d} \sum_{\mathbf{k}} \left(\langle \Psi | \hat{\psi}_{\mathbf{k}\uparrow}^\dagger \hat{\psi}_{\mathbf{k}\uparrow} | \Psi \rangle - \langle \Psi | \hat{\psi}_{\mathbf{k}\downarrow}^\dagger \hat{\psi}_{\mathbf{k}\downarrow} | \Psi \rangle \right). \end{aligned} \quad (2.26)$$

By invoking Eq. (2.26) we can express the expectation values in Eq. (2.25) with respect to $\mathbf{\Delta} = \Delta_x \mathbf{e}_x + \Delta_y \mathbf{e}_y + \Delta_z \mathbf{e}_z$, where $\mathbf{e}_x, \mathbf{e}_y, \mathbf{e}_z$ refer to the unit vectors in the spin-space. Following this prescription we obtain the Hamiltonian of the Stoner model

$$\begin{aligned} \hat{H}_{SM} - \mu \hat{N} &= \frac{L^d}{4g} \left[|\mathbf{\Delta}|^2 - (gn)^2 \right] \\ &+ \sum_{\mathbf{k}\alpha\beta} \left[\left(\varepsilon_{\mathbf{k}} + \frac{gn}{2} - \mu \right) \delta_{\alpha\beta} - \frac{\mathbf{\Delta} + B_{\mathbf{k}} \mathbf{e}_z}{2} \cdot \boldsymbol{\sigma}_{\alpha\beta} \right] \hat{\psi}_{\mathbf{k}\alpha}^\dagger \hat{\psi}_{\mathbf{k}\beta}, \end{aligned} \quad (2.27)$$

where the total density reads

$$n = \frac{1}{L^d} \sum_{\mathbf{k}} \langle \Psi | \hat{\psi}_{\mathbf{k}\uparrow}^\dagger \hat{\psi}_{\mathbf{k}\uparrow} + \hat{\psi}_{\mathbf{k}\downarrow}^\dagger \hat{\psi}_{\mathbf{k}\downarrow} | \Psi \rangle. \quad (2.28)$$

The Hamiltonian of Eq. (2.27) represents an ensemble of non-interacting spins with each particular one corresponding to a different quasimomentum, \mathbf{k} . These non-interacting

spins are subjected to an effective magnetic field. The latter stems from the actual applied magnetic field $B_{\mathbf{k}}$ and an effective contribution based on the polarization of the non-interacting spins Δ . \hat{H}_{SM} can be easily diagonalized for each- k , yielding the spin-dependent dispersion relations as a function of the Stoner parameter

$$E_{\mathbf{k}}^{\pm}(\Delta) = \left(\varepsilon_{\mathbf{k}} + \frac{gn}{2L^d} \right) \pm \frac{|\Delta + B_{\mathbf{k}}\mathbf{e}_z|}{2} \quad (2.29)$$

Note that also the eigenstates of \hat{H}_{SM} can be expressed in terms of fermionic field operators $\hat{f}_{\mathbf{k}\pm}^{\dagger}(\Delta) = c_{\mathbf{k}\uparrow}^{\pm}(\Delta)\hat{\psi}_{\mathbf{k}\uparrow}^{\dagger} + c_{\mathbf{k}\downarrow}^{\pm}(\Delta)\hat{\psi}_{\mathbf{k}\downarrow}^{\dagger}$ implying that within the Stoner model the itinerant spin-1/2 fermions can be mapped to an ensemble of non-interacting fermionic quasi-particles under the effect of a self-consistent field [107]. Accordingly, their ground state at temperature T is characterized by the Fermi-Dirac distribution

$$\langle \Psi | \hat{f}_{\mathbf{k}\pm}^{\dagger}(\Delta) \hat{f}_{\mathbf{k}\pm}(\Delta) | \Psi \rangle = \left[1 + \exp \left(\frac{E_{\mathbf{k}}^{\pm}(\Delta) - \mu}{k_B T} \right) \right]^{-1}. \quad (2.30)$$

Therefore the knowledge of the solution for every Δ and μ allows us to express the solution of the Stoner model in terms of the physical parameters g and n by solving Eq. (2.26) and (2.28) for the Stoner parameter and chemical potential. For a \mathbf{k} -dependent external magnetic field such a solution is non-trivial and it requires a numerical treatment. However, in the case of a homogeneous external magnetic field $B_{\mathbf{k}} = B_0$ the ground state properties of the Stoner model can be analyzed in an intuitive manner. Indeed, in this case the expansion coefficients $c_{\mathbf{k}\alpha}^{\pm}(\Delta)$, with $\alpha \in \{\uparrow, \downarrow\}$ are \mathbf{k} -independent and accordingly the electronic spins have to be polarized in the direction of $\Delta/|\Delta|$ for $|\Delta| \neq 0$. Furthermore, Eq. (2.27) reveals that the ground state of the Stoner model needs to satisfy $\Delta \times \mathbf{e}_z = 0$, as in the opposite case the polarization of the particles along $\Delta/|\Delta|$ would precess around the z axis and therefore this state could not be stationary. Note also that

$$\begin{aligned} \frac{\langle \Psi | \hat{H}_{SM} | \Psi \rangle}{N} &= \frac{(gn)^2 - |\Delta|^2}{4gn} - \frac{1}{2} B_0 \mathbf{e}_z \cdot \frac{\Delta}{gn} - \frac{dk_B T}{2n} \left(\frac{mk_B T}{2\pi\hbar^2} \right)^{d/2} \\ &\times \left[\text{Li}_{\frac{d}{2}+1} \left(-e^{\frac{2\mu - |\Delta + B_0 \mathbf{e}_z|}{2k_B T}} \right) + \text{Li}_{\frac{d}{2}+1} \left(-e^{\frac{2\mu + |\Delta + B_0 \mathbf{e}_z|}{2k_B T}} \right) \right], \end{aligned} \quad (2.31)$$

where $\text{Li}_p(x)$ refers to the polylogarithm function, rendering the polarization of the Fermi gas along the z axis (i.e. parallel to the magnetic field) preferable to reduce the energy stemming from the interaction between the polarization and the external magnetic field $\propto B_0$. This constitutes a significant simplification as the ground state of the Stoner model for $B_{\mathbf{k}} = B_0 \geq 0$ is then characterized by $\Delta = \Delta_z \mathbf{e}_z$, with $\Delta_z \geq 0$, implying that Eq. (2.26) for Δ_x and Δ_y are trivially satisfied. The Stoner gap parameter Δ_z and the chemical potential μ can be expressed in terms of the interaction parameter g and the density n as a function of temperature T by solving the coupled set of transcendental equations

$$\text{Li}_{\frac{d}{2}} \left(-e^{\frac{2\mu \pm (\Delta_z + B_0)}{2k_B T}} \right) = -\frac{n}{2} \left(\frac{2\pi\hbar^2}{mk_B T} \right)^{\frac{d}{2}} \left(1 \pm \frac{\Delta_z}{ng} \right). \quad (2.32)$$

THEORETICAL FRAMEWORK

Notice that $\Delta_z/(gn) \in [0, 1]$ and expresses the polarization of the spin of the system along the z direction. Accordingly, $\Delta_z/(gn)$ can be employed as the order parameter of ferromagnetism.

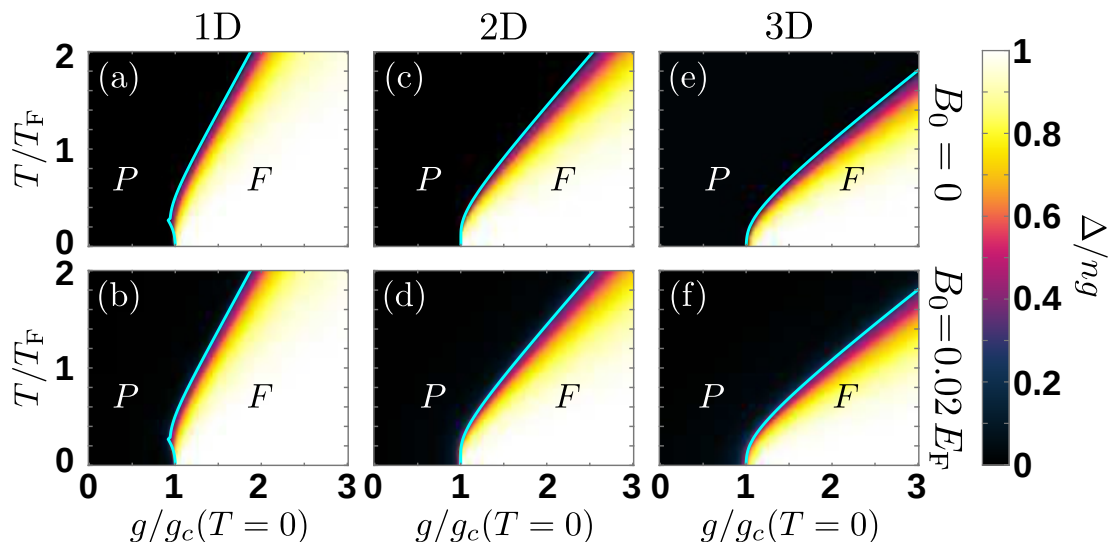


Figure 2.1: Phase diagram of the Stoner model of Eq. (2.27) in terms of the temperature T (in units of the Fermi one, T_F) and interaction strength g for (a), (b) one, (c), (d) two and (e), (f) three spatial dimensions. In all cases the magnetic field is homogeneous taking the values (a), (c), (e) $B_0 = 0$ and (b), (d), (f) $B_0 = 0.02E_F$, where E_F is the Fermi energy. The regimes corresponding to the paramagnetic and the ferromagnetic phase are denoted by P and F respectively. The solid blue line provides the critical interaction strength, $g_c(T)$, as captured by Eq. (2.33) for $B_0 = 0$.

The finite temperature phase diagram resulting from the solution of Eq. (2.32) is provided in Fig. 2.1. It becomes evident that independently of the dimensionality $d = 1, 2, 3$ and for $B_0 = 0$, there are two phases appearing in the corresponding phase diagram. Namely, the paramagnetic phase (see regions labeled as P) characterized by $\Delta_z = 0$, and the ferromagnetic one (labeled as F) having $\Delta_z > 0$. The paramagnetic phase appears when the interaction is smaller than a critical value $g < g_c(T)$, while the system transits to the ferromagnetic phase in the opposite case. This second-order transition can be explained intuitively in view of the Hamiltonian of Eq. (2.23) where only the kinetic energy and the short-range interaction terms contribute. Indeed, for small interactions the pairing of two fermions with opposite spin into the same single-particle state, such that $\langle \Psi | \hat{\psi}_{\mathbf{k}\uparrow}^\dagger \hat{\psi}_{\mathbf{k}\uparrow} | \Psi \rangle = \langle \Psi | \hat{\psi}_{\mathbf{k}\downarrow}^\dagger \hat{\psi}_{\mathbf{k}\downarrow} | \Psi \rangle$ is energetically preferable since it decreases the volume of occupied quasimomenta in \mathbf{k} space and hence the kinetic energy. However, in the large interaction limit such a pairing process costs a large energy since the interaction energy E_I scales with the spin component overlap $E_I \sim g \int d^d x n_\uparrow(\mathbf{x}) n_\downarrow(\mathbf{x}) = gn^2[1 - \Delta_z/(gn)]$, see also Eq. (2.31). Accordingly, the system prefers the spin of its constituting particles to polarize along an (arbitrary for

$B_0 = 0$) direction to reduce the interaction energy of the system [104]. The critical interaction strength $g_c(T)$, can be evaluated by taking the $\Delta_z \rightarrow 0^+$ limit of Eq. (2.32) yielding

$$g_c(T) = \left(\frac{1}{2} \frac{dn}{d\mu} \Big|_{\Delta_z=0} \right)^{-1}, \quad (2.33)$$

which in the particular case of $T = 0$ reads $g_c(T = 0)D(E_F) = 1$, with $D(E_F)$ is the single-particle density of states at the Fermi energy, corresponding to the well-known Stoner criterion [107]. As it can be seen in Fig. 2.1, the critical temperature prediction of Eq. (2.33) matches well with the transition points between the ferromagnetic and paramagnetic phases. The positive shift of the $g_c(T)$ with the temperature is qualitatively expected as a higher temperature typically leads to larger kinetic energies for the system. The order parameter of the Stoner model, $\Delta_z/(gn)$, is only weakly perturbed for weak magnetic fields, here $B_0 = 0.02 E_F$. Despite the fact that $\Delta_z > 0$ even within the paramagnetic region [see Eq. (2.31)], there is still a large and sharp increase of Δ_z in the vicinity of $g_c(T)$, indicating the presence of a second-order phase transition [281] from the paramagnetic to the ferromagnetic phase.

2.2.2 Stoner model and beyond: Description of ferromagnetism in condensed matter settings

For condensed matter systems the zero-ranged interactions introduced in the Hamiltonian of Eq. (2.23) should be understood as an approximation to the actual screened Coulomb interactions [282] experienced by two electrons in the conduction band of the lattice created by the ionic cores of the material. Accordingly, the Hamiltonian of Eq. (2.23) can be thought as the continuum limit of the single-band Hubbard model [283–286]

$$\hat{H}_{Hub} = -t \sum_{\langle i,j \rangle} \sum_{\alpha \in \{\uparrow, \downarrow\}} \hat{a}_{i\alpha}^\dagger \hat{a}_{j\alpha} + U \sum_i \hat{a}_{i\uparrow}^\dagger \hat{a}_{i\downarrow}^\dagger \hat{a}_{i\downarrow} \hat{a}_{i\uparrow}, \quad (2.34)$$

with t the tunnelling rate, U the on-site interaction and $\langle i, j \rangle$ indicating summation over all neighbouring sites. This limit is valid for $n_e^d V_s \ll 1$, where n_e is the density of the electrons in the band to be described by the Hubbard model and V_s refers to the volume of the lattice unit cell. Nevertheless, the validity of the Hamiltonian of Eq. (2.23) can be extended to the $n_e^d V_s \lesssim 1$ case if $\epsilon_{\mathbf{k}} = \hbar^2 \mathbf{k}^2 / 2m$ is substituted with the appropriate dispersion relation for the lattice under consideration. The typical Fermi energy for metals is of the order of several eV [107]. In addition, the Zeeman splitting for electrons reads $B_0 = g_s \mu_B |\mathbf{B}|$, where $g_s \approx 2$ is the gyromagnetic ratio of the electron, $\mu_B \approx 5.788 \times 10^{-5}$ eV/T refers to the Bohr magneton and $|\mathbf{B}|$ is the magnitude of the applied magnetic field. Therefore, a Zeeman splitting e.g. of $B_0 = 0.02 E_F$ [see Fig. 2.1] corresponds to an extremely large magnetic field of $|\mathbf{B}| \sim 100$ T. As a consequence, the effect of the external magnetic field on the magnetization of the material is negligible and thus in a condensed matter setting we can clearly focus on the $B_0 = 0$ limit.

THEORETICAL FRAMEWORK

The Fermi temperature for a metal is rather high, namely, $T_F = E_F/k_B \sim 10^4$ K. By comparing this value with the phase diagram [see Fig. 2.1(e)] a material at room temperature is close to the zero temperature limit of the Stoner model, as $T/T_F \approx 10^{-2}$. This implies that the Stoner criterion for ferromagnetism $gD(E)/L^3 > 1$ can be applied. Indeed, the ferromagnetic metals Fe, Co, Ni possess a large density of states close to the Fermi energy [107, 287] and therefore their ferromagnetic behaviour can be qualitatively described by the Stoner model [104]. In addition, these materials show a pronounced difference in the spin-resolved density of states for the spin- \uparrow and spin- \downarrow components in the vicinity of the Fermi energy which supports the development of a Stoner gap, $\Delta_z \neq 0$. However, even in this case there are strong quantitative deviations with the experimental observations [107]. The most well known regards the Curie temperature T_C , which is the temperature that ferromagnetic materials lose their permanent magnetization. It turns out that the Curie temperature is highly overestimated by the Stoner model, which predicts $T_C \approx T_F \sim 10^4$ K, while the measured value ranges from $T_c \approx 627$ K for Ni to $T_C \approx 1390$ K for Co.

There are also conceptual problems regarding Stoner ferromagnetism. In particular, the Stoner model of Eq. (2.27) implies that the ferromagnetic system is in a state of broken symmetry. While, the three-dimensional Hubbard model without additional magnetic field possesses an $O(3)$ symmetry, corresponding to the rotations of spin-space, the Stoner model for $|\Delta| \neq 0$ possesses only an $O(2)$ symmetry of rotations around the spin-axis defined by $\Delta/|\Delta|$. In order to achieve such a reduction of symmetry, spontaneous symmetry breaking should take place [281]. However, according to the Mermin-Wagner theorem [111], which has been extended to the case of the Hubbard model [288–290], the $O(3)$ continuous symmetry cannot be broken if the Fermi gas possesses $d \leq 2$ dimensions. In contrast to this theorem, as Fig. 2.1(a) and 2.1(d) reveals the Stoner model predicts that there is a $|\Delta| \neq 0$ phase for $d = 1, 2$. This discrepancy can be attributed to the inability of the employed mean-field theory to describe spin-wave excitations [108, 109]. Interestingly, it was already noted by Slater in 1937 [108] that for investigating the temperature variation of magnetization of the system an appropriate spin-wave theory should be employed. The spin-waves correspond to spatial-dependent fluctuations in the orientation of $\Delta/|\Delta|$ and their quanta correspond to quasi-particles called magnons which are the Goldstone bosons of the broken $O(3)$ symmetry. For $d \leq 2$ thermal fluctuations are supposed to excite long-wavelength spin-waves, destroying the long-range ferromagnetic order for any finite temperature in the thermodynamic limit.

Even within the zero-temperature limit, further inconsistencies arise when comparing the viewpoint of Stoner ferromagnetism with the theorems regarding the energetic ordering of the different manifolds of total spin S . In particular, it is known that the ground state of Eq. (2.23) for $d = 1$ has a total spin of $S = 0$ for even and $S = 1/2$ for odd total particle numbers [110]. In addition, the eigenenergies have to satisfy $E(S) < E(S')$, for $S < S'$, where $E(S)$ is the energetically lowest eigenenergy with total spin S . In contrast, the Stoner model predicts a ferromagnetic transition at zero temperature when $gD(E)/L > 1$ is satisfied. Similarly, it has been shown by Lieb

in 1989 [112] that for any bipartite lattice (even in the case of broken translational symmetry) the ground state at half filling, i.e. $N_e = N_s$, where N_e is the number of particles and N_s the number of sites, possesses spin equal to $S = \frac{N_A - N_B}{2(N_A + N_B)} N_s$, where N_A, N_B refers to the number of A and B sites in a unit cell. This implies that all bipartite lattices with equal number of A and B sites cannot support ferromagnetism at half filling. Cases of such lattices include for instance the square, rectangular and honeycomb lattice for $d = 2$, the cubic and triclinic lattice for $d = 3$. The Stoner criterion, $gD(E_F) \geq 1$, is unable to incorporate such geometric effects as it only involves the density of states at the Fermi energy and as a consequence it can violate the Lieb theorem [112]. A particular case of agreement refers to the honeycomb lattice where the density of states at half filling is zero (since the Fermi energy lies exactly at the energy level of the Dirac points) and as a consequence the Stoner model predicts that ferromagnetism is impossible. However, counterexamples are far more common. For instance, regarding a square or cubic lattice at half filling the density of states is maximal at the Fermi energy, indicating that according to the Stoner criterion these lattices are prone to exhibit ferromagnetic phenomena in sharp contrast to the Lieb theorem [112]. The condition $N_A \neq N_B$ also provides an interesting caveat to Stoner ferromagnetism. If this condition is satisfied for a particular lattice configuration, its Fermi energy for half filling lies within a dispersionless (flat) band and consequently a very large (infinite in the thermodynamic limit) density of states is involved at the Fermi level [291, 292]. Here the Stoner model predicts a ferromagnetic transition for non-vanishing repulsion, however, according to the Lieb theorem in the presence of correlations ferrimagnetism [293] is exhibited.

As evident from the above despite the success of the Stoner model in predicting the development of a gap between the states of spin- \uparrow and spin- \downarrow electrons in ferromagnetic metals [107], this model is too simplistic to capture the intricacies of ferromagnetism in condensed matter setups. In recent years more involved Hartree-Fock mean field methodologies addressing the Hubbard model were proposed, which are able to rectify some of the above mentioned issues by properly accounting for geometric lattice effects and inhomogeneous phases [113]. Nevertheless, it is generally believed that the Hubbard model at finite doping can appropriately capture the basics of ferromagnetism, with no need for involving multi-band models or explicit exchange interactions among the electrons [114].

A major result that supports the conjecture that the Hubbard model can adequately describe the phenomenon of itinerant ferromagnetism in metals is put forward by Nagaoka in 1966 [294]. In particular, it was proven that the ground state of the Hubbard model on a bipartite system in the limit of $U \rightarrow \infty$ and for $N_e = N_s - 1$, i.e. a single particle lower than half filling, is ferromagnetic in the sense that its ground state possesses total spin $S = \frac{N_e}{2}$ [294]. This finding led to a new era of investigations [114, 295, 296], however, to our knowledge there is no rigorous generalization of the Nagaoka ferromagnetism to finite U or $N_e < N_s - 1$.

2.3 Stationary and magnetic properties of confined spin-1/2 Fermi gases in one-dimension

The direct realization of the above mentioned Stoner instability in ultracold Fermi gases in its simplest form as described by Eq. (2.27) was not possible [94,96]. The inability of the experiment to observe such a phenomenon is attributed to the fast decay of repulsive Fermi gases to diatomic molecular bound states [95]. This process occurs in the three and two dimensional settings, due to the attractive character of the actual interatomic potential [77]. This fact necessitates the development of novel techniques for the adequate characterization of ferromagnetism. In particular, spin-dynamics [97] and pump-probe spectroscopy [100,101] has been employed for the characterization of the magnetic properties of the metastable repulsive fraction of a Fermi gas in three dimensions. Here we propose an alternative bottom-up approach by considering the magnetic properties of a repulsive 1D Fermi gas, which does not suffer from the competing process of molecule formation [77]. In particular, the magnetic properties of 1D Fermi gases can be mapped to a spin-chain model in the limiting case of infinite interactions [128–133] and as we will demonstrate within this thesis the same is true within the opposite regime of weak interactions [134,135]. This mapping between itinerant and localized magnetic systems is of crucial importance due to the well-understood character of the magnetic properties of the latter allowing for the understanding of the related phenomena emerging in the former [107].

An important hindrance of employing 1D fermions for the study of ferromagnetism is that according to the Lieb-Mattis theorem [110] the ground state is of antiferromagnetic character independently of the type and strength of the trapping potential and of the involved interactions. Within our studies we can easily bypass this issue by considering the excited state of such Fermi gases and in particular their fully polarized states or spatial domains of polarized particles, which can easily be implemented in the ultracold environment [97,125]. Moreover, the apparent drawback of an antiferromagnetic ground state provides further insights into the inner-workings of magnetic systems. As we will argue, the fact that the ground state of a Fermi gas is always antiferromagnetic is a consequence of the Anderson kinetic exchange interactions [142] which competes with ferromagnetism. In this light the Lieb-Mattis theorem can be interpreted as the proof that the Anderson exchange interactions always dominate the ferromagnetic processes [139–141] that emanate in those setups.

In the following, we will present the Hamiltonian and review the basic spin symmetries of 1D Fermi ensembles. Then we will continue by examining the basic non-interacting, weakly and strongly interacting magnetic properties of such Fermi systems.

2.3.1 Hamiltonian and basic symmetries

The Hamiltonian of 1D spinor fermi gases according to Eq. (2.16) and Eq. (2.18) reads

$$\begin{aligned} \hat{H} = \sum_{\alpha \in \{\uparrow, \downarrow\}} \int dx \hat{\psi}_{\alpha}^{\dagger}(x) \left(-\frac{\hbar^2}{2m} \frac{d^2}{dx^2} + V(x) \right) \hat{\psi}_{\alpha}(x) \\ + g \int dx \hat{\psi}_{\uparrow}^{\dagger}(x) \hat{\psi}_{\downarrow}^{\dagger}(x) \hat{\psi}_{\downarrow}(x) \hat{\psi}_{\uparrow}(x). \end{aligned} \quad (2.35)$$

It possesses important spin-symmetries as it commutes with the spin-operators

$$\hat{S}_i = \frac{\hbar}{2} \sum_{\alpha, \alpha' \in \{\uparrow, \downarrow\}} \int dx \hat{\psi}_{\alpha}^{\dagger}(x) \sigma_{\alpha\alpha'}^i \hat{\psi}_{\alpha'}(x). \quad (2.36)$$

with $i \in \{x, y, z\}$ and $\sigma_{\alpha\alpha'}^i$ being the spin- i Pauli matrix. First, notice that the \hat{S}_z operator can be also expressed as $\hat{S}_z = \hbar(\hat{N}_{\uparrow} - \hat{N}_{\downarrow})/2$. This combined with the fact that \hat{H} commutes with the total particle operator $\hat{N} = (\hat{N}_{\uparrow} + \hat{N}_{\downarrow})$ implies that the number of particles within each individual component is a conserved quantity. Therefore, for a N particle Fermi gas each different $S_z \in \{-\frac{N}{2}, -\frac{N}{2} + 1, \dots, \frac{N}{2}\}$ manifold of states can be treated independently. The \hat{S}_x and \hat{S}_y symmetries are also important. Indeed, these symmetries imply that the spin-ladder operators, $\hat{S}_{\pm} = \hat{S}_x \pm i\hat{S}_y$, also commute with the Hamiltonian. In turn, the total-spin operator $\hat{S}^2 = \hat{S}_+ \hat{S}_- + \hat{S}_z(\hat{S}_z - 1)$, also commutes both with the Hamiltonian, \hat{H} , and the \hat{S}_z operators. Consequently, for each state there are two good quantum numbers namely S and S_z , with the available values of the total spin S depending on the number of spin- \uparrow and spin- \downarrow atoms since $S \in \{|S_z|, |S_z| + 1, \dots, \frac{N}{2}\}$. The \hat{S}_{\pm} symmetries have an additional consequence as if we assume an eigenstate of the system, $|\Psi; S, S_z\rangle$, with quantum numbers S and S_z then also the states $|\Psi; S, S_z + \frac{1}{2}\rangle = \hat{S}_+ |\Psi; S, S_z\rangle / \sqrt{(S - S_z)(S + S_z + 1)}$ and $|\Psi; S, S_z - \frac{1}{2}\rangle = \hat{S}_- |\Psi; S, S_z\rangle / \sqrt{(S + S_z)(S - S_z + 1)}$ (in the case that $S \geq S_z \pm 1$) are eigenstates of the Hamiltonian and are energetically degenerate with $|\Psi; S, S_z\rangle$. Of course, this also implies that states with spin $S \neq 0$ are a part of a degenerate eigenstate manifold consisting of at least $2S + 1$ states.

The above properties greatly aid in the characterization of the eigenspectrum of \hat{H} . Note that due to the commutation of the \hat{S}_{\pm} operator with \hat{H} the whole eigenspectrum of the N particle spin-1/2 Fermi gas can be generated by studying the eigenspectrum of a single configuration in terms of N_{\uparrow} and N_{\downarrow} states. The latter configuration refers to the case of $N_{\uparrow} = N_{\downarrow}$ for even N and the configuration $N_{\uparrow} = N_{\downarrow} + 1$ for odd N . Furthermore, even in the case that a homogeneous magnetic field is applied such that $\hat{H}' = \hat{H} + B_0 \hat{S}_z$, the eigenstates of \hat{H}' are exactly equivalent to the $B_0 = 0$ case. Their corresponding eigenenergy is, however, shifted by $\hbar B_0 S_z$, where S_z is the corresponding spin quantum number. Therefore, the eigenspectrum of the Hamiltonian \hat{H} is relevant also for more realistic systems that additionally account for the Zeeman splitting of the hyperfine levels.

Figure 2.2 provides an explicit example for the eigenspectrum of a spin-1/2 Fermi system within the interaction range, $g \geq -1 \sqrt{\hbar^3 \omega / m}$. The corresponding physical

THEORETICAL FRAMEWORK

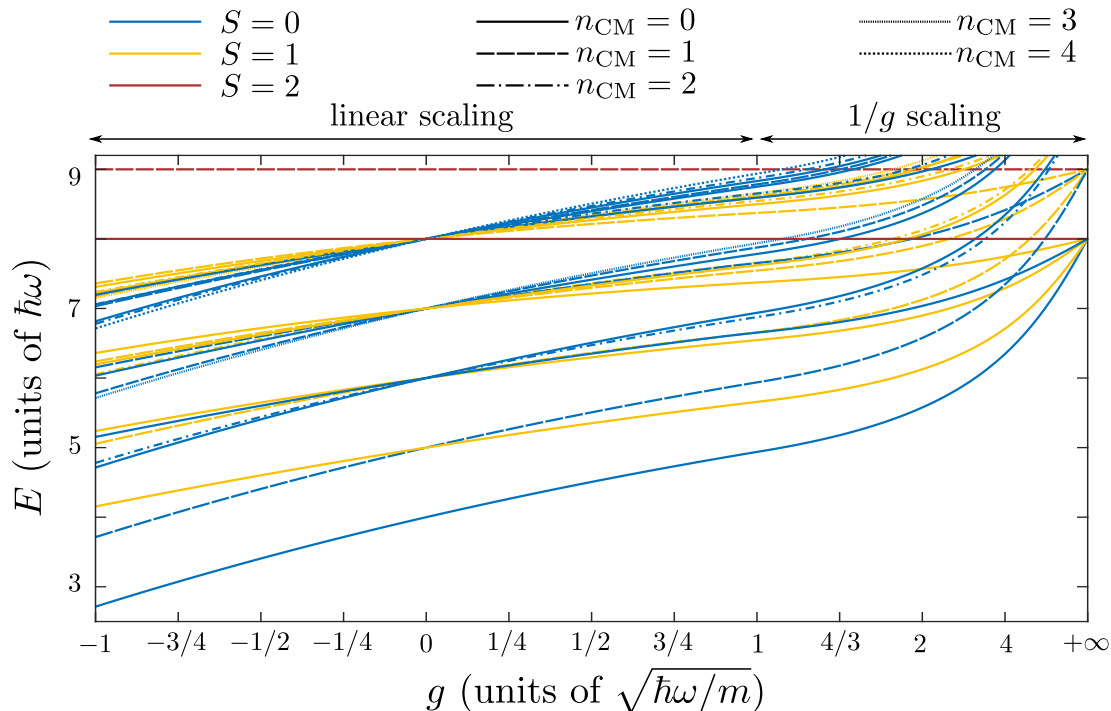


Figure 2.2: The 65 energetically lowest eigenenergies for $N = 4$ spin-1/2 fermions confined in a parabolic trap versus the interaction strength g , obtained within ML-MCTDH. The total spin S for each eigenstate is encoded in the color of the lines indicating also the degree of degeneracy, $2S + 1$, for each state. The line pattern indicates the degree of excitation for the center of mass, n_{CM} . Notice also that for $|g| < 1$ linear scaling of the interaction axis is employed while for $g > 1$ we switch to $1/g$ scaling.

system refers to $N = 4$ parabolically confined, $V(x) = (m\omega^2 x^2)/2$, fermions. The 65 energetically lowest eigenenergies of the system are depicted referring to 31 distinct manifolds of degenerate eigenstates. In agreement to the above discussion the degree of degeneracy of these manifolds relies on the total spin of the eigenstates S and it is given by $2S + 1$. Indeed, each manifold can be spanned by the eigenstates referring to the different allowed $S_z = -S, -S + 1, \dots, S$ which are related by the ladder-operators \hat{S}_{\pm} . The eigenspectrum of Fig. 2.2 exhibits a prominent structure in terms of the different involved S manifolds. In particular, notice the almost linear dependence of the eigenenergies on g for weak attractions or repulsions ($|g| < 1/2$) and the $\approx 1/g$ increase of the eigenenergies within the strong interaction regime $g > 4$. Nevertheless, we will postpone the detailed discussion of the exhibited magnetic properties in the interaction regimes $g = 0$, $|g| \ll 1$ and $g \gg 1$, which will be analyzed in Sec. 2.3.2, 2.3.3 and 2.3.5 respectively.

Before proceeding, notice that for the complete characterization of the eigenspec-

trum the symmetries of the Hamiltonian stemming from the external potential $V(x)$ are crucial. Of course, there are no generally applicable statements that can be made since each different confinement potential has to be individually examined. For the harmonic trap considered in Fig. 2.2 a relevant symmetry is the relative coordinate and center of mass separation [297]. Indeed, the Hamiltonian operator for the center of mass

$$\hat{H}_{\text{CM}} = \frac{1}{2Nm} \underbrace{\left(-i\hbar \sum_{\alpha \in \{\uparrow, \downarrow\}} \int dx \hat{\psi}_{\alpha}^{\dagger}(x) \frac{d}{dx} \hat{\psi}_{\alpha}(x) \right)^2}_{\equiv \hat{P}} + \frac{Nm\omega^2}{2} \underbrace{\left(\sum_{\alpha \in \{\uparrow, \downarrow\}} \int dx x \hat{\psi}_{\alpha}^{\dagger}(x) \hat{\psi}_{\alpha}(x) \right)^2}_{\equiv \hat{X}}, \quad (2.37)$$

commutes with the many-body Hamiltonian, \hat{H} of Eq. (2.35). Therefore, the eigenstates of the confined fermions can be characterized in terms of the degree of excitation of the center of mass, n_{CM} . In addition, due to this symmetry the eigenstates with excited center of mass can be constructed from the corresponding ones with $n_{\text{CM}} = 0$ by (repeatedly) applying the creation operator $\hat{a}_{\text{CM}}^{\dagger} = \sqrt{Nm\omega/(2\hbar)}[\hat{X} + i/(Nm\omega)\hat{P}]$. Note that each such excitation increases the energy of the eigenstate by $\hbar\omega$. In view of these properties the whole spectrum consisting of 65 eigenenergies presented in Fig. (2.2) can be constructed in terms of 14 different eigenstates, with $S_z = 0$ and $n_{\text{CM}} = 0$. This large reduction in the number of independent states appearing in the eigenspectrum shows the prominent role of symmetries in reducing the computational effort of many-body simulations [298] and providing a valuable sanity check of different approaches [299].

2.3.2 Non-interacting many-body eigenspectrum

A many-body wavefunction basis for expressing the N -body spectrum of the spin-1/2 fermions can be derived in terms of the single-particle eigenspectrum of the confining potential [146]. Such a construction is particularly useful away from the strong interaction limit where the interactions dominate the behaviour of the system. The starting point is to express the eigenstates of the many-body system in the $g = 0$ case in terms of the single-particle eigenstates (SPES), $\phi_i(x)$, $i = 0, 1, \dots$, of the system. Indeed, by defining the creation and annihilation operators of the spin- \uparrow and spin- \downarrow atoms

$$\hat{a}_{i\uparrow}^{\dagger} = \int dx \phi_i(x) \hat{\psi}_{\uparrow}^{\dagger}(x) \text{ and } \hat{a}_{i\uparrow} = \int dx \phi_i^*(x) \hat{\psi}_{\uparrow}(x), \quad (2.38)$$

the many-body Hamiltonian reads

$$\hat{H} = \underbrace{\sum_i \sum_{\alpha \in \{\uparrow, \downarrow\}} \epsilon_i \hat{a}_{i\alpha}^{\dagger} \hat{a}_{i\alpha}}_{\equiv \hat{H}_0} + g \underbrace{\sum_{i,j,k,l} U_{ijkl} \hat{a}_{i\uparrow}^{\dagger} \hat{a}_{j\downarrow}^{\dagger} \hat{a}_{k\downarrow} \hat{a}_{l\uparrow}}_{\equiv \hat{H}_I}. \quad (2.39)$$

THEORETICAL FRAMEWORK

Here ϵ_i correspond to the single-particle eigenenergies (SPEE), while the interaction matrix elements refer to $U_{ijkl} = \int dx \phi_k^*(x)\phi_l^*(x)\phi_i(x)\phi_j(x)$. Accordingly, the creation and annihilation operators obey the anticommutation relations $\{\hat{a}_{i\alpha}, \hat{a}_{j\alpha'}^\dagger\} = \delta_{ij}\delta_{\alpha\alpha'}$ and $\{\hat{a}_{i\alpha}, \hat{a}_{j\alpha'}\} = \{\hat{a}_{i\alpha}^\dagger, \hat{a}_{j\alpha'}^\dagger\} = 0$ [146]. These imply that each single-particle state can be occupied either singly, by a particle of either spin, or doubly, by two particles of opposite spin. The latter configuration is commonly referred to as a doublon. For $g = 0$ the many-body eigenspectrum is rather trivial. The ground state(s) consists of the state(s)

$$|\text{GS}_\alpha\rangle = \left(\hat{a}_{\lfloor \frac{N}{2} \rfloor \alpha}^\dagger \right)^{\text{mod}(N,2)} \left[\prod_{i=0}^{\lfloor \frac{N}{2} \rfloor - 1} \hat{a}_{i\uparrow} \hat{a}_{i\downarrow} \right]^\dagger |0\rangle, \quad (2.40)$$

where $\alpha \in \{\uparrow, \downarrow\}$ corresponds to the spin of the ground state which is relevant for odd N . The ground state eigenenergy is equal to $E = \text{mod}(N, 2)\epsilon_{\lfloor N/2 \rfloor - 1} + 2 \sum_{i=0}^{\lfloor N/2 \rfloor - 1} \epsilon_i$ [146]. Furthermore, all other eigenstates with the same S_z can be generated by applying one or multiple single-particle excitation operators $\hat{T}_{ij}^\alpha = \hat{a}_{i\alpha}^\dagger \hat{a}_{j\alpha}$, with $i \neq j$. Indeed, when \hat{T}_{ij}^α acts on a many-body eigenstate it generates a different orthogonal one with an energy difference $\epsilon_i - \epsilon_j$ to the initial eigenstate. Finally, the states with different S_z can be generated by employing the \hat{S}_+ and \hat{S}_- operators and as discussed previously they are energetically degenerate with the initial eigenstate.

It is instructive to elaborate on the issue of degeneracy of the many-body eigenspectrum for $g = 0$. Notice that exact degeneracies do not occur in the 1D single-particle spectrum for a confined system, as the underlying SPES have to be normalizable, see also Ref. [247]. However, degeneracies can occur due to the different configuration of particles contributing to a many-body eigenstate [K1,K2]. Indeed, the allowed eigenenergies for $g = 0$ read

$$E_0 = \sum_i \epsilon_i (n_{i\uparrow} + n_{i\downarrow}). \quad (2.41)$$

Equation (2.41) reveals that there are two classes of degeneracies that can arise in the many-body eigenspectrum. An example of the first kind of degeneracy occurs if the condition

$$\epsilon_i + \epsilon_j = 2\epsilon_k \quad (2.42)$$

holds for three different SPEE. In this case, each eigenstate $|\Psi_0\rangle$ has to be degenerate with $|\Psi_{\alpha\alpha'}^A\rangle = \hat{T}_{ik}^\alpha \hat{T}_{jk}^{\alpha'} |\Psi_0\rangle$ and $|\Psi_{\alpha\alpha'}^B\rangle = \hat{T}_{ki}^\alpha \hat{T}_{kj}^{\alpha'} |\Psi_0\rangle$, for all α, α' that yield $|\Psi_{\alpha\alpha'}^A\rangle \neq 0 \neq |\Psi_{\alpha\alpha'}^B\rangle$. The above generalize when more than three SPEE are involved, for instance in the case that four different SPEE fulfill

$$\epsilon_i + \epsilon_j = \epsilon_k + \epsilon_l. \quad (2.43)$$

A similar argument can be employed in order to create degenerate many-body eigenstates related to the eigenenergy coincidence of more than four single-particle levels. The second kind of degeneracy stems from the fact that given a many-body eigenstate its energy depends only on the sum of spin- \uparrow and spin- \downarrow atoms, $n_i = n_{i\uparrow} + n_{i\downarrow}$, that

occupy a given SPES. This implies that a lower bound for the degeneracy of a given eigenstate is 2^{N-2N_d} , where N_d is the number of doublons, as the spin of each fermion not forming a doublon can either be spin- \uparrow or spin- \downarrow without affecting the energy of the many-body eigenstate. This lower bound is exhausted whenever a degeneracy of the first kind is not possible. A useful tool for categorizing the non-interacting many-body eigenstates is the vector quantity $\vec{n} = (n_0, n_1, \dots)$ that tracks the occupation of each SPES independently of the spin of the involved fermions. By using \vec{n} we can distinguish between the degeneracies of the first and the second type as the former involve many-body eigenstates of different \vec{n} , while the latter refer to eigenstates with equal \vec{n} .

The above properties can be easily identified in the eigenspectrum of $N = 4$ parabolically confined fermions depicted in Fig. 2.2. In particular, the ground state belongs to the configuration $\vec{n} = (2, 2, 0, \dots)$ and reads $|\text{GS}\rangle = \hat{a}_{1\downarrow}^\dagger \hat{a}_{1\uparrow}^\dagger \hat{a}_{0\downarrow}^\dagger \hat{a}_{0\uparrow}^\dagger |0\rangle$, where $\hat{a}_{i\alpha}^\dagger$ are the creation operators referring to the SPES of the harmonic oscillator potential. The ground state is unique (recall that $N_d = 2$) and possesses an energy of $E_{\text{GS}} = 4\hbar\omega$. The excited states with $S_z = 0$ can be obtained by applying the operators \hat{T}_{ij}^α and the energetically lowest ones correspond to $|\text{Ex}_\alpha\rangle = \hat{T}_{21}^\alpha |\text{GS}\rangle$, belonging to the $\vec{n} = (2, 1, 1, 0, \dots)$ configuration with energy $E_{\text{Ex}} = 5\hbar\omega$. Due to the presence of one doublon the eigenstates should be quadruply degenerate, with the other two states referring to $|\text{Ex}_{\uparrow\uparrow}\rangle = \hat{S}_+ \hat{T}_{21}^\uparrow |\text{GS}\rangle$ and $|\text{Ex}_{\downarrow\downarrow}\rangle = \hat{S}_+ \hat{T}_{21}^\downarrow |\text{GS}\rangle$. The quadruple degeneracy of this energy manifold can be verified by observing that two eigenenergy manifolds of $S = 0$ and $S = 1$ become degenerate for $g = 0$ and $E = 5\hbar\omega$ in Fig. 2.2. The degeneracy due to SPEE coincidence becomes apparent in the next manifold of degenerate states at $E_{\text{Ex}2} = 6\hbar\omega$. In this case there are three different configurations, namely the $\vec{n} = (2, 1, 0, 1, 0, \dots)$, $\vec{n} = (1, 2, 1, 0, \dots)$ and $\vec{n} = (2, 0, 2, 0, \dots)$ referring to the same energy, since $\epsilon_1 + \epsilon_3 = 2\epsilon_2 = 2\hbar\omega$, satisfying the condition of Eq. (2.42). Consequently, the degeneracy of this manifold is $4 + 4 + 1 = 9$, which can be verified by Fig. 2.2 by observing that three branches of the $S = 0$ eigenstates and two referring to the $S = 1$ ones become degenerate for $E = 6\hbar\omega$ and $g = 0$. These arguments can be applied to degenerate manifolds of increasing energy and thus generate the whole non-interacting eigenspectrum in terms of the SPES and SPEE.

Regarding the magnetic properties of non-interacting spin-1/2 Fermi gases we expect that since their many-body eigenspectrum is highly spin-independent their behaviour has to be paramagnetic [134]. However, their eigenstates are in general highly degenerate and therefore very susceptible to perturbations. There are also several hints that point towards the fact that interactions can modify the magnetic properties of Fermi gases. As mentioned previously the SU(2) symmetry of the interacting Hamiltonian refers to the invariance under rotations of the total spin of the system and not each individual particle. In contrast, the full Hamiltonian depends on the correlations between the spins of individual atoms, which are affected by modifying their individual spins. Another hint towards this direction is provided by the excitation operator \hat{T}_{ij}^α which does not commute with \hat{S}_+ , \hat{S}_- and \hat{S}^2 implying that the non-interacting eigenstates generated from $|\text{GS}_\alpha\rangle$, by applying \hat{T}_{ij}^α operators, might not be eigenstates of the interacting system $g \neq 0$, since in general they do not possess a well defined S

THEORETICAL FRAMEWORK

Term (\hat{H}_U)	Description	U	ΔE_0
$\hat{a}_{i\uparrow}^\dagger \hat{a}_{i\downarrow}^\dagger \hat{a}_{i\downarrow} \hat{a}_{i\uparrow}$	Interaction energy of a doublon	$\int dx \phi_i^4$	0
$\hat{a}_{i\uparrow}^\dagger \hat{a}_{j\downarrow}^\dagger \hat{a}_{j\downarrow} \hat{a}_{i\uparrow}, i \neq j$	Inter-SPES interaction energy	$\int dx \phi_i^2 \phi_j^2$	0
$\hat{a}_{i\uparrow}^\dagger \hat{a}_{j\downarrow}^\dagger \hat{a}_{i\downarrow} \hat{a}_{j\uparrow}, i \neq j$	Spin exchanging interaction	$\int dx \phi_i^2 \phi_j^2$	0
$\hat{a}_{i\uparrow}^\dagger \hat{a}_{i\downarrow}^\dagger \hat{a}_{j\downarrow} \hat{a}_{j\uparrow}, i \neq j$	Hopping of a doublon	$\int dx \phi_i^2 \phi_j^2$	$2(\epsilon_i - \epsilon_j)$
$\hat{a}_{i\uparrow}^\dagger \hat{a}_{k\downarrow}^\dagger \hat{a}_{k\downarrow} \hat{a}_{j\uparrow}, i \neq j$	Density-mediated hopping	$\int dx \phi_i \phi_j \phi_k^2$	$\epsilon_i - \epsilon_j$
$\hat{a}_{k\uparrow}^\dagger \hat{a}_{i\downarrow}^\dagger \hat{a}_{j\downarrow} \hat{a}_{k\uparrow}, i \neq j$	Spin-exchanging density-mediated hopping	$\int dx \phi_i \phi_j \phi_k^2$	$\epsilon_i - \epsilon_j$
$\hat{a}_{i\uparrow}^\dagger \hat{a}_{k\downarrow}^\dagger \hat{a}_{j\downarrow} \hat{a}_{k\uparrow}, i \neq j$	Creation of a doublon	$\int dx \phi_i \phi_j \phi_k^2$	$2\epsilon_k - (\epsilon_i + \epsilon_j)$
$\hat{a}_{i\uparrow}^\dagger \hat{a}_{j\downarrow}^\dagger \hat{a}_{k\downarrow} \hat{a}_{k\uparrow}, i \neq j$	Annihilation of a doublon	$\int dx \phi_i \phi_j \phi_k^2$	$(\epsilon_i + \epsilon_j) - 2\epsilon_k$
$\hat{a}_{i\uparrow}^\dagger \hat{a}_{j\downarrow}^\dagger \hat{a}_{k\downarrow} \hat{a}_{l\uparrow},$ $i, j, k, l \text{ distinct}$	Double hopping	$\int dx \phi_i \phi_j \phi_k \phi_l$	$\epsilon_i + \epsilon_j - \epsilon_k - \epsilon_l$

Table 2.1: Categorization of all interaction terms appearing in an 1D spin-1/2 Fermi gas. U indicates the coupling constant in terms of the overlaps of the SPES, $\phi_i(x)$. Here, the SPES are assumed real since a confined system is considered. ΔE_0 refers to the energy difference before and after the application of the interaction term to a many-body eigenstate for $g = 0$.

quantum number.

2.3.3 Magnetic properties of weakly interacting systems

In order to get a better understanding of the interacting system it is instructive to study the qualitative character of the different interaction terms that appear in the Hamiltonian of Eq. (2.39). These interaction terms can be categorized in ten classes according to their effect when applied to a $g = 0$ many-body eigenstate. This categorization is provided in Table 2.1. Particularly important are the terms that couple states being degenerate for $g = 0$, since they might lift the degeneracy between the involved states [K1, K2]. There are three classes of such terms possessing this property, which are identified in Table 2.1 since they possess $\Delta E_0 = 0$, where $\Delta E_0 = \langle \Psi | \hat{H}_U \hat{H}_0 \hat{H}_U | \Psi \rangle - \langle \Psi | \hat{H}_0 | \Psi \rangle$. Here, \hat{H}_U denotes the particular class of terms contributing to \hat{H}_I . The first such class corresponds to the doublon interaction energy terms

$$\hat{H}_U^{\text{doub}} = \sum_i g U_{iiii} \hat{a}_{i\uparrow}^\dagger \hat{a}_{i\downarrow}^\dagger \hat{a}_{i\downarrow} \hat{a}_{i\uparrow}. \quad (2.44)$$

They result in the linear increase of the energy with g of all states possessing doublons. Second, the inter-SPES interaction contributions

$$\hat{H}_U^{\text{inter}} = \sum_{i \neq j} g U_{ijji} \hat{a}_{i\uparrow}^\dagger \hat{a}_{j\downarrow}^\dagger \hat{a}_{j\downarrow} \hat{a}_{i\uparrow}, \quad (2.45)$$

which encode the interaction energy of two fermions with anti-oriented spins residing in different SPES. Finally, the spin exchange interaction terms

$$\hat{H}_U^{\text{exc}} = \sum_{i \neq j} g U_{ijij} \hat{a}_{i\uparrow}^\dagger \hat{a}_{j\downarrow}^\dagger \hat{a}_{i\downarrow} \hat{a}_{j\uparrow}, \quad (2.46)$$

allowing two fermions in different SPES to exchange their spin. Therefore, for small enough g we expect that the above mentioned terms described in Eq. (2.44), (2.45) and (2.46) contribute dominantly to the lifting of degeneracy between each degenerate manifold of states (see Ref. [K1, K2] and [135]). We can therefore justify for small g the approximation of the full-interaction term as [K2]

$$\hat{H}_I \approx \hat{H}_U^{\text{doub}} + \hat{H}_U^{\text{inter}} + \hat{H}_U^{\text{exc}} = g \left[\sum_i U_i \hat{n}_{i\uparrow} \hat{n}_{i\downarrow} - \sum_{j \neq i} J_{ij} \left(\hat{\mathbf{S}}_i \cdot \hat{\mathbf{S}}_j - \frac{1}{4} \hat{n}_i \hat{n}_j \right) \right], \quad (2.47)$$

with $U_i = \int dx \phi_i^4(x)$ and $J_{ij} = \int dx \phi_i^2(x) \phi_j^2(x)$. It can be seen that the approximation of Eq. (2.47) introduces ferromagnetic spin-exchange interactions for repulsively interacting Fermi gases ($g > 0$) between the different singly occupied SPES and accordingly anti-ferromagnetic spin-exchange interactions for attractively interacting fermions ($g < 0$). The above imply that indeed for non-zero interactions the few-body 1D Fermi gas exhibits non-trivial magnetic properties.

The approximate interaction term in Eq. (2.47) can be used within degenerate state first-order perturbation theory in order to lift the degeneracy of the eigenstates observed within the $g = 0$ case [135], [K1, K2]. In particular, notice that Eq. (2.47) conserves the spatial configuration in terms of \vec{n} of the non-interacting states and therefore allows for the decoupling of the spectrum of the 1D Fermi gas with respect to distinct \vec{n} . This decoupling leads to the mapping of the eigenstates of a configuration \vec{n} to a Heisenberg-type spin-chain Hamiltonian consisting of $N - 2N_d$ spins and incorporating long-range interactions [K1]. Notice that $J_{ij} > 0$ and accordingly a ferromagnetic (antiferromagnetic) ground state for each different \vec{n} spin-chain is ensured for $g > 0$ ($g < 0$) [107]. The only scaling of the terms in Eq. (2.47) with g at this limit is a homogeneous linear increase of the interaction strengths and accordingly we expect the eigenenergies to scale linearly within the $|g| \ll 1$ interaction regime.

The above mentioned expectation can be verified e.g. for $N = 4$ parabolically confined atoms shown in Fig. 2.2. In line with the above argumentation we observe that the eigenenergies increase linearly within $|g| < 1/2$. In particular, the slope of the eigenstates characterized by smaller $S = 0$ is larger than the corresponding ones for $S = 1$, with the states possessing $S = 2$ having a constant energy. This fact indicates

THEORETICAL FRAMEWORK

that the fermions behave ferromagnetically and antiferromagnetically for positive and negative interactions respectively, in accordance to the predictions of Eq. (2.47). Deviations from the magnetic order imposed by this approximate form of the interaction Hamiltonian seem to be insignificant except for the case of large interactions $g \gg 1$. Notice that the behaviour presented in Fig. 2.2 indicated that Eq. (2.47) can be applied to qualitatively obtain valid results within the $g \approx 1$ interaction regime, although the increase of the eigenenergies deviates from the predicted linear trend.

In particular, one of the main goals of the works [K1,K2] are to demonstrate that the approximation of Eq. (2.47) adequately describes and characterizes the magnetic properties of 1D spin-1/2 Fermi gases for weak and intermediate interactions. Additionally, Ref. [K1,K2] generalize Eq. (2.47) and extend its validity in the moderate interaction $g \approx \epsilon_{i+1} - \epsilon_i$ regime and in the case of broken SU(2) symmetry. At first glance, the approximation that Eq. (2.47) provides may seem *ad hoc*. Particularly, in the cases that the SPEE satisfy Eq. (2.42) or Eq. (2.43), for different i, j, k, l , there are additional degeneracies between states possessing different \vec{n} in the many-body eigen-spectrum for $g = 0$. These states can couple due to interactions involving doublon creation or annihilation or correlated double hopping, see also Table 2.1. However, detailed calculations in [K1,K2] and [135] demonstrate that the approximate form of Eq. (2.47) indeed provides the basic underlying framework for understanding the magnetic properties emanating in the excited states of the confined 1D Fermi gas.

Apart from the numerical evidence provided in the above mentioned works there are some qualitative arguments that support this behaviour. First, except for the harmonic oscillator case of equidistant SPEE, in general the energy differences between distinct SPEE are not equal and thus Eq. (2.42) and (2.43) are rarely satisfied, for very specific combinations of i, j, k, l , with these indices typically attaining quite different values. This in turn implies that the involved coupling strengths $U_{ijkk} = U_{kkij} = \int dx \phi_i(x)\phi_j(x)\phi_k^2(x)$ or $U_{ijkl} = \int dx \phi_i(x)\phi_j(x)\phi_k(x)\phi_l(x)$ are much smaller than the ones involved in Eq. (2.47) and thus coupling effects are negligible. Moreover, even in the case of a harmonic oscillator there is an additional symmetry at play, namely the separation of the relative and the center-of-mass coordinates, Eq. (2.37). The latter finally prohibits the above mentioned states to couple with one another. Note here that even when this symmetry is weakly broken, with the SPEE remaining roughly equidistant, Ref. [K1] reveals that effects beyond Eq. (2.47) remain negligible.

Although as mentioned above exact degeneracies in the SPEE are impossible in 1D setups [247], the double-well or the multi-well confinement provide examples of external potentials where quasi-degeneracies occur. In these cases the validity condition $|g| \ll \epsilon_{i+1} - \epsilon_i$ of Eq. (2.47) breaks down and one expects that it is inadequate for describing the magnetic properties of the system. However, in Ref. [K2], we show that a generalization of Eq. (2.47) that properly accounts for the magnetic mechanisms emanating in double-well confined fermionic ensembles is rather straightforward, with the system maintaining to a large degree its ferromagnetic correlations for repulsive interparticle interaction strengths, $g > 0$.

2.3.4 Strongly interacting 1D spin-1/2 fermions

In the strong interaction regime, namely $g \ll \epsilon_{i+1} - \epsilon_i$, the SPES are no longer an adequate basis for characterizing the interacting many-body eigenspectrum. Indeed, it is known that the diagonalization of the many-body Hamiltonian of Eq. (2.39) over a finite set of SPES leads to unphysical results as $g \rightarrow \infty$ [300]. The above demonstrate the large degree of interparticle correlations that is manifested for strong zero-range repulsions. An important step in understanding the behavior of spinor fermionic ensembles is the realization that in the limit of strong interactions $g \rightarrow \infty$ these systems constitute examples of Tonks-Girardeau gases.

The concept of a Tonks-Girardeau gas has been originally introduced in terms of an 1D infinitely repulsive gas of spinless bosons [301]. A Tonks-Girardeau gas behaves similarly to an ensemble of distinguishable impenetrable particles, but in addition, it satisfies the proper for the indistinguishable character of its constituents particle exchange properties. It is known [129, 302] that infinitely interacting spin-1/2 fermions form a Tonks-Girardeau gas and a convenient basis for examining their eigenspectrum can be constructed via employing a mapping to impenetrable particles. The magnetic properties of a spin-1/2 fermionic gas proximal to the Tonks-Girardeau regime are particularly interesting due to their involved underlying exchange statistics of the spatial and spin degrees of freedom. For this reason, the properties of the above mentioned fermionic systems (especially in the few-body regime) are well-studied, mostly by employing appropriate spin-chain models in the vicinity of the $g \rightarrow \infty$ limit, see Ref. [128–133] and Sec. 2.3.5. Below, we provide an outline for the construction of the many-body basis appropriate for the study of strongly interacting spin-1/2 fermions and provide an intuitive interpretation regarding the character of the involved states.

According to the Tonks-Girardeau framework for infinitely repulsive zero-range interactions the spin-1/2 fermions behave as a collection of impenetrable atoms. This implies that two fermions cannot reside at the same position and they cannot permeate one another since such a process involves the crossing of an interaction potential barrier of infinite amplitude, $V(x_i, x_j) \sim \lim_{g \rightarrow \infty} g\delta(x_i - x_j)$. However, the process of two fermions permeating one another cannot be formulated in a transparent and rigorous manner due to the wavefunction symmetrization properties of the many-body setup stemming from the fermionic nature of its constituents. To address this issue it is useful to study an analogous setup consisting of distinguishable impenetrable particles. The advantages of such a study are twofold. First, the distinguishable character of the particles allows for a straightforward description of the process where one particle permeates another. For instance, such a process can be characterized by the transfer of population from a configuration where $x_i < x_j$ for two particles labeled i and j to a configuration with $x_i > x_j$. Second, given the eigenspectrum of the setup involving distinguishable particles the eigenstates of the system consisting of indistinguishable particles but obeying the same Hamiltonian can be evaluated by taking into account the proper symmetrization of the many-body wavefunction. Notice that the above is true for any atomic species or mixture and not particularly for spinor fermions, showcasing the generality

THEORETICAL FRAMEWORK

of this approach. The Hamiltonian referring to distinguishable impenetrable particles is equivalent to a non-interacting one, see also Eq. (2.35), reading

$$\hat{H} = \sum_{i=1}^N \left[-\frac{\hbar^2}{2m} \frac{d^2}{dx_i^2} + V(x_i) \right], \quad (2.48)$$

with $V(x)$ the external potential and m the atomic mass. Also, hard-wall (Dirichlet) boundary conditions are incorporated for $x_i = x_j$ and $i \neq j \in \{1, \dots, N\}$. The description of the stationary properties of this system is more transparent because the ordering of the x_i coordinates of distinguishable particles is well-defined since the corresponding many-body wavefunction, $\Psi_d(x_1, x_2, \dots, x_N)$ does not involve the symmetrization of those coordinates. The ability to define the ordering of the x_i is particularly important since both the Hamiltonian and the boundary conditions are symmetric under any permutation of the particle indices, i.e. $x_1, x_2, \dots, x_N \rightarrow x_{P_i(1)}, x_{P_i(2)}, \dots, x_{P_i(N)}$, with $P_i(1), P_i(2), \dots, P_i(N)$ being the i -th permutation of the indices $1, 2, \dots, N$. This symmetry properties allows us to invoke the so-called sector wavefunctions for expressing the eigenstates of the gas of distinguishable atoms, $\Psi_d^{j,k}(x_1, x_2, \dots, x_N)$. In particular, the eigenstates of Eq. (2.48) read

$$\Psi_d^{j,k}(x_1, x_2, \dots, x_N) = \Psi_0^k(x_{P_j(1)}, x_{P_j(2)}, \dots, x_{P_j(N)}). \quad (2.49)$$

Here $\Psi_0^k(x_1, x_2, \dots, x_N)$, for $k = 1, 2, \dots$ refer to the sector wavefunctions, possessing the property $\Psi_0^k(x_1, x_2, \dots, x_N) \neq 0$ if $x_1 < x_2 < \dots < x_N$ and $\Psi_0^k(x_1, x_2, \dots, x_N) = 0$ otherwise. Note that the eigenstates $\Psi_d^{j,k}(x_1, x_2, \dots, x_N)$ with different $j = 1, 2, \dots, N!$, are degenerate since the Hamiltonian of Eq. (2.48) is invariant under any particle exchange. Accordingly, the energy of each eigenstate of Eq. (2.49) depends solely on k which refers to the appropriate sector wavefunction.

As it can be readily seen, in order to span the eigenspectrum of the impenetrable distinguishable particles we have to determine the sector wavefunctions $\Psi_0^k(x_1, x_2, \dots, x_N)$. This can be easily achieved by considering a spinless non-interacting Fermi gas. Indeed, this setup obeys the non-interacting Hamiltonian of Eq. (2.48) and in addition owing to the Pauli exclusion principle all of its eigenstates satisfy the Dirichlet boundary conditions, i.e. $\Psi_f^k(x_1, \dots, x_i, \dots, x_j = x_i, \dots, x_N) = 0$ for all $i \neq j \in \{1, 2, \dots, N\}$. Therefore, the eigenstates of spinless fermions can be viewed as a set of particular solutions for the eigenvalue problem defined by Eq. (2.48) when the appropriate boundary conditions are taken into account. Notice that the spinless fermion eigenstates additionally incorporate the proper antisymmetrization of the many-body wavefunction for the spatial coordinates of all fermions. This property implies that there is an one-to-one correspondence between spinless fermionic many-body eigenstates and sector wavefunctions, namely

$$\Psi_f^k(x_1, x_2, \dots, x_N) = \frac{1}{\sqrt{N!}} \sum_{i=1}^{N!} (-1)^{\text{sign} P_i} \Psi_0^k(x_{P_i(1)}, x_{P_i(2)}, \dots, x_{P_i(N)}), \quad (2.50)$$

where $\text{sign}P_i$ is the parity of the P_i permutation of the atomic indices. Notice that the many-body wavefunctions of the spinless Fermi gas are trivial to evaluate since they can be constructed in terms of the corresponding SPES via employing the Slater determinants

$$\Psi_f^{\vec{l}}(x_1, x_2, \dots, x_N) = \frac{1}{\sqrt{N!}} \sum_{i=1}^{N!} (-1)^{\text{sign}P_i} \phi_{l_1}(x_{P_i(1)}) \phi_{l_2}(x_{P_i(2)}) \dots \phi_{l_N}(x_{P_i(N)}). \quad (2.51)$$

In this expression, we have replaced the index k by the vector valued $\vec{l} = (l_1, l_2, \dots, l_N)$, with $l_1 < l_2 < \dots < l_N$, which contains the indices of the occupied SPES for the sake of clarity. Therefore, the different sector wavefunctions are obtained by inverting Eq. (2.50). This process yields

$$\Psi_0^{\vec{l}}(x_1, x_2, \dots, x_N) = \sqrt{N!} \theta(x_1, x_2, \dots, x_N) \Psi_f^{\vec{l}}(x_1, x_2, \dots, x_N), \quad (2.52)$$

where $\theta(x_1, x_2, \dots, x_N) = 1$ if $x_1 < x_2 < \dots < x_N$ and $\theta(x_1, x_2, \dots, x_N) = 0$ otherwise. Equations (2.49) and (2.52), define the many-body eigenbasis of distinguishable particles that diagonalizes the Hamiltonian of Eq. (2.48) and satisfies the appropriate boundary conditions. In particular, the eigenspectrum consists of distinct degenerate manifolds of dimension $N!$ referring to the distinct particle orderings but the same sector wavefunction. The energy of each degenerate manifold is $E = \sum_{i=1}^N \epsilon_i$, where ϵ_i refers to the i -th lowest SPEE of the single-particle Hamiltonian.

The crucial point that relates the eigenstates of the distinguishable atoms to the corresponding ones for spin-1/2 fermions is that the Hamiltonian of the latter for $g \rightarrow \infty$ is equivalent to the one of Eq. (2.48). Accordingly, in order to extract the eigenspectrum of a spin-1/2 Fermi gas we have to impose the appropriate, for this case, particle exchange properties of the many-body wavefunction. In particular, for a given spin-configuration the proper linear combinations of the eigenstates of the distinguishable system $\Psi_d^{j,k}(x_1, x_2, \dots, x_N)$ can be evaluated so that the total wavefunction possesses the appropriate for spin-1/2 fermions particle exchange symmetry.

The above imply that in order to span the eigenbasis of impenetrable spin-1/2 fermions we can focus only on the spatial- and spin-configuration for $x_1 < x_2 < \dots < x_N$. Notice that, for a given state of a particular sector the state of all other sectors is fixed due to the total antisymmetry of the fermionic wavefunction. Therefore, the only degrees-of-freedom available to the system is first the choice of the sector wavefunction, which determines the energy of the eigenstate, and second the choice of the spin-configuration. By taking into account the above the eigenbasis of the system can be written in a compact form in the second quantization picture

$$|\vec{l}; \vec{\alpha}\rangle = \sqrt{N!} \int d^N x \theta(x_1, \dots, x_N) \Psi_f^{\vec{l}}(x_1, \dots, x_N) \hat{\psi}_{\alpha_1}^\dagger(x_1) \dots \hat{\psi}_{\alpha_N}^\dagger(x_N) |0\rangle, \quad (2.53)$$

where $\alpha = (\alpha_1, \alpha_2, \dots, \alpha_N)$, with $\alpha_i = \{\uparrow, \downarrow\}$. It can be verified that the above mentioned states are orthonormal, i.e. $\langle \vec{l}; \vec{\alpha} | \vec{l}'; \vec{\alpha}' \rangle = \delta_{\vec{l}\vec{l}'} \delta_{\vec{\alpha}\vec{\alpha}'}$. Furthermore, their energy

THEORETICAL FRAMEWORK

depends only on the spatial configuration \vec{l} , $E\{|\vec{l}; \vec{\alpha}\rangle\} = \sum_{i=1}^N \epsilon_i$, similarly to the distinguishable case for $g \rightarrow \infty$, implying that the eigenstates are arranged in degenerate manifolds of dimension of 2^N , referring in this case to the different available spin-configurations.

Let us now elaborate on the physical meaning of Eq. (2.53). First, note that in general the ordering of indistinguishable particles is meaningless due to the (anti)symmetry of the many-body wavefunction under particle exchange. However, the states defined by Eq. (2.53) are special since the particles are sequentially created such that their positions satisfy $x_1 < x_2 < \dots < x_N$ and in addition each created particle, e.g. at $x = x_i$, possesses a well-defined spin, here α_i . The eigenstates $|\vec{l}; \vec{\alpha}\rangle$ are addressable by *in situ* images of the atomic density that provide simultaneous spatial and spin resolution. Indeed, if we order the imaged particles according to their position in the image, with $i = 1$ being the leftmost and $i = N$ being the rightmost one, we know that for $|\vec{l}; \vec{\alpha}\rangle$ the probability that the i -th particle possesses spin α_i is equal to unity. Furthermore, the probability to find an i -th particle at a certain position is given by

$$\rho_i(x) = N! \int d^N x \delta(x - x_i) \theta(x_1, x_2, \dots, x_N) |\Psi_{\vec{l}}^{\vec{\alpha}}(x_1, x_2, \dots, x_N)|^2. \quad (2.54)$$

The above imply that the particles constituting the states $|\vec{l}; \vec{\alpha}\rangle$ are spatially ordered in a well-defined and experimentally detectable manner despite the fact that the involved particles are indistinguishable.

Note here that the above mentioned degree of degeneracy of the states $|\vec{l}; \vec{\alpha}\rangle$ is much larger than the one expected just by considering the symmetries of the system at finite interaction strength, Eq. (2.35). In analogy to the $g = 0$ case, for infinite interactions $g \rightarrow \infty$ the energy of the system is invariant under the spin-flip of any individual particle and accordingly the system behaves paramagnetically. This invariance does not hold for finite interaction strengths. As already mentioned, in this case the involved interaction depends on the spin-spin correlations of each particle pair, which are modified by the spin-flip of individual fermions. Therefore, we expect that for strong but not infinite interactions, such that $0 < 1/|g| \ll 1$, the eigenstates $|\vec{l}; \vec{\alpha}\rangle$ with the same \vec{l} but different $\vec{\alpha}$, couple leading to the lifting of their degeneracy and importantly giving also rise to non-trivial magnetic properties.

2.3.5 Spin-chain models for strongly interacting 1D systems

A. Derivation of the spin-chain model

In order to evaluate the spectral properties of spin-1/2 fermions in the strongly interaction regime degenerate perturbation theory for small $1/g$ is employed [128–133]. Let us define a Taylor expansion of the Hamiltonian \hat{H} for small $1/g$ [129]

$$\hat{H}(1/g) = \lim_{1/g \rightarrow 0} \hat{H} + \frac{1}{g} \lim_{1/g \rightarrow 0} \frac{d\hat{H}}{d(1/g)} + \dots = \lim_{1/g \rightarrow 0} \hat{H} - \frac{1}{g} \lim_{1/g \rightarrow 0} \left(g^2 \frac{d\hat{H}}{dg} \right) + \dots \quad (2.55)$$

Consequently, the perturbation operator reads

$$\hat{H}_{\text{pert}} = - \lim_{1/g \rightarrow 0} g^2 \int dx \hat{\psi}_{\uparrow}^{\dagger}(x) \hat{\psi}_{\downarrow}^{\dagger}(x) \hat{\psi}_{\downarrow}(x) \hat{\psi}_{\uparrow}(x). \quad (2.56)$$

A major problem in this perturbative formulation is that all matrix elements of the perturbation operator $\langle \vec{l}; \vec{\alpha} | \hat{H}_{\text{pert}} | \vec{l}; \vec{\alpha}' \rangle = 0$ vanish when expressed in the Tonks-Girardeau basis, $|\vec{l}; \vec{\alpha}'\rangle$, since within each of the corresponding basis states it is impossible to have two particles at exactly the same position. To rectify this problem we assume that we can form sector wavefunctions that approach asymptotically the proper ones in the Tonks-Girardeau limit, i.e. $\tilde{\Psi}_0^k(x_1, \dots, x_N) \rightarrow \Psi_0^k(x_1, \dots, x_N)$ for $g \rightarrow \infty$, and additionally satisfy the Bethe-Peierls [303] boundary conditions

$$\left. \frac{\partial \tilde{\Psi}_0^k(x_1, \dots, x_N)}{\partial(x_i - x_j)} \right|_{x_i \rightarrow x_j^+} - \left. \frac{\partial \tilde{\Psi}_0^k(x_1, \dots, x_N)}{\partial(x_i - x_j)} \right|_{x_i \rightarrow x_j^-} = \frac{2mg}{\hbar^2} \tilde{\Psi}_0^k(x_1, \dots, x_N) \Big|_{x_i = x_j}, \quad (2.57)$$

for all $i \neq j \in \{1, 2, \dots, N\}$. These boundary conditions can be justified by considering that the Hamiltonian \hat{H} instead of defining a many-body system of 1D particles, corresponds to a single-particle Hamiltonian in N -dimensions. In this picture each interaction term $g\delta(x_i - x_j)$ corresponds to a delta-barrier along the hypersurface $x_i = x_j$ of the N -dimensional space. From elementary quantum-mechanics [247] it is well-known that such a delta barrier results to a discontinuity in the first derivative of the wavefunction at its position which is proportional to the barrier strength. Then, the wavefunction amplitude leads to the expression of Eq. (2.57). Notice that crossing a barrier implies that the fictitious N -dimensional particle tunnels from a region characterized by $x_i > x_j$ to one corresponding to $x_i < x_j$ and therefore during tunnelling the particle ordering changes. Of course, in the many-body picture this tunneling process corresponds to two particles tunneling through one another. Therefore, we can interpret the fact that the matrix elements $\langle \vec{l}; \vec{\alpha} | \hat{H}_{\text{pert}} | \vec{l}; \vec{\alpha}' \rangle = 0$ vanish as a manifestation of the impenetrable nature of the particles in the $g \rightarrow \infty$ limit. However, in the actual physical case the particles are impenetrable only asymptotically. In this sense, there is always a probability that the particles tunnel through one another which tends to vanish as $g \rightarrow \infty$. The above implies that in order to obtain non-trivial results, the matrix elements of \hat{H}_{pert} need to be calculated in the case that the particles are not impenetrable and afterwards the impenetrable limit, $g \rightarrow \infty$ should be taken.

To this end, let us assume that the eigenfunctions close to $1/g = 0$ read

$$|\tilde{\Psi}; \vec{l}, \vec{\alpha}\rangle = \int d^N x \sqrt{N!} \tilde{\theta}(x_1, \dots, x_N) \tilde{\Psi}_0^{\vec{l}}(x_1, \dots, x_N) \hat{\psi}_{\alpha_1}^{\dagger}(x_1) \dots \hat{\psi}_{\alpha_N}^{\dagger}(x_N) |0\rangle, \quad (2.58)$$

where $\tilde{\theta}(x_1, \dots, x_N) = 1$ for $x_1 \leq x_2 \leq \dots \leq x_N$ and $\tilde{\theta}(x_1, \dots, x_N) = 0$ otherwise.

THEORETICAL FRAMEWORK

Then, the involved matrix elements read as follows

$$\begin{aligned}
\langle \tilde{\Psi}; \vec{l}, \vec{\alpha} | \hat{H}_{\text{pert}} | \tilde{\Psi}; \vec{l}, \vec{\alpha}' \rangle = & \\
-g^2 N! \sum_{i=1}^{N-1} \left[\prod_{j=1}^{i-1} \delta_{\alpha_j \alpha'_j} \right] \left[\prod_{j=i+2}^N \delta_{\alpha_j \alpha'_j} \right] & \left(\delta_{\alpha_i \alpha'_i} \delta_{\alpha_{i+1} \alpha'_{i+1}} - \delta_{\alpha_i \alpha'_{i+1}} \delta_{\alpha_{i+1} \alpha'_i} \right) \\
\times \int \sum_{i=1}^{N-1} dx_j dx & \prod_{j=i+2}^N dx_j \tilde{\theta}(x_1, \dots, x_i = x, x_{i+1} = x, \dots, x_N) \\
& \times |\tilde{\Psi}_0^{\vec{l}}(x_1, \dots, x_i = x, x_{i+1} = x, \dots, x_N)|^2.
\end{aligned} \tag{2.59}$$

Moreover, the term $|\tilde{\Psi}_0^{\vec{l}}(x_1, \dots, x_i = x, x_{i+1} = x, \dots, x_N)|^2$ can be substituted by employing the boundary condition

$$\begin{aligned}
|\tilde{\Psi}_0^{\vec{l}}(x_1, \dots, x_i = x, x_{i+1} = x, \dots, x_N)|^2 = & \\
\frac{\hbar^4}{4m^2 g^2} \left| \lim_{x_i \rightarrow x_{i+1}^-} \left(\frac{\partial \tilde{\Psi}_0^k(x_1, \dots, x_N)}{\partial x_i} - \frac{\partial \tilde{\Psi}_0^k(x_1, \dots, x_N)}{\partial x_{i+1}} \right) \right. & \\
\left. - \lim_{x_i \rightarrow x_{i+1}^+} \left(\frac{\partial \tilde{\Psi}_0^k(x_1, \dots, x_N)}{\partial x_i} - \frac{\partial \tilde{\Psi}_0^k(x_1, \dots, x_N)}{\partial x_{i+1}} \right) \right|^2. &
\end{aligned} \tag{2.60}$$

This equation becomes greatly simplified when the limit $g \rightarrow \infty$ is applied. First, the second limit vanishes as $\tilde{\Psi}_0^{\vec{l}}(x_1, \dots, x_N) \rightarrow \Psi_0^{\vec{l}}(x_1, \dots, x_N) = 0$ for $x_i > x_{i+1}$. Second, the derivative of $\Psi_0^{\vec{l}}(x_1, \dots, x_N)$ along the barrier has to vanish since the amplitude of the wavefunction tends to zero at each individual point along its extent for $g \rightarrow \infty$. Therefore, it holds

$$\frac{\partial \tilde{\Psi}_0^k(x_1, \dots, x_N)}{\partial (x_i + x_{i+1})} = 0 \Rightarrow \frac{\partial \tilde{\Psi}_0^k(x_1, \dots, x_N)}{\partial x_i} = -\frac{\partial \tilde{\Psi}_0^k(x_1, \dots, x_N)}{\partial x_{i+1}}. \tag{2.61}$$

By employing Eq. (2.60) and (2.61) the matrix elements of Eq. (2.59) acquire the simplified form

$$\begin{aligned}
\langle \tilde{\Psi}; \vec{l}, \vec{\alpha} | \hat{H}_{\text{pert}} | \tilde{\Psi}; \vec{l}, \vec{\alpha}' \rangle = - \sum_{i=1}^{N-1} \frac{J_i^{\vec{l}}}{4} \left[\prod_{j=1}^{i-1} \delta_{\alpha_j \alpha'_j} \right] \left[\prod_{j=i+2}^N \delta_{\alpha_j \alpha'_j} \right] & \\
\times \left[\sigma_{\alpha_i \alpha'_i} \cdot \sigma_{\alpha_{i+1} \alpha'_{i+1}} - \delta_{\alpha_i \alpha'_i} \delta_{\alpha_{i+1} \alpha'_{i+1}} \right], &
\end{aligned} \tag{2.62}$$

where $\sigma_{\alpha\alpha'}$ is the Pauli vector and the property of the Pauli matrices $\sigma_{\alpha\beta} \cdot \sigma_{\gamma\delta} = 2\delta_{\alpha\delta}\delta_{\beta\gamma} - \delta_{\alpha\beta}\delta_{\gamma\delta}$ was employed. The coupling parameters $J_i^{\vec{l}}$ read

$$J_i^{\vec{l}} = \frac{2\hbar^4 N!}{m^2} \int d^N x \delta(x_i - x_{i+1}) \tilde{\theta}(x_1, \dots, x_N) \left| \frac{\partial \tilde{\Psi}_0^{\vec{l}}(x_1, \dots, x_N)}{\partial x_i} \right|^2. \tag{2.63}$$

These are obviously positive, i.e. $J_i^{\vec{l}} > 0$. Eq. (2.62) reveals that the spin of each particle spin experiences an effective antiferromagnetic interaction with its “nearest neighbour”. This effect becomes more evident by relating the above mentioned matrix elements with the corresponding ones emanating in an antiferromagnetic Heisenberg spin-chain model with nearest neighbor interactions, namely

$$\langle \vec{\Psi}; \vec{l}, \vec{\alpha} | \hat{H}_{\text{pert}} | \vec{\Psi}; \vec{l}, \vec{\alpha}' \rangle = \langle \vec{\alpha} | \sum_{i=1}^{N-1} J_i^{\vec{l}} \left(\hat{\mathbf{S}}_i \cdot \hat{\mathbf{S}}_{i+1} - \frac{1}{4} \right) | \vec{\alpha}' \rangle, \quad (2.64)$$

here $|\vec{\alpha}\rangle = |\alpha_1\rangle \otimes |\alpha_2\rangle \otimes \cdots \otimes |\alpha_N\rangle$ refer to the states of a spin-chain consisting of N localized spin-1/2 particles and $\hat{\mathbf{S}}_i$ being the corresponding spin-operators acting on the i -th spin.

Let us now elaborate on the physical meaning of Eq. (2.64). First, note that in general the ordering of indistinguishable particles is meaningless due to the (anti)symmetry of the many-body wavefunction under particle exchange. However, the states defined by Eq. (2.58) are special since the particles are sequentially created such that their spatial positions satisfy $x_1 < x_2 < \cdots < x_N$ and in addition each created particle, e.g. at $x = x_i$, possesses a well-defined spin, here α_i . This in turn implies that if all N particles in the state $|\vec{l}, \vec{\alpha}\rangle$ are imaged in a spatially and spin-resolved manner, then their spin-configuration when reading the spin of each particle from the left ($x \rightarrow -\infty$) to the right ($x \rightarrow +\infty$) will yield $\alpha = (\alpha_1, \alpha_2, \dots, \alpha_N)$ with probability equal to 1. In this way, the spin of the particles constituting the states $|\vec{l}, \vec{\alpha}\rangle$ is spatially ordered in a well defined manner. Therefore, a well-posed question is to ask what is the probability for strongly interacting atoms initialized in a particular spin-configuration $\vec{\alpha}$ to reach a different configuration $\vec{\alpha}'$ after some time t . The answer is given by the time-evolution of the effective spin-system described by Eq. (2.64). Particularly, it states that the dynamics of the spin degree of freedom of strongly interacting fermions is equivalent to the one described by a Heisenberg spin chain of N localized spins experiencing inhomogeneous interactions given by $2J_i^{\vec{l}}/g$. Similarly, one can map the strongly-interacting eigenstates to the stationary states of the spin-chain model of Eq. (2.64). By paraphrasing Ref. [129] we can argue that Eq. (2.64) provides a realization of quantum magnetism of localized spins without the need to localize the atoms via the use of external potentials.

B. Relation of the strongly-interacting eigenstates and the corresponding spin-chain model

The analysis of the eigenspectrum of $N = 4$ parabolically confined interacting particles agrees to a large degree with the findings presented above, see Fig. 2.2. In particular it can be seen that the eigenenergies increase proportionally to $\propto 1/g$ as the strong interaction regime is approached for $g > 4$. To get a better appreciation for the eigenstates in this strong interaction regime Fig. 2.3 provides several observables relevant for the characterization of all states within the lowest in energy manifold with $n_{\text{CM}} = 0$, in the case of $N_{\uparrow} = N_{\downarrow} = 2$. Recall, that the states with different value of S_z can

THEORETICAL FRAMEWORK

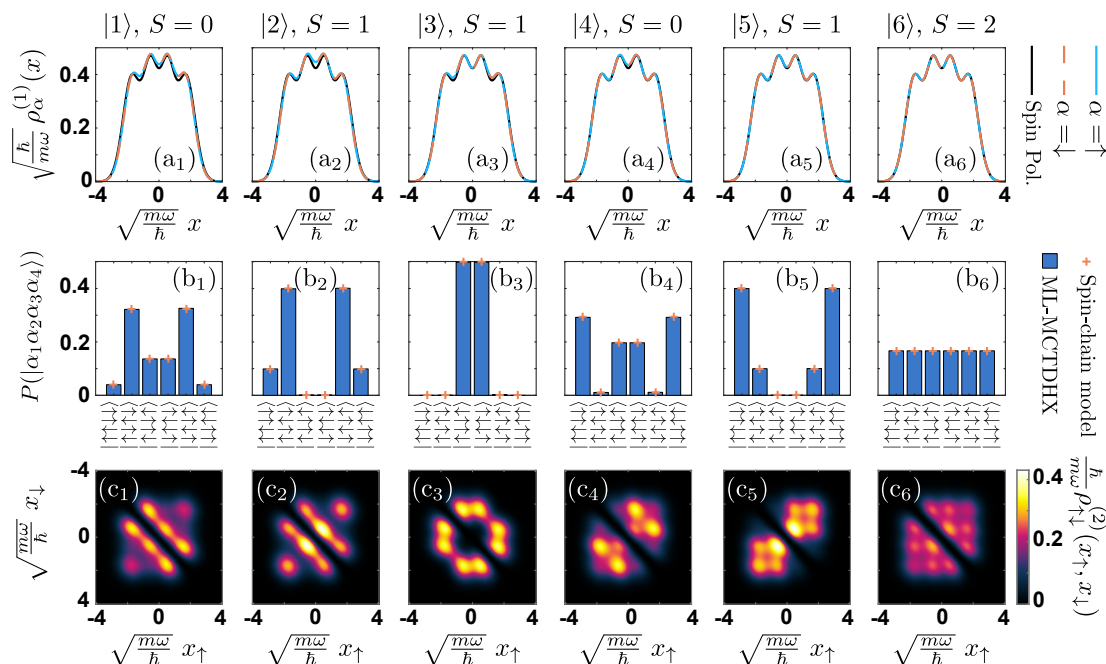


Figure 2.3: (a₁)–(a₆) Spin-resolved one-body densities, $\rho_\alpha^{(1)}(x)$, $\alpha \in \{\uparrow, \downarrow\}$, (b₁)–(b₆) Spatially resolved spin-configuration probabilities, $P(|\alpha_1\alpha_2\alpha_3\alpha_4\rangle)$ (see text) and (c₁)–(c₆) interspecies two-body densities, $\rho_{\uparrow\downarrow}^{(2)}(x_\uparrow, x_\downarrow)$, for the lowest six eigenstates, $|i\rangle$, $i = 1, \dots, 6$, of the Hamiltonian \hat{H} [Eq. (2.35)]. In all cases $N_\uparrow = N_\downarrow = 2$ and $1/g = 0.06$. For comparison, (a₁)–(a₆) also incorporate the one-body density for the ground state of a spin-polarized system with $N = 4$ (rescaled by a factor of 1/2 to compensate for the increased N). The histograms of (b₁)–(b₆) result from the sampling over 1000 simulated single-shot images of the ML-MCTDHX obtained eigenstates.

be constructed in terms of these $S_z = 0$ states by employing the spin-raising, \hat{S}_+ , or spin-lowering, \hat{S}_- operators.

Figure 2.3 (a₁)–(a₆) presents the one-body densities, $\rho_\alpha^{(1)}(x) = \langle i | \hat{\psi}_\alpha^\dagger(x) \hat{\psi}_\alpha(x) | i \rangle$, corresponding to the lowest 6 eigenstates, $|i\rangle$, $i = 1, \dots, 6$ of the Hamiltonian of Eq. (2.35) within the strong interaction regime, $g = (0.06)^{-1} \approx 16.7$. Importantly, these density distributions are almost completely equivalent for all distinct eigenstates. This is in agreement, to our discussion in Sec. 2.3.4. Indeed, the spatial degrees-of-freedom of the low-lying eigenstates of a strongly interacting system are expected to be characterized in terms of the lowest in energy sector wavefunction, $\Psi_0^l(x_1, \dots, x_N)$ [Eq. (2.52)]. In particular, we observe that the density distributions are proximal to the corresponding one for $N = 4$ spin-polarized Fermions in line to our argumentation in Sec. 2.3.4. This pronounced agreement motivates that the different eigenstates of the system can be characterized in terms of the different occupied spin states. However, such a characterization is not possible on the level of single-particle density, since the

corresponding distributions for spin- \uparrow and spin- \downarrow fermions lie perfectly on top of one another. This is a result of the reflection symmetry of the spin with respect to the xy spin-plane holding within the $N_\uparrow = N_\downarrow = 2$ configuration⁵, implying that the exchange of spin- \uparrow atoms with spin- \downarrow ones does not affect the state of the system.

To characterize the different spin-states contributing to each eigenstate, $|i\rangle$, we employ the spatially resolved spin-configuration probability, $P(|\alpha_1\alpha_2\dots\alpha_N\rangle)$, see Fig. 2.3(b₁)–(b₆). This observable probes the spatial ordering of the fermionic spins in a particular configuration $|\alpha_1\alpha_2\dots\alpha_N\rangle$. This configuration can be revealed by spin and spatial resolved imaging. In this case, the leftmost particle would be found in the spin-state α_1 , the one to its right would be in the α_2 state and so on, see also Sec. 2.3.5A. In terms of the spin-chain model of Eq. (2.64), $P(|\alpha_1\alpha_2\dots\alpha_N\rangle) = \sum_{\vec{l}} |\langle \tilde{\Psi}, \vec{l}, (\alpha_1\alpha_2\dots\alpha_N) | i \rangle|^2$. In the Tonks-Girardeau limit there is almost only one occupied spatial configuration, $\vec{l} = (0, 1, 2, \dots, N)$ (Sec. 2.3.4), which corresponds to the lowest in energy sector wavefunction and thus the spatially resolved spin-configuration probability, $P(|\alpha_1\alpha_2\dots\alpha_N\rangle)$, directly probes the many-body state of the system. To obtain $P(|\alpha_1\alpha_2\alpha_3\alpha_4\rangle)$ we simulate single-shot images via Monte-Carlo sampling (for details see Ref. [210, 304, 305] and [K1]) of the $N_\uparrow + N_\downarrow$ -body density distribution, $\hat{\rho}^{(N_\uparrow+N_\downarrow)} = |i\rangle\langle i|$, obtained within ML-MCTDHX. Then we identify the corresponding spatial configuration $|\alpha_1\alpha_2\alpha_3\alpha_4\rangle$ for each image and finally we make a histogram over a set of single-shot simulations (here we employ a set size of 1000 images for each distinct $|i\rangle$), obtaining in this way an estimation for $P(|\alpha_1\alpha_2\alpha_3\alpha_4\rangle)$. Notice that single-atom resolution for few-fermion systems is now possible by spatially-resolved fluorescence imaging [306–308] rendering this observable also experimentally accessible. Focussing on the ML-MCTDHX data [see the histograms in Fig. 2.3(b₁)–(b₆)] it is evident that the distinct eigenstates of the system, $|i\rangle$ possess radically different $P(|\alpha_1\alpha_2\dots\alpha_N\rangle)$, thus indicating the different spin-order in each of these states. In addition the prediction for $P(|\alpha_1\alpha_2\alpha_3\alpha_4\rangle)$ within the spin-chain model of Eq. (2.64) given by the crosses in Fig. 2.3(b₁)–(b₆) captures very well the spin-order emanating within our *ab initio* ML-MCTDHX calculations, revealing its validity within this strong interaction regime.

The magnetic properties in this regime, despite not being easily identifiable within the level of single-particle densities, can crucially affect the correlations emanating in the system. To highlight this point we present the intercomponent two-body densities $\rho_{\uparrow\downarrow}^{(2)}(x_\uparrow, x_\downarrow) = \langle i | \hat{\psi}_\uparrow^\dagger(x_\uparrow) \hat{\psi}_\downarrow^\dagger(x_\downarrow) \hat{\psi}_\downarrow(x_\downarrow) \hat{\psi}_\uparrow(x_\uparrow) | i \rangle$ for the eigenstates $|i\rangle$, $i = 1, \dots, 6$ in Fig. 2.3(b₁)–(b₆). The two-body densities for different eigenstates are prominently different. In particular, their shape reflects the dominant spin-configuration for each eigenstate. This is more evident for the eigenstates with $S = 1$, $|2\rangle$, $|3\rangle$ and $|5\rangle$ where the dominant states are the Neel $|\uparrow\downarrow\uparrow\downarrow\rangle$ ($|\downarrow\uparrow\downarrow\uparrow\rangle$), core-shell domain wall $|\uparrow\downarrow\uparrow\downarrow\rangle$ ($|\downarrow\uparrow\uparrow\downarrow\rangle$) and single domain-wall $|\uparrow\uparrow\downarrow\downarrow\rangle$ ($|\downarrow\downarrow\uparrow\uparrow\rangle$) states respectively. Indeed, in these cases the two-body densities prominently feature the corresponding correlation patterns. For instance, in Fig. 2.3(b₃) we can see that the two-body density possesses non zero values only in the case that $|x_\uparrow| \gtrsim 1 \gtrsim |x_\downarrow|$ or $|x_\downarrow| \gtrsim 1 \gtrsim |x_\uparrow|$, indicating the presence of two domain-

⁵Note that this property is independent of the total particle number $N = N_\uparrow + N_\downarrow$ and holds for all $S_z = \frac{N_\uparrow - N_\downarrow}{2} = 0$ configurations.

walls among the spin-components at $x \approx \pm 1$. Similarly, in Fig. 2.3(b₅) the presence of a single domain-wall at $x = 0$ results in the two-body density being non-zero only for $x_{\uparrow}x_{\downarrow} < 0$. Overall this example $N = 4$ -body system showcases that, despite the fact that the single-particle distribution of a strongly interacting spin-1/2 gas is largely fixed to the distribution of a spin-polarized gas, the correlations are very sensitive to variations of the magnetic order emerging in the system. The magnetic properties are, in turn, dictated by the presence of antiferromagnetic effective spin-spin interactions captured by the spin-chain model of Eq. (2.64).

C. Origin of the spin-spin interactions

Finally, let us examine on the origin of mechanism that generates the effective spin-spin interactions for strongly interacting spin-1/2 Fermi gases. According to Sec. 2.3.5 the spin-exchange mechanism at play refers to two fermions transmitting through one another, a process which is possible for $1/g > 0$. This process possesses spin-dependence as two fermions with the same spin are impenetrable due to the Pauli exclusion principle and have to backscatter even for finite $g > 0$ while two atoms with opposite spin can transmit through one another. This in turn implies that “adjacent” fermions possessing opposite spin have a lower kinetic energy since they are less confined than in the case of particles occupying the same spin-state. This naturally leads to the emergence of effective antiferromagnetic interactions for repulsive interparticle coupling strengths. Although, not clearly stated in the ultracold-atom literature this process can be related to the well-known phenomenon of the Anderson kinetic exchange interaction [142], emanating for lattice trapped systems. Indeed, Anderson has shown [142] that for a lattice of unit filling, $n_e = 1$, and repulsive interactions the spin of the fermions occupying each lattice site experiences antiferromagnetic interactions with a coupling strength $J = 4t^2/U$, where t is the hopping parameter and U the onsite interaction. Ogata and Shiba [309] generalized this result to finite filling factors, $n_e \in [0, 2]$

$$J(n_e) = \frac{4t^2}{U} n_e \left(1 - \frac{\sin(2\pi n_e)}{2\pi n_e} \right). \quad (2.65)$$

The effective coupling $J(n_e)$ decreases from the value $J(n_e = 1) = 4t^2/U$, for $n_e < 1$, due to the fact that the fermions are not necessarily nearest neighboring as the lattice filling decreases. Therefore, the kinetic energy benefit of antiferromagnetic spin-spin correlations is significantly decreased. Finally, Matveev [310] used this result to calculate the spin-exchange coupling for zero-range strongly interacting particles in the case of $V(x) = 0$ by extrapolating the result of Eq. (2.65) to vanishing lattice length $\alpha \rightarrow 0$ and relating the Hubbard parameters to the corresponding ones of a continuum system as $t = \hbar^2/(2ma^2)$, $U = g/a$ and $n_e = na$, where n is the density. As a result, the following couplings were obtained

$$J[V(x) = 0] = \frac{2\pi^2}{3} \frac{\hbar^4 n^3}{m^2 g}. \quad (2.66)$$

The comparison of Eq. (2.66) with the corresponding one for the parabolically confined case by employing Eq. (2.63) was performed within the Local Density and Thomas-Fermi approximations in Ref. [129] demonstrating excellent agreement of the order of 1% for as low as $N = 6$ particles. This last proof of Ref. [129] demonstrates that the antiferromagnetic character of the spin-chain model of Eq. (2.64) is a direct manifestation of the Anderson kinetic exchange [142]. In our studies [K1, K2] we show that the influence of this interaction is also significant for weak and intermediate interactions and its interplay with the ferromagnetic Hund interactions [139–141], stemming from the weak coupling expansion of Eq. (2.47), gives rise to the intriguing magnetic properties emanating in the latter interaction regimes.

2.4 Bose and Fermi polarons

2.4.1 The Fröhlich Hamiltonian

The Bose polaron problem originated from Landau's prediction of an electron being self trapped in the polarization field it induces to its surrounding crystal [148]. Although, Pekar was the first to develop a model to describe this quasi-particle in the strong coupling limit [149, 150], Fröhlich was the first to develop a *phenomenological* Hamiltonian for the description of this phenomenon in both the weak and the strong interaction limits [152]. The idea of Fröhlich was that the polarization field of a crystal can be described by two contributions, $\mathbf{P}(\mathbf{r}) = \mathbf{P}_{\text{IR}}(\mathbf{r}) + \mathbf{P}_{\text{UV}}(\mathbf{r})$, with $\mathbf{P}_{\text{IR}}(\mathbf{r})$ stemming from the deformation of the crystal and $\mathbf{P}_{\text{UV}}(\mathbf{r})$ referring to the induced polarization of the ionic electron clouds. The crucial observation is that both of these modes can be described by classical oscillator models [219] since $\mathbf{P}_{\text{IR}}(\mathbf{r})$ is related to lattice vibrations and $\mathbf{P}_{\text{UV}}(\mathbf{r})$ to the Lorentz oscillator discussed in section 2.1.2. Therefore, he concluded that the equations of motion of these polarization contributions read

$$\begin{aligned} \ddot{\mathbf{P}}_{\text{IR}}(\mathbf{r}, t) + \omega_{\text{IR}}^2 \mathbf{P}_{\text{IR}}(\mathbf{r}, t) &= \overbrace{\frac{\omega_{\text{IR}}^2}{4\pi} \left(\frac{1}{\epsilon_{\infty}} - \frac{1}{\epsilon_0} \right)}^{\equiv 1/\gamma_{\text{IR}}} \mathbf{D}(\mathbf{r}; \mathbf{r}_{\text{el}}(t)), \\ \ddot{\mathbf{P}}_{\text{UV}}(\mathbf{r}, t) + \omega_{\text{UV}}^2 \mathbf{P}_{\text{UV}}(\mathbf{r}, t) &= \overbrace{\frac{\omega_{\text{UV}}^2}{4\pi} \left(1 - \frac{1}{\epsilon_{\infty}} \right)}^{\equiv 1/\gamma_{\text{UV}}} \mathbf{D}(\mathbf{r}; \mathbf{r}_{\text{el}}(t)), \end{aligned} \quad (2.67)$$

where $\mathbf{D}(\mathbf{r}; \mathbf{r}_{\text{el}}(t))$ is the electrical displacement created by the moving electron, ω_{IR} , ω_{UV} are the frequencies of the corresponding oscillators and ϵ_0 , ϵ_{∞} are the static and high-frequency dielectric constants of the material. Notice here that all quantities are measured in cgs units as is customary done in condensed-matter literature. The factors γ_{IR} and γ_{UV} in the right hand side of Eq. (2.67) stem from the requirement that within linear response $\mathbf{P}(\mathbf{r}) = (\epsilon(\omega) - 1)/(4\pi)\mathbf{E}(\mathbf{r})$ and $\mathbf{D}(\mathbf{r}) = \epsilon(\omega)\mathbf{E}(\mathbf{r})$ for both $\omega \rightarrow 0$ and $\omega \rightarrow \infty$ limits. In addition, $\mathbf{P}_{\text{IR}}(\mathbf{r}) = \mathbf{0}$ for $\omega \rightarrow \infty$ was employed, occurring due to the large mass of the ions when compared to the electrons which also implies $\omega_{\text{IR}} \ll \omega_{\text{UV}}$.

THEORETICAL FRAMEWORK

The corresponding equation of motion for the electron is simply $\dot{\mathbf{p}}_{\text{el}}(t) = -4\pi e\mathbf{P}(\mathbf{r}, t)$. The above permit the derivation of the classical Hamiltonian describing the coupling of the electron to the induced polarization field

$$H = \frac{\mathbf{p}_{\text{el}}^2}{2m_e} + \int d^3r \left\{ \frac{\gamma_{\text{IR}}}{2} \left[\dot{\mathbf{P}}_{\text{IR}}^2(\mathbf{r}, t) + \omega_{\text{IR}}^2 \mathbf{P}_{\text{IR}}(\mathbf{r}, t) \right] - \mathbf{D}(\mathbf{r}; \mathbf{r}_{\text{el}}(t)) \cdot \mathbf{P}_{\text{IR}}(\mathbf{r}, t) \right\} \\ + \int d^3r \left\{ \frac{\gamma_{\text{UV}}}{2} \left[\dot{\mathbf{P}}_{\text{UV}}^2(\mathbf{r}, t) + \omega_{\text{UV}}^2 \mathbf{P}_{\text{UV}}(\mathbf{r}, t) \right] - \mathbf{D}(\mathbf{r}; \mathbf{r}_{\text{el}}(t)) \cdot \mathbf{P}_{\text{UV}}(\mathbf{r}, t) \right\}. \quad (2.68)$$

A further assumption in deriving the Fröhlich Hamiltonian is that the electron is slow moving. This has two important consequences, first the magnetic field generated by the motion of the electron can be ignored resulting to an electric displacement that follows the Maxwell equations $\nabla \cdot \mathbf{D}(\mathbf{r}; \mathbf{r}_{\text{el}}) = 4\pi e\delta(\mathbf{r} - \mathbf{r}_{\text{el}})$ and $\nabla \times \mathbf{D}(\mathbf{r}; \mathbf{r}_{\text{el}}) = \mathbf{0}$. With the latter further implying that $\nabla \times \mathbf{P}(\mathbf{r}; t) = \mathbf{0}$ due to the linear response of the material. Consequently, a polarization potential $\Phi_P(\mathbf{r}; t) = -4\pi \int \mathbf{P}(\mathbf{r}; t) \cdot d\mathbf{r}$ can be defined. In addition, the part of the Hamiltonian referring to $\mathbf{P}_{\text{UV}}(\mathbf{r}, t)$ can be thought to contribute a constant shift of the energy since for a slow a moving electron, $\mathbf{P}_{\text{UV}}(\mathbf{r}, t)$ can follow its motion adiabatically, i.e. $\ddot{\mathbf{P}}_{\text{UV}}(\mathbf{r}; t) = \mathbf{0}$, and thus contributes as time-independent potential in the frame of reference of the electron $\Phi_{\text{UV}}(\mathbf{r} - \mathbf{r}_{\text{el}}) \approx -e^2(1 - 1/\epsilon_\infty)/|\mathbf{r} - \mathbf{r}_{\text{el}}|$. With these assumptions the potential $\Phi_{\text{IR}}(\mathbf{r}; t)$ can be evaluated. Subsequently the classical Hamiltonian of Eq. (2.68) can be quantized by imposing the quantization rules $[\mathbf{e}_\mu \cdot \hat{\mathbf{r}}_{\text{el}}, \mathbf{e}_\nu \cdot \hat{\mathbf{p}}_{\text{el}}] = i\hbar\delta_{\mu\nu}$ and $[\mathbf{e}_\mu \cdot \hat{\mathbf{P}}_{\text{IR}}, \mathbf{e}_\nu \cdot \gamma_{\text{IR}}(d\hat{\mathbf{P}}_{\text{IR}}/dt)] = i\hbar\delta_{\mu\nu}$, with $\mathbf{e}_\mu, \mathbf{e}_\nu$ denoting the unit vectors and $\mu, \nu = \{x, y, z\}$.

The final form of the Fröhlich Hamiltonian reads

$$\hat{H} = \frac{\hat{\mathbf{p}}_{\text{el}}^2}{2m_e} + \hbar\omega_{\text{IR}} \sum_{\mathbf{q}} \left(\hat{b}_{\mathbf{q}}^\dagger \hat{b}_{\mathbf{q}} + \frac{1}{2} \right) + i\hbar\omega_{\text{IR}} \sqrt{\frac{4\pi\alpha}{\ell_{\text{IR}}^{-1}V}} \sum_{\mathbf{q}} \frac{1}{q} \left(\hat{b}_{\mathbf{q}}^\dagger e^{-i\mathbf{q} \cdot \hat{\mathbf{r}}_{\text{el}}} - \hat{b}_{\mathbf{q}} e^{i\mathbf{q} \cdot \hat{\mathbf{r}}_{\text{el}}} \right), \quad (2.69)$$

where $\alpha = \frac{2\pi e^2 \ell_{\text{IR}}^{-1}}{\hbar\gamma_{\text{IR}}\omega_{\text{IR}}^3}$ is the dimensionless interaction parameter of the electron with the polarization field and $\ell_{\text{IR}} = \sqrt{\hbar/(2m_e\omega_{\text{IR}})}$ is the characteristic length scale for the motion of the electron. The ladder operators $\hat{b}_{\mathbf{q}}^\dagger, \hat{b}_{\mathbf{q}}$ correspond to the creation and annihilation operators respectively of the field $\hat{\mathbf{P}}_{\text{IR}}(\mathbf{r}) = [\hbar/(2\gamma_{\text{IR}}\omega_{\text{IR}})]^{1/2}[\hat{\mathbf{B}}(\mathbf{r}) + \hat{\mathbf{B}}^\dagger(\mathbf{r})]$ expressed in momentum space coordinates. The corresponding real space field operators are given by $\hat{\mathbf{B}}(\mathbf{r}) = \sum_{\mathbf{q}} \frac{\mathbf{q}/q}{\sqrt{V}} \hat{b}_{\mathbf{q}} e^{i\mathbf{q} \cdot \mathbf{r}}$ and the Hermitian conjugate expression for $\hat{\mathbf{B}}^\dagger(\mathbf{r})$.

The Fröhlich Hamiltonian permits solutions for weak coupling strength α , via second-order Reileigh-Schrödinger perturbation theory [247], which correspond to the so-called Fröhlich polaron, with energy $E_{\text{Fr}} = -\alpha\hbar\omega_{\text{IR}}$ and effective mass $m^* = (1 + \alpha/6)m_e$. In addition, the Fröhlich Hamiltonian also captures the solution in the high energy limit that was attributed to Pekar. Indeed, the variationally optimized approximation of the total state of the system by a tensor product of the states of the electron and the polarization field, $|\Psi\rangle = |\Psi_{\text{el}}\rangle \otimes |\Psi_P\rangle$, yields a polaron energy $E_{\text{Pe}} = -25/256\alpha^2$ and an effective mass $m^* = 0.02\alpha^4 m_e$. Based on the above mentioned energy estimates the crossover among the two polaronic behaviours was estimated at around $\alpha \approx 10$. To bridge the crossover among the two polaronic theories

Feynman devised a variational method based on the path integral approach [160] which is able to correctly predict the properties of the polaron for all α . The accuracy of the Feynman path integral method has been numerically verified by several quantum Monte Carlo techniques [311–314] and also experimentally by measurements of the electron mobility in semiconductors [315, 316].

Before proceeding to the study of the ultracold atom analogue of the polaron let us note that the phenomenological Hamiltonian of Eq. (2.69), is supported by *ab initio* methods and it is relevant for qualitative and sometimes quantitative calculations for polar semiconductors [161]. In particular, by using the local density approximation [317] within the framework of the density functional theory [318, 319] the electron Hamiltonian in the presence of electron-phonon coupling reads

$$\begin{aligned} \hat{H} = & \sum_{\mathbf{q},n,s} E_{\mathbf{q},n,s} \hat{c}_{\mathbf{q},n,s}^\dagger \hat{c}_{\mathbf{q},n,s} + \sum_{\mathbf{q},\nu} \omega_{\mathbf{q},\nu} \hat{b}_{\mathbf{q},\nu}^\dagger \hat{b}_{\mathbf{q},\nu} + \sum_{\mathbf{q}} V(\mathbf{q}) \hat{\rho}_{\mathbf{q}}^\dagger \hat{\rho}_{\mathbf{q}} \\ & + \frac{1}{\sqrt{2N}} \sum_{\mathbf{q},\mathbf{q}',n,n',s} \omega_{\mathbf{q},\nu} \left[\gamma_{n,n'}(\mathbf{q}, \mathbf{q}', \nu) \hat{c}_{\mathbf{q}',n',s}^\dagger \hat{c}_{\mathbf{q}-\mathbf{q},n,s} \hat{b}_{\mathbf{q},\nu} + h.c. \right], \end{aligned} \quad (2.70)$$

where $\hat{c}_{\mathbf{q},n,s}^\dagger$ ($\hat{c}_{\mathbf{q},n,s}$) and $\hat{b}_{\mathbf{q},\nu}^\dagger$ ($\hat{b}_{\mathbf{q},\nu}$) refer to the electron and phonon creation (annihilation) operators respectively. Furthermore, $E_{\mathbf{q},n,s}$ is the dispersion relation of electrons in the band n with spin $s \in \{\uparrow, \downarrow\}$, $\omega_{\mathbf{q},\nu}$ is the dispersion relation of phonons in the mode ν , $V(\mathbf{q})$ are the electron-electron interaction integrals and $\hat{\rho}_{\mathbf{q}} = \sum_{\mathbf{q}',n,s} \hat{c}_{\mathbf{q},n,s}^\dagger \hat{c}_{\mathbf{q},n,s}$ is the electron density fluctuation operator. Finally, $\gamma_{n,n'}(\mathbf{q}, \mathbf{q}', \nu)$ refer to the electron-phonon coupling matrix elements. In principle, there exist also electron-phonon coupling terms that are of quadratic or higher-order in the phonon operators, however, they are small and relevant only if the phonons are not coupled by the linear electron-phonon interaction contained in Eq. (2.70) [161]. Electron-doped polar semiconductors, such as n-GaAs, involve only a small number of electrons in their conduction band acting as carriers. For this reason their conduction properties do not depend largely on the details regarding their lattice structure since only electrons of quasimomentum $q \ll \pi/a$, where a is the lattice spacing, are relevant. This allows in principle for approximations that neglect the influence of the ionic potential such as Eq. (2.69) for the study of their properties. According to [161] the matrix elements of the electron-phonon coupling can be approximated by single-band models as $\gamma_{n,n'}(\mathbf{q}, \mathbf{q}', \nu) \approx \gamma(\mathbf{q})$, except from the case that the orbitals n and n' are degenerate. Within these approximations $\gamma(\mathbf{q})$ is sensitive on the type of phonons that are coupled to the motion of electrons. For polar semiconductors, such as GaAs, it turns out that the matrix element scales as $\gamma(\mathbf{q}) \propto 1/|\mathbf{q}|$ in the low q limit for optical phonons ($\omega_{\mathbf{q},\nu} = \omega_0$ for $q \rightarrow 0$) which are coupled with the electrons via polar interactions. Accordingly, the Fröhlich model is indeed realized in these systems. Notice that except from the case of the large polaron examined here, different polaron models, such as the small polaron model attributed to Holstein [172, 173], can be realized by considering the coupling of electrons with phonons of a different character.

2.4.2 Impurities in a weakly interacting Bose gas

The starting point for the derivation of an analogous polaron model to Eq. (2.69) applicable in ultracold experiments [179] is the Hamiltonian of a two component mixture [see also Eq. (2.8) and Eq. (2.19)] in the absence of external confining potential

$$\begin{aligned} \hat{H} = & \int d^d r \hat{\Psi}_B^\dagger(\mathbf{r}) \left[-\frac{\hbar^2}{2m_B} \nabla^2 + \frac{g_{BB}}{2} \hat{\Psi}_B^\dagger(\mathbf{r}) \hat{\Psi}_B(\mathbf{r}) \right] \hat{\Psi}_B(\mathbf{r}) \\ & + \int d^d r \hat{\Psi}_I^\dagger(\mathbf{r}) \left[-\frac{\hbar^2}{2m_I} \nabla^2 + g_{BI} \hat{\Psi}_B^\dagger(\mathbf{r}) \hat{\Psi}_B(\mathbf{r}) \right] \hat{\Psi}_I(\mathbf{r}), \end{aligned} \quad (2.71)$$

with $\Psi_\sigma(\mathbf{r})$ referring to the creation operators of the $\sigma = B$ bath and $\sigma = I$ impurity species with masses m_B and m_I respectively. The interaction strengths are parametrized by g_{BB} for the intraspecies interactions of the bath and g_{BI} corresponds to the interspecies interaction strength. The relation between these interaction strengths and the corresponding scattering lengths a_{BB} and a_{BI} depends on the number of spatial dimensions d . Notice here that the density operator of the bath $\hat{\psi}_B^\dagger(\mathbf{x})\hat{\psi}_B(\mathbf{x})$ acts as a matter-wave potential for the impurities a fact that will be of relevance later on [see Eq. (2.75) and Sec. 2.4.4].

The definition of a BEC implies that the $\mathbf{q} = \mathbf{0}$ mode of the bath species is predominantly occupied by $N_c \approx N_B$ atoms. This enables us to simplify the Hamiltonian of Eq. (2.71) by expressing the bath field operators in momentum space as $\hat{\Psi}_B(\mathbf{r}) = L^{-d/2}[\hat{\psi}_{\mathbf{q}=\mathbf{0}} + \sum_{\mathbf{q} \neq \mathbf{0}} \exp(i\mathbf{q} \cdot \mathbf{r})\hat{\psi}_{\mathbf{q}}]$ and approximating $\hat{\psi}_{\mathbf{q}=\mathbf{0}}^\dagger = \hat{\psi}_{\mathbf{q}=\mathbf{0}} = \sqrt{N_B} \approx \sqrt{N_c}$ since $N_B \approx N_c \gg 1$ is assumed. This replacement gives a hierarchy to the intraspecies interaction terms of the bath appearing in Eq. (2.71). Indeed, the BEC self-interaction term $\propto \hat{\psi}_{\mathbf{q}=\mathbf{0}}^\dagger \hat{\psi}_{\mathbf{q}=\mathbf{0}}^\dagger \hat{\psi}_{\mathbf{q}=\mathbf{0}} \hat{\psi}_{\mathbf{q}=\mathbf{0}}$ is quartic in $\hat{\psi}_{\mathbf{q}=\mathbf{0}}$ and accordingly scales with $g_{BB}N_B^2$, similarly quadratic terms scale like $g_{BB}N_B$, linear ones according to $g_{BB}N_B^{1/2}$ and terms with no $\hat{\psi}_{\mathbf{q}=\mathbf{0}}$ scale with g_{BB} . The thermodynamic limit is defined as the limit where $g_{BB} \rightarrow 0$ and $N_B \rightarrow \infty$ such as $g_{BB}N_B = \text{constant}$, implying that only the quartic and quadratic terms are relevant in this limit. Indeed, the approximation where the linear and constant terms in $\hat{\psi}_{\mathbf{q}=\mathbf{0}}$ are dropped consists the so-called Bogoliubov approximation [23]. Within this approximation the bath Hamiltonian reads

$$\hat{H}_B^{\text{Bog}} = E_0 + \sum_{\mathbf{q} \neq \mathbf{0}} \frac{\hbar^2 \mathbf{q}^2}{2m_B} \hat{\psi}_{\mathbf{q}}^\dagger \hat{\psi}_{\mathbf{q}} + \frac{g_{BB}n}{2} \sum_{\mathbf{q} \neq \mathbf{0}} \left(2\hat{\psi}_{\mathbf{q}}^\dagger \hat{\psi}_{\mathbf{q}} + \hat{\psi}_{\mathbf{q}}^\dagger \hat{\psi}_{\mathbf{q}}^\dagger + \hat{\psi}_{\mathbf{q}} \hat{\psi}_{\mathbf{q}} \right), \quad (2.72)$$

where $E_0 = g_{BB}nN_B/2 + \sum_{\mathbf{q}=\mathbf{0}} m_B(g_{BB}n)^2/(2q^2)$ is a constant energy shift, and $n = N_B/V$ is the density of the bath atoms. The Hamiltonian \hat{H}_B^{Bog} is quadratic in $\hat{\psi}_{\mathbf{q}}$ and accordingly it can be diagonalized via the Bogoliubov transformation defined by $\hat{\psi}_{\mathbf{q}} = u_{\mathbf{q}}\hat{b}_{\mathbf{q}} + v_{-\mathbf{q}}^*\hat{b}_{-\mathbf{q}}^\dagger$ and $\hat{\psi}_{\mathbf{q}}^\dagger = v_{-\mathbf{q}}\hat{b}_{-\mathbf{q}} + u_{\mathbf{q}}^*\hat{b}_{\mathbf{q}}^\dagger$, with

$$u_{\mathbf{q}} = \frac{1}{\sqrt{2}} \sqrt{\frac{1 + \xi^2 q^2}{\xi q \sqrt{2 + \xi^2 q^2}}} + 1, \quad v_{\mathbf{q}} = -\frac{1}{\sqrt{2}} \sqrt{\frac{1 + \xi^2 q^2}{\xi q \sqrt{2 + \xi^2 q^2}}} - 1, \quad (2.73)$$

while $\xi = \hbar(2m_B g_{BBn})^{-1/2}$ denotes the healing length. Notice that u_q and v_q depend solely on the amplitude of the wavenumber $|q|$, when compared to $1/\xi$. Finally, the Hamiltonian of Bogoliubov phonons reads

$$\hat{H}_B^{\text{Bog}} = E'_0 + \sum_{\mathbf{q} \neq \mathbf{0}} \underbrace{\hbar c |\mathbf{q}| \sqrt{1 + \frac{\xi^2 q^2}{2}}}_{\equiv \omega_{\mathbf{q}}} \hat{b}_{\mathbf{q}}^\dagger \hat{b}_{\mathbf{q}}, \quad (2.74)$$

with $c = \sqrt{g_{BBn}/m_B}$ and $E'_0 = E_0 - 1/2 \sum_{\mathbf{q} \neq \mathbf{0}} (\hbar^2 q^2 / (2m_B) + g_{BBn} - \hbar \omega_{\mathbf{q}})$. The Bogoliubov dispersion relation exhibits an interplay in its character for different values of $|q|$. For $q \ll 1/\xi$ the dispersion is proximal to acoustic phonons, namely $\omega_{\mathbf{q}} \approx c|q|$, while for $q \gg 1/\xi$ the dispersion becomes particle-like, i.e. $\omega_{\mathbf{q}} \approx \hbar^2 q^2 / (2m_B) + m_B c^2$. Importantly, in the latter limit ($q \gg 1/\xi$) the phonon operators are also particle-like $\hat{b}_{\mathbf{q}} \approx \hat{\psi}_{\mathbf{q}}$, $\hat{b}_{\mathbf{q}}^\dagger \approx \hat{\psi}_{\mathbf{q}}^\dagger$.

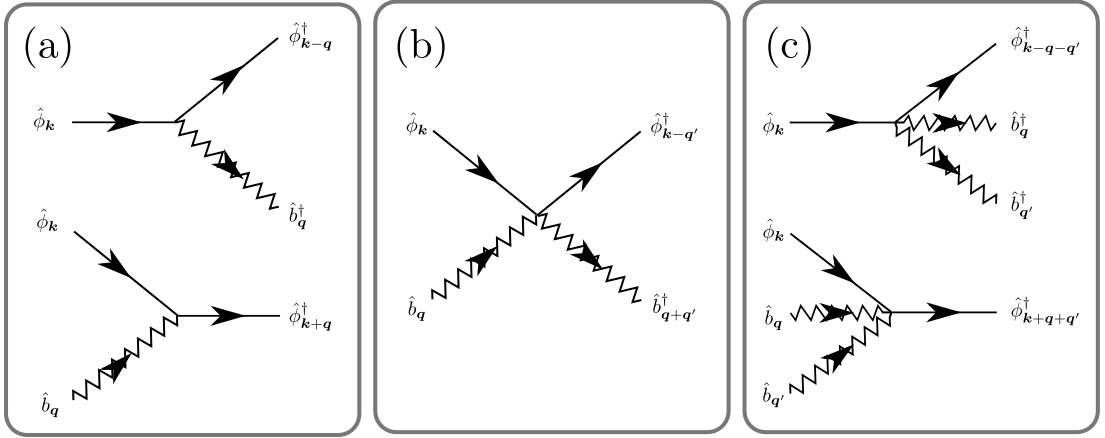


Figure 2.4: Feynman diagrams of the phonon-impurity interaction terms (interaction vertices) involved within the Bogoliubov approximation. (a) Three point vertex corresponding to the emission (top) an absorption (bottom) of a phonon by the impurity. (b) Four point vertex corresponding to elastic scattering of the impurity with a phonon and (c) four point vertex corresponding to the simultaneous absorption or emission of two phonons by the impurity.

The creation or annihilation of Bogoliubov phonons affects the density of the bath and accordingly it leads to the modification of the matter-wave potential that affects the impurity see Eq. (2.71). It is therefore instructive to express the bath density operator

in terms of the Bogoliubov phonon creation and annihilation operators yielding

$$\begin{aligned}
\hat{\Psi}_B^\dagger(x)\hat{\Psi}_B(x) &= n + \frac{\sqrt{N_B}}{L^d} \sum_{\mathbf{q}} \left(e^{i\mathbf{q}\cdot\mathbf{r}} \hat{\psi}_{\mathbf{q}} + e^{-i\mathbf{q}\cdot\mathbf{r}} \hat{\psi}_{\mathbf{q}}^\dagger \right) + \frac{1}{L^d} \sum_{\mathbf{q},\mathbf{q}'} e^{-i(\mathbf{q}'-\mathbf{q})\cdot\mathbf{r}} \hat{\psi}_{\mathbf{q}'}^\dagger \hat{\psi}_{\mathbf{q}} \\
&= n + \frac{\sqrt{N_B}}{L^d} \sum_{\mathbf{q}} e^{i\mathbf{q}\cdot\mathbf{r}} \left[(u_{\mathbf{q}} + v_{\mathbf{q}}) \hat{b}_{\mathbf{q}} + (u_{-\mathbf{q}}^* + v_{-\mathbf{q}}^*) \hat{b}_{-\mathbf{q}}^\dagger \right] \\
&+ \frac{1}{L^d} \sum_{\mathbf{q},\mathbf{q}'} e^{-i(\mathbf{q}'-\mathbf{q})\cdot\mathbf{r}} \left[(u_{\mathbf{q}'}^* u_{\mathbf{q}} + v_{\mathbf{q}'}^* v_{\mathbf{q}}) \hat{b}_{\mathbf{q}'}^\dagger \hat{b}_{\mathbf{q}} + v_{-\mathbf{q}'} u_{\mathbf{q}} \hat{b}_{-\mathbf{q}'} \hat{b}_{\mathbf{q}} \right. \\
&\quad \left. + u_{\mathbf{q}'}^* v_{-\mathbf{q}'}^* \hat{b}_{\mathbf{q}'}^\dagger \hat{b}_{-\mathbf{q}}^\dagger \right].
\end{aligned} \tag{2.75}$$

Therefore, within the Bogoliubov approximation the interaction of the impurity with the atoms involves four different processes, with their relative prominence scaled by the bath density n and the healing length ξ . First, the homogeneous density of the condensed bath atoms shifts the energy of the system by an amount given by $g_{BI}n$. Second, the impurity can change its momentum by creating $\propto \hat{\phi}_{\mathbf{k}-\mathbf{q}}^\dagger \hat{b}_{\mathbf{q}}^\dagger \hat{\phi}_{\mathbf{k}}$ or absorbing a phonon $\propto \hat{\phi}_{\mathbf{k}+\mathbf{q}}^\dagger \hat{b}_{\mathbf{q}} \hat{\phi}_{\mathbf{k}}$, here $\hat{\phi}_{\mathbf{k}}$ are the field operators for the impurity. A sketch of these processes in terms of Feynman diagrams is given in Fig. 2.4(a). Note that the characteristic energy scale of such events is given by $\sim E_{\text{pI}} = g_{BI} \sqrt{n \xi^{-d}}$. Finally, there are additional terms describing the elastic scattering of impurities with the phonons of the BEC $\propto \hat{\phi}_{\mathbf{k}-\mathbf{q}'}^\dagger \hat{b}_{\mathbf{q}+\mathbf{q}'}^\dagger \hat{b}_{\mathbf{q}} \hat{\phi}_{\mathbf{k}}$ [see Fig. 2.4(b)] or the simultaneous creation $\propto \hat{\phi}_{\mathbf{k}-\mathbf{q}'-\mathbf{q}'}^\dagger \hat{b}_{\mathbf{q}'}^\dagger \hat{b}_{\mathbf{q}}^\dagger \hat{\phi}_{\mathbf{k}}$ or absorption $\propto \hat{\phi}_{\mathbf{k}+\mathbf{q}'+\mathbf{q}'}^\dagger \hat{b}_{\mathbf{q}'} \hat{b}_{\mathbf{q}} \hat{\phi}_{\mathbf{k}}$ of two phonons by the impurity [see Fig. 2.4(c)]. The energy scale of the latter quartic terms is of the order of $\sim E_{\text{pI4}} = g_{BI} \xi^{-d}$. Similarly to Sec. 2.4.1 the Bogoliubov-Fröhlich Hamiltonian results by neglecting the above mentioned quartic terms [see Fig. 2.4(b), 2.4(c)] involving two phonon operators. Within these approximations the Bogoliubov-Fröhlich Hamiltonian reads

$$\hat{H}^{BF} = \frac{\hat{p}_I^2}{2m_I} + \frac{1}{L^d} \sum_{\mathbf{q}} \left[\hbar\omega_{\mathbf{q}} \hat{b}_{\mathbf{q}}^\dagger \hat{b}_{\mathbf{q}} + V_{\mathbf{q}} e^{i\mathbf{q}\cdot\hat{\mathbf{r}}_I} (\hat{b}_{\mathbf{q}} + \hat{b}_{-\mathbf{q}}^\dagger) \right], \tag{2.76}$$

where $V_{\mathbf{q}} = g_{BI} \sqrt{n} \left(\frac{\xi^2 q^2}{2 + \xi^2 q^2} \right)^{1/4}$ refers to the $|\mathbf{q}|$ -dependent matrix elements of the impurity-phonon coupling and the Hamiltonian terms that contribute as shifts of the total energy are dropped. The fact that the quartic terms are neglected limits the regime of applicability of Eq. (2.76) to small g_{BI} such as $E_{\text{pI4}}/E_{\text{p}} \ll 1 \Rightarrow g_{BI} \ll \hbar c \xi^2$, where $E_{\text{p}} = \hbar c / \xi$ is the characteristic energy scale of the phonons. Notice here that except from the coupling strength of the impurity phonon coupling, $\alpha = \alpha_{BI}^2 / (\alpha_{BB} \xi) \sim (E_{\text{pI2}}/E_{\text{p}})^2$, the mass imbalance of the bath and impurity atoms m_B/m_I provides a second independent dimensionless parameter of the Bogoliubov-Fröhlich Hamiltonian giving rise to a more complex phase diagram than in the condensed matter case of Eq. (2.69).

To comprehend the interplay of these two parameters it is helpful to transform H^{BF} to the frame comoving with the polaron. This is achieved via the Lee-Low-Pines

unitary transformation [320–322] $\hat{U}_{LLP} = \exp(i \hat{\mathbf{r}}_I \cdot \sum_{\mathbf{q}} \mathbf{q} \hat{b}_{\mathbf{q}}^{\dagger} \hat{b}_{\mathbf{q}})$ yielding

$$\hat{H}^{LLP} = g_{BI}n + \frac{1}{L^d} \sum_{\mathbf{q}} \left[\omega_{\mathbf{q}} \hat{b}_{\mathbf{q}}^{\dagger} \hat{b}_{\mathbf{q}} + V_{\mathbf{q}} (\hat{b}_{\mathbf{q}} + \hat{b}_{-\mathbf{q}}^{\dagger}) \right] + \frac{1}{2m_I} \left(\hat{\mathbf{p}}_I - \sum_{\mathbf{q}} \hbar \mathbf{q} \hat{b}_{\mathbf{q}}^{\dagger} \hat{b}_{\mathbf{q}} \right)^2. \quad (2.77)$$

First, notice that $[\hat{\mathbf{p}}_I, \hat{H}^{LLP}] = 0$ and accordingly in this frame of reference the momentum of the impurity is a constant of motion. In particular, the last term contains a contribution that is quartic in the Bogoliubov phonon operators and thus introduces an effective phonon-phonon interaction. The energy scale of the system is fixed by the energy of phonons $\hbar c/\xi = \sqrt{2}g_{BB}n$ and the impurity phonon interaction scales with $\alpha \propto g_{BI}^2$ which can be tuned by g_{BI} . Consequently, the value of m_B/m_I controls the induced phonon-phonon interaction strength. Therefore, the ultracold environment allows for the systematic study of effects stemming from the Bose polaron mobility by employing impurities of different masses m_I and the phonon-impurity coupling which is tunable by Fano-Feshbach resonances that affect g_{BI} . Notice that the above are in direct contrast to the small polaron model of Eq. (2.69) discussed in Sec. 2.4.1 where the mobility of the polaron is essentially fixed by the phonon frequency as the kinetic energy of electrons is $E_K \sim \hbar^2/(2m_e \ell_{\text{IR}}) = \hbar \omega_{\text{IR}}$.

2.4.3 The phase-diagram of Bose polarons

As it was made evident in the previous section the behaviour of Bose-polarons depends on two aspects, namely, the polaron mobility and the phonon-impurity coupling which can be controlled independently [178]. This fact results to a richer phase diagram for the Bose polarons than their equivalent in condensed matter systems. To work out the corresponding phases it is important to understand how the weak (Fröhlich polaron [152]) and strong (Pekar polaron [149–151]) regimes identified for the case of the polarons in semiconductors (see Sec. 2.4.1) translate in the case of ultracold bosons.

In the particular case of $m_I \rightarrow \infty$ the Hamiltonian in the frame co-moving with the polaron, \hat{H}^{LLP} [see Eq. (2.77)], becomes quadratic and can be solved exactly by employing a displacement operator, $|\Psi\rangle = \exp[\sum_{\mathbf{q}} a_{\mathbf{q}}^*(\alpha) \hat{b}_{\mathbf{q}} - a_{\mathbf{q}}(\alpha) \hat{b}_{\mathbf{q}}^{\dagger}] |\Psi_{\text{BEC}}\rangle \otimes |\mathbf{p}_I\rangle$ [178, 323]. The state $|\Psi_{\text{BEC}}\rangle$ corresponds to the state of the bath in the absence of phonons, i.e. $\hat{b}_{\mathbf{q}} |\Psi_{\text{BEC}}\rangle = 0$ for all \mathbf{q} , and $|\mathbf{p}_I\rangle$ is the state of the impurity at a particular polaron momentum \mathbf{p}_I . This implies a finite and α -dependent number of phonons, $\langle \Psi | \hat{b}_{\mathbf{q}}^{\dagger} \hat{b}_{\mathbf{q}} | \Psi \rangle = |a_{\mathbf{q}}(\alpha)|^2/2$, in the ground state of the polaron and accordingly a well-defined polaron in the heavy impurity limit. By decreasing m_I/m_B induced phonon-phonon interactions are introduced, see Eq. (2.77), and the system is not exactly solvable by the above approach. Assuming that the influence of the mobility is small m_I/m_B a mean-field theory can be established based on a displacement operator ansatz similar to the solution for $m_I \rightarrow 0$ for the coupled state of phonons and impurity. The results of this mean-field theory are to lowest order consistent with the ones stemming from perturbation theory for small α and finite m_I [178]. Accordingly, the polaron that is described by this mean-field approach is the ultracold analogue of the Fröhlich

THEORETICAL FRAMEWORK

polaron emanating in condensed matter systems. The regime of applicability of the Lee-Low-Pines mean field theory defines the weak coupling regime of the Bogoliubov-Fröhlich model.

Similarly to the Pekar polaron [149–151] the strong coupling limit of the Bogoliubov-Fröhlich model corresponds to the regime where the impurity becomes self-localized due to its large interaction with the bath phonons [180]. The state of the system in this limit is described by a product ansatz wavefunction $|\Psi_{pI}\rangle = |\Psi_p\rangle \otimes |\Psi_I\rangle$ but expressed in terms of real space coordinates. The strong coupling wavefunction is a good approximation of the system in the case of large effective masses, implying $\alpha \ll 1$ and $m_I/m_B \ll 1$ since in this case the impurity evolves almost adiabatically in the potential created by the phononic cloud. Notice also, that the two-ansatze are equivalent in the $m_I \rightarrow \infty$ limit⁶ with both reproducing the exact solution that exists in this regime.

Therefore the mass of the impurity plays a crucial role for the Bogoliubov-Fröhlich polaron as the weak and strong coupling limits coincide in the limit $m_I/m_B \rightarrow \infty$. As m_I/m_B decreases a crossover regime between this two regions appears similarly to the case of polarons in semiconductors. In this case, there is an open question whether this regime can be well understood within the variational framework of Feynmann path integral or whether in the regime $m_I/m_B \approx 1$ a new phase consisting of a mobility dominated polaron appears [178, 323]. For three-spatial dimensions Quantum Monte Carlo approaches [186] and Renormalization Group methods [187] have been applied within this regime revealing that the properties of the polaronic states significantly deviate from the corresponding predictions of the Feynman theory [160]. Their results hint towards the emergence of a novel mobility dominated regime for the polarons at $m_I \approx m_B$ and coupling strengths α lying in the crossover of the Fröhlich ($\alpha \rightarrow 0$) and Pekar polaron ($\alpha \rightarrow \infty$) regimes. However, the experimental verification of the above is still lacking. This mobility dominated regime is particularly interesting because in novel materials such as organic semiconductors [155–157], found e.g. in plastic photovoltaics [324], the lattice vibrations cannot follow the movement of electrons adiabatically and accordingly mobility effects are significant.

In the case of two-spatial dimensions, $d = 2$, there is no theoretical consensus on the phase-diagram of the Bose polaron with different theoretical frameworks currently available in the literature providing conflicting results [189, 323]. In particular, and also to the best of our knowledge presently there is no experimental realization of Bose polarons in two-dimensions. One-dimensional polarons are even less explored theoretically, but experimental realizations are already present in the literature [9, 89]. The study of Bose polarons within the mobility-dominated regime for 1D systems is one of the main topics we have explored within the works [K4–K6].

⁶Notice that in this regime $m^* \propto m_I \rightarrow \infty$ and therefore the dispersion relation of the polaron is p_I independent, implying that localized states are eigenstates of the system.

2.4.4 The effective potential

In section 2.4.2 we have provided the derivation of the Fröhlich Hamiltonian for the case that the system is not confined, $V(\mathbf{r}) = 0$, however, if a trap is imposed to the system there are some crucial changes that need to be considered. A particularly important modification is that the expansion of the field operators of the bath in terms of phonon operators changes within the Bogoliubov approximation. In order to derive this expansion in the case that a trap is considered first the Gross-Pitaevski equation

$$\mu\Psi(\mathbf{r}) = \left[-\frac{\hbar^2}{2m_B}\nabla^2 + V(\mathbf{r}) + g_{BB}|\Psi(\mathbf{r})|^2 \right] \Psi(\mathbf{r}), \quad (2.78)$$

where μ is the chemical potential, has to be solved yielding the order parameter $\Psi(\mathbf{r})$. In turn the order parameter corresponds to the macroscopically occupied single-particle wavefunction of the condensate $\Psi(\mathbf{r})/\sqrt{N_B}$. Subsequently, in order to evaluate the phonon spectrum the above mentioned Gross-Pitaevskii equation is linearized by considering small fluctuations around the order parameter and employing the ansatz, $\Psi_{BdG}(\mathbf{r}) = \Psi(\mathbf{r}) + (u(\mathbf{r})e^{i\omega t} + v^*(\mathbf{r})e^{i\omega^*t})$. This process generates the so-called Bogolubov-de Gennes equations of motion and their solution results to an expansion of the field operator of the form, $\hat{\Psi}_B(\mathbf{r}) = \Psi(\mathbf{r}) + \sum_j [u_j(\mathbf{r})\hat{b}_j + v_j^*(\mathbf{r})\hat{b}_j^\dagger]$. Plugging this expansion into the bath-impurity interaction term, see Eq. (2.71), generates except from a phonon-phonon impurity, as for the $V(\mathbf{r}) = 0$ case, a potential term for the motion of the impurity that reads

$$\hat{V}_{\text{eff}} = g_{BI} \int d^d\mathbf{r} |\Psi(\mathbf{r})|^2 \hat{\Psi}_I^\dagger(\mathbf{r}) \hat{\Psi}_I(\mathbf{r}). \quad (2.79)$$

The scaling of this term is $E_{\text{eff}} = gn$ and it is only suppressed when the interactions between the impurity and the BEC are much smaller than the corresponding inter-species ones of the bose gas $E_{\text{eff}}/E_p \ll 1 \Rightarrow g_{BI}/g_{BB} \ll \sqrt{2}$. Of course, the regime of vanishing coupling among the impurity and the BEC $g_{BI}/g_{BB} \ll 1$ is not particularly interesting and accordingly as long as there is confinement in the system the effective potential of Eq. (2.79) has to be taken into account.

For typical experimental conditions the Thomas-Fermi approximation is valid [23]. Within this approximation the kinetic energy of the condensed atoms is neglected and the solution of the Gross-Pitaevski equation reads $\Psi(\mathbf{r}) = \sqrt{[\mu - V_B(\mathbf{r})]/g_{BB}}\theta(\mu - V_B(\mathbf{r}))$. The above implies that the total confinement of the impurity becomes

$$V_{\text{tot}}(\mathbf{r}) = \begin{cases} V_I(\mathbf{r}) - \frac{g_{BI}}{g_{BB}}V_B(\mathbf{r}) & \text{if } V_B(\mathbf{r}) < \mu \\ V_I(\mathbf{r}) & \text{if } V_B(\mathbf{r}) > \mu \end{cases}, \quad (2.80)$$

where $V_I(\mathbf{r})$ is the confining potential in the absence of a coupling with the bath species ($g_{BI} = 0$). Equation (2.80) reveals that the confining potential of the impurities is severely modified in the presence of an interacting BEC. In particular, in the case that the bath and impurity particles refer to the same atomic species, then the impurity potential reads $V_I(\mathbf{r}) \approx V_B(\mathbf{r})$, implying that the strength of the confinement

THEORETICAL FRAMEWORK

within the BEC is renormalized by $V_I(\mathbf{r}) \rightarrow (1 - g_{BI}/g_{BB})V_I(\mathbf{r})$, within the spatial extent of the BEC. This renormalization of the impurity's trapping potential has dire consequences since for $g_{BI} = g_{BB}$ the impurity is unconfined as long as it is within the BEC and for $g_{BI} > g_{BB}$ it is actually expelled from the spatial extent of the BEC and phase separation is induced. On the contrary, if $g_{BI} < 0$ the potential that the impurity experiences is stronger than in its absence. An estimation of the relative prominence of phonon-impurity interactions when compared to the effective potential yields $E_{\text{pl2}}/E_{\text{eff}} \propto \frac{(g_{BB}N_B)^\beta}{\sqrt{N_B}}$, with $\beta = 1/3$, $\beta = 1/2$ and $\beta = 0.6$ for one, two and three dimensions respectively. Considering that $g_{BB}N_B$ controls the depletion of the Bose gas and therefore cannot become arbitrarily large the above fact leads to the conclusion that the effective potential is always more prevalent for extensive in particle number confined BECs. The exploration of the impurity dynamics in different regimes of g_{BI} within the above-discussed effective potential framework consists one of the main themes of our works [K4–K6].

2.4.5 Non-linear effects in BECs and their relevance in polaron physics

A basic feature of quasi-particles is their finite quasi-particle residue, $Z = |\langle \Psi(|g| > 0) | \Psi(g = 0) \rangle|^2$, where $|\Psi(|g| > 0)\rangle$ is the state containing the quasi-particle and $|\Psi(g = 0)\rangle$ refers to the ground state of the system in the absence of coupling. Therefore, a necessary condition for a correlated state of an impurity with the phononic excitations of a BEC to be characterized as a Bose polaron refers to $0 < Z < 1$. A famous example where the quasi-particle picture breaks down due to the violation of the above condition is the Anderson orthogonality catastrophe phenomenon. The latter refers to an ensemble of polarized fermions perturbed by a localized potential. It has been shown that in this case the overlap of states with and without the localized potential vanishes as the $N \rightarrow \infty$ limit is approached.

In the case of a BEC the concept of Anderson orthogonality catastrophe can be generalized as follows. A BEC involves a large amount of condensed particles, $N_c \approx N_B$, with N_B denoting the total number of bosons, which occupy a single mesoscopic wavefunction (order parameter), $\Psi_0(x)$. Let us now assume an infinitesimally small perturbation of $\Psi_0(x)$ such that $\Psi_0(x) \rightarrow \Psi'_0(x)$, with $\int dx \Psi_0^*(x)\Psi'_0(x) = 1 - \delta P$ and $\Delta P \ll 1$. Then the overlap between the resulting many-body wavefunctions will tend to zero exponentially with the number of condensed atoms as $\langle \Psi_0 | \Psi'_0 \rangle = (1 - \delta P)^{N_c} \propto e^{-\delta P N}$. The above implies that even an infinitesimal change of the order parameter of the BEC leads to a phenomenon analogous to the Anderson orthogonality catastrophe [190–192]. In the literature there are several processes that lead to the modification of the order parameter of the BEC. First, note that collective modes such as the dipole and the breathing mode of a BEC also involve alterations of the order parameter scaling with the amplitude of the excitation. A particularly relevant example when considering Bose polarons is the formation of solitary waves. An effect that is important on its own right since studies both within, as well as, beyond the mean-field Gross-Pitaevskii approximation, see Eq. (2.78), have shown that dark solitons can be spontaneously

generated via e.g. dragging an impurity barrier through a 1D BEC. In the case of a polaron system under consideration the impurity can be thought of as a matter-wave barrier and as a result when its momentum becomes larger than a critical one we expect similar to the aforementioned dynamics. Note also that the complex-valued $\Psi_0(x)$ containing such a dark-soliton involves a phase winding as the spatial extent where the dark soliton lies is crossed and as a consequence its overlap with the order parameter in the absence of such an excitation is significantly smaller than unity, approaching zero in the case of slow solitons. Similar effects also arise in higher dimensional setups which include the formation of vortex and vortex line configurations in two- and three dimensional BECs respectively when perturbed by a rapidly moving obstacle.

Another important phenomenon that might contribute to a vanishing polaron residue is the phase separation [202–206]. This process is well studied both within the mean-field approximation, as well as, in the correlated case [210]. It refers to the occurrence of an instability when the interspecies interactions between two Bose gases exceed a threshold value when compared to the intraspecies ones. Indeed, it can be shown that for $g_{AB} \geq \sqrt{g_{AA}g_{BB}}$, where g_{AA} , g_{BB} are the intraspecies interactions for the A and B species and g_{AB} is the interspecies interaction, the BECs are immiscible, i.e. they tend to minimize their density overlap, while in the opposite case, $g_{AB} < \sqrt{g_{AA}g_{BB}}$, the gases are miscible [207]. The related dynamics occurring after this instability of the system is triggered has been characterized, both within the Gross-Pitaevskii framework, as well as in the case that correlations are properly considered [208, 210]. It has been demonstrated that upon crossing the miscibility-immiscibility threshold by means of quenching the interspecies interaction strength, the density of the different BEC components forms filament-like structures with a particular interaction-dependent wave-vector [210]. Interestingly, the behaviour between this wavevector and the interaction strength is modified in the presence of correlations. Of course, such filamentation process implies a dramatic alteration of the order parameter of the involved BECs, associated also with a significant depletion of the condensed atoms in the correlated case. Hence, also in this case a strongly decaying overlap between the time-evolved and the initial state is expected during the dynamics. Notice that the effective potential, Sec. 2.4.4, already hints towards the development of a phase separated state for $g_{BI} > g_{BB}$ and accordingly such a phenomenon seems to be particularly relevant in the case of Bose polarons.

Although these non-linear dynamics are well-studied for one and two dimensional systems, within the mean field approximation [207]. Studies that probe the beyond mean field correlated dynamics have appeared only recently mainly focussing in the case of 1D [208–210]. As previously mentioned polarons have been nowadays observed only in one and three dimensions, leading to the conclusion that studying the properties of the 1D polaron offers an ideal testbed for clarifying the relation of non-linear phenomena to the polaronic ones. Indeed, considering the possibility of emergent non-linear excitations motivates us to conjecture that 1D Bose polarons will not be, in principle, long-lived structures. In particular, one of our aims is to characterize under which conditions the above-mentioned non-linear phenomena can lead to the de-

cay of polaronic quasi-particles. To examine the lifetime of Bose structures a time-resolving spectroscopic scheme needs to be employed. For this reason we rely mainly on Ramsey spectroscopy which allows us to access the structure factor of the polaronic state [K4, K5]. Another powerful approach employed within this thesis is pump-probe spectroscopy [K6] which opens the possibility to investigate the dynamical formation and decay of Bose polarons. The above mentioned spectroscopic schemes are introduced in sections 2.5.3 and 2.5.4.

2.4.6 Extension to Fermi polarons

Ultracold atom setups allow for studying the dependence of various effects on the particle statistics [22, 24]. In this spirit the Fermi polaron [98, 116, 117, 144, 145, 181, 184] is the fermionic analogue of the Bose polaron [9, 89, 91, 179, 180, 182, 183] with the BEC being substituted by a spin-polarized Fermi gas. The two quasi-particles are radically different since the extensive gas is a superfluid in the bosonic case [23], while for fermions it corresponds to impenetrable particles, as two fermions cannot occupy the same single-particle state due to the Pauli principle [146]. In addition, due to the short-ranged character of the interatomic interactions, the particles of the Fermi gas are not interacting among themselves and the only possible interaction channel is provided by the impurity-bath coupling. The Fermi polaron therefore constitutes a novel and rather interesting state of matter, that has a quite different character from its bosonic analogue. Fermi polarons can be thought as extremely spin-imbalanced Fermi ensembles [92, 117, 181] and therefore they can provide insights for elusive phenomena. More specifically, Impurities possessing an attractive interaction with their environment thus forming attractive Fermi polarons can be related to the development of a Fulde-Ferrell-Larkin-Ovchinnikov (better known as FFLO) phase [325–327] for spin-imbalanced superconductors [328]. Similarly, the lifetime of repulsive impurities forming repulsive Fermi polarons probes the stability of an extremely spin-imbalanced repulsive Fermi gas against the formation of Feshbach molecules and thus can be relevant for studies of ferromagnetism [117].

Fermi polarons are well-studied in two and three dimensional setups. The quasi-particle properties in such setups can be well-understood within the variational Framework of the Chevy ansatz [329]. In particular, the state of the polaron is approximated by

$$|\Psi_{\text{FP}}\rangle = \left(\sqrt{Z} \hat{a}_{\mathbf{q}=0\downarrow}^\dagger + \sum_{\{\mathbf{q}|q \leq k_F\}} \sum_{\{\mathbf{q}'|q' > k_F\}} \phi_{\mathbf{q}, \mathbf{q}'} \hat{a}_{\mathbf{q}'\uparrow}^\dagger \hat{a}_{\mathbf{q}\uparrow} \hat{a}_{\mathbf{q}-\mathbf{q}'\downarrow}^\dagger \right) |\text{FS}\rangle, \quad (2.81)$$

where $\hat{a}_{\mathbf{q}\alpha}$ and $\hat{a}_{\mathbf{q}\alpha}^\dagger$ correspond to the fermionic creation and annihilation operators respectively, acting on the state characterized by the wavevector \mathbf{q} . Here, $a = \uparrow$ refers to bath fermions while $\alpha = \downarrow$ corresponds to the impurity. Additionally, k_F refers to the Fermi momentum and $|\text{FS}\rangle$ is the state of the ideal Fermi gas (Fermi sea) of spin- \uparrow atoms. For zero temperature $|\text{FS}\rangle = \prod_{\{\mathbf{q}|q \leq k_F\}} \hat{a}_{\mathbf{q}\uparrow}^\dagger |0\rangle$, with $|0\rangle$ being the vacuum state. The Chevy ansatz, Eq. (2.81), incorporates $\phi_{\mathbf{q}, \mathbf{q}'}$ as variational parameters, with

the corresponding quasi-particle residue being $Z = 1 - \sum_{\{\mathbf{q}|q \leq k_F\}} \sum_{\{\mathbf{q}'|q' > k_F\}} |\phi_{\mathbf{q}, \mathbf{q}'}|^2$. This ansatz resembles the first-order perturbative correction to the wavefunction of a free impurity in the presence of interactions, however, the ansatz parameters $\phi_{\mathbf{q}, \mathbf{q}'}$ are calculated variationally by the minimization of $\langle \Psi_{\text{FP}} | \hat{H}_h | \Psi_{\text{FP}} \rangle$ [329], where \hat{H}_h is given by Eq. (2.23). This seemingly *ad hoc* approximation is supported within diagrammatic methods. Indeed, the variational minimalization of $\langle \Psi_{\text{FP}} | \hat{H}_h | \Psi_{\text{FP}} \rangle$ can be shown to be equivalent to truncating the self-energy of the impurity, $\Sigma(\mathbf{p}; E)$, to the first non-trivial order of the corresponding the ladder expansion [330, 331].

The Chevy ansatz reproduces the energy of the repulsive and attractive polaron for positive and negative scattering lengths exhibited respectively in 3D fermionic ensembles [135, 144]. Noticeably, it has been shown experimentally that the attractive polaron persists for strong positive scattering lengths, $a > (0.847k_F)^{-1}$, in agreement to the Chevy ansatz prediction [144]. In addition, the Chevy ansatz possesses also support from *ab initio* methods since its predictions are largely reproduced by employing Quantum Monte Carlo calculations [332, 333]. Surprisingly, the Chevy ansatz seems to be adequate to characterize the Fermi polaron on the wavefunction level. Indeed, the quasi-particle residue and effective mass of the Fermi polaron is well-predicted as comparisons with experiment [135, 334, 335] and Quantum Monte Carlo reveal [186]. The Chevy ansatz is also effective in correctly characterizing the Fermi polaron in 2D ensembles [116]. This large success of Chevy ansatz, despite its simplicity, is quite surprising, leading some authors to investigate the underlying theoretical reasons that lead to its remarkable accuracy [332, 336].

However, it is not clear whether a similar expansion can be employed to describe 1D setups. This is because of the concept of the Anderson orthogonality catastrophe [190–192]. Indeed, it can be shown that the Anderson orthogonality catastrophe is exhibited for all different impurity-bath mass ratios for an 1D system [191, 192]. In particular, the overlap between the interacting state of a system consisting of $N_\uparrow + 1_\downarrow$ atoms, $|\Psi_{N_\uparrow+1_\downarrow}\rangle$ and the corresponding non interacting ground state $|\Psi_{N_\uparrow}\rangle \otimes |\Psi_{1_\downarrow}\rangle$ decreases with system size as $\langle \Psi_{N_\uparrow+1_\downarrow} | [|\Psi_{N_\uparrow}\rangle \otimes |\Psi_{1_\downarrow}\rangle] \rangle \propto N_\uparrow^{-\gamma/2}$, where $\gamma > 0$ is a constant depending on the mass ratio m_\uparrow/m_\downarrow and interaction strength g . This result implies that $Z \rightarrow 0$ for $N_\uparrow \rightarrow \infty$, invalidating any expansion similar to Eq. (2.81) as it implies the generation of an infinite series of particle-hole excitations. Equivalently, it implies that quasi-particles such as the Fermi polaron cannot exist in one-dimension [186, 337, 338]. Nevertheless, a recent experiment has shown [185] that thermodynamic properties of the $N_\uparrow + 1_\downarrow$ 1D Fermi system [339, 340] can be reclaimed for N_\uparrow as low as $N_\uparrow = 8$. Owing to this experimental advance it is not clear whether the Anderson orthogonality catastrophe precludes the creation of a well-defined Fermi polaron. The exploration of this possibility is the main topic of our work [K3].

2.5 Radiofrequency spectroscopy

The purpose of this section is to outline several applications of radiofrequency spectroscopy for the study of ultracold atoms [143, 220]. Within this section we treat atoms

mainly as two level systems, an approximation which within the context of many ultracold experiments is excellent, see also Sec. 2.1. Indeed, in such setups magnetic fields of the order of 100 G are employed allowing for the selective coupling of individual hyperfine states by radiofrequency fields [125, 246, 274]. This selective coupling stems from the large quadratic Zeeman shift within this regime that heavily detunes all other possible transitions except the selected one [274]. Another important feature of ultracold atom setups is their relatively long timescales of time-evolution that range from a few to hundreds of ms, referring to the center-of-mass motion of the atoms [22, 23]. In addition, the exhibited coherence times are even longer exceeding the timescale of a second. The above allow for the application of both adiabatic and diabatic spectroscopic techniques, where the particles are transferred among the different hyperfine levels within much longer or shorter timescales with respect to their center-of-mass motion, respectively [143]. The large coherence time also allows for any decoherence effects to be neglected within a good approximation.

In the following we analyze the basic features of adiabatic and diabatic spin-dynamics and its relevance for spectroscopic applications by utilizing a simple example system. Subsequently, we examine the protocols of injection, ejection, Ramsey and pump-probe spectroscopy and outline their relevance for probing ultracold atom setups.

2.5.1 Adiabatic and diabatic spin-dynamics and importance for spectroscopic applications

Understanding how particles move when subjected to out-of-equilibrium scenarios involving interactions among themselves and their environment is one of the key paradigms of the study of ultracold atoms [37]. Of course, in order to address this dynamics tunable probes should be developed that are sensitive to the details of atomic motion. For the construction of such probes it is particularly important that the correlations of the state of the probe and its environment are well-understood such that useful information about the latter can be obtained upon studying the former. Within radiofrequency spectroscopy the motional (center-of-mass) state of the atoms is coupled with an additional (pseudo)spin degree-of-freedom referring to their internal atomic hyperfine state [91, 98, 116, 144, 182, 183]. As discussed in previous sections [see e.g. Sec. 2.2 and Sec. 2.3] such processes can possibly give rise to complex correlated dynamics and novel emergent phenomena (see also [K1, K2]). However, despite the fundamental interest in understanding the dynamics within these regimes, the latter are not relevant for spectroscopic applications since they are currently not well-understood. In contrast, within the regimes where the transfer between the different hyperfine levels is either much slower (adiabatic) or much faster (diabatic) than the corresponding timescale of atomic motion, the spin dynamics are predictable and well-characterized. In particular, this controllable dynamics provides important information for the state of the system [143]. Indeed, for diabatic spectroscopy⁷ the spatial distribution and coher-

⁷Henceforth with the term diabatic or adiabatic spectroscopy we denote the spectroscopic techniques utilizing pulses that induce diabatic or adiabatic spin-transfer dynamics respectively. Notice that the

ence of the atomic wavepacket is probed, while for adiabatic spectroscopy information regarding the energy content in terms of eigenenergies and eigenstates of the system is accessible.

A. Example model

In order to provide a clearer picture for adiabatic and diabatic spectroscopy, we present here a simple example that allows for the identification of the basic features of both regimes of spin-dynamics. We consider a single atom in a spin-dependent harmonic trap. This simple model allows for a comprehensive understanding of the basic principles of the different spectroscopic schemes since it allows for the coupling of the atomic spin and motion, without the inclusion of complicating factors occurring in interacting many-body systems. The Hamiltonian of the system reads

$$\begin{aligned} \hat{H} = \int dx \left[\sum_{\alpha \in \{\uparrow, \downarrow\}} \hat{\psi}_{\alpha}^{\dagger}(x) \left(-\frac{\hbar^2}{2m} \frac{d^2}{dx^2} \right) \hat{\psi}_{\alpha}(x) + \frac{m\omega^2}{2} x^2 \hat{\psi}_{\downarrow}^{\dagger}(x) \hat{\psi}_{\downarrow}(x) \right. \\ \left. + \frac{m\omega^2}{2} (x - x_0)^2 \hat{\psi}_{\uparrow}^{\dagger}(x) \hat{\psi}_{\uparrow}(x) + \frac{\hbar\Omega_R(t)}{2} \left(\hat{\psi}_{\uparrow}^{\dagger}(x) \hat{\psi}_{\downarrow}(x) + \hat{\psi}_{\downarrow}^{\dagger}(x) \hat{\psi}_{\uparrow}(x) \right) \right. \\ \left. - \frac{\hbar\Delta}{2} \left(\hat{\psi}_{\uparrow}^{\dagger}(x) \hat{\psi}_{\uparrow}(x) - \hat{\psi}_{\downarrow}^{\dagger}(x) \hat{\psi}_{\downarrow}(x) \right) \right], \end{aligned} \quad (2.82)$$

where m is the atomic mass, ω and x_0 refer to the trapping frequency and the spatial offset of the parabolic confinement of the spin- \uparrow with respect to the spin- \downarrow ones. Finally, $\Omega_R(t) = \Omega_R e^{-\frac{\pi(\Omega_R t)^2}{\phi^2}}$ corresponds to the Rabi frequency of the Gaussian-shaped pulse with phase angle ϕ . The Gaussian shape of this pulse enables the different broadening effects to be distinguished from one another while being of experimental relevance [143]. Finally, Δ is the detuning of the pulse with respect to the atomic transition. An important aspect in the following is that for an isolated spin the probability to find a particle in the spin- \uparrow state is given for $0 < \phi \leq \pi$ by a Gaussian distribution having the form

$$P_{\uparrow}(\Delta, \phi) = \sin^2 \left(\frac{\phi}{2} \right) \exp \left[-W^2 \left(\frac{\phi}{\pi} \right) \frac{\Delta^2}{\Omega_R^2} \right]. \quad (2.83)$$

The inverse width of the lineshape is $W(x) \approx \sqrt{\pi/2}x + 0.07771 \times x^{3.709}$ within an accuracy of 10^{-4} . Here, the first term is determined by employing first-order time-dependent perturbation theory and the second one by fitting an exponential function to the exact data for $W(x) - \sqrt{\pi/2}x$. The increase of the width of the Gaussian lineshape exhibited in Eq. (2.83) is an example of a power broadening [219]. The amplitude of the Gaussian is exactly $\sin^2(\phi/2)$ being a manifestation of the so-called pulse-area theorem [219]. This theorem states that for $\Delta = 0$ the transfer efficiency between the states depends only on the time integral of the pulse intensity $\phi = \int_{-\infty}^{\infty} dt \Omega_R(t)$ rather than its shape.

corresponding pulses will also be referred to as diabatic or adiabatic ones.

THEORETICAL FRAMEWORK

As a last remark notice the use of the rotating wave approximation in Eq. (2.82). The rotating wave approximation is excellent in the relevant regime for spectroscopic applications in ultracold ensembles addressing different hyperfine levels. This is due to the fact the typical energy scale of the hyperfine splitting is $h \times \text{MHz}$, while the intended Rabi frequencies, being of the order of the inverse timescale of atomic motion $\Omega_R \sim \text{kHz}$, are much smaller.

B. Diabatic regime

Diabatic spin-dynamics occurs when the motion of the particles can be neglected within the timescale that the spins transit between the spin- \uparrow and spin- \downarrow states. In the simple model of Eq. (2.82) the timescale for spin-transfer is given by π/Ω_R , while the atomic motion occurs within $\sim \pi/\omega$. Accordingly, the diabatic regime is accessed for $\Omega_R \gg \omega$. Due to the inability of atoms to move for $t < \pi/\Omega_R$ within this regime the kinetic energy in Eq. (2.82) can be neglected. In this case the Hamiltonian can be approximated by an integral over localized spins, i.e. $\hat{H} \approx \hat{H}_0 + \int dx \hat{H}(x)$, with

$$\begin{aligned} \hat{H}(x) = & \frac{\hbar\Omega_R}{2} e^{-\frac{\pi(\Omega_R t)^2}{\phi^2}} \left(\hat{\psi}_\uparrow^\dagger(x) \hat{\psi}_\downarrow(x) + \hat{\psi}_\downarrow^\dagger(x) \hat{\psi}_\uparrow(x) \right) \\ & - \frac{1}{4} (2\hbar\Delta - m\omega^2 x_0^2 - 2m\omega^2 x_0 x) \left(\hat{\psi}_\uparrow^\dagger(x) \hat{\psi}_\uparrow(x) - \hat{\psi}_\downarrow^\dagger(x) \hat{\psi}_\downarrow(x) \right), \end{aligned} \quad (2.84)$$

and \hat{H}_0 denoting a spin-independent term contributing to a net shift of the energy

$$\hat{H}_0 = \frac{1}{4} \int dx [m\omega^2 x^2 + m\omega^2 (x - x_0)^2] \left(\hat{\psi}_\uparrow^\dagger(x) \hat{\psi}_\uparrow(x) + \hat{\psi}_\downarrow^\dagger(x) \hat{\psi}_\downarrow(x) \right). \quad (2.85)$$

Accordingly, in the diabatic limit the spin-dynamics of the itinerant spin can be mapped to an analogous system consisting of an ensemble of localized and non-interacting spins. This ensemble possesses a spatially dependent detuning and its dynamics is driven by a homogeneous in space pulse. The absence of effective spin-spin interactions is indicative of the semiclassical nature of this approximation. Assuming that initially the system is prepared in the ground state of the spin- \downarrow configuration subject to Eq. (2.84), the probability to find a spin- \uparrow particle after the application of the pulse is

$$\begin{aligned} P_\uparrow(\Delta, \phi) = & \left\{ 1 + \left[W \left(\frac{\phi}{\pi} \right) \frac{x_0}{\alpha_t} \frac{\omega}{\Omega_R} \right]^2 \right\}^{-\frac{1}{2}} \sin^2 \left(\frac{\phi}{2} \right) \\ & \times \exp \left[-\frac{W^2 \left(\frac{\phi}{\pi} \right)}{\Omega_R^2} \frac{\left(\Delta - \frac{m\omega^2 x_0^2}{2\hbar} \right)^2}{1 + \left[W \left(\frac{\phi}{\pi} \right) \frac{x_0}{\alpha_t} \frac{\omega}{\Omega_R} \right]^2} \right], \end{aligned} \quad (2.86)$$

where $\alpha_t = \sqrt{\hbar/(m\omega)}$ is the confinement length scale. The result of Eq. (2.86) provides a great insight into the dynamics. First, the spectrum exhibits a single peak at the position $\hbar\Delta = \frac{m\omega^2 x_0^2}{2}$, which corresponds to the energy expectation value of a coherent

state with average zero momentum and displaced by x_0 from the trap center. Indeed, within the diabatic regime the spatial distribution of the atom cannot change during the short timescale of transfer among the hyperfine states. Accordingly, the atom transits from its ground state for spin- \downarrow to a coherent state for spin- \uparrow that possess a spatial wavefunction equivalent to the initial one. Note here that the prefactor of the Gaussian distribution is smaller than unity even in the resonant case, namely $\Delta = m\omega^2 x_0^2/2$ [see Eq. (2.86)] revealing that the transfer of spin- \downarrow atoms to the spin- \uparrow state is not perfect. In particular, it reduces the fraction of the displacement, x_0 , over the trapping length-scale, as α_t increases. Nevertheless, this correction is relatively small as it is scaled by $\omega/\Omega_R \ll 1$ within the diabatic regime. The origin of this correction can be traced back to Eq. (2.84), where it can be seen that the spatially dependent detuning is a linear function of x with the slope given by x_0 . Of course, if the slope of the detuning is large, then some parts of the density of the spin- \downarrow atom will lie beyond the resonance condition of the pulse $|\Delta - m\omega^2 x^2/(2\hbar)| < \Omega_R$. Consequently, these will not be transferred to the spin- \uparrow state after the application of the pulse resulting to a reduced overall efficiency. Finally, let us comment that the main broadening mechanism is the power broadening. In particular, the lineshape remains Gaussian with a comparable but slightly increased width when compared to the fixed spin case, Eq. (2.83). This increase stems from the part of the density that is off-resonant.

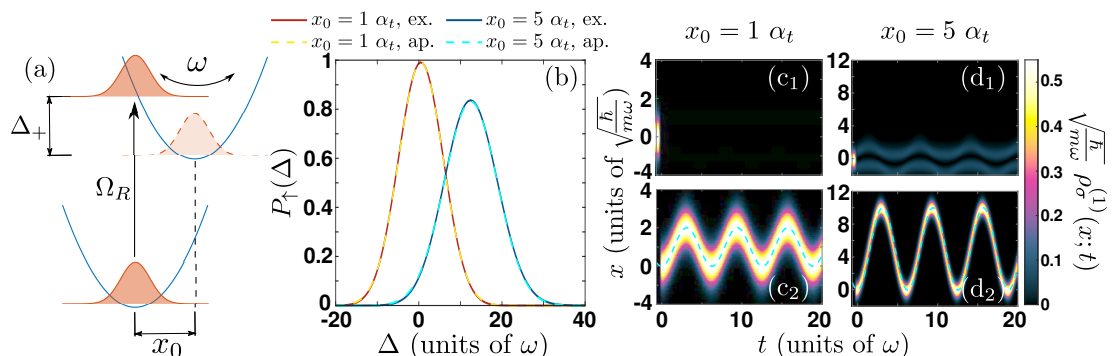


Figure 2.5: (a) Schematic illustration of the transfer between the spin states within the diabatic regime. (b) Spin transfer spectra for $\Omega_R = 10 \omega$, $x_0 = 1 \alpha_t$ and $x_0 = 5 \alpha_t$ (see legend) and comparison with the approximate profile of Eq. (2.84). Density evolution of the (c₁), (d₁) spin- \uparrow and the (c₂), (d₂) spin- \downarrow component for (c₁), (c₂) $x_0 = 1 \alpha_t$ and (d₁), (d₂) $x_0 = 5 \alpha_t$ and $\Omega_R = 10 \omega$ for the resonant cases $\Delta = 0.5 \omega$ and $\Delta = 12.5 \omega$ respectively. Light blue dashed lines in (c₂) and (d₂) demonstrate the expected trajectory corresponding to a coherent state with zero momentum at $x = 0$ created at $t = 0$.

It is instructive to compare the approximate yet analytical results of Eq. (2.86) to an exact simulation of Eq. (2.82). Figure 2.5(b) provides a comparison between the exact injection spectrum for $\Omega = 10 \omega$ [Eq. (2.82)] and the analytical prediction obtained within the diabatic approximation [Eq. (2.86)]. It can be seen that the

THEORETICAL FRAMEWORK

exact spectrum closely follows the approximate one, showing a peak at a finite value of Δ/ω , given by $\Delta_+ = \frac{m\omega^2 x_0^2}{2\hbar} = \frac{\omega x_0^2}{2\alpha_t^2}$. Notice also that for resonant detunings and in the $x_0 = 1 \alpha_t$ case the transfer to the spin- \uparrow is almost perfect $P_{\uparrow}(\Delta_+) > 0.99$, while for $x_0 = 5 \alpha_t$ the transfer efficiency is significantly lower than unity, specifically $P_{\uparrow}(\Delta_+) \approx 0.83$. As mentioned previously, according to the diabatic approximation, the mechanism responsible for the reduction of the transfer efficiency is that of the edges of the initial density distribution, recall that $\rho_{\sigma}^{(1)}(x; t) = \langle \Psi(t) | \hat{\psi}_{\sigma}^{\dagger}(x) \hat{\psi}_{\sigma}(x) | \Psi(t) \rangle$, with $\sigma \in \{\uparrow, \downarrow\}$, become off-resonant when a steep detuning gradient emanates in the spatial extent of the initial density. Indeed, this process can be verified within the exact calculation. For $x_0 = 1 \alpha_t$ we observe that for $t > 0$ the density of the spin- \downarrow atoms is almost completely nullified, see Fig. 2.5(c₁). However, for $x_0 = 5 \alpha_t$, Fig. 2.5(d₁) reveals that the density within the edges of the initial spin- \downarrow configuration remains in the same component after the application of the pulse, as the former seem to be outside the resonant region. Furthermore, we can demonstrate that a coherent state of the spin- \uparrow configuration is populated after the diabatic pulse. In particular, Fig. 2.5(c₁) and 2.5(d₂) demonstrate that the dipole oscillations undergone by the density transferred to the spin- \uparrow configuration match the trajectory of a coherent state generated at $x(t=0) = 0$, namely, $x(t) = x_0 - x_0 \cos(\omega t)$.

The above examined example reveals the key features of diabatic spectroscopy. The defining aspect of this spectroscopic scheme is that it addresses the state of the system in terms of dynamically evolving wavepackets the properties of which can be manipulated by modifying the overall preparation scheme. Indeed, the application of a diabatic pulse results to the creation of a wavepacket with an almost identical shape to the initial one, which enables the probing of different properties of the system by varying its initial state. This is a desirable feature for the study of e.g. the quasiparticle states of a many-body system since they possess typically a large overlap with the corresponding non-interacting states [179, 329] which can be employed to initialize a diabatic pulse scheme, see also Sec. 2.4.5. The spectroscopic signal provided by the shift of the spectral line probes the energy of the excited wavepacket with an uncertainty stemming from the intensity of the pulse. Therefore, a lower intensity, in terms of Ω_R , is preferable in order to suppress this broadening effect and accordingly increase the spectral resolution. However, due to the semiclassical character of the excited wavepacket the spectral response is not adequate to fully characterize the initial state. Finally, for most applications the characteristic energy associated with the pulse, $\hbar\Omega_R$, has to be kept much larger than the fluctuations of the detuning in the spatial extent of the wavepacket to ensure that its entirety satisfies the criterion $|\Delta(x)| < \Omega_R$ at resonance and therefore making an efficient transfer between the hyperfine states possible.

C. Adiabatic regime

Adiabatic spin-dynamics occurs when the rate of transfer among the spin- \uparrow and spin- \downarrow states is much lower than the inverse characteristic timescale of atomic motion. This implies that within the adiabatic regime the energy scale related to the Rabi frequency,

$\hbar\Omega_R$ is much smaller than the characteristic one for the atomic (center-of-mass) motion. Consequently, the latter corresponds to the dominant energy scale of the system. Within our example system, Eq. (2.82), it is thus instructive to express the Hamiltonian in terms of the different eigenstates in the case $\Omega_R = 0$. To achieve this, we expand the field operators as

$$\hat{\psi}_\downarrow^\dagger(x) = \sum_{n=0}^{\infty} \varphi_n(x) \hat{a}_n^\dagger, \quad \text{and,} \quad \hat{\psi}_\uparrow^\dagger(x) = \sum_{n=0}^{\infty} \varphi_n(x - x_0) \hat{b}_n^\dagger, \quad (2.87)$$

where $\varphi_n(x)$ corresponds to the n -th eigenfunction of the harmonic oscillator and \hat{a}_n^\dagger and \hat{b}_n^\dagger refer to the creation operators of the corresponding modes. By employing Eq. (2.87) the Hamiltonian of Eq. (2.82) can be expressed as follows

$$\begin{aligned} \hat{H} = & \frac{\hbar(\Delta + 1)}{2} \hat{N} + \sum_{n=0}^{\infty} \hbar\omega n \hat{a}_n^\dagger \hat{a}_n + \sum_{n=0}^{\infty} \hbar(\omega n - \Delta) \hat{b}_n^\dagger \hat{b}_n \\ & + \frac{\hbar\Omega_R}{2} e^{-\frac{(\Omega_R t)^2}{\pi}} \sum_{n=0}^{\infty} \sum_{m=0}^{\infty} \left(\left\langle n \left| \hat{D} \left(\frac{x_0}{\sqrt{2}\alpha t} \right) \right| m \right\rangle \hat{a}_n^\dagger \hat{b}_m + h.c. \right), \end{aligned} \quad (2.88)$$

where \hat{N} is the particle number operator, $\hat{D}(\alpha) = \exp(\alpha\hat{a}^\dagger - \alpha^*\hat{a})$ is the displacement operator and $|n\rangle = (\hat{a}^\dagger)^n / \sqrt{n!} |0\rangle$ is the n -th eigenstate of the harmonic oscillator. The relation between the eigenfunction and eigenstates reads $\varphi_n(x) \equiv \langle x|n\rangle$. The interpretation of Eq. (2.88) is that the eigenenergies of spin- \uparrow and spin- \downarrow states form two ladders of equidistant levels with a spacing given by $\hbar\omega$, which are offsetted by the detuning of the pulse, $\hbar\Delta$ [see Fig. 2.6(a)]. In principle, the pulse couples all of the spin- \uparrow states with all of the spin- \downarrow ones with a state-dependent amplitude $Z_{n,m}\Omega_R \leq \Omega_R$, where $Z_{n,m} = |\langle n|\hat{D}(x_0/\sqrt{2}\alpha t)|m\rangle| \leq 1$ is referred to as the Frank-Condon coefficient [219]. In order to transfer the spin- \uparrow atom to the spin- \downarrow configuration the condition

$$|E_n^\uparrow - E_m^\downarrow| \sim \hbar|Z_{n,m}\Omega_R|, \quad (2.89)$$

needs to be satisfied [see also Eq. (2.83)], where E_n^\uparrow and E_m^\downarrow refer to the energy of the involved spin- \uparrow and spin- \downarrow state respectively. This condition can only hold for distinct pairs of spin- \uparrow and spin- \downarrow states [see Fig. 2.6(a)]. Indeed, let us suppose that a spin- \downarrow state with index m and a spin- \uparrow state which possesses an index n satisfy Eq. (2.89). In this case the spin- \uparrow states $n \pm 1$ will not be able to satisfy the resonance condition with the m th spin- \downarrow one since $|E_{n\pm 1}^\uparrow - E_m^\downarrow| > ||E_n^\uparrow - E_m^\downarrow| - \hbar\omega| \approx \hbar\omega \gg \hbar\Omega_R$. Therefore, the system can be treated within the adiabatic approximation as a collection of non-interacting spin-1/2 particles with a spin-dependent Rabi-frequency, $Z_{n,m}\Omega_R$, and detuning $\Delta - n\omega$ [see Fig. 2.6(a)]. The shift of the Rabi-frequency, however, implies that the flip angle of the pulse does not refer to its bare value, ϕ , for an isolated spin but it is rather equal to $\tilde{\phi}_{n,m} = Z_{n,m}\phi$. The latter further results to the variation of its value for each different pair of states, n, m . The spectrum in the adiabatic case for a system initialized in the ground-state of spin- \downarrow reads

$$P_\uparrow(\Delta, \phi) = \sum_{n=0}^{\infty} \sin^2 \left(\frac{Z_{n,0}\phi}{2} \right) \exp \left[-W^2 \left(\frac{Z_{n,0}\phi}{\pi} \right) \frac{(\Delta - n\omega)^2}{Z_{n,0}^2 \Omega_R^2} \right]. \quad (2.90)$$

THEORETICAL FRAMEWORK

Note that spectrum consists of several non-overlapping peaks at $\Delta = n\omega$, with $n = 0, 1, 2, \dots$ (recall that $\Omega_R \ll \omega$ within the adiabatic regime). Each peak of the adiabatic spectrum possesses similar characteristics to a corresponding one referring to a localized spin with $\phi \rightarrow Z_{n,0}\phi$ and $\Omega_R \rightarrow Z_{n,0}\Omega_R$. Note that within adiabatic spectroscopy the perfect preparation of any particular spin- \uparrow state is possible as long as the flip angle is set to $\phi = \pi/Z_{n,0}$.

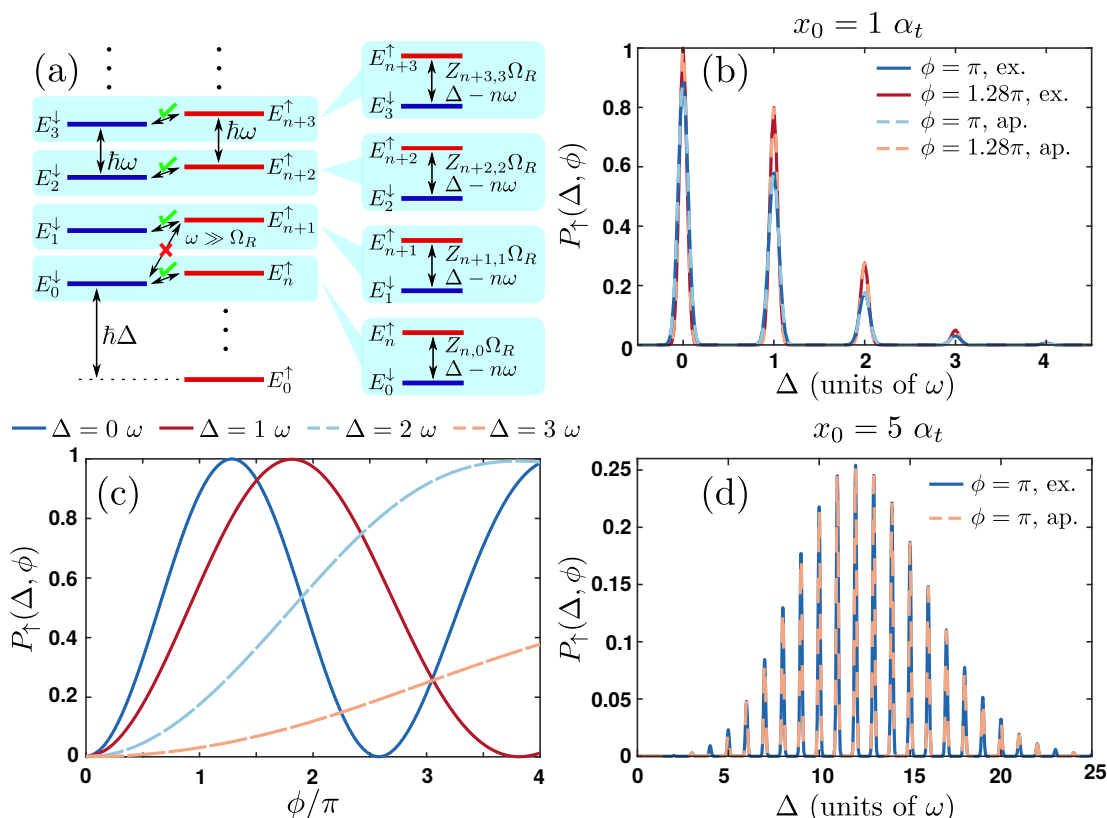


Figure 2.6: (a) Coupling scheme between the different eigenstates within the adiabatic spectroscopy regime. (b) Spin transfer spectra for $\Omega_R = 0.1\omega$, $x_0 = 1$ and $\phi = \pi, 1.28\pi$ when compared to the approximate profile of Eq. (2.90). (c) Transfer probability for the first four resonances and varying ϕ with $\Omega_R = 0.1\omega$, $x_0 = 1$ (see legend). (d) Spin transfer spectra for $\Omega_R = 0.1\omega$, $x_0 = 5$ and $\phi = \pi$.

Figure 2.6(b) demonstrates the spectrum obtained for $\Omega_R = 0.1\omega$ and $x_0 = 1$, within Eq. (2.82) when contrasted to the spectrum obtained within the adiabatic approximation, Eq. (2.90). It can be seen that the approximate spectrum matches almost perfectly the exact one for the employed flip angles $\phi = \pi$ and $\phi = 1.28\pi \approx \pi/Z_{0,0}$. The observed difference in the heights of the peaks for different Δ can be understood within the picture of the renormalization of the flip angle of the pulse, namely $\phi \rightarrow Z_{n,0}\phi$.

The basic features of the adiabatic spectroscopy is that it involves transitions between distinct eigenstates of the system, which is in direct contrast to the transitions between wavepacket states that diabatic spectroscopy resolves. Adiabatic spectroscopy provides information on the eigenenergies of the system being related to the position of the resonances [219]. Furthermore, their Frank-Condon overlaps with the initial state are imprinted in the heights of the corresponding spectral features. In addition, since the employed intensities are small there is no significant broadening of the spectral lines, in contrast to the diabatic case. In principle, adiabatic spectroscopy can be employed to prepare a system at any state that possesses a finite Frank-Condon overlap with the initial state. However, in practice such a preparation scheme becomes largely inefficient, since the time that the pulse should be applied increases with reducing $Z_{n,0}$. This increase of the exposure time implies that imperfections of the employed setup such as decoherence or variations of the applied field become important for the accurate description of the system [143, 219, 220]. Note also that the Frank-Condon overlap characterizing the transitions among different states of a many-body system can decrease drastically upon increasing the system size [190–192]. This is particularly relevant for spinor systems embedded within a more extensive structureless gas. In this case, the excited states of the spinor system are decaying by transferring energy to their environment, which, owing to its extensiveness, dramatically limits the Frank-Condon overlap of the state accessed after the decay. Such a decay process leads to a lifetime broadening [219] accompanied with a reduced amplitude of the spectral peaks. As a countermeasure to this process larger Rabi-frequencies could be employed so that $\Omega_R > \Gamma$, where Γ is the decay rate of the state. However, in the case that Γ is of the order of the characteristic timescale of atomic motion, this measure is ineffective and spectroscopic techniques relying on diabatic pulses such as Ramsey spectroscopy [see Sec. 2.5.3] have to be employed [143].

2.5.2 Injection and ejection spectroscopy

The simplest spectroscopic techniques that can be employed for the study of structures emanating in Bose and Fermi gases refer to the injection and ejection spectroscopy [91, 98, 116, 144, 182, 183]. Within these spectroscopic schemes, two different hyperfine levels are involved, the first one, denoted here as spin- \uparrow , corresponds to the configuration the behaviour of which is to be studied, while the second one, spin- \downarrow , is a different hyperfine level where the system possesses well-known properties. The difference of the two spectroscopic techniques lies in the initial preparation of the spin degree-of-freedom of the system. Within ejection or direct spectroscopy [144, 183] the system is prepared in the ground state $|\Psi_{0\uparrow}\rangle$ of the configuration that is to be probed, spin- \uparrow , and subsequently a pulse is applied so as to drive the atoms to the spin- \downarrow configuration. Injection or indirect spectroscopy is the reverse process [91, 98, 116, 182], i.e. the atoms are initially prepared in the spin- \downarrow ground state, $|\Phi_{0\downarrow}\rangle$, and then by applying a radiofrequency pulse the population is transferred to the configuration under study, namely the spin- \uparrow state. The spectroscopic signal in both processes is the fraction of atoms that has been successfully transferred after the application of the

THEORETICAL FRAMEWORK

pulse to the spin-state that is different from the one that the system was initially prepared [98, 116, 144].

Ejection and injection spectroscopy are particularly suited for the study of the system corresponding to the spin- \uparrow configuration in terms of its eigenstates and eigenenergies. This is achieved by ensuring that the applied pulse operates within the adiabatic spin-transfer regime, see Sec. 2.5.1C. In the single spin case $N_s = 1$ and within the adiabatic regime of ejection spectroscopy the energy of the initial $|\Psi_{0\uparrow}\rangle$ can be identified in terms of its relation to the known eigenenergies of the spin- \downarrow configuration corresponding to $|\Phi_{i\downarrow}\rangle$ by examining the position of the different spectroscopic resonances. In addition, the analysis of the heights of each individual peak of the ejection spectrum reveals the Frank-Condon overlaps $Z_{0,i} = |\langle\Psi_{0\uparrow}|\hat{S}_+|\Phi_{i\downarrow}\rangle|$, between the above mentioned states. Within adiabatic injection spectroscopy for $N_s = 1$ the states of the spin- \uparrow configuration possessing a finite Frank-Condon overlap with the ground state $|\Psi_{0\downarrow}\rangle$ can be populated, with their energy being imprinted in the location of the spectral peaks. Similarly, their overlap with the initial state, $Z_{i,0} = |\langle\Psi_{i\uparrow}|\hat{S}_+|\Phi_{0\downarrow}\rangle|$, is captured by the amplitude of the spectral features. Another, advantage of these spectroscopy schemes is that realizations utilizing different phase angles ϕ of the applied pulse can be used to probe Rabi oscillations [116] between the initial spin- \downarrow and the final spin- \uparrow states, yielding information regarding the coherence properties of the system.

When applied to systems containing a large number of spins, $N_s > 1$, injection and ejection spectroscopy work optimally when states with a high Frank-Condon overlap are addressed $Z_{i,j} \approx 1$ and in particular in the case that the involved spins are largely non-interacting and exhibit a slow rate of decoherence. In this case, the energy shifts between the sectors with different S_z , as well as, the coupling matrix elements between S_z and $S_z \pm 1$ states are roughly constant and the system can be treated as an effective pseudospin- $N_s/2$ single spin system. In this case the $N_s = 1$ results outlined above also carry over to $N_s > 1$ allowing for a straightforward characterization of the system via injection or ejection spectroscopy [91, 98, 116, 144, 182, 183]. In the more complicated case where the $Z_{i,j} \ll 1$ and/or spin-spin interactions are prominent a more careful analysis is required and additional observables must be employed since the above mentioned mapping is no longer possible, see also [K3]. The decoherence effects might be suppressed by employing stronger pulses, however different spectroscopic techniques might be preferable in this case (see also the discussion in Sec. 2.5.3).

Let us also note in passing that pulses resulting to diabatic spin-transfer are not particularly useful within injection and ejection spectroscopy. Indeed, due to the large intensities of such pulses the atomic motion is negligible during their application and therefore the corresponding spectrum provides information only regarding the semiclassical energy $\hbar \rightarrow 0$ of the spins (see Sec. 2.5.1B) which in turn offers only a crude characterization of the involved states [341]. In addition, injection and ejection spectroscopy do not utilize the strength of diabatic pulses referring to the formation of dynamically evolving wavepacket states after their application.

Finally, let us note that both the injection [91, 98, 116, 182] and ejection [144, 183] spectroscopy have been applied for investigating experimentally the polaron problem.

Indeed, injection spectroscopy has been employed as the workhorse for examining the equilibrium properties of Bose and Fermi polarons since it allows for addressing also the excited states of the system. In particular, injection spectroscopy allows for the experimental realization of the repulsive Bose [91, 182] or Fermi [98, 116] polaron, that constitutes an excited state of the composite bath impurity system in two and three spatial dimensions. Nevertheless, injection spectroscopy does not provide information regarding the dynamics of impurities or the polaron formation and lifetime, motivating the development of time-dependent spectroscopy schemes that are able to resolve the intriguing polaron dynamics.

2.5.3 Ramsey spectroscopy

A powerful alternative to injection and ejection radiofrequency spectroscopy is the so-called Ramsey spectroscopy [145, 147]. In particular, the injection and ejection techniques mainly rely on a large Frank-Condon coefficient among the initial and the finite state, i.e. $\langle \Psi_f | \hat{S}_+ | \Phi_i \rangle \approx 1$ allowing for adiabatic pulses to be efficiently employed. This is especially relevant in the many-body case, involving multiple spins. In particular the violation of the above mentioned condition leads to a complex dynamical response. This complex response of the system although theoretically interesting implies that the injection and ejection spectra cannot adequately characterize the system if not supported by the measurement of additional observables. Another drawback of these schemes is that they do not possess any time-resolution. Indeed, a state that is decaying to multiple different ones is only characterized by a lifetime dependent broadening of the corresponding spectral line [143, 219], see Sec. 2.5.1C.

Ramsey spectroscopy rectifies these issues by providing information regarding the decay rate exhibited by a state with a finite lifetime [145]. More specifically, Ramsey spectroscopy relies on the application of two hard $\pi/2$ pulses with a varying dark time in between them and possibly different polarizations, see Fig. 2.7(a). A hard pulse refers to an intense pulse resulting to diabatic spin-transfer for which the coupling of the spatial degree of freedom with the spin one can be neglected. Namely, for a hard pulse $P_{\uparrow}(\Delta, \phi) \approx \sin^2(\phi/2)$ for Δ close to resonance, see also Eq. (2.86). This scheme can be described better by invoking the concept of the Bloch sphere, see Fig. 2.7(b). In this picture, the application of a hard pulse can be regarded as a rotation of the total spin of the ensemble on this Bloch sphere along a particular spin-axis which can be related to the polarization of the pulse. Initially the system is prepared in a long-lived spin- \downarrow state and therefore the spin of the system lies in the South pole of the Bloch sphere corresponding to a spin $S_z = -\frac{N_s}{2}$, where N_s is the number of spins [Fig.2.7(c)]. Then the sequence is initiated by the first $\pi/2$ pulse that rotates the spin of the system along the y axis of the Bloch sphere by an angle of $\pi/2$. The fact that the pulse is hard implies that all of the spins after the end of this pulse end up in the superposition state $\frac{|\uparrow\rangle + |\downarrow\rangle}{\sqrt{2}}$, i.e. their spin is aligned along the x axis, see Fig. 2.7(b). Subsequently, the system is left to evolve in the absence of fields for a dark-time, t_d . During this dark-time the spin of the system precesses along the equator of the Bloch sphere due to the different energies of the spin- \uparrow and spin- \downarrow states [2.7(b), (c)]. Subsequently, the

THEORETICAL FRAMEWORK

$\langle S_x(t_d) \rangle$ and $\langle S_y(t_d) \rangle$ projections of the total-spin, $\langle \mathbf{S}(t_d) \rangle = \langle \Psi(t_d) | \hat{\mathbf{S}} | \Psi(t_d) \rangle$, can be probed by applying a second $\pi/2$ pulse along the y or x spin-axis (i.e. possessing a phase difference of $\Delta\theta = 0$ or $\Delta\theta = \pi/2$ to the first one) respectively. This last sequence rotates the spin so that the polarization of the particles along the z axis, $\langle S_z(t_d + t_e) \rangle$ after the second pulse refers to the value of $\langle S_x(t_d) \rangle$ or $\langle S_y(t_d) \rangle$ before the second pulse is applied, see Fig. 2.7(c).

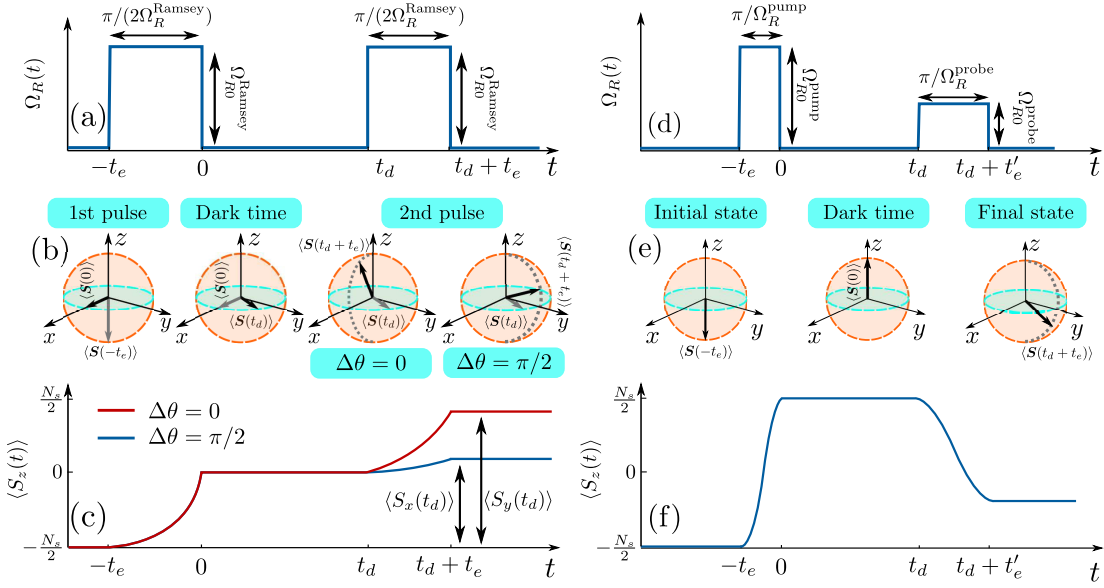


Figure 2.7: Schematic illustration of (a), (b), (c) the Ramsey and (d), (e), (f) the pump-probe spectroscopy schemes. (a), (d) Indicative pulse sequences expressed in terms of the time-dependence of the Rabi-frequency on the applied radiofrequency field, $\Omega_R(t)$. (b), (d) Bloch sphere representations demonstrating the anticipated behaviour of the total spin $\langle \mathbf{S}(t) \rangle$ at certain times during the dynamics. $\Delta\theta$ refers to the phase difference among the two pulses of the Ramsey scheme. (c), (f) Dynamical evolution of the z projection of total spin $\langle S_z(t) \rangle$.

For spatially fixed non-interacting spins Ramsey spectroscopy yields the rather trivial result of $\langle \Psi(t_d) | \hat{S}_x + i\hat{S}_y | \Psi(t_d) \rangle = \frac{N_s}{2} \exp(i\frac{E_\uparrow - E_\downarrow}{\hbar}t_d)$, where E_α corresponds to the energy of the spin- α state, with $\alpha \in \{\uparrow, \downarrow\}$. However, in the case that either the spins interact or the spin- \uparrow state is coupled to another degree of freedom, the situation becomes more complicated. Indeed, in this case the first $\pi/2$ pulse maps the system from the state $|\Psi(-t_e)\rangle = |\Psi_0\rangle \otimes |\downarrow\rangle^{\otimes N_s}$ to the state $|\Psi(0)\rangle = 2^{-N_s/2}(1 + \hat{S}_+)^{N_s} |\Psi(-t_e)\rangle$, where N_s is the number of constituent spins, which during the dark time undergoes non-trivial dynamics.

Particularly enlightening is the case of $N_s = 1$ [92, 147] where the spin is coupled to one or several auxiliary degrees-of-freedom. In this case and for ideal Ramsey pulses, i.e. $\Omega_R^{\text{Ramsey}} \rightarrow \infty$, $t_e \sim \pi/(2\Omega_R^{\text{Ramsey}}) \rightarrow 0$, the components of the spin during the

dark-time read

$$C(t_d) = \langle \Psi(t_d) | \hat{S}_x + i\hat{S}_y | \Psi(t_d) \rangle = \frac{1}{2} \langle \Psi(-t_e) | \hat{S}_- e^{\frac{i}{\hbar}(\hat{H} - E_0)t_d} \hat{S}_+ | \Psi(-t_e) \rangle. \quad (2.91)$$

Eq. (2.91) shows that the amplitude of the contrast $|C(t_d)| = \sqrt{\langle \hat{S}_x(t_d) \rangle^2 + \langle \hat{S}_y(t_d) \rangle^2}$ provides information on the overlap of the time-evolved state projected to the spin- \uparrow configuration, $|\Psi_{\uparrow}(t_d)\rangle = e^{-\frac{i}{\hbar}\hat{H}t_d}\hat{S}_+|\Psi(-t_e)\rangle$ with the initial state with spin- \downarrow , $|\Psi(-t_e)\rangle$. The decrease of the amplitude of the contrast, $|C(t_d)|$, implies that the energy imported to the system by the initial $\pi/2$ -pulse is redistributed to the degrees-of-freedom that are coupled to the spin. Therefore, Ramsey spectroscopy allows for tracking the time-dependence of such energy transfer processes and the identification of the lifetime of such states. In addition the phase of $\langle \Psi(t_d) | \hat{S}_x + i\hat{S}_y | \Psi(t_d) \rangle$ corresponds to the phase difference accumulated during the dark time, with respect to the initial state. In particular, the Ramsey contrast can be expressed in terms of the structure factor $C(t_d) = \langle \Psi_0 | e^{+i\hat{H}'_0 t_d/\hbar} e^{-i\hat{H}' t_d/\hbar} | \Psi_0 \rangle \equiv S(t_d)$, where $S(t)$ is the structure factor of the spinless system and the spin-independent Hamiltonians that read $\hat{H}'_0 \equiv [(\downarrow |^{\otimes N_s} \hat{H} | \downarrow)^{\otimes N_s}]$ and $\hat{H}' \equiv [(\uparrow |^{\otimes N_s} \hat{H} | \uparrow)^{\otimes N_s}]$. Therefore, the appropriate selection of the spin- \downarrow state allows for the experimental characterization of the spin- \uparrow configuration enabling the study of the structures emerging therein.

Notice that the mapping of the Ramsey contrast to the structure factor does not hold for $N_s > 1$ since in this case the former reads

$$C(t_d) = \frac{1}{2^{N_s}} \sum_{n=0}^{N_s-1} \frac{N_s - m}{m + 1} \binom{N_s}{m}^2 \langle \Psi(-t_e) | (\hat{S}_-)^{m+1} e^{\frac{i\hat{H}t_d}{\hbar}} \hat{S}_+ e^{-\frac{i\hat{H}t_d}{\hbar}} (\hat{S}_+)^m | \Psi(-t_e) \rangle. \quad (2.92)$$

It is straightforward to check that Eq. (2.92) reduces to Eq. (2.91) for $N_s = 1$. However, these two expressions have very different physical interpretation. Indeed, Eq. (2.92) reveals that the Ramsey contrast in the many-body case is a function of the overlaps of the time-evolved many-body states with m and $m + 1$ spin- \uparrow particles for $m = 0, 1, \dots, N_s - 1$. Correlations between the spin- \uparrow particles can dramatically affect the values of these overlaps for distinct m and accordingly they cannot be related in the generic case to the structure factor of a single excitation referring to the term with $m = 0$. One additional caveat of Eq. (2.92) is that the amplitude of the contrast crucially depends on the relative phase between the different terms involving a different number of spin- \uparrow atoms. This implies a relaxation rate of the Ramsey signal due to the decoherence of the spin in the different involved S_z sectors of a many-body system. Therefore, in contrast to the $N_s = 1$ case, for $N_s > 1$ a dynamically decreasing $|C(t_d)|$ does not necessarily imply energy migration among the spin and the degrees-of-freedom that are coupled to it, since spin-spin correlations also play an important role. The above complicating factors of the many-body Ramsey spectroscopy can be circumvented in the absence of two-body correlations allowing the system to be treated within mean-field theory [92, 147]. However, in the correlated case the interpretation of the Ramsey response of a system consisting of $N_s > 1$ spins is rather challenging and in general it should be supported by other independent observables.

With respect to the impurity problem, Ramsey spectroscopy has been applied recently [145] to study the heteronuclear Fermi-polaron in order to reveal the formation and fate of such quasi-particles. Motivated by this application we have also exploited Ramsey spectroscopy extensively [K4, K5] to demonstrate the decay dynamics of confined Bose polarons in the strongly interacting regime. Due to the recent shift of the community's focus in addressing the intricate Bose and Fermi polaron dynamics [9, 89, 145, 342–347] experiments.

2.5.4 Pump-probe spectroscopy

The pump-probe spectroscopy scheme is a time-resolving spectroscopy approach that allows also for spectral resolution [143]. As we discussed above Ramsey spectroscopy yields information about the proximity of the time-evolving state to the initial one both with respect to the actual overlap of the states as well as their relative phase. However, it is not able to reveal how the energy of the system is redistributed. This issue can be solved within pump-probe spectroscopy.

In the most general case pump-probe spectroscopy consists of a sequence of two pulses. The first one is the pump pulse which acts on a degree of freedom of the system leading to its excitation and subsequent out of equilibrium dynamics. The second pulse being referred to as the probe pulse is applied after a variable delay time from the pump one and its role is to characterize the induced dynamics, Fig. 2.7(d), (e), (f). The second pulse can either probe the state [100, 101] of the degree-of-freedom excited by the first pulse or a different one that is also optically addressable, see e.g. [348–355]. Herewith, we focus on the former case, as we deem it more relevant for applications in ultracold atoms. An important aspect of pump-probe spectroscopy is the field-free evolution of the system during the time interval between the two pulses, the so-called dark time. Within this time interval the initial excitation has time to energetically redistribute among the different dynamical modes of the system, as was also the case in Ramsey spectroscopy. However, in contrast to Ramsey spectroscopy within pump-probe spectroscopy this energy redistribution can be probed directly by the second pulse that allows for finite spectral resolution of the dynamics of the system. Essentially, the proposed pump-probe sequence refers to the ejection spectroscopy of an excitation (selectively) induced by a diabatic injection pulse. A notable drawback of the pump-probe technique is that the temporal and spectral resolution provided by this approach are limited by the Heisenberg time-energy uncertainty relation [247] and therefore a compromise between the two uncertainties has to be found. Accordingly, Ramsey spectroscopy is typically better in identifying the decay rate of a spin-excited state, while pump-probe spectroscopy allows for identifying how the energy is redistributed among the different degrees-of-freedom of the system. Finally, let us stress that the pump-probe framework can be employed in a variety of different setups [348–355] providing important information inaccessible by other spectroscopic techniques.

Within the ultracold setting pump-probe spectroscopy has played a pivotal role in addressing the development of anti-bunching correlations in the repulsive metastable branch of mass-balanced Fermi gases for positive scattering lengths [100, 101]. This

development as already mentioned in previous sections, see for instance Sec. 2.2, revitalized the interest in the study of the ferromagnetic properties in ultracold Fermions [94, 96–98, 100, 101]. In addition to the above mentioned application, the pump-probe spectroscopy technique is a powerful tool for studying the Bose and Fermi polarons especially focussing on understanding their dynamical properties. In particular, within our work [K6] we have employed pump-probe spectroscopy to monitor the dynamical energy redistribution emanating after the decay of strongly repulsively interacting Bose polarons. Another feature of pump-probe spectroscopy that can be utilized in the future is its relative robustness when the number of involved spinor atoms is increased when compared to Ramsey and injection or ejection spectroscopy. Indeed, this characteristic of the pump-probe scheme allows to address questions related to the crossover from the polaron limit of a single impurity [K6] embedded in an extensive environment to the two component gas case where both components have almost equal prevalence in the dynamics [100, 101]. These questions are particularly relevant in the Fermi polaron case [98, 116, 117, 144, 145, 181, 184] the study of which is largely tied to realizing few-body analogues of extensive phases, see also Sec. 2.4.6.

2.6 Many-Body Methodological Approach: ML-MCTDHX

the adequate description of quantum many-body systems is a highly challenging task due to the difficulty of modelling the effect of quantum correlations. The latter refer to statistical dependencies of the states of the constituent particles of the system, stemming from the non-trivial structure of the underlying many-body wavefunction describing them. Indeed, quantum correlations cannot be properly captured by the widely used mean-field theories and their variants since they are generically neglected. Instead, addressing the many-body Schrödinger equation, at least up to a certain degree, is required for appropriately taking quantum correlations into account. Such an approach is, of course, quite computationally challenging, since the dimensionality of the this partial differential equation increases linearly with number of particles, and therefore, an exponential scaling of the number of available states is involved as the system size increases.

A prominent class of numerical approaches that allow for the study of quantum correlations refers to the *ab initio* and numerically exact methods. *Ab initio* implies that the method addresses directly the many-body Schrödinger equation and does not invoke any further assumptions for its simplification. In turn, numerically exact means that by increasing the computational effort of the calculation one can obtain, in principle, results that are as precise as the numerical precision of the computing machine allows. The simplest and most well-known example of such a method is the so-called full configuration interaction (also known as the exact diagonalization) approach [107, 300, 356]. Within this numerical technique the state of each particle is restricted to a finite-dimensional subspace of the available Hilbert space, and subsequently all possible configurations that the particles can occupy are considered as the basis of the corresponding many-body Hilbert space. This approach allows for solving the corresponding many-

THEORETICAL FRAMEWORK

body Schrödinger equation within this truncated many-body basis by employing standard linear-algebra techniques. The *ab initio* character of this technique stems from the absence of approximations, besides the truncation of the underlying single-particle basis. Configuration interaction is also numerically exact because as a larger number of single-particle basis states are considered the accuracy of the method is increased. Therefore, asymptotically the accuracy is only limited by the numerical one. Nevertheless, the capacity of this method to feasibly perform calculations is severely limited by the system size since the complexity scales exponentially with the particle number of the system. Several sophisticated numerical approaches have been developed that severely improve this aspect of computational complexity when compared to configuration interaction while retaining an *ab initio* and numerically exact character. Indicatively, we mention, here, the density matrix renormalization methods [357, 358], the matrix product states approaches [359–362], several Quantum Monte Carlo techniques including the diagrammatic [313, 336, 363] and diffusion [189, 364, 365] ones. Furthermore, there exist several variational methods exploiting powerful ansätze [300] that can, on the one hand, efficiently truncate the many-body Hilbert space for computational efficiency, while on the other hand, they are general enough such that they can represent the whole many-body Hilbert space at a particular limit, ensuring this way numerical accuracy.

The numerical approach that we shall employ to tackle the correlated dynamics of ultracold atomic mixtures presented within this thesis belongs to this latter category of variational *ab initio* and numerically exact methods. Namely, it refers to the Multi-Layer Multi-Configuration Time-Dependent Hartree method for bosonic and fermionic mixtures (ML-MCTDHF) [366–368]. The ML-MCTDHF approach is a member of the family of numerical techniques that are descendants of the Multi-Configuration Time-Dependent Hartree (MCTDH) method [369, 370]. The distinctive feature of this class of numerical approaches is that they employ a variational ansatz involving a time-dependent and variationally optimized basis for expressing the many-body wavefunction of the system. This ansatz allows for a rather computationally efficient treatment of the quantum dynamics as compared to the case where a stationary basis is employed, as e.g. within the configuration interaction approach. MCTDH has been a very successful method for simulating the quantum dynamics of distinguishable molecular degrees-of-freedom in quantum chemistry (see for instance Ref. [370] and references therein) and has inspired several related approaches, employed for the study of a wide range of distinct physical systems. For our purposes the most relevant such extensions regard the Multi-Configuration Time-Dependent Hartree methods for fermions (MCTDHF) [371, 372] and for bosons (MCTDHB) [373, 374] which enable the treatment of indistinguishable particles of fermionic and bosonic character respectively. ML-MCTDHF is the successor to these methods as it enables the simulation of bosonic and fermionic ensembles [375], as well as, any mixture thereof. In particular, it uses a multi-layered structure [376–378] of the many-body wavefunction ansatz which provides access to the correlations developed among the distinct species of a multicomponent mixture in an efficient manner.

In the following we provide a brief description of the ML-MCTDHX method [366] especially when applied to the class of systems described in Ref. [K1–K6]. Subsequently, we discuss several aspects regarding its convergence and its relevance for the study of the particular setups employed within this thesis.

2.6.1 Basic elements of the ML-MCTDHX approach

The key feature of ML-MCTDHX is that it relies on a time-dependent and variationally optimized many-body basis set in order to represent the instantaneous many-body wavefunction. Despite its increased numerical efficiency, ML-MCTDHX further constitutes a versatile platform for tackling a wide variety of many-body scenarios involving fermionic and bosonic particles. Indeed, its multi-layer ansatz for the total wavefunction is based on a coarse-graining cascade, where strongly correlated degrees of freedom are grouped together and treated as subsystems, which mutually couple to each other. This layered structure of the ML-MCTDHX ansatz allows for its adaptation to the system specific intra- and inter-species correlations patterns, which in turn enables the efficient and accurate simulation of a large class of many-body systems.

In principle, ML-MCTDHX is able to treat systems involving any number of bosonic or fermionic species. In addition, there is no restriction to the spatial dimensionality of each species, while they can also be coupled with a spin degree-of-freedom of an arbitrary magnitude S . Of course, for increasing complexity of the system and, equivalently, the variational many-body wavefunction, the numerical effort becomes substantially larger. For our purposes we restrict our discussion to the case of a binary ultracold 1D gas possessing an additional spin-1/2 degree-of-freedom for one of the constituting species. Importantly, the particle exchange symmetry of the indistinguishable particles constituting each species is explicitly taken into account within ML-MCTDHX. However, in the following we will employ a unified notation for expressing the corresponding many-body wavefunction ansatz and equations of motion in both the bosonic and fermionic cases, and only briefly comment on the differences that the distinct statistics introduce.

A. The Hamiltonian

Before analyzing the ML-MCTDHX ansatz and the corresponding equations of motion, let us briefly discuss the typical form of the considered many-body Hamiltonian. The most generic form of Hamiltonian treated within this thesis, refers to a mixture of two species A and B externally confined along one spatial axis. In addition, the species B possesses a spin-1/2 degree-of-freedom the states of which are possibly coupled by an external field. The species possess intra- and interspecies interactions depending on the spin of the B particles. The most general Hamiltonian describing the above-mentioned physical scenario reads

$$\hat{H} = \sum_{\alpha \in \{A, \uparrow, \downarrow\}} \hat{H}_{\alpha\alpha} + \hat{H}_{\uparrow\downarrow} + \sum_{\alpha \in \{A, \uparrow, \downarrow\}} \hat{V}_{\alpha\alpha} + \hat{V}_{\uparrow\downarrow} + \hat{W}_{A\uparrow} + \hat{W}_{A\downarrow}. \quad (2.93)$$

THEORETICAL FRAMEWORK

The first kind of terms appearing in Eq. (2.93), are the single-particle ones which can either be diagonal or off-diagonal on the spin-indices

$$\hat{H}_{\alpha\alpha'} \equiv \int dx \hat{\Psi}_\alpha^\dagger(x) h_{\alpha\alpha'} \left(x, \frac{d}{dx} \right) \hat{\Psi}_{\alpha'}(x), \quad (2.94)$$

where $h_{\alpha\alpha'}(x, \frac{d}{dx}) = \langle x\alpha | \hat{h}(\hat{x}, \hat{p}) | x\alpha' \rangle$ are the matrix elements of the corresponding single-particle operator in the configuration space, $|x\alpha\rangle = \hat{\Psi}_\alpha^\dagger(x)|0\rangle$. Here, for the sake of simplicity, we have encoded the particle exchange statistics of the species with spin-state α in the proper commutation ($\zeta = 1$) or anticommutation ($\zeta = -1$) properties of the corresponding field operators, i.e. $[\hat{\Psi}_\alpha(x), \hat{\Psi}_\alpha^\dagger(x')]_\zeta = \hat{\Psi}_\alpha(x)\hat{\Psi}_\alpha^\dagger(x') - \zeta\hat{\Psi}_\alpha^\dagger(x')\hat{\Psi}_\alpha(x) = \delta(x - x')$. The kinetic energy contribution and the spin-independent potential terms contribute to the diagonal elements in the spin-indices $\hat{H}_{\alpha\alpha}$, while spin-dependent potentials or spin-orbit coupling terms (not discussed within this thesis) contribute to the non-diagonal part, $\hat{H}_{\uparrow\downarrow}$.

The interaction terms read

$$\hat{K}_{\alpha\alpha'} = \int dx_1 dx_2 \hat{\Psi}_\alpha^\dagger(x_1) \hat{\Psi}_{\alpha'}^\dagger(x_2) k_{\alpha\alpha'}(x_1, x_2) \hat{\Psi}_{\alpha'}(x_2) \hat{\Psi}_\alpha(x_1), \quad (2.95)$$

where $k_{\alpha\alpha'} = \langle x_1\alpha; x_2\alpha' | \hat{k}(\hat{x}_1, \hat{x}_2) | x_1\alpha; x_2\alpha' \rangle$ denote the interaction matrix elements in the two particle configuration space, $|x\alpha; x'\alpha'\rangle = \hat{\Psi}_\alpha^\dagger(x)\hat{\Psi}_{\alpha'}^\dagger(x')|0\rangle$. For convenience, in Eq. (2.93), we have introduced different notation for the distinct types of interaction. The interspecies interactions are denoted as $\hat{W}_{\alpha\alpha'} \equiv \hat{K}_{\alpha\alpha'}$ and $w_{\alpha\alpha'}(x_1, x_2) \equiv k_{\alpha\alpha'}(x_1, x_2)$, for $\alpha = A$ and $\alpha' \in \{\uparrow, \downarrow\}$. While, the intraspecies interaction terms correspond to all other cases of $\alpha, \alpha' \in \{A, \uparrow, \downarrow\}$ and are defined as $\hat{V}_{\alpha\alpha'} \equiv \hat{K}_{\alpha\alpha'}$ and $v_{\alpha\alpha'}(x_1, x_2) \equiv k_{\alpha\alpha'}(x_1, x_2)$. Let us remark again that the interactions employed throughout this thesis are zero-ranged, namely $k_{\alpha\alpha'}(x_1, x_2) = \delta(x_1 - x_2)$ and as a consequence for a fermionic species with spin-state α , $\hat{V}_{\alpha\alpha} = 0$ holds, since $(\hat{\Psi}_\alpha^\dagger(x))^2 = 0$. However, it is instructive to consider within this section the more general case that includes also finite range interactions, where all terms appearing in Eq. (2.93) are non-trivial.

B. Many-body ansatz

Let us now elaborate on the many-body ansatz that we employ in order to solve within the ML-MCTDHX approach the many-body Schrödinger equation $i\frac{d}{dt}|\Psi(t)\rangle = \hat{H}|\Psi\rangle$. Notice that herewith $\hbar = 1$ and \hat{H} is defined as in Eq. (2.93). As a first step, in order to account for the development of interspecies correlations the many-body wavefunction is expanded in terms of D distinct natural species functions, $|\tilde{\Psi}_k^\sigma(t)\rangle$, $i = 1, \dots, D$, for the species $\sigma = A$ and $\sigma = B$ that form the so-called truncated Schmidt decomposition of order D [379], namely

$$|\Psi(t)\rangle = \sum_{k=1}^D \sqrt{\lambda_k(t)} |\tilde{\Psi}_k^B(t)\rangle \otimes |\tilde{\Psi}_k^A(t)\rangle, \quad (2.96)$$

where λ_k refer to the corresponding expansion (Schmidt) coefficients. Note here that the expansion of Eq. (2.96) has a pronounced physical interpretation. Indeed, in the case of entanglement among the species two or more λ_k 's possess non zero values adhering to the intraspecies correlations emanating in the system [379]. In the opposite case of the absence of entanglement $\lambda_1 = 1$ and $\lambda_k = 0$, for $k = 2, \dots, D$ and accordingly, Eq. (2.96) has a tensor product form. For computational convenience, the Schmidt decomposition within the ML-MCTDHX ansatz is encoded via the equivalent form

$$|\Psi(t)\rangle = \sum_{k,l=1}^D A_{kl}(t) |\Psi_k^B(t)\rangle \otimes |\Psi_l^I(t)\rangle, \quad (2.97)$$

which is connected to the Schmidt decomposition via a unitary transformation $|\tilde{\Psi}^\sigma(t)\rangle = \hat{U}(t)|\Psi^\sigma(t)\rangle$, and therefore contains equivalent information with Eq. (2.96).

To properly account for the intraspecies correlations emanating in the system each $|\Psi_k^\sigma(t)\rangle$, $k = 1, \dots, D$, is then expanded in terms of a time-dependent number-state basis

$$|\Psi_k^\sigma(t)\rangle = \sum_{\vec{n}} C_{k;\vec{n}}^\sigma(t) |\vec{n}(t)\rangle^\sigma, \quad (2.98)$$

where $A_{k;\vec{n}}^\sigma(t)$ refer to the expansion coefficients and $\vec{n} = (n_1, \dots, n_{M_\sigma})$ is the vector of particle occupations of each of the M_σ distinct time-dependent single-particle functions, $|\phi_j^\sigma(t)\rangle$, $j = 1, \dots, M_\sigma$, that satisfy $\sum_{j=1}^{M_\sigma} n_j = N_\sigma$. These number states are defined in terms of time-dependent single-particle functions according to the following expansion

$$|\vec{n}(t)\rangle^\sigma = \frac{1}{\sqrt{\prod_{j=1}^{M_\sigma} n_j!}} \prod_{j=1}^{M_\sigma} [\hat{a}_{j;\sigma}^\dagger(t)]^{n_j} |0\rangle, \quad (2.99)$$

where the creation and annihilation operators $\hat{a}_{i;\sigma}(t)$, $\hat{a}_{j;\sigma}^\dagger(t)$ correspond to creation or annihilation of a particle in the $|\phi_j^\sigma(t)\rangle$, $j = 1, \dots, M_\sigma$ state. These operators follow the proper commutation or anticommutation relations for the σ species, $[\hat{a}_{i;\sigma}(t), \hat{a}_{j;\sigma}^\dagger(t)]_{\zeta_\sigma} = \delta_{ij}$.

Finally the single-particle functions themselves are expressed in terms of a time-independent single-particle basis, $\chi_l(x)$. The latter expansion for the A species that do not possess a spin degree-of-freedom reads

$$|\phi_j^A(t)\rangle = \underbrace{\sum_{k=1}^M \phi_{j;l}^A(t) \int dx \chi_l(x) \hat{\Psi}_A^\dagger(x)}_{\equiv \hat{a}_{j;A}^\dagger(t)} |0\rangle. \quad (2.100)$$

While for the spinor species B the spin-1/2 degree-of-freedom is explicitly taken into account

$$|\phi_j^B(t)\rangle = \underbrace{\left[\sum_{k=1}^M \int dx \phi_{j;l\uparrow}^B(t) \chi_l(x) \hat{\Psi}_{\uparrow}^\dagger(x) + \phi_{j;l\downarrow}^B(t) \chi_l(x) \hat{\Psi}_{\downarrow}^\dagger(x) \right]}_{\equiv \hat{a}_{j;B}^\dagger(t)} |0\rangle. \quad (2.101)$$

THEORETICAL FRAMEWORK

Accordingly, the time-evolution of the many-body wavefunction, $|\Psi(t)\rangle$, is determined by the time-evolution of the expansion coefficients $A_{kl}(t)$, $C_{k,\vec{n}}^\sigma(t)$ and $\phi_{j;l}^\sigma(t)$, which can be obtained by solving the ML-MCTDHX equations of motion. The later are determined by employing a variational principle such as the Dirac-Frenkel one [380,381] or the Lagrangian one [382] and utilizing the wavefunction expansion explicated in Eq. (2.97), (2.98), (2.100) and (2.101).

C. The ML-MCTDHX equations of motion

A suitable framework to derive the ML-MCTDHX equations of motion is the Langrange variational principle, namely

$$S = \int_{t_i}^{t_f} d\tau \langle \Psi(\tau) | \hat{H} - i \frac{d}{d\tau} | \Psi(\tau) \rangle, \quad (2.102)$$

where \hat{H} is given by Eq. (2.93) and $|\Psi(t)\rangle$ is expanded according to Eq. (2.97), (2.98), (2.100) and (2.101). We further introduce the constraint of the wavefunction normalization $\langle \Psi(t) | \Psi(t) \rangle = 1$, as well as, the species and single-particle function orthogonality $\langle \Psi_k^\sigma(t) | \Psi_l^\sigma(t) \rangle = \delta_{kl}$ and $\langle \phi_i^\sigma(t) | \phi_j^\sigma(t) \rangle = \delta_{ij}$ respectively, for both species $\sigma \in \{A, B\}$.

Note here that due to the structure of the ML-MCTDHX ansatz of Eq. (2.97), (2.98), (2.100) and (2.101) the variational principle Eq. (2.102), does not provide a unique solution for $A_{kl}(t)$, $C_{k,\vec{n}}^\sigma(t)$ and $\phi_{j;l}^\sigma(t)$. Indeed, by performing proper unitary transformations for the different coefficients the same information regarding the time-evolution can be encoded among the coefficients in distinct ways, without altering the overall many-body state of the system $|\Psi(t)\rangle$. In the related literature this property is referred to as the ‘‘gauge degree of freedom of multiconfiguration time-dependent Hartree methods’’. Within our implementation the gauge fixing is implemented by demanding that the increment of the species and single-particle functions is orthogonal to their instantaneous values, namely

$$\langle \Psi_k^\sigma(t) | \frac{d}{dt} | \Psi_l^\sigma(t) \rangle = 0 \quad \text{and} \quad \langle \phi_i^\sigma(t) | \frac{d}{dt} | \phi_j^\sigma(t) \rangle = 0, \quad (2.103)$$

where $k, l = 1, \dots, D$ and $i, j = 1, \dots, M_\sigma$. For this choice, the equations of motion obtain an intuitive form. In particular, $A_{kl}(t)$ obeys

$$i \frac{dA_{kl}}{dt} = \sum_{r,s=1}^M \langle \Psi_k^A(t) | \langle \Psi_l^B(t) | \hat{H} | \Psi_r^A(t) \rangle | \Psi_s^B(t) \rangle A_{rs}(t), \quad (2.104)$$

possessing exactly the same form as the many-body Schrödinger equation, but notably the matrix elements of the Hamiltonian has a time-dependence stemming from the time-evolving species-functions. The equation of motion for $C_{k,\vec{n}}^\sigma$ is

$$i \frac{dC_{k,\vec{n}}^\sigma}{dt} = {}^\sigma \langle \vec{n}(t) | (1 - \hat{P}_\sigma) \left\{ \left(\hat{H}_\sigma + \hat{V}_\sigma \right) | \Psi_k^\sigma(t) \rangle + \sum_{p,q,r,s=1}^D [(\rho_\sigma^{(N_\sigma)})^{-1}]_{k;p} [\rho_{\sigma\bar{\sigma}}^{(N_\sigma+N_{\bar{\sigma})}]_{pr;qs} \langle \Psi_r^{\bar{\sigma}}(t) | \hat{W}_{\sigma\bar{\sigma}} | \Psi_s^{\bar{\sigma}}(t) \rangle | \Psi_q^\sigma(t) \rangle \right\}, \quad (2.105)$$

here $\sigma \in \{A, B\}$ and $\bar{\sigma}$ is defined as $\bar{\sigma} \neq \sigma$. For this reason we have employed the definitions $\hat{H}_A = \hat{H}_{AA}$ and $\hat{V}_A = \hat{V}_{AA}$, but $\hat{H}_B = \hat{H}_{\uparrow\uparrow} + \hat{H}_{\downarrow\downarrow} + \hat{H}_{\uparrow\downarrow}$ and $\hat{V}_B = \hat{V}_{\uparrow\uparrow} + \hat{V}_{\downarrow\downarrow} + \hat{V}_{\uparrow\downarrow}$, as well as $\hat{W}_{AB} = \hat{W}_{A\uparrow} + \hat{W}_{A\downarrow}$. The single-species density matrices, appearing in Eq. (2.105), read

$$\begin{aligned} \left[\hat{\rho}_A^{(N_A)} \right]_{k';k} &= \langle \Psi_{k'}^A(t) | \hat{\rho}_A^{(N_A)} | \Psi_k^A(t) \rangle = \sum_{l=1}^D A_{k'l}^* A_{kl}, \\ \left[\hat{\rho}_B^{(N_B)} \right]_{l';l} &= \langle \Psi_{l'}^B(t) | \hat{\rho}_B^{(N_B)} | \Psi_l^B(t) \rangle = \sum_{k=1}^D A_{k'l'}^* A_{kl}, \end{aligned} \quad (2.106)$$

with $\left[(\rho_\sigma^{(N_\sigma)})^{-1} \right]_{k;p}$ denoting the inverse of the corresponding matrix. Similarly, the two species density matrix is defined as

$$\left[\hat{\rho}_{AB}^{(N_A+N_B)} \right]_{k'l';kl} = \langle \Psi_{k'}^A(t) | \langle \Psi_{l'}^B(t) | \hat{\rho}_{AB}^{(N_A+N_B)} | \Psi_k^A(t) \rangle | \Psi_l^B(t) \rangle = A_{k'l'}^* A_{kl}. \quad (2.107)$$

The final quantity to be defined is the projector $\hat{P}_\sigma = \sum_{k=1}^M |\Psi_k^\sigma(t)\rangle \langle \Psi_k^\sigma(t)|$, which ensures that the gauge fixing condition $\langle \Psi_k^\sigma(t) | \frac{d}{dt} | \Psi_l^\sigma(t) \rangle = 0$ is satisfied for all $k, l = 1, \dots, D$.

Finally, the equation of motion for the single-particle functions reads

$$\begin{aligned} i \frac{d}{dt} |\phi_j^\sigma(t)\rangle &= (1 - \hat{P}_\sigma^{(1)}) \left\{ \hat{h}_\sigma |\phi_j^\sigma(t)\rangle \right. \\ &+ \sum_{p,q,r,s=1}^{M_\sigma} [(\rho_\sigma^{(1)})^{-1}]_{j;p} [\rho_{\sigma\sigma}^{(2)}]_{pr;qs} \langle \phi_r^\sigma(t) | \hat{v}_\sigma(\hat{x}_1, \hat{x}_2) | \phi_s^\sigma(t) \rangle |\phi_q^\sigma(t)\rangle \\ &\left. + \sum_{p,q,r,s=1}^{M_\sigma} [(\rho_\sigma^{(1)})^{-1}]_{j;p} [\rho_{\sigma\bar{\sigma}}^{(2)}]_{pr;qs} \langle \phi_r^{\bar{\sigma}}(t) | \hat{w}_{\sigma\bar{\sigma}}(\hat{x}_1, \hat{x}_2) | \phi_s^{\bar{\sigma}}(t) \rangle |\phi_q^\sigma(t)\rangle \right\}. \end{aligned} \quad (2.108)$$

Similarly to Eq. (2.105), also in this case $\sigma \in \{A, B\}$ and $\bar{\sigma} \neq \sigma$ hold. The definitions of the first-quantization operators are $\hat{h}_A = \hat{h}_{AA}$ and $\hat{v}_A = \hat{v}_{AA}$ regarding the scalar A species. For the spinor species we have

$$\hat{h}_B = \hat{h}_{\uparrow\uparrow} |\uparrow\rangle\langle\uparrow| + \hat{h}_{\downarrow\downarrow} |\downarrow\rangle\langle\downarrow| + \hat{h}_{\uparrow\downarrow} (|\uparrow\rangle\langle\downarrow| + |\downarrow\rangle\langle\uparrow|), \quad (2.109)$$

for the single-particle terms and

$$\begin{aligned} \hat{v}_B &= \hat{v}_{\uparrow\uparrow} |\uparrow\rangle_1 |\uparrow\rangle_2 \langle\uparrow|_2 \langle\uparrow| + \hat{v}_{\downarrow\downarrow} |\downarrow\rangle_1 |\downarrow\rangle_2 \langle\downarrow|_2 \langle\downarrow| \\ &+ \hat{v}_{\uparrow\downarrow} (|\uparrow\rangle_1 |\downarrow\rangle_2 \langle\uparrow|_2 \langle\downarrow| + |\downarrow\rangle_1 |\uparrow\rangle_2 \langle\downarrow|_2 \langle\uparrow|), \end{aligned} \quad (2.110)$$

for the corresponding interspecies interaction ones. Finally, the interspecies interaction operator reads $\hat{w}_{AB} = \hat{w}_{A\uparrow} |\uparrow\rangle_B \langle\uparrow| + \hat{w}_{A\downarrow} |\downarrow\rangle_B \langle\downarrow|$. The one and two-body

density operators are defined in terms of the time-dependent creation and annihilation operators as

$$\begin{aligned} [\hat{\rho}_\sigma^{(1)}]_{i;j} &= \langle \Psi(t) | \alpha_{i;\sigma}^\dagger(t) \alpha_{j;\sigma}(t) | \Psi(t) \rangle, \\ [\hat{\rho}_{\sigma\sigma'}^{(2)}]_{ij;kl} &= \langle \Psi(t) | \alpha_{i;\sigma}^\dagger(t) \alpha_{j;\sigma'}^\dagger(t) \alpha_{l;\sigma'}(t) \alpha_{k;\sigma}(t) | \Psi(t) \rangle. \end{aligned} \quad (2.111)$$

The final quantity to be defined is the projector $\hat{P}_\sigma^{(1)} = \sum_{j=1}^{M_\sigma} |\phi_j^\sigma(t)\rangle \langle \phi_j^\sigma(t)|$, which ensures that the gauge fixing condition $\langle \phi_i^\sigma(t) | \frac{d}{dt} | \phi_j^\sigma(t) \rangle = 0$ is satisfied for all $i, j \in \{1, \dots, M_\sigma\}$.

As a last remark, let us briefly discuss the basic properties of the ML-MCTDHX equations of motion. The equation-of-motion for the $A_{i,j}(t)$ coefficients, Eq. (2.104), yields D^2 coupled linear differential equations. These equations correspond to a configuration interaction approach within the time-dependent and variationally optimized many-body basis. Regarding the expansion of species functions and the $C_{k,\vec{n}}^\sigma(t)$ coefficients there are $D(\dim\{|\vec{n}(t)\rangle^A\} + \dim\{|\vec{n}(t)\rangle^B\})$ non-linear integrodifferential equations. Here, the dimension of the many-body basis is $\dim\{|\vec{n}(t)\rangle^\sigma\} = \binom{N_\sigma + (1 + \delta_{\sigma B})M_\sigma - 1}{N_\sigma}$ for a bosonic and $\dim\{|\vec{n}(t)\rangle^\sigma\} = \binom{(1 + \delta_{\sigma B})M_\sigma}{N_\sigma}$ for a fermionic species σ . Finally, the equations-of-motion for the $M_A + M_B$ single-particle functions, yield a further set of $\mathcal{M}(M_A + 2M_B)$ non-linear integrodifferential equations.

2.6.2 Limiting cases of the ML-MCTDHX approach and convergence

Having analyzed the basic ingredients of ML-MCTDHX methodology, an important question that we need to address is how one can judge the accuracy of this approach. As it was made evident in Sec. 2.6.1B and 2.6.1C, ML-MCTDHX relies on a variationally optimized truncation of the many-body Hilbert space at each particular time-instant of the quantum evolution. The order of the truncation is given by the number of basis states employed within each layer of the ML-MCTDHX ansatz. Accordingly, each ML-MCTDHX calculation is inherently characterized by the set of parameters $C = \{D, M_A, M_B, \mathcal{M}\}$. One of the main tasks that need to be performed, in order to estimate the reliability of a given ML-MCTDHX calculation, is to appreciate the convergence of the approach as a function of the set of parameters C .

In order to better the convergence of the method we provide below a few remarks regarding the limiting cases of the ML-MCTDHX approach. Considering a minimal ML-MCTDHX calculation with $M_\sigma = 1$ for a bosonic species σ , it can be shown that the equation-of-motion for $|\phi_1^\sigma(t)\rangle$, Eq. (2.108), is equivalent to the Gross-Pitaevskii equation [383, 384]. Consequently, the species σ does not possess any correlations since the probability to find any two particles at two certain positions are completely independent $\rho_{\alpha\alpha'}^{(2)}(x_1, x_2) = \rho_\alpha^{(1)}(x_1)\rho_{\alpha'}^{(1)}(x_2)$, where the spin-states α, α' correspond to the available ones of species σ . Similarly, for $M_\sigma = N_\sigma$ and a fermionic σ species the equations of motion correspond to the well-known Hartree-Fock equations [275, 276]. In addition, all correlations except from the trivial ones, stemming from

the fermionic nature of the particles, are neglected. In particular, due to the Wick theorem, $\rho_{\alpha\alpha'}^{(2)}(x_1, x_2) = [1 - |g_{\alpha\alpha'}^{(1)}(x_1, x_2)|^2]\rho_{\alpha}^{(1)}(x_1)\rho_{\alpha'}^{(1)}(x_2)$ within the Hartree-Fock case, where $g_{\alpha\alpha'}^{(1)}(x, x') = \langle \Psi | \hat{\Psi}_{\alpha'}^\dagger(x') \hat{\Psi}_\alpha(x) | \Psi \rangle / [\rho_{\alpha'}^{(1)}(x')\rho_{\alpha}^{(1)}(x)]^{1/2}$ is the one-body coherence function. Notice that if one of the above mean-field cases is true, the Schmidt decomposition of Eq. (2.96) dictates that $D = 1$, corresponding to a product state ansatz neglecting the entanglement among the species A and B . Therefore, in the simplest case where $D = 1$ and M_A, M_B satisfying the mean-field condition, the ML-MCTDHX method corresponds to a mean-field approach where all non-trivial correlations are neglected.

The above are to be contrasted to the opposite case. Considering $M_A = \mathcal{M}$ and $M_B = 2\mathcal{M}$, it follows that $\hat{P}_\sigma^{(1)} = 1$. Further, assuming a non-truncated Schmidt decomposition with $D = \min(\dim\{|\vec{n}(t)\rangle^A\}, \dim\{|\vec{n}(t)\rangle^B\})$, it can be proven that $\hat{P}_\sigma = 1$. In the above expressions the unity operator 1 is understood within the accuracy provided by the primitive basis of a finite dimension \mathcal{M} . Substituting the projection operators \hat{P}_σ and $\hat{P}_\sigma^{(1)}$ in Eq. (2.105) and (2.108) yields $\frac{d}{dt}C_{k,\vec{n}}^\sigma(t) = 0$ and $\frac{d}{dt}|\phi_j^\sigma(t)\rangle = 0$. Therefore, in this limit the many-body basis is time-independent. The ML-MCTDHX approach in this case reduces to the full-configuration interaction method, which is the prototypical *ab initio* and numerically exact method, see also Eq. (2.104). This implies that as the number of basis states in ML-MCTDHX is increased from the minimal value the approach is able to capture the effect of quantum correlations and as $C = \{\min(\dim\{|\vec{n}(t)\rangle^A\}, \dim\{|\vec{n}(t)\rangle^B\}), \mathcal{M}, 2\mathcal{M}, \mathcal{M}\}$ is approached, it takes all correlations into account.

Another relevant feature of the ML-MCTDHX multi-layered ansatz is the ability to treat intra- and inter-species correlations independently. In particular, $D = 1$ can also be employed outside of the mean-field regime (i.e. $M_\sigma \neq 1$ for bosons and $M_\sigma \neq N_\sigma$ for fermions). This allows us to find the best approximation of the many-body state by increasing M_σ , and therefore including intraspecies correlations, while the entanglement among the species is excluded. This approach corresponds to the species mean-field case. When the species mean-field is compared to full ML-MCTDHX calculations it is able to exploit the role of entanglement in the studied system [366, 385, 386]. Similarly, the number of Schmidt modes can be set to $D = \min(\dim\{|\vec{n}(t)\rangle^A\}, \dim\{|\vec{n}(t)\rangle^B\})$, even though the number of single-particle functions does not satisfy the configuration interaction criterion $M_A = \mathcal{M}$ and $M_B = 2\mathcal{M}$. This approach can be useful when the system under study involves strong interspecies correlations. In this case the ML-MCTDHX reduces to one of the proposed multi-species methods MCTDH-BB (MCTDH for Bose-Bose mixtures), MCTDH-BF (MCTDH for Bose-Fermi mixtures) and MCTDH-FF (MCTDH for Bose-Fermi mixtures) [387], depending on the statistics of the individual components.

The above show that depending on the particular set of parameters $C = \{D, M_A, M_B, \mathcal{M}\}$, different orders of approximation can be realized. In contrast, to the configuration interaction method the multiple parameters that control the accuracy of the ML-MCTDHX method can be tuned independently in order to adapt the many-body ansatz to the correlation patterns emerging in the system. In this way, ML-MCTDHX can achieve

as precise results as the configuration interaction approach but with a much reduced computational effort, allowing for the treatment of mesoscopic systems. Practically, in order to ensure convergence each one of the parameters D , M_A and M_B is increased, and the results corresponding to different sets of C and C' are compared. Typically, these comparisons rely on the observables of interest for the particular application, since they are usually good indicators for the variation of the many-body wavefunction for distinct C . Nevertheless, convergence indicators might involve particular quantities based on the deviation of an appropriate observable, such as the one-body density, for two sets of parameters C and C' . Another, convergence indicator is provided by utilizing the eigenvalues of the one-body density matrix, n_i and the Schmidt weights λ_i . The related convergence checks involve the comparison of their temporal evolution for different C or the verification that the value corresponding to minimum one, $\min(n_i)$ and $\min(\lambda_i)$, does not exceed a given threshold, typically 10^{-4} . For a detailed discussion on how the convergence tests are performed we refer the interested reader to Ref. [366]. Note also that convergence is also tested with respect to \mathcal{M} . In this case, we employ large increments of \mathcal{M} , since the effect of this parameter on the computational effort is typically small.

2.6.3 Efficiency of ML-MCTDHX method for addressing the impurity problem

Before proceeding, it is important to mention that the ML-MCTDHX ansatz of Eq. (2.97), (2.98), (2.100) and (2.101) is particularly suited for exploring the properties of a small number of impurities, especially when they are embedded in a BEC. First, recall that a Bose gas corresponds to a perfect BEC if and only if one single-particle state is occupied by all constituting particles. This fact implies that the many-body state of a perfect BEC is described exactly for $M_A = 1$. In practice, away from the thermodynamic limit the BEC is slightly depleted, but for small intraspecies interactions this depletion is suppressed, especially when considering moderate particle numbers, e.g. $N_A \approx 100$ and weak intraspecies interactions. For such setups convergence is achieved for a small number of $M_A < 4$. Strikingly, it has been shown [200, 210, 386, 388], that in this case, even the non-equilibrium dynamics of a Bose gas proximal to a BEC state can be accurately explored by involving only such a small number of single-particle states.

In addition, it is well-known that the quasi-particle states such as polarons involve a large overlap with the ground state of the system involving non-interacting impurities with its environment [161]. Note that this is also true in the case of Fermi polarons [329]. Therefore, the expected entanglement among the impurities and the bath is rather small, implying that a Schmidt decomposition of low order, $D \approx 6 - 9$, see also Eq. (2.96), suffices for the accurate representation of such quasiparticle states. Therefore, the study of the expected correlation properties of the Bose polaron problem motivates by itself a truncation scheme of the many-body wavefunction in terms of a small number of single-particle and single species basis states which lies at the heart of the ML-MCTDHX framework. Indeed, this fact allows for the optimal truncation of

the many-body wavefunction and the numerically efficient treatment of the stationary and dynamical properties of impurities immersed in a bosonic environment. Similarly, also in the case of a fermionic environment the small amount of entanglement involved in a Fermi polaron problem, allows us to efficiently reach system sizes referring to the crossover from few- to many-body physics predicted experimentally in Ref. [185].

2.6.4 Advantages of spectroscopic simulations

As it was discussed in Sec. 2.5 radiofrequency spectroscopy allows to experimentally address several important properties of the system under study such as the dynamical structure factor. The purpose of this section is to demonstrate that the simulation of such spectroscopy schemes is also of theoretical relevance since they offer an optimal way for addressing properties of the system, with minimal cost when compared to their direct evaluation and without employing any additional approximations.

The structure factor of a many-body system is defined as

$$S(t) = \langle \Psi(0) | \exp(+\frac{i}{\hbar} \hat{H}_0 t) \exp(-\frac{i}{\hbar} \hat{H} t) | \Psi(0) \rangle. \quad (2.112)$$

Despite the simple form of this quantity its calculation is quite challenging. The reason is that it relies on the many-body overlap of two distinct many-body wavefunctions, namely $|\Psi_0(t)\rangle = \exp(-\frac{i}{\hbar} \hat{H}_0 t) |\Psi(0)\rangle$ and $|\Psi(t)\rangle = \exp(-\frac{i}{\hbar} \hat{H} t) |\Psi(0)\rangle$. Such an overlap cannot be expressed in terms of few-body operators and therefore the full many-body wavefunction have to be utilized in its calculation. If the states $|\Psi_0(t)\rangle$ and $|\Psi(t)\rangle$ are expressed in terms of the same many-body basis, $|\vec{n}\rangle$, the many-body overlap corresponds to a vector-vector multiplication

$$\langle \Psi_0(t) | \Psi(t) \rangle = \sum_{\vec{n}} A_{0;\vec{n}}^*(t) A_{\vec{n}}(t). \quad (2.113)$$

Accordingly, given $A_{\vec{n}}^*$ and $A_{\vec{n}}$ the computational cost of calculating $\langle \Psi_0 | \Psi(t) \rangle$ scales proportionately to the size of the underlying many-body basis i.e. exponentially with the system size in terms of the particle number N . The computational cost for calculating $A_{\vec{n}}$ strongly depends on the many-body wavefunction ansatz employed by the computational method and it is generally non-negligible (except in the case of the configuration interaction methods). Within (ML-)MCTDHX, a time-dependent many-body basis $|\vec{n}\rangle = |\vec{n}(t)\rangle$ is employed in order to greatly reduce the required many-body basis size for the accurate representation of the time-evolved wavefunction $|\Psi(t)\rangle$. However, this implies that in order to evaluate a many-body overlap as in Eq. (2.113) the transformation matrix between the distinct many-body bases has to be evaluated. In the case of MCTDHF and MCTDHB the corresponding matrix elements correspond to Slater determinants and permanents respectively,

$$\langle \vec{n}(t) | \vec{m}(t) \rangle = \frac{1}{\sqrt{N!}} \sum_{i=1}^{N!} \zeta^{\text{sign} P_i} \langle \phi_{n_1}(t) | \phi_{m_{P_i(1)}}(t) \rangle \dots \langle \phi_{n_N}(t) | \phi_{m_{P_i(N)}}(t) \rangle, \quad (2.114)$$

THEORETICAL FRAMEWORK

where $\zeta = 1$ for bosons and $\zeta = -1$ for fermions. For multi-species systems similar overlap integrals need to be evaluated independently for each node. Therefore, even though the number of elements contributing to the vector-vector multiplication is significantly reduced due to the variationally optimal truncation of the many-body basis, there is a large overhead stemming from the transformation among the different many-body bases that two different ML-MCTDHX calculations involve. A more efficient route to perform such an evaluation is to employ a basis that is simultaneously optimized to represent both many-body wavefunctions $|\Psi(t)\rangle$ and $|\Psi_0(t)\rangle$. This can be achieved within ML-MCTDHX by employing an additional pseudospin degree of freedom such that the total wavefunction $|\tilde{\Psi}(0)\rangle$ reads

$$|\tilde{\Psi}(0)\rangle = \frac{1}{\sqrt{2}}|\Psi(0)\rangle \otimes |\uparrow\rangle + \frac{1}{\sqrt{2}}|\Psi_0(0)\rangle \otimes |\downarrow\rangle, \quad (2.115)$$

and it evolves according to the Hamiltonian

$$\hat{H} = \hat{H}_0 \hat{\mathbb{P}}_{\downarrow} + \hat{H} \hat{\mathbb{P}}_{\uparrow}, \quad (2.116)$$

where $\hat{\mathbb{P}}_{\alpha}$ corresponds to the projection operator to the spin-state $\alpha \in \{\uparrow, \downarrow\}$. By following this prescription the overlap $\langle \Psi(t) | \Psi_0(t) \rangle$ maps exactly to the expectation value of the spin operators $\langle \Psi(t) | \Psi_0(t) \rangle = \langle \tilde{\Psi}(t) | \hat{S}_x + i \hat{S}_y | \tilde{\Psi}(t) \rangle$. The latter can be calculated very efficiently since it comprises of an operator acting only on a single degree of freedom possessing only two available states. The time-evolution of the system characterized by $\tilde{s} \equiv \{\hat{H}, |\tilde{\Psi}(t)\rangle\}$, see Eq. (2.115), (2.116) can be addressed within the ML-MCTDHX methodology of spinor systems see Sec. 2.6.1. The corresponding computational cost is not much larger than the one corresponding to the individual systems $s_1 \equiv \{\hat{H}, |\Psi(t)\rangle\}$ and $s_2 \equiv \{\hat{H}_0, |\Psi_0(t)\rangle\}$. Indeed, the additional spin-degree of freedom is related to an increase of the primitive single-particle states, while the correlations contributing to $|\tilde{\Psi}(t)\rangle$ are equivalent to the ones emanating in $|\Psi(t)\rangle$ and $|\Psi_0(t)\rangle$. Accordingly the numbers of single-particle and single species functions that need to be employed in order to achieve convergence for \tilde{s} is slightly larger than the corresponding ones of the individual systems s_1 and s_2 . Notice that the above system \tilde{s} , characterized by Eq. (2.115) and (2.116), resulted from considerations regarding the optimization of the structure factor, Eq. (2.112), calculations within ML-MCTDHX. Nevertheless, \tilde{s} models the process of Ramsey spectroscopy and in particular the time evolution during the dark time see Sec. 2.5.3. Furthermore, $\langle \tilde{\Psi}(t) | \hat{S}_x + i \hat{S}_y | \tilde{\Psi}(t) \rangle$ refers to the main observable addressed by a Ramsey sequence, see Eq. (2.91). As a consequence, we conclude that spectroscopic simulations might offer an useful tool for extracting quantities of interest from the many-body dynamics of a system in the absence of approximations. The above imply that apart from a field of fundamental research, spinor setups provide an efficient framework to monitor properties of a large class of systems even on the methodological level.

Chapter 3

Outline of scientific contributions

3.1 Itinerant ferromagnetism in 1D few-fermion gases

The phenomenon of itinerant ferromagnetism is thought of being qualitatively well-described in terms of the Stoner model [104]. As also discussed in Sec. 2.2.1, Stoner ferromagnetism occurs for strong short-range repulsive interactions between fermions with anti-oriented spins. In that case, the involved large interaction energy counteracts the kinetic energy benefit obtained by pairing two fermions with opposite spin in a particular single-particle state making such configurations unfavourable. The ground state of the ferromagnet refers either to a state with phase-separated or particle-imbalanced spin-components. However, the experimental verification of this form of ferromagnetism in ultracold atom ensembles has provided to date somewhat inconclusive evidence [94, 96–98, 100, 101], mainly due to the competition of ferromagnetic phenomena with the process of Feshbach molecule creation [95] (see also Sec. 2.3).

Below, we outline our strategy to compare the magnetic properties of the excited states of spin-1/2 1D few-body fermionic gases with the expected ones within the Stoner model. Indeed, as already mentioned in detail in Sec. 2.3, ultracold 1D setups provide an alternative promising route for the study of itinerant ferromagnetism since they are characterized by short-range interactions of tunable strength accompanied by a suppressed rate of Feshbach molecule formation [77] in the interaction regime where itinerant ferromagnetism is expected. To expose the emergence of ferromagnetic phenomena we have focussed on identifying the stability properties of the spin-polarized [K1] and phase separated states [K2] while properly accounting for all correlations emanating in the system. It turns out that these two classes of states are favored in the ferromagnetic regime of the Stoner model, allowing us to directly examine its validity in the presence of correlations.

3.1.1 Dynamical stability of parabolically trapped spin-polarized fermions [K1]

The study of the stability of the spin-polarized states constitutes an excellent starting point for any study that deals with ferromagnetic phenomena, since these states can be unambiguously characterized as ferromagnetic. Indeed, for a spin-polarized ensemble all the magnetic moments of the fermions are oriented in the same well-defined direction and accordingly both the magnetization and the pairwise spin-alignment are maximal. Note that the spin-polarization and spin-alignment in the are generically not equivalent. For instance, a linear superposition of two spin-polarized states with opposite orientations, e.g. the NOON state defined as $|\text{NOON}\rangle = (|\uparrow\uparrow\dots\uparrow\rangle + |\downarrow\downarrow\dots\downarrow\rangle)/\sqrt{2}$, possesses maximal spin-alignment, since any two spins are perfectly aligned among themselves. But importantly, it does not have maximal polarization since $\langle\text{NOON}|\hat{\mathbf{S}}|\text{NOON}\rangle = \mathbf{0}$, with $\hat{\mathbf{S}}$ being the total spin vector.

The distinction between the pairwise spin-alignment and spin-polarization, enables us to examine the validity of the Stoner model for describing the response of fully-polarized states subjected to perturbations. Within the Stoner model the spin of each atom is interacting with the mean effective magnetic field resulting from the spin of all other atoms (see also the discussion in Sec. 2.2.1). This framework dictates that ferromagnetic phenomena emanate when this effective magnetic field, the so-called Stoner gap parameter, Δ becomes non-zero [104]. Importantly, the Stoner gap is proportional to the magnitude of the spin-polarization, $P^{(1)}$, namely $|\Delta| \propto gP^{(1)}$, where g is the interaction strength between anti-oriented spins. Therefore, within the Stoner model the phenomenon of ferromagnetism relies on the stability of the spin-polarization of the fermionic ensemble.

Within [K1] we devise a setup that allows us to identify whether this picture of ferromagnetism, inherently connected with the spin-polarization, adequately describes the magnetic phenomena emanating within repulsively interacting Fermi gases. In particular, we utilize an initial fully spin-polarized state realizing the highest possible value of $|\Delta|$ for a particular value of g . Subsequently, the stability of the initially imprinted polarization is probed by employing an inhomogeneous magnetic field perpendicular to the polarization axis. This choice of spatially-dependent magnetic field breaks the spin-symmetries of the many-body system that would otherwise prevent the decay of spin-polarization. This allows us to isolate the effects stemming from the presence of contact interactions in the spin-dynamics of the system and explicate their relation to the stability properties of spin-polarization and spin-alignment.

In particular, we observe that the spin-polarization of the system is not stable for any-interaction strength. However, ferromagnetic order is realized in the form of stable spin-spin correlations, implying that an almost perfect pairwise spin-alignment is present beyond a certain threshold value of interaction strength g for both attractive and repulsive couplings, provided that the system does not approach the Tonks-Girardeau limit for $g \rightarrow \infty$. This signifies that a different mechanism, rather than the emergence of a Stoner gap, $|\Delta| > 0$, explains the ferromagnetic properties of the system. This mechanism refers to an effective ferromagnetic spin-spin interaction

among the fermions. The origin of this interaction can be traced back to the weak-coupling expansion of the interaction Hamiltonian referring to a Fermi gas, see Eq. (2.47). To expose the importance of this mechanism we develop an effective spin-chain model based on the presence of the above mentioned effective ferromagnetic interaction, which is an extension of the one employed within Ref. [135]. The success of this model in capturing the essence of the *ab initio* results, demonstrates to the best of our knowledge for the first time, the importance of the weak-coupling expansion for understanding the inherent magnetic order of confined systems in the weak and moderate interaction regimes. Importantly, during the demagnetization dynamics a NOON state, $|\text{NOON}\rangle = \hat{U}(\theta)(|\uparrow\uparrow\dots\uparrow\rangle + |\downarrow\downarrow\dots\downarrow\rangle)/\sqrt{2}$, characterized by net zero spin-polarization but perfect spin-alignment is (almost perfectly) realized, up to a homogeneous rotation of all spins, $\hat{U}(\theta)$. The emergence of such a highly-entangled state explicates the importance of correlations among spin-states for the adequate description of the spin-dynamics and, quite strikingly, provides an avenue to realize such highly entangled states in fermionic ultracold ensembles. Indeed, within Ref. [K1] we explicitly explore the possibility of an experimental implementation of our setup. As we demonstrate by performing single-shot image simulations [200], state-of-the-art experiments are able to identify the different regimes of spin-dynamics and explicitly characterize the spin-polarization and spin-alignment properties of the fermionic ensemble.

One important difference of the spin-chain models stemming from Eq. (2.47) to the Stoner model, Eq. (2.27), is that the former constitute multi-band models while the latter refers to a single band. As we have outlined in Sec. 2.2.2 it is an open question whether effects that originate from the coupling of multiple bands are required in order to properly describe itinerant ferromagnetism in condensed matter systems [114]. If we have to draw an analogy between the parabolically confined gas examined in [K1] and a specific condensed matter setup, we have to acknowledge that the solid-state analogue of a harmonically trapped Fermi gas is the electronic state of a single atom. Therefore, our findings within this work motivate but cannot address whether ferromagnetic spin-spin interactions stemming from the coupling of different “bands” are essential for itinerant ferromagnetism. To proceed along these lines, it is crucial to investigate how the ferromagnetic properties of the system generalize from the case of a single-well trap to a multi-well system. Such a generalization, when expressed in terms of an analogous condensed matter system, would probe the crossover from the electronic state of a single atom to the corresponding one of a crystal lattice and it is therefore a highly desirable and also a non-trivial extension.

3.1.2 Relation of ferromagnetism and phase separation [K2]

Motivated by the possible extension of our results in [K1] towards the analogue of a condensed matter crystal we examine, in [K2], the double-well case, which, in the sense outlined above, is analogous to a diatomic molecule. Indeed, a double-well setup offers the simplest framework to identify the interplay of ferromagnetism and the hybridization of the single-particle states belonging to distinct wells due to tunnelling. Note that in [K1] we have shown that, for a single-well, repulsive zero-range interactions lead to

OUTLINE OF SCIENTIFIC CONTRIBUTIONS

the development of ferromagnetic correlations among the unpaired particles. Therefore, an intriguing prospect is to examine whether the composite system with two such wells being coupled via tunnelling retains such a ferromagnetic order. Furthermore, the magnetic properties of the double-well system might diverge significantly from those expected within the well-established Stoner framework [104]. Thus their characterization is also important at a more fundamental level.

In the latter context, one particularly relevant concept is the interplay of ferromagnetism and phase separation, which according to the Stoner model is prevalent in spatially inhomogeneous systems. Concretely, within the Stoner framework, inhomogeneous systems can be treated by substituting the global value of the gap parameter with a local one, $\Delta \rightarrow \Delta(x)$ [389, 390]. Notice that, $|\Delta(x)| \propto P^{(1)}(x)$, with $P^{(1)}(x)$ denoting the local spin-polarization [389, 390]. In this case Stoner ferromagnetism can appear even for population balanced spin- \uparrow and spin- \downarrow particles, such that $S_z = 0$. Ferromagnetism is then manifested by the formation of ferromagnetic domains. The ferromagnetic domains refer to spatial regions possessing a high magnitude of spin-polarization $|P^{(1)}(x)| \gg 0$ that are separated by domain-walls. These correspond essentially to regions where the value of $P^{(1)}(x)$ continuously changes magnitude and possibly direction, interpolating between the $P^{(1)}(x)$ values characterizing the respective adjacent domains. Obviously, the above imply the development of a pronounced phase separation among the spin- \uparrow and spin- \downarrow atoms.

Experimentally, by artificially preparing a phase separated state within a 3D Fermi gas, it has been found that the initially prepared phase separation is metastable [97], with its decay attributed to the formation of Feshbach molecules [95]. However, more recent pump-probe studies have shown that no macroscopic phase separation can be observed [100, 101]. Their findings reveal, instead, that the maximum size of ferromagnetic domains is of the order of only a few interparticle spacings. In particular, they have proposed the existence of a quantum emulsion state [123, 124] where the Fermi gas is in a state where Feshbach molecules and unpaired fermions coexist, with the latter showing phase separation in the scale of a few interparticle spacings. Therefore, the above experiments can be interpreted in a way that they support the presence of a ferromagnetic instability similar to the Stoner model one. Nevertheless, the complicating factor of Feshbach molecule formation prevents them from providing a decisive test for the Stoner mechanism. Within the literature referring to 1D Fermi gases, which do not exhibit Feshbach molecule formation, there are several findings that support the interplay of magnetic properties and phase separation [130, 135–138]. However, there is not any systematic study elaborating on this relation and comparing it to the scheme that the Stoner model provides.

A significant part of the above outstanding open questions can be addressed by investigating the magnetic properties of the simple setup examined in [K2]. Particularly, we have employed a few-fermion system confined in a double-well potential in a population-balanced state where the spin- \uparrow particles occupy the left well, while the spin- \downarrow fermions occupy the right one. For this system, the Stoner model predicts that beyond a critical interaction strength the tunnelling dynamics, characterizing the

$g = 0$ case, will cease to exist as the fermions will become localized in their corresponding wells, rendering the phase separation stable. Strikingly, in [K2] we explicitly demonstrate that this expectation is not realized within the correlated case. Instead of a stable phase separation we observe an interaction regime where the phase separation is metastable and the spin- \uparrow and spin- \downarrow particles, periodically and collectively, tunnel among the wells over a large time scale in comparison to the corresponding non-interacting one ($g = 0$).

We analyze this dynamical feature of the magnetic properties of the fermionic ensemble which in detail within [K2]. For this, a new tight-binding model that extends the XXZ Heisenberg models of Ref. [135] and [K1] was developed based on the weak-coupling expansion of Eq. (2.47). Specifically, this model consists of an ensemble of Hubbard dimers for the particles occupying the different “bands” of the double-well potential, referring to the distinct manifolds of quasi-degenerate single-particle eigenstates (SPES). These bands are coupled by ferromagnetic spin-spin interactions, acting locally on each particular well. Based on this model, we have shown that during the metastable decay dynamics of the phase separation, the system exhibits stable ferromagnetic spin-spin correlations within each of the wells of the external trap throughout the time-evolution. This behaviour is persevered even when the SU(2) symmetry associated with the total spin of the system is broken by a spin-dependent linear gradient potential. The exhibited dynamics in this latter case are in analogy to the one observed for a parabolic confinement [K1].

These results have important implications for the understanding of ferromagnetism in itinerant systems. In particular, the ferromagnetic Hund interaction which is responsible for the stable intrawell ferromagnetic correlations is shown to act only among single-particle states that possess a significant density-density overlap. Indeed, the above imply that the distinct SPES interact ferromagnetically for a harmonic trap, while the same is true only for the states localized within a particular well for a double-well confinement. Furthermore, the metastability of the phase separation for the double-well setup is attributed to the tunneling among the wells. In turn the tunneling, introduces antiferromagnetic Anderson exchange interactions, leading to the dephasing of the eigenstates with ferromagnetic correlations that are involved in the decay dynamics of the initial state. However, these Anderson exchange interactions are found to be extremely weak and, as a consequence, the phase separation within this interaction regime can be stabilized even for small amplitude spin-dependent potentials that break the SU(2) symmetry.

In conclusion, the findings of Ref. [K1, K2] provide a solid starting point for developing a bottom-up characterization of itinerant ferromagnetism. Our approach, generalizes the concept of Stoner instability which relies on the relative prominence of kinetic and interaction energies, in the sense that it reveals a more fundamental interplay of competing spin-spin correlation effects. Indeed, within our studies, the overall magnetic behaviour of our few-body setups is driven by the competition of antiferromagnetic interactions, stemming from the kinetic energy benefit of such a spin-alignment and the ferromagnetic spin-spin couplings, stemming from the density-density repulsion of anti-

oriented spins. The simultaneous presence of the above mentioned competing spin-spin interactions seems to be a pivotal point, since it promotes the development of higher-order spin-spin correlations. In particular, as explicated within the arguably quite simple spin-chain models that we have employed, the system is forced to compromise between developing ferromagnetic and antiferromagnetic spin-spin correlations. Indeed, due to the simultaneous presence of spin-spin interactions favouring opposite magnetic orders, the dynamics drive the system away from the product states of either ferromagnetic (spin-polarized, phase separated) or antiferromagnetic (e.g. Neel-like [107, 391]) nature favoring configurations that involve a high degree of entanglement. The bottom-up approach for the study of itinerant ferromagnetism can provide important insights in a large class of fermionic systems. In particular, we envisage several avenues for further research which will be outlined in detail later on, see Chapter 5.

3.2 Spectroscopic properties of Bose and Fermi Polarons

The second part of this thesis addresses the correlation mechanisms and dynamics of Fermi [K3] and Bose polarons [K4–K6] in 1D. More specifically, we focus on unveiling the existence and stability properties of these quasi-particles. Major findings of our investigations are the existence of well-defined and long-lived repulsive Fermi polarons and the unstable character of Bose polarons for strong impurity-bath repulsions. Importantly, the emergent interactions among polarons mediated by their environment are also explored in some detail. To characterize these states we mainly rely on spectroscopic probes, which expose the utility of spinor ultracold atoms as a tool to analyze the emergent order in composite systems and provide a strong connection to state-of-the-art experiments.

3.2.1 Reverse radiofrequency spectroscopy of Fermi polarons in few-body ensembles [K3]

Our study into the Fermi polaron problem focusses on the existence of this quasi-particle within an 1D (confined) setup. As already mentioned in Sec. 2.4.5, fermionic ensembles perturbed by a localized impurity potential exhibit the phenomenon of the Anderson orthogonality catastrophe [190–192]. This effect implies that the ground state of the system involving the impurity potential is orthogonal to the one without it in the thermodynamic limit. Here, the thermodynamic limit refers to the case that the number of fermions tends to infinity as their density is kept fixed. Note that a localized impurity potential can be mapped to an infinitely heavy impurity, possessing short-range interactions with its environment. It follows that in the infinite mass limit the presence of a quasi-particle such as a Fermi polaron, referring to an impurity coupled with the excitations of its fermionic environment, is ill-defined for all dimensions. Notably, it is shown that in 1D setups the Anderson orthogonality catastrophe phenomenon occurs for every mass ratio [192], rendering the concept of a Fermi polaron ill-defined in the thermodynamic limit of 1D systems.

In direct contrast to the above mentioned result, the recent experiment of Ref. [185] has demonstrated that certain properties of 1D composite Fermi systems quickly converge to the corresponding ones of the thermodynamic limit. In particular, ejection spectroscopy studies [185] reveal that the interaction energy of a single impurity immersed in Fermi gas quickly converges to the thermodynamic limit prediction by McGuire [339, 340], even for small particle numbers $N_F = 8$. These show that several important properties of 1D Fermi systems in their thermodynamic limit are also present in setups with a small particle number. This result is quite counterintuitive, given that 1D systems exhibit Anderson orthogonality catastrophe. Indeed, since the state of the interacting system in the thermodynamic limit is orthogonal to the corresponding non-interacting one, it is surprising that it possesses similar properties to a few-body system where the states with zero and finite interaction are not orthogonal. Note that the Anderson orthogonality catastrophe refers to a decrease of the overlap between the non-interacting, $|\Psi_0\rangle$, and interacting states, $|\Psi_{\text{int}}\rangle$, that scales polynomially with the particle number, i.e. $\langle\Psi_0|\Psi_{\text{int}}\rangle \propto N_F^{-\gamma/2}$, with an mass and interaction dependent exponent $\gamma > 0$ [192]. Therefore the Anderson orthogonality catastrophe phenomenon slowly sets in as the particle number increases. As a consequence, the results of Ref. [185] can be interpreted as indicating the existence of the Fermi polaron in 1D systems, that vanishes only asymptotically for $N \rightarrow \infty$.

Motivated by the above, we directly examine the polaronic properties emanating in impurities embedded in a Fermi gas. To this end, we have employed injection spectroscopy by utilizing an adiabatic pulse that drives the impurities from their spin- \downarrow state which is non-interacting with their host to the corresponding spin- \uparrow which involves a finite interaction among the impurities and their environment. The adiabatic character of the spectroscopic scheme allows us to directly address the many-body state overlap of the polaronic and non-interacting states and therefore to directly probe the Anderson orthogonality catastrophe. In addition, we have employed a mass-imbalanced setup where the impurities correspond to ^{40}K atoms while their environment refers to ^6Li ones. Except for the experimental relevance of the above mentioned system, the mass-imbalanced case has been selected, since the distinct bath and impurity species do not exhibit a spinor character that would complicate the interpretation of their response due to magnetic effects as in Ref. [K1, K2].

By examining the injection spectrum of such few-body setups we reveal the existence of several excitation pathways for the Fermi polaron, which we subsequently analyze in detail. Importantly, we observe that the presence of an initially excited impurity gives rise to a significantly modified spectrum when comparing to the corresponding ground state. In the case of two ^{40}K impurities the excitation pathways of the ground and excited impurity states cause interference effects to occur during the spin-transfer dynamics, resulting in a complex spectrum. In the case of strong interactions among the two atomic species, this interference gives rise to multiple distinct spectral peaks, from which only one is of a two-polaron character while the remaining ones refer to different motionally excited states of a single Fermi polaron. We verify that this behaviour is not observable for weaker impurity-bath interactions where only

one spectroscopic resonance is prominent. The polaron energy shift and residue are also studied, indicating, quite expectedly, the increasing positive shift of the repulsive Fermi polaron for stronger interaction strengths. This mechanism is also associated with the decrease of the polaron residue. In line with recent studies [98], the presence of induced interactions between the polarons is indicated by a positive shift of the two-polaron resonance when compared to the single polaron one. However, the non-sizeable nature of this shift, being of the order of 2%, suggests that in order to infer the presence of induced interactions an alternative measure is needed. Inspecting the relative distance between the resulting quasiparticles, a quantity that can be probed experimentally via in situ spin-resolved single-shot measurements [210, 304, 305], we observe its decrease which concordantly dictates the presence of induced interactions. The latter are found to be attractive despite the repulsive nature of the impurity-bath interactions in the system. This fact persists upon enlarging the fermionic sea and considering different atomic species.

As a last remark, let us note that the Fermi polarons are, quite surprisingly, found to be long lived structures. To examine their lifetime we have employed a Ramsey-like spectroscopy scheme where we excite the impurities to their polaronic state and after a variable dark time we apply a second pulse, identical to the first one, to transfer them back to the state that is not interacting with their environment. The fraction of atoms transferred to the non-interacting state by the second pulse, \mathcal{F} , constitutes our main observable. This sequence reveals irrespectively of the particular state or the interaction strength that the polarons remain coherent during the dynamics and there is no sign of a decay of the repulsive 1D Fermi polaron.

3.2.2 Ramsey spectroscopy of the Bose polaron and evidence towards an orthogonality catastrophe phenomenon [K4]

Having unveiled the presence of a stable Fermi polaron in 1D, we next turn our attention to the study of the stability of the Bose polaron. This premise seems at first somewhat strange since the Bose polaron is thought to be stable even in 1D. This is because the form of the Bogoliubov-Fröhlich Hamiltonian, Eq. (2.76), is independent of the dimensionality of the system [179]. Moreover, recent experiments have also realized 1D Bose polaron states. However, as also mentioned in Sec. 2.4.5, ultracold atom ensembles encompass a variety of competing effects regarding the Bose polaron formation. These refer to the possible pathways via which different non-linear excitations of the BEC host can be manifested, when it is perturbed by a mobile impurity. Here, we are particularly interested in two such mechanisms, namely the emergence of phase separation, characterized by the immiscibility of the BEC plus impurity mixture [202–207] and the pattern formation [200, 207–210, 386, 388], stemming from the violation of the Landau criterion for a rapidly moving impurity.

The above motivate the use of Ramsey spectroscopy for the study of such states, which are generically expected not to be long-lived. Recall here that the Ramsey spectroscopic scheme does not rely on a finite overlap of the many-body states characterized by vanishing and finite interactions between the impurity and its environment, i.e. the

Frank-Condon coefficient, see also Sec. 2.5.3. Accordingly, within this framework we are able to track the impurity dynamics even in the case that the state accessed by the interacting system is almost completely orthogonal to the non-interacting one. Another benefit of the Ramsey spectroscopy is that it allows for the time-dependent characterization of the dynamics of the impurity by tracking the stability properties of the Bose polarons in terms of the spectroscopic contrast.

The description of the employed spectroscopic protocol has been provided in detail in Sec. 2.5.3. Here we only briefly recapitulate it below. Initially, the impurity is prepared in its pseudospin- \downarrow state, which is not interacting with the bosonic environment, such that both the impurity and the bosonic bath are in their corresponding ground state configurations. To trigger the dynamics, an intense $\pi/2$ radiofrequency pulse acts upon the spin degree of freedom of the impurity, which maps the pseudospin- \downarrow impurity to the superposition state $|\psi_S\rangle_i \equiv \frac{|\uparrow\rangle + |\downarrow\rangle}{\sqrt{2}}$ [145]. Subsequently, the system is left to evolve in the absence of radiofrequency fields for a dark time $t = t_d$. After this step the real and imaginary parts of the Ramsey contrast can be probed by measuring the magnetization of the pseudospin impurity along the x and y pseudospin axes respectively. Importantly, since a single impurity is employed the Ramsey contrast is equivalent to the structure factor $\langle \Psi(t) | \hat{S}_x + i\hat{S}_y | \Psi(t) \rangle = S(t)$ (see also Eq. 2.91). In this work we are mostly interested in the absolute value of the structure factor, $|S(t)|$, yielding the Lodschmidt echo, or fidelity, of the polaronic state with the initial one, which is inherently connected with the concept of the quasi-particle residue [92, 147].

The Ramsey spectroscopy of repulsive Bose polarons reveals, that for impurity-bath interactions smaller than the intraspecies ones of the BEC, namely $g_{BI} \leq g_{BB}$, the structure factor possesses an oscillatory behaviour in time with $0 < |S(t)| \leq 1$. This finding signifies that for these interaction regimes the Bose polaron is a well defined and stable quasiparticle. A valuable tool for the characterization of the dynamics is provided by an effective potential approach which allows for qualitatively understanding the behaviour of the system. This effective potential regards the density of the bosonic bath acting merely as a repulsive potential for the impurity, and thus modifying its effective confinement. More specifically, for $g_{BI} < g_{BB}$, this effective potential corresponds to a harmonic oscillator with a modified trapping frequency, $\omega_{\text{eff}} = \omega \sqrt{1 - g_{BI}/g_{BB}}$, where ω is the frequency of the original externally imposed parabolic potential. The above imply that the population of the impurity, which is transferred to the spin- \uparrow state and is exposed to a finite interaction with the bosonic host, experiences a weaker confinement $\omega_{\text{eff}} < \omega$ compared to its initial state. In turn a breathing mode is induced for the spin- \uparrow atoms which can be clearly observed by examining the time-evolution of the spin-resolved impurity density. This breathing mode is associated with a periodic modulation of the density overlap between the spin- \downarrow and spin- \uparrow states, leading to the exhibited behaviour of $|S(t)|$. In the case of $g_{BI} \approx g_{BB}$ a similar phenomenology is observed, however the imprint of the dynamics to the Ramsey signal is more pronounced. In this case, the effective potential can be shown to possess an almost square-well shape. Accordingly, the initial pulse induces a prominent dynamics for the spin- \uparrow density of the impurity. The later diffuses within the BEC background by breaking up into two

OUTLINE OF SCIENTIFIC CONTRIBUTIONS

filament-like structures [208–210], and subsequently revives at the trap center. The above imply that the value of the structure factor reduces to $|S(t)| \approx 0$ for the times that the spin- \uparrow forms filaments and reaches a value $|S(t)| \approx 1$ when the density revives. The stability of these oscillations of $|S(t)|$ against damping indicate the long-lived nature of the Bose polaron that persists within the $g_{BI} \approx g_{BB}$ interaction regime. This will be further explicated later on, via the use of pump-probe spectroscopy, see also Sec. 3.2.4.

However, the situation becomes drastically different when the bath-impurity interactions are significantly larger than the intraspecies ones, i.e. $g_{BI} > g_{BB}$. In that case, after a brief time interval, roughly $t < 20\omega^{-1}$, where $|S(t)|$ exhibits an oscillatory pattern with a decaying amplitude, the structure factor saturates to a value $|S(t)| \rightarrow 0$. By inspecting the corresponding one-body density of the spin- \uparrow configuration we observe that initially the density of the impurity splits into two filaments which are expelled from the spatial extent of the BEC. The dynamics in this case is reminiscent of the one occurring when a binary Bose gas is quenched from the miscible to the immiscible phase [208–210], triggering in this way the phase separation. After this initial expansion, the filaments perform damped oscillations around the Thomas-Fermi radius of the BEC. Obviously, this attenuation of the dynamics implies that the energy of the impurity is not constant in time and consequently it cannot be explained solely based on the effective potential, in contrast to $g_{BI} \leq g_{BB}$. The above mentioned phenomenon is referred to as the (temporal) orthogonality catastrophe, since the state of the many-body system at long times $t \geq 100\omega^{-1}$ is almost orthogonal to the initial one.

To qualitatively comprehend the mechanism leading to the temporal orthogonality catastrophe, we consider the Landau criterion for the superfluidity of the BEC [201] when the latter is perturbed by a mobile impurity [197, 199, 200]. The deformation of the effective potential for $g_{BI} > g_{BB}$, gives us, also in this case, an intuitive picture regarding the motion of the impurity within its environment. In particular, for $g_{BI} > g_{BB}$, the effective potential possesses a double-well structure, with the initial state of the impurities being on the top of the potential barrier and the corresponding potential minima located at the edges of the BEC, i.e. at $x = \pm R_{TF}$, where R_{TF} denotes the Thomas-Fermi radius of the environment. The repulsive character of this potential expels the impurity from the trap center, leading to its acceleration. This acceleration implies that increasing values of impurity momentum are accessed, enabling the violation of the Landau criterion for the superfluidity of the BEC background [200]. In particular, when the velocity of the impurity exceeds a critical value, phononic excitations are induced in its bosonic host [201], resulting to the transfer of energy from the impurity to the BEC, which is indeed observed in our calculations. This transfer of energy is the mechanism that leads to the apparent dissipation of the spin- \uparrow impurity dynamics and the accumulation of the corresponding density at the periphery of the Bose gas at $x = \pm R_{TF}$.

The study of Ref. [K4] provides important information regarding the Bose polaron properties and the characterization of the distinct regimes of polaron dynamics when the bath-impurity interactions are abruptly switched on. However, an important concept

that is not discussed within this study refers to induced polaron-polaron interactions mediated by their host. This subject is particularly important, since it gives rise to composite structures, such as the bipolaron [162, 164, 166, 365], referring to a bound state of polarons emanating due to their induced attraction. Such states are thought to be important in a variety of systems, however they still lack a decisive experimental identification and characterization.

3.2.3 Multiple Bose polarons and their induced interactions [K5]

In order to examine the effect of induced interactions in Bose polaron systems we focus on the case of a small impurity number (mainly referring to two) and examine the properties of the resulting polaronic states with respect to the case where no interaction effects are exhibited. The main tools for this characterization are the examination of the ground state of two impurities embedded in a parabolically confined Bose gas and Ramsey spectroscopy to monitor the polaron generation and decay. As discussed in Sec. 2.5.3, Ramsey spectroscopy is not particularly suited for studies of multiple polaron states, since the relation of the Ramsey contrast and the dynamical structure factor, holding for $N_I = 1$, does not carry over to $N_I > 1$. Nevertheless, as we explicitly demonstrate in Ref. [K5] this spectroscopic scheme provides significant insights for the polaron dynamics also when considering multiple impurities.

As a first attempt to address the question of impurity-impurity interactions mediated by their environment we resort to the equilibrium properties of two Bose polarons. Similarly, to the Fermi polaron case the difference in the Bose polaron energy between a two-polaron state and a single-polaron one hardly reveals the presence of any induced polaron-polaron interactions. A notable exception is the case of strong impurity-bath attractions. There, a large energy decrease is observed for the two-polaron case, even when the impurities interact repulsively via s -wave interactions, suggesting the presence of a strong impurity-impurity induced effective attraction.

Motivated by our findings regarding Fermi polarons [K3], we demonstrate that the relative distance among the impurities is, also in the bosonic case, a valuable quantity to characterize the polaron-polaron interactions. To elucidate the imprint of induced interactions in the relative distance of the impurities, we compare our findings to an effective potential approach [K4]. In particular, this approach takes into account the deformation of the impurity density due to its interaction with the bosonic environment for $g_{BI} \neq 0$, but it completely neglects the effects stemming from induced impurity-impurity interactions, which are mediated by the density fluctuations of the BEC. Therefore, the effective potential consists our benchmark regarding non-interacting impurities which we employ for the identification and characterization of their induced interactions. When these density fluctuations of the BEC are taken into account within our fully correlated ML-MCTDHF calculations (Sec. 2.6), the presence of a polaron-polaron attraction is revealed by the reduced value of the impurity-impurity distance when compared to the effective potential prediction. Particularly, in the case that the s -wave scattering among the impurities is zero, $g_{II} = 0$, the distance between them is shown to be smaller than the prediction of the effective potential for all $g_{BI} \neq 0$, indi-

OUTLINE OF SCIENTIFIC CONTRIBUTIONS

cating the presence of induced attraction, independently of the repulsive or attractive character of g_{BI} . However, in the case of repulsive s -wave interactions among the impurities, $g_{II} > 0$, there is a large reduction of the strength of the induced interactions. Importantly, the relative distance between the impurities is larger than the corresponding one for $g_{II} = 0$, showing that the s -wave repulsion between the impurities largely counteracts the induced attraction mediated by the bosonic host. Strikingly, in the intermediate and temporal orthogonality catastrophe regimes, $g_{BI} \gtrsim g_{BB}$, the relative distance for $g_{II} > 0$ indicates a sizable net repulsion of the impurities, since its value becomes larger than the effective potential prediction.

A particularly important aspect of our study is the exploration of the attractive bath-impurity interaction regime. Regarding the above mentioned stationary properties we observe pronounced induced interactions in the $g_{BI} < 0$ regime. In particular, for strong $g_{BI} < 0$, associated with a large decrease of the polaron energy, we identify the emergence of the bipolaron [162, 164, 166, 365]. The latter refers to a composite structure of two polarons which are bound together by the strong attractive impurity-impurity mediated interactions. By examining the dynamics for $g_{BI} < 0$ in terms of the Ramsey spectroscopy we observe a response similar to the weakly repulsive impurity case, see also Sec. 3.2.2. This response is characterized by an oscillatory behaviour of the Ramsey contrast due to the presence of the attractive Bose polaron, indicating a stable polaron with residue, $Z < 1$. However, in this case, depending on the magnitude of $g_{BI} < 0$, the bosonic environment is prominently deformed. In particular, as a result of the attractive nature of the impurity-bath interactions the impurities experience an effectively stronger confining potential, leading to their increased localization tendency at the trap center. Accordingly, the bath particles are attracted to this increased impurity density, leading to the development of a BEC density peak which accompanies the impurity one. This additional structure and the associated strong excitation of the bosonic environment implies a significant reduction of the polaron residue. The above explain the prominent fluctuations of the Ramsey contrast associated with the large amplitude fluctuations of the dynamical structure factor in the course of the dynamics.

The study of the two and three impurity dynamics in the repulsive case yields similar results to the single impurity case ($N_I = 1$), analyzed in Ref. [K4]. In the Ramsey contrast three impurity-bath interaction regimes are mainly observed referring to weak, $0 < g_{BI} < g_{BB}$, intermediate, $g_{BI} \approx g_{BB}$, and strong, $g_{BI} > g_{BB}$, interactions. In the weak and strong coupling regimes the behaviour of the system is similar to $N_I = 1$, with the only difference being that for $g_{BI} > g_{BB}$ the temporal orthogonality catastrophe seems to occur faster for $N_I > 1$. The same information can be deduced from the time-evolution of the one-body density of the impurities. Significant deviations from the $N_I = 1$ case occur in the intermediate regime $g_{BI} \approx g_{BB}$. Here, the amplitude of the oscillations of the Ramsey contrast drops significantly at the later stages of the dynamics. This behaviour can be explained in terms of the emergence of mediated interactions, resulting in the development of impurity-impurity correlations, which lead to the dephasing of the single and two-polaron terms that contribute to the Ramsey contrast, see also Eq. (2.92). In agreement to this interpretation, the one-body density

for $N_I = 2$ is found to be almost identical to the corresponding one for $N_I = 1$, supporting that the discrepancy for different particle numbers is related to the emergence of induced correlations. As a final comment, the boundaries between the weak and strong interaction regimes are significantly affected by the increase of the impurity number, with the onset of the orthogonality catastrophe shifting to lower values of g_{BI}/g_{BB} for increasing N_I .

3.2.4 Pump-Probe spectroscopy of Bose polarons: lifetime and relaxation of the quasiparticle structures [K6]

Having identified the existence of polaronic excitations in Ref. [K4, K5], we turn our attention to the study of their dynamical formation, lifetime and decay. To identify these properties, a protocol that provides access to the spectral features of the impurities state, during distinct stages of the dynamics, needs to be employed. As mentioned in Sec. 2.5.4, such a time-dependent spectroscopic scheme is provided by the so-called pump-probe spectroscopy, which allows for probing the dynamics with simultaneous temporal and spectral resolution. Indeed, within this scheme we can identify the evolution of the energy distribution among the different excited modes of the system and from that infer the formation or death of quasi-particle excitations.

In Ref [K6] we assume the pump-probe spectroscopic scheme that is briefly outlined below. Initially, the impurities reside in a particular spin state, $|\downarrow\rangle$, characterized by zero interaction between them and their bosonic environment. In addition, both the impurities and the bath are assumed to be in their corresponding ground states. At $t = -t_e$ a strong pump pulse is applied in order to transfer, as efficiently as possible, the impurities from their spin- \downarrow state to the spin- \uparrow one. The latter is resonantly interacting with the bath with an interaction strength g_{BI} . After this pump sequence an optical blast transition annihilates the remaining spin- \downarrow atoms, resulting to the projection of the spin degree-of-freedom to the $|\uparrow\rangle$ state. Subsequently, the system is left to evolve in the absence of a coupling among the spin-states for a dark time, t_d . After the end of this dark time the nonequilibrium dynamics of the impurities is monitored via the application of a pump pulse that transfers the spin- \uparrow impurities to their spin- \downarrow state. The employed spectroscopic signal is the fraction of impurity atoms that are transferred to the spin- \downarrow state after the end of the pump pulse.

Before proceeding further, it is instructive to elaborate on the parameters employed within our pump-probe setup and their relevance for exposing the dynamical formation of the polaron. In particular, a strong pump pulse is applied, resulting in a spatial configuration of the many-body system that remains as proximal as possible to the initial one, while all the spins are flipped. More specifically, the pump pulse satisfies $\frac{1}{N_I!} \langle \Psi(0) | (\hat{S}_+)^{N_I} | \Psi(-t_e) \rangle \approx 1$, where $\hat{S}_+ = \hat{S}_x + i\hat{S}_y$ refers to the spin-rising operator and $|\Psi(-t_e)\rangle$, $|\Psi(0)\rangle$ to the many-body state before or after the pulse respectively. The above ensure that polarons are not able to form during the pump pulse, as the spatial state of the mixture remains largely unperturbed during its application. The corresponding parameters of the probe pulse are selected, such that they compromise between the spectral and temporal resolution of the polaron dynamics. Indeed, a

OUTLINE OF SCIENTIFIC CONTRIBUTIONS

strong probe pulse inevitably results to a significant power broadening, implying a lower spectral resolution (since the error in the determination of the position of spectral lines scales as $\delta\Delta^{\text{probe}} \approx \Omega_{R0}^{\text{probe}}$). Furthermore, a probe pulse of lower intensity, despite its higher spectral resolution, relies on longer pulse times in order to obtain a measurable spectroscopic signal. For longer probe pulses the dynamics of the spatial degree-of-freedom of the system is not suppressed during their application, reducing the obtained temporal resolution of the system dynamics. As a heuristic argument the spectral resolution can be related with the temporal one via the Heisenberg uncertainty equation $\delta E \delta t \approx \hbar$, yielding $\delta t_d \approx (\delta\Delta^{\text{probe}})^{-1} \approx (\Omega_{R0}^{\text{probe}})^{-1}$. For a trapped system the relevant energy and time scales are $\hbar\omega$ and ω^{-1} respectively. Consequently, a natural choice for the Rabi frequency of the probe pulse is $\Omega_{R0}^{\text{probe}} = 1$ so as to balance the resolution of pump-probe spectroscopy for both time and energy. This choice of $\Omega_{R0}^{\text{probe}} = 1$ is adopted throughout our work [K6].

Based on the above mentioned protocol we have qualitatively characterized the dynamics of the impurities in terms of the quasi-particle formation. To achieve this, we rely on paradigmatic cases, referring to the regimes of different qualitative responses, identified in [K4, K5]. Below we summarize the information that we were able to extract regarding the dynamical formation, the decay of polaronic excitations and their dependence on the bath-impurity interaction strength.

For attractive bath-impurity interactions strong evidence for stable polaronic excitations has been provided in Ref. [K5]. In Ref. [K6], we put this expectation to a test by considering the case of $g_{BI} = -|g_{BB}| = -0.5$. The dynamics for $N_I = 1$ is characterized by a system that remains close to its initial state and populates well-defined polaronic states having a large residue, for all times $t_d < 300$. However, introducing multiple impurities, their energy is not as well defined as in the single-impurity case. The large uncertainty in the impurity energy can be attributed to the emergence of large impurity-impurity induced interactions, resulting to collisional broadening of the spectral line. For large times we observe that the impurities mainly reside in a polaronic state with well-defined energy, but the reduced amplitude of this peak implies a dramatically reduced contrast when compared to the single-impurity case. This fact can be also regarded as an evidence for the presence of induced interactions. Similar arguments also hold for fermionic impurities, however, the features of induced interactions become less prominent than in the bosonic case.

For repulsive impurity-bath interactions, Ref. [K4, K5] reveal the appearance of three distinct regimes of dynamical response. First the regime of small interactions, $g_{BI} < g_{BB}$, where a dynamics similar to the case of attractive interactions is expected. Second, the regime around $g_{BI} = g_{BB}$, where the periodic evolution between the initial state and a state characterized by filament formation has been observed. Finally, the regime of orthogonality catastrophe, for $g_{BI} > g_{BB}$, where the impurity is expelled from the bosonic environment and subsequently it progressively gets accumulated in the periphery of the Bose gas. The case of weakly interacting impurities, $g_{BI} < g_{BB}$, is not discussed in Ref. [K6] for the sake of brevity, as it is completely analogous to the case of attractive interactions (see also [K5]). For this reason, in this work, we focus on

SPECTROSCOPIC PROPERTIES OF BOSE AND FERMI POLARONS

the dynamical formation of Bose polarons, by considering two examples, namely the $g_{BI} \approx g_{BB}$ and $g_{BI} > g_{BB}$ regimes, which exhibit a more involved dynamical response.

Our results for $g_{BI} = g_{BB} = 0.5$, reveal the appearance of fringes in the probe spectrum for times corresponding to the delocalization of the initial wavepacket. This pattern can be explained by the interference of the two filaments of the impurity density [K4]. In particular, the emergence of this pattern is a signature of at least two many-body states being predominantly occupied during the dynamics, which, due to their coherence, lead to the manifestation of fringes in the probe spectrum. This argument is further supported by the almost perfect coherence between the filaments, as captured by the one-body coherence function. The contrast of these fringes appears to possess a larger amplitude in the single-impurity case, rather than for $N_I = 2$ bosonic impurities. This effect can be attributed to the presence of impurity-impurity induced interactions for $N_I = 2$, which lead to the reduction of the coherence of the ensemble. Revival events are also identified for larger times, when a well-defined polaronic peak similar to the one for $t = 0$ is exhibited. The revival of the polaronic resonance also occurs for large evolution times and for both impurity numbers, demonstrating the robustness of the polaron in the $g_{BI} = g_{BB}$ regime. As a final comment note that the exchange symmetry of the impurities seems to not affect the stability properties of the Bose polaron, since the pump-probe spectra for $N_I = 2$ fermions are qualitatively similar to the bosonic case.

As already established in Ref. [K4,K5], for large interactions, e.g. $g_{BI} = 3g_{BB} = 1.5$, we observe the phenomenon of the temporal orthogonality catastrophe. For $t_d = 0$ and for $N_I = 1$, two dominant polaronic peaks occur. The first one is close to the resonance of the pump pulse, Δ_+ , resembling the initial distribution, while the second is shifted to larger values. Both of these peaks decay significantly already for $t_d = 2$, giving rise to a much wider distribution centered around Δ_+ , as well as, to a significant peak at $\Delta^{\text{probe}} = 0$, indicating the presence of quasi-free particles. This behaviour demonstrates that the temporal orthogonality catastrophe, which leads to a finite lifetime of polaronic excitations, is at least as fast as the formation of these excitations themselves. Furthermore, the dynamical behaviour imprinted in the probe spectrum remains qualitatively equivalent, as the number of impurities increases. Quantitatively, the decay of the polarons is faster for $N_I = 2$, as already for $t_d = 0$, the amplitude of the polaron peaks is significantly reduced when compared to the $N_I = 1$ case. Induced interactions are also manifested for this value of dark-time, as the dominant peak at $\Delta^{\text{probe}} = \Delta_+$ splits into two for $N_I = 2$. For larger t_d the distribution of energies along different dynamical modes saturates, leading to the manifestation of a quasi-stable state. The most prevalent feature of this energy distribution is the quasi-free particle peak, which possesses a large amplitude $\langle \hat{N}_\downarrow(t_d) \rangle / N_I \approx 0.5$, alongside a wide distribution of lower amplitude, around $\Delta^{\text{probe}} \approx \Delta_+$. The only notable difference between the spectra for different particle numbers is the presence of fringes in the probe spectrum with $N_I = 1$. This can be attributed to the larger single-particle coherence, due to the absence of induced impurity-impurity interactions. Fermionic impurities behave similarly to bosonic ones. However, for fermions the initial stages of the temporal orthogonality catastrophe

OUTLINE OF SCIENTIFIC CONTRIBUTIONS

seem to occur for smaller times. Indeed, in the corresponding $t_d = 0$ spectrum a rather wide feature is observed in the vicinity of Δ_+ , in contrast to the sharp peaks in the $N_I = 1$ and the bosonic $N_I = 2$ cases. Nevertheless, the subsequent evolution of the probe spectra in the case of fermionic impurities is qualitatively similar to the bosonic one with some minor shifts in the positions of the spectral lines, owing to the different statistics.

An intriguing aspect of the polaronic dynamics in the strongly interacting regime is the eigenstate thermalization of the ensemble, following the orthogonality catastrophe. In particular, it is found that the pump-probe spectrum for large dark times of the order of $\sim 100\omega^{-1}$ saturates, being largely independent of the precise value of the dark time, impurity number and even their bosonic or fermionic flavor. By directly fitting the one-body density matrix of the impurity to an appropriate thermal distribution we can demonstrate that the final state of the impurity, corresponds to an eigenstate thermalized one. The corresponding effective temperature is found to be rather large when compared to the energy scale of the trap further exposing the incoherent nature of the state accessed after the temporal orthogonality catastrophe.

Concluding, the results of [K4–K6] demonstrate the important role of the inhomogeneity of the BEC density and the modification of the polaronic properties due to the presence of an effective potential, see Eq. (2.80). In particular, we are able to characterize the regimes of qualitatively distinct dynamics and provide signatures of induced interactions where the concept of the effective potential plays a prominent role. The identification of trap-induced effects, provided herein, is highly relevant for future Bose polaron experiments and offers several new prospects for further study, a subject that is further discussed in Chapter 5.

Chapter 4

Scientific Contributions

4.1 Magnetic properties of 1D degenerate few-fermion gases

4.1.1 Probing ferromagnetic order in few-fermion correlated spin-flip dynamics

PAPER • OPEN ACCESS

Probing ferromagnetic order in few-fermion correlated spin-flip dynamics

To cite this article: G M Koutentakis *et al* 2019 *New J. Phys.* **21** 053005

View the [article online](#) for updates and enhancements.

Recent citations

- [Flux-driven quantum spin liquids in kagome optical lattices](#)
Hoi-Yin Hui *et al*
- [Dissipative correlated dynamics of a moving impurity immersed in a Bose-Einstein condensate](#)
S I Mistakidis *et al*
- [One-dimensional mixtures of several ultracold atoms: a review](#)
Tomasz Sowiski and Miguel Ángel García-March



PAPER

Probing ferromagnetic order in few-fermion correlated spin-flip dynamics

OPEN ACCESS

RECEIVED

14 December 2018

REVISED

20 March 2019

ACCEPTED FOR PUBLICATION

29 March 2019

PUBLISHED

6 May 2019

Original content from this work may be used under the terms of the [Creative Commons Attribution 3.0 licence](https://creativecommons.org/licenses/by/4.0/).

Any further distribution of this work must maintain attribution to the author(s) and the title of the work, journal citation and DOI.

G M Koutentakis^{1,2,3}, S I Mistakidis¹  and P Schmelcher^{1,2}¹ Zentrum für Optische Quantentechnologien, Universität Hamburg, Fachbereich Physik, Luruper Chaussee 149, D-22761 Hamburg, Germany² The Hamburg Centre for Ultrafast Imaging, Universität Hamburg, Luruper Chaussee 149, D-22761 Hamburg, Germany³ Author to whom any correspondence should be addressed.E-mail: gkoutent@physnet.uni-hamburg.de**Keywords:** ultracold fermions, quantum gases, quantum magnetism, ferromagnetism, out-of-equilibrium dynamics, few-body systems

Abstract

We unravel the dynamical stability of a fully polarized one-dimensional ultracold few-fermion spin-1/2 gas subjected to inhomogeneous driving of the itinerant spins. Despite the unstable character of the total spin-polarization the existence of an interaction regime is demonstrated where the spin-correlations lead to almost maximally aligned spins throughout the dynamics. The resulting ferromagnetic order emerges from the build up of superpositions of states of maximal total spin. They comprise a decaying spin-polarization and a dynamical evolution towards an almost completely unpolarized NOON-like state. Via single-shot simulations we demonstrate that our theoretical predictions can be detected in state-of-the-art ultracold experiments.

1. Introduction

Magnetism constitutes a principal feature of a large class of materials and represents a macroscopic phenomenon of quantum origin [1–3]. In conductors the magnetic properties of the delocalized (itinerant) electrons are qualitatively understood in terms of the Stoner instability [4]. To verify and emulate the latter mechanism ultracold fermionic ensembles have been employed [5–7]. However, the nature of the interparticle interaction exhibited in three-dimensional ultracold gases hindered the study of itinerant ferromagnetism as the repulsive Fermi gas is metastable due to bosonic Feshbach molecule formation [8]. Utilizing fast interaction quenches, it has been shown that no ferromagnetic phase can be achieved as the decay into molecules is faster than the formation of ferromagnetic domains [6, 7]. Instead, recent pump-probe experiments [9] indicate that the formation rate of ferromagnetic domains with a size comparable to the interatomic separation is larger than the corresponding molecular decay rate. Furthermore, ferromagnetic properties have been observed indirectly either by the spectroscopic study of strongly particle-imbalanced [10, 11] (supplemented by [12]) and particle-balanced [9] two-component Fermi mixtures or by employing a binary Fermi gas prepared in a magnetic domain wall structure [13]. The latter experimental evidence poses the question whether stable ferromagnetism can be observed in the absence of molecule formation.

A controllable setting that can shed light on such inquiries is the experimentally accessible few-fermion quasi-one dimensional (1D) gas [14]. Owing to its 1D character, a shallow two-body bound state for effectively repulsive interactions is absent and thus the molecule formation is suppressed. Moreover, the experimental [15, 16] and theoretical [17–21] study of the magnetic properties of few-fermion systems has led to the insight that for near zero and infinite interactions there is an approximate mapping of the 1D spin-1/2 Fermi gas to an effective spin-chain model [22–28]. Most importantly, these spinor systems possess experimentally accessible eigenstates of ferromagnetic nature⁴, namely the interaction-independent spin-polarized states. Consequently, the study of the dynamical stability of these ferromagnetic states is essential for our understanding of the

⁴ For our purposes, a state is defined as ferromagnetic when it is characterized by maximal spin alignment and polarization.

magnetic properties of 1D systems. The study of the mechanisms emanating in 1D systems might in turn provide important insights for higher dimensional settings.

We study the dynamical stability of the fully polarized 1D parabolically-confined few-fermion spin-1/2 gas under the effect of inhomogeneous Rabi coupling of the spin-states. This coupling scheme introduces a spatially dependent spin-flip transition amplitude and thus probes the stability of the initial state by breaking the spin-symmetries of the unperturbed system (see below). An argumentation based on the Hartree–Fock (HF) framework of the Stoner model testified within the time-dependent Hartree–Fock (TDHF) [29] showed that the spin-polarization of the Fermi gas is stable for interparticle repulsions that exceed the kinetic and spin-flip contributions [30, 31]. Inspecting the correlated spin-flip dynamics within the latter interaction regime (where TDHF predicts stable ferromagnetism) we reveal that the many-body (MB) spin–spin correlator exhibits ferromagnetic spin–spin correlations throughout the dynamics. Moreover and in contrast to the TDHF results the MB state of the ferromagnetically correlated gas shows an unstable polarization fluctuating between fully polarized and almost completely unpolarized. This outcome cannot be retrieved within the HF description and exposes the crucial role of correlations in the magnetic properties of spin-1/2 fermions even away from the strongly interacting regime. We show that the decay of the polarization and the emerging correlated spin-order can be understood by generalizing the spin-chain model of [28]. The coupling of the initial state to lower spin- S values is found to cause the dephasing of the collective Larmor precession of the spins. This dephasing dynamically leads the system to an almost equal superposition of the two ferromagnetic fully polarized states of opposite spin-orientation i.e. a NOON-like state [32, 33] with zero total polarization. For weaker and stronger interactions lying outside the above-mentioned ferromagnetically ordered regime the system undergoes a demagnetization dynamics which is identified and characterized. Our results generalize to other particle numbers within the few-body regime. The employed setup can be implemented in state-of-the-art ^{40}K experiments and the corresponding findings can be probed by fluorescence imaging techniques. Additionally, we showcase that our findings can be generalized to a broader class of dynamical scenarios characterized by different initial states and Rabi-coupling potentials. We explicitly demonstrate the robustness of our results against common noise sources exhibited in such experiments by performing simulations of single-shot images.

The presentation of our results proceeds as follows. In section 2 we discuss the setup and the basic observables used for the interpretation of the spin-dynamics. In section 3 we present our results for the correlated spin-flip dynamics employing the Multi-Configuration Time-Dependent Method for Fermions (MCTDHF) [34–39] and interpret them in terms of two approximate methods for the case $N = 3$. Section 4 provides a generalization of our findings to the case of $N = 5$ fermions. In section 5 we also demonstrate that the observed dynamical phenomena persist for different initial states and inhomogeneous Rabi-couplings. A possible experimental probe of our predictions and its feasibility are discussed in section 6. In section 7 we summarize our results and provide an outlook. Appendix A addresses our numerical methodology based on MCTDHF. The numerical implementation of the single-shot simulations for spinor fermions is briefly discussed in appendix B. Finally, in appendix C we derive the effective spin-chain model for our system.

2. Setup

We consider an interacting system of N spin-1/2 fermions of mass m , confined in an 1D parabolic trap of frequency ω . The interparticle interaction emanating in such systems is well-described by the s -wave contact interaction of strength, g [40]. The latter can be manipulated by exploiting either Fano-Feshbach or confinement induced resonances [8]. The MB Hamiltonian that models such a system reads $\hat{H} = \hat{H}_0 + \hat{H}_I$, where the single-particle Hamiltonian \hat{H}_0 is

$$\hat{H}_0 = \sum_{\alpha \in \{\uparrow, \downarrow\}} \int dx \hat{\psi}_\alpha^\dagger(x) \left(-\frac{\hbar^2}{2m} \frac{d^2}{dx^2} + \frac{1}{2} m \omega^2 x^2 \right) \hat{\psi}_\alpha(x). \quad (1)$$

The corresponding interparticle interaction term is encoded by

$$\hat{H}_I = g \int dx \hat{\psi}_\uparrow^\dagger(x) \hat{\psi}_\uparrow^\dagger(x) \hat{\psi}_\uparrow(x) \hat{\psi}_\downarrow(x), \quad (2)$$

where $\hat{\psi}_\alpha(x)$ denotes the fermionic field-operator with spin $\alpha \in \{\uparrow, \downarrow\}$. The Hamiltonian \hat{H} exhibits several crucial spin-symmetries. It can be shown that \hat{H} commutes with each component of the total spin-vector operator

$$\hat{S} = \frac{\hbar}{2} \sum_{\alpha\alpha'} \int dx \hat{\psi}_\alpha^\dagger(x) \boldsymbol{\sigma}_{\alpha\alpha'} \hat{\psi}_{\alpha'}(x), \quad (3)$$

where $\boldsymbol{\sigma}$ denotes the Pauli vector. Additionally, it possesses a SU(2) symmetry stemming from its commutation with the total spin-magnitude operator

$$\hat{S}^2 = \frac{3N\hbar^2}{4} + \underbrace{\frac{\hbar^2}{4} \sum_{\alpha, \alpha', \beta, \beta'} \int d^2x (\sigma_{\alpha, \alpha'} \cdot \sigma_{\beta, \beta'}) \hat{\psi}_{\alpha}^{\dagger}(x_1) \hat{\psi}_{\beta}^{\dagger}(x_2) \hat{\psi}_{\beta'}(x_2) \hat{\psi}_{\alpha'}(x_1)}_{=\sum_{i \neq j} \hat{S}_i \cdot \hat{S}_j}. \quad (4)$$

These symmetries imply that the eigenvalues of \hat{S}_z and \hat{S}^2 define good quantum numbers. Consequently, the ferromagnetic fully spin-polarized state, $|\Psi_F\rangle = \prod_{i=0}^{N-1} \int dx \phi_i(x) \hat{\psi}_{\uparrow}^{\dagger}(x) |0\rangle$, where $\phi_i(x)$ refers to the i th eigenfunction of the 1D harmonic oscillator, is the energetically lowest eigenstate of \hat{H} (note that $\hat{H}_I |\Psi_F\rangle = 0$) with total spin eigenvalues $S = S_z = \frac{N}{2}$.

To controllably probe the stability of such a ferromagnetic state $|\Psi(0)\rangle = |\Psi_F\rangle$ under coherent processes that break both \hat{S}_z and \hat{S}^2 symmetries we employ an inhomogeneous Rabi coupling between the spin \uparrow and \downarrow states. Note here that similar Rabi-coupling techniques have been employed in several experiments e.g. see [41–44] involving binary bosonic mixtures. The resulting Hamiltonian of the total system reads

$$\hat{H} = \hat{H}_0 + \hat{H}_S + \hat{H}_I, \quad (5)$$

where the externally-imposed Rabi coupling term is

$$\hat{H}_S = B_0 \sum_{\alpha, \alpha'} \int dx e^{-\frac{x^2}{2w^2}} \hat{\psi}_{\alpha}^{\dagger}(x) \sigma_{\alpha, \alpha'}^x \hat{\psi}_{\alpha'}(x). \quad (6)$$

In particular, \hat{H}_S induces spin-flip transitions with a spatially dependent transition amplitude, modelled by a Gaussian of width w and intensity B_0 . This coupling scheme can be realized in ultracold experiments by optical Raman dressing of the two lowest hyperfine levels of ^{40}K (see also section 4). We choose the values $w = 2$ and $B_0 = 2.5/\sqrt{8\pi}$ (in harmonic oscillator units) leading to an average precession (Larmor) frequency, $\omega_L \approx 0.85$, for the spins which is lower than all collective mode frequencies (e.g. $\omega_R \approx 2$ for the breathing mode). This choice enables us to avoid spin segregation phenomena [28] occurring when the length scale of the modulation w is smaller than that of the trap $l_{\omega} = \sqrt{\hbar/m\omega}$.

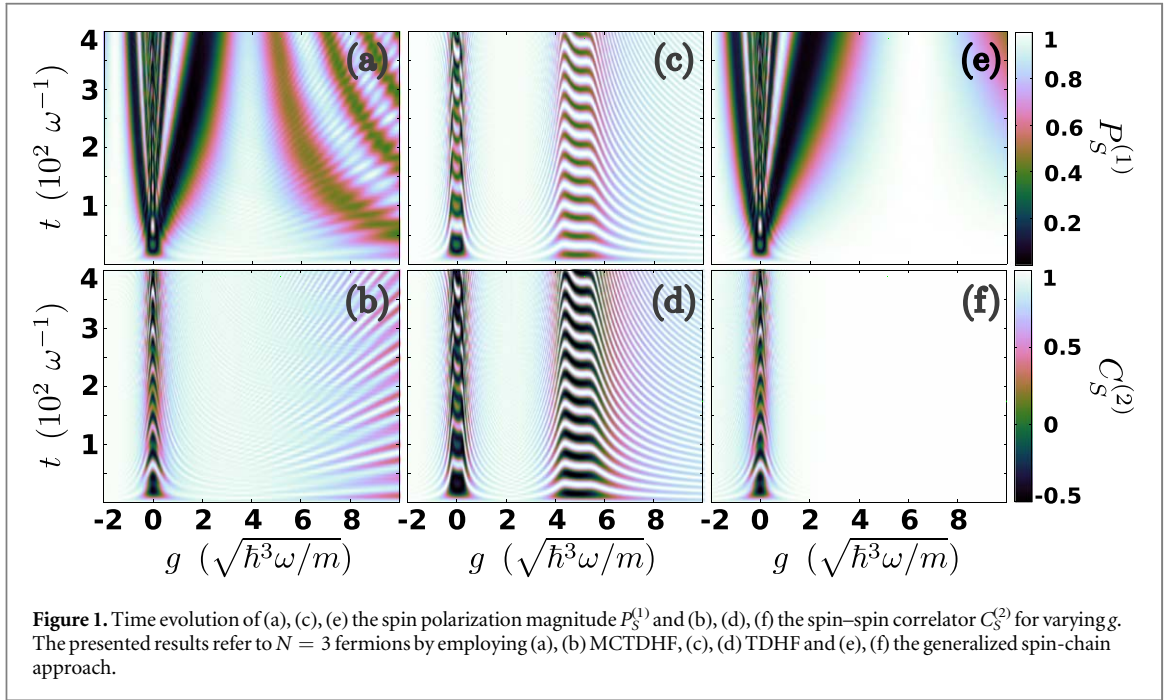
Our goal is to inspect the stability of the ferromagnetism when the \hat{H}_S term, equation (6), is abruptly switched on at $t = 0$. To achieve this we track two main observables, directly related with the system's broken symmetries. Namely, the normalized spin polarization magnitude $P_S^{(1)} = \frac{2}{\hbar N} |\langle \hat{S} \rangle|$ and the spin–spin correlator $C_S^{(2)} = \frac{4\langle \hat{S}^2 \rangle - 3N}{\hbar^2 N(N-1)} = \frac{\sum_{i \neq j} \langle \hat{S}_i \cdot \hat{S}_j \rangle}{\hbar^2 N(N-1)}$. $P_S^{(1)}$ expresses the averaged spin-order (magnetization) and refers to the magnitude of the polarization. Due to its one-body character $P_S^{(1)}$ does not probe the correlations that might emerge in the system despite being affected by them. For this purpose we employ the spin–spin correlator, $C_S^{(2)}$, which probes the alignment of each two spins and serves as an indicator for the distinction of ferromagnetic $C_S^{(2)} \approx 1$, antiferromagnetic $C_S^{(2)} \approx -1$ and paramagnetic $C_S^{(2)} \approx 0$ spin–spin correlations.

3. Analysis of the spin-flip dynamics

3.1. Many-body correlated spin-flip dynamics

Figures 1(a) and (b) present our MB results for the paradigmatic case of $N = 3$ fermions obtained via MCTDHF, that enables us to capture all interparticle correlation effects [34–39]. The MCTDHF method is a variational, numerically exact, *ab initio* method for solving the time-dependent MB Schrödinger equation which includes all correlation effects. It is based on expanding the MB wavefunction in terms of a time-dependent variationally optimized basis. In this way it enables us to efficiently truncate the MB Hilbert space relevant for our system by using a computationally feasible basis size. The MCTDHF method exhibits increased numerical efficiency when compared to an expansion relying on a time-independent basis since the number of basis states can be significantly reduced. A detailed discussion on the capabilities and the MB wavefunction ansatz of the above-mentioned method is presented in appendix A.

For weak repulsive or attractive interactions, $|g| < 0.5$, a rapid demagnetization (see the decaying behaviour of $P_S^{(1)}$) is observed, accompanied by a loss of the spin alignment, $C_S^{(2)}$, at a time scale ~ 20 . Partial revivals of both $P_S^{(1)}$ and $C_S^{(2)}$ appear over regular time intervals for later times. Our results for this interaction interval are compliant with the spin-dynamics analysed in [28, 45] and we shall refer to this regime as the weak- g demagnetization regime. Indeed within this regime each of the particles precesses with a different Larmor frequency leading to the loss of the polarization magnitude $P_S^{(1)}$ after a few precession cycles. For intermediate interactions of either sign, i.e. $0.5 < |g| < 4$, the decay and revival of $P_S^{(1)}$ also occurs but at a drastically increased time-scale (which increases further for larger $|g|$) when compared to the weak- g demagnetization regime. In contrast, $C_S^{(2)}$ indicates that the spins are close to be maximally aligned (e.g. $C_S^{(2)} \geq 0.85$ for $2 < g < 4$ and $C_S^{(2)} \geq 0.95$ for $g \sim -2$ in figure 1(b)) throughout the evolution, signifying ferromagnetic spin-correlations. Therefore, ferromagnetism is unstable in this interaction interval as the polarization ($P_S^{(1)}$) of the ensemble features large fluctuations despite the ferromagnetic order captured by $C_S^{(2)}$ which is almost perfect. Hence, we

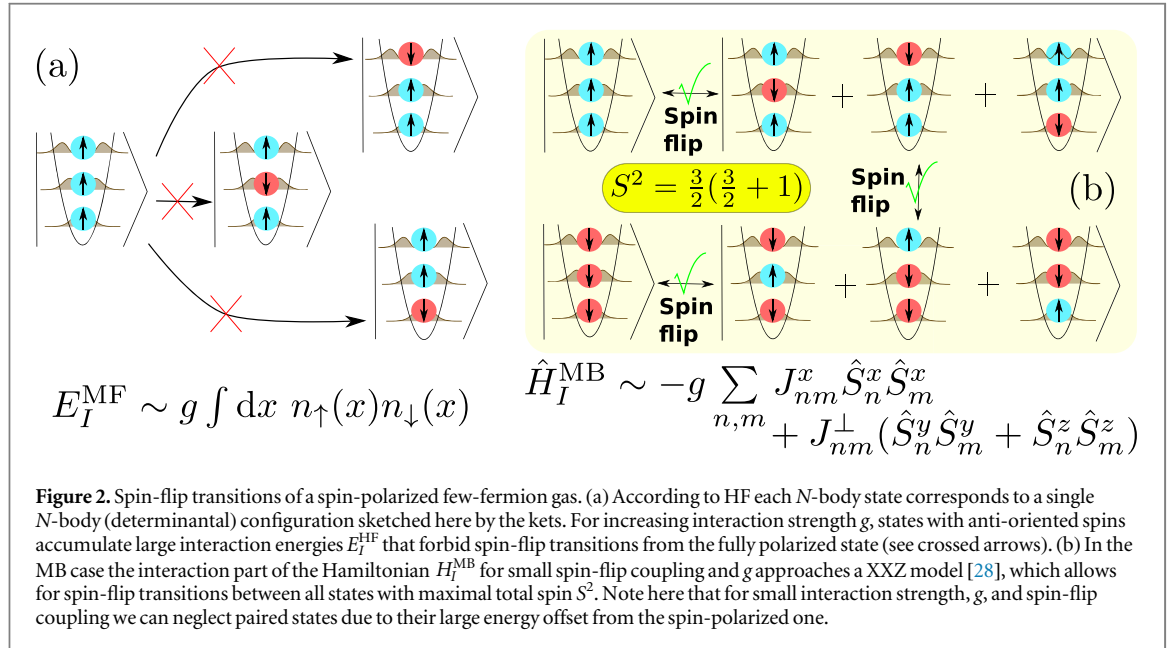


refer to this regime as ferromagnetically ordered. In particular, it involves a different spin-order than ferromagnetism, as its order is inferred by the ferromagnetic spin–spin correlations rather than the polarization. For $g > 4$ a suppression of the ferromagnetic spin–spin correlations occurs as the amplitude of the $C_S^{(2)}$ oscillations increases for stronger g , see figure 1(b). For instance, at $g \approx 10$, $C_S^{(2)}$ fluctuates between the values 0.5 and unity. $P_S^{(1)}$ is also oscillatory taking values between unity and $1/3$, with a significantly smaller oscillation frequency than $C_S^{(2)}$ (see figure 1(a)). In the following this interaction interval ($g > 4$) is referred to as the strong- g demagnetization regime.

3.2. Spin-flip dynamics within TDHF

To demonstrate the crucial role of correlations within the MB dynamics we compare the above MB findings with the TDHF approximation presented in figures 1(c) and (d). For weak $|g|$ ($|g| < 0.5$) the demagnetization dynamics is qualitatively captured by the TDHF approximation. However, upon increasing $|g|$, (in particular for $0.5 < |g| < 4$) TDHF predicts no loss of $P_S^{(1)}$ in contrast to the MB case (compare figures 1(a) and (c)), while a similar spin-correlation dynamics is observed compare figures 1(b) and 1(d). This behaviour of the TDHF can be interpreted in terms of the Stoner model [4, 30], see figure 2(a). Indeed, within HF the interaction energy of contact interacting spin-1/2 fermions is proportional to the density overlap between the two spin-components [4, 30]. Therefore, for large enough g the system initialized in a spin-polarized state characterized by zero interaction energy, cannot access states with a single (or more) spin-flips due to their large interaction energy. Thus, each of the spins has to precess with the same frequency resulting in the constant polarization magnitude, $P_S^{(1)}$. For strong $g > 4$, Rabi oscillations between the ferromagnetic initial state $|\Psi_F\rangle$ (characterized by $P_S^{(1)} = 1$, $C_S^{(2)} = 1$) and the paired HF ground states $|\Psi_\alpha^{\text{HF}}\rangle \sim \int d^3x \phi_0(x_1) \phi_0(x_2) \phi_1(x_3) \psi_\uparrow^\dagger(x_1) \psi_\downarrow^\dagger(x_2) \psi_\alpha^\dagger(x_3) |0\rangle$ (referring to $P_S^{(1)} = 1/3$, $C_S^{(2)} = -1/2$) take place. This indicates that the interparticle repulsion between the paired fermions exactly balances the energy benefit of their pairing in the same state and corresponds to the Stoner instability of the ground state. It is important to note here that these Rabi oscillations are absent in the MB case, see also figures 1(c) and (d) for $g \approx 5$.

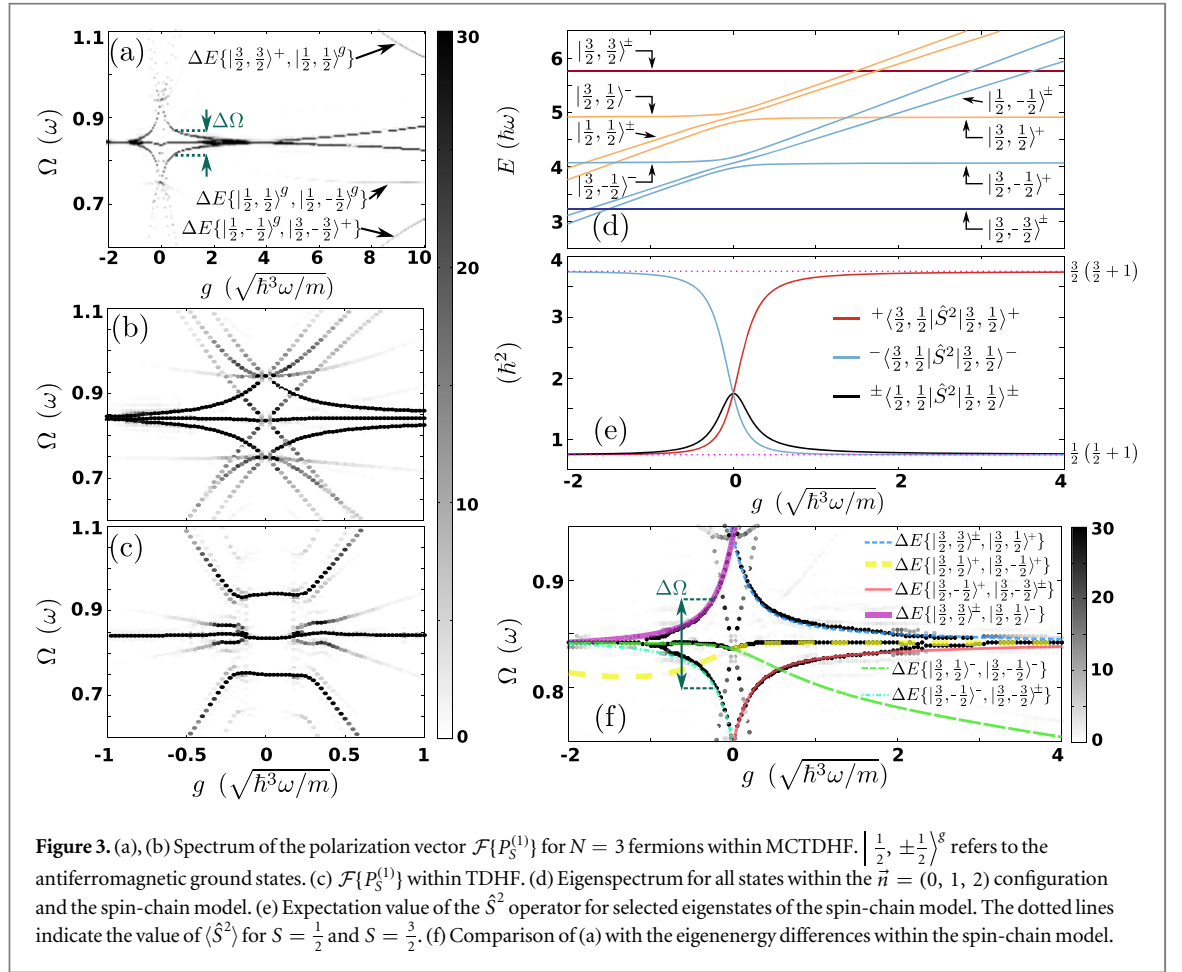
Concluding, the ferromagnetically ordered regime exhibited in the MB case corresponds to a stable ferromagnetic one within the HF framework. This observation exposes the correlated nature of the ferromagnetically ordered regime. In both cases the interaction regime is limited to intermediate values of g and in particular to $0.5 < |g| < 4$ (see figures 1(b), (d)). However, for $g > 4$ the mechanism that breaks the spin-order differs. In the HF case the ground state Stoner instability takes place which is forbidden for any finite repulsive interaction in the MB case [46, 47]. Instead, it is known that the unpaired states of maximum S (see figure 1(b)) and the MB antiferromagnetic ground states exhibit a crossing in the Tonks-Girardeau limit [16–21]. In our case due to the breaking of the $SU(2)$ symmetry the above consist an avoided crossing [27, 48, 49] which is approached for increasing $g > 4$. As we shall argue in section 3.4, the fluctuations of $C_S^{(2)}$ in the strong- g demagnetization regime for the MB case can be attributed to this avoided crossing.



3.3. Effective spin-chain model

To uncover the main mechanisms responsible for the emergence of the ferromagnetically ordered regime ($0.5 < |g| < 4$) we employ an extended version of the spin-chain model (see appendix C) presented in [28]. Our spin-chain model incorporates additional effective magnetic field terms (for details see appendix C) when compared to [28], that are necessary for the treatment of generic spin-1/2 fermion systems with a single conserved spin-component (here \hat{S}_x). Within this model the N -body wavefunction is decomposed as $|\Psi(t)\rangle = \sum_{\vec{n}} |\Psi_{\vec{n}}(t)\rangle$ with $|\Psi_{\vec{n}}(t)\rangle = \sum_{\vec{\alpha}} A_{\vec{n};\vec{\alpha}}(t) \hat{c}_{n_1\alpha_1}^\dagger \dots \hat{c}_{n_N\alpha_N}^\dagger |0\rangle$. The operator $\hat{c}_{n\alpha}^\dagger$ creates a fermion in the eigenstate $|\chi_n^\alpha\rangle = \int dx \chi_n^\alpha(x) \hat{\psi}_\alpha^\dagger(x) |0\rangle$ of $\hat{H}_0 + \hat{H}_S$, see equations (1) and (6) $\vec{n} = (n_1, \dots, n_N)$ and $\vec{\alpha} = (\alpha_1, \dots, \alpha_N)$ denote the spatial and spin configuration respectively. The crucial approximation in this model is that all the interaction terms, $\hat{H}_I^{\delta\vec{n}}$, that couple different spatial configurations \vec{n} can be neglected. By setting $\hat{H}_I^{\text{eff}} \equiv \hat{H}_I - \hat{H}_I^{\delta\vec{n}}$, the different spatial configurations \vec{n} are decoupled. It can be shown that the time-evolution of each $|\Psi_{\vec{n}}(t)\rangle$ can be described by an XXZ spin-chain consisting of N -spins [28]. The employed approximation limits the expected range of validity of the spin-chain model to small interaction values, $g < \sqrt{\hbar\omega^3/m} = 1$, where the interaction energy is smaller than the energy spacing between the single-particle eigenstates.

The polarization dynamics within the spin-chain model comply with the MB results within the weak- g demagnetization ($|g| < 0.5$) and the ferromagnetically ordered regime ($0.5 < |g| < 4$) compare figures 1(e) and (a). Moreover, by comparing $C_S^{(2)}$ (see figures 1(b) and (f)) between the two methods we observe that the spin-correlation dynamics is almost identical in the weak- g demagnetization regime, where the approximations that the spin-chain model employs are valid. On the contrary, in the ferromagnetically ordered regime the ferromagnetic spin-correlations are overestimated by the spin-chain method [hardly visible in figures 1(b) and (f)]. Finally, for increasing interactions ($g > 4$) no strong- g demagnetization regime appears within the spin-chain model, signifying the break down of its validity. This behaviour is clearly imprinted in $C_S^{(2)}$ for large g (compare figures 1(f) and (b) for $g \approx 8$). To interpret the spin-chain dynamics in the ferromagnetic and strong- g demagnetization regime we note that the configuration $\vec{n} = (0, 1, 2)$ possesses approximately 99.72 % of the contribution to $|\Psi(0)\rangle$ and thus it almost completely dictates the dynamics of the system within the spin-chain approximation. The MB polarization $P_S^{(1)}$ dynamics within the ferromagnetically ordered regime is well-captured by the spin-chain model allowing us to conclude that this behaviour emerges due to the spin-dynamics of the different states (characterized by distinct $\vec{\alpha}$) within the dominant $\vec{n} = (0, 1, 2)$ spatial configuration. In contrast, the (small) depletion of $C_S^{(2)}$ in the same regime (see figure 1(b)) is absent in the spin-chain approximation, leading to the conclusion that it stems from the neglected couplings to different spatial configurations, contained in $\hat{H}_I^{\delta\vec{n}}$. The latter couplings, however, are not as strong as to prohibit the spin-chain model to capture the spin-order emerging within the MB evolution in this interaction regime. Regarding the absence of a strong- g demagnetization regime we remark here that the coupling between the antiferromagnetic ground states belonging to the spatial configuration $\vec{n} = (0, 0, 1)$ and the initially populated states of the dominant $\vec{n} = (0, 1, 2)$ configuration is neglected by the spin-chain model.



At this point it becomes clear that the ferromagnetic order exhibited in 1D spin-1/2 Fermi gases greatly deviates from the standard HF description. Additionally, the emerging spin-order is different than the one perceived as ferromagnetic in the literature. Indeed, its defining characteristic is the stability of the spin–spin correlations rather than the polarization. The spin-chain model seems to capture well some of the characteristics of this emerging order. In the following by analysing in parallel the MB and spin-chain dynamics we will shed light onto the underlying microscopic mechanisms of the ferromagnetically ordered regime.

3.4. Analysis of the microscopic mechanisms

To identify the underlying mechanisms of the MB spin-dynamics we invoke the spectrum of the spin-polarization, namely $\mathcal{F}\{P_S^{(1)}\}(\Omega) = |\int dt e^{i\Omega t} P_S^{(1)}(t)|^2$, presented in figures 3(a) and (b) for $-2 < g < 10$ and $|g| < 1$ respectively. Recall that each branch in the spectrum of $P_S^{(1)}$ corresponds to an energy difference between two eigenenergies of \hat{H} , (see equation (5)). For $g = 0$ three distinct Larmor frequencies⁵ occur that correspond to the three energy differences among the occupied single-particle eigenstates in the spatial configuration $\vec{n} = (0, 1, 2)$. For $g \neq 0$ a multitude of interaction-dependent frequency branches emerge from each Larmor frequency. The failure of TDHF to capture even on the qualitative level the spin dynamics even for low g is evident in $\mathcal{F}\{P_S^{(1)}\}(\Omega)$. Indeed, the TDHF captures only one frequency per particle for $|g| < 0.1$ (see figure 3(c)) in contrast to the multitude of interaction-dependent frequency branches emerging from each Larmor frequency in the correlated case (see figure 3(b)). Thus we can conclude that the build up of correlations in the MB case even for very small g completely invalidates the HF picture for the spin dynamics. Such correlations are of particular importance in the ferromagnetically ordered regime. In this case, three dominant branches appear in the vicinity of $\Omega \approx 0.85$ (see also figure 3(b) for $g \approx 1$) within the correlated case that lead to the beating dynamics of $P_S^{(1)}$, observed in figures 1(a), (b).

The origin of the above-mentioned frequencies can be exposed by comparing $\mathcal{F}\{P_S^{(1)}\}$, with the energy differences of the eigenstates of the spin-chain model. As anticipated by our discussion in section 3.3 the eigenstates of the configuration $\vec{n} = (0, 1, 2)$ are expected to well capture the $P_S^{(1)}$ dynamics. The eigenspectrum

⁵ Note here the perturbative nature of \hat{H}_S , equation (6), which is manifested by the fact that the Larmor frequency of the occupied states does not deviate more than 12% from its average value $\Omega_L \approx 0.85$.

of the spin-chain Hamiltonian $\hat{H}_n = \hat{H}_{(0,1,2)}$ is presented in figure 3(d). The spin-chain eigenstates within the weak- g demagnetization regime ($|g| < 0.5$) are ordered in terms of increasing S_x due to the Zeeman effect induced by the effective magnetic field along the x axis that \hat{H}_S , equation (6), introduces. Within this weak- g demagnetization regime an avoided crossing between the distinct eigenstates of the same $S_x = \pm \frac{1}{2}$ occurs which can be attributed to the breaking of the \hat{S}^2 symmetry by the inhomogeneity of the \hat{H}_S term. The states of the spin-chain model can be labelled as $|S, S_x\rangle^\ell$ in the repulsive ($\ell = +$) and attractive ($\ell = -$) part of the ferromagnetically ordered regime ($0.5 < |g| < 4$). This is possible because S is an approximate good quantum number within this interaction range. This property can be identified by examining the expectation value of $\langle \hat{S}^2 \rangle \equiv \langle S, S_x | \hat{S}^2 | S, S_x \rangle^\ell$. Figure 3(e) presents this expectation value for the states with $S_x = \frac{1}{2}$ and varying interaction strength. It becomes evident that for increasing $|g|$ the $\langle \hat{S}^2 \rangle$ of one of these states [i.e. $|\frac{3}{2}, \frac{1}{2}\rangle^+$ and $|\frac{3}{2}, \frac{1}{2}\rangle^-$ in the case of $g > 0$ and $g < 0$ respectively] approaches the value $\langle \hat{S}^2 \rangle = \frac{3}{2}(\frac{3}{2} + 1)$, indicating that $S \approx \frac{3}{2}$. Moreover, the states $\{|\frac{3}{2}, \frac{1}{2}\rangle^-, |\frac{3}{2}, \frac{1}{2}\rangle^\pm\}$ and $\{|\frac{3}{2}, \frac{1}{2}\rangle^+, |\frac{3}{2}, \frac{1}{2}\rangle^\pm\}$ in the case of $g > 0$ and $g < 0$ respectively tend to $\langle \hat{S}^2 \rangle = \frac{1}{2}(\frac{1}{2} + 1)$. We remark here that the states with $S_x = -\frac{1}{2}$ exhibit a similar behaviour as the aforementioned $S_x = \frac{1}{2}$ case and the eigenstates $|\frac{3}{2}, \pm\frac{3}{2}\rangle^\pm$ correspond to fully polarized states along the x axis with $\langle \hat{S}^2 \rangle = \frac{3}{2}(\frac{3}{2} + 1)$ for all g (not shown here for brevity). By employing the spin-chain eigenspectrum, figure 3(d), we can identify all the energy branches appearing in figure 3(b) with the corresponding eigenenergy differences of the spin-chain model. Most importantly, figure 3(f) presents this identification within the ferromagnetically ordered regime ($0.5 < |g| < 4$). As it can be seen the energy differences between the spin-chain eigenstates with $S \approx \frac{3}{2}$, $\Delta E \{|\frac{3}{2}, S_x\rangle^\ell, |\frac{3}{2}, S_x'\rangle^{\ell'}\}$, possess the main contribution to $\mathcal{F}\{P_S^{(1)}\}$ in the ferromagnetically ordered regime as they match well with the dominant energy branches appearing in the MB dynamics. Based on this identification we can draw several conclusions regarding the order exhibited within the ferromagnetically ordered regime. First, the ferromagnetic spin-correlations emanate from the predominant occupation of MB eigenstates with $S \approx 3/2$ each characterized by a different value of S_x . The frequency difference $\Delta\Omega$ between the highest ($\Delta E \{|\frac{3}{2}, \frac{3}{2}\rangle^\pm, |\frac{3}{2}, \frac{1}{2}\rangle^\ell\}$) and lowest lying ($\Delta E \{|\frac{3}{2}, -\frac{1}{2}\rangle^\ell, |\frac{3}{2}, -\frac{3}{2}\rangle^\pm\}$) of the above-mentioned dominant branches (see also figure 3(d)) results in the dephasing of the initial superposition. In terms of the spin- \uparrow and spin- \downarrow states this means that the system performs spin-flips between the different states with $S = \frac{3}{2}$ and varying S_z leading to the decay of $P_S^{(1)}$, see figure 2(b). The corresponding timescale is $\tau_D \approx \frac{\pi}{\Delta\Omega}$. $\Delta\Omega$ is attributed to the energy shift of the $|\frac{3}{2}, \pm\frac{1}{2}\rangle^\ell$ states from being equidistantly spaced which is induced by an avoided crossing at $g = 0$, as in figure 3(d). The increase of $|g|$ within the ferromagnetically ordered regime, leads to a decrease of $\Delta\Omega$ (or equivalently increase of τ_D) giving rise to the observed $P_S^{(1)}$ dynamics (figures 1(a) and (e)).

Regarding the strong- g demagnetization regime (see figure 3(a) for $g > 4$) the frequency branches that correspond to the $|\frac{3}{2}, \pm\frac{1}{2}\rangle^+$ states deviate from $\Omega \approx 0.85$ as they couple to the antiferromagnetic ground states of $S \approx \frac{1}{2}$ and $S_x = \pm\frac{1}{2}$ character. Due to the same mechanism additional branches also appear in $\mathcal{F}\{P_S^{(1)}\}$ (see the corresponding arrows in figure 3(a)) that contribute to the complex $P_S^{(1)}$ dynamics exhibited in this interaction regime (see figure 1(a)) and results in the oscillatory patterns of $C_S^{(2)}$ (see figure 1(b), and also our discussion in section 3.2).

3.5. Characterization of entanglement in the ferromagnetically ordered regime

The separation of the energy scales $\Delta\Omega \sim 0.05$ (see figure 3(c)) and the average Larmor frequency, $\Omega_L = \frac{1}{3\hbar} \Delta E \{|\frac{3}{2}, \frac{3}{2}\rangle, |\frac{3}{2}, -\frac{3}{2}\rangle\} \sim 0.85$ observed in figure 3, enables us to further characterize the superpositions that emerge in the ferromagnetically ordered regime. To this end we introduce the precessing bases $|\frac{3}{2}, S_{y'(t)}\rangle = e^{i\frac{1}{2}\hat{S}_x\Omega_L t} |\frac{3}{2}, S_j\rangle$ ($j \in \{x, y, z\}$) and project the MB wavefunction obtained within MCTDHF to these basis states. Note that if all the particles were collectively precessing with the frequency Ω_L then $|\langle \frac{3}{2}, S_{z'(t)} = \frac{3}{2} | \Psi(t) \rangle|$ would be constant in time. However, as we have already established in section 3.2, this is not the case. Figure 4(a) presents the results of this projection for a representative case ($g = 2$) within the ferromagnetically ordered regime. We observe a low-frequency ($\sim \Delta\Omega$) population transfer from the state $|\frac{3}{2}, S_{z'(t)} = \frac{3}{2}\rangle$ to the state $|\frac{3}{2}, S_{z'(t)} = -\frac{1}{2}\rangle$. For $t > 350$ the latter mechanism results in $\langle \hat{S}_{z'(t)} \rangle \approx 0$, as $|\frac{3}{2}, S_{z'(t)} = -\frac{1}{2}\rangle$ possesses approximately a three times larger population as compared to $|\frac{3}{2}, S_{z'(t)} = \frac{3}{2}\rangle$. The nature of this superposition can be understood by transforming to the orthogonal precessing axis, $y'(t)$ (see figure 4(b)). In this case the populations of $|\frac{3}{2}, S_{y'(t)} = \frac{3}{2}\rangle$ and $|\frac{3}{2}, S_{y'(t)} = -\frac{3}{2}\rangle$ are almost equal for $t > 350$, signifying the tendency to dynamically approach a NOON state, characterized by $\langle \hat{S}_{y'(t)} \rangle \approx 0$, i.e. $|\Psi(t_0)\rangle \sim \frac{1}{\sqrt{2}} (|\frac{3}{2}, S_{y'(t)} = \frac{3}{2}\rangle + e^{i\phi} |\frac{3}{2}, S_{y'(t)} = -\frac{3}{2}\rangle)$ with a relative phase ϕ . These results combined with the conserved

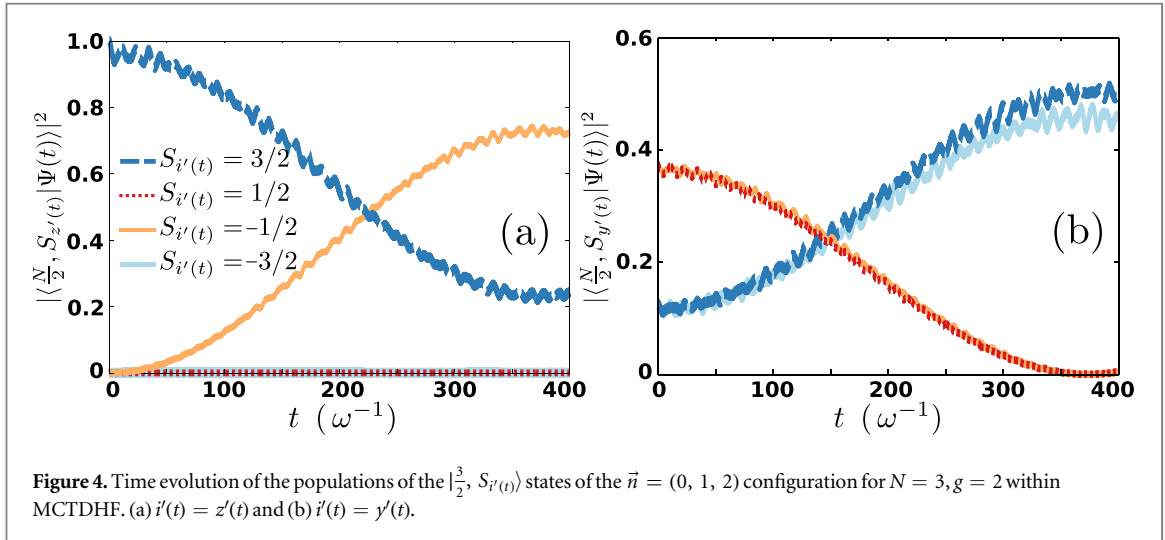


Figure 4. Time evolution of the populations of the $|\frac{3}{2}, S_{i'(t)}\rangle$ states of the $\vec{n} = (0, 1, 2)$ configuration for $N = 3, g = 2$ within MCTDHF. (a) $i'(t) = z'(t)$ and (b) $i'(t) = y'(t)$.

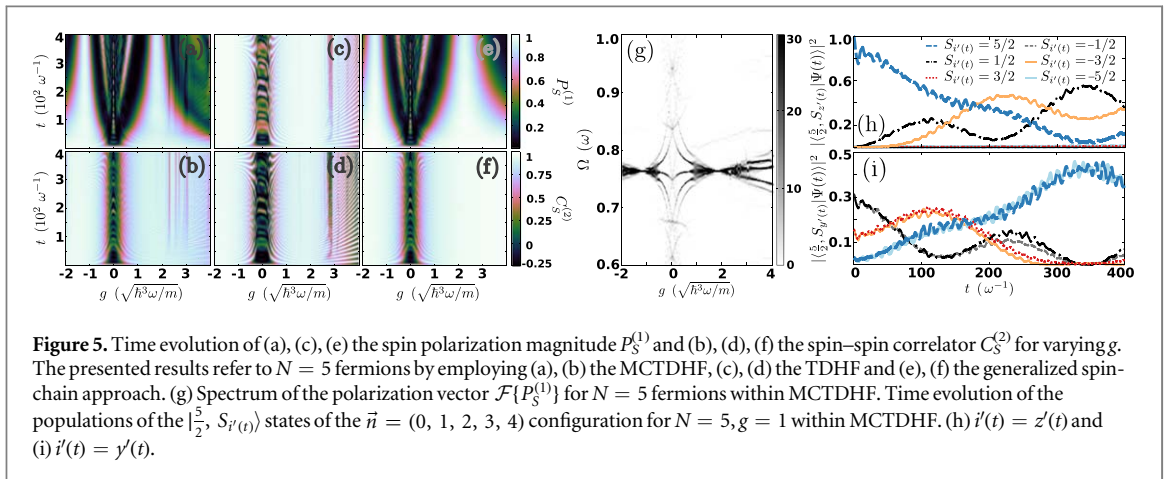


Figure 5. Time evolution of (a), (c), (e) the spin polarization magnitude $P_S^{(1)}$ and (b), (d), (f) the spin-spin correlator $C_S^{(2)}$ for varying g . The presented results refer to $N = 5$ fermions by employing (a), (b) the MCTDHF, (c), (d) the TDHF and (e), (f) the generalized spin-chain approach. (g) Spectrum of the polarization vector $\mathcal{F}\{P_S^{(1)}\}$ for $N = 5$ fermions within MCTDHF. Time evolution of the populations of the $|\frac{5}{2}, S_{i'(t)}\rangle$ states of the $\vec{n} = (0, 1, 2, 3, 4)$ configuration for $N = 5, g = 1$ within MCTDHF. (h) $i'(t) = z'(t)$ and (i) $i'(t) = y'(t)$.

quantity $\langle \hat{S}_x \rangle = 0$ explain the decay of the total magnetization $P_S^{(1)} \rightarrow 0$ for $t > 350$. Accordingly, the spin-dynamics within the ferromagnetically ordered regime describes the dynamical evolution of a fully polarized state to a superposition one consisting of two antiparallel-oriented fully polarized states.

4. Spin dynamics for $N = 5$ fermions

We next demonstrate the robustness of our main findings for the case of larger particle numbers by examining a system consisting of $N = 5$ fermions.

Figures 5(a)–(f) present $P_S^{(1)}$ and $C_S^{(2)}$ for $N = 5$ fermions within the three different approaches employed above, i.e. the MCTDHF, TDHF and spin-chain approach. A similar spin-dynamics as for the $N = 3$ case is observed for both quantities, but in different interaction regimes, caused by the increase of N . The ferromagnetically ordered regime occurs in the range $0.5 < |g| < 2$, where both $P_S^{(1)}$ and $C_S^{(2)}$ possess a value proximal to unity within the TDHF approach (see figures 5(c) and (d)). In the same range the MB treatment provided by MCTDHF reveals that $P_S^{(1)}$ is decaying (see figure 5(a)), a feature which is also well captured by the spin-chain method (see figure 5(e)). The only additional structures that emerge in the MB spin-flip dynamics when compared to the $N = 3$ case are very narrow interaction windows where $C_S^{(2)}$ gets significantly depleted from unity (see figure 5(b), $g \approx 2.5$). These regions can be attributed to avoided crossings between the different spin-states of the dominant spatial configuration $\vec{n} = (0, 1, 2, 3, 4)$ with states characterized by spatial configurations with double occupations of single-particle spatial mode(s) [e.g. $\vec{n}' = (0, 1, 2, 2, 3)$].

Inspecting $\mathcal{F}\{P_S^{(1)}\}$ for $N = 5$ fermions, see figure 5(g), similar microscopic mechanisms to the $N = 3$ case can be observed in both the weak- g and the ferromagnetically ordered regime. Despite the fact that more states are involved, the main features essentially remain the same. The weak- g demagnetization regime originates from the multitude of branches emerging from the five available non-interacting Larmor frequencies. However, only five (which can be identified as the energy differences between the $|\frac{5}{2}, S_x\rangle^\ell$ states) possess a significant amplitude

for $|g| > 0.5$. The frequency difference, $\Delta\Omega$, between the highest and lowest lying of the above five branches (see figure 5(g)) gives rise to the decay of $P_S^{(1)}$ within the ferromagnetically ordered regime observed in figure 5(a).

Finally, we show that even the superpositions emerging in the dynamics are of the same character as for $N = 3$ fermions. To reveal this we construct the precessing basis analogously to the case $N = 3$, namely $|\frac{5}{2}, S_j'(t)\rangle = e^{i\frac{1}{2}\hat{S}_x\Omega_L t}|\frac{5}{2}, S_j\rangle$, $\Omega_L = \frac{1}{5\hbar}\Delta E\{|\frac{5}{2}, \frac{5}{2}\rangle, |\frac{5}{2}, -\frac{5}{2}\rangle\}$ and expand the MB wavefunction in terms of the latter. Figures 5(h) and (i) present the results of this expansion for the axes $z'(t)$ and $y'(t)$ respectively and for $g = 1$ within the ferromagnetically ordered regime. Figure 5(h) demonstrates that the collective precession of the spins characterized by $|\langle\frac{5}{2}, S_{z'(t)} = \frac{5}{2}|\Psi(t)\rangle|^2 = 1$ gets quickly dephased. At later times $t \approx 350$ the dephasing of the collective Larmor precession leads to the formation of a NOON-like state characterized by $|\langle\frac{5}{2}, S_{y'(t)} = \frac{5}{2}|\Psi(t)\rangle|^2 = |\langle\frac{5}{2}, S_{y'(t)} = -\frac{5}{2}|\Psi(t)\rangle|^2 \approx 1/2$ (see figure 5(i)), compliant with our $N = 3$ results.

5. Generalization to other dynamical systems

Below we demonstrate that the above identified ferromagnetic properties are not restricted to the previously examined out-of-equilibrium scenario. Indeed, we will show that the 1D spin-1/2 Fermi gas exhibits a similar spin-dynamics for different initial states characterized by $S \approx \frac{N}{2}$ within the ferromagnetic-like regime, which, furthermore, does not depend on the exact form of the Rabi coupling potential⁶. The special feature of the specific dynamical protocol investigated in the previous sections is that it can be readily implemented in state-of-the-art experiments (see also section 6).

It can be shown that any initial state which is dominated by the states of the $\vec{n} = (0, \dots, N - 1)$ spatial configuration with $S = \frac{N}{2}$ possesses a similar spin-spin correlation dynamics to the ferromagnetic one,

$|\Psi_F\rangle = \prod_{i=0}^2 \int dx \phi_i(x) \hat{\psi}_\uparrow^\dagger(x) |0\rangle$. The reason is that the time-evolution of the expectation value of \hat{S}^2 reads

$$\langle\Psi(t)|\hat{S}^2|\Psi(t)\rangle = \sum_{S_x=-\frac{N}{2}}^{\frac{N}{2}} \left| \left\langle\Psi(t)\left|\frac{3}{2}; S_x\right.\right\rangle \right|^2 \left\langle\frac{3}{2}; S_x\left|e^{\frac{i}{\hbar}\hat{H}\hat{S}^2}e^{-\frac{i}{\hbar}\hat{H}}\left|\frac{3}{2}; S_x\right.\right\rangle\right| + \mathcal{O}\left(1 - \sum_{S_x=-\frac{N}{2}}^{\frac{N}{2}} \left| \left\langle\Psi(t)\left|\frac{3}{2}; S_x\right.\right\rangle \right|^2\right). \quad (7)$$

This equation stems from the fact that the quantum numbers $S = \frac{N}{2}$ and $S_x \in \{-\frac{N}{2}, \dots, \frac{N}{2}\}$ uniquely identify a single N -body state of the $\vec{n} = (0, \dots, N - 1)$ configuration. Additionally, the \hat{S}_x operator commutes with both \hat{S}^2 and \hat{H} cancelling all cross terms that would appear in the first term of equation (7). Therefore, within the ferromagnetically ordered regime where $\langle\Psi(t)|\hat{S}^2|\Psi(t)\rangle \approx \frac{N}{2}(\frac{N}{2} + 1)$, for $|\Psi(0)\rangle = |\Psi_F\rangle$, all of the contributing expectation values need to satisfy $\langle\frac{N}{2}; S_x|e^{\frac{i}{\hbar}\hat{H}\hat{S}^2}e^{-\frac{i}{\hbar}\hat{H}}|\frac{N}{2}; S_x\rangle \approx \frac{N}{2}(\frac{N}{2} + 1)$, since the probabilities are positive definite, i.e. $|\langle\Psi(t)|\frac{3}{2}; S_x\rangle|^2 > 0$. This implies that for all initial states which satisfy $\sum_{S_x=-\frac{N}{2}}^{\frac{N}{2}} |\langle\Psi(0)|\frac{3}{2}; S_x\rangle|^2 \approx 1$ the correlation dynamics within the ferromagnetically ordered regime is stable.

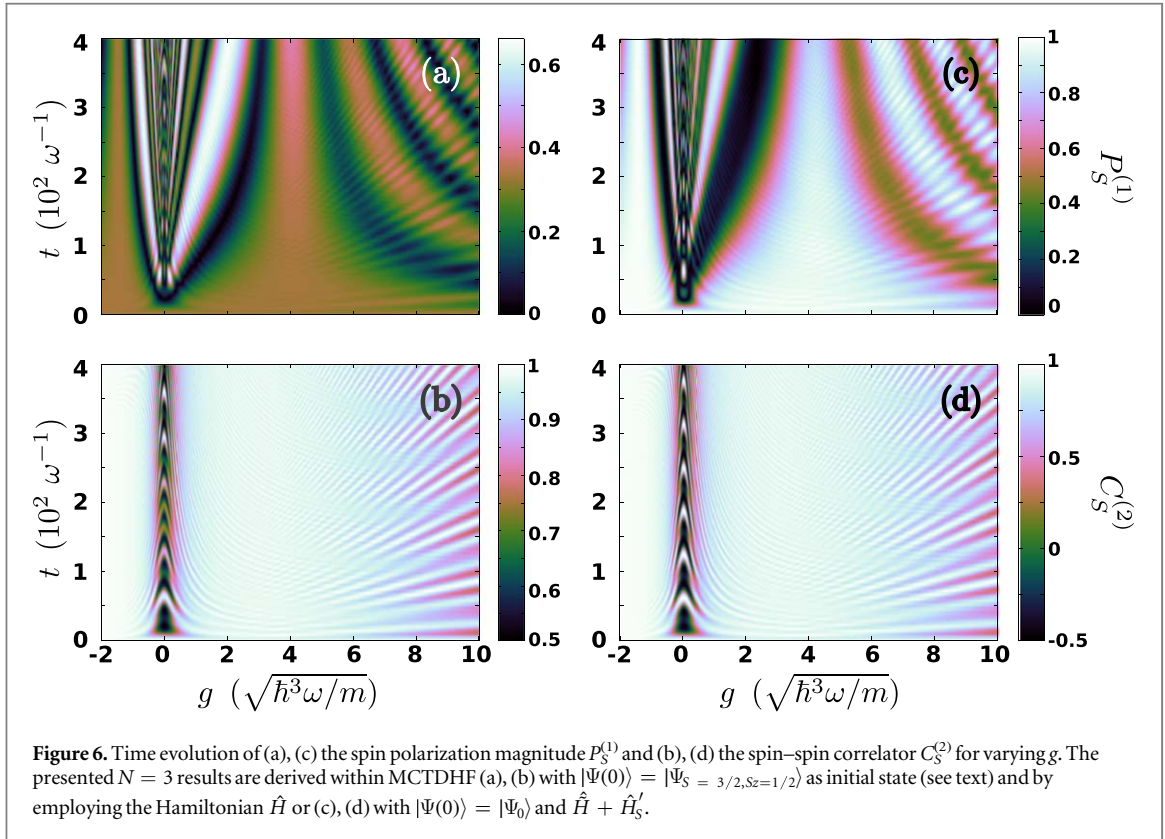
To provide concrete numerical evidence supporting the above-mentioned theoretical argument, we present in figure 6, the time-evolution of the polarization, $P_S^{(1)}$, and the spin-spin correlator, $C_S^{(2)}$, utilizing the Hamiltonian of equation (5), in the case of the initial state [16]

$$|\Psi_{S=3/2, S_z=1/2}\rangle = \int \frac{d^3x}{\sqrt{3!}} \begin{vmatrix} \phi_0(x_1) & \phi_0(x_2) & \phi_0(x_3) \\ \phi_1(x_1) & \phi_1(x_2) & \phi_1(x_3) \\ \phi_2(x_1) & \phi_2(x_2) & \phi_2(x_3) \end{vmatrix} \hat{\psi}_\uparrow^\dagger(x_1) \hat{\psi}_\uparrow^\dagger(x_2) \hat{\psi}_\uparrow^\dagger(x_3) |0\rangle. \quad (8)$$

As it can be clearly seen the correlation dynamics (see figure 6(b)) is almost identical to the one observed in section 3.1 for the fully spin-polarized initial state, $|\Psi_F\rangle = \prod_{i=0}^2 \int dx \phi_i(x) \hat{\psi}_\uparrow^\dagger(x) |0\rangle$ (see also figure 1(b)). Most importantly, the ferromagnetically ordered regime appears in the $0.5 < |g| < 4$ interaction range, characterized by $C_S^2 \approx 1$, while losses of spin-alignment (i.e. $C_S^2 < 1$) are found outside of this interaction regime. The polarization dynamics (see figure 6(a)), however, shows different patterns from the dynamics obtained with $|\Psi_F\rangle$, since the initial polarization in the present case is $P_S^{(2)} = \frac{1}{3}$ rather than unity. Nevertheless, within the ferromagnetically ordered regime we observe large fluctuations of the polarization while the spin-spin correlator is almost constant, similarly to the dynamics that the system with $|\Psi(0)\rangle = |\Psi_F\rangle$ follows (see figures 1(a), (b)).

According to our previous discussion (see section 2) the Rabi-coupling between the spin- \uparrow and the spin- \downarrow states is assumed to be weak and the characteristic length of its modulation is larger than the length scale of the trap, $\sqrt{\frac{\hbar}{m\omega}}$. Due to these assumptions it is reasonable to approximate the Rabi-coupling potential by its Taylor series. We can, thus, demonstrate that our results generalize to all Rabi-coupling potentials with a non-vanishing

⁶ Here we assume a weak and spatially slowly varying coupling of the spin- \uparrow and spin- \downarrow states.



second-order derivative⁷ by showing that a similar dynamics as in section 3.1 can be obtained for the parabolic spin-coupling potential

$$\hat{H}'_S = \frac{1}{2}m(\Delta\omega)^2 \int dx x^2 \sum_{\alpha,\beta} \hat{\psi}_\alpha^\dagger(x) \sigma_{\alpha\beta}^x \hat{\psi}_\beta(x). \quad (9)$$

For our simulations we employ $\Delta\omega = \sqrt{0.1}$, while the system is initialized in the fully polarized state, $|\Psi_F\rangle$, though as argued above a similar dynamics takes place when the system is initialized in the $|\Psi_{S=3/2, S_z=1/2}\rangle$ state (results not shown here for brevity). As it can be seen, the behaviour of the system in terms of the spin-polarization, $P_S^{(1)}$ (see figure 6(c)) and the spin–spin correlations, $C_S^{(2)}$ (see figure 6(d)) is almost identical to the case of \hat{H}_S , equation (6) (see also figures 1(a) and (b)), with deviations occurring only within the $g \approx 0$ region (compare figures 6(c) and (b)). We also note that in the case of strong spin-dependent potentials, where the exact shape of the Rabi-coupling potential might play an important role, spin segregation phenomena are induced [28, 45]. These compete with the ferromagnetic order identified here, as the overlap of the spin-densities provides an upper bound for $\langle \hat{S}^2 \rangle$ and therefore such investigations lie beyond the scope of this work.

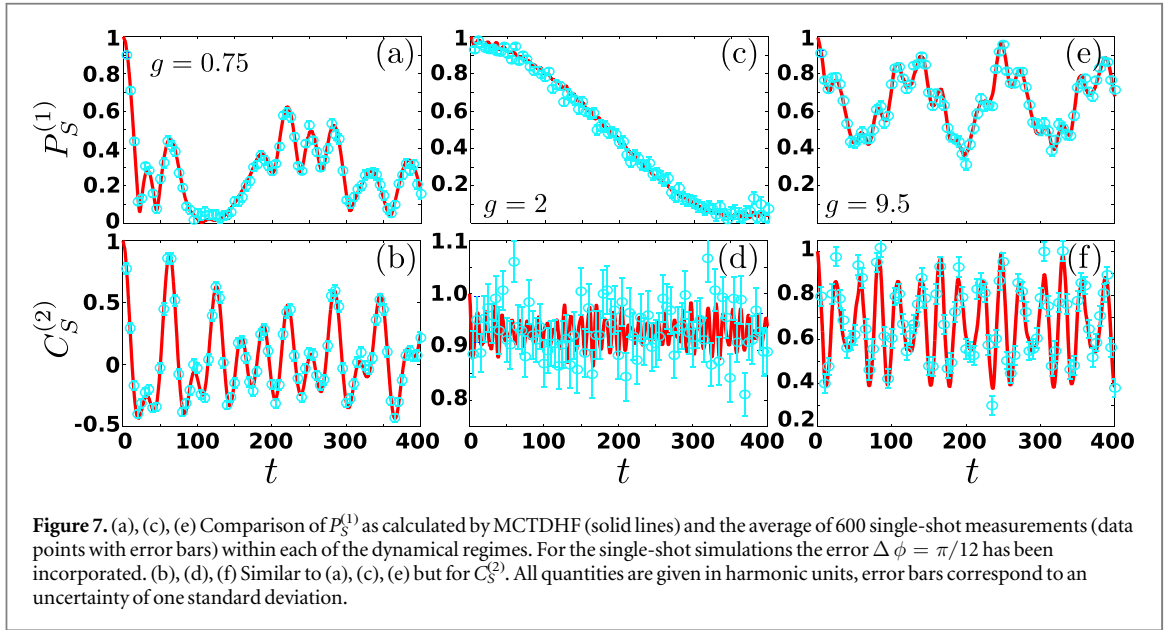
6. Experimental realization

Our setup can be realized using ^{40}K atoms under the influence of a Raman coupling of the two energetically lowest hyperfine states, while the observables $P_S^{(1)}$ and $C_S^{(2)}$ are accessible by fluorescence imaging. Below we propose a possible experimental realization in order to probe our findings. The robustness of the suggested measurement scheme is demonstrated by comparing our MCTDHF results with simulated sets of single-shot images that contain additional noise emulating this way the noise sources inherent in a corresponding experiment [14–16].

The effective Rabi coupling scheme, see \hat{H}_S equation (6), can be achieved by employing a two-photon resonant, $\delta = 0$, Raman transition via two Gaussian focussed laser beams. To incorporate non-negligible interatomic interactions one needs to apply a bias magnetic field close to the point of an s -wave broad Fano-Feshbach resonance [8]. For ^{40}K atoms a broad s -wave Fano-Feshbach resonance between the hyperfine states $|\uparrow\rangle = |^2S_{1/2}; F = \frac{9}{2}, m_F = -\frac{9}{2}\rangle$ and $|\downarrow\rangle = |^2S_{1/2}; F = \frac{9}{2}, m_F = -\frac{7}{2}\rangle$, is located at the magnetic field strength $B_{\text{FF}} = 202.10 \text{ G}$ [50].

Fluorescence imaging is commonly used to probe the state of the system in few-atom ($N < 10$) experiments [14]. Here a certain number of atoms is ejected from the trap and recaptured into a magneto-optical trap [51].

⁷The Homogeneous term that is also contributing to the Taylor expansion of H_S , equation (6), preserves both of the \hat{S}_z and \hat{S}^2 symmetries of \hat{H} and consequently the its only effect is to shift the collective Larmor precession frequency.



Subsequently, the number of ejected particles can be inferred by measuring the intensity of the scattered light. We show that $P_S^{(1)}$ and $C_S^{(2)}$ can be experimentally detected using fluorescence imaging. $P_S^{(1)}$ and $C_S^{(2)}$ depend on the average and the variance of the magnitude of the spin polarization respectively. Because of the employed Raman scheme the Hamiltonian (6) is implemented in the interaction picture. This implies that in the Schrödinger picture and in the absence of the Raman fields the orientation of the spin-vector precesses around the z spin-axis with frequency $\omega_{\uparrow\downarrow} = 2\pi \times [44.8 + 0.156\text{G}^{-1}(B - B_{\text{FF}})]\text{MHz}$ (where B refers to the bias magnetic field). $\omega_{\uparrow\downarrow}$ corresponds to the energy offset between the $|\uparrow\rangle$ and $|\downarrow\rangle$ states of ^{40}K for magnetic fields in the vicinity of B_{FF} . As a consequence only the spin-polarization along the z axis (i.e. population-imbalance in the occupation of the hyperfine states $|\uparrow\rangle$, $|\downarrow\rangle$) in spin-space can be directly probed. To measure the spin-state in such atomic systems Ramsay spectroscopy is employed to coherently rotate the rotating x or y axes in the interaction picture to the stationary z axis, which is common for both pictures. A Ramsay spectroscopy sequence (described in the interaction picture) is utilized. Initially all of the atoms are prepared in the N -body state $|\Psi(0)\rangle$, namely all atoms reside in the $|\uparrow\rangle$ hyperfine state. At time $t = 0$ the inhomogeneous Raman coupling of the hyperfine states is suddenly switched on and the fermions are exposed to it for time t . By the end of this process, the MB wavefunction has evolved from $|\Psi(0)\rangle$ to $|\Psi(t)\rangle$ (in the interaction picture) under the influence of \hat{H} . At time t , the Raman coupling is suddenly switched off and the system evolves for a dark time t_{dark} . Within this time interval the reestablished symmetries of the Hamiltonian $\hat{H}_0 + \hat{H}_I$ (see equations (3), (4)) prohibit any change to \mathbf{S} and S^2 . To measure the S_x or S_y components we need to rotate the desired spin component to the z axis by applying a $-\sigma_y$ or σ_x , $\frac{\pi}{2}$ -pulse respectively by means of spatially homogeneous two-photon-resonant optical Raman fields with the appropriate phase shift, ϕ , from the inhomogeneous one (for S_z no $\frac{\pi}{2}$ -pulse is used and the sequence continues directly with the next step). This sequence stops the precession dynamics of the desired spin component in the Schrödinger picture as it is mapped to the stationary z axis. In the following, all the spin- \downarrow are removed from the trap by applying a high-intensity resonant laser pulse at time t_{ex} [16]. The surviving atoms are loaded into the magneto-optical trap (at $t = t_{\text{meas}}$) and counted to provide a measurement for the spin polarization $S_i = \frac{2N_i - N}{2}$ along the selected axis $i \in \{x, y, z\}$.

As a proof-of-principle of the above-mentioned imaging procedure we simulate single experimental measurements, where we take into account a random error in the phase $\Delta\phi$. We employ a generalized version of the recent single-shot implementation offered by Multi-Layer Multi-Configuration Hartree method for atomic Mixtures (ML-MCTDHX) [36] (see [52–55] and appendix B for details) and evaluate $P_S^{(1)}$ and $C_S^{(2)}$ from the simulated experimental data. Note that $\Delta\phi$ might be induced by variations in the optical path of the $-\sigma_y$ or σ_x , $\frac{\pi}{2}$ -pulse Raman beams. To incorporate this source of error we simulate experimental measurements for each of the x , y and z components of the spin vector and incorporate a random rotation by $\delta\phi$ along the z axis that follows a Gaussian distribution of width $\Delta\phi$.

Figures 7(a) and (b) offer a comparison of our MCTDHF data with the simulated experimental estimates based on 600 single-shot realizations containing an error $\Delta\phi = \pi/12$. We observe that despite the latter error the single-shot results follow closely the MCTDHF data and reproduce both the spin polarization $P_S^{(1)}$, as well as, the correlation dynamics $C_S^{(2)}$. The uncertainty of the simulated single-shot results is of the order ~ 0.05 .

Agreement between the MCTDHF data and the single-shot estimates is observed also for the ferromagnetically ordered (see figures 7(c) and (d)) and the strong- g demagnetization regime (see figures 7(e) and (f)). Therefore, we conclude that the error in the phase ϕ is not prohibitive for accurate measurements of $P_S^{(1)}$ and $C_S^{(2)}$ as long as it is kept sufficiently smaller than $\frac{\pi}{2}$.

7. Summary and outlook

We have explored the spin-flip dynamics of few ultracold fermions subject to spatially inhomogeneous external driving of the spins. In particular, we showed that in this case the polarization of the confined Fermi gas cannot be stabilized for any interaction strength. A result that lies in contrast to the picture of ferromagnetism provided by the celebrated Stoner model. Most importantly, a stable correlation-induced ferromagnetic spin-order emerges in spite of the strongly fluctuating polarization for moderate interactions. We have characterized the emerging spin-order by comparing *ab initio* simulations with an effective spin-chain model in the few-body case. The influence of correlations and the emergence of entangled NOON-like states during the dynamical evolution of the system has been explicitly demonstrated. In the weak and strong interaction limit the behaviour of the system is characterized by a significant depletion of the spin–spin correlator which can be related to the corresponding avoided crossings appearing in the eigenspectrum. Our setup is experimentally accessible in ^{40}K few-atom experiments by employing a Raman coupling scheme of the two energetically lowest hyperfine states. The observables $P_S^{(1)}$ and $C_S^{(1)}$ can be measured by employing Ramsay spectroscopy and fluorescence imaging.

It is known that the properties of itinerant magnetism vary depending on the confining potential [56]. Studying the stability of ferromagnetism in the case of a double well potential or an optical lattice can yield further insights into the magnetic properties exhibited in 1D systems. Notice, also, that the spin-chain model presented here is easily extendable to higher dimensional settings. The investigation on whether a similar order occurs in higher dimensional settings also provides an intriguing perspective for future study. Another interesting prospect is to examine the demagnetization dynamics of few-fermions when exposed to Rashba and Dresselhaus spin–orbit coupling [57, 58]. This might establish a link to relevant condensed matter systems where such demagnetization mechanisms are well-studied [59–61]. Such dynamics have recently been examined in the case of thermal Fermi gases in the collisionless regime [62–64].

Acknowledgments

This work is supported by the Cluster of Excellence ‘Advanced Imaging of Matter’ of the Deutsche Forschungsgemeinschaft (DFG) - EXC 2056 - project ID 390715994. SIM and PS gratefully acknowledge financial support by the Deutsche Forschungsgemeinschaft (DFG) in the framework of the SFB 925 ‘Light induced dynamics and control of correlated quantum systems’.

Appendix A. The computational method: ML-MCTDHF and the spinor variant of MCTDHF

Our approach to solve the MB Schrödinger equation $(i\hbar\partial_t - \hat{H})|\Psi(t)\rangle = 0$ relies on the ML-MCTDHF [36]. In particular we employ a reduction of the ML-MCTDHF method for spin-1/2 fermions being referred in the following as the spinor-variant of MCTDHF. MCTDHF has been applied extensively for the treatment of fermions with or without spin-degrees of freedom, in a large class of condensed matter, atomic and molecular physics scenarios (see e.g. [65–70]) and recently also applied in the field of ultracold atoms [35–39, 71]. The key idea of MCTDHF lies in the usage of a time-dependent (t-d) and variationally optimized MB basis set, which allows for the optimal truncation of the total Hilbert space. The ansatz for the MB wavefunction is taken as a linear combination of t-d Slater determinants $|\vec{n}(t)\rangle$, with t-d weight coefficients $A_{\vec{n}}(t)$

$$|\Psi(t)\rangle = \sum_{\vec{n}} A_{\vec{n}}(t) |\vec{n}(t)\rangle. \quad (\text{A1})$$

Each t-d Slater determinant is expanded in terms of M t-d variationally optimized single-particle functions (SPFs) $|\phi_l(t)\rangle$, $l = 1, 2, \dots, M$ with occupation numbers $\vec{n} = (n_1, \dots, n_M)$. The SPFs are subsequently expanded in a primitive basis $\{|k, s\rangle\}$, being the tensor product of a discrete variable representation (DVR) basis for the spatial degrees of freedom $\{|k\rangle\}$ of dimension M_p and the two-dimensional spin basis $\{|\uparrow\rangle, |\downarrow\rangle\}$

$$|\phi_j(t)\rangle = \sum_{k=1}^{M_p} \sum_{\alpha=\{\uparrow,\downarrow\}} C_{k\alpha}^j(t) |k\rangle |\alpha\rangle. \quad (\text{A2})$$

$C_{k\alpha}^j(t)$ refer to the corresponding t-d expansion coefficients. Note here that each t-d SPF is a general spinor wavefunction of the form $|\phi_j(t)\rangle = \int dx [\chi_j^\uparrow(x)\hat{\psi}_\uparrow^\dagger(x) + \chi_j^\downarrow(x)\hat{\psi}_\downarrow^\dagger(x)]|0\rangle$ and hence the employed method is termed as the spinor-variant of MCTDHF. The time-evolution of the N -body wavefunction under the effect of the Hamiltonian \hat{H} reduces to the determination of the A -vector coefficients and the SPFs, which in turn follow the variationally obtained MCTDHF equations of motion [34–36]. In the limiting case of $M = N$, the method reduces to the TDHF method, while for the case of $M = 2M_p$, it is equivalent to a full configuration interaction approach (commonly referred to as ‘exact diagonalization’ in the literature) within the basis $\{|k, s\rangle\}$.

For our implementation we have used a harmonic oscillator DVR, which results after a unitary transformation of the commonly employed basis of harmonic oscillator eigenfunctions, as a primitive basis for the spatial part of the SPFs. To study the dynamics, we propagate the wavefunction by utilizing the appropriate Hamiltonian within the MCTDHF equations of motion. To verify the accuracy of the numerical integration, we impose the following overlap criteria $|\langle\Psi|\Psi\rangle - 1| < 10^{-8}$ for the total wavefunction and $|\langle\varphi_i|\varphi_j\rangle - \delta_{ij}| < 10^{-9}$ for the SPFs. To infer about convergence, we increase the number of SPFs and DVR basis states such that the observables of interest ($P_S^{(1)}, C_s^{(2)}$) do not change within a given relative accuracy which is in our case 10^{-4} . More specifically, we have used $M_p = 60, M = 26$ and $M_p = 80, M = 20$ for the $N = 3$ and the $N = 5$ case respectively. Note that a full configuration interaction treatment of the above-mentioned systems in the employed primitive bases would require 280 840 number-states for $N = 3$ and 820 384 032 ones for $N = 5$.

Appendix B. Single-shot procedure in spin-1/2 Fermi gases

The single-shot simulation procedure relies on a sampling of the MB probability distribution, being available within the ML-MCTDHF framework. In a spinor Fermi gas the single-shot procedure is altered significantly when compared to the single component case [52–54]. Here the role of entanglement between particles in different spin states plays an important role. For example consider the procedure that the spin- \uparrow atoms are imaged before the spin- \downarrow atoms. Then, the total number of spin- \uparrow atoms N_\uparrow^{imag} that will be imaged is not *a priori* known due to the breaking of the S_z symmetry. However, after imaging all of the spin- \uparrow atoms the number of spin- \downarrow atoms is exactly known $N_\downarrow^{\text{imag}} = N - N_\uparrow^{\text{imag}}$ since the total number of atoms N is definite.

To capture the entanglement between the different spin states the MB wavefunction obtained by ML-MCTDHF should be expressed such that the entanglement between the spin states is evident. The spin-1/2 Fermi gas under consideration is a bipartite system [72, 73] since the spatial degree of freedom for each particle in the spin- \uparrow or spin- \downarrow state resides in the Fock space $\mathcal{F}^\uparrow, \mathcal{F}^\downarrow$ respectively. The latter results in a total Fock space $\mathcal{F}^{S=1/2} = \mathcal{F}^\uparrow \otimes \mathcal{F}^\downarrow$. Then, the MB wavefunction can be expressed in the Schmidt decomposition form (herewith we omit the temporal dependence for simplicity)

$$|\Psi\rangle = \sum_{k=1}^K \sqrt{\lambda_k} |\Psi_k^\uparrow\rangle |\Psi_k^\downarrow\rangle. \quad (\text{B1})$$

The coefficient λ_k is referred to as the natural occupation of the species function k ⁸. Note that, $|\Psi_k^\alpha\rangle \in \mathcal{F}^\alpha$ and as such the number of α -spin particles varies for different Schmidt modes, k . A state of the bipartite system (see equation (B1)) cannot be expressed as a direct product of two states from the two subsystem Fock spaces \mathcal{F}^α if at least two coefficients λ_k are nonzero. In the latter case the system is referred to as entangled [74]. The Schmidt decomposition of the MB wavefunction is obtained as follows. The reduced density matrix for one of the spin states, let it be α , is evaluated i.e. $\rho^\alpha = \text{Tr}_{\alpha'}[|\Psi\rangle\langle\Psi|]$, where α' refers to the spin state orthogonal to α and subsequently diagonalized resulting in its Schmidt representation $\rho^\alpha = \sum_{k=1}^M \lambda_k |\Psi_k^\alpha\rangle\langle\Psi_k^\alpha|$. Then, the corresponding species wavefunction of the spin state α' can be calculated by $|\Psi_k^{\alpha'}\rangle = \frac{1}{\sqrt{\lambda_k}} \langle\Psi_k^\alpha|\Psi\rangle$.

The single-shot process in spinor gases represents a generalization of the single-shot process for a mixture with a definite number of atoms in each species [55]. This generalization is based on the treatment of the vacuum state $|0^\alpha\rangle$. Before each step of the single-shot process the existence of particles in the imaged spin state is checked. To perform the latter a random number in the interval $P_{\text{rand}} \in [0, 1]$ is compared with $\lambda_{\tilde{k}}$, where \tilde{k} is the Schmidt mode for which $|\Psi_{\tilde{k}}^\alpha\rangle = |0^\alpha\rangle$ holds. If $P_{\text{rand}} < \lambda_{\tilde{k}}$ the imaging of the spin state α ends and the MB wavefunction is projected to $|\tilde{\Psi}\rangle = |0^\alpha\rangle \otimes |\Psi_{\tilde{k}}^{\alpha'}\rangle$. Then the simulation of the imaging of the α' spin state is initiated. The MB wavefunction in this case is the species wavefunction $|\Psi_{\tilde{k}}^{\alpha'}\rangle$ and as such the single-shot procedure reduces to the well-established single species case (see [52–54] and also the discussion below). For $P_{\text{rand}} > \lambda_{\tilde{k}}$ a particle in the spin state α is imaged. First, a random position is drawn according to the constraint

⁸ The upper bound for summation reads $K = \min(\dim(\mathcal{F}^\uparrow), \dim(\mathcal{F}^\downarrow))$ and it is therefore infinite in the general case even after considering that the \mathcal{F}^\uparrow and \mathcal{F}^\downarrow are restricted by the condition $N_\uparrow, N_\downarrow < N$. However, spinor MCTDHF truncates the dimension of each Fock space to $\dim(\mathcal{F}^\alpha) = \sum_{N_\alpha=0}^N \frac{M!}{N_\alpha!(M-N_\alpha)!}$. For realistic applications even the latter value is too high and most of the λ_k 's have a numerical-zero value. To cure this problem we truncate the Schmidt decomposition further by setting $K = \min(K^{\text{eff}})$ obeying $\lambda_{k>K^{\text{eff}}} < 10^{-12}$.

$\rho_\alpha^{(1)}(x'_1) = \langle \Psi | \hat{\psi}_\alpha^\dagger(x'_1) \hat{\psi}_\alpha(x'_1) | \Psi \rangle > l_1$ where l_1 refers to a random number within the interval $[0, \max\{\rho_\alpha^{(1)}(x)\}]$. Then we project the N -body wavefunction to the $(N - 1)$ -body one by employing the operator $\frac{1}{N} \hat{\psi}_\alpha(x'_1)$, where $\mathcal{N} = \sqrt{\langle \Psi | \hat{\psi}_\alpha^\dagger(x'_1) \hat{\psi}_\alpha(x'_1) | \Psi \rangle}$ is a normalization factor. The latter process directly affects the Schmidt coefficients λ_k 's (entanglement weights) and thus despite the fact that the spin- α' atoms have not been imaged yet, both $\rho_\uparrow^{(1)}(x) = \langle \Psi | \hat{\psi}_\uparrow^\dagger(x) \hat{\psi}_\uparrow(x) | \Psi \rangle$ and $\rho_\downarrow^{(1)}(x) = \langle \Psi | \hat{\psi}_\downarrow^\dagger(x) \hat{\psi}_\downarrow(x) | \Psi \rangle$ change. This can be easily understood by employing again the Schmidt decomposition. Indeed after this first measurement the $(N - 1)$ -particle MB wavefunction reads

$$|\tilde{\Psi}^{(-1)}\rangle = \sum_k \sqrt{\tilde{\lambda}_k^{(-1)}} |\tilde{\Psi}_k^{\alpha(-1)}\rangle |\Psi_k^{\alpha'}\rangle, \quad (\text{B2})$$

where $|\tilde{\Psi}_k^{\alpha(-1)}\rangle = \frac{1}{N_k} \hat{\psi}_\alpha(x'_1) |\Psi_k^\alpha\rangle$ refer to the species wavefunction after the imaging and

$N_k = \sqrt{\langle \Psi_k^\alpha | \hat{\psi}_\alpha^\dagger(x'_1) \hat{\psi}_\alpha(x'_1) | \Psi_k^\alpha \rangle}$ denotes the corresponding normalization factor. Finally, the Schmidt coefficients read $\tilde{\lambda}_k^{(-1)} = \lambda_k N_k / \sum_m \lambda_m N_m^2$. The above-mentioned procedure is repeated N_α^{imag} times until the condition $\| \langle 0^\alpha | \tilde{\Psi}^{(-N_\alpha^{\text{imag}})} \rangle \| = 1$ is reached or if a random number satisfying $P_{\text{rand}} < \lambda_k^{(-N_\alpha^{\text{imag}})}$ is selected. The resulting distribution of positions $(x'_1, \dots, x'_{N_\alpha^{\text{imag}}})$ is convoluted with a point spread function leading to a single-shot $\mathcal{A}^\alpha(\tilde{x})$ for the spatial configuration of spin- α particles, where \tilde{x} refers to the spatial coordinates within the image. It is worth mentioning at this point that, in the special case for which the probability of $N_\alpha^{\text{imag}} = N$ is zero, it can be easily shown that upon annihilating the last spin- α particle (provided that $P_{\text{rand}} > \lambda_k^{(-N_\alpha^{\text{imag}}+1)}$ is chosen) the $(N - N_\alpha^{\text{imag}})$ -particle MB wavefunction becomes

$$|\tilde{\Psi}^{(-N_\alpha^{\text{imag}})}\rangle = |0^\alpha\rangle \otimes \sum_{k \neq \tilde{k}} \frac{\sqrt{\tilde{\lambda}_k^{(-N_\alpha^{\text{imag}}+1)}} \langle x'_{N_\alpha^{\text{imag}}} | \Phi_k^\alpha \rangle}{\sum_{m \neq \tilde{k}} \sqrt{\tilde{\lambda}_k^{(-N_\alpha^{\text{imag}}+1)}} |\langle x'_{N_\alpha^{\text{imag}}} | \Phi_k^\alpha \rangle|^2} |\Psi_k^{\alpha'}\rangle. \quad (\text{B3})$$

After this last step the entanglement between the spin states has been destroyed and the single component wavefunction of the spin α' atoms $|\tilde{\Psi}^{(-N_\alpha^{\text{imag}})}\rangle$ corresponds to the second term on the right hand side of equation (B3).

In this way, it becomes evident that after the imaging of spin α particles the resulting wavefunction $|\tilde{\Psi}^{(-N_\alpha^{\text{imag}})}\rangle = |\Psi^{\alpha'}\rangle$ (see equation (B3)) is a non-entangled $(N - N_\alpha^{\text{imag}})$ -particle MB wavefunction and its corresponding single-shot procedure is the same as in the single species case [52]. The latter is well-established (for details see [52, 53]) and here it is only briefly outlined below. We first calculate $\rho_{\alpha'}^{(1)}(x)$ from the MB wavefunction $|\tilde{\Psi}^{(-N_\alpha^{\text{imag}})}\rangle = |\Psi^{\alpha'}\rangle$. Then, a random position x_1'' is drawn obeying $\rho_{\alpha'}^{(1)}(x_1'') > l_2$ where l_2 is a random number in the interval $[0, \max\{\rho_{\alpha'}^{(1)}(x)\}]$. Next, one particle located at position x_1'' is annihilated and $\rho_{\alpha'}^{(1)'}(x)$ is calculated from $|\tilde{\Psi}^{(-N_\alpha^{\text{imag}}-1)}\rangle = [\rho_{\alpha'}^{(1)}(x_1'')]^{-1/2} \hat{\psi}_{\alpha'}(x_1'') |\tilde{\Psi}^{(-N_\alpha^{\text{imag}})}\rangle$. To proceed, a new random position x_2'' is drawn from $\rho_{\alpha'}^{(1)'}(x; t_{im})$. Following this procedure for $N - N_\alpha^{\text{imag}}$ steps we obtain the distribution of positions $(x_1'', \dots, x_{N-N_\alpha^{\text{imag}}}'')$ which is then convoluted with a point spread function resulting in a single-shot image $\mathcal{A}^{\alpha'}(\tilde{x}' | \mathcal{A}^\alpha(\tilde{x}))$.

Appendix C. Spin-chain approach

The spin-chain Hamiltonian builds upon the spin dependent eigenstates, $|\chi_n^\alpha\rangle$, of the non-interacting Hamiltonian $\hat{H}_0 + \hat{H}_S$, where α, n denote the spin and spatial modes. To simplify the notation below, we perform a rotation in spin-space by employing the unitary operator $\hat{U} = e^{i\frac{\pi}{4}\hat{S}_y}$ such that the x axis (see main text) is mapped to the z axis and thus the spin-modes correspond to $\alpha \in \{\uparrow, \downarrow\}$. The n th spatial mode is considered as singly occupied if either $|\chi_n^\uparrow\rangle$ or $|\chi_n^\downarrow\rangle$ is occupied, doubly occupied if both are occupied and unoccupied if neither is occupied. Then the spatial configurations are defined by $\vec{n} = (n_1, \dots, n_N)$ where n_i refers to the occupied spatial modes. There are 2^{N-2D} (D denotes the number of double occupations) distinct states that correspond to the same spatial configuration, \vec{n} , corresponding to the different available spin-configurations $\vec{\alpha} = (\alpha_1, \dots, \alpha_N)$. Consequently, a basis state of the N -body system, $|\vec{n}; \vec{\alpha}\rangle = \hat{c}_{n_1 \alpha_1}^\dagger \dots \hat{c}_{n_N \alpha_N}^\dagger |0\rangle$, is completely defined by its spin and spatial configurations $\vec{\alpha}$ and \vec{n} respectively.

To derive the effective Hamiltonian of the spin-chain model, \hat{H}^{eff} , we neglect all terms that couple states of different spatial configurations. The non-interacting Hamiltonian $\hat{H}_0 + \hat{H}_S$ is diagonal on the basis states $|\vec{n}, \vec{\alpha}\rangle$ and thus its exact form is incorporated in the effective spin-chain Hamiltonian, \hat{H}^{eff} . However, the same is not true for the interaction term \hat{H}_I . According to the above-mentioned approximation, the general form of the effective

interaction term, \hat{H}_I^{eff} , contains all the terms in \hat{H}_I that preserve the spatial configuration of the state they act on. There are only two terms in \hat{H}_I that possess the latter property and are linearly independent, namely the \hat{H}_I^{shift} and \hat{H}_I^{exc} terms. $\hat{H}_I^{\text{shift}} = g \sum_{m,n=0}^{m_{\text{max}}} u_{mm}^{nm} \hat{c}_{n\uparrow}^\dagger \hat{c}_{m\downarrow}^\dagger \hat{c}_{m\downarrow} \hat{c}_{n\uparrow}$ accounts for the energy shift of the single-particle modes due to interaction, where $u_{mp}^{nq} = \int dx [\chi_n^\uparrow(x) \chi_m^\downarrow(x)]^* \chi_p^\downarrow(x) \chi_q^\uparrow(x)$ denote the corresponding interaction integrals. $\hat{H}_I^{\text{exc}} = g \sum_{m=0}^{m_{\text{max}}} \sum_{n \neq m} u_{nm}^{mn} \hat{c}_{m\uparrow}^\dagger \hat{c}_{n\downarrow}^\dagger \hat{c}_{m\downarrow} \hat{c}_{n\uparrow}$ allows for the exchange of the single-particle modes after a collision event. Therefore, the effective Hamiltonian reads $\hat{H}^{\text{eff}} = \hat{H}_0 + \hat{H}_S + \hat{H}_I^{\text{eff}}$, where $\hat{H}_I^{\text{eff}} = \hat{H}_I^{\text{shift}} + \hat{H}_I^{\text{exc}}$.

To cast \hat{H}^{eff} in the spin-chain form we define the spin operators for each spatial mode $\hat{\sigma}_n^0 = \hat{c}_{n\uparrow}^\dagger \hat{c}_{n\uparrow} + \hat{c}_{n\downarrow}^\dagger \hat{c}_{n\downarrow}$, $\hat{\sigma}_n^z = \hat{c}_{n\uparrow}^\dagger \hat{c}_{n\uparrow} - \hat{c}_{n\downarrow}^\dagger \hat{c}_{n\downarrow}$, $\hat{\sigma}_n^+ = \hat{c}_{n\uparrow}^\dagger \hat{c}_{n\downarrow}$ and $\hat{\sigma}_n^- = \hat{c}_{n\downarrow}^\dagger \hat{c}_{n\uparrow}$. The effective MB Hamiltonian \hat{H}^{eff} conserves the spatial modes for each spatial configuration $\vec{n} = (n_1, \dots, n_N)$ as it commutes with the projection operators

$$\hat{P}_{\vec{n}} = \sum_{\alpha_1=\{\uparrow,\downarrow\}} \dots \sum_{\alpha_N=\{\uparrow,\downarrow\}} \hat{c}_{n_1\alpha_1}^\dagger \dots \hat{c}_{n_N\alpha_N}^\dagger |0\rangle \langle 0| \hat{c}_{n_N\alpha_N} \dots \hat{c}_{n_1\alpha_1}. \quad (\text{C1})$$

Employing this projection operator, we can derive the spin-chain Hamiltonian, $\hat{H}_{\vec{n}} = \hat{P}_{\vec{n}} \hat{H}^{\text{eff}} \hat{P}_{\vec{n}}$, for each configuration \vec{n} with no double occupations (i.e. $n_i \neq n_j, \forall i, j$), corresponding to the N -spin XXZ spin-chain

$$\hat{H}_{\vec{n}} = \varepsilon_{\vec{n}}(g) + \sum_{i=1}^N h_{n_i}(g) \hat{\sigma}_{n_i}^z - g \sum_{i=1}^{N-1} \sum_{j=i+1}^N [J_{n_i n_j}^\perp \hat{\sigma}_{n_i}^+ \hat{\sigma}_{n_j}^- + J_{n_i n_j}^{\perp*} \hat{\sigma}_{n_i}^- \hat{\sigma}_{n_j}^+] + J_{n_i n_j}^z \hat{\sigma}_{n_i}^z \hat{\sigma}_{n_j}^z. \quad (\text{C2})$$

The spin-spin interactions are given by the overlap integrals $J_{nm}^\perp = u_{nm}^{mn}$ and $J_{nm}^z = \frac{1}{4}(u_{nm}^{nm} + u_{mn}^{mm})$. The interaction-dependent energy shift $\varepsilon_{\vec{n}}(g)$ and the local magnetic field $h_{n_i}(g)$ read

$$\begin{aligned} \varepsilon_{\vec{n}}(g) &= \sum_{i=1}^N \frac{E_{n_i}^\uparrow + E_{n_i}^\downarrow}{2} + g \sum_{i=1}^{N-1} \sum_{j=i+1}^N J_{n_i n_j}^z, \\ h_{n_i}(g) &= \frac{E_{n_i}^\uparrow - E_{n_i}^\downarrow}{2} + g \sum_{j=1, j \neq i}^N \frac{u_{n_i n_j}^{n_i n_j} - u_{n_i n_j}^{n_j n_i}}{4}. \end{aligned} \quad (\text{C3})$$

The configurations with D double occupations have to be treated separately because the creation operator of a double occupancy $\hat{c}_{n\uparrow}^\dagger \hat{c}_{n\downarrow}^\dagger$ possesses a non-trivial commutation relation with the $\hat{\sigma}_n^0$ one, $[\hat{\sigma}_m^0, \hat{c}_{n\uparrow}^\dagger \hat{c}_{n\downarrow}^\dagger] = 2\delta_{nm} \hat{c}_{n\uparrow}^\dagger \hat{c}_{n\downarrow}^\dagger$. In this case, it turns out that the projected Hamiltonian, $\hat{H}_{\vec{n}}$, is expressed in terms of a $(N - 2D)$ -spin XXZ Hamiltonian, $\hat{H}_{\vec{m}}^{(2D)}$, with \vec{m} being a $(N - 2D)$ -particle configuration composed of the singly occupied states of \vec{n} . The $\hat{H}_{\vec{n}}$ and $\hat{H}_{\vec{m}}^{(2D)}$ are related via the creation operator of all the double occupations $\hat{M}_{\vec{k}}^\dagger \equiv \prod_{j=0}^{D-1} \hat{c}_{k_j\downarrow}^\dagger \hat{c}_{k_j\uparrow}^\dagger$, where \vec{k} is the vector of doubly occupied modes in \vec{n} , as $\hat{H}_{\vec{n}} = \hat{M}_{\vec{k}}^\dagger \hat{H}_{\vec{m}}^{(2D)} \hat{M}_{\vec{k}}$. $\hat{H}_{\vec{m}}^{(2D)}$ has exactly the same form as equation (C2) but the energy shift, $\varepsilon_{\vec{m}}^{(2D)}(g)$, and local magnetic field, $h_{m_i}^{(2D)}(g)$, possess additional contributions when compared to the ones in equation (C3). Namely,

$$\begin{aligned} \varepsilon_{\vec{m}}^{(2D)}(g) &= \varepsilon_{\vec{m}}(g) + \sum_{i=1}^D 2\varepsilon_{k_i}^0 + g \left[\sum_{i=1}^D 2J_{k_i k_i}^z + \sum_{i=1}^{D-1} \sum_{j=i+1}^D 4J_{k_i k_j}^z + \sum_{i=1}^D \sum_{j=1}^{N-2D} J_{k_i m_j}^z \right], \\ h_{m_i}^{(2D)}(g) &= h_{m_i}(g) + g \sum_{j=1}^D \frac{u_{k_j k_j}^{m_i m_i} - u_{m_i m_i}^{k_j k_j}}{2}. \end{aligned} \quad (\text{C4})$$

The weight of each spatial configuration to the MB wavefunction $|\Psi(t)\rangle$ is constant in time as the $w_{\vec{n}} = \langle \Psi(t) | \hat{P}_{\vec{n}} | \Psi(t) \rangle$ are conserved. Therefore, the time evolution of the MB wavefunction within the spin-chain approximation reads

$$|\Psi(t)\rangle = \sum_{\vec{n}} \sqrt{w_{\vec{n}}} e^{-i\hat{H}_{\vec{n}} t} |\Psi_{\vec{n}}(0)\rangle, \quad (\text{C5})$$

where $|\Psi_{\vec{n}}(0)\rangle = \frac{1}{\sqrt{w_{\vec{n}}}} \hat{P}_{\vec{n}} |\Psi(0)\rangle$ is the normalized initial wavefunction for each XXZ spin-chain.

The generalization of the presented method compared to the one developed in [28] is the inclusion of the interaction-dependent local magnetic potential (see equations (C2) and (C4)), which vanishes for a linear gradient as the one considered in [28] in the present case such a term is important for obtaining the correct behaviour of the polarization magnitude $P_S^{(1)}$ in the ferromagnetically ordered regime. Within our implementation we numerically diagonalize the one-body Hamiltonian, $\hat{H}_0 + \hat{H}_S$, by employing the basis consisting of the 80 energetically lowest eigenstates of the harmonic oscillator and truncate the summation over \vec{n} of equation (C5) by taking into account only the contributions of the spatial mode configurations with $|w_{\vec{n}}| > 10^{-12}$. This truncation results in 1520 and 38304 configurations for $N = 3$ and $N = 5$ fermions respectively.

ORCID iDs

SI Mistakidis  <https://orcid.org/0000-0002-5118-5792>

References

- [1] Vollhardt D, Blumer N and Kollar M 2001 Metallic Ferromagnetism—an electronic correlation phenomenon *Lecture Notes in Physics* vol 580 (Berlin: Springer)
- [2] Brando M, Belitz D, Grosche F M and Kirkpatrick T R 2016 *Rev. Mod. Phys.* **88** 025006
- [3] Sachdev S 2008 *Nat. Phys.* **4** 173
- [4] Stoner E 1933 *Phil. Mag.* **15** 1018
- [5] Jo G-B, Lee Y-R, Choi J-H, Christensen C A, Kim T H, Thywissen J H, Pritchard D E and Ketterle W 2009 *Science* **325** 1521
- [6] Sanner C, Su E J, Huang W, Keshet A, Gillen J and Ketterle W 2012 *Phys. Rev. Lett.* **108** 240404
- [7] Pekker D, Babadi M, Sensarma R, Zinner N, Pollet L, Zwierlein M W and Demler E 2011 *Phys. Rev. Lett.* **106** 050402
- [8] Chin C, Grimm R, Julienne P and Tiesinga E 2010 *Rev. Mod. Phys.* **82** 1225
- [9] Amico A, Scazza F, Valtolina G, Tavares P E S, Ketterle W, Inguscio M, Roati G and Zaccanti M 2018 *Phys. Rev. Lett.* **121** 253602
- [10] Kohstall C, Zaccanti M, Jag M, Trenkwalder A, Massignan P, Bruun G M, Schreck F and Grimm R 2012 *Nature* **485** 615
- [11] Scazza F, Valtolina G, Massignan P, Recati A, Amico A, Burchianti A, Fort C, Inguscio M, Zaccanti M and Roati G 2017 *Phys. Rev. Lett.* **118** 083602
- [12] Li W and Cui X 2017 *Phys. Rev. A* **96** 053609
- [13] Valtolina G, Scazza F, Amico A, Burchianti A, Recati A, Enss T, Inguscio M, Zaccanti M and Roati G 2017 *Nat. Phys.* **13** 709
- [14] Serwane F, Zürn G, Lompe T, Ottenstein T B, Wenz A N and Jochim S 2011 *Science* **332** 336
- [15] Wenz A N, Zürn G, Murmann S, Brouzos I, Lompe T and Jochim S 2013 *Science* **342** 457
- [16] Murmann S, Deuretzbacher F, Zürn G, Bjerlin J, Reimann S M, Santos L, Lompe T and Jochim S 2015 *Phys. Rev. Lett.* **115** 215301
- [17] Gharashi S E and Blume D 2013 *Phys. Rev. Lett.* **111** 045302
- [18] Brouzos I and Schmelcher P 2013 *Phys. Rev. A* **87** 023605
- [19] Bugnion P O and Conduit G J 2013 *Phys. Rev. A* **87** 060502(R)
- [20] Sowiński T, Grass T, Dutta O and Lewenstein M 2013 *Phys. Rev. A* **88** 033607
- [21] Lindgren E J, Rotureau J, Forssén C, Volosniev A G and Zinner N T 2014 *New J. Phys.* **16** 063003
- [22] Levinsen J, Massignan P, Bruun G M and Parish M M 2015 *Sci. Adv.* **1** e1500197
- [23] Deuretzbacher F, Becker D, Bjerlin J, Reimann S M and Santos L 2014 *Phys. Rev. A* **90** 013611
- [24] Volosniev A G, Fedorov D V, Jensen A S, Valiente M and Zinner N T 2014 *Nat. Commun.* **5** 5300
- [25] Yang L, Guan L and Pu H 2015 *Phys. Rev. A* **91** 043634
- [26] Cui X and Ho T-L 2014 *Phys. Rev. A* **89** 023611
- [27] Cui X and Ho T-L 2014 *Phys. Rev. A* **89** 013629
- [28] Koller A P, Wall M L, Mundinger J and Rey A M 2016 *Phys. Rev. Lett.* **117** 195302
- [29] Grochowski P T, Karpiuk T, Brewczyk M and Rzażewski K 2017 *Phys. Rev. Lett.* **119** 215303
- [30] Salasnich L and Penna V 2017 *New J. Phys.* **19** 043018
- [31] Penna V and Salasnich L 2019 *J. Phys. B: At. Mol. Opt. Phys.* **52** 035301
- [32] Giovannetti V, Lloyd S and Maccone L 2011 *Nat. Photon.* **5** 222–9
- [33] Jones J A, Karlen S D, Fitzsimons J, Ardavan A, Benjamin S C, Briggs G A D and Morton J J L 2009 *Science* **324** 1166
- [34] Alon O E, Streltsov A I and Cederbaum L S 2007 *J. Chem. Phys.* **127** 154103
- [35] Fasshauer E and Lode A U J 2016 *Phys. Rev. A* **93** 033635
- [36] Cao L, Bolsinger V, Mistakidis S I, Koutentakis G M, Krönke S, Schurer J M and Schmelcher P 2017 *J. Chem. Phys.* **147** 044106
- [37] Erdmann J, Mistakidis S I and Schmelcher P 2018 *Phys. Rev. A* **98** 053614
- [38] Erdmann J, Mistakidis S I and Schmelcher P 2019 *Phys. Rev. A* **99** 013605
- [39] Mistakidis S I, Katsimiga G C, Koutentakis G M and Schmelcher P 2019 *New J. Phys.* **21** 043032
- [40] Olshanii M 1998 *Phys. Rev. Lett.* **81** 938
- [41] Tommasini P, de Passos E J V, de Toledo Piza A F R, Hussein M S and Timmermans E 2003 *Phys. Rev. A* **67** 023606
- [42] Nicklas E, Strobel H, Zibold T, Gross C, Malomed B A, Kevrekidis P G and Oberthaler M K 2011 *Phys. Rev. Lett.* **107** 193001
- [43] Stamper-Kurn D M and Ueda M 2013 *Rev. Mod. Phys.* **85** 1191
- [44] Bernier N R, Dalla Torre E G and Demler E 2014 *Phys. Rev. Lett.* **113** 065303
- [45] Koller A P, Mundinger J, Wall M L and Rey A M 2015 *Phys. Rev. A* **92** 033608
- [46] Lieb E and Mattis D 1962 *Phys. Rev.* **125** 164
- [47] Sowiński T 2018 *Condens. Matter* **3** 7
- [48] Volosniev A G, Petrosyan D, Valiente M, Fedorov D V, Jensen A S and Zinner N T 2015 *Phys. Rev. A* **91** 023620
- [49] Guan Q and Blume D 2015 *Phys. Rev. A* **92** 023641
- [50] Regal C A, Greiner M and Jin D S 2004 *Phys. Rev. Lett.* **92** 040403
- [51] Pethick C J and Smith H 2002 *Bose–Einstein Condensation in Dilute Gases* (Cambridge: Cambridge University Press)
- [52] Sakmann K and Kasevich M 2016 *Nat. Phys.* **12** 451
- [53] Lode A U and Bruder C 2017 *Phys. Rev. Lett.* **118** 013603
- [54] Katsimiga G C, Mistakidis S I, Koutentakis G M, Kevrekidis P G and Schmelcher P 2017 *New J. Phys.* **19** 123012
- [55] Mistakidis S I, Katsimiga G C, Kevrekidis P G and Schmelcher P 2018 *New J. Phys.* **20** 043052
- [56] Zintchenko I, Wang L and Troyer M 2016 *Eur. Phys. J. B* **89** 180
- [57] Bychkov A and Rashba E I 1984 *J. Phys. C: Solid State Phys.* **17** 6039
- [58] Dresselhaus G 1955 *Phys. Rev.* **100** 580
- [59] Dyakonov M I and Perel V I 1971 *Zh. Eksp. Teor. Fiz.* **60** 1954
Dyakonov M I and Perel V I 1971 *Sov. Phys. JETP* **33** 1053
- [60] Elliot R J 1954 *Phys. Rev.* **96** 266
- [61] Yafet Y 1983 *Phys. Lett. A* **98** 287
- [62] Stanescu T D, Zhang C and Galitski V 2007 *Phys. Rev. Lett.* **99** 110403
- [63] Natu S S and Sarma S Das 2013 *Phys. Rev. A* **88** 033613

- [64] Radić J, Natu S S and Galitski V 2014 *Phys. Rev. Lett.* **112** 095302
- [65] Zanghellini J, Kitzler M, Fabian C, Brabec T and Scrinzi A 2003 *Laser Phys.* **13** 1064
- [66] Kato T and Kono H 2004 *Chem. Phys. Lett.* **392** 533
- [67] Caillat J, Zanghellini J, Kitzler M, Koch O, Kreuzer W and Scrinzi A 2005 *Phys. Rev. A* **71** 012712
- [68] Nest M, Klamroth T and Saalfrank P 2005 *J. Chem. Phys.* **122** 124102
- [69] Hochstuhl D, Bauch S and Bonitz M 2010 *J. Phys.: Conf. Ser.* **220** 012019
- [70] Haxton D J, Lawler K V and McCurdy C W 2011 *Phys. Rev. A* **83** 063416
- [71] Cao L, Mistakidis S I, Deng X and Schmelcher P 2017 *Chem. Phys.* **482** 303
- [72] Horodecki R, Horodecki P, Horodecki M and Horodecki K 2009 *Rev. Mod. Phys.* **81** 865
- [73] Horodecki P, Horodecki R and Horodecki M 1998 *Acta Phys. Slov.* **48** 3
- [74] Roncaglia M, Montorsi A and Genovese M 2014 *Phys. Rev. A* **90** 062303

4.1.2 Interplay of phase separation and itinerant magnetism for correlated few fermions in a double-well

PAPER • OPEN ACCESS

Interplay of phase separation and itinerant magnetism for correlated few fermions in a double-well

To cite this article: G M Koutentakis *et al* 2020 *New J. Phys.* **22** 063058

View the [article online](#) for updates and enhancements.



PAPER

Interplay of phase separation and itinerant magnetism for correlated few fermions in a double-well

OPEN ACCESS

RECEIVED
16 January 2020REVISED
24 April 2020ACCEPTED FOR PUBLICATION
6 May 2020PUBLISHED
26 June 2020

Original content from
this work may be used
under the terms of the
[Creative Commons
Attribution 4.0 licence](#).

Any further distribution
of this work must
maintain attribution to
the author(s) and the
title of the work, journal
citation and DOI.

G M Koutentakis^{1,2}, S I Mistakidis¹  and P Schmelcher^{1,2} ¹ Center for Quantum Optical Technologies, University of Hamburg, Department of Physics, Luruper Chaussee 149, 22761 Hamburg, Germany² The Hamburg Centre for Ultrafast Imaging, Universität Hamburg, Luruper Chaussee 149, 22761 Hamburg, GermanyE-mail: gkoutent@physnet.uni-hamburg.de**Keywords:** ultracold fermions, quantum gases, quantum magnetism, ferromagnetism, phase separation, out-of-equilibrium dynamics, few-body systems

Abstract

We explore the stability of the phase separation phenomenon in few-fermion spin-1/2 systems confined in a double-well potential. It is shown that within the SU(2) symmetric case, where the total spin is conserved, the phase separation cannot be fully stabilized. An interaction regime characterized by metastable phase separation emerges for intermediate interactions which is inherently related with ferromagnetic spin–spin correlations emerging within each of the wells. The breaking of the SU(2) symmetry crucially affects the stability properties of the system as the phase separated state can be stabilized even for weak magnetic potential gradients. Our results imply an intricate relation between the phenomena of phase separation and ferromagnetism that lies beyond the view of the Stoner instability.

1. Introduction

Understanding the properties of itinerant magnetism has been a long-standing problem in condensed matter physics [1, 2]. Its importance stretches beyond this field of study since it impacts the behaviour of a large class of quantum systems encountered e.g. in atomic physics [3, 4]. The emergence of ferromagnetism in systems of spatially delocalized short-range repulsively interacting spinor fermions has been historically qualitatively understood in the framework of the Stoner instability [5]. Within this framework ferromagnetism is related to the phase separation of the different spin components and the formation of ferromagnetic domains [6–8]. Ultracold atoms provide a fertile platform to investigate such quantum many-body (MB) phenomena due to their exceptional tunability [3]. Indeed, several experiments utilizing ensembles of ultracold fermions have attempted to implement and study the Stoner instability [9–13] but their results have been somewhat inconclusive [14, 15].

The phase separation of Fermi systems has been studied in the case of strong attractive interactions [16–18] where the phenomenon of spin-segregation for weak attraction or repulsion has been identified [19–21]. However, only recently experiments attempted to address the relation between ferromagnetism and phase separation in the case of a repulsively interacting Fermi-gas [11, 13]. For instance, it has been demonstrated [11] that an artificially prepared phase separated state becomes metastable for strong repulsions which in turn implies the presence of a ferromagnetic instability. Accordingly, by employing pump-probe spectroscopy the emergence of short-range two-body anti-correlations in the repulsive Fermi-gas supporting some sort of ferromagnetic order has been revealed [13], while the possibility of macroscopic phase separation has been ruled out. These experimental evidences indicate that the relation between phase separation and magnetism might be more intricate and involved than it appears within the framework of the Stoner instability manifested within the Hartree–Fock theory. Nevertheless, competing processes such as the Feshbach molecule formation [22, 23] and its possible enhancement by coherent processes [14] have hindered the experimental progress in this direction. As a consequence a complete

understanding on how and via which mechanism phase separation and ferromagnetism are related remains still elusive.

Here we propose that one-dimensional (1D) few-body systems offer an ideal platform to provide insight into these fundamental questions. Besides the suppression of the above-mentioned competing processes which render the magnetic properties of 1D spin-1/2 fermions experimentally addressable [24, 25], the corresponding theoretical understanding of these properties is also advanced. Indeed, the availability of numerically-exact methods [26–28] and the development of powerful spin-chain models [29–36] allows for the accurate modeling of the magnetic properties emerging in 1D systems in the cases of strong [29–34] and weak [35, 36] interactions. Regarding the occurrence of phase separation previous studies revealed the role of the breaking of the SU(2) symmetry, associated with the conservation of the total spin of the system. Moreover, manifestations of the interplay between the magnetic properties and the phase separation have also been reported [35–40]. Below, we provide some characteristic examples. It has been demonstrated [37, 38] that contrary to mean-field treatments phase separation does not occur during the interaction-quench dynamics of an SU(2) symmetric system. However, the ground state of a system with weakly broken SU(2) symmetry is known [39, 40] to be phase separated in the case of infinite repulsion. In contrast, it has been shown that a parabolically confined initially spin-polarized Fermi-gas in the case of weak interactions prefers a state of largely miscible spin components even when perturbed by a spin dependent potential which weakly breaks the SU(2) symmetry [35]. In particular, for sufficiently weak spin-dependent potentials a ferromagnetic order despite the miscible character of the Fermi-gas has been established [36]. However, a systematic study that clarifies the relation between the phase separation and the magnetic properties of 1D fermions unifying, also, the above results is currently absent. Furthermore, the comparison of the underlying mechanisms provided by such a unification with the expectations of the Stoner instability might provide invaluable insights into the study of magnetic phenomena emerging in more complex systems.

Here we attempt to bridge this apparent gap in the literature by studying the stability of the phase separated state during the correlated dynamics of fermionic ensembles confined in a double-well (DW). The employed DW confinement allows for the experimental implementation of the phase separated initial state [11, 41]. This initial state is allowed to evolve for different values of the interaction strength and the degree of the dynamical phase separation between the spin components is monitored. To capture the correlated out-of-equilibrium dynamics of this spinor fermion system we resort to the multilayer multiconfiguration time-dependent Hartree method for atomic mixtures (ML-MCTDHX) [28]. Focussing on an SU(2) invariant system and following the above-mentioned procedure we find that for weak interactions the phase separation is unstable. While for increasing repulsion an interaction regime where the phase separated state becomes metastable is unveiled. To identify the emergence of this metastable state and its relation with the magnetic properties of the system we invoke an effective tight-binding model. The metastability of the phase separated state is shown to be inherently connected with the appearance of a quasi-degenerate manifold of eigenstates characterized by intra-well ferromagnetic correlations of both wells but a varying total spin. The occurrence of this manifold is attributed to the ferromagnetic Hund exchange interactions [42–44] appearing within each well of the DW setup. Moreover, the low-frequency tunneling dynamics that leads to the decay of the metastable initial state provides a manifestation of the antiferromagnetic Anderson kinetic exchange interactions [45]. These interactions act between the wells and result in the lifting of the degeneracy among states exhibiting intra-well ferromagnetic correlations.

For larger interactions, the interband coupling introduced by cradle-like processes [46–48] is shown to result in a fastly decaying dynamics of the phase separation, thus limiting the interaction regime where this metastability of the initial state is exhibited. The breaking of the SU(2) symmetry is found to substantially affect the dynamics of the system. Indeed, the initial phase separated state of the system can be stabilized by applying a linear magnetic potential gradient to the system. This stabilization is much more prevalent in the case of intermediate interactions due to the occurrence of quasi-degenerate eigenstates with different total spin. Our results demonstrate the relation of the phase separation to the stability of the intra-well ferromagnetic order. Indeed, the interplay of the Anderson and Hund exchange interactions is found to dictate the behaviour of the system in terms of these two above phenomena implying that their relation is more intricate than what is qualitatively expected in view of the Stoner instability.

This paper is structured as follows. In section 2 we introduce our setup and discuss its inherent spin symmetries. Section 3 presents the MB dynamics of our system and showcases the important features of the related eigenspectrum. An effective tight-binding model of our system is introduced in section 4 which is subsequently utilized to expose the magnetic properties of the system during the dynamics. In section 4 we study the dynamics in the case of a broken SU(2) symmetry. Finally, in section 6 we conclude and provide future perspectives. In appendices A and B we generalize our results for more particles and different barrier

heights respectively. Appendix C provides the derivation of the Anderson effective kinetic exchange interaction for our DW setup and appendix D describes the employed numerical approach, namely the ML-MCTDHX method.

2. Description of the system and relevant observables

2.1. Hamiltonian and symmetries

We consider an interacting system consisting of N spin-1/2 fermions of mass m being confined in an 1D DW trap. The latter is composed by a harmonic oscillator with frequency ω and a Gaussian barrier. Such a system is described by the MB Hamiltonian $\hat{H} = \hat{H}_0 + \hat{H}_1$, where \hat{H}_0 and \hat{H}_1 correspond to its non-interacting and interacting parts respectively. The Hamiltonian, \hat{H} , expressed in harmonic oscillator units ($\hbar = m = \omega = 1$), reads

$$\hat{H} = \underbrace{\sum_{\alpha} \int dx \hat{\psi}_{\alpha}^{\dagger}(x) \left(-\frac{1}{2} \frac{d^2}{dx^2} + \frac{1}{2} x^2 + V_0 e^{-\frac{x^2}{2w^2}} \right) \hat{\psi}_{\alpha}(x)}_{\equiv \hat{H}_0} + g \underbrace{\int dx \hat{\psi}_{\downarrow}^{\dagger}(x) \hat{\psi}_{\uparrow}^{\dagger}(x) \hat{\psi}_{\uparrow}(x) \hat{\psi}_{\downarrow}(x)}_{\equiv \hat{H}_1}, \quad (1)$$

where $\hat{\psi}_{\alpha}(x)$ denotes the fermionic field operator with spin- $\alpha \in \{\uparrow, \downarrow\}$. V_0 and w refer to the height and width of the Gaussian barrier respectively. In the ultracold regime, g describes the effective 1D s -wave contact interaction strength between anti-aligned spins. This effective interaction strength, g , is known to be related with the transverse confinement length and the 3D s -wave scattering length [49]. The above imply that the interaction strength is experimentally tunable with the aid of confinement-induced and Fano–Feshbach resonances [22]. The Hamiltonian of equation (1) is invariant under rotations in spin-space as it commutes with the total \hat{S}_z , $\hat{S}_{\pm} = \hat{S}_x \pm i\hat{S}_y$ spin operators. The corresponding individual spin operators, \hat{S}_k , are defined as

$$\hat{S}_k = \frac{1}{2} \int dx \sum_{\alpha, \beta} \hat{\psi}_{\alpha}^{\dagger}(x) \sigma_{\alpha, \beta}^k \hat{\psi}_{\beta}(x), \quad (2)$$

with σ^k , $k \in \{x, y, z\}$, referring to the corresponding Pauli matrix. The system additionally possesses an SU(2) symmetry since \hat{H} (equation (1)) commutes with the total spin operator, $\hat{S}^2 = \hat{S}_+ \hat{S}_- + \hat{S}_z(\hat{S}_z - 1)$. As we shall demonstrate later on, this symmetry has a deep impact on the eigenspectrum of the system.

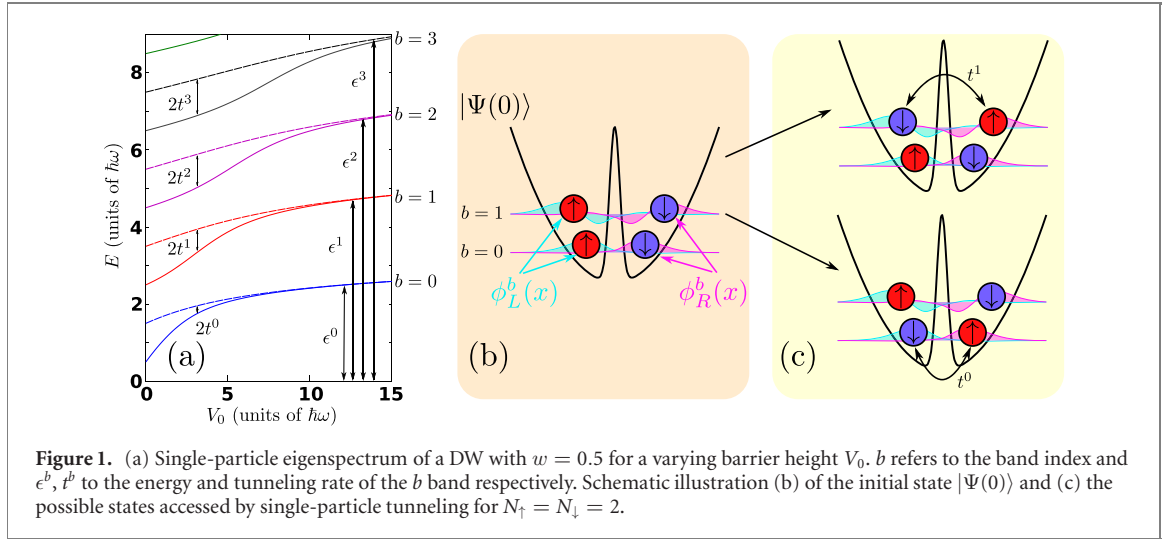
The behaviour of the single-particle Hamiltonian \hat{H}_0 for varying V_0 and w is well-known [50, 51] and depicted in figure 1(a). For $V_0 = 0$ the harmonic oscillator potential is retrieved and the single-particle spectrum consists of equidistant states. As V_0 is increased, gradually all the eigenenergies, starting with the energetically two lowest ones, form quasi-degenerate pairs of different parity states (herewith called bands). Employing linear combinations of the two eigenstates forming the band, b , it is possible to construct the so-called Wannier states, $\phi_s^b(x)$, which are localized either in the left, $s = L$ or the right well, $s = R$ [52]. The single-particle dynamics of a system initialized in such a Wannier state is rather simple as the particle tunnels from each well to the other during the evolution with a frequency given by the energy difference, $2t^b$, between the two quasi-degenerate states which form the corresponding band.

2.2. Initial state characterization

The purpose of this work is to examine whether a phase separated state can be stabilized in the presence of interactions and reveal its relation to the (ferro)magnetic properties of the system. A promising candidate for such an investigation is the initial state

$$|\Psi(0)\rangle = \prod_{b=0}^{N_{\uparrow}-1} \underbrace{\int dx \phi_L^b(x) \hat{\psi}_{\uparrow}^{\dagger}(x)}_{\equiv \hat{a}_{L\uparrow}^{b\dagger}} \prod_{b=0}^{N_{\downarrow}-1} \underbrace{\int dx \phi_R^b(x) \hat{\psi}_{\downarrow}^{\dagger}(x)}_{\equiv \hat{a}_{R\downarrow}^{b\dagger}} |0\rangle, \quad (3)$$

where $N_{\uparrow} = \frac{N}{2}$ spin- \uparrow and $N_{\downarrow} = \frac{N}{2}$ spin- \downarrow fermions are localized in the left and right wells respectively (see figure 1(b) for $N = 4$). Recall that $\phi_s^b(x)$ denotes the Wannier state corresponding to the $s \in \{L, R\}$ well and band b . Herein, we intend to address the dynamics of a system initialized in the state described by equation (3), especially focussing on the stability properties of the phase separation. Evidently, in the non-interacting case each one of the constituting particles will perform its individual tunneling oscillation with a frequency $2t^b$ and, consequently, the phase separation imprinted in the initial state will be



periodically lost and recovered during the time-evolution. However, in the case of $g \neq 0$ the individual tunneling channels of each of the particles couple due to the interparticle interaction. The interaction between the spin components is particularly important since the system accesses via tunneling, states possessing a substantial density overlap for anti-aligned spins yielding an interaction energy $E_I \sim g \sum_{s \in L,R} \int dx |\phi_s^b(x)|^2 |\phi_s^{b'}(x)|^2$, see for instance figure 1(c). Employing a mean-field argumentation one arrives at the conclusion that the tunneling among the wells slows down and eventually terminates as the repulsion increases. This is due to the large interaction energy of a spin- \uparrow and a spin- \downarrow atom occupying the same well when compared to the interaction energy contained in $|\Psi(0)\rangle$ where the spin components are phase separated. However, the interparticle interaction possibly induces two- (or more) body correlations crucially affecting the dynamics of the system. As we shall demonstrate later on this is indeed the case and the dynamics for $g \neq 0$ is more involved than what is expected by the above-mentioned mean-field argumentation.

2.3. Magnetization imbalance and MB eigenstate categorization in terms of bands

To monitor the degree of phase separation between the spin components during the dynamics of the system we employ the experimentally accessible measure [11, 41]

$$M = \frac{1}{2}(M_\uparrow - M_\downarrow), \quad \text{with } M_\alpha = \frac{1}{N_\alpha} \left(\int_{-\infty}^0 dx \rho_\alpha^{(1)}(x; t) - \int_0^\infty dx \rho_\alpha^{(1)}(x; t) \right). \quad (4)$$

Here $\rho_\alpha^{(1)}(x; t) = \langle \Psi(t) | \hat{\psi}_\alpha^\dagger(x) \hat{\psi}_\alpha(x) | \Psi(t) \rangle$ is the spin-dependent, $\alpha \in \{\uparrow, \downarrow\}$, one-body density. Notice that both the Hamiltonian, equation (1), and the initial state, equation (3), are invariant under the transformation $x \rightarrow -x$, $|\uparrow\rangle \rightarrow |\downarrow\rangle$ and $|\downarrow\rangle \rightarrow |\uparrow\rangle$, implying that $M_\uparrow + M_\downarrow = 0$ is conserved during the dynamics. The quantity M takes its extreme values $M = 1$ and $M = -1$ when the particles within each of the wells are fully-polarized, a situation equivalent to a perfect phase separation. The sign of M in this case depends on whether the spin- \uparrow particles reside in the left ($M = 1$), as is the case for $|\Psi(0)\rangle$, or right ($M = -1$) well. In the case that $M = 0$ the spin- \uparrow and spin- \downarrow particles are distributed over both wells showing that the spin components are miscible. Since $M \neq 0$ corresponds to states magnetized along the x spatial-axis (see also equation (3)), M will be herewith referred to as magnetization imbalance.

Furthermore, let us note that for large barrier heights and weak or intermediate interactions, we expect that the band-gaps between the non-interacting bands constitute the largest energy scale of the system, see figure 1(a). As a consequence, the energetic characterization of the MB eigenstates in terms of non-interacting bands will be of great importance in the following. We assign each eigenstate of the non-interacting N -body system, $|\Psi_{g=0}\rangle$ to an energetic class by employing the vector $\vec{n}_B = (n_B^0, n_B^1, \dots)$. This vector contains the occupation numbers of each of the non-interacting bands, $n_B^b = \langle \Psi_{g=0} | \hat{n}_{L\uparrow}^b + \hat{n}_{R\uparrow}^b + \hat{n}_{L\downarrow}^b + \hat{n}_{R\downarrow}^b | \Psi_{g=0} \rangle$ ($0 \leq n_B^b \leq 4$), with $\hat{n}_{s\alpha}^b$ being the number operator that counts the number of spin- α particles residing in the Wannier state $\phi_s^b(x)$. Accordingly, each eigenstate of the interacting system, $g \neq 0$, will be assigned to an energy class, \vec{n}_B , if it constitutes a superposition of non-interacting eigenstates of this particular class. For instance the initial state, $|\Psi(0)\rangle$, belongs to the $\vec{n}_B = (2, 2, 0, \dots)$ class for $N = 4$, see also figure 1(b). Indeed, the initial state for $N = 4$ contains two fermions in the 0th band ($n_B^0 = 2$) and two additional ones residing in the 1st excited band ($n_B^1 = 2$).

3. Many-body eigenspectrum and correlated dynamics

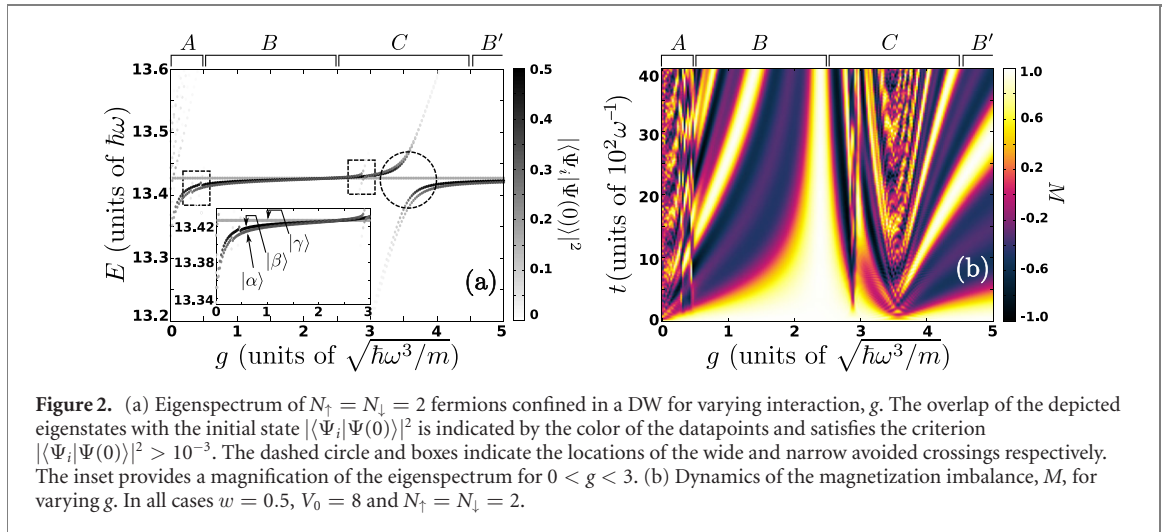
In this section we examine the eigenspectrum of the full MB Hamiltonian \hat{H} (see equation (1)) in the case of $N = 4$ fermions. Then we analyze the correlated dynamics of such a system initialized in the state $|\Psi(0)\rangle$ (equation (3)) and subsequently left to evolve within \hat{H} . This investigation permits us to identify the emergent phase separation behaviour between the spin components for varying interaction strength. To track the correlated dynamics of this system we employ ML-MCTDHX [28] and, in particular, its reduction for spin-1/2 fermions (for more details see appendix C). ML-MCTDHX is an *ab initio* variational method that takes all correlations into account enabling us to reveal their influence into the static properties and in particular the dynamics of MB systems. We generalize our results to the $N > 4$ case in appendix A.

3.1. Many-body eigenspectrum

The eigenspectrum of \hat{H} (equation (1)), for $N_\uparrow = N_\downarrow = 2$ fermions and varying g , is presented in figure 2(a), in the case of a relatively deep ($V_0 = 8$, $w = 0.5$) DW potential. The overlap of the MB interacting eigenstates, $|\Psi_i\rangle$ with the initial state, $|\Psi(0)\rangle$ is indicated by the different colors in figure 2(a). Based on the eigenspectrum we can identify four different interaction regimes, indicated by A, B, C and B' in figure 2(a), where the overlap of the initial state, $|\Psi(0)\rangle$ with the MB eigenstates $|\Psi_i\rangle$ of \hat{H} exhibits a qualitatively different behaviour. In addition, by expanding each eigenstate $|\Psi_i\rangle$ in the number states of the Wannier basis, $\phi_s^b(x; t)$, (not shown here for brevity) we are able to infer its energetic class, \vec{n}_B (see section 2.3) which is important for identifying the interband processes contributing to the eigenspectrum and dynamics.

For weak interactions, $g < 0.5$ within the interaction regime A we observe that multiple eigenstates (the ones with $E > 13.42$ are hardly visible in figure 2(a)) contribute to the initial state. We remark that these states belong to the energy class $\vec{n}_B = (2, 2, 0, \dots)$ according to the energy categorization given in section 2.3. The energies of the eigenstates with $E > 13.42$ increases for increasing g , while their overlap with the initial state decreases, see figure 2(a) for $0 < g < 0.5$. For $g \approx 0.5$ only three of the aforementioned eigenstates with $E < 13.43$ possess a significant overlap with $|\Psi(0)\rangle$ see also the inset of figure 2(a). Additionally, narrow avoided crossings (see the dashed box in figure 2(a) for $g \approx 0.2$) emerge but overall the MB eigenspectrum is only slightly modified. These narrow avoided crossings result from the coupling of states belonging to the energy classes $\vec{n}_B = (3, 0, 1, 0, \dots)$ and $\vec{n}_B = (2, 2, 0, \dots)$ by a weak two-particle interband transfer process.

Entering the interaction regime B, $0.5 < g < 2.5$, we observe that the three eigenstates of \hat{H} possessing the dominant overlap with $|\Psi(0)\rangle$, are quasi-degenerate. In terms of increasing energetic order we refer to these eigenstates as $|\alpha\rangle$, $|\beta\rangle$ and $|\gamma\rangle$, see also the inset of figure 2(a). The existence of the quasi-degenerate predominantly occupied eigenstates within the B and also B' ($4.5 \leq g < 5$) interaction regimes implies that the time-scales of the dynamical evolution, which are associated with the energy differences of these quasi-degenerate states, are rather large. Therefore, these interaction regimes are very promising for studying the dynamical stability of the phase separation exhibited by the initial state $|\Psi(0)\rangle$. Note that the physical reasoning behind the emergence of this quasi-degenerate eigenstate manifold will be the main focus of section 4. At $g \approx 3.5$ the three aforementioned quasi-degenerate eigenstates show a wide avoided crossing (see the dashed circle in figure 2(a)) with the eigenstates of the $\vec{n}_B = (3, 1, 0, \dots)$ energy class within the interaction regime C, $2.5 < g < 4$. As we shall explicate later on, this interband avoided crossing is the fermionic analogue of the so-called cradle mode that has been identified in the interaction quench dynamics of spinless lattice trapped bosonic ensembles [46–48]. For larger repulsions, $g > 4.5$, the quasi-degeneracy of the predominantly occupied eigenstates reappears giving rise to the B' interaction regime. The eigenspectrum for these interactions ($g > 4.5$) possesses a similar structure to the one observed within the interaction regime B. Note that the Tonks–Girardeau limit of our system is approached for $g > 5$ (not shown here for brevity). The Tonks–Girardeau regime for a spin-1/2 Fermi system is approached in the limit of large repulsions, $g \rightarrow \infty$. In this case the system behaves similarly to an ensemble of hard-core (impenetrable) particles and its eigenstates can be expressed in terms of the ones of a spinless Fermi gas [29, 53, 54]. Specifically, for the strongly repulsive limit and for the DW confinement considered herein [34] the eigenspectrum features an avoided crossing between the aforementioned quasi-degenerate states and the ones belonging to the energetically lowest class $\vec{n}_B = (4, 0, \dots)$. The eigenspectrum in this case can be theoretically described by using standard spin-chain techniques [34]. We remark that the state $|\gamma\rangle$ possesses an interaction independent eigenenergy, associated with its fully antisymmetric character under particle exchange.



3.2. Correlated dynamics

To inspect the stability of the phase separation encoded in $|\Psi(0)\rangle$ for different interaction strengths we let the system initialized in the state $|\Psi(0)\rangle$ of equation (3) to evolve in time and subsequently we track the magnetization imbalance, M (equation (4)), during the out-of-equilibrium dynamics. To provide a further interpretation of the participating dynamical modes we relate our findings regarding the phase separation to the eigenspectrum of \hat{H} (equation (1)), see also figure 2(a). For weak interactions, i.e. $0 < g < 0.5$, the phase separated, $|\Psi(0)\rangle$, state is shown to be unstable especially when the non-interacting limit is approached. Indeed, as already identified in the eigenspectrum (see figure 2(a) for the interaction regime A) multiple eigenstates contribute to the MB dynamics whose occupation results in a fast decay of the phase separation. This is indeed justified by inspecting the corresponding time-evolution of M showing fast oscillations of small amplitude (figure 2(b)). The dynamics is better captured by the evolution of the spin- α one-body density, $\rho_{\alpha}^{(1)}(x; t)$, see figures 3(a₁) and (a₂). Here, the dominant process is single particle tunneling. More precisely, the particles occupying the first excited band tunnel between the wells with much higher frequency than the particles occupying the lowest band. This can be identified by comparing the rate of tunneling of the two humped density structure ($b = 1$ band) appearing in figure 3(a₁) with the tunneling of the density residing near the center of the well ($b = 0$ band) within the time-interval $0 < t < 100$. Additionally, an interaction induced dephasing, due to the involvement of the multitude of eigenstates identified in figure 2(a), is evident as $|\Psi(0)\rangle$ does not completely revive during the time evolution.

Further monitoring the dynamical evolution of the system we observe that the phase separated state, $|\Psi(0)\rangle$ (equation (3)), is a long-lived metastable state within the interaction regime B. Indeed, for $0.5 < g < 2.5$ we can infer the decay of the phase separation, imprinted in the magnetization imbalance, M and its subsequent revival (figure 2(b)). This process is relatively fast for weak interactions within the interaction regime B. For instance, the phase separated state $|\Psi(0)\rangle$ decays to a miscible state with $M = 0$ at $t \approx 500$ for $g = 1$. Qualitatively similar dynamics occurs but it is shown to be significantly slower for $1 < g < 4$, e.g. at $g = 2$, $M = 0$ is reached for $t \approx 2000$, while the life-time of $|\Psi(0)\rangle$ exceeds $t = 4000$ for $g \approx 2.5$ (figure 2(b)). The metastability of $|\Psi(0)\rangle$ is accordingly well-justified since its life-times are much larger than the inverse of the characteristic tunneling rate of the ground, $\pi/(2t^0) \approx 42$, and the first excited band, $\pi/(2t^1) \approx 190$. To shed light into the dynamical evolution of $|\Psi(0)\rangle$ we also inspect the one-body densities of the spin components, $\rho_{\alpha}^{(1)}(x; t)$ (figures 3(b₁) and (b₂)) at $g = 1$. Indeed, at $t \approx 500$ $\rho_{\uparrow}^{(1)}(x; t)$ and $\rho_{\downarrow}^{(1)}(x; t)$ are delocalized over both wells and they are almost perfectly overlapping which is in accordance to the value $M = 0$ (see figure 2(b)). Note here that the absence of any signature of phase separation within each of the wells justifies the use of M as a measure of phase separation. Subsequently, the density of each component accumulates in the opposite well, than it was residing initially, but a small density portion remains in the initially populated well. Finally, at $t \approx 2700$ an almost perfect revival of $|\Psi(0)\rangle$ occurs. For larger evolution times, the above-mentioned dynamics is repeated in a periodic manner. Regarding the underlying tunneling mechanisms, the evolution of $\rho_{\alpha}^{(1)}(x; t)$ is indicative of a low-frequency two-body correlated tunneling dynamics for both spin components, as the entire density of two spin-aligned fermions seems to tunnel among the wells without being deformed. In addition, a contribution stemming from a single-particle tunneling process is also visible in figures 3(b₁) and (b₂), notice for instance the dynamics of the faint two-humped structure for $t \approx 600$, $t \approx 1200$ and $t = 1800$. In the following section it will be shown that the occurrence of the interaction regime B can be explained by examining the spin-order exhibited in the system.

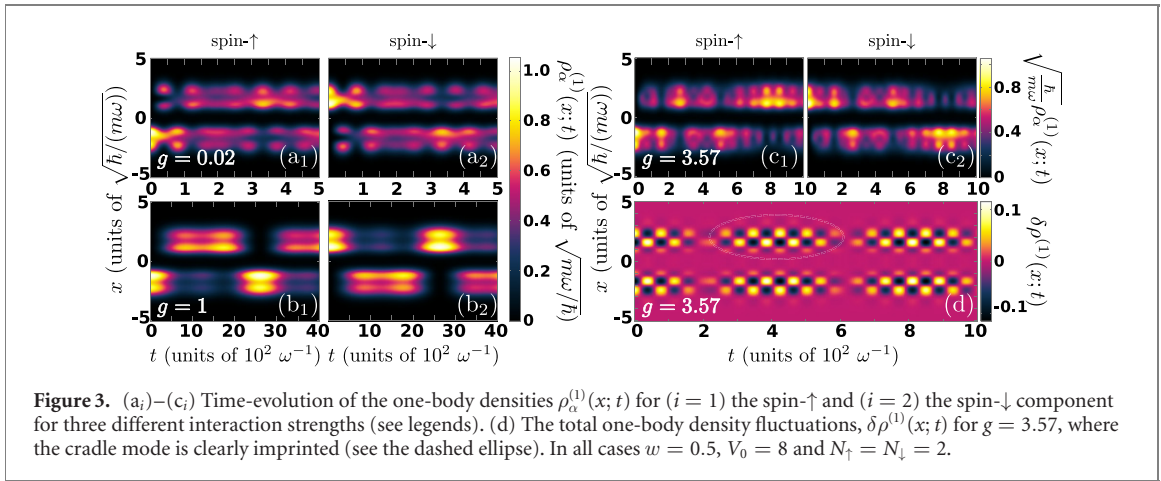


Figure 3. (a₁)–(c₂) Time-evolution of the one-body densities $\rho_{\alpha}^{(1)}(x; t)$ for ($i = 1$) the spin- \uparrow and ($i = 2$) the spin- \downarrow component for three different interaction strengths (see legends). (d) The total one-body density fluctuations, $\delta\rho^{(1)}(x; t)$ for $g = 3.57$, where the cradle mode is clearly imprinted (see the dashed ellipse). In all cases $w = 0.5$, $V_0 = 8$ and $N_{\uparrow} = N_{\downarrow} = 2$.

For strong interactions, $g > 2.5$, the eigenstates belonging to the energy class $\vec{n}_B = (3, 1, 0, \dots)$ cross with the predominantly occupied eigenstates of the class $\vec{n}_B = (2, 2, 0, \dots)$ as shown in figure 2(a) at $g \approx 3.5$. The states of the two energy classes exhibit two avoided crossings (indicated in figure 2(a) by the dashed circle) due to the interband interaction-induced coupling which is a manifestation of the cradle mode [46–48]. This resonant behaviour is directly imprinted on M , which shows a strong dependence of the lifetime of $|\Psi(0)\rangle$ on the value of g , see figure 2(b) at $g \approx 2.8$ and $g \approx 3.5$. The spin-dependent one-body densities also show a tunneling behaviour similar to the weakly interacting case, compare figures 3(c₁) and (a₁). The cradle mode is manifested as a dipole-like oscillation within each well. To explicitly demonstrate its existence we invoke the total one-body density fluctuations [46–48] defined as

$$\delta\rho^{(1)}(x; t) = \sum_{\alpha \in \{\uparrow, \downarrow\}} \left[\rho_{\alpha}^{(1)}(x; t) - \frac{1}{T} \int_0^T dt' \rho_{\alpha}^{(1)}(x; t') \right]. \quad (5)$$

Indeed, $\delta\rho^{(1)}(x; t)$ reveals dipole-like oscillations within both wells (see for instance figure 3(d) around $t \approx 400$ i.e. the encircled region) and a beating dynamics for the intensity of the cradle mode. This beating can be understood by inspecting the eigenspectrum of the system (figure 2(a)), where two almost perfectly overlapping cradle resonances can be identified at $g \approx 3.5$, yielding two cradle frequencies of comparable magnitude. Notice that the cradle mode exhibited in our system is slightly different from its bosonic counterpart [46–48] as it does not involve overbarrier transport between the different wells but rather a direct interband population transfer within a particular well. The absence of overbarrier transport can be identified in figure 3(d) as the density fluctuations in the spatial region of the barrier, $x \approx 0$ are vanishing.

4. Interpretation of the magnetic properties and the effective tight-binding model

Having appreciated the magnetic properties of the system within the fully-correlated ML-MCTDHX approach, we next proceed by constructing a reduced effective model. This model as we shall discuss below facilitates the qualitative interpretation of the correlated MB dynamics. In particular, the qualitative understanding of the underlying magnetic properties of the system via the effective model enables the identification of the decay mechanisms of the phase separation in a straightforward and intuitive way, allowing also, for comparisons with previous studies.

4.1. The effective tight-binding model

As already mentioned in section 2, the band-gaps constitute the largest energy-scale of the system for both weak and intermediate interactions. It is therefore, well-justified to assume that a corresponding tight-binding model might sufficiently capture the observed dynamics. Within such a tight-binding model the Wannier states, $\phi_s^b(x)$, with $s \in \{L, R\}$, constitute the basis states of the MB Hamiltonian. The non-interacting Hamiltonian reads

$$\hat{H}_0 = - \sum_{b=0}^{\infty} \sum_{\alpha \in \{\uparrow, \downarrow\}} t^b \left(\hat{a}_{R\alpha}^{b\dagger} \hat{a}_{L\alpha}^b + \hat{a}_{L\alpha}^{b\dagger} \hat{a}_{R\alpha}^b \right) + \sum_{b=0}^{\infty} \sum_{\alpha \in \{\uparrow, \downarrow\}} \epsilon^b \left(\hat{n}_{L\alpha}^b + \hat{n}_{R\alpha}^b \right),$$

where ϵ^b is the average energy of the non-interacting eigenstates forming the band, b . Also, $\hat{a}_{s\alpha}^{b\dagger}$ ($\hat{a}_{s\alpha}^b$) is the operator that creates (annihilates) a spin- α particle in the Wannier state $\phi_s^b(x)$ and $\hat{n}_{s\alpha}^b \equiv \hat{a}_{s\alpha}^{b\dagger} \hat{a}_{s\alpha}^b$. The exact

form of the interaction term, \hat{H}_I , involves all matrix elements between the different Wannier states and it is, thus, quite complicated in appearance. Within the lowest-band approximation the Fermi–Hubbard model circumvents this issue by considering only on-site interactions and neglecting all density-induced tunneling effects [55]. It constitutes a valid approximation for large V_0 , where the underlying Wannier basis-states are well-localized to the corresponding wells. Additionally, g should define a sufficiently smaller energy scale than the band gap, ensuring that no significant interaction-induced interband tunneling, such as the cradle mode, occurs. Fermi–Hubbard models have been very successful in describing various effects emerging in a variety of settings where DW or lattice potentials are involved [56, 57].

Therefore, it is tempting to approximate the exact interaction term, \hat{H}_I , by the following effective one

$$\hat{H}_I^{\text{dir}} = g \left[\sum_{b=0}^{\infty} U^b (\hat{n}_{L\uparrow}^b \hat{n}_{L\downarrow}^b + \hat{n}_{R\uparrow}^b \hat{n}_{R\downarrow}^b) + \sum_{b \neq b' \in [0, \infty)} J^{bb'} (\hat{n}_{L\uparrow}^b \hat{n}_{L\downarrow}^{b'} + \hat{n}_{R\uparrow}^b \hat{n}_{R\downarrow}^{b'}) \right], \quad (6)$$

where $J^{bb'} = \int dx |\phi_L^b(x)|^2 |\phi_L^{b'}(x)|^2 = \int dx |\phi_R^b(x)|^2 |\phi_R^{b'}(x)|^2$ and $U^b = J^{bb}$ refer to the inter and intraband on-site interactions respectively. However, as it can be easily verified the last term of equation (6) breaks the SU(2) symmetry of \hat{H} (equation (1)), since it does not commute with \hat{S}^2 . In order to avoid this artificial symmetry breaking one needs, also, to include into the effective Hamiltonian the term

$$\hat{H}_I^{\text{exc}} = -g \sum_{b \neq b' \in [0, \infty)} J^{bb'} (\hat{a}_{L\uparrow}^{b\dagger} \hat{a}_{L\downarrow}^{b'\dagger} \hat{a}_{L\uparrow}^{b'} \hat{a}_{L\downarrow}^b + \hat{a}_{R\uparrow}^{b\dagger} \hat{a}_{R\downarrow}^{b'\dagger} \hat{a}_{R\uparrow}^{b'} \hat{a}_{R\downarrow}^b + \hat{a}_{L\uparrow}^{b\dagger} \hat{a}_{L\downarrow}^{b'\dagger} \hat{a}_{L\uparrow}^b \hat{a}_{L\downarrow}^{b'} + \hat{a}_{R\uparrow}^{b\dagger} \hat{a}_{R\downarrow}^{b'\dagger} \hat{a}_{R\uparrow}^b \hat{a}_{R\downarrow}^{b'}). \quad (7)$$

The term \hat{H}_I^{exc} , which is present in the exact \hat{H}_I of equation (1), incorporates the effect where two fermions in different bands but on the same well can exchange their spin due to their mutual interaction. Models that extend the Hubbard model in a similar manner to the above-mentioned have been employed in the context of the metal-insulator transition appearing in d -electron systems, for a review see [58].

Including all of the above-mentioned terms into an effective tight-binding Hamiltonian results in the following multi-band tJU model

$$\begin{aligned} \hat{H}_{\text{eff}} = & - \sum_{b=0}^{\infty} \sum_{\alpha \in \{\uparrow, \downarrow\}} t^b (\hat{a}_{R\alpha}^{b\dagger} \hat{a}_{L\alpha}^b + \hat{a}_{L\alpha}^{b\dagger} \hat{a}_{R\alpha}^b) + g \sum_{b=0}^{\infty} U^b (\hat{n}_{L\uparrow}^b \hat{n}_{L\downarrow}^b + \hat{n}_{R\uparrow}^b \hat{n}_{R\downarrow}^b) \\ & - g \sum_{b \neq b' \in [0, \infty)} J^{bb'} \left[\hat{\mathbf{S}}_L^b \cdot \hat{\mathbf{S}}_L^{b'} + \hat{\mathbf{S}}_R^b \cdot \hat{\mathbf{S}}_R^{b'} - \frac{1}{4} (\hat{n}_L^b \hat{n}_L^{b'} + \hat{n}_R^b \hat{n}_R^{b'}) \right] + \sum_{b=0}^{\infty} \sum_{\alpha \in \{\uparrow, \downarrow\}} \epsilon^b (\hat{n}_{L\alpha}^b + \hat{n}_{R\alpha}^b), \quad (8) \end{aligned}$$

where $\hat{\mathbf{S}}_s^b = \hat{S}_{x;s}^b \mathbf{i} + \hat{S}_{y;s}^b \mathbf{j} + \hat{S}_{z;s}^b \mathbf{k}$ with $\hat{S}_{k;s}^b = \frac{1}{2} \sum_{\alpha, \beta} \sigma_{\alpha\beta}^k \hat{a}_{s\alpha}^{b\dagger} \hat{a}_{s\beta}^b$, $k \in \{x, y, z\}$, $s \in \{L, R\}$ and $\mathbf{i}, \mathbf{j}, \mathbf{k}$ refer to the unit vectors in spin-space and $\hat{n}_s^b = \hat{n}_{s\uparrow}^b + \hat{n}_{s\downarrow}^b$. tJ models, where the on-site interaction term vanishes as double site occupations are adiabatically eliminated, have been originally employed to describe magnetic phenomena in condensed matter physics [59–61] and later for the interpretation of some aspects of superconductivity [62–64]. Physically, the effective Hamiltonian of equation (8) describes a collection of Hubbard-dimers for each band, b , that are coupled by ferromagnetic (in the repulsive case $g > 0$) on-site exchange interaction (second line of equation (8)) and are off-setted by the corresponding band energy (third line of equation (8)). On-site interband exchange interactions, such as those encoded in equation (8), are known as Hund interactions in condensed matter physics [42–44]. The tight-binding approximation is only valid for $t^b/E^b \ll 1$ or equivalently large V_0 . An additional limitation of the tJU model (equation (8)) is that $gU^b/E^b \ll 1$ allowing for the interaction-driven interband processes to be safely neglected. Within this model states of different energy classes, \vec{n}_B do not couple and as a consequence all the elements of \vec{n}_B are conserved. As we have previously established within the full MB system (that does not possess this symmetry) such interband effects do not alter the eigenspectrum significantly within the interaction regimes A and B .

Below we argue why this model leads to a *metastable*, phase separated, state $|\Psi(0)\rangle$, in the case of intermediate repulsions, qualitatively explaining the magnetic order exhibited within the interaction regime B .

4.2. Magnetic properties of the effective model

Let us first discuss the relevant properties of the N -body eigenspectrum of the tJU model. We operate in the $t^b/(gU^b) \ll 1$ limit, where we can neglect the tunneling term $\propto t^b$. Indeed, for the system examined in section 3 the criterion $\frac{gU^b}{t^b} \gg 1$ is well-satisfied³ within the interaction regime B , $0.5 < g < 3$. In view of the

³ For $V_0 = 8$ and $w = 0.5$ the relevant scales for $N = 4$ are $\frac{gU^1}{t^1} \approx 11.38g$ and $\frac{gU^0}{t^0} \approx 71.44g$.

decoupling of different energy classes \vec{n}_B within the effective tJU model we will focus on the particular energetic class that the initial state, $|\Psi(0)\rangle$, belongs to, namely, \vec{n}'_B . This class is defined as $n_B^b = 2$ for $b < N/2$ and $n_B^b = 0$ otherwise⁴.

Focussing on the simplest case of $t^b = 0$, for all involved b , the effective Hamiltonian can be expanded in two intra-well Hamiltonian terms $\hat{H}_{\text{eff}} = \hat{H}_R + \hat{H}_L$ that are decoupled among them. By projecting these Hamiltonian terms into the energy class \vec{n}'_B the former reads

$$\hat{P}_B \hat{H}_s \hat{P}_B = g \sum_{b=0}^{\frac{N}{2}-1} U^b \hat{n}_{s\uparrow}^b \hat{n}_{s\downarrow}^b - g \sum_{b=0}^{\frac{N}{2}-1} \sum_{b' \neq b} J^{bb'} \left[\hat{S}_s^b \cdot \hat{S}_s^{b'} - \frac{1}{4} \hat{n}_s^b \hat{n}_s^{b'} \right] + \sum_{b=0}^{\frac{N}{2}-1} \epsilon^b \hat{n}_s^b, \quad (9)$$

where \hat{P}_B is the projection operator into \vec{n}'_B . Equation (9) corresponds to a ferromagnetic Heisenberg model, incorporating additional energy shifts depending on the particle occupation $\propto \hat{n}_s^b$, $s \in \{L, R\}$. For $g > 0$ the sum of these energy shifts contained within \hat{H}_L and \hat{H}_R is minimized in the case that no double occupations of a particular site occur, i.e. $\langle \Psi | \hat{n}_s^b \hat{n}_s^b | \Psi \rangle = 0$ for all b and s . The spin configuration for $t^b = 0$ can be characterized by the quantum numbers S, S_L, S_R , where $\hat{S}_s^2 = \sum_{b,b'} \hat{S}_s^b \cdot \hat{S}_s^{b'}$, refers to the total spin within the $s \in \{L, R\}$ well. It is well-known that ferromagnetic Heisenberg models exhibit ferromagnetic ground states [65] and as a consequence the ground states of equation (9) correspond to the largest possible values of S_L and S_R . Notice, also, that $|\Psi(0)\rangle$ is characterized by maximum S_L and S_R , since the spin-state within each well is fully spin-polarized. As a consequence, we can conclude that $|\Psi(0)\rangle$ belongs to a degenerate manifold of dimension $N/2$ at an energy $E = E_B = 2 \sum_{b=0}^{N/2-1} \epsilon^b$. This manifold consists of the states $|\Phi(t^b = 0); S\rangle$ with quantum numbers $S_L = S_R = \frac{N}{4}$ but varying total spin $S \in \{0, 1, \dots, \frac{N}{2}\}$ (see also below). In addition, the eigenstates $|\Phi(t^b = 0); S\rangle$ get energetically well-separated from the other states with $\vec{n}_B = \vec{n}'_B$ as the gap between them scales linearly with g , see equation (9).

The inclusion of the tunneling term for $t^b \neq 0$ induces couplings between the above-mentioned degenerate states resulting in the lifting of their degeneracy. Indeed, by treating the tunneling term in equation (8) within second order perturbation theory (see appendix C), we can show that in the $t^b \ll gU^b$ limit the effective Hamiltonian projected on the manifold of degenerate states spanned by $|\Phi(t^b = 0); S\rangle$ reads

$$\hat{P}_D \hat{H}_{\text{eff}} \hat{P}_D = E_B + \sum_{b=0}^{\frac{N}{2}-1} \frac{4(t^b)^2}{g\tilde{U}^b} \left(\hat{S}_L^b \cdot \hat{S}_R^b - \frac{1}{4} \right), \quad (10)$$

where \hat{P}_D is the projection operator $\hat{P}_D = \sum_{S=0}^{\frac{N}{2}} |\Phi(t^b = 0); S\rangle \langle \Phi(t^b = 0); S|$ and the interaction parameter \tilde{U}^b refers to $\tilde{U}^b = \sum_{b=0}^{\frac{N}{2}-1} J^{b_0 b}$. Equation (10) provides great insight into the structures imprinted in the intra-well ferromagnetically correlated states within the tJU model in the case of non-vanishing tunneling. Indeed, the inclusion of tunneling for $t^b \neq 0$ results to an apparent antiferromagnetic Heisenberg exchange interaction for $g > 0$, known as the Anderson kinetic exchange interaction [45]. Note that the total spin $\hat{S} = \hat{S}_L + \hat{S}_R$ commutes with $\hat{P}_D \hat{H}_{\text{eff}} \hat{P}_D$ implying that the eigenstates of the tJU model $|\Phi; S\rangle$ reduce within the zeroth order approximation to the ones for $t^b = 0$, i.e. $|\Phi; S\rangle = |\Phi(t^b = 0); S\rangle + \mathcal{O}(\frac{t^b}{gU^b})$. Regarding their eigenenergies, the tJU eigenstates, $|\Phi; S\rangle$ are expected to be energetically ordered in terms of increasing S due to the antiferromagnetic character of the Anderson exchange interaction and be quasi-degenerate possessing energy shifts among them of the order of $\Omega_d^b \sim \frac{(t^b)^2}{gU^b} \ll t^b$.

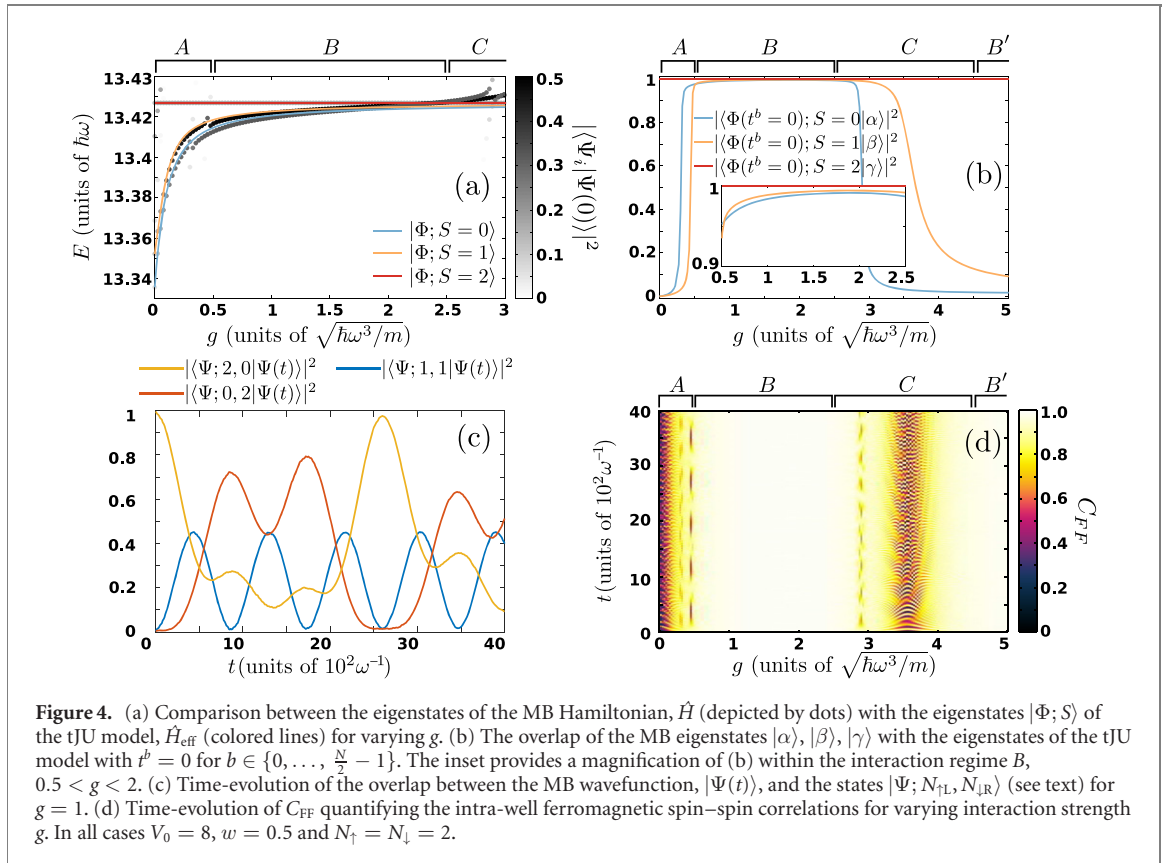
The above properties of the tJU eigenspectrum imply that the initial state $|\Psi(0)\rangle$ being a superposition of the eigenstates $|\Phi; S\rangle$ dephases during the time-evolution with a slow timescale $\sim \min_b(\pi/\Omega_d^b)$. In particular $|\Psi(0)\rangle$ can be expanded in terms of these eigenstates by utilizing the Clebsch–Gordan coefficients

leading to $\langle \Phi; S | \Psi(0) \rangle \approx \langle \Phi(t^b = 0); S | \Psi(0) \rangle = \sqrt{\frac{(2S+1)(\frac{N}{2}!)^2}{(\frac{N}{2}-S)!(\frac{N}{2}+S+1)!}}$. Moreover, the maximum values of

$S_L = \frac{N}{4}$ and $S_R = \frac{N}{4}$ which characterize the eigenstates $|\Phi; S\rangle \approx |\Phi(t^b = 0); S\rangle$ imply intra-well ferromagnetic correlations for particles occupying the same well⁵ and stem from the ferromagnetic Hund exchange interactions contributing to the multi-band tJU model of equation (8). Therefore, the emergence of the interaction regime B can be attributed to the dominant contribution of the intra-well ferromagnetic correlations when compared to the above-mentioned effective antiferromagnetism stemming from t^b , see equation (10). We remark here that the nature of this effective antiferromagnetism has been identified and studied by employing spin-chain models tailored to operate in the vicinity of the Tonks–Girardeau limit,

⁴ Since we operate in the manifold of states with $S_z = 0$ we are obviously restricted to even particle numbers.

⁵ Note that within this particular configuration in terms of \vec{n}_B and \vec{n}_D , the total spin within the s well solely depends on the corresponding spin–spin correlator, $\hat{P}_D \hat{S}_s^2 \hat{P}_D = \frac{N}{2} \frac{1}{2} (\frac{1}{2} + 1) + 2 \sum_{b>b'} \hat{S}_s^b \cdot \hat{S}_s^{b'}$.

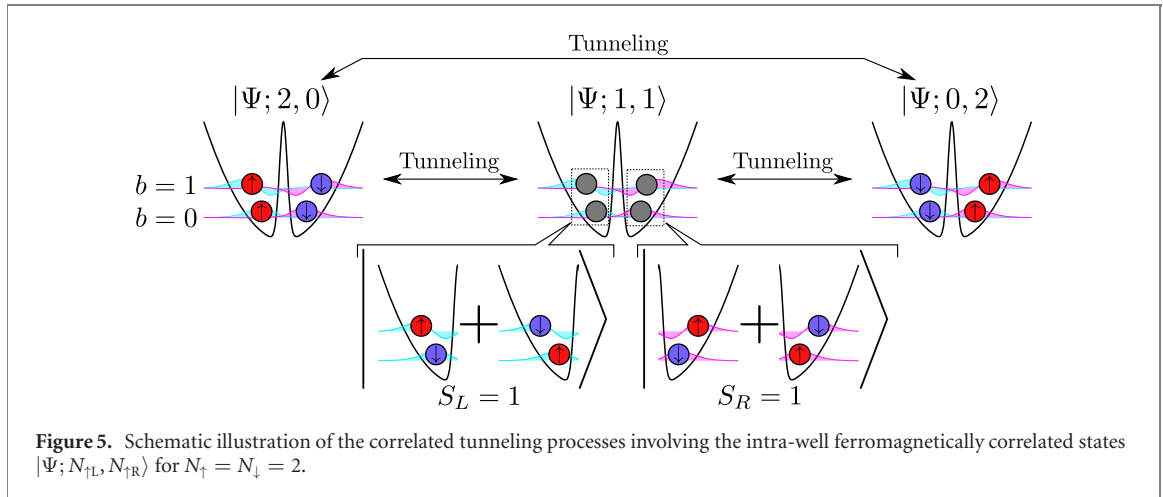


$g \rightarrow \infty$ [29–34]. Note also that this notion of antiferromagnetism does not conflict with our notion of ferromagnetism as the first is an effective magnetic phenomenon induced by the tunneling, t^b , while the second is a result of the exchange interaction term in equation (7).

4.3. Comparison with ML-MCTDHX

Before analyzing further the magnetic properties of the system and their connection to the emergent tunneling dynamics let us first establish that the magnetic properties exhibited in the framework of the tJU model carry forward to the fully correlated case. To this end we shall compare the eigenspectra obtained within the tJU model with the ML-MCTDHX method.

The relevant eigenenergies within the tJU model (equation (8)) appear in figure 4(a) as colored lines referring to the case $N = 4$. Here the three eigenstates $|\Phi; S\rangle$, with $S = 0, 1, 2$ possess three distinct eigenenergies at $g \approx 0$. The energy difference between the $S = 0$ and $S = 1$ states is given by t^0 and the one between the $S = 1$ and $S = 2$ corresponds to t^1 . This decrease of the single-particle energy of $|\Phi; S = 1\rangle$ and $|\Phi; S = 0\rangle$ stems from the occurrence of one and two doublons respectively in the $g \approx 0$ case. The formation of these doublons implies the double occupation of the single-particle state $[\phi_L^b(x) + \phi_R^b(x)]/\sqrt{2}$, with $b = 0, 1$. For increasing g the energy of the $S = 1$ and $S = 0$ eigenstates is larger due to the involvement of these doublons which contribute a substantial amount of interaction energy. Most importantly, for $0.5 < g < 2.5$ (interaction regime B) the energies of the eigenstates $|\Phi; S\rangle$ converge towards the eigenenergy of $|\Phi; S = 2\rangle$, possessing $E_{S=2}(g) = E_B \approx 13.424$, and this leads to the formation of the quasi-degenerate manifold, identified also in figure 2(a). It can also be checked that the energy differences between the states $|\Phi; S\rangle$ are consistent with equation (10) possessing a characteristic energy scale of $\Omega_d^1 \approx 0.033/g$. Figure 4(a) further reveals that the eigenstates of the tJU model follow closely the behaviour of the eigenstates of the MB system, represented as dots in figure 4(a), within both the interaction regimes A and B. There are a few discrepancies associated with the avoided crossings emerging in the interaction regimes A and C which, as also mentioned in section 3, stem from the couplings between states with different \vec{n}_B . Such couplings are indeed neglected within the tJU model. Nevertheless, the agreement within the interaction regime B is almost perfect and it can be further shown that the key ingredients of the magnetic order within the tJU model are also exhibited within the fully correlated case. Indeed, the overlaps between the MB eigenstates $|\alpha\rangle, |\beta\rangle, |\gamma\rangle$ and the initial state, $|\Psi(0)\rangle$ agree well with those found within the effective tJU description (see figure 4(a)), namely, $|\langle\alpha|\Psi(0)\rangle|^2 \approx |\langle\Phi; S = 0|\Psi(0)\rangle|^2 = \frac{1}{3}$, $|\langle\beta|\Psi(0)\rangle|^2 \approx |\langle\Phi; S = 1|\Psi(0)\rangle|^2 = \frac{1}{2}$ and $|\langle\gamma|\Psi(0)\rangle|^2 \approx |\langle\Phi; S = 2|\Psi(0)\rangle|^2 = \frac{1}{6}$. Furthermore, in figure 4(b) we



demonstrate the large overlap of the MB eigenstates $|\alpha\rangle$, $|\beta\rangle$ and $|\gamma\rangle$ with the eigenstates, $|\Phi(t^b = 0); S\rangle$, of the tJU model for $t^b \ll gU^b$ within the interaction regime B . Indeed, this overlap is in excess of 95% (see also the inset of figure 4(b)), a result which is also consistent with the values obtained within the tJU model for the overlaps $|\langle \Phi; S | \Phi(t^b = 0); S \rangle|^2$ (not shown for brevity). The above mentioned findings explicitly showcase that the magnetic order exhibited in the interaction regime B within the tJU model carries forward to the MB case. However, for stronger interactions and as the interaction regime C is approached, e.g. see figure 4(b) at $g \approx 2.5$, the overlap of the MB eigenstates and the $|\Phi(t^b = 0); S\rangle$ states decreases. This feature is beyond the tJU model description and occurs due to the interband coupling caused by the presence of the cradle mode.

4.4. Relation of the magnetic properties to the tunneling dynamics

Having identified the magnetic order of the interaction regime B within the full MB approach by comparing to an effective model, we subsequently showcase the relation of these magnetic properties to the tunneling dynamics of the system, see also figures 3(b₁) and (b₂). To unravel this interplay we define the states with $S_L = S_R = \frac{N}{2}$ and a definite spin projection $S_{z;s} = \sum_b S_{z;s}^b$ within each of the wells, namely

$$|\Psi; N_{\uparrow L}, N_{\uparrow R}\rangle = (\hat{S}_{-;L} \hat{S}_{+;R})^{\frac{N}{2} - N_{\uparrow L}} |\Psi(0)\rangle. \quad (11)$$

Here $\hat{S}_{\pm;s} = \sum_b \hat{S}_{x;s}^b \pm i \hat{S}_{y;s}^b$ refer to the spin increasing and lowering operators within the $s \in \{L, R\}$ well. Note that it can be verified that the states $|\Psi; N_{\uparrow L}, N_{\uparrow R}\rangle$ are related to the states $|\Phi(t^b = 0); S\rangle$ by a unitary transformation. But in contrast to $|\Phi(t^b = 0); S\rangle$ the states $|\Psi; N_{\uparrow L}, N_{\uparrow R}\rangle$ have a definite number of spin- \uparrow and spin- \downarrow particles within each well. The expansion of $|\Psi; N_{\uparrow L}, N_{\uparrow R}\rangle$ in the basis $|\Phi(t^b = 0); S\rangle$ can be easily obtained by employing the Clebsch–Gordan coefficients [66].

The introduction of this new basis relates the phenomenon of quasidegeneracy of the states $|\Phi(t^b = 0); S\rangle$ exhibited both within the tJU model ($|\Phi; S\rangle \approx |\Phi(t^b = 0); S\rangle$) and the full MB case ($|\alpha\rangle \approx |\Phi(t^b = 0); S = 0\rangle$, $|\beta\rangle \approx |\Phi(t^b = 0); S = 1\rangle$ and $|\gamma\rangle \approx |\Phi(t^b = 0); S = 2\rangle$), see figure 4(b), with the emergent tunneling processes. Owing to the unitary transformation between the states $|\Psi; N_{\uparrow L}, N_{\uparrow R}\rangle$ and the approximate eigenstates $|\Phi(t^b = 0); S\rangle$, the accumulation of relative phases between the eigenstates during the dynamics (due to their different eigenenergies, see figure 4(a) and equation (10)), corresponds to a population transfer between the $|\Psi; N_{\uparrow L}, N_{\uparrow R}\rangle$ states and hence to an apparent tunneling dynamics within the spin components. For the particular case of $N = 4$ particles this mechanism is illustrated in figure 5. Notice that due to the strongly-correlated nature of the involved states (see also figure 5) such a mechanism is absent within the Hartree–Fock mean-field theory since $|\Psi; N_{\uparrow L} = 1, N_{\downarrow R} = 1\rangle$ cannot be written as a single Slater determinant.

To explicitly demonstrate the occurrence of this tunneling mechanism we present in figure 4(c) the overlap of the time-dependent wavefunction, $|\Psi(t)\rangle$, with the states $|\Psi; N_{\uparrow L}, N_{\uparrow R}\rangle$ for $g = 1$ (interaction regime B). For $0 < t < 500$ we observe a population transfer process from the initial state $|\Psi(0)\rangle = |\Psi; 2, 0\rangle$ to the states $|\Psi; 1, 1\rangle$ and $|\Psi; 0, 2\rangle$. Recall that these two processes have, also, been identified in the time evolution of $\rho_{\sigma}^{(1)}(x; t)$ (see figures 3(b₁) and section 3). Most importantly, the intricate relation of the tunneling dynamics to the magnetic properties of the system is now evident via employing the unitary transformation connecting the states $|\Psi; N_{\uparrow L}, N_{\uparrow R}\rangle$ to the eigenstates $|\Phi(t^b = 0); S\rangle$. For later times $t \approx 2600$ an almost perfect revival of the state $|\Psi; 2, 0\rangle$ is exhibited owing to the commensurability of the frequencies of these particle transfer processes. Indeed, the two-body tunneling process $|\Psi; 2, 0\rangle \leftrightarrow |\Psi; 0, 2\rangle$ is found to

possess a roughly three times smaller frequency than the single-particle tunneling mode $|\Psi; 2, 0\rangle \leftrightarrow |\Psi; 1, 1\rangle$ (see figure 4(c)).

4.5. Spin–spin correlations

Having described in detail the interconnection of the magnetic properties of the system and its tunneling dynamics we are able to shed light onto the relation of ferromagnetism and phase separation. The ferromagnetic order of a Fermi gas is characterized by the spin polarization and the spin–spin correlations of the system. The total spin polarization and the total spin of the system, the latter being related to the spin–spin correlator [36], are constant during the dynamics due to the symmetries of the Hamiltonian (equation (1)). As a consequence no global ferromagnetic order can appear during the dynamics due to the conservation laws stemming from the above symmetries. However, as the tJU model reveals the intra-well magnetic properties are important for the adequate description of the system. In this spirit, the quantity M besides being a measure of the phase separation also quantifies the spin polarization within each well (equation (4)). An adequate quantity that captures the intra-well magnetic correlations is also hinted by the effective tJU model. This refers to the total spin within each of the wells, $\langle \Psi(t) | \hat{S}_s^2 | \Psi(t) \rangle$, with $s \in \{L, R\}$. In particular, we can employ a more refined quantity by involving some of the magnetic properties of the system identified within the tJU model. As we have previously discussed, the subset of states $|\Phi(t^b = 0); S\rangle$ are characterized by ferromagnetic spin–spin correlations within each well since $S_L = S_R = 1$. Specifically, $|\Phi(t^b = 0); S\rangle$ are the only states within the configuration $\vec{n}_B = (2, 2, 0, \dots)$ that exhibit this property (see also section 4.2). It is thus instructive to evaluate the overlap of the MB wavefunction, $|\Psi(t)\rangle$ with the states $|\Phi(t^b = 0); S\rangle$, i.e. $C_{\text{FF}} = \sum_{S=0}^2 |\langle \Phi(t^b = 0); S | \Psi(t) \rangle|^2$. C_{FF} is an adequate quantity for studying the spin–spin correlation properties of the system, as it constitutes a lower bound for the values of the intra-well spin–spin correlator $\langle \Psi(t) | \hat{S}_L^2 | \Psi(t) \rangle \geq 2C_{\text{FF}}$ and $\langle \Psi(t) | \hat{S}_R^2 | \Psi(t) \rangle \geq 2C_{\text{FF}}$. Accordingly, large values of C_{FF} indicate that both wells are *simultaneously* characterized by intra-well ferromagnetic spin–spin correlations.

The time evolution of C_{FF} is presented in figure 4(d) for varying interaction strength g . For weak interactions, within the interaction regime A, C_{FF} exhibits rapid fluctuations between zero and unity manifesting the periodic decay and revival of the intra-well ferromagnetic spin–spin correlations of the initial state, $|\Psi(0)\rangle$. Recall that the phase separation, and hence the intra-well spin polarization, is unstable in this interaction regime exhibiting decay and revival oscillations, see also figures 2(b), 3(a₁) and (a₂). However, in the interaction regime B, we observe that the spin–spin correlations within each well are ferromagnetic since $C_{\text{FF}} = 1$. Indeed, the value of C_{FF} is almost constant and possesses a large value being of the order of $C_{\text{FF}} \approx 0.98$, see figure 4(d). The weak fluctuations of C_{FF} around this average value, further, showcase the stability of the intra-well ferromagnetic order. Note also that the intra-well spin polarization quantified by M is characterized as metastable within the interaction regime B. Entering the interaction regime C ($2.5 < g < 4.5$) we observe that C_{FF} exhibits multi-frequency oscillations. These oscillations can be explained in terms of the observed resonance of the cradle mode which introduces an interband coupling⁶, see also figures 2(a) and 3(d). For even stronger interactions, i.e. within the interaction regime B', the intra-well ferromagnetic order is reestablished and it is characterized by large and almost constant values of C_{FF} during the dynamics.

The above results manifest the close relation between the intra-well ferromagnetic order identified in a DW trap and the ferromagnetic order emerging in a harmonic trap with weakly broken SU(2) symmetry, as it has been demonstrated in reference [36]. This order appears for intermediate interactions where the ferromagnetic Hund exchange interaction, stemming from spin-exchange interaction processes, see e.g. equation (7), dominates and leads to largely stable ferromagnetic spin–spin correlations but a fluctuating polarization. The different imposed potential alters the manifestation of this ferromagnetic order during the dynamics. In the case of the DW the ferromagnetic order is exhibited locally within each of the wells and as discussed above implies a metastable phase separated state for the system. In contrast, in the case of a harmonic trap the emergent ferromagnetic order affects the global values of the spin polarization and total spin implying miscibility of the contributing spin components [36]. This difference stems from the Hund exchange interaction between two fermions which is only sizable if the involved single particle states (i.e. the orbitals) possess a significant density overlap, see also equation (7). To understand this analogy further in the following section we study the dynamics of the DW by employing an additional potential that breaks the SU(2) symmetry of the system.

⁶ Recall that the cradle mode involves states of the $\vec{n}_B = (3, 1, 0, \dots)$ energetic class. Due to the presence of three particles in the first band this number-state class cannot support states with $S_L = S_R = 1$ and its influence is detrimental to the ferromagnetic order.

5. SU(2) violating case

Up to this point, we have identified the metastability of the phase separated state in a DW due to the presence of the SU(2) invariance of the system. Also we have characterized the emerging metastability of the phase separated state appearing for intermediate interactions and connected it to the magnetic properties of the system. Next we aim to show that the phase separated state is stable within region B even in the case that the SU(2) symmetry is weakly broken. Also, in analogy to reference [36] the intra-well ferromagnetic correlations are shown to persist within this region. Moreover, the implications regarding the magnetic order exhibited in a DW are briefly discussed.

To study the case of a system with broken SU(2) symmetry we employ a linear gradient of the magnetic field which shifts the energies of the spin- \uparrow and spin- \downarrow fermions in a spatially-dependent manner. The corresponding term which is incorporated in the MB Hamiltonian of equation (1), reads

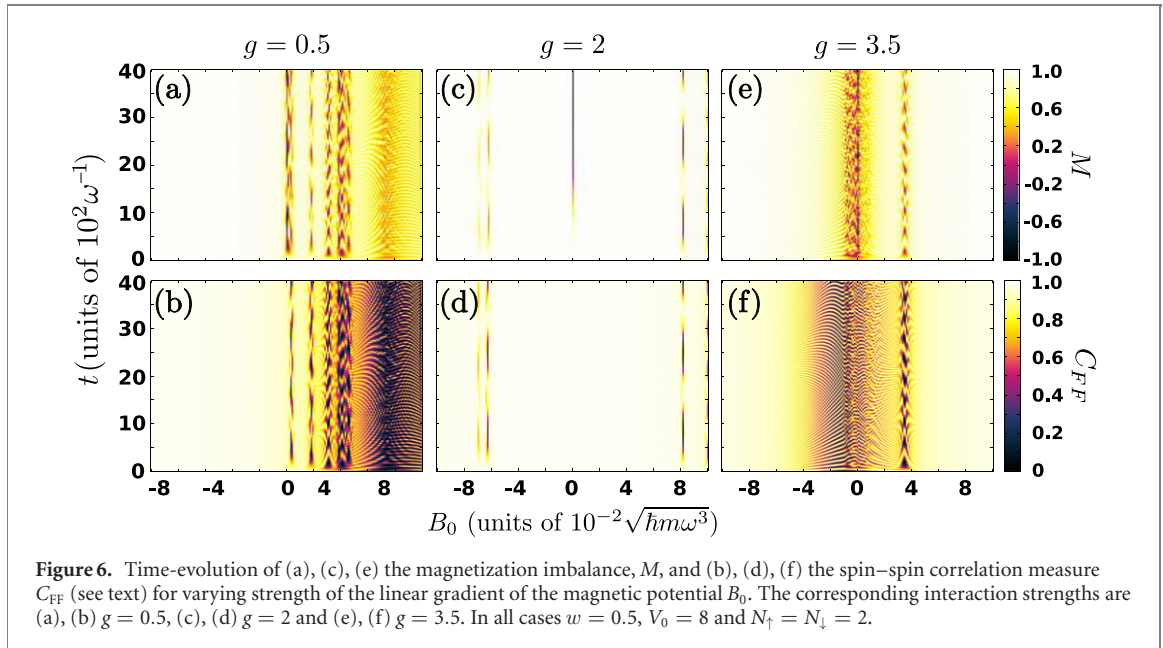
$$\hat{H}_g = B_0 \int dx x \hat{\psi}_\alpha^\dagger(x) \sigma_{\alpha\alpha'}^z \hat{\psi}_{\alpha'}(x). \quad (12)$$

The value of B_0 determines the energy offset between the two wells for the different spin components. A positive value of B_0 means that it is energetically preferable for the spin- \uparrow atoms to occupy the right-well and the spin- \downarrow atoms the left-well. Accordingly, when $B_0 < 0$ it is favorable for the spin- \uparrow and spin- \downarrow atoms to occupy the left and the right-well respectively.

Figure 6 illustrates the time-evolution of the magnetization imbalance M and C_{FF} which quantifies the degree of intra-well ferromagnetic correlations, for varying B_0 at three different values of g corresponding to the interaction regimes A , B and C . We observe that in the weakly-interacting case (belonging to the interaction regime A in figures 6(a) and (b)) and for $B_0 < 0$ both M and C_{FF} are stable throughout the time-evolution indicating that the system remains close to its initial state. For $B_0 > 0$ a multitude of resonances appear at different intervals of B_0 involving prominent tunneling as captured by M (figure 6(a)). Also, C_{FF} reveals that the state of the system is driven away from the $S_L = S_R = 1$ manifold (figure 6(b)) since $C_{\text{FF}} < 1$. These resonances correspond to possible tunneling pathways where the spin- \uparrow particles occupying initially the left-well of the DW resonantly tunnel to the right-well (or to the opposite direction for the spin- \downarrow atoms) leading to the decay of the intra-well ferromagnetic order.

For $g = 2$ (interaction regime B) it can be deduced that besides the very narrow region around the SU(2) symmetric case, i.e. at $B_0 = 0$, the phase separated initial state is stable for $|B_0| < 0.04$ as $M(t) \approx 1$ throughout the evolution (see figure 6(c)). Notice also that within these values of $|B_0|$ the ferromagnetic intra-well order is stable as indicated by $C_{\text{FF}}(t) \approx 1$ (figure 6(d)). The stable phase separated state appears due to the quasi-degeneracy of the states $|\alpha\rangle$, $|\beta\rangle$, $|\gamma\rangle$ in the SU(2) preserving case for the interaction regime B . As stated in the previous sections these states, owing to their intra-well ferromagnetic correlations, lie in an energy region of the MB spectrum where no other eigenstates appear and are quasi-degenerate characterized by a different value of the total spin S (see also figure 4(a)). Recall that these states possess $C_{\text{FF}} \approx 1$ indicating their intra-well ferromagnetic character. Moreover, their energetic ordering in terms of increasing S manifests the presence of the weak antiferromagnetic Anderson exchange interaction, (see section 4.2 and equation (10)). By breaking the SU(2) symmetry with the additional spin-dependent potential described by equation (12) the states $|\alpha\rangle$, $|\beta\rangle$ and $|\gamma\rangle$ couple with one another resulting in the formation of eigenstates with definite number of spin- \uparrow and spin- \downarrow atoms in each of the wells (results not shown here for brevity). Therefore, for decreasing $B_0 < 0$ the initial state, $|\Psi(0)\rangle$, becomes the lowest-in-energy state with $S_L = S_R = 1$, while it corresponds to the highest-in-energy eigenstate of the same manifold of states for $B_0 > 0$. In both cases the phase separation of this state is stable as imprinted also in the time evolution of $M(t)$ for $|B_0| < 0.04$ (see figure 6(c)). In the vicinity of $B_0 \approx 0$, $M(t)$ is depleted during the time-evolution while $C_{\text{FF}}(t) \approx 1$ throughout the dynamics. The appearance of this region is explained by the fact that the couplings between the states $|\alpha\rangle$, $|\beta\rangle$ and $|\gamma\rangle$ associated with \hat{H}_g are smaller than their energy differences due to the Anderson kinetic exchange interaction (being of the order of $\frac{t^b}{gU^b}$). The latter implies a large but finite life-time of the phase separation of the initial state, in agreement with the SU(2) preserving case $B = 0$. In addition, further resonances appear when $|B_0| > 0.04$ for $g = 2$ (see figure 6(c)). More specifically, the resonances at $B_0 > 0.04$ correspond to tunneling resonances in a similar fashion to the case of the interaction regime A (figure 6(a)). The positive shift of these resonances when compared to the corresponding ones appearing for $g = 0.5$ is attributed to the increased interaction energy of the states accessed by tunneling. For $B_0 < -0.04$ another set of resonances occurs in figure 6(c) that correspond to interband processes similar to the aforementioned cradle mode. These resonances emerge due to the coupling of different bands induced by the interactions.

Within the interaction regime C the stability properties of the phase separation are similar to the corresponding ones of the interaction regime A , compare in particular figures 6(e) and (f) to figures 6(a)



and (b) respectively. For large $B_0 < 0$ the initial state is stable (see figures 6(e) and (f)), however, for $B_0 \approx 0$ the phase separation and intra-well ferromagnetic order as imprinted in $M(t)$ and $C_{FF}(t)$ respectively fluctuate during the dynamics. This fluctuating behaviour can be explained by the inter-band coupling that occurs within this interaction regime suppressing the intra-well ferromagnetic order of the initially phase separated state (see also figures 4(c) and (d)). Turning to large $B_0 > 0$ the phase separation is stable (see in particular figure 6(e)) since $M(t) \approx 1$. However, for $B_0 \approx 0.04$ a resonance associated with the narrow avoided crossings identified in figure 2(a) for $g \approx 3$ is observed.

The above discussed stability properties of the phase separated state, especially within the interaction regime B , provide direct insight into the magnetic properties of the $SU(2)$ violating system. First, the fact that the phase separated state, $|\Psi(0)\rangle$, which is not an eigenstate of \hat{S}^2 , becomes an eigenstate of the system, $\hat{H} = \hat{H}_0 + \hat{H}_\uparrow + \hat{H}_g$, even for a relatively small breaking of the $SU(2)$ symmetry shows that, as also identified previously, for a DW there is no global ferromagnetic order imprinted in S^2 . This is in contrast to the case of the harmonic confinement as it has been demonstrated in reference [36]. Instead, for a DW trap the instability of the S^2 becomes more pronounced for intermediate interactions. This property can be understood by inspecting the effective tJU model (equation (8)). For fermions confined in a DW, ferromagnetic Hund interactions occur *only* between particles that reside in the same well and as a consequence only the intra-well ferromagnetic correlations are robust within each well. An observation that is also supported by the apparent stability of the phase separated state except for the cases within the interaction regimes B and C where inter-band couplings are involved, see figures 6(b)–(d) and (f). Most importantly, for intermediate interactions supporting the intra-well ferromagnetic order (see figure 6(c)) the phase separated state is stabilized even for a very weak breaking of the $SU(2)$ symmetry. This feature of the DW system can be understood by the fact that the extremely weak Anderson kinetic exchange interaction is the only magnetic mechanism that can possibly prohibit the coupling of states with different S for a system with broken $SU(2)$ symmetry. On the contrary, the intra-well ferromagnetic order is stable independently of whether the $SU(2)$ symmetry is preserved or it is weakly broken as the intra-well ferromagnetic correlations are protected by the much stronger Hund exchange interaction. The above imply that within the interaction regime B dominated by ferromagnetic intra-well correlations an instability occurs which is triggered by the breaking of the $SU(2)$ symmetry. This instability leads to the formation of two polarized ferromagnetic domains of the spin components as the system phase separates almost perfectly among the two wells.

6. Conclusions

We have explored the stability of the phase separated state of interacting spin-1/2 fermions confined in DW potentials. Most importantly, we have revealed an interaction regime characterized by a metastable phase separation for moderate interactions. By invoking an effective tight-binding model, we unveil that the metastability of the phase separation is related to the formation of a quasi-degenerate manifold of states

described by ferromagnetic intra-well spin–spin correlations but varying total spin. The formation of this quasi-degenerate manifold of states can be intuitively understood by the inclusion of an effective ferromagnetic Hund interaction, stemming from the spin exchange interaction between two interacting particles residing at the same well. This exchange interaction cannot be neglected due to the large spatial overlap of the particles occupying different bands but the same well of the DW. The breaking of the SU(2) symmetry is found to substantially alter the behaviour of the system in this interaction regime where the ferromagnetic correlations dominate. Indeed, the phase separated state becomes stable even when we break the SU(2) symmetry by employing a very weak linear gradient of the magnetic potential.

The description of the magnetic properties of 1D fermions in terms of the ferromagnetic Hund interaction provides a unifying viewpoint on the relation between phase separation and ferromagnetism. Most importantly, it provides a theoretical framework via which the stability of ferromagnetic correlations in the absence of SU(2) symmetry (see also [36]) can be understood. In particular, the ferromagnetic correlations are found to be stable only within the spatial regions where the Hund interaction is strong, i.e. within each of the wells of a DW and not between them. In this picture the ferromagnetic correlations of the system are not directly related with the phase separation in contrast to the conventional Stoner instability viewpoint. Instead, the effective antiferromagnetism induced by the Anderson kinetic exchange interaction is responsible for the absence of phase separation in SU(2) symmetric systems. Indeed, when this effective antiferromagnetism is weak the system is found to be unstable towards phase separation. More precisely, in the case of a DW potential these two phenomena are indeed related. In the interaction regime where the ferromagnetic Hund interaction dominates the Anderson kinetic exchange interaction leading to stable intra-well ferromagnetic correlations, even a weak breaking of the SU(2) symmetry enforces the system to phase separate.

Our work sets several avenues of further study that can be pursued. First, notice the absence of any obvious limitation of the underlying mechanisms that would make them incapable of describing higher dimensional settings. The examination of higher dimensional settings is therefore a promising next step for understanding the ferromagnetic properties emerging in DW systems. Also, the tunability of the phase separation by weakly breaking the SU(2) symmetry gives rise to the prospect of controlling the formation of ferromagnetic domains in the case of DW or lattice systems. Certainly, the generalization of our results for mass-imbalanced settings might provide an alternative promising way of breaking the SU(2) symmetry compared to spin-dependent potentials [40, 67–71]. Finally, the inclusion of various inherent effects that break the SU(2) symmetry of a Fermi system such as spin–orbit coupling or weak spin-dependent interactions might allow cold atoms to form realistic models that better emulate the ferromagnetic properties encountered in real materials.

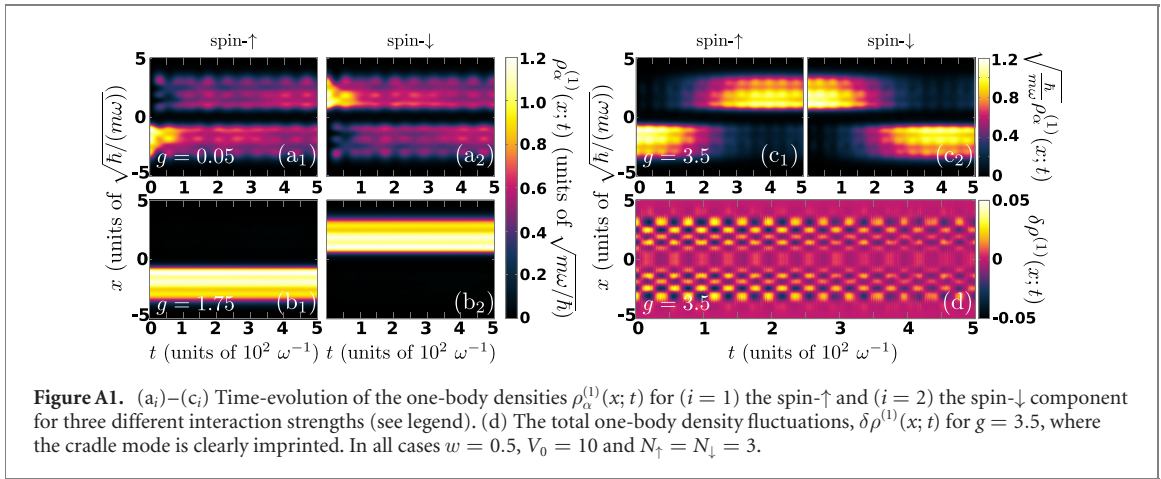
Acknowledgments

This work is funded by the Cluster of Excellence ‘CUI: Advanced Imaging of Matter’ of the Deutsche Forschungsgemeinschaft (DFG)—EXC 2056—project ID 390715994. SIM gratefully acknowledges financial support in the framework of the Lenz-Ising Award of the University of Hamburg.

Appendix A. Six fermion dynamics

The discussion in section 4.2 reveals that within the effective model description an overall similar dynamical behaviour of the system is expected independently of the particle number (see also footnote 4) To verify this expectation within the fully correlated approach we investigate the dynamical behaviour of a system consisting of $N = 6$ fermions and identify the underlying phenomenology associated with the different interaction regimes A, B and C in the corresponding spin- α one-body densities, $\rho_\alpha^{(1)}(x; t)$, illustrated in figure A1.

In particular, for weak interactions ($g = 0.05$) the one-body density of both spin- \uparrow and spin- \downarrow fermions exhibits a tunneling dynamics among the wells, see figures A1(a₁) and (a₂). In this case, each of the particles occupying the three energetically lowest bands performs an individual tunneling oscillation with a frequency close to the one associated with the band it occupies, t^b , see for instance the fast tunneling of the three-humped structure emerging in $\rho_\alpha^{(1)}(x; t)$ in comparison to the overall slower tunneling dynamics. This observed dynamics is in line to the one emerging within the interaction regime A for $N = 4$ particles (compare figure 3(a) with figure A1(a)). For increasing interactions, $g = 1.75$, no tunneling oscillations are observed and the phase separation appears to be almost completely stable within the time scales we have studied, see figures A1(b₁) and (b₂). This behaviour of the one-body density is characteristic for the

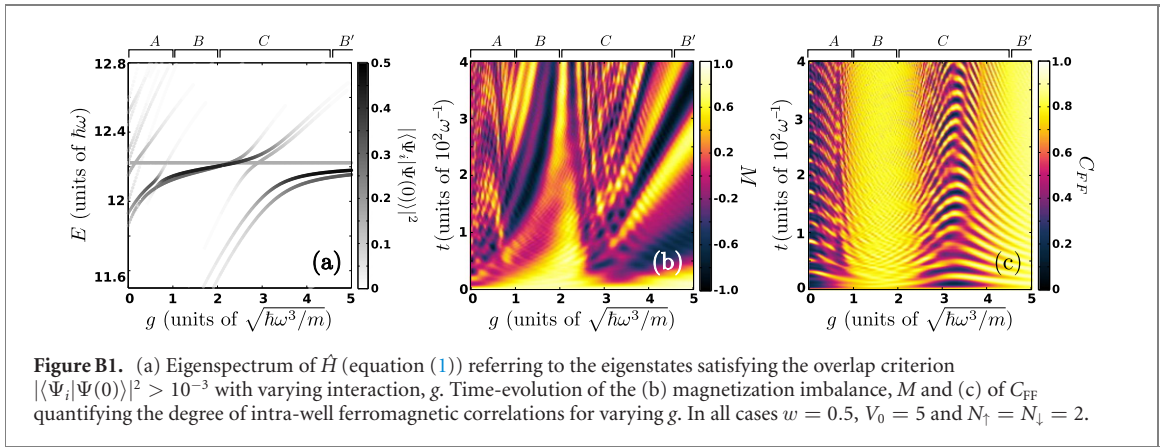


interactions belonging to the regime *B*, where as identified in the $N = 4$ particle case the tunneling dynamics slows down dramatically (see also figure 3(b)) as a consequence of the formation of the quasi-degenerate manifold of eigenstates with ferromagnetic intra-well correlations. Finally, the cradle mode being the characteristic feature of the interaction regime *C* (see also figures 3(c) and (d)) can also be observed for $N = 6$. Inspecting the dynamics of the one-body density for $g = 3.5$ (figure A1(c)), we observe a collective tunneling mode of the density among the wells, as well as, deformations of the one-body density within each of the occupied sites possessing a much larger frequency than the tunneling mode. By employing the temporal fluctuations of the total one-body density, $\delta\rho^{(1)}(x; t)$ (see figure A1 (d)) these deformations can be related to the emergence of the cradle mode, verifying the existence of the interaction regime *C* in the $N = 6$ case.

Appendix B. Shallow double-well case

As we have discussed in the main text (see sections 4.5 and 5) the relation of the phase separation phenomenon and the ferromagnetism depends on the shape of the external potential imposed on the atoms. Indeed, it is found that despite the fact that the same microscopic mechanisms are at play for a parabolically or a DW trapped spin-1/2 Fermi system, the manifestation of the above-mentioned phenomena differs significantly. The purpose of this section is to study the dependence of the stability properties of the phase separated state, $|\Psi(0)\rangle$, equation (3) on the barrier height of the DW potential. To achieve this we study the case of a shallower DW with $V_0 = 5$ and $w = 0.5$ and compare with the case of $V_0 = 8$.

The eigenspectrum for a shallow DW is presented in figure B1(a). The qualitative structures emerging in the eigenspectrum for $V_0 = 5$ are similar to the case of $V_0 = 8$ (compare figure B1(a) with figure 2(a)). However, there are also prominent quantitative differences which, as we shall explain below, lead to a different dynamical behaviour. Within the regime *A*, $0 < g < 1$, the role of eigenstates with high energy (see figure B1(a) for $E > 12.2$ and $g < 1$) is very pronounced as they accumulate a population larger than in their deep DW counterpart, see also figure 2(a). In the dynamics of the shallow DW this translates to a much faster loss of M (see e.g. figure B1(b) for $g < 1$) when compared to the case of the deep DW (figure 2(b)) which is accompanied with the loss of intra-well ferromagnetic correlations imprinted in C_{FF} , see figure B1(c). Of course, this difference is simply caused by the larger tunneling rates, t^b involved in the $V_0 = 5$ case (figure 1(a)). The differences between the two setups become more interesting in the intermediate interaction regime, *B*, for $1 < g < 2.5$. In the shallow DW case three eigenstates dominate similarly to $V_0 = 8$, but their spacing is quantitatively larger in the shallower DW (compare figure B1(a) with figure 2(a) for $g \approx 2$). This is not surprising since the spacing of these eigenstates (see also section 4.2) is proportional to $\frac{t^b}{gU^b}$ which decreases with increasing V_0 . In addition, and in direct contrast to the $V_0 = 8$ case higher-lying eigenstates (see figure B1(a) for $1 < g < 2.5$ and $E > 12.3$) and most importantly lower-lying ones (see figure B1(a) for $1 < g < 2.5$ and $E > 11.8$) are involved in the dynamics within this regime. Accordingly the dynamics of M and C_{FF} shows that in the shallow DW case the initial state cannot be characterized as metastable for any interaction in the regime *B*. Indeed, the magnetization imbalance $M(t)$ (figure B1(b)) is greatly suppressed for $t > 100$ possessing values $M(t) < 0.6$ for all interactions in $1 < g < 2.5$. Regarding the spin–spin correlations it can be seen that $C_{FF}(t)$ is almost stable during the dynamics except for a very fast decay at initial times $t < 4$ (see figure B1(c)). During the time-evolution it



acquires values of the order of $C_{\text{FF}} \approx 0.8$, for all interactions within the regime B showcasing predominantly ferromagnetic intra-well correlations. The above implies that while the mechanisms at play in the shallow DW case are similar to the ones emerging in the case of a deeper DW, the apparent phenomenology is altered due to the pronounced involvement of lower-lying states. These lower-lying states are able to alter the dynamics within the regime B because, as it can be seen by inspecting the eigenspectrum for $g \approx 3$ the cradle resonances are much wider in the case of a shallower DW thus affecting a broader interaction regime than for $V_0 = 8$.

In the case of $V_0 = 5$ the regime C appears in the interaction range $2 < g < 4.5$. The phenomenology taking place within C is completely analogous to the case of $V_0 = 8$. Indeed, the tunneling is prevalent within this regime as imprinted in the fluctuating behaviour of the magnetization imbalance $M(t)$ (see figure B1(b)). In addition, the intra-well spin–spin correlations imprinted in $C_{\text{FF}}(t)$ can be also seen to fluctuate similarly to the case of $V_0 = 8$ (compare figure B1(c) with figure 4(d)). For even stronger interactions the regime B' is accessed where the fluctuations of M slow down dramatically when compared to the regions A and C (see figure B1(b)), while $C_{\text{FF}}(t)$ is almost constant during the dynamics possessing values $C_{\text{FF}}(t) \approx 0.9$. In addition, by inspecting the eigenspectrum (figure B1(a)) it can be deduced that in this regime a quasi-degenerate manifold of the predominantly occupied eigenstates begins to form similarly to the regime B' encountered for $V_0 = 8$.

In conclusion, the nature of the microscopic mechanisms that govern the stability properties of phase separation are not altered as the depth of the DW changes. However, because of their direct competition, in particular between the exchange interaction and the combined effects of the tunneling and the cradle mode, the observed dynamics differs significantly as the barrier height, V_0 decreases. Indeed, the mechanisms competing with the exchange interaction become more prevalent for a shallower DW as it is also clearly imprinted in the corresponding eigenspectrum. This renders the intra-well ferromagnetic order unable to completely dominate the dynamics for every interaction strength, resulting in the absence of stable ferromagnetic intra-well correlations and its direct imprint on the dynamics i.e. the metastability of the phase separation.

Appendix C. Anderson kinetic exchange interaction

The purpose of this section is to provide the explicit derivation of the effective antiferromagnetic interaction acting upon the different wells of our DW setup. This antiferromagnetic interaction is similar to the Anderson kinetic exchange interaction which couples the different sites of a lattice within the Hubbard model [45]. Although such an effective magnetic term can be derived within the resolvent formalism by invoking less assumptions, here we opt to employ the standard Reyleigh–Schrödinger second order perturbation theory due to its mathematical (and physical) clarity.

The terms appearing in the Hamiltonian of the tJU model (equation (8)) can be separated into two Hamiltonian terms⁷ that solely act within each of the wells, \hat{H}_s , with $s \in \{\uparrow, \downarrow\}$, and a Hamiltonian part corresponding to the coupling between them, \hat{H}_{LR} . By performing this separation the effective Hamiltonian

⁷ In order to make the notation less cumbersome we drop the index eff, however all of the Hamiltonian terms mentioned in this section are to be considered within the effective tJU model.

reads $\hat{H}_{\text{eff}} = \hat{H}_R + \hat{H}_L + \hat{H}_{LR}$. The intra-well Hamiltonian terms,

$$\hat{H}_s = +g \sum_{b=0}^{\infty} U^b \hat{n}_{s\uparrow}^b \hat{n}_{s\downarrow}^b - g \sum_{b \neq b' \in \{0, \infty\}} J^{bb'} \left[\hat{\mathbf{S}}_s^b \cdot \hat{\mathbf{S}}_s^{b'} - \frac{1}{4} \hat{n}_s^b \hat{n}_s^{b'} \right] + \sum_{b=0}^{\infty} \epsilon^b \hat{n}_s^b, \quad (C1)$$

correspond to ferromagnetic Heisenberg models with additional occupation dependent terms $\propto \hat{n}_s^b$. The intra-well coupling

$$\hat{H}_{LR} = - \sum_{b=0}^{\infty} \sum_{\alpha \in \{\uparrow\downarrow\}} t^b \left(\hat{a}_{R\alpha}^{b\dagger} \hat{a}_{L\alpha}^b + \hat{a}_{L\alpha}^{b\dagger} \hat{a}_{R\alpha}^b \right) \quad (C2)$$

describes the tunneling among the wells. Our intention is to perturbatively treat \hat{H}_{LR} and show that it acts as an effective antiferromagnetic interaction between the particles occupying the same band but different wells.

According to the discussion in sections 2.2 and 4.2 we are particularly interested in the configuration with no doublons and a single occupation of each Wannier state up to the $b = \frac{N}{2} - 1$ band. The projection of \hat{H}_s to this particular configuration results in the Heisenberg model

$$\hat{P}_B \hat{H}_s \hat{P}_B = \frac{E_B}{2} - g \sum_{b \neq b' \in \{0, \frac{N}{2}-1\}} J^{bb'} \left[\hat{\mathbf{S}}_s^b \cdot \hat{\mathbf{S}}_s^{b'} - \frac{1}{4} \right], \quad (C3)$$

which possesses the degenerate ground states

$$\left| \frac{N_s}{2}, N_{\uparrow s} - \frac{N_s}{2} \right\rangle_s \equiv \sqrt{\frac{(N_s - N_{\uparrow s})!}{N_s! N_{\uparrow s}!}} \left(\sum_{b=0}^{\infty} \hat{S}_{+;s}^b \right)^{N_{\uparrow s}} \left(\prod_{b=0}^{N_s-1} \hat{a}_{+;s}^b \right)^\dagger |0\rangle, \quad (C4)$$

where $\hat{S}_{+;s}^b \equiv \hat{a}_{s\uparrow}^{b\dagger} \hat{a}_{s\downarrow}^b$, $N_L = N_R = \frac{N}{2}$ and we have parametrized these states by the number of spin- \uparrow atoms contained in each well. Then the ground state manifold of the system $\hat{P}_B (\hat{H}_L + \hat{H}_R) \hat{P}_B$ possesses an energy $E^{(0)} = E_B = 2 \sum_{b=0}^{\frac{N}{2}-1} \epsilon^b$ and it is spanned by the states $|\Psi; N_{\uparrow L}, N_{\uparrow R}\rangle = |\frac{N}{4}, N_{\uparrow L} - \frac{N}{4}\rangle_L \otimes |\frac{N}{4}, N_{\uparrow R} - \frac{N}{4}\rangle_R$, with $N_{\uparrow L} + N_{\uparrow R} = \frac{N}{2}$ (see also equation (11)).

Note here that the action of \hat{H}_{LR} on the basis of the ground state manifold $|\Psi; N_{\uparrow L}, N_{\uparrow R}\rangle$ is rather simple due to its product state character. Indeed $\hat{H}_{LR} |\Psi; N_{\uparrow L}, N_{\uparrow R}\rangle$ can be expressed via the action of the creation and annihilation operators on the single-well ferromagnetic states $|\frac{N_s}{2}, N_{\uparrow s} - \frac{N_s}{2}\rangle_s$. Indeed the annihilation operator creates a vacancy to the single-well ferromagnetic states

$$\hat{a}_{s\alpha}^{b_0} \left| \frac{N_s}{2}, N_{\uparrow s} - \frac{N_s}{2} \right\rangle_s = (-1)^{N_s + b_0} \left[\delta_{\alpha\downarrow} \sqrt{\frac{N_s - N_{\uparrow s}}{N_s}} \left| \frac{N_s - 1}{2}, N_{\uparrow s} - \frac{N_s - 1}{2} \right\rangle_s^{b_0} + \delta_{\alpha\uparrow} \sqrt{\frac{N_{\uparrow s}}{N_s}} \left| \frac{N_s - 1}{2}, N_{\uparrow s} - 1 - \frac{N_s - 1}{2} \right\rangle_s^{b_0} \right]. \quad (C5)$$

Nevertheless the resulting states are ferromagnetic since they possess maximal S_s and read

$$\left| \frac{N_s - 1}{2}, N_{\uparrow s} - \frac{N_s - 1}{2} \right\rangle_s^{b_0} \equiv \sqrt{\frac{(N_s - N_{\uparrow s} - 1)!}{(N_s - 1)! N_{\uparrow s}!}} \left(\sum_{b=0}^{\infty} \hat{S}_{+;s}^b \right)^{N_{\uparrow s}} \left(\prod_{b=0}^{b_0-1} \hat{a}_{s\downarrow}^b \prod_{b=b_0+1}^{N_s-1} \hat{a}_{s\downarrow}^b \right)^\dagger |0\rangle. \quad (C6)$$

Furthermore, the creation operator, $\hat{a}_{s\alpha}^{b_0\dagger}$, maps the ferromagnetic states to the corresponding $|\frac{N_s-1}{2}, N_{\uparrow s} - \frac{N_s-1}{2}\rangle_s^{b_0}$ state with an additional doublon at the b_0 th band. More specifically,

$$\hat{a}_{s\alpha}^{b_0\dagger} \left| \frac{N_s}{2}, N_{\uparrow s} - \frac{N_s}{2} \right\rangle_s = (-1)^{N_s + b_0} \hat{a}_{s\uparrow}^{b_0\dagger} \hat{a}_{s\downarrow}^{b_0} \left[\delta_{\alpha\uparrow} \sqrt{\frac{N_s - N_{\uparrow s}}{N_s}} \left| \frac{N_s - 1}{2}, N_{\uparrow s} - \frac{N_s - 1}{2} \right\rangle_s^{b_0} - \delta_{\alpha\downarrow} \sqrt{\frac{N_{\uparrow s}}{N_s}} \left| \frac{N_s - 1}{2}, N_{\uparrow s} - 1 - \frac{N_s - 1}{2} \right\rangle_s^{b_0} \right]. \quad (C7)$$

Importantly, the intra-well ferromagnetic states with vacancy, $|\frac{N_s-1}{2}, N_{\uparrow s} - \frac{N_s-1}{2}\rangle_s^{b_0}$, are eigenstates of the Hamiltonian of the corresponding well, \hat{H}_s as they satisfy the following eigenvalue equation

$$\hat{H}_s \left| \frac{N_s - 1}{2}, N_{\uparrow s} - \frac{N_s - 1}{2} \right\rangle_s^{b_0} = \left(\frac{E_B}{2} - \epsilon^b \right) \left| \frac{N_s - 1}{2}, N_{\uparrow s} - \frac{N_s - 1}{2} \right\rangle_s^{b_0}. \quad (C8)$$

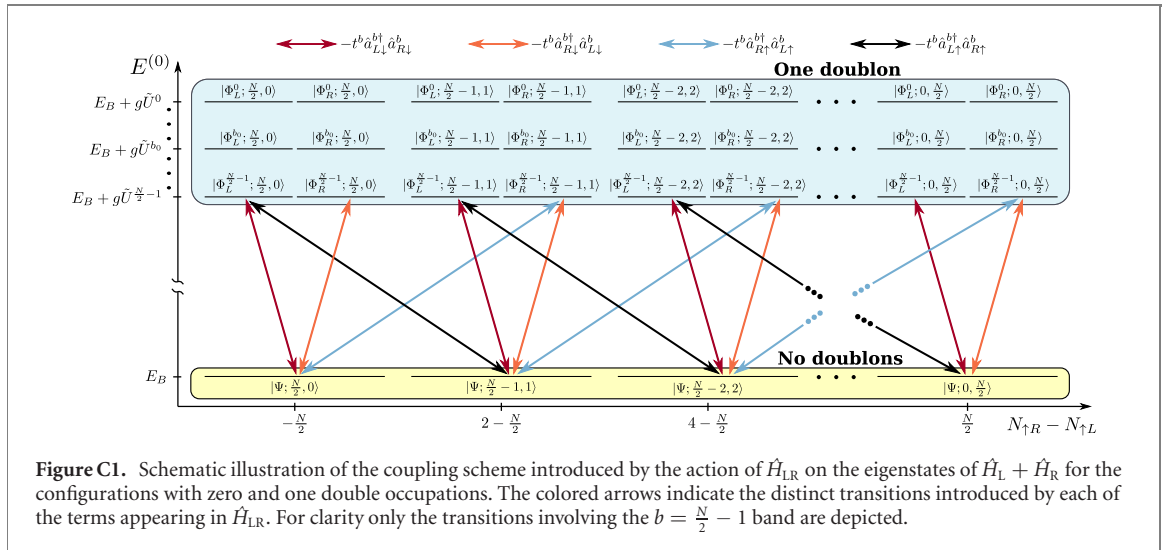


Figure C1. Schematic illustration of the coupling scheme introduced by the action of \hat{H}_{LR} on the eigenstates of $\hat{H}_L + \hat{H}_R$ for the configurations with zero and one double occupations. The colored arrows indicate the distinct transitions introduced by each of the terms appearing in \hat{H}_{LR} . For clarity only the transitions involving the $b = \frac{N}{2} - 1$ band are depicted.

By employing the commutation relations of the creation operator of a doublon $\hat{a}_{s\uparrow}^{b\dagger} \hat{a}_{s\downarrow}^{b\dagger}$, namely $[\hat{n}_s^b, \hat{a}_{s\uparrow}^{b\dagger} \hat{a}_{s\downarrow}^{b\dagger}] = 2\delta_{bb'} \delta_{ss'} \hat{a}_{s\uparrow}^{b'\dagger} \hat{a}_{s\downarrow}^{b'\dagger}$, $[\hat{n}_{s\uparrow}^b \hat{n}_{s\downarrow}^b, \hat{a}_{s\uparrow}^{b\dagger} \hat{a}_{s\downarrow}^{b\dagger}] = \delta_{bb'} \delta_{ss'} \hat{a}_{s\uparrow}^{b'\dagger} \hat{a}_{s\downarrow}^{b'\dagger}$ and $[\hat{S}_s^b, \hat{a}_{s\uparrow}^{b'\dagger} \hat{a}_{s\downarrow}^{b'\dagger}] = \mathbf{0}$, it can be shown that the states containing an additional doublon satisfy the following eigenvalue equation

$$\hat{H}_s \hat{a}_{s\uparrow}^{b_0\dagger} \hat{a}_{s\downarrow}^{b_0\dagger} \left| \frac{N_s - 1}{2}, N_{\uparrow s} - \frac{N_s - 1}{2} \right\rangle_s^{b_0} = \left(\frac{E_B}{2} + \epsilon^{b_0} + g\tilde{U}^{b_0} \right) \hat{a}_{s\uparrow}^{b_0\dagger} \hat{a}_{s\downarrow}^{b_0\dagger} \left| \frac{N_s - 1}{2}, N_{\uparrow s} - \frac{N_s - 1}{2} \right\rangle_s^{b_0}, \quad (C9)$$

where $\tilde{U}^{b_0} = \sum_{b=0}^{\frac{N}{2}-1} J^{b_0 b}$ (recall that $U^{b_0} = J^{b_0 b_0}$), and as a consequence also constitute eigenstates of \hat{H}_s .

By using equations (C5) and (C7) we can show that each term appearing in \hat{H}_{RL} couples each state $|\Psi; N_{\uparrow L}, N_{\uparrow R}\rangle$ to a single state containing one doublon. This coupling scheme is schematically depicted in figure C1. Here the state $|\Phi_s^{b_0}; N_{\uparrow L}, N_{\uparrow R}\rangle$ refers to the \vec{n}_B state possessing a double occupancy at the b_0 th band of the s -well and $N_{\uparrow L}$ and $N_{\uparrow R}$ spin- \uparrow atoms in the left and right well respectively. For $s = R$ this state possessing a doublon reads $|\Phi_R^{b_0}; N_{\uparrow L}, N_{\uparrow R}\rangle = |\frac{N/2-1}{2}, N_{\uparrow L} - \frac{N/2-1}{2}\rangle_L^{b_0} \otimes \hat{a}_{R\downarrow}^{b_0\dagger} \hat{a}_{R\uparrow}^{b_0\dagger} |\frac{N/2-1}{2}, N_{\uparrow R} - 1 - \frac{N/2-1}{2}\rangle_R^{b_0}$ and for $s = L$, $|\Phi_L^{b_0}; N_{\uparrow L}, N_{\uparrow R}\rangle = \hat{a}_{L\uparrow}^{b_0\dagger} \hat{a}_{L\downarrow}^{b_0\dagger} |\frac{N/2-1}{2}, N_{\uparrow L} - 1 - \frac{N/2-1}{2}\rangle_L^{b_0} \otimes |\frac{N/2-1}{2}, N_{\uparrow R} - \frac{N/2-1}{2}\rangle_R^{b_0}$. Moreover, it can be shown that $|\Phi_s^{b_0}; N_{\uparrow L}, N_{\uparrow R}\rangle$ are eigenstates of $\hat{H}_L + \hat{H}_R$ and are degenerate. Indeed, the following eigenvalue equation holds

$$(\hat{H}_L + \hat{H}_R) |\Phi_s^{b_0}; N_{\uparrow L}, N_{\uparrow R}\rangle = (E_B + g\tilde{U}^{b_0}) |\Phi_s^{b_0}; N_{\uparrow L}, N_{\uparrow R}\rangle. \quad (C10)$$

Therefore, by employing the basis states $|\Psi; N_{\uparrow L}, N_{\uparrow R}\rangle$ and $|\Phi_s^{b_0}; N_{\uparrow L}, N_{\uparrow R}\rangle$ the couplings between states possessing no and one double occupation induced by \hat{H}_{RL} are intuitive. Indeed, the tunneling terms $\hat{a}_{R\sigma}^{b_0\dagger} \hat{a}_{L\sigma}^{b_0}$ ($\hat{a}_{L\sigma}^{b_0\dagger} \hat{a}_{R\sigma}^{b_0}$) create a double occupancy on the right (left) well of the b_0 th band and shift $N_{\uparrow L} - N_{\uparrow R}$ by two in the case that $\sigma = \uparrow$. For instance, the tunneling term $\hat{a}_{R\uparrow}^{b_0\dagger} \hat{a}_{L\uparrow}^{b_0}$ (blue arrows in figure C1) transfers the spin- \uparrow particle of the state $|\Psi; N_{\uparrow L}, N_{\uparrow R}\rangle$ from the left to the right well of the b_0 th band resulting in the formation of a double occupancy on the right well of this band and modifying the occupation of spin- \uparrow particles to $N_{\uparrow L} - 1$ for the left and $N_{\uparrow R} + 1$ for the right well.

The approach followed to obtain the dominant perturbative correction to the eigenstates of $\hat{H}_L + \hat{H}_R$, $|\Psi; N_{\uparrow L}, N_{\uparrow R}\rangle$, in the presence of the coupling term \hat{H}_{RL} is explicated below. First, we define the Hilbert space spanned by the degenerate eigenstates $|\Psi; N_{\uparrow L}, N_{\uparrow R}\rangle$ as \mathcal{H}_0 . Obviously since the states within \mathcal{H}_0 are not directly coupled by \hat{H}_{LR} the first order perturbative correction to their energy vanishes. In order to obtain the first non-trivial correction to the energy of those degenerate states we have to treat the coupling term \hat{H}_{LR} within second order perturbation theory. Let us define the perturbative eigenstates up to second order in perturbation theory as $|S_i\rangle \approx |S_i^{(0)}\rangle + |S_i^{(1)}\rangle + |S_i^{(2)}\rangle$ with $|S_i^{(0)}\rangle \in \mathcal{H}_0$. Accordingly, the corresponding perturbative eigenenergies read, $E_i \approx E^{(0)} + E_i^{(2)}$, with $E^{(0)} = E_B$. Then, the second order correction to the eigenenergy of $|S_i\rangle$, $E_i^{(2)}$ is given by

$$\langle S_i^{(0)} | \sum_{k \notin \mathcal{H}_0} \frac{\hat{H}_{LR} |\Psi_k\rangle \langle \Psi_k | \hat{H}_{LR}}{E^{(0)} - E_k^{(0)}} | S_j^{(0)} \rangle = \delta_{ij} E_i^{(2)}, \quad (C11)$$

where $|\Psi_k\rangle$ and $E_k^{(0)}$ correspond to the eigenstates and eigenenergies of $\hat{H}_L + \hat{H}_R$ within the complementary space of \mathcal{H}_0 . Equation (C11) implies that in order to obtain $E_i^{(2)}$ the operator in the bracket should be

diagonalized within \mathcal{H}_0 . The eigenvectors resulting from this diagonalization correspond to the zeroth order correction of the eigenstate, $|S_i^{(0)}\rangle$. Having found the zeroth order correction to the eigenstate the first order correction to it can be derived by employing

$$|S_i^{(1)}\rangle = \sum_{k \notin \mathcal{H}_0} \frac{\langle \Psi_k | \hat{H}_{LR} | S_i^{(0)} \rangle}{E^{(0)} - E_k^{(0)}} |\Psi_k\rangle \quad (\text{C12})$$

and finally the second order correction can be similarly obtained by

$$|S_i^{(2)}\rangle = \sum_{m \notin \mathcal{H}_0} \langle \Psi_m | \sum_{k \notin \mathcal{H}_0} \frac{\hat{H}_{LR} |\Psi_k\rangle \langle \Psi_k | \hat{H}_{LR}}{(E^{(0)} - E_m^{(0)})(E^{(0)} - E_k^{(0)})} |S_i^{(0)}\rangle |\Psi_m\rangle. \quad (\text{C13})$$

The fact that the states $|\Phi_s^b; N_{\uparrow L}, N_{\uparrow R}\rangle$ which are coupled to the \mathcal{H}_0 manifold (see figure C1 and equation (C10)) are degenerate greatly simplifies equation (C11). Indeed the latter can be expressed as

$$\langle S_i^{(0)} | \sum_{b=0}^{\infty} \sum_{\alpha, \alpha' \in \{\uparrow, \downarrow\}} \frac{2(t^b)^2}{g\tilde{U}^b} \left(\hat{a}_{L\alpha}^{b\dagger} \hat{a}_{R\alpha}^b \hat{a}_{R\alpha'}^{b\dagger} \hat{a}_{L\alpha'}^b + \hat{a}_{R\alpha}^{b\dagger} \hat{a}_{L\alpha}^b \hat{a}_{L\alpha'}^{b\dagger} \hat{a}_{R\alpha'}^b \right) |S_j^{(0)}\rangle = \delta_{ij} E_i^{(2)} \quad (\text{C14})$$

and by introducing the spin-operators \hat{S}_s^b an effective antiferromagnetic Heisenberg exchange interaction term is obtained

$$\langle S_i^{(0)} | \sum_{b=0}^{\infty} \frac{4(t^b)^2}{g\tilde{U}^b} \left(\hat{S}_L^b \cdot \hat{S}_R^b - \frac{1}{4} \right) |S_j^{(0)}\rangle = \delta_{ij} E_i^{(2)}. \quad (\text{C15})$$

Obviously, this Heisenberg exchange interaction term possesses the S^2 [SU(2)] symmetry and as a consequence the zeroth order correction $|S^{(0)}\rangle$ can be identified with the states of definite S , $|\Phi(t^b = 0); S\rangle \in \mathcal{H}_0$. Then the first order $|S^{(1)}\rangle$ and the second order $|S^{(2)}\rangle$ corrections to the wavefunction correspond to the occupation of states possessing one and two double occupations respectively. In the limit $\frac{t^b}{g\tilde{U}^b} \ll 1$ the occupation of these states becomes highly suppressed and as a consequence these corrections can be neglected. Indeed, as figure 4(b) reveals such corrections even beyond the effective tJU model contribute to a correction less than 2% to the fully correlated many-body eigenstates within the interaction regime B . Within the above mentioned approximation the \hat{H}_{RL} coupling term can then be substituted with the one of the effective Anderson exchange interaction

$$\hat{H}_{RL} \approx \hat{H}_{RL}^{\text{And}} = \sum_{b=0}^{\infty} \frac{4(t^b)^2}{g\tilde{U}^b} \left(\hat{S}_L^b \cdot \hat{S}_R^b - \frac{1}{4} \right), \quad (\text{C16})$$

which corresponds exactly to the form of the effective antiferromagnetic interaction appearing in equation (10) of the main text.

Appendix D. The computational method: ML-MCTDHF

To solve the MB Schrödinger equation $(i\hbar\partial_t - \hat{H}) |\Psi(t)\rangle = 0$ we rely on the multilayer multiconfiguration time-dependent Hartree method for atomic mixtures [28] (ML-MCTDHX). More specifically, a reduction of the ML-MCTDHX method for spin-1/2 fermions is employed which is referred to as the spinor-variant of the multiconfiguration time-dependent Hartree method for Fermions (MCTDHF). MCTDHF has been applied extensively for the treatment of fermions with or without spin-degrees of freedom, in a large class of condensed matter, atomic and molecular physics scenarios (see e.g. [72–77]) and recently also applied in the field of ultracold atoms [28, 36–38, 67, 78, 79]. MCTDHF is a variational method the key idea of which is to employ a time-dependent (TD) and variationally optimized MB basis set, which allows for the optimal truncation of the MB Hilbert space. The ansatz of the MCTDHF method can be summarized as follows. First, the MB wavefunction, $|\Psi(t)\rangle$ is expanded on a TD number-state basis

$$|\Psi(t)\rangle = \sum_{\vec{n}} A_{\vec{n}}(t) |\vec{n}(t)\rangle, \quad (\text{D1})$$

where $A_{\vec{n}}(t)$ are the corresponding TD expansion coefficients. The TD number states $|\vec{n}(t)\rangle$ each possessing different occupation numbers $\vec{n} = (n_1, \dots, n_D)$ read

$$|\vec{n}(t)\rangle = \left[\prod_{i=1}^D \hat{a}^{n_i}(t) \right]^\dagger |0\rangle. \quad (\text{D2})$$

As equation (D2) reveals the time-dependence of this MB basis stems from the utilization of D different TD creation operators, $\hat{a}_j^\dagger(t)$, $j = 1, \dots, D$. These operators create a fermion in the TD and variationally optimized single particle function (SPF)

$$|\phi_j(t)\rangle = \hat{a}_j^\dagger(t)|0\rangle = \int dx \left[\phi_{j\uparrow}(x; t)\hat{\psi}_\uparrow^\dagger(x) + \phi_{j\downarrow}(x; t)\hat{\psi}_\downarrow^\dagger(x) \right] |0\rangle, \quad (\text{D3})$$

where the variational parameters $\phi_{j\alpha}(x; t)$ refer to the spatial distribution of the spin- α part of the j th SPF and $\hat{\psi}_\alpha(x)$ is the spin- α fermionic field operator. The operators $\hat{a}_j(t)$ satisfy the standard fermionic anti-commutation relations $\{\hat{a}_i(t), \hat{a}_j^\dagger(t)\} = \delta_{ij}$ and thus the MCTDHF ansatz takes explicitly into account the particle symmetry of the system. Note here that we have used the term spinor-variant when referring to our implementation of MCTDHF as each SPF, $|\phi_j(t)\rangle$, in our case is a general spinor wavefunction (see equation (D3)). By employing the above mentioned ansatz equations (D1)–(D3) the time-evolution of the N -body wavefunction, $|\Psi(t)\rangle$ under the effect of the Hamiltonian \hat{H} reduces to the determination of the coefficients $A_{\vec{n}}(t)$ and the components of the SPFs, $\phi_{j\uparrow}(x; t)$, $\phi_{j\downarrow}(x; t)$. The latter in turn follow the variationally obtained MCTDHF equations of motion [28]. In the limiting case of $D = N$, the method reduces to the time-dependent Hartree–Fock approach neglecting all two-body and higher-order correlations. In the opposite limiting case of $D = 2M_p$, where M_p is the dimension of the basis for the SPF coefficients, MCTDHF is equivalent to a full configuration interaction approach (commonly referred to as ‘exact diagonalization’ in the literature). The major advantage of the MCTDHF method when compared to methods employing a stationary single-particle basis is that the employed time-dependent basis is able to adapt to the correlation patterns emerging in the system during the dynamics and thus a smaller set of basis states is required for numerical convergence.

For our implementation we discretize the spatial coordinate by employing a harmonic oscillator discrete variable representation (DVR), which results after a unitary transformation of the commonly employed basis of harmonic oscillator eigenfunctions. To study the dynamics, we propagate the wavefunction by utilizing the appropriate Hamiltonian within the MCTDHF equations of motion. To verify the accuracy of the numerical integration, we impose the following overlap criteria $|\langle\Psi|\Psi\rangle - 1| < 10^{-8}$ for the total wavefunction and $|\langle\phi_i|\phi_j\rangle - \delta_{ij}| < 10^{-9}$ for the SPFs. To testify convergence, we increase the number of SPFs and DVR basis states such that the observables of interest (M , C_{FF}) do not change within a given level of accuracy which is in our case 10^{-4} . More specifically, we have used $M_p = 80$, $D = 16$ and $M_p = 80$, $D = 18$ for the $N = 4$ and the $N = 6$ case respectively. Note that a full configuration interaction treatment of the above-mentioned systems in the employed primitive bases would require 2.63×10^7 number states for $N = 4$ and 2.12×10^{10} ones for $N = 6$.

ORCID iDs

S I Mistakidis  <https://orcid.org/0000-0002-5118-5792>

P Schmelcher  <https://orcid.org/0000-0002-2637-0937>

References

- [1] Vollhardt D, Blumer N and Kollar M 2001 *Metallic Ferromagnetism—An Electronic Correlation Phenomenon (Lecture Notes in Physics vol 580)* (Berlin: Springer)
- [2] Brando M, Belitz D, Grosche F M and Kirkpatrick T R 2016 *Rev. Mod. Phys.* **88** 025006
- [3] Giorgini S, Pitaevskii L P and Stringari S 2008 *Rev. Mod. Phys.* **80** 1215
- [4] Silverstein S D 1969 *Phys. Rev. Lett.* **23** 139
- [5] Stoner E 1933 *Phil. Mag.* **15** 1018
- [6] Grochowski P T, Karpiuk T, Brewczyk M and Rzażewski K 2017 *Phys. Rev. Lett.* **119** 215303
- [7] Salasnich L and Penna V 2017 *New J. Phys.* **19** 043018
- [8] Penna V and Salasnich L 2019 *J. Phys. B: At. Mol. Opt. Phys.* **52** 035301
- [9] Jo G-B, Lee Y-R, Choi J-H, Christensen C A, Kim T H, Thywissen J H, Pritchard D E and Ketterle W 2009 *Science* **325** 1521
- [10] Sanner C, Su E J, Huang W, Keshet A, Gillen J and Ketterle W 2012 *Phys. Rev. Lett.* **108** 240404
- [11] Valtolina G, Scazza F, Amico A, Burchianti A, Recati A, Enss T, Inguscio M, Zaccanti M and Roati G 2017 *Nat. Phys.* **13** 709
- [12] Scazza F et al 2017 *Phys. Rev. Lett.* **118** 083602
- [13] Amico A, Scazza F, Valtolina G, Tavares P E S, Ketterle W, Inguscio M, Roati G and Zaccanti M 2018 *Phys. Rev. Lett.* **121** 253602
- [14] Pekker D, Babadi M, Sensarma R, Zinner N, Pollet L, Zwierlein M W and Demler E 2011 *Phys. Rev. Lett.* **106** 050402
- [15] Li W and Cui X 2017 *Phys. Rev. A* **96** 053609
- [16] Shin Y, Zwierlein M W, Schunck C H, Schirotzek A and Ketterle W 2006 *Phys. Rev. Lett.* **97** 030401
- [17] Partridge G B, Li W, Kamar R I, Liao Y-a. and Hulet R G 2006 *Science* **311** 503
- [18] Shin Y-I, Schunck C H, Schirotzek A and Ketterle W 2008 *Nature* **451** 689
- [19] Du X, Luo L, Clancy B and Thomas J E 2008 *Phys. Rev. Lett.* **101** 150401
- [20] Du X, Zhang Y, Petricka J and Thomas J E 2009 *Phys. Rev. Lett.* **103** 010401
- [21] Pegahan S, Kangara J, Arakelyan I and Thomas J E 2019 *Phys. Rev. A* **99** 063620

- [22] Chin C, Grimm R, Julienne P and Tiesinga E 2010 *Rev. Mod. Phys.* **82** 1225
- [23] Kangara J, Cheng C, Pegahan S, Arakelyan I and Thomas J E 2018 *Phys. Rev. Lett.* **120** 083203
- [24] Serwane F, Zürn G, Lompe T, Ottenstein T B, Wenz A N and Jochim S 2011 *Science* **332** 336
- [25] Murmann S, Deuretzbacher F, Zürn G, Bjerlin J, Reimann S M, Santos L, Lompe T and Jochim S 2015 *Phys. Rev. Lett.* **115** 215301
- [26] Sowiński T, Grass T, Dutta O and Lewenstein M 2013 *Phys. Rev. A* **88** 033607
- [27] Brandt B B, Yannouleas C and Landman U 2015 *Nano Lett.* **15** 7105
- [28] Cao L, Bolsinger V, Mistakidis S I, Koutentakis G M, Krönke S, Schurer J M and Schmelcher P 2017 *J. Chem. Phys.* **147** 044106
- [29] Deuretzbacher F, Becker D, Bjerlin J, Reimann S M and Santos L 2014 *Phys. Rev. A* **90** 013611
- [30] Volosniev A G, Fedorov D V, Jensen A S, Valiente M and Zinner N T 2014 *Nat. Commun.* **5** 5300
- [31] Levinsen J, Massignan P, Bruun G M and Parish M M 2015 *Sci. Adv.* **1** e1500197
- [32] Yang L, Guan L and Pu H 2015 *Phys. Rev. A* **91** 043634
- [33] Cui X and Ho T-L 2014 *Phys. Rev. A* **89** 013629
- [34] Yannouleas C, B Brandt B and Landman U 2016 *New J. Phys.* **18** 073018
- [35] Koller A P, Wall M L, Mundinger J and Rey A M 2016 *Phys. Rev. Lett.* **117** 195302
- [36] Koutentakis G M, Mistakidis S I and Schmelcher P 2019 *New J. Phys.* **21** 053005
- [37] Erdmann J, Mistakidis S I and Schmelcher P 2019 *Phys. Rev. A* **99** 013605
- [38] Kwasniok J, Mistakidis S I and Schmelcher P 2019 arXiv:1911.12839
- [39] Cui X and Ho T-L 2014 *Phys. Rev. A* **89** 023611
- [40] Dehkharghani A S, Volosniev A G and Zinner N T 2016 *J. Phys. B: At. Mol. Opt. Phys.* **49** 085301
- [41] Sowiński T, Gajda M and Rzażewski K 2016 *Europhys. Lett.* **113** 56003
- [42] Haule K and Kotliar G 2009 *New J. Phys.* **11** 025021
- [43] Hu J 2013 *Phys. Rev. X* **3** 031004
- [44] Georges A, de Medici L and Mravlje J 2013 *Annu. Rev. Condens. Matter Phys.* **4** 137
- [45] Anderson P W 1959 *Phys. Rev.* **115** 2
- [46] Mistakidis S I, Cao L and Schmelcher P 2014 *J. Phys. B: At. Mol. Opt. Phys.* **47** 225303
- [47] Mistakidis S I, Cao L and Schmelcher P 2015 *Phys. Rev. A* **91** 033611
- [48] Mistakidis S I, Koutentakis G M and Schmelcher P 2018 *Chem. Phys.* **509** 106
- [49] Olshanii M 1998 *Phys. Rev. Lett.* **81** 938
- [50] Müller-Kirsten H J W 2012 *Introduction to Quantum Mechanics: Schrödinger Equation and Path Integral* (Singapore: World Scientific)
- [51] Shin Y I 2012 *PhD Thesis* Massachusetts Institute of Technology
- [52] Wannier G H 1937 *Phys. Rev.* **52** 191
- [53] Girardeau M 1960 *J. Math. Phys.* **1** 516
- [54] Girardeau M D and Minguzzi A 2007 *Phys. Rev. Lett.* **99** 230402
- [55] Hubbard J 1963 *Proc. R. Soc. A* **276** 238
- [56] Lewenstein M, Sanpera A, Ahufinger V, Damski B, SenDe A and Sen U 2007 *Adv. Phys.* **56** 243
- [57] Esslinger T 2010 *Annu. Rev. Condens. Matter Phys.* **1** 129
- [58] Imada M, Fujimori A and Tokura Y 1998 *Rev. Mod. Phys.* **70** 1039
- [59] Spalek J and Oleś A M 1977 *Physica B* **86** 375
- [60] Chao K A, Spalek J and Oleś A M 1978 *Phys. Rev. B* **18** 3453
- [61] Spalek J, Oleś A M and Chao K A 1978 *Phys. Rev. B* **18** 3748
- [62] Spalek J 1988 *Phys. Rev. B* **37** 533
- [63] Gros C 1988 *Phys. Rev. B* **38** 931
- [64] Lee P A, Nagaosa N and Wen X-G 2006 *Rev. Mod. Phys.* **78** 17
- [65] Mattis D C 1988 *The Theory of Magnetism* (Berlin: Springer)
- [66] Cohen-Tannoudji C 1977 *Quantum Mechanics* (New York: Wiley)
- [67] Erdmann J, Mistakidis S I and Schmelcher P 2018 *Phys. Rev. A* **98** 053614
- [68] Volosniev A G 2017 *Few-Body Syst.* **58** 54
- [69] Peçak D, Gajda M and Sowiński T 2016 *New J. Phys.* **18** 013030
- [70] Peçak D and Sowiński T 2016 *Phys. Rev. A* **94** 042118
- [71] Parajuli B, Peçak D and Chien C-C 2019 *Phys. Rev. A* **100** 063623
- [72] Zanghellini J, Kitzler M, Fabian C, Brabec T and Scrinzi A 2003 *Laser Phys.* **13** 1064
- [73] Kato T and Kono H 2004 *Chem. Phys. Lett.* **392** 533
- [74] Caillat J, Zanghellini J, Kitzler M, Koch O, Kreuzer W and Scrinzi A 2005 *Phys. Rev. A* **71** 012712
- [75] Nest M, Klamroth T and Saalfrank P 2005 *J. Chem. Phys.* **122** 124102
- [76] Hochstuhl D, Bauch S and Bonitz M 2010 *J. Phys.: Conf. Ser.* **220** 012019
- [77] Haxton D J, Lawler K V and McCurdy C W 2011 *Phys. Rev. A* **83** 063416
- [78] Cao L, Mistakidis S I, Deng X and Schmelcher P 2017 *Chem. Phys.* **482** 303
- [79] Mistakidis S I, Katsimiga G C, Koutentakis G M and Schmelcher P 2019 *New J. Phys.* **21** 043032

4.2 Spectroscopic properties of Bose and Fermi Polarons

4.2.1 Repulsive Fermi polarons and their induced interactions in binary mixtures of ultracold atoms

PAPER • OPEN ACCESS

Repulsive Fermi polarons and their induced interactions in binary mixtures of ultracold atoms

To cite this article: S I Mistakidis *et al* 2019 *New J. Phys.* **21** 043032

View the [article online](#) for updates and enhancements.

Recent citations

- [Ion-induced interactions in a Tomonaga-Luttinger liquid](#)
A. B. Michelsen *et al*
- [Thermal crossover, transition, and coexistence in Fermi polaronic spectroscopies](#)
Hiroyuki Tajima and Shun Uchino
- [Quench Dynamics and Orthogonality Catastrophe of Bose Polarons](#)
S. I. Mistakidis *et al*



PAPER

Repulsive Fermi polarons and their induced interactions in binary mixtures of ultracold atoms

OPEN ACCESS

RECEIVED

12 December 2018

REVISED

1 March 2019

ACCEPTED FOR PUBLICATION

15 March 2019

PUBLISHED

15 April 2019

Original content from this work may be used under the terms of the [Creative Commons Attribution 3.0 licence](https://creativecommons.org/licenses/by/4.0/).

Any further distribution of this work must maintain attribution to the author(s) and the title of the work, journal citation and DOI.

S I Mistakidis^{1,3,4} , G C Katsimiga^{1,3}, G M Koutentakis^{1,2,3} and P Schmelcher^{1,2}¹ Center for Optical Quantum Technologies, Department of Physics, University of Hamburg, Luruper Chaussee 149, D-22761 Hamburg Germany² The Hamburg Centre for Ultrafast Imaging, Universität Hamburg, Luruper Chaussee 149, D-22761 Hamburg, Germany³ These authors have contributed equally to this work.⁴ Author to whom any correspondence should be addressed.E-mail: smistaki@physnet.uni-hamburg.de**Keywords:** Fermi polarons, correlations, induced interactions, radiofrequency spectroscopy**Abstract**

We explore repulsive Fermi polarons in one-dimensional harmonically trapped few-body mixtures of ultracold atoms using as a case example a ${}^6\text{Li}$ - ${}^{40}\text{K}$ mixture. A characterization of these quasiparticle-like states, whose appearance is signaled in the impurity's radiofrequency spectrum, is achieved by extracting their lifetime and residua. Increasing the number of ${}^{40}\text{K}$ impurities leads to the occurrence of both single and multiple polarons that are entangled with their environment. An interaction-dependent broadening of the spectral lines is observed suggesting the presence of induced interactions. We propose the relative distance between the impurities as an adequate measure to detect induced interactions independently of the specifics of the atomic mixture, a result that we showcase by considering also a ${}^6\text{Li}$ - ${}^{173}\text{Yb}$ system. This distance is further shown to be indicative of the generation of entanglement independently of the size of the bath (${}^6\text{Li}$) and the atomic species of the impurity. The generation of entanglement and the importance of induced interactions are revealed with an emphasis on the regime of intermediate interaction strengths.

1. Introduction

The properties and interactions of impurities immersed in a complex many-body (MB) environment represents a famous example of Landau's quasiparticle theory [1]. The concept of a polaron, where an impurity immersed in a bath couples to the excitations of the latter forming an effective free particle, plays a central role in our understanding of quantum matter. Applications range from semiconductors [2], high T_c superconductors [3], and liquid Helium mixtures [4, 5] to polymers and proteins [6, 7]. Population imbalanced ultracold Fermi gases [8] with their tunable interactions, offer an ideal platform for studying the impurity problem as well as the effective interactions between Fermi polarons.

Most of the experimental and theoretical studies on this topic have initially been focusing on attractive Fermi polarons [9–14]. Only very recently quasiparticle formation in fermionic systems associated with strong repulsive interactions have been experimentally realized first in the context of narrow [15] and subsequently for universal broad Feshbach resonances (FR) [16, 17]. They have triggered a new era of theoretical investigations regarding the properties of repulsive Fermi polarons [18–25]. These metastable states—that can decay into molecules in two- and three-dimensions (3D)—are of fundamental importance since their existence and longevity offers the possibility of stabilizing repulsive Fermi gases. As a result exotic quantum phases and itinerant ferromagnetism [26–33] could be explored. While for finite impurity mass Fermi polarons constitute well-defined quasiparticles in these higher dimensional systems [34–36], the quasiparticle picture is shown to be ill-defined in the thermodynamic limit of one-dimensional (1D) settings [37–39]. However, important aspects of the physics in this limit have been identified in few-body experiments evading such difficulties [40, 41]. Besides the fundamental question of the existence of coherent quasiparticles in such lower dimensional settings [41–53], far less insight is nowadays experimentally available regarding the notion of induced interactions

between polarons [54–65]. In this direction, 1D systems represent the cornucopia for studying effective interactions between quasiparticle-like states, since their role is expected to be enhanced in such settings [39].

In this work, we simulate the experimental process of reverse radiofrequency (rf) spectroscopy [15, 16, 66, 67] using as a case example a mixture consisting of ^{40}K Fermi impurities coupled to a few-body ^6Li Fermi sea and demonstrate the accumulation of polaronic properties. We predict and characterize the excitation spectrum of these states and derive their lifetimes and residues. Most importantly here, we identify all the dominant microscopic mechanisms that lead to polaron formation. By increasing the number of ^{40}K impurities immersed in a ^6Li bath, we verify the existence of single as well as multi-polaron states both for weak and strong interspecies repulsion. In line with recent studies [16, 68] the presence of induced interactions between the polarons is indicated by a positive resonance shift further accompanied by a spectral broadening. However, the non-sizeable nature of this shift, being of the order of 2%, suggests that in order to infer about the presence of induced interactions an alternative measure is needed. Inspecting the relative distance between the resulting quasiparticles, a quantity that can be probed experimentally via *in situ* spin-resolved single-shot measurements [69], we observe its decrease which concordantly dictates the presence of induced interactions [70]. The latter are found to be attractive despite the repulsive nature of the fundamental interactions in the system. This fact persists upon enlarging the fermionic sea [57] and considering different atomic species. We find that the decrease of the relative distance is inherently connected to the generation of entanglement. The von-Neumann entropy [71] reveals equally the entanglement and is sensitive to the number of impurities.

This work is structured as follows. Section 2 presents our setup and MB treatment. In section 3 we discuss the excitation spectrum of the fermionic mixture and identify polaronic states. We also extract their residues and lifetimes. In section 4 we quantify the degree of entanglement between the impurity atom(s) and the bath. The induced interactions between the two impurity atoms are analyzed and related to the generation of entanglement. We summarize our findings and provide an outlook in section 5. Appendix A contains a discussion of our numerical implementation regarding the process of rf spectroscopy. The applicability of the employed model in the context of effective range corrections is shown in appendix B. Appendix C showcases the behavior of the energy of the polaron versus the particle number of the bath. Finally, in appendix D we provide further details of our numerical findings presented in the main text.

2. Theoretical framework

2.1. Model system

Our system consists of $N_L = 5$ spinless ^6Li fermions each with mass m_L , which serve as a bath for the spin-1/2 $N_K = 1, 2$ ^{40}K impurities of mass m_K . Each species is trapped in a 1D harmonic potential with frequency $\omega_K = 0.6 \omega_L$ in line with previous ^6Li - ^{40}K experiments [68, 72–74]. The MB Hamiltonian of the system reads

$$\hat{H} = \hat{H}_L^0 + \sum_a \hat{H}_a^0 + \hat{H}_I + \hat{H}_S, \quad (1)$$

where $\hat{H}_L^0 = \int dx \hat{\Psi}_L^\dagger(x) \left(-\frac{\hbar^2}{2m_L} \frac{d^2}{dx^2} + \frac{1}{2} m_L \omega_L^2 x^2 \right) \hat{\Psi}_L(x)$, is the Hamiltonian describing the trapped motion of the majority ^6Li atoms with trap frequency ω_L . The corresponding non-interacting Hamiltonian of the minority ^{40}K atoms is $\hat{H}_a^0 = \int dx \hat{\Psi}_a^\dagger \left(-\frac{\hbar^2}{2m_K} \frac{d^2}{dx^2} + \frac{1}{2} m_K \omega_K^2 x^2 \right) \hat{\Psi}_a(x)$, where $a = \{\uparrow, \downarrow\}$ denotes the spin component. In both of the above-mentioned cases $\hat{\Psi}_i(x)$ is the fermionic field-operator for either the majority ($i = L$) or the impurity ($i = K$) atoms. The contact interspecies interaction term of effective strength $g > 0$ between a spin- \uparrow impurity particle and the bath is given by $\hat{H}_I = g \int dx \hat{\Psi}_L^\dagger(x) \hat{\Psi}_\uparrow^\dagger(x) \hat{\Psi}_\uparrow(x) \hat{\Psi}_L(x)$ ⁵. The non-resonant interaction of the spin- \downarrow state with the ^6Li bath can be neglected when compared to \hat{H}_I . Moreover, the effective interaction strength g [75] can be experimentally tuned either by means of FR [76] or confinement induced resonances [75]. It is important to stress at this point that a bound state of a Feshbach molecule occurs for all scattering lengths in one-dimension. However it can be demonstrated [77, 78] that its effect is negligible for repulsive interactions sufficiently away from the infinite interaction limit such as the ones considered herein (see also appendix A). We also note that in the considered few-body case it can be shown that the effective range corrections to the interaction term \hat{H}_I stemming from the presence of narrow FR are negligible, see appendix B. Finally, $\hat{H}_S = \frac{\hbar \Omega_R^0}{2} \hat{S}_x - \frac{\hbar \Delta}{2} \hat{S}_z$, where Ω_R^0 denotes the Rabi frequency, and Δ the detuning of the rf field in the absence of the ^6Li bath. Here, $\hat{S} = \int dx \sum_{ab} \hat{\Psi}_a^\dagger(x) \sigma_{ab} \hat{\Psi}_b(x)$ is the total spin operator while σ denotes the Pauli vector. We assume, $\Omega_R^0 \ll \omega_L$ such that $\Omega_R^0 \ll \Delta_{+i}$ (Δ_{+i} denotes the location of the resonance to the i th state identified in the rf spectra) thus allowing for a spectroscopic study of the polaronic structures, see also appendix A.

⁵ Note that the effective interaction strength is given in terms of the scattering length a_0 as $g = (2\pi\hbar^2 a_0 (m_L + m_K)) / (m_L m_K)$.

2.2. The MB approach

To theoretically address the impurity problem, we use a variational method, namely the Multi-Layer Multi-Configuration Time-Dependent Hartree method for atomic mixtures (ML-MCTDHX), that takes into account all particle correlations [79, 80]. Such a non-perturbative inclusion of correlations allows us to calculate the impurity spectrum and thus identify the emergent polaron states.

The MB wavefunction, $|\Psi(t)\rangle_{\text{MB}}$ is constructed as a linear combination of a set of M time-dependent wavefunctions for each of the species being referred to as species wavefunctions, $|\Psi_i^\sigma(t)\rangle$. Here $\sigma \in \{L, K\}$, $i = 1, \dots, M$ and

$$|\Psi(t)\rangle_{\text{MB}} = \sum_{i,j=1}^M A_{ij}(t) |\Psi_i^L(t)\rangle |\Psi_j^K(t)\rangle, \quad (2)$$

where $A_{ij}(t)$ denote the time-dependent expansion coefficients. Equation (2) is equivalent to a truncated Schmidt decomposition of rank M [71, 81, 82]. Indeed, the spectral decomposition of the expansion coefficients A_{ij} reads $A_{ij}(t) = \sum_{k=1}^M U_{ik}^{-1}(t) \sqrt{\lambda_k(t)} U_{kj}(t)$ where $\sqrt{\lambda_k(t)}$ refer to the Schmidt weights. As a consequence the MB wavefunction can be written as a truncated Schmidt decomposition i.e. $|\Psi(t)\rangle_{\text{MB}} = \sum_{k=1}^M \sqrt{\lambda_k(t)} |\tilde{\Psi}_k^L(t)\rangle |\tilde{\Psi}_k^K(t)\rangle$.

Subsequently each of the species wavefunctions is expanded on the time-dependent number-state basis, $|\vec{n}(t)\rangle^\sigma$, with time-dependent weights $B_{i;\vec{n}}^\sigma(t)$

$$|\Psi_i^\sigma(t)\rangle = \sum_{\vec{n}} B_{i;\vec{n}}^\sigma(t) |\vec{n}(t)\rangle^\sigma. \quad (3)$$

Each time-dependent number state corresponds to a Slater determinant of the m^σ time-dependent variationally-optimized single-particle functions (SPFs) $|\phi_l^\sigma(t)\rangle$, $l = 1, 2, \dots, m^\sigma$ with occupation numbers $\vec{n} = (n_1, \dots, n_{m^\sigma})$. Each of the SPFs is subsequently expanded in a primitive basis. For the ^6Li atoms the primitive basis $\{|k\rangle\}$ consists of a discrete variable representation (DVR) of dimension \mathcal{M} . For ^{40}K the primitive basis $\{|k, s\rangle\}$, refers to the tensor product of a the aforementioned DVR basis for the spatial degrees of freedom and the two-dimensional spin basis $\{|\uparrow\rangle, |\downarrow\rangle\}$,

$$|\phi_j^K(t)\rangle = \sum_{k=1}^{\mathcal{M}} \sum_{\alpha=\{\uparrow, \downarrow\}} C_{jk\alpha}^K(t) |k\rangle |\alpha\rangle. \quad (4)$$

$C_{jk\alpha}^K(t)$ refer to the corresponding time-dependent expansion coefficients. Note here that each time-dependent SPF for the ^{40}K is a general spinor wavefunction of the form $|\phi_j^K(t)\rangle = \int dx [\chi_j^\uparrow(x) \hat{\Psi}_\uparrow^\dagger(x) + \chi_j^\downarrow(x) \hat{\Psi}_\downarrow^\dagger(x)] |0\rangle$ (see also [33]). The time-evolution of the N -body wavefunction under the effect of the Hamiltonian \hat{H} reduces to the determination of the A -vector coefficients and the expansion coefficients of each of the species wavefunctions and SPFs. Those, in turn, follow the variationally obtained ML-MCTDHX equations of motion [80]. It is important to mention here that in order obtain the eigenstates involving one and two polarons of the interacting MB system we use the method of improved relaxation [80] within ML-MCTDHX. We remark that the system in its stationary state reduces to a binary mixture of bath and spin- \uparrow atoms. In this way the general ansatz of equation (2) becomes that of equation (8) (see also the discussion in section 4). For a detailed discussion on this ansatz we refer the reader to [80–82].

In the limiting case of $M = 1$ and $m^\sigma = N^\sigma$ the method reduces to the two-species coupled time-dependent Hartree–Fock method, while for the case of $M = \min\left[\binom{m^L}{N^L}, \binom{m^K}{N^K}\right]$, $m^L = \mathcal{M}$ and $m^K = 2\mathcal{M}$, it is equivalent to a full configuration interaction approach (commonly referred to as ‘exact diagonalization’ in the literature) within the employed primitive basis. Another important reduction of the method is the so-called species mean-field (SMF) approximation [80, 81]. In this context the entanglement between the species is ignored while the correlations within each of the species are taken into account. More specifically, the system’s wavefunction is described by only one species wavefunction, i.e. $|\Psi_i^L(t)\rangle = |\Psi_i^K(t)\rangle = 0$ for $i \neq 1$. Subsequently each species wavefunction is expressed in terms of the time-dependent number state basis of equation (3) consisting of different time-dependent variationally optimized SPFs. As a result the total wavefunction of the system takes the tensor product form

$$|\Psi(t)\rangle_{\text{SMF}} = |\Psi_1^L(t)\rangle \otimes |\Psi_1^K(t)\rangle. \quad (5)$$

3. Reverse rf spectroscopy

3.1. Excitation spectrum

In order to probe the excitation spectrum of the ^{40}K impurities we simulate reverse rf spectroscopy [15, 16, 66, 67]. This process follows the protocol explicated below. The initial state of the system consists of the

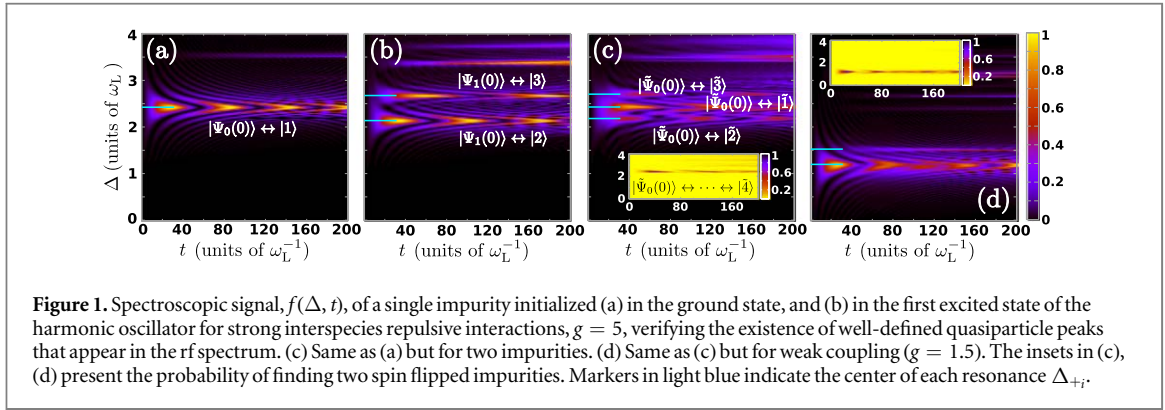


Figure 1. Spectroscopic signal, $f(\Delta, t)$, of a single impurity initialized (a) in the ground state, and (b) in the first excited state of the harmonic oscillator for strong interspecies repulsive interactions, $g = 5$, verifying the existence of well-defined quasiparticle peaks that appear in the rf spectrum. (c) Same as (a) but for two impurities. (d) Same as (c) but for weak coupling ($g = 1.5$). The insets in (c), (d) present the probability of finding two spin flipped impurities. Markers in light blue indicate the center of each resonance Δ_{+i} .

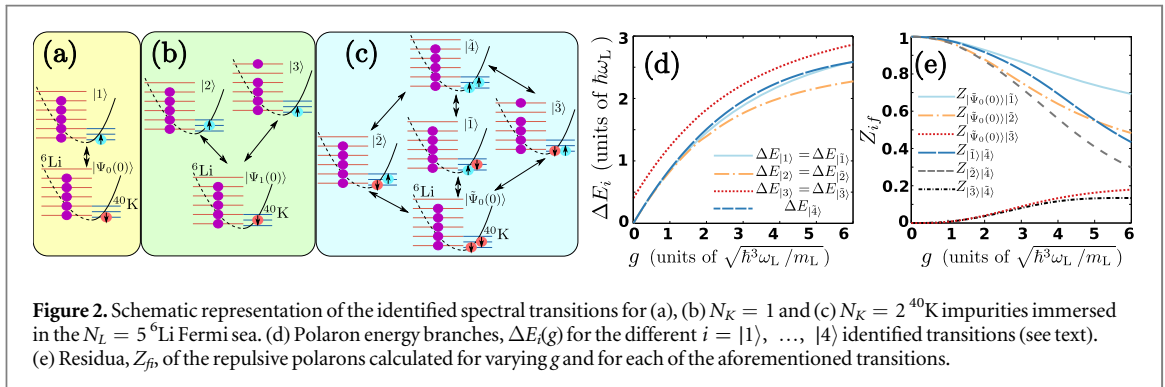


Figure 2. Schematic representation of the identified spectral transitions for (a), (b) $N_K = 1$ and (c) $N_K = 2$ ^{40}K impurities immersed in the $N_L = 5$ ^6Li Fermi sea. (d) Polaron energy branches, $\Delta E_i(g)$ for the different $i = |1\rangle, \dots, |4\rangle$ identified transitions (see text). (e) Residua, Z_{if} , of the repulsive polarons calculated for varying g and for each of the aforementioned transitions.

^6Li atoms in their N_L -body non-interacting ground state $|\Psi_L(0)\rangle = \prod_{i=0}^{N_L-1} \int dx \phi_i^L(x) \hat{\Psi}_L^\dagger(x) |0\rangle$. $\phi_i^L(x)$ refers to the i th energetically excited eigenstate of \hat{H}_L^0 . For $N_K = 1$ the ^{40}K impurity is prepared in the non-interacting spin- \downarrow state, and it is either in its ground state or in its first excited state (see also the discussion below). Namely $|\Psi_j(0)\rangle = \int dx \phi_j^K(x) \hat{\Psi}_\downarrow^\dagger(x) |\Psi_L(0)\rangle$, where $j \in \{0, 1\}$ while $\phi_j^K(x)$ refer to the eigenstates of \hat{H}_\downarrow^0 . We then drive the impurity atom to the resonantly interacting spin- \uparrow state, by applying a rectangular rf pulse (see also appendix A) with bare Rabi frequency $\Omega_R^0 = 4\pi \times 10^{-2}$ (harmonic oscillator units $\hbar = m_L = \omega_L = 1$ are adopted here). Our simulated spectroscopic signal presented in figures 1(a), (b) is the fraction of impurity atoms transferred after a pulse $f(\Delta, t) = \frac{\langle N_\uparrow \rangle}{N_K}$, with $\langle N_\uparrow \rangle$ being the number of spin flipped impurities, measured for varying rf detuning $\Delta = \nu_{\text{rf}} - \nu_0$ and pulse time t . ν_0 denotes the frequency of the non-interacting transition between the spin- \downarrow and spin- \uparrow states and ν_{rf} is the applied frequency (see also appendix A).

Starting from $|\Psi_0(0)\rangle$ and for fixed strong interspecies repulsions ($g = 5$) we observe a resonance for $\Delta_{+|1\rangle} = 2.430 \pm 0.002$ (see figure 1(a)), possessing a Rabi frequency $\Omega_R = 0.1072 \pm 0.0021$. These values stem from fitting $\tilde{\Omega}_R(\Delta) = \sqrt{(\Omega_R)^2 + (\Delta - \Delta_{+i})^2}$ to the simulated rf spectra. This resonance corresponds to the lowest energetically interacting state of a spin- \uparrow impurity with the ^6Li bath (figure 2(a)) verifying the existence of a repulsive polaron in our 1D setup. Further resonances corresponding to higher excited states can be identified as e.g. for $\Delta_+ \approx 3.6$ possessing a much lower Rabi frequency. To identify the transition that leads to the occurrence of the above-mentioned quasiparticle peak, i.e. $|\Psi_0(0)\rangle \leftrightarrow |1\rangle$ schematically illustrated in figure 2(a), we first compute the energy, $E_i(g)$, ($i = |1\rangle$) for this configuration. The resulting energy difference, $\Delta E_i(g) = [E_i(5) - E_i(0)]/n$, with $E(0)$ being the energy of the initial state and n the order of the transition, is the one that matches the location of the observed resonance. The corresponding polaronic energy branch shows a monotonic increase for increasing interspecies repulsion (see the light blue line in figure 2(d)), a behavior that is consistent with the experimental [16] and the theoretical predictions [18–21] in higher dimensional settings.

As a next step we consider a single impurity being initialized in its first excited state $|\Psi_1(0)\rangle$. This is of importance for the case of $N_K = 2$ impurities for which more transitions are possible. In sharp contrast to the $|\Psi_0(0)\rangle$ case, two dominant polaron peaks appear in the rf spectrum of figure 1(b) centered at $\Delta_{+|2\rangle} = 2.152 \pm 0.001$ ($\Omega_R = 0.0899 \pm 0.0012$) and $\Delta_{+|3\rangle} = 2.688 \pm 0.002$ ($\Omega_R = 0.05072 \pm 0.022$) respectively. These two quasiparticle peaks occur at lower and higher values of Δ respectively, when compared to the $\Delta_{+|1\rangle}$ resonance. The width of the resonance centered at $\Delta_{+|3\rangle}$ is significantly sharper compared to the lower-lying one as it possesses lower Ω_R . The corresponding transitions in this case namely $|\Psi_1(0)\rangle \leftrightarrow |2\rangle$, and

$|\Psi_1(0)\rangle \leftrightarrow |3\rangle$ are shown in figure 2(b). The relevant energy branches, $\Delta E_{|2\rangle}(g)$, $\Delta E_{|3\rangle}(g)$, for increasing g are depicted in figure 2(d). It is evident that for $g \leq 1.5$ all the aforementioned resonances except the transition $|\Psi_1(0)\rangle \leftrightarrow |3\rangle$, are overlapping since $\Delta E_{|1\rangle}(g) \simeq \Delta E_{|2\rangle}(g)$. However, $\Delta E_{|3\rangle}(g)$ possesses a non-zero value even for $g \approx 0$ as the involved states are already distinct (figure 2(b)).

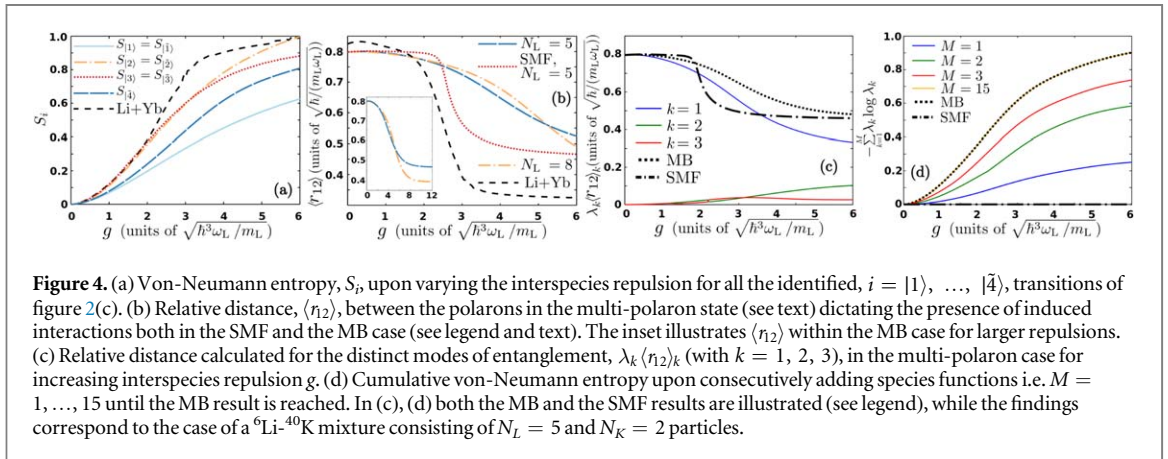
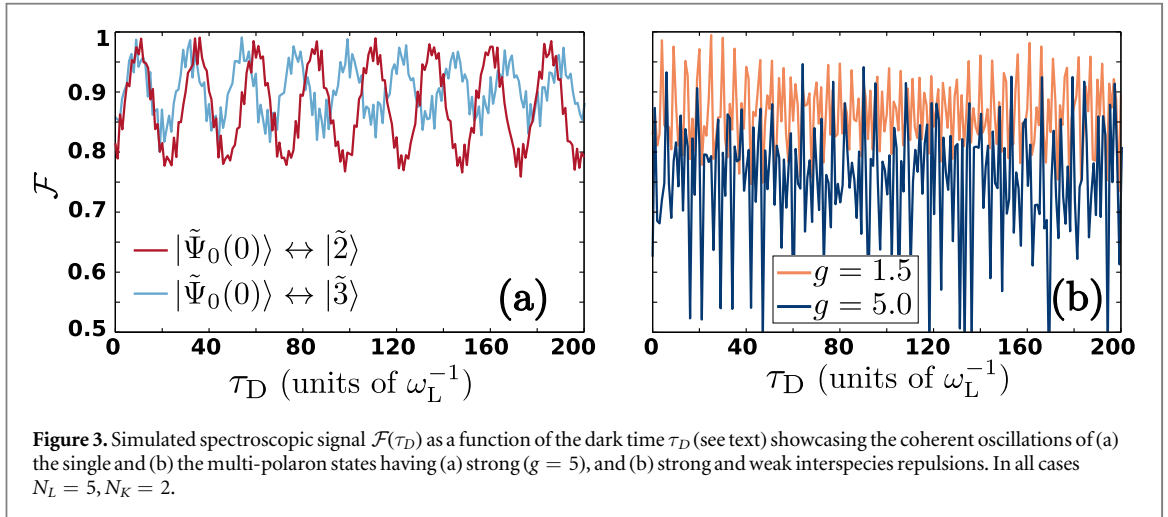
To probe the existence of effective interactions between polarons we next consider the case of two ^{40}K impurities immersed in the ^6Li sea. Figure 1(c) shows the rf spectrum for $N_K = 2$, and $g = 5$. Here, three narrowly spaced resonances can be observed, see the broad structure centered around $\Delta = 2.4$ in figure 1(c). This broadening together with an overall small upshift with respect to the above single impurity cases, has been argued to be indicative of the presence of induced interactions between the polarons [16, 68] that we will explore below. The resonances are located at $\Delta_{+|2\rangle} = 2.195 \approx \Delta E_{|2\rangle}$ ($\Omega_R = 0.0836 \pm 0.0004$), $\Delta_{+|\bar{1}\rangle} = 2.441 \approx \Delta E_{|\bar{1}\rangle}$ ($\Omega_R = 0.0745 \pm 0.001$), and $\Delta_{+|\bar{3}\rangle} = 2.722 \approx \Delta E_{|\bar{3}\rangle}$ ($\Omega_R = 0.0577 \pm 0.0005$) respectively. The relevant transitions are $|\tilde{\Psi}_0(0)\rangle \leftrightarrow |\bar{2}\rangle$, and $|\tilde{\Psi}_0(0)\rangle \leftrightarrow |\bar{3}\rangle$ for the outer resonances, in direct analogy with the ones found in the single impurity case of figure 2(b). More importantly herein, the central resonance accounts not only for a transition $|\tilde{\Psi}_0(0)\rangle \leftrightarrow |\bar{1}\rangle$ but it also involves several second-order processes namely $|\tilde{\Psi}_0(0)\rangle \leftrightarrow \dots \leftrightarrow |\bar{4}\rangle$ and thus corresponds to a multi-polaron state (figure 2(c)). We showcase this, by calculating the probability of finding two particles with spin- \uparrow (see the inset in figure 1(c)). It is the appearance of this $|\bar{4}\rangle$ state that leads to higher-order transitions via the virtual occupation of $|\bar{4}\rangle$ (figure 2(c)). The observed upshift of all spectral lines is attributed to the occurrence of this state. Strikingly enough, the energy of this two-polaron state, $\Delta E_{|\bar{4}\rangle}$, almost coincides with the single polaron one, $\Delta E_{|\bar{1}\rangle}$, i.e. it exhibits a deviation of 1.9% which is of the same order as the observed upshift (figure 2(d)). Note that such a two-polaron resonance is also present for weaker interactions located at $\Delta_+ \approx 1.175$, see figure 1(d) and its inset for $g = 1.5^6$. Thus, increasing the number of impurities does not significantly affect the energy of the polaron or the multi-polaron state formed, in accordance with the absence of a significant shift of the corresponding energy in current experimental settings [16]. The origin of the above-mentioned positive shift can be further attributed to the difference between the effective and bare mass of the impurities [9, 16], as well as to the presence of induced interactions between the polarons [56, 58, 63]. Therefore the position of the resonance might not be an adequate experimental probe for the presence of induced interactions. Indeed, the observed energy shift between the energy of the single and two impurities is rather small, being of the order of 1.9%, and therefore given the current experimental resolution it might even not be easily experimentally detectable. Instead as we shall demonstrate below the spatial separation of the impurities is the relevant quantity and can be probed by current state-of-the-art experimental methods.

3.2. Residue and lifetime of the polaron

To further characterize the polarons we employ their residue, Z_{fi} , which is a measure of the overlap between the dressed polaronic state and the initial non-interacting one after a single spin flip [25, 39]. It is important to note here that in one-dimension the quasiparticle residue acquires a finite value for any finite N_L . Indeed, the Anderson orthogonality catastrophe occurs only in the thermodynamic limit $N_L \rightarrow \infty$ [39, 83] rendering the quasiparticle picture ill defined. We have used two independent ways for determining Z_{fi} . Initially, with the aid of Fermi's golden rule, $\Gamma_{i \rightarrow f} = \frac{\pi \hbar}{2} (\Omega_R^0)^2 \sum_f Z_{fi} \delta(\omega - \omega_f)$, where $Z_{fi} \equiv |\langle f | \hat{S}_x | i \rangle|^2$, we can deduce that the residue is related to our simulated rf procedure via $Z_{fi} = (\Omega_R / \Omega_R^0)^2 \equiv Z_{fi}^{\text{rf}}$ [15, 16]. For the three polaron peaks identified in figure 1(c) the above gives: $Z_{|\tilde{\Psi}_0(0)\rangle|\bar{2}\rangle}^{\text{rf}} = 0.5107 \pm 0.0136$, $Z_{|\tilde{\Psi}_0(0)\rangle|\bar{1}\rangle}^{\text{rf}} = 0.7277 \pm 0.0285$, and $Z_{|\tilde{\Psi}_0(0)\rangle|\bar{3}\rangle}^{\text{rf}} = 0.1629 \pm 0.0141$. Additionally, one can calculate the quasiparticle weight by invoking its definition. The corresponding Z_{if} 's are presented in figure 1(e) upon varying g . For increasing g Z_{if} decreases being dramatically steeper for the multi-polaron state, $Z_{|\bar{1}\rangle|\bar{4}\rangle}$, when compared to the single polaron case $Z_{|\tilde{\Psi}_0(0)\rangle|\bar{1}\rangle}$. This result supports the observation that polarons consist of well-defined quasiparticles in the single impurity limit [17]. Importantly here, very good agreement in evaluating Z_{fi} is observed between the two approaches as can be seen by comparing e.g. at $g = 5$ $Z_{|\tilde{\Psi}_0(0)\rangle|\bar{3}\rangle} = 0.1627$ shown in figure 2(e) to $Z_{|\tilde{\Psi}_0(0)\rangle|\bar{3}\rangle}^{\text{rf}}$.

The coherence properties of the above-identified polarons can be directly inferred by measuring their lifetime. Due to the 1D confinement and due to the fact that in the Hamiltonian of equation (1) incoherent two- and three-body recombination processes are ignored [20, 21, 25, 39, 84], only coherent oscillations are expected and indeed observed. Figures 3(a) and (b) summarize our findings for $N_K = 2$ both for weak and strong coupling. To obtain these lifetimes a two-pulse rf scheme is adopted, mimicking the experimental procedure [15], which is briefly outlined here (see appendix A for details). For a specific resonance a π -pulse is applied transferring the atoms from their initial spin- \downarrow to their polaronic spin- \uparrow state. Then the particles are left to evolve in the absence of an rf field, $\Omega_R^0 = 0$, for a variable (dark) time, τ_D . After this dark time a second π -pulse is used driving the impurities from the interacting (spin- \uparrow state) to their non-interacting (spin- \downarrow) state. The signature of

⁶ For $g = 1.5$ the corresponding separation of the spectral lines is suppressed resulting to a broadened central peak and a single and sharper side peak when compared to the $g = 5$ case.



this process is the fraction of atoms transferred to the spin- \downarrow state during the second pulse divided by the transferred atoms during the first pulse. Namely

$$\mathcal{F}(\tau_D) = \frac{\left[f\left(\frac{\pi}{\Omega_R}\right) - f\left(\frac{2\pi}{\Omega_R} + \tau_D\right) \right]}{f\left(\frac{\pi}{\Omega_R}\right)}. \quad (6)$$

Note that the presence of excitations as well as higher-order transitions, signify the non-adiabatic nature of this procedure. Thus a phase difference between the distinct polaronic states contributing to the MB wavefunction is accumulated during the dark time leading in turn to the observed oscillations (figure 3). Evidently, for single particle transitions a dominant oscillation frequency can be deduced (figure 3(a)), whereas multiple ones occur in the corresponding two-polaron case (figure 3(b)) due to the virtual occupation of the $|\bar{4}\rangle$ state.

4. Entanglement and induced interactions

To unravel the entangled nature of both the single and the two-polaron states we next invoke the von-Neumann entropy [71]. It is important to stress here that the polaronic states refer to stationary states of the binary mixture consisting of bath and spin- \uparrow atoms. For this binary system ($\sigma = L, \uparrow$) the von-Neumann entropy reads $S_i = -\text{Tr}_\sigma[\rho^\sigma \log(\rho^\sigma)]$, with $\rho^\sigma = -\text{Tr}_\sigma[|\Psi\rangle\langle\Psi|]$ being the species density matrix. In figure 4(a) S_i is shown for all of the above transitions, namely $i = |1\rangle, \dots, |\bar{4}\rangle$, as a function of the coupling strength. In all cases a monotonic increase of S_i is observed when entering deeper into the repulsive regime. Strikingly enough, the entropy is found to be significant not only for the two-polaron state but also for the single polaron ones suggesting that these quasiparticles are in general entangled. However notice the deviation between the single ($S_{|1\rangle}$) and the two-polaron state ($S_{|\bar{4}\rangle}$) which is of the order of 20% for large repulsions.

Turning our attention to the two-polaron state, we aim to reveal the presence of induced interactions. As discussed above one cannot necessarily infer about the latter by solely considering the energies. Therefore we employ the relative distance between the two ^{40}K impurities that constitute the multi-polaron state for variable g . The relative distance reads

$$\langle r_{12} \rangle = \frac{\int dx_1 dx_2 |x_1 - x_2| \langle \Psi | \hat{\Psi}_\uparrow^\dagger(x_1) \hat{\Psi}_\uparrow^\dagger(x_2) \hat{\Psi}_\uparrow(x_2) \hat{\Psi}_\uparrow(x_1) | \Psi \rangle}{\langle \Psi | \hat{N}_\uparrow (\hat{N}_\uparrow - 1) | \Psi \rangle}, \quad (7)$$

where $\hat{\Psi}_\uparrow(x_1)$ denotes the fermionic field operator that annihilates a fermion at position x_1 . \hat{N}_\uparrow is the number operator that measures the number of fermions residing in the spin- \uparrow state. Such a quantity can be directly probed experimentally by performing *in situ* spin-resolved single-shot measurements on the \uparrow -state of ^{40}K [69]. Each image offers an estimate of the relative distance between the polarons provided that the position uncertainty is relatively low [69]. Then $\langle r_{12} \rangle$ is obtained by averaging over several such images. Evidently (see figure 4(b)) stronger repulsions result in a significant decrease of $\langle r_{12} \rangle$ that drops to almost half of its initial value for $g \geq 5$. In this way, $\langle r_{12} \rangle$ clearly captures the manifestation of attractive induced interactions present in the system saturating for even larger g (see the inset in figure 4(b)). As shown in figure 4(b) this behavior of $\langle r_{12} \rangle$ holds equally for larger particle numbers of the bath, i.e. $N_L = 8$, and different atomic species, e.g. a ^6Li - ^{173}Yb mixture possessing $\omega_{\text{Yb}} = 0.125 \omega_L$ [85, 86]. This indicates that $\langle r_{12} \rangle$ captures the presence of induced interactions independently of the specifics of the atomic mixture. It becomes also apparent that heavier impurities lead to even stronger attraction emerging from drastically smaller interactions. Most importantly, by calculating $\langle r_{12} \rangle$ in the non-entangled SMF approximation (see also equation (5)), it can be clearly deduced that its shape, being much smoother in the MB approach (figure 4(b)), bears information regarding the generation of entanglement (see also our discussion below). Recall that in this latter SMF case the wavefunction ansatz assumes the form $|\Psi\rangle_{\text{SMF}} = |\tilde{\Psi}^L\rangle \otimes |\tilde{\Psi}^\uparrow\rangle$, which is the most general ansatz that excludes entanglement but includes intraspecies correlations.

Therefore, $\langle r_{12} \rangle$ is indicative of the generation of entanglement, as dictated by the growth rate of S_t for varying g , in MB systems. Indeed, the relation between the generation of entanglement and the $\langle r_{12} \rangle$ can be understood as follows. In order to connect the relative distance with the generation of entanglement we must first recall that the system under consideration is a bipartite composite system whose MB wavefunction, $|\Psi\rangle_{\text{MB}}$, can be expressed in terms of the truncated Schmidt decomposition of rank M as

$$|\Psi\rangle_{\text{MB}} = \sum_{k=1}^M \sqrt{\lambda_k} |\tilde{\Psi}_k^L\rangle |\tilde{\Psi}_k^\uparrow\rangle. \quad (8)$$

Here $|\tilde{\Psi}_k^L\rangle$ and $|\tilde{\Psi}_k^\uparrow\rangle$ denote the species wavefunction of the bath and the impurity respectively. The weights λ_k in decreasing order are referred to as the natural occupations of the k th species function, and $\sqrt{\lambda_k} |\tilde{\Psi}_k^L\rangle |\tilde{\Psi}_k^\uparrow\rangle$ denotes the k th mode of entanglement. Then the expectation value $\langle r_{12} \rangle$ in terms of the Schmidt coefficients λ_k reads

$$\langle r_{12} \rangle = \sum_{k=1}^M \lambda_k \int dx_1 dx_2 |x_1 - x_2| \frac{\langle \hat{\Psi}_k^\dagger | \hat{\Psi}_\uparrow^\dagger(x_1) \hat{\Psi}_\uparrow^\dagger(x_2) \hat{\Psi}_\uparrow(x_2) \hat{\Psi}_\uparrow(x_1) | \hat{\Psi}_k^\dagger \rangle}{\langle \Psi | \hat{N}_\uparrow (\hat{N}_\uparrow - 1) | \Psi \rangle} \equiv \sum_{k=1}^M \lambda_k \langle r_{12} \rangle_k. \quad (9)$$

It becomes apparent by the above expression that the interplay of two different quantities has to be taken into account in order to extract the dominant contribution that leads to the final shape of $\langle r_{12} \rangle$ when including all the relevant correlations. Namely the Schmidt weights, λ_k , and the two-body correlator $\langle r_{12} \rangle_k$ of the k th mode of entanglement. In figure 4(c) $\lambda_k \langle r_{12} \rangle_k$ is illustrated for each of the first three individual species functions $k = 1, 2, 3$, and for the case of a ^6Li - ^{40}K mixture consisting of $N_L = 5$, $N_K = 2$ fermions. Also in the same figure we have included the corresponding full MB result depicted with the dashed dotted black line, as well as the relevant outcome in the non-entangled SMF case (see the dashed black line in figure 4(c)). Notice the abrupt decrease of $\langle r_{12} \rangle$ in the SMF case when compared to the much smoother decay observed in the presence of entanglement. It is exactly this comparison of the MB outcome to the SMF one which reveals that the relative distance itself via its shape bears information regarding the generation of entanglement in the system. Additionally, as can be clearly deduced from this figure the dominant contribution to the final shape of $\langle r_{12} \rangle$ stems from $\lambda_1 \langle r_{12} \rangle_1$ (see solid blue line in figure 4(c)) which corresponds to the first mode of entanglement. It is important to note here, that the form of this dominant mode, $\lambda_1 \langle r_{12} \rangle_1$, in the MB case is greatly altered when compared to the non-entangled, $\langle r_{12} \rangle_{\text{SMF}}$, case. Therefore it becomes apparent that besides this dominant contribution also higher order modes of entanglement weighted by $\lambda_2, \lambda_3, \dots$ are significant in retrieving the MB outcome indicating the strongly entangled nature of the system.

Turning to the von-Neumann entropy recall that the latter can be written in terms of the Schmidt coefficients as follows: $S_M = -\sum_{k=1}^M \lambda_k \log \lambda_k$. The corresponding $S_{|\bar{a}\rangle} \equiv S_M$ upon consecutively adding higher

order contributions is shown in figure 4(d). Indeed inspecting figure 4(d) it becomes evident that in order to retrieve the full MB result the higher-lying Schmidt coefficients, namely $k > 1$, are the ones that predominantly contribute to the final shape of S_M . This result is in sharp contrast to the behavior of the relative distance which is mainly determined by the first mode of entanglement characterized by the leading order Schmidt coefficient, namely the λ_1 . Notice also that in the same figure we have included the corresponding SMF result (see the dashed black line in figure 4(d)) just to showcase that in this case the von-Neumann entropy is zero due to the absence of entanglement.

It becomes evident by the above discussion that both the von-Neumann entropy and the relative distance dictate the generation of entanglement in the MB system but by taking into account different contributions. Additionally, since both quantities are given in terms of the Schmidt coefficients being subject to the constraint $1 - \lambda_1 = \sum_{i=1}^M \lambda_i$, when $\Delta r_{12}(g) = \langle r_{12} \rangle_{\text{MB}} - \langle r_{12} \rangle_{\text{SMF}}$ is finite then also $\Delta S_M(g) = S_{\text{MB}} - S_{\text{SMF}}$ is finite. Moreover, $S_M(g)$ is used to showcase that polarons are indeed entangled with their environment. However, since S_M cannot be measured experimentally, one can infer about the generation of entanglement in the MB system via the shape of $\langle r_{12} \rangle$ which can be probed via *in situ* spin-resolved single-shot measurements that are nowadays available [69]. It is also worth commenting at this point that the above results can be generalized to any type of mixture not necessarily a fermionic one.

5. Conclusions

We have investigated the existence and emergent properties of single and multiple repulsive polarons in 1D harmonically confined fermionic mixtures both for weak and strong interspecies interactions. In particular, we have simulated the corresponding experimental process of rf spectroscopy using different fermionic mixtures consisting of a single or two impurities coupled to a few-body Fermi sea. Analysing the obtained rf excitation spectrum it is indeed shown that these impurities accumulate polaronic properties. Most importantly, we identify all dominant microscopic mechanisms that lead to the polaron formation. We verify that by increasing the number of impurities immersed in a bath with fixed particle number both single and multi-polaron states occur independently of the interaction strength. The corresponding polaronic states are characterized by extracting their residues and lifetimes. We find that the residue exhibits a decreasing tendency for increasing interspecies interaction strengths. This decrease is found to be much more prominent for a multi-polaron than a single polaron state. On the other hand the spectroscopic signal shows an oscillatory behavior with variable dark time indicating the longevity of the polarons.

Turning to the induced interactions between the polarons we show that their presence is first dictated by a positive resonance shift in the rf spectrum accompanied by a consequent spectral broadening. This latter finding is in accordance with the recent experimental observations in three-dimensional setups. However, the above-mentioned shift possesses a small amplitude, being of the order of 2%. This implies that in order to infer about the presence of induced interactions an alternative measure is needed. Our alternative measure for probing the presence of induced interactions is the relative distance between the polarons. It can be experimentally probed via *in situ* spin-resolved single-shot measurements. Attractive induced interactions are indeed captured by this quantity and shown to persist upon enlarging the fermionic sea or considering different fermionic species. The shape of the relative distance for increasing interspecies interactions is found to be also indicative of the presence of entanglement in the MB system. To quantify the degree of entanglement between the impurity and the bath we resort to the von-Neumann entropy which acquires finite values and in particular increases for larger interactions. The degree of entanglement is found to be crucial for the case of a single and for two impurities, being larger in the latter case.

Our investigation of strongly correlated 1D repulsive fermi polarons and multi-polaron states opens up the possibility of further studies of quantum impurities in lower dimensional settings. In particular a straightforward extension of our results would be to consider bosonic or fermionic impurities of the same or higher concentration in a bosonic bath and study the consequent formation of quasiparticles. An imperative prospect would be to examine the existence and properties of such quasiparticle states in the 1D to the 3D crossover, an investigation that calls for further experimental studies. Another interesting direction is to unravel the few to MB crossover regarding the size of the bath in order to reveal its impact on the emergent polaronic properties. Certainly the study of dressed impurities in the strongly interacting regime where the polaron picture is expected to break down is an intriguing perspective.

Acknowledgments

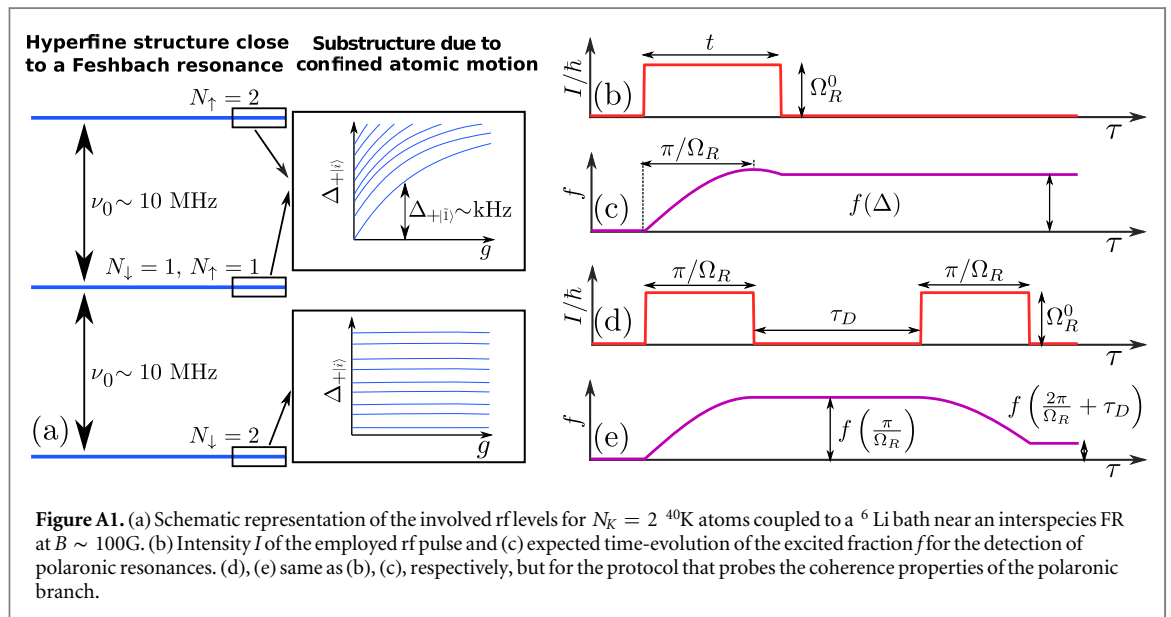
The authors acknowledge fruitful discussions with AG Volosniev, NT Zinner and A Recati. GMK and PS acknowledge the support by the cluster of Excellence ‘Advanced Imaging of Matter’ of the Deutsche Forschungsgemeinschaft (DFG)—EXC 2056—project ID 390715994.

Appendix A. Details of the reverse rf spectroscopy

The purpose of this section is to elaborate on the model that allows for the simulation of rf spectroscopy [15, 16]. The latter has been employed in the main text for the identification of the polaronic resonances and the subsequent characterization of their coherence properties.

In our case few ^{40}K atoms are immersed in an environment consisting of ^6Li atoms close to an interspecies magnetic FR [76]. Such resonances occur at magnetic fields of the order of 100 G [72, 73, 87], where the ground state of ^{40}K atoms, $|^2S_{1/2}; F = \frac{9}{2}\rangle$, experiences a sizeable quadratic Zeeman shift [88]. This Zeeman shift allows us to address selectively the distinct m_F transitions provided that the employed intensity of the rf pulse results in a Rabi frequency Ω_R much smaller than the Zeeman splitting of the involved hyperfine levels. In this work we consider two such hyperfine levels of ^{40}K denoted as $|\uparrow\rangle, |\downarrow\rangle$ that can be identified and resonantly coupled for a rf photon frequency ν_0 , corresponding to the Zeeman splitting between the two levels, in the absence of a ^6Li bath. In such a case, it suffices to treat the ^{40}K atoms as two-level systems. As the atoms are confined within a harmonic potential each of the hyperfine levels is further divided into states of different atomic motion. The average spacing between these sublevels corresponds to the harmonic trap frequency, ω_K being of the order of kHz in typical few-atom experiments [40, 77, 89]. In the vicinity of a FR the energy of these sublevels strongly depends on the interspecies interaction strength g between the ^{40}K atoms in the resonantly-interacting hyperfine state and the ^6Li environment. Accordingly the energy of each motional state shifts by $\Delta_{\pm}(g)$, from the corresponding non-interacting one. In few-atom experiments this shift is of the order of the trapping frequency ($\sim\text{kHz}$).

Figure A1(a) schematically demonstrates the rf spectral lines in the case of $N_K = 2$, including resonant interactions between the $|\uparrow\rangle$ particles and the ^6Li environment. Three well-separated energy level manifolds occur corresponding to the different configurations of N_{\uparrow} and N_{\downarrow} , with $N_{\uparrow} + N_{\downarrow} = N_K$, separated by the Zeeman splitting ν_0 . Each of these manifolds exhibits a substructure of different energy levels of atomic motion. For the configuration $N_{\uparrow} = 0$ and $N_{\downarrow} = 2$ this substructure is interaction-independent in sharp contrast to the $N_{\uparrow} = 1, N_{\downarrow} = 1$ and $N_{\uparrow} = 2, N_{\downarrow} = 0$ configurations as the $|\downarrow\rangle$ atoms do not interact with neither the $|\uparrow\rangle$ ^{40}K or the ^6Li atoms. Reverse rf spectroscopy can be employed to identify these interaction energy shifts provided that the Rabi frequency satisfies $\Omega_R < \Delta_{\pm} \sim \text{kHz}$. This allows us to invoke the rotating wave approximation as $\Omega_R \sim \text{kHz} \ll \nu_0 \sim 10\text{ MHz}$. Employing this approximation the Hamiltonian for the internal state of the ^{40}K atoms, in the interaction picture of the $\uparrow\downarrow$ transition, reads $\hat{H}_S = -\frac{\hbar\Delta}{2}\hat{S}_z + \frac{\hbar\Omega_R^0}{2}\hat{S}_x$. The latter is exactly the form employed in the main text. Ω_R^0 and Δ refer to the Rabi frequency and detuning with respect to the resonance of



the $\uparrow\downarrow$ transition at $g = 0$. We remark that the $|\uparrow\rangle$ and $|\downarrow\rangle$ states in the Schrödinger and interaction pictures are equivalent, so our conclusions are invariant under this frame transformation.

One-dimensional (1D) ensembles offer a clean realization of few-body rf spectroscopy as the existing bound state of a Feshbach molecule possesses a binding energy of the order of $\epsilon_b = -2 \hbar \omega_\perp$ [90] at the confinement-induced resonance, i.e. $g_{1D} \rightarrow \infty$. Since current state-of-the-art few-body 1D experiments have been consistently described by pure 1D models [77, 78] the effect of the bound state for repulsive interactions sufficiently below the $g_{1D} \rightarrow \infty$ regime is negligible. Indeed in order to ensure the validity of the 1D description $\omega_\perp \gg N\omega_L$ must hold, where N denotes the total particle number. In the worst case scenario considered in the main text, namely that of $N_L = 8$, and $N_K = 2$, and in particular when $\omega_\perp = N\omega_L$ then $\epsilon_b \approx -20 \hbar \omega_L$. However, the detuning parameter, Δ , used herein is maximally $4 \hbar \omega_L$. Therefore it lies far below the above threshold of $|\epsilon_b|$. The same line of argumentation holds for the corresponding binding energy at the magnetic FR where $\epsilon_b = -0.606 \hbar \omega_\perp$ [90]. Additionally, few-body systems involve low-densities thus drastically reducing the incoherent processes such as two- and three-body recombination and resulting in increased coherence times. The above allows us to assume a coherent evolution during the simulated experimental sequence.

To identify the resonances corresponding to polaronic states we employ the rf pulse shape depicted in figure A1(b). The system is initialized in the non-interacting ground state where the ^{40}K atoms are spin-polarized in their $|\downarrow\rangle$ state and a rectangular pulse of frequency ν , and detuning Δ is employed. This pulse is further characterized by an exposure time t and a Rabi-frequency Ω_R^0 . Different realizations utilize different detunings Δ but the same t and Ω_R^0 . In the duration of the pulse the system undergoes Rabi-oscillations (see figure A1(c)) whenever the detuning Δ is close to a resonance $\Delta \approx \Delta_+$. The employed spectroscopic signal is the fraction of atoms transferred to the $|\uparrow\rangle$ hyperfine state, namely $f(\Delta, t) = \frac{\langle N_\uparrow \rangle}{N_K}$. We remark that different pulse shapes have been simulated e.g. Gaussian-shaped pulses, which do not alter the presented results. To infer about the coherence properties of the polaronic states we employ a Ramsey like process, see figure A1(d). Initially, we prepare the system in the same non-interacting ground state as in the previously examined protocol and apply a rectangular π -pulse on a polaronic resonance. This sequence transfers the atoms from the ground state to the polaronic state in an efficient manner. Then we let the system evolve in the absence of rf fields, $\Omega_R^0 = 0$, for a dark time, τ_D . Finally, we apply a second π -pulse identical to the first one to transfer the atoms from the polaronic to the initial ground state. The spectroscopic signal is the fraction of atoms that have been excited to the polaronic branch by the first pulse and subsequently deexcited by the second one divided by the total number of excited atoms, $\mathcal{F}(\tau_D) = \frac{f(\pi/\Omega_R) - f(2\pi/\Omega_R + \tau_D)}{f(\pi/\Omega_R)}$, see also figure A1(e).

Appendix B. Effective range corrections

Below we briefly discuss the applicability of the Hamiltonian employed in the current work (see equation (1) in the main text). Notice that this model Hamiltonian assumes that contact interactions dominate the dynamics, ignoring effective range corrections. It is well-known that a ^6Li - ^{40}K mixture features narrow FR [73] with the broader ones being at 114 G [72] and 155 G [15] magnetic field respectively. Among these two resonances the former has been suggested as the most promising and at the same time experimentally feasible that can be used to reach the universal regime being s -wave dominated and satisfying the condition $k_F R^* \ll 1$ [72]. Here, $k_F = \sqrt{\frac{2mN\omega_L}{\hbar}}$ is the Fermi momentum where m , N is the mass and particle number of the relevant component while R^* is the range parameter. In contrast, the latter FR which is also the narrower of the two, suffers from effective range corrections that in turn alter the physics of polarons [15] resulting in enhanced lifetimes of these

Table B1. Effective range parameter, $k_F R^*$, calculated for a ^6Li - ^{40}K mixture showcasing the validity of the single-channel 1D model Hamiltonian used in the main text. The experimental axial trapping frequency is $\omega_\parallel \equiv \omega_L = 2\pi \times 75 \text{ Hz}$ [69], and the range parameter at resonance reads $R^* = 1.43 \times 10^{-7}$ [15]. Note also that $m_L = 6 \times 9.96 \times 10^{-27}$ and $m_K = 40/6 m_L$.

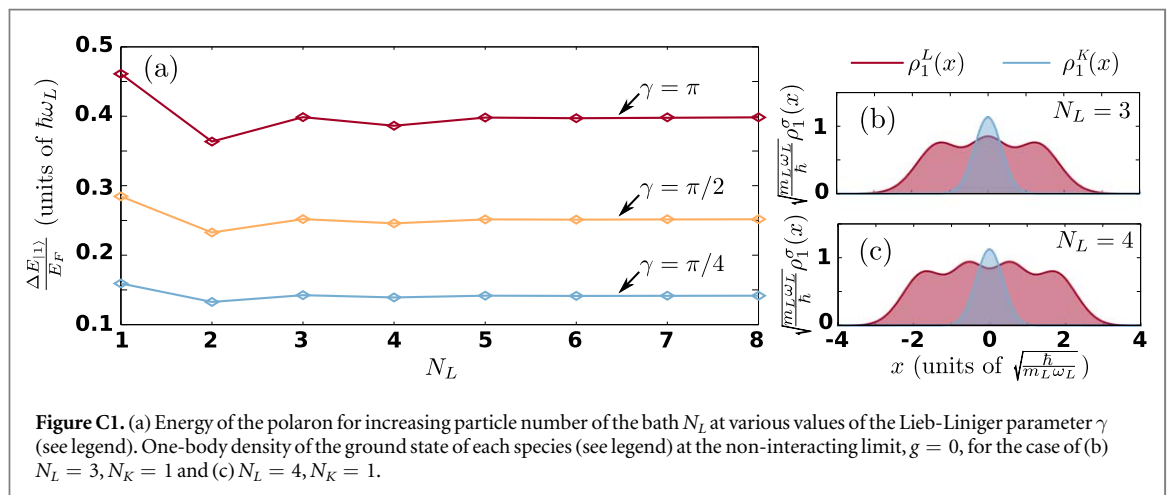
Effective range		
Number of particles	$(k_F R^*)_{^6\text{Li}}$	$(k_F R^*)_{^{40}\text{K}}$
$N = 1$	0.0426	0.0852
$N = 2$	0.0603	0.1206
$N = 5$	0.0953	0.1906
$N = 8$	0.1205	0.241

repulsive states. In order to showcase that the model Hamiltonian used herein accurately describes the dynamics of repulsive fermi polarons below we provide estimates of the effective range parameter $k_F R^*$ for the narrower FR at 155 G, and for all the cases investigated in the main text. Our results are summarized in table B1. In particular, in order to calculate the effective range correction $k_F R^*$ for the different cases studied in this work, we use as a range parameter $R^* = 2700 \times 5.29 \times 10^{-11}$ m [15], and as a characteristic axial trapping frequency $\omega_{\parallel} \equiv \omega_L = 2\pi \times 75$ Hz [69]. Note also that $m_L = 6 \times 1.66 \times 10^{-27}$ kg and $m_K = 40/6 m_L$. As it can be clearly seen in all cases of interest here (see the boldface values in table B1), $k_F R^*$ is sufficiently smaller than unity. The latter verifies the applicability of the model used and thus the universal behavior, by means of a negligible R^* , of the physics addressed herein. Finally, we remark that for the second fermionic mixture considered in this work, namely the ${}^6\text{Li}$ - ${}^{173}\text{Yb}$ one, it is predicted that such a mixture features broad FRs and thus the model Hamiltonian used again accurately describes the polaron dynamics [85].

Appendix C. Polaron energy versus the particle number of the bath

Let us investigate the behavior of the polaron energy while approaching the MB limit by increasing the number of the bath particles N_L . It is known [40] that the polaron energy scales proportionally to the square root of the bath particle number, i.e. $\Delta E_{|1\rangle}(g) = E_{|1\rangle}(g) - E_{|\Psi_0(0)\rangle}(g) \propto \sqrt{N_L}$. Here, $E_{|1\rangle}(g)$ [$E_{|\Psi_0(0)\rangle}$] denotes the ground state energy of the interacting (non-interacting) $(N_L + 1)$ -body system. In order to obtain a non-divergent polaron energy $\Delta E_{|1\rangle}(g)$ for $N_L \rightarrow \infty$ we rescale it with the corresponding Fermi energy $E_F = N_L \hbar \omega_L$. Note that in the presence of a harmonic trap E_F refers to the energy of the energetically lowest unoccupied single-particle eigenstate [40]. Therefore, the rescaled polaron energy is proportional to $\Delta E_{|1\rangle}/E_F \propto 1/\sqrt{N_L}$. Moreover, in order to obtain a dimensionless interaction parameter that scales similarly to the polaron energy with respect to N_L we define the so-called Lieb-Liniger parameter $\gamma = \frac{\pi m g}{\hbar^2 k_F}$, where $k_F = \sqrt{2m_L E_F}/\hbar$ is the Fermi momentum. The interaction interval used in the main text is $0 < g < 5$ which corresponds to $0 < \gamma < \frac{3\pi}{2}$.

To provide some representative examples of the convergence of $\Delta E_{|1\rangle}/E_F$ for increasing N_L and fixed γ we choose the values $\gamma = \frac{\pi}{4}, \frac{\pi}{2}, \pi$, see figure C1(a). As it can be seen, for $N_L \geq 5$ the polaron energy exhibits a saturated behavior. The latter observation essentially indicates that the particle number of the bath $N_L = 5$ captures adequately the behavior of the Fermi polaron at the MB level. On the other hand, for smaller particle numbers i.e. $N_L \leq 4$ we observe that $\Delta E_{|1\rangle}/E_F$ depends strongly on N_L . This effect can be attributed to the behavior of the one-body density of the bath which exhibits a local maximum (minimum) in the vicinity of $x = 0$ for an odd (even) particle number N_L . Since the impurity is localized around $x = 0$ the scaled interaction energy is larger for an odd compared to an even particle number of the bath. To provide a concrete example in figures C1 (b), (c) we demonstrate the ground state one-body densities of each species at the non-interacting limit for the systems $N_L = 3, N_K = 1$ and $N_L = 4, N_K = 1$ respectively. We observe that in the case of $N_L = 3, N_K = 1$ the densities of the ${}^6\text{Li}$ and ${}^{40}\text{K}$ possess a larger spatial overlap compared to the case of $N_L = 4, N_K = 1$. As a consequence the corresponding interaction energy between the species is larger for $N_L = 3$ than the $N_L = 4$ system. In turn, this explains the larger rescaled energy of the polaron in the case of an odd than an even particle number of the bath.



Appendix D. Remarks on the MB numerical method: ML-MCTDHX

To address the MB dynamics during rf spectroscopy we rely on the Multi-Layer Multi-Configuration Time-Dependent Hartree method for Atomic Mixtures [80] (ML-MCTDHX). The main distinctive features of the employed method are outlined below. First, within ML-MCTDHX the total MB wavefunction is expanded with respect to a time-dependent and variationally optimized MB basis. This allows us to achieve convergence by employing a drastically reduced number of time-dependent basis states compared to methods relying on a time-independent basis. Second, the symmetry of the atomic species being either bosonic or fermionic is explicitly employed by considering the expansion of the MB wavefunction in terms of the number-states spanned by the underlying time-dependent basis. Finally, the multi-layer ansatz for the total wavefunction is based on a coarse-graining cascade, where strongly correlated degrees of freedom are grouped together and treated as subsystems mutually coupling to each other. The latter enables us to tailor the employed MB wavefunction ansatz according to the specific intra- and interspecies correlation patterns emanating in different setups. The latter renders ML-MCTDHX a versatile tool for simulating the dynamics of multispecies systems. In particular this work employs a reduction of the ML-MCTDHX method for mixtures of two fermionic species one of which possesses an additional spin-1/2 degree of freedom.

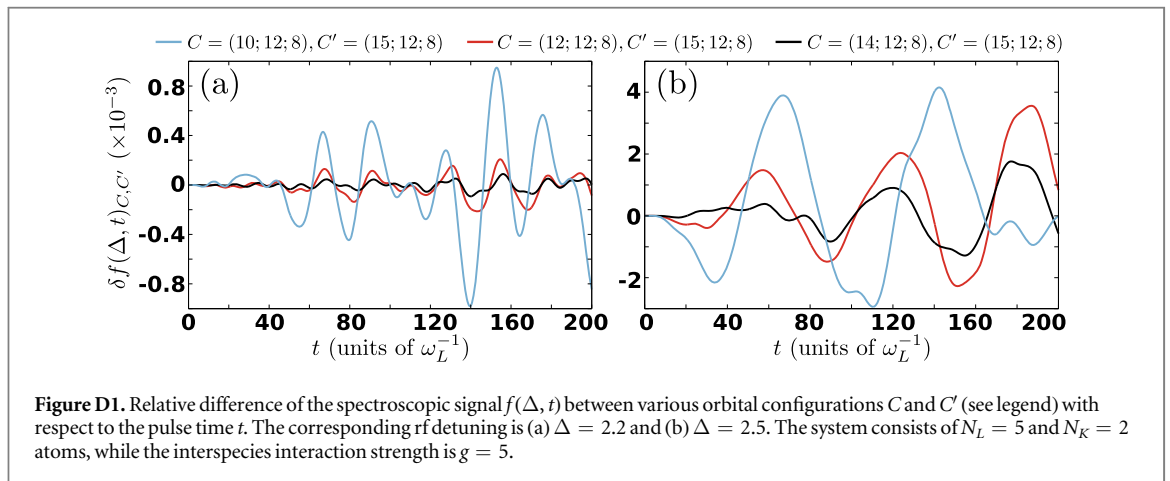
For our implementation we have used a harmonic oscillator DVR, resulting after a unitary transformation of the commonly employed basis of harmonic oscillator eigenfunctions, as a primitive basis for the spatial part of the SPFs. To study the dynamics of the spinor system we propagate the wavefunction of equation (2) by utilizing the appropriate Hamiltonian within the ML-MCTDHX equations of motion.

To infer about convergence we demand that all the observables of interest (f , \mathcal{F}) do not change within a given relative accuracy (see also below). In order to achieve the above criterion we increase the DVR basis states, \mathcal{M} , as well as the number of species wavefunctions, M , and SPFs m^σ (with $\sigma = A, B$ denoting each of the species). More specifically, for the two different mixtures presented in the main text namely the ${}^6\text{Li}$ - ${}^{40}\text{K}$ and the ${}^6\text{Li}$ - ${}^{173}\text{Yb}$ mixture the number of grid points used are $\mathcal{M} = 80$ and $\mathcal{M} = 150$ respectively. Additionally, for the cases investigated in the main text i.e. $N_L = 5$ and $N_K = 1$, $N_L = 5$ and $N_K = 2$, $N_L = 8$ and $N_K = 2$, and $N_L = 5$ and $N_{\text{Yb}} = 2$, the corresponding configurations satisfying the aforementioned convergence criterion are $C = (6; 10; 6)$, $C = (15; 12; 8)$, $C = (14; 14; 8)$ and $C = (15; 10; 10)$ respectively. The orbital configuration C follows the notation $C = (M; m^A; m^B)$. It is important to note here that e.g. for the case of $N_L = 5$ and $N_K = 1$, with $C = (6; 10; 6)$ the truncated Hilbert space for the corresponding rf simulation involves 2864 coefficients, while for an exact diagonalization treatment it would require the inclusion of 1.9232×10^9 coefficients rendering the latter simulation infeasible. The same result also holds for all the cases explored in the main text. E.g. for $N_L = 5$ and $N_K = 2$ with $C = (15; 12; 8)$ the inclusion of 14.125 coefficients is needed within the ML-MCTDHX approach, while the number of coefficients that should be taken into account using exact diagonalization is 7.5966×10^{10} . Finally, for the ${}^6\text{Li}$ - ${}^{173}\text{Yb}$ mixture with $N_L = 5$, $N_{\text{Yb}} = 2$ and $C = (15; 10; 10)$ the corresponding coefficients within ML-MCTDHX are 7680 while the inclusion of 6.6111×10^{12} coefficients is needed for a full configuration interaction treatment.

Finally, let us also briefly showcase the numerical convergence of our results with respect to an increasing number of species functions M . We employ e.g. the time-evolution of the spectroscopic signal, $f(\Delta, t)_C$, at a certain rf-detuning Δ for the system consisting of $N_L = 5$ and $N_K = 2$ fermions. To infer about convergence we calculate the deviation of $f(\Delta, t)_{C'}$ between the $C' = (15; 12; 8)$ and other numerical configurations $C = (M; 12; 8)$, namely

$$\delta f(\Delta, t)_{C,C'} = f(\Delta, t)_{C'} - f(\Delta, t)_C. \quad (\text{D1})$$

Figure D1 presents $\delta f(\Delta, t)_{C,C'}$ for the case of $N_L = 5$ and $N_K = 2$ at $g = 5$ when considering a pulse characterized by a detuning $\Delta = 2.2$ and $\Delta = 2.5$ respectively. Recall that these values of Δ lie in the vicinity of the first two energetically lowest lying resonances of the rf spectrum discussed in the main text, see also figure 1(c). Evidently, a systematic convergence of $\delta f(\Delta, t)_{C,C'}$ is achieved for both $\Delta = 2.2$ and $\Delta = 2.5$. For instance, comparing $\delta f(\Delta, t)_{C,C'}$ at $\Delta = 2.2$ between the $C' = (15; 12; 8)$ and $C = (14; 12; 8)$ ($C = (10; 12; 8)$) approximations we can infer that the corresponding relative difference lies below 0.01% (0.1%) throughout the evolution, see figure D1(a). Also, as illustrated in figure D1(b) for $\Delta = 2.5$ the corresponding $\delta f(\Delta, t)_{C,C'}$ between the configurations $C' = (15; 12; 8)$ and $C = (14; 12; 8)$ ($C = (10; 12; 8)$) shows a deviation which reaches a maximum value of the order of 0.15% (0.4%) at large pulse times. Finally, we note that a similar analysis has been performed for all other rf-detunings Δ and interspecies interaction strengths shown in the main text and found to be converged (results not shown here for brevity).



ORCID iDs

S I Mistakidis  <https://orcid.org/0000-0002-5118-5792>

References

- [1] Landau L D 1957 *Sov Phys JETP* **3** 920
- [2] Gershenson M E, Podzorov V and Morpurgo A F 2006 *Rev. Mod. Phys.* **78** 973
- [3] Dagotto E 1994 *Rev. Mod. Phys.* **66** 763
- [4] Bardeen J, Baym G and Pines D 1967 *Phys. Rev.* **156** 207
- [5] Baym G and Pethick C 1991 *Landau Fermi-Liquid Theory: Concepts and Applications* (New York: Wiley)
- [6] Deibel C and Dyakonov V 2010 *Rep. Prog. Phys.* **73** 096401
- [7] Davydov A 1973 *J. Theor. Biol.* **38** 559
- [8] Pęcak D, Gajda M and Sowiński T 2016 *New J. Phys.* **18** 013030
- [9] Schirotzek A, Wu C-H, Sommer A and Zwierlein M W 2009 *Phys. Rev. Lett.* **102** 230402
- [10] Nascimbène S, Navon N, Jiang K J, Tarruell L, Teichmann M, McKeever J, Chevy F and Salomon C 2009 *Phys. Rev. Lett.* **103** 170402
- [11] Punk M, Dumitrescu P T and Zwirger W 2009 *Phys. Rev. A* **80** 053605
- [12] Chevy F and Mora C 2010 *Rep. Prog. Phys.* **73** 112401
- [13] Zhang Y, Ong W, Arakelyan I and Thomas J E 2012 *Phys. Rev. Lett.* **108** 235302
- [14] Tajima H and Uchino S 2018 *New J. Phys.* **20** 073048
- [15] Kohstall C, Zaccanti M, Jag M, Trenkwalder A, Massignan P, Bruun G M, Schreck F and Grimm R 2012 *Nature* **485** 615
- [16] Scazza F, Valtolina G, Massignan P, Recati A, Amico A, Burchianti A, Fort C, Inguscio M, Zaccanti M and Roati G 2017 *Phys. Rev. Lett.* **118** 083602
- [17] Koschorreck M, Pertot D, Vogt E, Fröhlich B, Feld M and Köhl M 2012 *Nature* **485** 619
- [18] Cui X and Zhai H 2010 *Phys. Rev. A* **81** 041602(R)
- [19] Pilati S, Bertaina G, Giorgini S and Troyer M 2010 *Phys. Rev. Lett.* **105** 030405
- [20] Massignan P and Bruun G 2011 *Eur. Phys. J. D* **65** 83
- [21] Schmidt R and Enss T 2011 *Phys. Rev. A* **83** 063620
- [22] Schmidt R, Enss T, Pietilä V and Demler E 2012 *Phys. Rev. A* **85** 021602
- [23] Ngampruetikorn V, Levinsen J and Parish M M 2012 *Europhys. Lett.* **98** 30005
- [24] Massignan P, Yu Z and Bruun G M 2013 *Phys. Rev. Lett.* **110** 230401
- [25] Schmidt R, Knap M, Ivanov D A, You J-S, Cetina M and Demler E 2018 *Rep. Prog. Phys.* **81** 024401
- [26] Duine R A and MacDonald A H 2005 *Phys. Rev. Lett.* **95** 230403
- [27] Chang S-Y, Randeria M and Trivedi N 2011 *Proc. Natl Acad. Sci.* **108** 51
- [28] Pekker D, Babadi M, Sensarma R, Zinner N, Pollet L, Zwierlein M W and Demler E 2011 *Phys. Rev. Lett.* **106** 050402
- [29] Sanner C, Su E J, Huang W, Keshet A, Gillen J and Ketterle W 2012 *Phys. Rev. Lett.* **108** 240404
- [30] He L, Liu X-J, Huang X-G and Hu H 2016 *Phys. Rev. A* **93** 063629
- [31] Valtolina G, Scazza F, Amico A, Burchianti A, Recati A, Enss T, Inguscio M, Zaccanti M and Roati G 2017 *Nat. Phys.* **13** 704
- [32] Li W and Cui X 2017 *Phys. Rev. A* **96** 053609
- [33] Koutentakis G M, Mistakidis S I and Schmelcher P 2018 arXiv:1804.07199
- [34] Zöllner S, Bruun G M and Pethick C J 2011 *Phys. Rev. A* **83** 021603(R)
- [35] Parish M M 2011 *Phys. Rev. A* **83** 051603(R)
- [36] Bour S, Lee D, Hammer H-W and Meissner U-G 2015 *Phys. Rev. Lett.* **115** 185301
- [37] Rosch A and Kopp T 1995 *Phys. Rev. Lett.* **75** 1988
- [38] Castella H 1996 *Phys. Rev. B* **54** 17422
- [39] Massignan P, Zaccanti M and Bruun G M 2014 *Rep. Prog. Phys.* **77** 034401
- [40] Wenz A N, Zürn G, Murmann S, Brouzos I, Lompe T and Jochim S 2013 *Science* **342** 457
- [41] Gharashi S E, Yin X Y, Yan Y and Blume D 2015 *Phys. Rev. A* **91** 013620
- [42] Yang C N 1967 *Phys. Rev. Lett.* **19** 1312
- [43] Mathey L, Wang D-W, Hofstetter W, Lukin M D and Demler E 2004 *Phys. Rev. Lett.* **93** 120404
- [44] Leskinen M J, Nummi O H T, Massel F and Torma P 2010 *New J. Phys.* **12** 073044
- [45] Catani J, Lamporesi G, Naik D, Gring M, Inguscio M, Minardi F, Kantian A and Giamarchi T 2012 *Phys. Rev. A* **85** 023623

- [46] Casteels W, Tempere J and Devreese J T 2012 *Phys. Rev. A* **86** 043614
- [47] Doggen E V H and Kinnunen J J 2013 *Phys. Rev. Lett.* **111** 025302
- [48] Mao R, Guan X W and Wu B 2016 *Phys. Rev. A* **94** 043645
- [49] Parisi L and Giorgini S 2017 *Phys. Rev. A* **95** 023619
- [50] Pastukhov V 2017 *Phys. Rev. A* **96** 043625
- [51] Volosniev A G and Hammer H W 2017 *Phys. Rev. A* **96** 031601
- [52] Mistakidis S I, Katsimiga G C, Koutentakis G M, Busch T and Schmelcher P 2018 arXiv:1811.10702
- [53] Mistakidis S I, Volosniev A G, Zinner N T and Schmelcher P 2018 arXiv:1809.01889
- [54] Klein A and Fleischhauer M 2005 *Phys. Rev. A* **71** 033605
- [55] Recati A, Fuchs J N, Peça C S and Zwerger W 2005 *Phys. Rev. A* **72** 023616
- [56] Mora C and Chevy F 2010 *Phys. Rev. Lett.* **104** 230402
- [57] Yu Z, Zöllner S and Pethick C J 2010 *Phys. Rev. Lett.* **105** 188901
- [58] Yu Z and Pethick C J 2012 *Phys. Rev. A* **85** 063616
- [59] Kinnunen J J and Bruun G M 2015 *Phys. Rev. A* **91** 041605(R)
- [60] Hu H, Mulkerin B C, Wang J and Liu X-J 2018 *Phys. Rev. A* **98** 013626
- [61] Dehkharghani A S, Volosniev A G and Zinner N T 2018 *Phys. Rev. Lett.* **121** 080405
- [62] Grusdt F, Astrakharchik G E and Demler E 2017 *New J. Phys.* **19** 103035
- [63] Camacho-Guardian A and Bruun G M 2018 *Phys. Rev. X* **8** 031042
- [64] Naidon P 2018 *J. Phys. Soc. Jpn.* **87** 043002
- [65] Camacho-Guardian A, Ardila L A P, Pohl T and Bruun G M 2018 *Phys. Rev. Lett.* **121** 013401
- [66] Gupta S, Hadzibabic Z, Zwierlein M W, Stan C A, Dieckmann K, Schunck C H, van Kempen E G M, Verhaar B J and Ketterle W 2003 *Science* **300** 1723
- [67] Regal C A and Jin D S 2003 *Phys. Rev. Lett.* **90** 230404
- [68] Cetina M et al 2016 *Science* **354** 96
- [69] Bergschneider A, Klinkhamer V M, Becher J H, Klemt R, Zürn G, Preiss P M and Jochim S 2018 *Phys. Rev. A* **97** 063613
- [70] Chen J, Schurer J M and Schmelcher P 2018 *Phys. Rev. Lett.* **121** 043401
- [71] Horodecki R, Horodecki P, Horodecki M and Horodecki K 2009 *Rev. Mod. Phys.* **81** 865
- [72] Tiecke T G, Goosen M R, Ludewig A, Gensemer S D, Kraft S, Kockelmans S J J M F and Walraven J T M 2010 *Phys. Rev. Lett.* **104** 053202
- [73] Naik D, Trenkwalder A, Kohstall C, Spiegelhalder F M, Zaccanti M, Hendl G, Schreck F, Grimm R, Hanna T M and Julienne P S 2011 *Eur. Phys. J. D* **65** 55
- [74] Cetina M, Jag M, Lous R S, Walraven J T M, Grimm R, Christensen R S and Bruun G M 2015 *Phys. Rev. Lett.* **115** 135302
- [75] Olshanii M 1998 *Phys. Rev. Lett.* **81** 938
- [76] Chin C, Grimm R, Julienne P and Tiesinga E 2010 *Rev. Mod. Phys.* **82** 1225
- [77] Murmann S, Deuretzbacher F, Zürn G, Bjerlin J, Reimann S M, Santos L, Lompe T and Jochim S 2015 *Phys. Rev. Lett.* **115** 215301
- [78] Deuretzbacher F and Santos L 2017 *Phys. Rev. A* **96** 013629
- [79] Alon O E, Streltsov A I and Cederbaum L S 2007 *J. Chem. Phys.* **127** 154103
- [80] Cao L, Bolsinger V, Mistakidis S I, Koutentakis G M, Krönke S, Schurer J M and Schmelcher P 2017 *J. Chem. Phys.* **147** 044106
- [81] Katsimiga G C, Koutentakis G M, Mistakidis S I, Kevrekidis P G and Schmelcher P 2017 *New J. Phys.* **19** 073004
- [82] Mistakidis S I, Katsimiga G C, Kevrekidis P G and Schmelcher P 2018 *New J. Phys.* **20** 043052
- [83] Anderson P W 1967 *Phys. Rev. Lett.* **18** 1049
- [84] Petrov D S 2003 *Phys. Rev. A* **67** 010703(R)
- [85] Hara H, Takasu Y, Yamaoka Y, Doyle J M and Takahashi Y 2011 *Phys. Rev. Lett.* **106** 205304
- [86] Khramov A, Hansen A, Dowd W, Roy R J, Makrides C, Petrov A, Kotochigova S and Gupta S 2014 *Phys. Rev. Lett.* **112** 033201
- [87] Wille E et al 2008 *Phys. Rev. Lett.* **100** 053201
- [88] Touchard F et al 1982 *Phys. Lett. B* **108** 169
- Bendali N, Duong H T and Vialle J L 1981 *J. Phys. B: At. Mol. Phys.* **14** 4231
- Arimondo E, Inguscio M and Violino P 1977 *Rev. Mod. Phys.* **49** 31
- [89] Serwane F, Zürn G, Lompe T, Ottenstein T B, Wenz A N and Jochim S 2011 *Science* **332** 336
- [90] Bloch I, Dalibard J and Zwerger W 2008 *Rev. Mod. Phys.* **80** 885

4.2.2 Quench Dynamics and Orthogonality Catastrophe of Bose Polarons

Quench Dynamics and Orthogonality Catastrophe of Bose PolaronsS. I. Mistakidis,¹ G. C. Katsimiga,¹ G. M. Koutentakis,^{1,2} Th. Busch,³ and P. Schmelcher^{1,2}¹*Center for Optical Quantum Technologies, Department of Physics, University of Hamburg, Luruper Chaussee 149, 22761 Hamburg, Germany*²*The Hamburg Centre for Ultrafast Imaging, Universität Hamburg, Luruper Chaussee 149, 22761 Hamburg, Germany*³*Quantum Systems Unit, OIST Graduate University, Onna, Okinawa 904-0495, Japan*

(Received 26 November 2018; published 8 May 2019)

We monitor the correlated quench induced dynamical dressing of a spinor impurity repulsively interacting with a Bose-Einstein condensate. Inspecting the temporal evolution of the structure factor, three distinct dynamical regions arise upon increasing the interspecies interaction. These regions are found to be related to the segregated nature of the impurity and to the Ohmic character of the bath. It is shown that the impurity dynamics can be described by an effective potential that deforms from a harmonic to a double-well one when crossing the miscibility-immiscibility threshold. In particular, for miscible components the polaron formation is imprinted on the spectral response of the system. We further illustrate that for increasing interaction an orthogonality catastrophe occurs and the polaron picture breaks down. Then a dissipative motion of the impurity takes place leading to a transfer of energy to its environment. This process signals the presence of entanglement in the many-body system.

DOI: [10.1103/PhysRevLett.122.183001](https://doi.org/10.1103/PhysRevLett.122.183001)

Introduction.—A valuable asset of ultracold atoms is the opportunity to track the real time dynamics of quantum many-body (MB) systems such as multicomponent quantum gases composed of different atomic species [1] or different hyperfine states of the same species [2,3]. In particular, the realization of highly population imbalanced atomic gases with tunable interactions [4–15] has already led to fundamentally new insights regarding Fermi [16–29] and very recently Bose polarons [30–40]. In this latter context the observation of coherent attractive and repulsive quasiparticles [41], even in the strongly interacting regime [42], refueled the scientific interest towards understanding their underlying dynamics.

Most of the theoretical studies regarding Bose polarons have been focused on a mean-field [43–46] description and on the Fröhlich model [47–52]. Only very recently theories going beyond the Fröhlich paradigm [53–59] and including higher-order correlations [60,61] have been developed, thereby allowing for the investigation of Bose polarons also in the intermediate and strong interaction regime. However, current experiments realized both in one [32–34] and three dimensions [41,42] probed the non-equilibrium dynamics of Bose polarons and necessitated the presence of higher-order correlations for an adequate description of the observed dynamics. Thus, the interplay of higher-order correlations during the out-of-equilibrium dynamics of bosonic impurities immersed in a Bose-Einstein condensate (BEC) is a key ingredient for advancing our understanding of the dynamics of such MB systems. On the theoretical side efforts concerning the nonequilibrium dynamics of Bose polarons [62–67] are

quite recent and remarkably only a few of them include quantum fluctuations [67–69].

In this Letter, motivated by current experiments [32,41,42,70,71] we explore the interaction quench dynamics of a spinor impurity coupled to a BEC. Focusing on repulsively interacting multicomponent bosonic systems in a one-dimensional (1D) harmonic trap, we showcase the dynamical dressing of the impurity when all particle correlations are taken into account. Three distinct dynamical regions with respect to the interspecies interaction strength are identified and captured by the structure factor, which is the spin polarization (contrast) of the impurity [72]. These regions are shown to be related to the miscible and immiscible character of the system and are indicative of the Ohmic character of the bath [66,73]. Their extent can be manipulated by adjusting the intraspecies repulsion of the BEC alias bath or by changing its particle number, thereby addressing the few to many-body crossover. This tunability is of significant importance since it leads to a longevity of the polaron and thus facilitates the control of quasiparticles. One of our key results consists of the interpretation of the Bose polaron dynamics in terms of an effective potential. The latter is found to be an adequate approximation in the weakly interacting case assuming the Thomas-Fermi approximation for the bath and generalizes the results of Ref. [74]. We demonstrate that deep in the immiscible phase, where entanglement is strong, the Bose polaron ceases to exist due to the orthogonality catastrophe [75,76]. In this strong interaction regime a dissipative motion of the impurity is observed accompanied by the population of several lower-lying excited states of the effective potential.

The latter involves now the single-particle density of the MB bath and provides only a very approximate picture of the impurity dynamics since entanglement is significant. This mechanism of dissipation in turn leads to a transfer of energy from the impurity to its environment also leading to a substantial entanglement in the system.

Model.—We consider a system consisting of a single impurity of mass m_I having an additional spin-1/2 degree of freedom. The impurity is in the superposition $|\Psi_S\rangle = \alpha|\uparrow\rangle + \beta|\downarrow\rangle$, with α, β denoting the different weights used that account for a partial or complete dressing of the single impurity. The impurity is immersed in a 1D harmonically confined BEC of $N_B = 100$ repulsively interacting atoms of mass m_B and trap frequency $\omega_B = \omega_I = 1.0$. The MB Hamiltonian of the system reads

$$\hat{H} = \hat{H}_B^0 + \sum_a \hat{H}_a^0 + \hat{H}_{BB} + \hat{H}_{BI}. \quad (1)$$

Here, $\hat{H}_B^0 = \int dx \hat{\Psi}_B^\dagger(x) [-(\hbar^2/2m_B)(d^2/dx^2) + \frac{1}{2}m_B\omega_B^2 x^2] \hat{\Psi}_B(x)$ is the Hamiltonian describing the motion of the BEC that serves as a bath for the impurity atom. $\hat{H}_a^0 = \int dx \hat{\Psi}_a^\dagger(x) [-(\hbar^2/2m_I)(d^2/dx^2) + \frac{1}{2}m_I\omega_I^2 x^2] \hat{\Psi}_a(x)$ ($a = \{\uparrow, \downarrow\}$) is the corresponding Hamiltonian for the impurity atom. In both cases $\hat{\Psi}_i(x)$ is the bosonic field-operator of either the majority ($i = B$) or the impurity ($i = a$) atoms. We focus on the case of equal masses $m_B = m_I = m$ [41]. $\hat{H}_{BB} = g_{BB} \int dx \hat{\Psi}_B^\dagger(x) \hat{\Psi}_B^\dagger(x) \hat{\Psi}_B(x) \hat{\Psi}_B(x)$ accounts for the contact intraspecies interaction of strength $g_{BB} > 0$ in the BEC component. $\hat{H}_{BI} = g_{BI} \int dx \hat{\Psi}_B^\dagger(x) \hat{\Psi}_\uparrow^\dagger(x) \hat{\Psi}_\uparrow(x) \hat{\Psi}_B(x)$ denotes the interaction between the bath and the part of the impurity being in the spin- \uparrow state, characterized by an effective strength $g_{BI} > 0$, while having a noninteracting spin- \downarrow component. Similar setups have been used in the context of fermionic impurities mostly focusing on the attractive side of interactions [77–81]. The multicomponent system is initially prepared in its ground-state configuration for fixed g_{BB} and $g_{BI} = 0$. We note that our results remain valid also for the case of weak interspecies interactions. Such an initial state preparation is experimentally realizable by means of radiofrequency spectroscopy [41,42,55,71,82] and Ramsey interferometry [71].

To derive the nonequilibrium dynamics of the spinor impurity, we use a nonperturbative method, namely, the multilayer multiconfiguration time-dependent Hartree method for atomic mixtures (ML-MCTDHX). Our method rests on expanding the MB wave function with respect to a variationally optimized time-dependent basis that spans the optimal subspace of the Hilbert space at each time instant. Its multilayer ansatz for the total wave function allows us to account for all intra- and interspecies correlations. In our case the latter are found to be more important than the former [83,84].

Our starting point is the ground state, $|\Psi_{BI}^0\rangle$, obeying the eigenvalue equation $(\hat{H} - \hat{H}_{BI})|\Psi_{BI}^0\rangle = E_0|\Psi_{BI}^0\rangle$, with E_0 denoting the corresponding eigenenergy. We then abruptly switch on at $t = 0$ the interspecies repulsion g_{BI} , and let the system evolve dynamically. The MB wave function following the quench reads

$$|\Psi(t)\rangle = \alpha e^{-i\hat{H}t/\hbar} |\Psi_{BI}^0\rangle |\uparrow\rangle + \beta e^{-iE_0t/\hbar} |\Psi_{BI}^0\rangle |\downarrow\rangle. \quad (2)$$

Results and discussion.—To investigate the nonequilibrium dynamics of the spinor impurity we first consider the case where the impurity is in an equal superposition, namely, $\alpha = \beta = (1/\sqrt{2})$, and determine the time evolution of the total spin polarization $|\langle \hat{S}(t) \rangle| = \sqrt{\langle \hat{S}_x(t) \rangle^2 + \langle \hat{S}_y(t) \rangle^2}$. Here, $\langle \hat{S}_z(t) \rangle = \langle \hat{S}_z(t=0) \rangle = 0$ since $[\hat{S}_z, \hat{H}] = 0$, while $\hat{S}_i = \int dx \sum_{ab} \hat{\Psi}_a^\dagger(x) \sigma_{ab}^i \hat{\Psi}_b(x)$ is the spin operator in the i th direction ($i = x, y, z$) and σ_{ab}^i are the Pauli matrices. This quantity is directly related to the so-called Ramsey response [71], namely, the structure factor that is the time-dependent overlap between the interacting and the noninteracting states $|\langle \Psi_{BI}^0 | e^{iE_0t/\hbar} e^{-i\hat{H}t/\hbar} | \Psi_{BI}^0 \rangle|^2 = |\langle \hat{S}(t) \rangle|^2 = |S(t)|^2$ [72]. $S(t) = |S(t)| e^{i\phi}$, with $\text{atan}\phi = \langle \hat{S}_x \rangle / \langle \hat{S}_y \rangle$, and the Hamiltonian, \hat{H} , after the quench, when the impurity is dressed, is given by Eq. (1).

Figures 1(a)–1(c) illustrate the evolution of the structure factor $|S(t)|$ (contrast) upon increasing the interspecies repulsion g_{BI} for different g_{BB} interactions and also for smaller system sizes. In all cases, three distinct dynamical regions can be inferred, namely, R_I , R_{II} , and R_{III} , which,

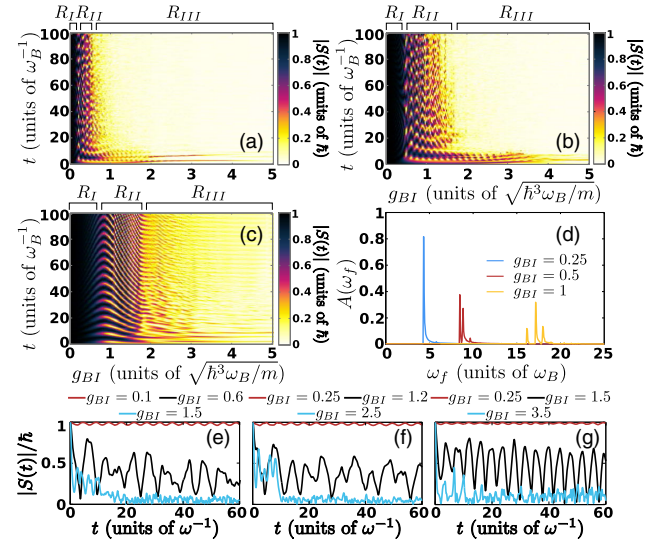


FIG. 1. Evolution of the contrast, $|S(t)|$, upon increasing g_{BI} for (a) $g_{BB} = 0.2$ and (b) $g_{BB} = 0.5$ with $N_B = 100$ and $N_I = 1$. (c) same as (b) but for $N_B = 10$. (d) Excitation spectrum, $A(\omega_f)$, indicating the emergent polaronic peaks for distinct g_{BI} (see legend) and $g_{BB} = 0.5$. (e),(f),(g) illustrate $|S(t)|$ of (a),(b),(c) for different g_{BI} (see legend).

e.g., for $g_{BB} = 0.5$ correspond to $0 \leq g_{BI}^{R_I} < 0.5$, $0.5 \leq g_{BI}^{R_{II}} < 1.65$, and $1.65 \leq g_{BI}^{R_{III}} < 5.0$, respectively. For short times a descent of $|S(t)|$ is observed [71,104]; see Figs. 1(e)–1(g), being sharper for larger g_{BI} . This descent occurs independently of the value of the intraspecies repulsion g_{BB} , compare Figs. 1(e) and 1(f). For larger evolution times $|S(t)|$ performs oscillations that become more pronounced upon increasing g_{BI} within R_I and exhibit a decaying amplitude in R_{II} . In contrast, entering R_{III} $|S(t)|$ exhibits an exponential decay indicating the orthogonality catastrophe. The degree of damping of $|S(t)|$ within R_I , R_{II} , and R_{III} is indicative of a sub-Ohmic, Ohmic, and super-Ohmic behavior of the bath, respectively (see also below). Comparing the temporal evolution of $|S(t)|$ for $g_{BB} = 0.2$ [Fig. 1(a)] to the one for $g_{BB} = 0.5$ [Fig. 1(b)] we observe that the extent of the above-mentioned dynamical regions (R_I , R_{II} , R_{III}) can be manipulated by adjusting g_{BB} . In particular, for larger g_{BB} an enhanced region of finite contrast that enters deeper into the regime of repulsive interspecies interactions can be achieved. This behavior is supported upon decreasing the number of bath particles to $N_B = 10$ [Fig. 1(c)]. In the latter few-body scenario coherent oscillations of $|S(t)|$ are observed [see Fig. 1(c) for $0.8 < g_{BI} < 1.8$] leading to a smoothly decreasing contrast as g_{BI} increases [105]. The aforementioned dynamics takes equally place when the initial superposition state of the spinor impurity involves different weights for each spinor component. This fact can be understood by analytically calculating $|\langle \hat{S}(t) \rangle|_{\alpha,\beta}$ when considering different weights α and β . Indeed, it holds $|\langle \hat{S}(t) \rangle|_{\alpha,\beta} = \sqrt{4\alpha^2\beta^2|S(t)|^2 + (|\alpha|^2 - |\beta|^2)^2}$, where $|S(t)|$ stems from the case $\alpha = \beta = 1/\sqrt{2}$.

As expected, the energy spectrum of the impurity is changed upon applying an interaction quench [81]. To quantify this we determine the Fourier transform of $S(t)$. At low impurity densities and weak interspecies interactions $S(t)$ is known to be proportional to the so-called spectral function of quasiparticles $A(\omega_f) = (1/\pi)\text{Re}\{\int_0^\infty dt e^{i\omega_f t} S(t)\}$ [71,72,81,106]. Figure 1(d) illustrates $A(\omega)$ for different interspecies repulsions ranging from small ($g_{BI}^{R_I} = 0.25$) to intermediate ($g_{BI}^{R_{II}} = 0.5$) and large ($g_{BI}^{R_{III}} = 1.0$) interactions, respectively. The observed peak at small g_{BI} located at $\omega = 4.435$ corresponds to the long-time evolution of a well-defined repulsive Bose polaron. In R_{II} two dominant peaks are imprinted in $A(\omega_f)$ centered at $\omega_1 = 8.482$ and $\omega_2 = 8.859$, respectively. These two peaks correspond to a well-defined quasiparticle dressed, for higher frequencies, by higher-order excitations of the BEC. Figures 2(a) and 2(c) depict the evolution of the impurity's one-body density, $\rho_\uparrow^{(1)}(x) = \langle \Psi(t) | \hat{\Psi}_\uparrow^\dagger(x) \hat{\Psi}_\uparrow(x) | \Psi(t) \rangle$, for small and intermediate values of g_{BI} . The observed out-of-equilibrium dynamics of the spinor impurity in both regions R_I and R_{II}

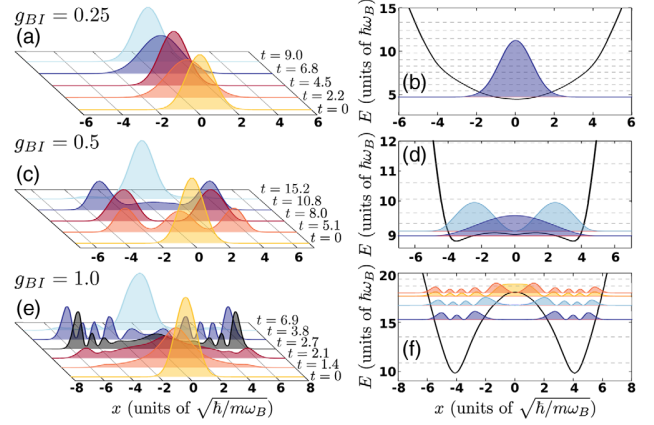


FIG. 2. Selected time instants during evolution of the impurity's one-body density for (a) $g_{BI} = 0.25$, (c) $g_{BI} = 0.5$, and (e) $g_{BI} = 1.0$ illustrating its dynamical dressing. Effective potential and example densities of the corresponding impurity eigenstates for the aforementioned (b) small, (d) intermediate, and (f) large g_{BI} values. Notice that the eigenenergies of V_{eff} are slightly shifted with respect to the polaronic energies obtained within the MB approach [see also Fig. 1(d) and the discussion in the main text]. In all cases dashed gray lines correspond to the energy levels of the effective potential.

can be well approximated by the dynamics in an effective potential. The latter is obtained by considering the bosonic bath as a static potential superimposed to the external harmonic trapping of the impurity, namely,

$$V_{\text{eff}} = \frac{1}{2} m_B \omega_B^2 x^2 + g_{BI} \rho_B^{(1)}(x), \quad (3)$$

where $\rho_B^{(1)}(x)$ is the single-particle density of the BEC at $t = 0$. It is important to stress that V_{eff} does not take into account the renormalization of the quasiparticle's zero-point energy occurring due to its dressing by the bath [68]. This deficit, however, shifts the eigenspectrum of the impurity in a homogeneous manner and, consequently, does not affect its dynamics. For small g_{BI} and fixed g_{BB} the Thomas-Fermi approximation, i.e., $\rho_B^{(1)}(x) = (1/g_{BB})(\mu_B - \frac{1}{2} m_B \omega_B^2 x^2)$ with μ_B being the chemical potential of the bath, is valid and $V_{\text{eff}} = \frac{1}{2} m_B \tilde{\omega}_B^2 x^2 + c$. Then V_{eff} is a parabola shifted by $c \equiv (g_{BI}/g_{BB})\mu_B$ possessing a modified trapping frequency [74], $\tilde{\omega}_B^2 \equiv [1 - (g_{BI}/g_{BB})]\omega_B^2 < \omega_B^2$ [see Fig. 2(b)]. In this case the impurity undergoes a breathing motion [Fig. 2(a)]. Note that the notion of V_{eff} can be extended to higher dimensions. However, relying solely on this approximation we can assess only the frequencies of the emergent dynamical modes i.e., the breathing mode, see also Ref. [84]. Contrary to this an increase of g_{BI} such that $g_{BI} > g_{BB}$ changes this effective potential picture. In this case the system enters the immiscible regime and the initial state involves higher-order excitations in the effective potential due to the stronger interaction of the impurity with the bosonic bath

[Fig. 2(c)]. For these intermediate g_{BI} interactions the impurity density develops a two-hump structure being pushed towards the boundaries of the bath and favoring a phase-separated state with the BEC that resides around the trap center (see the discussion below). It is for these intermediate values, indicating a miscible to an immiscible phase transition, that $V_{\text{eff}}(x)$ begins to deform into a double-well potential [Fig. 2(d)]. The impurity state corresponds then to the ground or the first excited state of this effective potential. Further increase of g_{BI} leads to the appearance of three dominant peaks in the impurity's excitation spectrum. These peaks are centered at $\omega_3 = 16.15$, $\omega_4 = 17.15$, and $\omega_5 = 17.97$, respectively [Fig. 1(d)], and correspond to even higher excited states of the quasiparticle. The relevant dynamical evolution of the impurity [Fig. 2(e)] showcases the deformation of its one-body density, with these higher excited states occupying the third up to sixth excited state of V_{eff} [Fig. 2(f)]. Entering deeper into the immiscible phase [Fig. 1(b)] results in a fast decay of the contrast at short timescales. Consequently, there is no clear polaronic signature in the relevant excitation spectrum, but rather a multitude of states are occupied in this effective double-well picture. This behavior is caused by the dissipative motion of the impurity leading to a partial transfer of its energy to the bath as we shall argue below.

To deepen our understanding of the dynamics of the spinor impurity we next examine the degree of miscibility between the spin components captured by the overlap integral

$$\Lambda^{\uparrow\downarrow}(t) = \frac{[\int dx \rho_{\uparrow}^{(1)}(x, t) \rho_{\downarrow}^{(1)}(x, t)]^2}{\int dx (\rho_{\uparrow}^{(1)}(x, t))^2 \int dx (\rho_{\downarrow}^{(1)}(x, t))^2}. \quad (4)$$

Here, e.g., the one-body density of the spin- \downarrow is $\rho_{\downarrow}^{(1)}(x, t) = \langle \Psi(t) | \Psi_{\downarrow}^{\dagger}(t) \Psi_{\downarrow}(t) | \Psi(t) \rangle$. $\Lambda^{\uparrow\downarrow}(t)$ takes values within the interval $[0, 1]$ with zero (unity) denoting the phase immiscible (miscible) spin components. Evidently, the three distinct dynamical regions captured by $|S(t)|$ leave their fingerprints in $\Lambda^{\uparrow\downarrow}(t)$ [Fig. 3(a)]. Note here that $\rho_{\downarrow}^{(1)}(x, t) = \rho_{\downarrow}^{(1)}(x, 0)$ and, therefore, $\Lambda^{\uparrow\downarrow}(t)$ is directly related to the contrast [see Fig. 1(b)]. Indeed, within R_I the spin components are maximally miscible, while within R_{II} they oscillate between miscibility and immiscibility. Finally, when the orthogonality catastrophe takes place in R_{III} they become immiscible. This spin segregation, in R_{III} , is manifested in the spatiotemporal evolution of $\rho_{\uparrow}^{(1)}(x, t)$ [Fig. 3(b)] [107]. Evidently, $\rho_{\uparrow}^{(1)}(x, t)$ breaks into two density fragments that perform damped oscillations symmetrically placed around the edges of the Thomas Fermi radius of the bath. These damped oscillations essentially indicate that the spin- \uparrow impurity is initially in a highly excited state of $V_{\text{eff}}(x)$ [see Fig. 3(e) for t_1] while

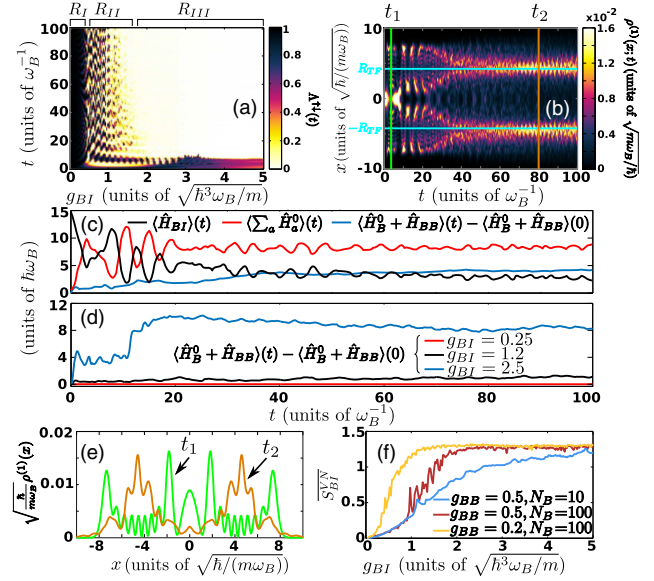


FIG. 3. (a) Evolution of the overlap $\Lambda^{\uparrow\downarrow}(t)$ between the spin- \uparrow and spin- \downarrow states of the impurity atom. (b) One-body density evolution of the spin- \uparrow atom. Horizontal solid lines indicate the position of the Thomas Fermi radius of the bath. (c) Expectation value of the energy (see legend). In both (b),(c) $g_{BI} = 1.7$. (d) Expectation value of the energy of the bath for different g_{BI} (see legend). (e) Density profiles at the time instants marked by the vertical solid lines in (b). (f) Time average of the von-Neumann entropy, \bar{S}_{BI}^{VN} , for increasing g_{BI} . In all cases $N_B = 100$, $N_I = 1$, and $g_{BB} = 0.5$.

for later times, e.g., t_2 , it populates a superposition of lower excited states. We remark here that $\rho_{\uparrow}^{(1)}(x, t)$ depicted in Fig. 3(e) is obtained from the correlated MB calculation while the interpretation in terms of V_{eff} provides an approximate picture of the impurity dynamics for these strong interactions. The latter behavior implies a transfer of energy from the impurity to the BEC environment [Fig. 3(c)] that is beyond the single-particle dynamics provided via V_{eff} . This energy transfer possesses contributions of different magnitude from each term of the above-mentioned superposition leading to different excitations of the BEC and hence it constitutes a manifestation of the entanglement present in the MB system. Since the kinetic energy of the impurity increases during evolution also an increase of its noninteracting energy $\langle \sum_a \hat{H}_a^0 \rangle$ is observed. Contrary to this excess of energy, a decrease of the interaction energy $\langle \hat{H}_{BI} \rangle$ occurs since the impurity is expelled to the edges of the BEC, where $\rho_B^{(1)}(x) \ll \rho_B^{(1)}(0)$. Indeed, $\langle \hat{H}_B^0 + \hat{H}_{BB} \rangle$ increases in the course of the dynamics capturing the transfer of energy from the impurity to the bath. This dissipation mechanism becomes pronounced within R_{III} . Figure 3(d) shows $\langle \hat{H}_B^0 + \hat{H}_{BB} \rangle$ during evolution for different g_{BI} . It becomes evident that within R_I the impurity does not dissipate energy to the bath since the

energy of the latter remains almost constant. However, within the region R_{II} the impurity starts to dissipate energy to the bath and this dissipation rate becomes maximal within R_{III} . This observation further supports the sub-Ohmic, Ohmic, and super-Ohmic behavior of the bath in the different regions. Moreover, to directly expose the presence of entanglement with respect to g_{BI} we invoke the von-Neumann entropy, $S_{BI}^{VN}(t) = -\sum_i \lambda_i(t) \log \lambda_i(t)$ [108]. Note that λ_i 's are the eigenvalues of the N_B -body density matrix $\rho_B^{(N_B)} = -\text{Tr}_I[|\Psi(t)\rangle\langle\Psi(t)|]$. Indeed, the time average \bar{S}_{BI}^{VN} [Fig. 3(f)] shows that the dressed impurity is entangled with the BEC within the regions R_I and R_{II} . By inspecting \bar{S}_{BI}^{VN} we observe that its slope becomes maximal in R_{II} and therefore the same holds for the generation of entanglement, see also Ref. [84]. Most importantly the system becomes strongly entangled within R_{III} , where the polaron ceases to exist, showcasing a plateau of $\bar{S}_{BI}^{VN}(t) \approx 1.2$ for fixed $g_{BB} = 0.5$ and for all $g_{BI} \gtrsim 1.65$.

Conclusions.—The correlated quench-induced dynamics of a trapped spinor impurity repulsively interacting with a BEC has been investigated. Inspecting the evolution of the spin polarization reveals three distinct dynamical regions with respect to the interspecies interaction strength. These regions are inherently related to the segregated nature of the multicomponent system and can be tuned by changing the intraspecies repulsion of the BEC or its particle number thereby addressing the few to many-body crossover. Within these three regions the birth, dynamical deformation, and death (orthogonality catastrophe) of the Bose polaron are unraveled. To interpret the impurity dynamics, an effective potential is derived being an adequate approximation for weak interspecies repulsions. For strong repulsions the system is strongly entangled and the impurity's motion becomes dissipative, transferring a part of its energy to the bath while being pushed to the edges of the BEC. Our results pave the way for manipulating the quasiparticle dynamics. An intriguing perspective for future endeavors is to consider more than one impurity where induced interactions can play an important role.

S. I. M. and P. S. gratefully acknowledge financial support by the Deutsche Forschungsgemeinschaft (DFG) in the framework of the SFB 925 “Light induced dynamics and control of correlated quantum systems.” G. M. K and P. S. acknowledge the support by the excellence cluster “The Hamburg Center for Ultrafast Imaging: Structure, Dynamics and Control of Matter at the Atomic Scale” of the DFG. This work was also supported by the OIST Graduate University.

G. C. K, S. I. M., and G. M. K. contributed equally to this work.

[1] G. Modugno, M. Modugno, F. Riboli, G. Roati, and M. Inguscio, *Phys. Rev. Lett.* **89**, 190404 (2002).

- [2] C. J. Myatt, E. A. Burt, R. W. Ghrist, E. A. Cornell, and C. E. Wieman, *Phys. Rev. Lett.* **78**, 586 (1997).
- [3] J. Stenger, S. Inouye, D. M. Stamper-Kurn, H.-J. Miesner, A. P. Chikkatur, and W. Ketterle, *Nature (London)* **396**, 345 (1998).
- [4] C.-H. Wu, J. W. Park, P. Ahmadi, S. Will, and M. W. Zwierlein, *Phys. Rev. Lett.* **109**, 085301 (2012).
- [5] M.-S. Heo, T. T. Wang, C. A. Christensen, T. M. Rvachov, D. A. Cotta, J.-H. Choi, Y.-R. Lee, and W. Ketterle, *Phys. Rev. A* **86**, 021602(R) (2012).
- [6] T. D. Cumby, R. A. Shewmon, M.-G. Hu, J. D. Perreault, and D. S. Jin, *Phys. Rev. A* **87**, 012703 (2013).
- [7] G. Roati, M. Zaccanti, C. D’Errico, J. Catani, M. Modugno, A. Simoni, M. Inguscio, and G. Modugno, *Phys. Rev. Lett.* **99**, 010403 (2007).
- [8] K. Pilch, A. D. Lange, A. Prantner, G. Kerner, F. Ferlaino, H.-C. Nägerl, and R. Grimm, *Phys. Rev. A* **79**, 042718 (2009).
- [9] A. Schirotzek, C.-H. Wu, A. Sommer, and M. W. Zwierlein, *Phys. Rev. Lett.* **102**, 230402 (2009).
- [10] C. Kohstall, M. Zaccanti, M. Jag, A. Trenkwalder, P. Massignan, G. M. Bruun, F. Schreck, and R. Grimm, *Nature (London)* **485**, 615 (2012).
- [11] M. Koschorreck, D. Pertot, E. Vogt, B. Fröhlich, M. Feld, and M. Köhl, *Nature (London)* **485**, 619 (2012).
- [12] Y. Zhang, W. Ong, I. Arakelyan, and J. E. Thomas, *Phys. Rev. Lett.* **108**, 235302 (2012).
- [13] N. Spethmann, F. Kindermann, S. John, C. Weber, D. Meschede, and A. Widera, *Phys. Rev. Lett.* **109**, 235301 (2012).
- [14] F. Scazza, G. Valtolina, P. Massignan, A. Recati, A. Amico, A. Burchianti, C. Fort, M. Inguscio, M. Zaccanti, and G. Roati, *Phys. Rev. Lett.* **118**, 083602 (2017).
- [15] N. J. Robinson, J. S. Caux, and R. M. Konik, *Phys. Rev. Lett.* **116**, 145302 (2016).
- [16] S. Nascimbène, N. Navon, K. J. Jiang, L. Tarruell, M. Teichmann, J. McKeever, F. Chevy, and C. Salomon, *Phys. Rev. Lett.* **103**, 170402 (2009).
- [17] M. Punk, P. T. Dumitrescu, and W. Zwerger, *Phys. Rev. A* **80**, 053605 (2009).
- [18] F. Chevy and C. Mora, *Rep. Prog. Phys.* **73**, 112401 (2010).
- [19] X. Cui and H. Zhai, *Phys. Rev. A* **81**, 041602(R) (2010).
- [20] S. Pilati, G. Bertainia, S. Giorgini, and M. Troyer, *Phys. Rev. Lett.* **105**, 030405 (2010).
- [21] P. Massignan and G. Bruun, *Eur. Phys. J. D* **65**, 83 (2011).
- [22] R. Schmidt and T. Enss, *Phys. Rev. A* **83**, 063620 (2011).
- [23] R. Schmidt, T. Enss, V. Pietilä, and E. Demler, *Phys. Rev. A* **85**, 021602(R) (2012).
- [24] V. Ngampruetikorn, J. Levinsen, and M. M. Parish, *Europhys. Lett.* **98**, 30005 (2012).
- [25] P. Massignan, Z. Yu, and G. M. Bruun, *Phys. Rev. Lett.* **110**, 230401 (2013).
- [26] P. Massignan, M. Zaccanti, and G. M. Bruun, *Rep. Prog. Phys.* **77**, 034401 (2014).
- [27] R. Schmidt, M. Knap, D. A. Ivanov, J.-S. You, M. Cetina, and E. Demler, *Rep. Prog. Phys.* **81**, 024401 (2018).
- [28] E. Burovski, V. Cheianov, O. Gamayun, and O. Lychkovskiy, *Phys. Rev. A* **89**, 041601(R) (2014).

- [29] O. Gamayun, O. Lychkovskiy, E. Burovski, M. Malcomson, V. V. Cheianov, and M. B. Zvonarev, *Phys. Rev. Lett.* **120**, 220605 (2018).
- [30] S. Palzer, C. Zipkes, C. Sias, and M. Köhl, *Phys. Rev. Lett.* **103**, 150601 (2009).
- [31] J. Tempere, W. Casteels, M. K. Oberthaler, S. Knoop, E. Timmermans, and J. T. Devreese, *Phys. Rev. B* **80**, 184504 (2009).
- [32] J. Catani, G. Lamporesi, D. Naik, M. Gring, M. Inguscio, F. Minardi, A. Kantian, and T. Giamarchi, *Phys. Rev. A* **85**, 023623 (2012).
- [33] T. Fukuhara, A. Kantian, M. Endres, M. Cheneau, P. Schauss, S. Hild, D. Bellem, U. Schollwöck, T. Giamarchi, C. Gross, I. Bloch, and S. Kuhr, *Nat. Phys.* **9**, 235 (2013).
- [34] R. Scelle, T. Rentrop, A. Trautmann, T. Schuster, and M. K. Oberthaler, *Phys. Rev. Lett.* **111**, 070401 (2013).
- [35] R. Schmidt, H. R. Sadeghpour, and E. Demler, *Phys. Rev. Lett.* **116**, 105302 (2016).
- [36] L. A. Peña Ardila and S. Giorgini, *Phys. Rev. A* **94**, 063640 (2016).
- [37] F. Grusdt, R. Schmidt, Y. E. Shchadilova, and E. Demler, *Phys. Rev. A* **96**, 013607 (2017).
- [38] A. G. Volosniev and H.-W. Hammer, *Phys. Rev. A* **96**, 031601(R) (2017).
- [39] N. E. Guenther, P. Massignan, M. Lewenstein, and G. M. Bruun, *Phys. Rev. Lett.* **120**, 050405 (2018).
- [40] D. Mayer, F. Schmidt, D. Adam, S. Haupt, J. Koch, T. Lausch, J. Nettersheim, Q. Bouton, and A. Widera, *J. Phys. B* **52**, 015301 (2019).
- [41] N. B. Jørgensen, L. Wacker, K. T. Skalmstang, M. M. Parish, J. Levinsen, R. S. Christensen, G. M. Bruun, and J. J. Arlt, *Phys. Rev. Lett.* **117**, 055302 (2016).
- [42] M.-G. Hu, M. J. Van de Graaff, D. Kedar, J. P. Corson, E. A. Cornell, and D. S. Jin, *Phys. Rev. Lett.* **117**, 055301 (2016).
- [43] G. E. Astrakharchik and L. P. Pitaevskii, *Phys. Rev. A* **70**, 013608 (2004).
- [44] F. M. Cucchiatti and E. Timmermans, *Phys. Rev. Lett.* **96**, 210401 (2006).
- [45] R. M. Kalas and D. Blume, *Phys. Rev. A* **73**, 043608 (2006).
- [46] M. Bruderer, A. Klein, S. R. Clark, and D. Jaksch, *Europhys. Lett.* **82**, 30004 (2008).
- [47] K. Sacha and E. Timmermans, *Phys. Rev. A* **73**, 063604 (2006).
- [48] M. Bruderer, A. Klein, S. R. Clark, and D. Jaksch, *Phys. Rev. A* **76**, 011605(R) (2007).
- [49] A. Privitera and W. Hofstetter, *Phys. Rev. A* **82**, 063614 (2010).
- [50] W. Casteels, J. Tempere, and J. T. Devreese, *Phys. Rev. A* **86**, 043614 (2012).
- [51] W. Casteels, J. Tempere, and J. T. Devreese, *Phys. Rev. A* **88**, 013613 (2013).
- [52] B. Kain and H. Y. Ling, *Phys. Rev. A* **94**, 013621 (2016).
- [53] W. Li and S. Das Sarma, *Phys. Rev. A* **90**, 013618 (2014).
- [54] L. A. Peña Ardila and S. Giorgini, *Phys. Rev. A* **92**, 033612 (2015).
- [55] Y. E. Shchadilova, R. Schmidt, F. Grusdt, and E. Demler, *Phys. Rev. Lett.* **117**, 113002 (2016).
- [56] S. P. Rath and R. Schmidt, *Phys. Rev. A* **88**, 053632 (2013).
- [57] F. Grusdt, G. E. Astrakharchik, and E. Demler, *New J. Phys.* **19**, 103035 (2017).
- [58] X. Li, G. Bighin, E. Yakaboylu, and M. Lemeshko, *Mol. Phys.*, **1** (2019).
- [59] B. Kain and H. Y. Ling, *Phys. Rev. A* **98**, 033610 (2018).
- [60] J. Levinsen, M. M. Parish, and G. M. Bruun, *Phys. Rev. Lett.* **115**, 125302 (2015).
- [61] R. S. Christensen, J. Levinsen, and G. M. Bruun, *Phys. Rev. Lett.* **115**, 160401 (2015).
- [62] M. B. Zvonarev, V. V. Cheianov, and T. Giamarchi, *Phys. Rev. Lett.* **99**, 240404 (2007).
- [63] J. Bonart and L. F. Cugliandolo, *Phys. Rev. A* **86**, 023636 (2012).
- [64] J. Bonart and L. F. Cugliandolo, *Europhys. Lett.* **101**, 16003 (2013).
- [65] A. G. Volosniev, H.-W. Hammer, and N. T. Zinner, *Phys. Rev. A* **92**, 023623 (2015).
- [66] A. Lampo, S. H. Lim, M. Á. García-March, and M. Lewenstein, *Quantum* **1**, 30 (2017).
- [67] F. Grusdt, K. Seetharam, Y. Shchadilova, and E. Demler, *Phys. Rev. A* **97**, 033612 (2018).
- [68] S. I. Mistakidis, A. G. Volosniev, N. T. Zinner, and P. Schmelcher, *arXiv:1809.01889*.
- [69] M. Drescher, M. Salmhofer, and T. Enss, *Phys. Rev. A* **99**, 023601 (2019).
- [70] M. Cetina, M. Jag, R. S. Lous, J. T. M. Walraven, R. Grimm, R. S. Christensen, and G. M. Bruun, *Phys. Rev. Lett.* **115**, 135302 (2015).
- [71] M. Cetina, M. Jag, R. S. Lous, I. Fritsche, J. T. M. Walraven, R. Grimm, J. Levinsen, M. M. Parish, R. Schmidt, M. Knap, and E. Demler, *Science* **354**, 96 (2016).
- [72] M. Knap, A. Shashi, Y. Nishida, A. Imambekov, D. A. Abanin, and E. Demler, *Phys. Rev. X* **2**, 041020 (2012).
- [73] J. Bonart and L. F. Cugliandolo, *Phys. Rev. A* **86**, 023636 (2012).
- [74] A. Sartori and A. Recati, *Eur. Phys. J. D* **67**, 260 (2013).
- [75] P. W. Anderson, *Phys. Rev. Lett.* **18**, 1049 (1967).
- [76] J. Goold, T. Fogarty, N. Lo Gullo, M. Paternostro, and T. Busch, *Phys. Rev. A* **84**, 063632 (2011).
- [77] F. Chevy, *Phys. Rev. A* **74**, 063628 (2006).
- [78] R. Combescot, A. Recati, C. Lobo, and F. Chevy, *Phys. Rev. Lett.* **98**, 180402 (2007).
- [79] R. Combescot and S. Giraud, *Phys. Rev. Lett.* **101**, 050404 (2008).
- [80] R. Combescot, S. Giraud, and X. Leyronas, *Europhys. Lett.* **88**, 60007 (2009).
- [81] M. M. Parish and J. Levinsen, *Phys. Rev. B* **94**, 184303 (2016).
- [82] S. I. Mistakidis, G. C. Katsimiga, G. M. Koutentakis, and P. Schmelcher, *New J. Phys.* **21**, 043032 (2019).
- [83] L. Cao, V. Bolsinger, S. I. Mistakidis, G. M. Koutentakis, S. Krönke, J. M. Schurer, and P. Schmelcher, *J. Chem. Phys.* **147**, 044106 (2017).
- [84] See Supplemental Material at <http://link.aps.org/supplemental/10.1103/PhysRevLett.122.183001> for the description of (i) impurity's breathing dynamics; (ii) the effective mass of the polaron; (iii) the ML-MCTDHX

- method, and (iv) the entanglement generation, which includes Refs. [86–104].
- [85] P. Siegl, S. I. Mistakidis, and P. Schmelcher, *Phys. Rev. A* **97**, 053626 (2018).
- [86] G. M. Koutentakis, S. I. Mistakidis, and P. Schmelcher, *Phys. Rev. A* **95**, 013617 (2017).
- [87] J. P. Ronzheimer, M. Schreiber, S. Braun, S. S. Hodgman, S. Langer, I. P. McCulloch, F. Heidrich-Meisner, I. Bloch, and U. Schneider, *Phys. Rev. Lett.* **110**, 205301 (2013).
- [88] J. W. Abraham and M. Bonitz, *Contrib. Plasma Phys.* **54**, 27 (2014).
- [89] L. Cao, S. Krönke, O. Vendrell, and P. Schmelcher, *J. Chem. Phys.* **139**, 134103 (2013).
- [90] G. C. Katsimiga, G. M. Koutentakis, S. I. Mistakidis, P. G. Kevrekidis, and P. Schmelcher, *New J. Phys.* **19**, 073004 (2017).
- [91] S. I. Mistakidis, G. C. Katsimiga, P. G. Kevrekidis, and P. Schmelcher, *New J. Phys.* **20**, 043052 (2018).
- [92] M. Roncaglia, A. Montorsi, and M. Genovese, *Phys. Rev. A* **90**, 062303 (2014).
- [93] G. M. Koutentakis, S. I. Mistakidis, and P. Schmelcher, *New J. Phys.*, <https://doi.org/10.1088/1367-2630/ab14ba> (2019).
- [94] J. Erdmann, S. I. Mistakidis, and P. Schmelcher, *Phys. Rev. A* **99**, 013605 (2019).
- [95] J. Frenkel, *Wave Mechanics*, 1st ed. (Clarendon Press, Oxford, 1934), pp. 423–428.
- [96] P. A. Dirac, *Proc. Cambridge Philos. Soc.* **26**, 376 (1930).
- [97] L. P. Pitaevskii and S. Stringari, *Bose-Einstein Condensation* (Oxford University Press, Oxford, 2003).
- [98] P. G. Kevrekidis, D. J. Frantzeskakis, and R. Carretero-González, *The Defocusing Nonlinear Schrödinger Equation* (SIAM, Philadelphia, 2015).
- [99] M. Naraschewski and R. J. Glauber, *Phys. Rev. A* **59**, 4595 (1999).
- [100] E. J. Mueller, T. L. Ho, M. Ueda, and G. Baym, *Phys. Rev. A* **74**, 033612 (2006).
- [101] O. Penrose and L. Onsager, *Phys. Rev.* **104**, 576 (1956).
- [102] P. Jain and M. Boninsegni, *Phys. Rev. A* **83**, 023602 (2011).
- [103] S. Bandyopadhyay, A. Roy, and D. Angom, *Phys. Rev. A* **96**, 043603 (2017).
- [104] R. A. Jalabert and H. M. Pastawski, *Adv. Solid State Phys.* **41**, 483 (2001).
- [105] Within the mean-field approximation for both $N_B = 100$ and $N_B = 10$ cases, $|S(t)|$ remains finite for $0 < g_{BI} < 5$ and thus the orthogonality catastrophe as captured by the contrast is absent.
- [106] P. Nozières and C. T. De Dominicis, *Phys. Rev.* **178**, 1097 (1969).
- [107] The spin- \downarrow component, being noninteracting, remains around the trap center for all times.
- [108] R. Horodecki, P. Horodecki, M. Horodecki, and K. Horodecki, *Rev. Mod. Phys.* **81**, 865 (2009).

Supplemental Material: Quench Dynamics and Orthogonality Catastrophe of Bose Polarons

BREATHING DYNAMICS OF THE IMPURITY WITHIN THE EFFECTIVE POTENTIAL APPROACH

To demonstrate the applicability of our effective potential approach given in Eq. (3) in the main text we investigate the breathing dynamics of the single impurity immersed in the bosonic bath. In order to capture the breathing dynamics [S2–S5] in all three dynamical regions (R_I , R_{II} and R_{III}) we consider a quench of the harmonic trapping frequency ω_I . Such a process aims at dynamically exciting the corresponding breathing mode of the impurity [S1].

In particular, we initialize the multi-component system in its ground state for $g_{BB} = 0.5$ and a chosen g_{BI} with harmonic oscillator frequencies $\omega_B = 1$ and $\omega_I = 0.95$. To trigger the dynamics we suddenly change at $t = 0$ the value of ω_I from 0.95 to 1.0, thus inducing a collective breathing mode. Measuring the center-off-mass motion [S2–S4] of the impurity we obtain its breathing frequency ω_I^{br} for a specific g_{BI} . Figure S1 shows ω_I^{br} for varying g_{BI} . As it can be seen, ω_I^{br} decreases within region R_I reaches a critical point around $g_{BI} \approx 0.5$ and thereafter it increases within region R_{II} and finally saturates close to $\omega_I^{br} \approx 3$ for $g_{BI} > 2$. We remark here that operating in the mean-field approximation, a similar behavior of ω_I^{br} within the miscible phase (R_I region in our case) but for a larger number of impurity particles has been reported in [S6].

Let us first compare the result of ω_I^{br} obtained via the many-body (MB) simulations with the effective model described in the main text. By employing also the Thomas-Fermi approximation the breathing frequency of the impurity reads $\omega_{br} = 2\tilde{\omega}_B$ [see the red dotted line in Fig. S1] where $\tilde{\omega}_B^2 = \left(1 - \frac{g_{BI}}{g_{BB}}\right)\omega_B^2$. Recall that this effective picture is valid only for weak (miscible) interactions namely when $g_{BB} \ll g_{BI}$. We indeed observe that for these interactions the effective potential predicts the correct breathing frequency except for the region $g_{BI} \approx g_{BB} = 0.5$.

To extend our analysis to the immiscible regime of interactions where the impurity probes spatial regions beyond the Thomas-Fermi radius, we next consider the general form of the effective potential $V_{eff}(x) = 1/2m\omega_B^2x^2 + g_{BI}\rho_B^{(1)}(x)$ introduced in Eq. (3) of the main text. Note that this $V_{eff}(x)$ does not incorporate the Thomas-Fermi approximation. Also, $\rho_B^{(1)}(x)$ is the numerically exact ground state density of the bath for $g_{BI} = 0$ and $g_{BB} = 0.5$. To test the accuracy of our effective potential we examine the breathing dynamics of a single particle trapped in $V_{eff}(x)$. As before we prepare the impurity in the ground state of $V_{eff}(x)$ with

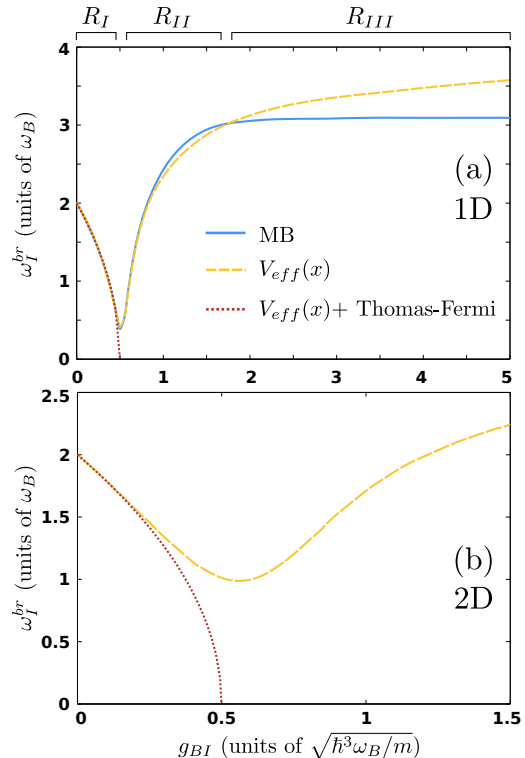


FIG. S1. (Color online) Breathing frequency, ω_I^{br} , of the Bose polaron as a function of the interspecies interaction strength in (a) one-dimension and (b) two-dimensions. The breathing motion is induced by quenching the trapping frequency of the impurity from 0.95 to 1.0. In all cases $N_B = 100$, $N_I = 1$ and $g_{BB} = 0.5$. Dotted red line refers to $\omega_{br} = 2\tilde{\omega}_B$ and dashed yellow line denotes the breathing frequency obtained within the effective potential picture (see text).

$\omega_I = 0.95$ and a specific g_{BI} and induce the breathing dynamics by quenching the frequency to 1.0. The resulting breathing frequency calculated via the center-of-mass motion is also presented in Fig. S1 (see the yellow dashed line) on top of the MB calculation (solid blue line). Evidently the single-particle picture obtained within our effective potential provides an adequate approximation of the full MB result especially for $0 < g_{BI} < 1$. Deviations between the effective model and the MB calculations are of the order of 8% for $g_{BI} \approx 2.5$, while they become significant for even larger g_{BI} . For these strong interactions the entanglement becomes strong rendering the effective potential an insufficient approach for describing the impurity dynamics.

The notion of the effective potential approximation can be easily extended to higher dimensions. Of course, relying exclusively on this approximation it is only possible to access the frequencies of the quench-induced dynamical modes, i.e. the breathing mode. To showcase

whether our predictions of the breathing frequency in one-dimension remain robust in higher dimensions we calculate next the breathing frequency in two-dimensions within the effective potential approximation. To induce the breathing dynamics we follow exactly the same procedure as in one-dimension (see the discussion above). Assuming an isotropic two-dimensional (2D) external harmonic trap, the effective potential reads $V_{eff}(r) = \frac{1}{2}m_B\omega_B^2r^2 + g_{BI}\rho_B^{(1)}(r)$, where $r = \sqrt{x^2 + y^2}$ and $\rho_B^{(1)}(r)$ is the single-particle density of the BEC at $t = 0$. Figure S1 (b) illustrates ω_I^{br} for the 2D trapped system upon varying g_{BI} . Additionally, $\rho_B^{(1)}(r)$ is obtained by solving the 2D Gross-Pitaevskii equation. For self consistency reasons ω_I^{br} is measured only in regions R_I and R_{II} since already for values of g_{BI} that belong to R_{II} the effective potential approximation is expected to fail. It is found that ω_I^{br} exhibits a similar behavior to its one-dimensional counterpart. In particular, ω_I^{br} decreases within region R_I , reaches a minimum located around $g_{BI} \approx 0.6$ and then it increases deeper in the region R_{II} [see yellow dashed line in Fig. S1 (b)]. Moreover, referring to weak g_{BI} the Thomas-Fermi approximation reads $\rho_B^{(1)}(r) = \frac{1}{g_{BB}}(\mu_B - \frac{1}{2}m_B\omega_B^2r^2)$. Here, μ_B denotes the chemical potential of the bath. Therefore combining the effective potential picture with the Thomas-Fermi approximation we deduce that $V_{eff}(r) = \frac{1}{2}m_B\tilde{\omega}_B^2r^2 + \tilde{c}$, being a parabola shifted by $\tilde{c} \equiv \frac{g_{BI}^2}{g_{BB}}\mu_B$ and exhibiting a modified trapping frequency $\tilde{\omega}_B^2 \equiv \left(1 - \frac{g_{BI}}{g_{BB}}\right)\omega_B^2 < \omega_B^2$. Utilizing this approximation the breathing frequency of the impurity is $\omega_{br} = 2\tilde{\omega}_B$ [see the red dotted line in Fig. S1 (b)]. As it can be seen, for $g_{BI} < 0.25$ the Thomas-Fermi approximation and the effective potential predict the same ω_{br}^I , while for $g_{BI} > 0.25$ strong deviations appear. Recall that close to $g_{BI} = 0.5$ the miscibility/immiscibility threshold is reached and the impurity probes also the spatial region at the edge of the BEC density. In this region the Thomas-Fermi profile, used herein, is not an adequate approximation for $\rho_B^{(1)}(r)$, a result that explains the observed deviations.

EFFECTIVE MASS

Having at hand the breathing frequency of the impurity atom we next calculate its effective mass m_{eff} . It has been recently shown [S12] that in the presence of an external harmonic trap the single-particle Hamiltonian that governs the impurity dynamics reads

$$\hat{H}_I^{eff} = \epsilon_{eff} + \frac{\hat{p}^2}{2m_I^{eff}} + \frac{1}{2}m_I^{eff}(\omega_I^{eff})^2\hat{x}^2. \quad (S1)$$

In this expression, ϵ_{eff} refers to the self-energy of the polaron. Also, ω_I^{eff} denotes the effective trapping of the polaron due to the combined effect of its interaction with

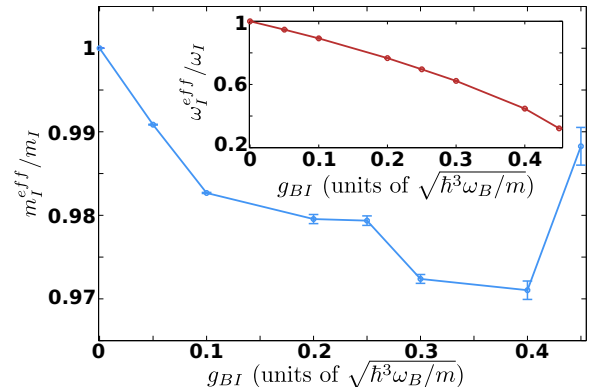


FIG. S2. (Color online) Effective mass of the polaron for increasing postquench interspecies interaction strength g_{BI} . The inset shows the effective trapping frequency of the polaron [see also Eq. (S1)] for varying g_{BI} . In all cases $N_B = 100$, $N_I = 1$, $g_{BB} = 0.5$ and the frequency of the external harmonic confinement is $\omega = 1$. The system is initialized in its ground state with $g_{BI} = 0$ and the dynamics is triggered via an interspecies interaction quench to a final value g_{BI} .

the bath and the presence of the external harmonic confinement, while m_I^{eff} is the effective mass of the polaron. It is also important to note that this effective Hamiltonian description is valid only within the miscible regime of interactions since it inherently involves the assumption that the impurity is effectively trapped by the bosonic bath. For more details regarding the construction of this model we refer the interested reader to [S12]. To calculate the effective mass of the polaron within the miscible regime of interactions, referring in our case to $g_{BI} < 0.5$, we perform the following analysis. We first measure the variance (size), $\langle x^2(t) \rangle$, of the impurity atom for a specific interspecies interaction quench amplitude relying on our numerical calculations performed in the main text. Independently, by solving Eq. (S1) we can show that

$$\begin{aligned} \langle x^2(t) \rangle &= \langle \Psi(t) | \hat{x}^2 | \Psi(t) \rangle = \frac{\langle \Psi(0) | \hat{p}^2 | \Psi(0) \rangle}{(m_I^{eff} \omega_I^{eff})^2} \\ &\times \sin^2(\omega_I^{eff} t) + \langle \Psi(t) | \hat{x}^2 | \Psi(t) \rangle \cos^2(\omega_I^{eff} t). \end{aligned} \quad (S2)$$

Assuming an initially non-interacting impurity, i.e. $g_{BI} = 0$, we obtain $\langle \Psi(0) | \hat{p}^2 | \Psi(0) \rangle = \frac{\hbar}{2}m_I\omega_I$ and $\langle \Psi(0) | \hat{x}^2 | \Psi(0) \rangle = \frac{\hbar}{2m_I\omega_I}$. A similar analytical relation to Eq. (S2) can also be obtained for $\langle \hat{p}^2(t) \rangle$. Here the unknown parameters that need to be determined are ω_I^{eff} and m_I^{eff} . To estimate these two parameters we perform a fitting of the analytical form of $\langle x^2(t) \rangle$ given by Eq. (S2) and $\langle p^2(t) \rangle$ to the numerically obtained $\langle x^2(t) \rangle$ and $\langle p^2(t) \rangle$. Figure S2 presents m_I^{eff} and ω_I^{eff} , as a result of the above-mentioned fitting, for increasing g_{BI} which always lies within the miscible regime of interactions where the polaron is also well defined. Recall that for stronger

interspecies interactions a dissipative motion of the impurity into the bosonic bath takes place signalling the onset of the orthogonality catastrophe of the Bose polaron. As it can be seen in Fig. S2, m_I^{eff} becomes smaller than the bare mass of the impurity for increasing interspecies interaction strengths. A trend that is also followed by ω_I^{eff} as it can be deduced by inspecting the inset depicted in Fig. S2. This behavior of m_I^{eff} being in line with the findings of Ref. [S12] is attributed to the presence of the external harmonic confinement and the interspecies correlations between the bath and the impurity.

THE MANY-BODY COMPUTATIONAL APPROACH: ML-MCTDHX

To simulate the MB quantum dynamics of the composite system discussed in the main text we utilize the Multi-Layer Multi-Configuration Time-Dependent Hartree method for Atomic Mixtures [S7] (ML-MCTDHX). ML-MCTDHX [S7, S8] is an ab-initio variational method for solving the time-dependent MB Schrödinger equation of atomic mixtures consisting either of bosonic [S10–S12] or fermionic [S14–S16] species. Within this approach the total MB wavefunction is expanded in terms of a time-dependent and variationally optimized basis, enabling us to capture the important correlation effects by using a computationally feasible basis size. In this way the system relevant subspace of the Hilbert space is spanned in an efficient manner at each time instant using a reduced number of basis states when compared to expansions relying on a time-independent basis. Most importantly, its multi-layer structure allows for tailoring the MB wavefunction ansatz to account for both intra- and interspecies correlations when simulating the dynamics of composite systems. Due to the above ML-MCTDHX constitutes a versatile tool for simulating the dynamics of multispecies systems.

Here, we employ ML-MCTDHX in order to study the quench-induced correlated dynamics of a particle imbalanced bosonic mixture. The mixture consists of a majority species being referred to as bath (B) in the following and a minority species which we shall call impurity (I) below. Most importantly, the minority atoms possess an additional spin-1/2 degree of freedom. To account for inter- and intraspecies correlations, the MB wavefunction ($|\Psi(t)\rangle$) is firstly expressed as a linear combination of D time-dependent species wavefunctions ($|\Psi_i^\sigma(t)\rangle$) for each of the $\sigma = B, I$ species

$$|\Psi(t)\rangle = \sum_{i,j=1}^D A_{ij}(t) |\Psi_i^B(t)\rangle |\Psi_j^I(t)\rangle. \quad (\text{S3})$$

Here $A_{ij}(t)$ refer to the corresponding time-dependent expansion coefficients. We remark that Eq. (S3) is connected to the truncated Schmidt decomposition of

rank D [S9–S11] via a unitary transformation, with the eigenvalues of $A_{ij}(t)$ being the well-known Schmidt weights, $\sqrt{\lambda_i(t)}$. Following this unitary transformation, U , we obtain $A_{ij} = U_{ik}^{-1} \sqrt{\lambda_k} U_{kj}$. Then the MB wavefunction is expressed in terms of different interspecies modes of entanglement taking the form $|\Psi(t)\rangle = \sum_{k=1}^D \sqrt{\lambda_k(t)} |\tilde{\Psi}_k^B(t)\rangle |\tilde{\Psi}_k^I(t)\rangle$ with $\sqrt{\lambda_k(t)} |\tilde{\Psi}_k^B(t)\rangle |\tilde{\Psi}_k^I(t)\rangle$ being referred to as the k -th mode of entanglement.

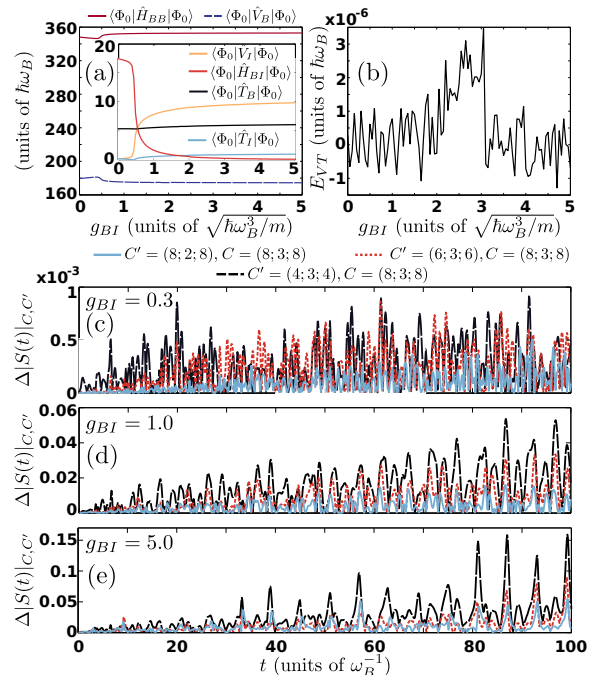


FIG. S3. (Color online) (a) Different energy contributions (see legend) of the ground state of the multicomponent system for varying interspecies interaction strength g_{BI} . (b) Outcome of the Virial theorem [see also Eq. (S6)] for increasing g_{BI} , obtained via the energy contributions shown in (a). We observe that $E_{VT} = 0$ for every g_{BI} verifying the Virial theorem for the ground states of our system setups. Evolution of the spin polarization deviations $\Delta|S(t)|_{C,C'}$ between the $C = (8; 3; 8)$ and other orbital configurations $C' = (D; d^A; d^B)$ (see legend) for (c) $g_{BI} = 0.3$, (d) $g_{BI} = 1$ and (e) $g_{BI} = 5$. In all cases $N_B = 100$, $N_I = 1$ and $g_{BB} = 0.5$.

Next each species wavefunction is expanded on the time-dependent number-state basis, $|\vec{n}(t)\rangle^\sigma$, as

$$|\Psi_i^\sigma(t)\rangle = \sum_{\vec{n}} B_{i;\vec{n}}^\sigma(t) |\vec{n}(t)\rangle^\sigma, \quad (\text{S4})$$

where $B_{i;\vec{n}}^\sigma(t)$ refer to the time-dependent coefficients. Each $|\vec{n}(t)\rangle^\sigma$ corresponds to a permanent of the d^σ time-dependent variationally optimized single-particle functions (SPFs) denoted by $|\phi_l^\sigma(t)\rangle$, $l = 1, 2, \dots, d^\sigma$ with occupation numbers $\vec{n} = (n_1, \dots, n_{d^\sigma})$. The SPFs are subsequently expanded within a time-independent primitive basis. For the majority species this primitive basis $\{|k\rangle\}$ consists of an \mathcal{M} dimensional discrete variable

representation (DVR). Regarding the impurity the primitive basis $\{|k, s\rangle\}$ corresponds to the tensor product of the DVR basis for the spatial degrees of freedom and the two-dimensional spin-1/2 basis $\{|\uparrow\rangle, |\downarrow\rangle\}$. In this way

$$|\phi_j^I(t)\rangle = \sum_{k=1}^{\mathcal{M}} \sum_{\alpha=\{\uparrow, \downarrow\}} C_{jk\alpha}^I(t) |k\rangle |\alpha\rangle, \quad (\text{S5})$$

where $C_{jk\alpha}^I(t)$ are time-dependent expansion coefficients. We remark that each SPF for the impurity atoms is a spinor wavefunction $|\phi_j^I(t)\rangle = \int dx [\chi_j^\uparrow(x)\hat{\Psi}_\uparrow^\dagger(x) + \chi_j^\downarrow(x)\hat{\Psi}_\downarrow^\dagger(x)]|0\rangle$ (for more details see also [S14]). To obtain the time-evolution of the $(N_B + N_I)$ -body wavefunction $|\Psi(t)\rangle$ under the influence of the Hamiltonian \hat{H} [see Eq. (1) in the main text] we determine the equations of motion [S7] for the coefficients $A_{\bar{n}}(t)$, $B_{i;\bar{n}}^\sigma(t)$ and $C_{jk\alpha}^I(t)$ by employing e.g. the Dirac-Frenkel [S17, S18] variational principle for the generalized ansatz [see Eqs. (S3), (S4)]. The latter refer to a set of D^2 ordinary (linear) differential equations of motion for the $A_{\bar{n}}(t)$ coefficients, coupled to a set of $D(\frac{(N_B+d^B-1)!}{N_B!(d^B-1)!} + \frac{(N_I+d^I-1)!}{N_I!(d^I-1)!})$ nonlinear integrodifferential equations for the species functions, and $d^B + d^I$ nonlinear integrodifferential equations for the SPFs. Finally, let us mention that ML-MCTDHX is able to operate within different approximation orders, for instance it reduces to the set of coupled mean-field (MF) Gross-Pitaevskii equations [S19, S20] when $D = d^B = d^I = 1$. Moreover it is capable of operating within the species mean-field (SMF) approximation [S7, S8, S10–S12] in which the entanglement between the species is neglected but intraspecies correlations are taken into account. In particular, in this latter case the N_σ -body state of each species is described by only one species function ($|\Psi_i^B(t)\rangle = |\Psi_i^I(t)\rangle = 0$ for $i \neq 1$) building upon distinct single-particle functions $|\phi_j^B(t)\rangle$ and $|\phi_k^I(t)\rangle$ with $j = 1, 2, \dots, d^B$ and $k = 1, 2, \dots, d^I$ respectively. Accordingly the total wavefunction of the system becomes $|\Psi(t)\rangle = |\Psi_1^B(t)\rangle \otimes |\Psi_1^I(t)\rangle$.

Within our implementation a sine discrete variable representation (sine-DVR) has been used as the primitive basis for the spatial part of the SPFs including $\mathcal{M} = 450$ grid points. The sine-DVR intrinsically introduces hard-wall boundaries at both edges of the numerical grid being in our case $x_\pm = \pm 40$. We have ensured that the location of these boundary conditions does not affect our results since we do not observe appreciable densities to occur beyond $x_\pm = \pm 25$. Another way to confirm the absence of edge effects in the simulations that were carried out and presented in the main text, is to estimate the time at which excitations travel towards the boundaries as detected by the local speed of sound of the bath. Indeed, all possible emergent system correlations will definitely travel with a speed smaller than the local speed of sound. The relevant time window for travelling a distance from the trap center to the spatial point $x_b > 0$ is $T = \int_0^{x_b} \frac{dx}{c(x)}$,

where the local speed of sound reads $c(x) = \sqrt{\frac{g_{BB}\rho_B^{(1)}(x)}{m}}$. This time increases dramatically when x_b lies beyond the Thomas-Fermi radius, which is in our case $R_{TF} \approx 4.2$. For instance, when $x_b = 6$ we obtain $T \approx 106$ while for $x_b \equiv x_+ = +40$ we find $T \approx 2 \times 10^{16}$. Therefore we can again deduce that within the considered simulation time $T = 100$, in the main text, edge effects do not play any role. To obtain the eigenstates of the MB system we rely on the so-called improved relaxation method [S7, S8] within ML-MCTDHX. To track the dynamics of the composite bosonic system we propagate in time the wavefunction [Eq. (S3)] by employing the appropriate Hamiltonian within the ML-MCTDHX equations of motion.

To conclude upon the reliability of our results, we increase the number of species functions D , SPFs d^B and d^I , and grid points \mathcal{M} , thus observing a systematic convergence of all the observables of interest, e.g. $S(t)$ and $\Lambda^{BI}(t)$. The Hilbert space truncation, i.e. the order of the used approximation, is designated by the considered orbital configuration space $C = (D; d^B; d^I)$. Convergence here means that for an increasing orbital configuration C the observables become almost insensitive within a given relative accuracy. We remark that all MB calculations presented in the main text refer to the configuration $C = (8; 3; 8)$.

In order to test from first principles the convergence of our results regarding the ground state of our system when varying g_{BI} we resort to the quantum Virial theorem. Referring to the ground state of our system, $|\Psi(0)\rangle$, the Virial theorem reads

$$\begin{aligned} E_{VT} \equiv & 2(\langle \Psi(0) | \hat{T}_B | \Psi(0) \rangle + \langle \Psi(0) | \hat{T}_I | \Psi(0) \rangle) \\ & - 2(\langle \Psi(0) | \hat{V}_B | \Psi(0) \rangle + \langle \Psi(0) | \hat{V}_I | \Psi(0) \rangle) \quad (\text{S6}) \\ & + (\langle \Psi(0) | \hat{H}_{BB} | \Psi(0) \rangle + \langle \Psi(0) | \hat{H}_{BI} | \Psi(0) \rangle) = 0. \end{aligned}$$

Here, the kinetic energy operators of the bath and the impurity are denoted by $\hat{T}_B = -\int dx \hat{\Psi}_B^\dagger(x) \frac{\hbar^2}{2m_B} \frac{d^2}{dx^2} \hat{\Psi}_B(x)$ and $\hat{T}_I = -\int dx \hat{\Psi}_I^\dagger(x) \frac{\hbar^2}{2m_I} \frac{d^2}{dx^2} \hat{\Psi}_I(x)$ respectively. Also, the corresponding potential energy operator for the bath is $\hat{V}_B = \int dx \hat{\Psi}_B^\dagger(x) \frac{1}{2} m_B \omega_B^2 x^2 \hat{\Psi}_B(x)$ and for the impurity reads $\hat{V}_I = \int dx \hat{\Psi}_I^\dagger(x) \frac{1}{2} m_I \omega_I^2 x^2 \hat{\Psi}_I(x)$. Furthermore, the operator of the intraspecies interaction energy of the bath is $\hat{H}_{BB} = g_{BB} \int dx \hat{\Psi}_B^\dagger(x) \hat{\Psi}_B^\dagger(x) \hat{\Psi}_B(x) \hat{\Psi}_B(x)$, while the operator of the interspecies interaction energy is $\hat{H}_{BI} = g_{BI} \int dx \hat{\Psi}_B^\dagger(x) \hat{\Psi}_\uparrow^\dagger(x) \hat{\Psi}_\uparrow(x) \hat{\Psi}_B(x)$. In all cases, $\hat{\Psi}_i(x)$ refers to the bosonic field operator of either the bath ($i = B$) or the impurity ($i = \uparrow, \downarrow$) atoms. The different energy contributions, given by Eq. (S6), are illustrated in Fig. S3 (a) for increasing g_{BI} . Calculating the quantum Virial theorem by taking into account all the aforementioned contributions [see Eq. (S6)] confirms that it is indeed fulfilled, since $E_{VT} \sim 10^{-6}$, for all the ground states of the system independently of g_{BI} [see Fig. S3 (b)]. The latter assures the convergence of all the ground state configurations considered herein.

As a next step, we also briefly discuss the convergence of our results in terms of a different number of species and single-particle functions. For this investigation we monitor during the nonequilibrium dynamics e.g. the spin polarization, $|S(t)|_C$, and we calculate its absolute deviation between the $C = (8; 3; 8)$ and other numerical configurations $C' = (D; d^A; d^B)$

$$\Delta |S(t)|_{C,C'} = \frac{||S(t)|_C - |S(t)|_{C'}|}{|S(t)|_C}. \quad (\text{S7})$$

Figure S3 presents $\Delta |S(t)|_{C,C'}$ for the multicomponent system under consideration with $N_B = 100$ and $N_I = 1$ following an interspecies interaction quench from $g_{BI} = 0$ to different finite values of g_{BI} . Closely inspecting Fig. S3, it becomes apparent that a systematic convergence of $\Delta |S(t)|_{C,C'}$ is achieved for all interspecies interactions used in the main text. For instance, comparing $\Delta |S(t)|_{C,C'}$ at $g_{BI} = 0.3$ between the $C = (8; 3; 8)$ and $C' = (6; 3; 6)$ [$C' = (8; 2; 8)$] approximations we deduce that the corresponding relative difference lies below 0.08% [0.04%] throughout the evolution, see Fig. S3 (a). However, for increasing g_{BI} the relative errors become larger, see Figs. S3 (b), (c). E.g. for $g_{BI} = 5$ which is the strongest interaction considered in the main text $\Delta |S(t)|_{C,C'}$ between the configurations $C = (8; 3; 8)$ and $C' = (6; 3; 6)$ [$C' = (8; 2; 8)$] exhibits a deviation which reaches a maximum value of the order of 7% [5%] at large propagation times. Finally, we remark that a similar analysis has been performed for all other interspecies interaction strengths discussed within the main text and found to be adequately converged (results not shown here for brevity).

FRAGMENTATION

The spectral representation of the reduced σ species one-body density matrix [S21] reads

$$\rho_\sigma^{(1)}(x, x'; t) = N_\sigma \sum_{\alpha=1}^{d^\sigma} n_\alpha^\sigma(t) \varphi_\alpha^\sigma(x, t) \varphi_\alpha^{*\sigma}(x', t), \quad (\text{S8})$$

where $\varphi_\alpha^\sigma(x, t)$ are the so-called natural orbitals of the $\sigma = B, I$ species and d^σ corresponds to the considered number of orbitals for the σ species. The corresponding population eigenvalues $n_\alpha^\sigma(t) \in [0, 1]$ (natural populations) characterize the degree of intraspecies correlations or fragmentation of the system [S10, S11, S22, S23]. Here we consider the natural orbitals to be normalized to unity i.e. $\int dx |\varphi_\alpha^\sigma(x)|^2 = 1$. Indeed, for only one macroscopically occupied orbital the system is said to be condensed, otherwise it is termed fragmented. It can be shown that for $n_1^\sigma(t) = 1$, $n_{i \neq 1}^\sigma(t) = 0$ the first natural orbital $\sqrt{N_\sigma} \varphi_1^\sigma(x^\sigma; t)$ reduces to the MF wavefunction $\varphi^\sigma(x^\sigma; t)$. Therefore, $1 - n_1^\sigma(t)$ offers a measure of the degree of the σ species fragmentation [S22, S23].

Finally let us remark that by employing the Schmidt decomposition of Eq. (S3) and the fact that $N_I = 1$ the one-body density matrix of the impurity reads

$$\rho_I^{(1)}(x, x'; t) = \sum_{k=1}^D \lambda_k(t) \tilde{\Psi}_k^I(x, t) \tilde{\Psi}_k^{I*}(x', t), \quad (\text{S9})$$

where $\tilde{\Psi}_k^I(x, t) = \langle x | \tilde{\Psi}_k^I \rangle$. Thus comparing Eq. (S8) with Eq. (S9) we can easily deduce that $n_k^I(t) = \lambda_k(t)$ for every k .

MANIFESTATION OF ENTANGLEMENT IN THE DEGREE OF MISCIBILITY

Let us now elaborate on the relation between the degree of miscibility and the entanglement occurring among the bath and the spinor impurity. As already discussed in the main text in order to expose the degree of phase separation, namely the degree of miscibility or immiscibility, between the bath and the spinor impurity we invoke the overlap integral function [S24, S25] which reads

$$\Lambda^{BI}(t) = \frac{\left[\int dx \rho_B^{(1)}(x; t) \rho_I^{(1)}(x; t) \right]^2}{\int dx \left(\rho_B^{(1)}(x; t) \right)^2 \times \int dx \left(\rho_I^{(1)}(x; t) \right)^2} \quad (\text{S10})$$

In this expression, $\rho_\sigma^{(1)}(x; t)$ denotes the one-body density of the $\sigma = B, I$ species. This function is normalized to unity taking values between $\Lambda = 0$ and $\Lambda = 1$ that signify complete or zero spatial overlap respectively on the single-particle level. Moreover according to our MB wavefunction expansion [see Eq. (S3)], the one-body density of the σ species, $\rho_\sigma^{(1)}(x; t)$, can be expressed with respect to different entanglement modes [S10, S11] as

$$\rho_\sigma^{(1)}(x; t) = \sum_{k=1}^D \lambda_k(t) \rho_k^{(1),\sigma}(x; t). \quad (\text{S11})$$

Here $\rho_k^{(1),\sigma}(x; t) = \langle \tilde{\Psi}_k^\sigma | \hat{\Psi}_\sigma^\dagger(x) \hat{\Psi}_\sigma(x) | \tilde{\Psi}_k^\sigma \rangle$ is the one-body density of the k -th species function. $\hat{\Psi}_\sigma^\dagger(x)$ [$\hat{\Psi}_\sigma(x)$] denotes the bosonic field operator that creates (annihilates) a σ species boson at position x . Moreover, $\lambda_k(t)$ refer to the corresponding Schmidt coefficients of the truncated Schmidt decomposition [see also Eq. (S3)]. We remark that the λ_k 's in decreasing order are known as natural species populations of the k -th species wavefunction $|\Psi_k^\sigma(t)\rangle$ of the σ -species. In turn, they represent a measure of the entanglement or interspecies correlations between the bath and the impurity. In particular, the system is said to be entangled [S10, S11, S13] when at least two different λ_k 's are nonzero. Recall that in this latter case the total MB state [Eq. (S3)] cannot be expressed as a direct product of two species states.

To proceed we define the general overlap integral between the one-body densities of different species wavefunctions corresponding to distinct modes of entanglement ($i \neq j$) and species ($\sigma \neq \sigma'$) as

$$K_{ij}^{\sigma\sigma'}(t) = \int dx \rho_i^{(1),\sigma}(x;t)\rho_j^{(1),\sigma'}(x;t). \quad (\text{S12})$$

Note that within the MF as well as the SMF approximations $\rho_i^{(1),\sigma}(x;t) = 0$ for $i > 1$ holds by definition,

$$\Lambda^{BI}(t) = \frac{[\sum_{i=1}^D \lambda_i^2 K_{ii}^{BI} + \sum_{i \neq j} \lambda_i \lambda_j K_{ij}^{BI}]^2}{[\sum_{i=1}^D \lambda_i^2 K_{ii}^{BB} + 2 \sum_{i < j} \lambda_i \lambda_j K_{ij}^{BI}][\sum_{i=1}^D \lambda_i^2 K_{ii}^{II} + 2 \sum_{i < j} \lambda_i \lambda_j K_{ij}^{IB}]}. \quad (\text{S13})$$

Of course in this most general case where a full MB description is considered and entanglement is strong, namely more than one species wavefunctions are significantly occupied, the relation of $\Lambda^{BI}(t)$ with the Schmidt coefficients λ_i where $i = 1, 2, \dots, D$ is complicated. To get a better insight of the aforementioned relation let us consider the following limiting cases. Within the MF and SMF approximations where entanglement between the bath and the impurity is absent (see also our discus-

since entanglement is ignored. In these non-entangled limits only $K_{11}^{\sigma\sigma'}$ acquires a non-zero value and hence it is relevant. Turning to a full MB description where several species wavefunctions are considered, and therefore entanglement is present, $K_{ij}^{\sigma\sigma'} \neq 0$ as long as there is a finite spatial overlap between the different species wavefunctions of the same ($\sigma = \sigma'$) or distinct ($\sigma \neq \sigma'$) species. Inserting now Eq. (S11) into Eq. (S10) and using Eq. (S12) we can re-express the overlap integral in terms of the Schmidt coefficients λ_i 's and $K_{ij}^{\sigma\sigma'}$. Indeed we obtain

sion above) it can be easily shown that $\Lambda^{BI}(t)$ becomes

$$\Lambda^{BI}(t) = \Lambda_0(t) \equiv \frac{[K_{11}^{BI}]^2}{K_{11}^{BB} K_{11}^{II}}, \quad (\text{S14})$$

as there is only a single (and hence dominant) mode in the corresponding Schmidt decomposition. Moreover when considering the weakly entangled case where $\lambda_1 \approx 1$ and $\lambda_j \ll 1$ with $j = 2, 3, \dots, D$ the overlap integral can be written with respect to the higher-order Schmidt coefficients as

$$\Lambda^{BI}(t) = \Lambda_0(t) \left[1 + 2 \sum_{j>1} \frac{\lambda_j(t)}{\lambda_1(t)} \left(\frac{K_{1j}^{BI}}{K_{11}^{BB}} + \frac{K_{j1}^{BI}}{K_{11}^{BB}} - \frac{K_{1j}^{II}}{K_{11}^{II}} - \frac{K_{1j}^{BB}}{K_{11}^{BB}} \right) \right] + \mathcal{O}\left(\left(\frac{\lambda_j}{\lambda_1}\right)^2\right). \quad (\text{S15})$$

We remark here that this weakly entangled case is actually realistic in a MB treatment only within the miscible phase since immiscible species are strongly entangled. It becomes evident that in this weakly entangled case the major contribution of $\Lambda^{BI}(t)$ stems from the dominant mode described by λ_1 and being encrypted in $\Lambda_0(t)$. However, there are small additional contributions to $\Lambda^{BI}(t)$ being of the order of λ_j/λ_1 . These latter contributions originate from the overlap between the one-body densities of the first $[\rho_1^{(1),\sigma}(x;t)]$ with the higher-order $[\rho_j^{(1),\sigma}(x;t), j > 1]$ modes of entanglement. It is important to stress that the species wavefunction of the first mode, $\Psi_1^\sigma(t)$, and therefore its density $\rho_1^{(1),\sigma}(x;t)$ is greatly altered in the full MB case when compared to the MF and SMF cases where entanglement is neglected. Concluding, $\Lambda^{BI}(t)$ captures the manifestation of entanglement even in such a weakly entangled scenario, while more traditional measures such as the Von-Neumann en-

tropy $S_{BI}^{VN} = -\sum_i \lambda_i(t) \log \lambda_i(t)$ are not sensitive to this change. Indeed S_{BI}^{VN} depends on the number and the weights (λ_i 's) of the entanglement modes. Therefore $\Lambda^{BI}(t)$ greatly supplements S_{BI}^{VN} regarding the identification of entanglement induced effects.

GENERATION OF ENTANGLEMENT AND FRAGMENTATION VERSUS THE DEGREE OF MISCIBILITY

To complete the physical picture we next focus on the dynamics between the impurity and the bath. For this purpose we employ the overlap integral $\Lambda^{B\uparrow}(t)$ [Fig. S4(a)] between the single-particle densities of the bath and the spin- \uparrow . As dictated by $\Lambda^{B\uparrow}(t)$ within R_I the impurity is partially miscible with the BEC while it is well separated within R_{III} . The link between $|S(t)|$ and $\Lambda^{B\uparrow}(t)$ is of significant importance not only due to

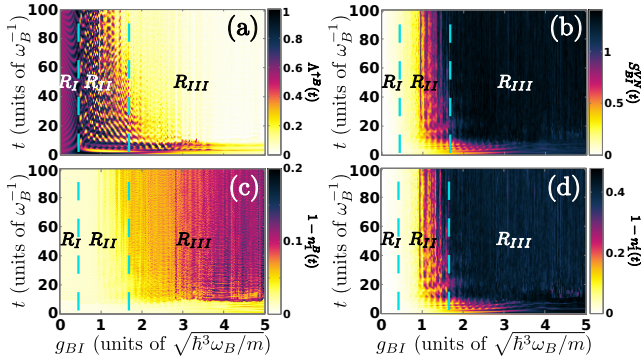


FIG. S4. (Color online) (a) Temporal evolution of the overlap, $\Lambda^{B\uparrow}(t)$, between the bath and the spin- \uparrow of the impurity atom (b) Evolution of the von-Neumann entropy, $S_{BI}^{VN}(t)$ for increasing g_{BI} . Deviation from unity of the first natural orbital of the (c) bath and (d) the impurity for varying g_{BI} . In all cases $N_B = 100$, $N_I = 1$ and $g_{BB} = 0.5$.

the experimental relevance of both quantities but most importantly because $\Lambda^{B\uparrow}(t)$ can be expressed in terms of the Schmidt coefficients, λ_i , see also Eqs. (S13) and (S15). For instance in the weakly entangled case where $\lambda_1 \approx 1$ and $\lambda_j \ll 1$

$$\frac{\Lambda^{B\uparrow}(t)}{\Lambda_0(t)} - 1 \propto \sum_{j>1} \frac{\lambda_j(t)}{\lambda_1(t)}, \quad (\text{S16})$$

with $\Lambda_0(t)$ being the overlap integral accounting only for the contribution of the first Schmidt coefficient λ_1 . Therefore $\Lambda^{B\uparrow}(t)$ can be used as a measure to probe the generation of entanglement in the MB system. However to directly visualize the degree of entanglement during the dynamics we employ the von-Neumann entropy, $S_{BI}^{VN}(t) = -\sum_i \lambda_i(t) \log \lambda_i(t)$ [S9]. The temporal evolution of $S_{BI}^{VN}(t)$ [Fig. S4(b)] shows that the dressed impurity is entangled with the BEC within the regions R_I and R_{II} . Most importantly the system becomes strongly entangled within R_{III} , where the polaron ceases to exist, showcasing a plateau of $S_{BI}^{VN}(t > 15) \approx 1.2$ for fixed $g_{BB} = 0.5$ and for all $g_{BI} \gtrsim 1.65$. This result is in turn related to the fragmented nature of the system [Figs. S4(c), S4(d)]. The latter is captured by the deviation from unity of the first natural orbital $1 - n_1^\sigma(t)$ of the σ -species. Since we consider a single impurity $n_1^I(t) = \lambda_1(t)$ follows $S_{BI}^{VN}(t)$. However, the bath fragmentation is almost zero in R_I and R_{II} and it is weak in R_{III} . Therefore it is the entanglement between the impurity and the bath that plays the crucial role in the quasiparticle formation, e.g. see that the growth rate of S_{BI}^{VN} becomes maximal in R_{II} , and not the fragmentation of the bath.

- [S1] S. Nascimbène, N. Navon, K. J. Jiang, L. Tarruell, M. Teichmann, J. McKeever, F. Chevy, and C. Salomon, Phys. Rev. Lett. **103**, 170402 (2009).
- [S2] P. Siegl, S. I. Mistakidis, and P. Schmelcher, Phys. Rev. A **97**, 053626 (2018).
- [S3] G. M. Koutentakis, S. I. Mistakidis and P. Schmelcher, Phys. Rev. A **95**, 013617 (2017).
- [S4] J. P. Ronzheimer, M. Schreiber, and S. Braun, Phys. Rev. Lett. **110**, 205301 (2013).
- [S5] J. W. Abraham and M. Bonitz, Contrib. Plasma Phys. **54**, 27 (2014).
- [S6] A. Sartori, and A. Recati, Europ. Phys. J. D **67**, 260 (2013).
- [S7] L. Cao, V. Bolsinger, S. I. Mistakidis, G. M. Koutentakis, S. Krönke, J. M. Schurer, and P. Schmelcher, J. Chem. Phys. **147**, 044106 (2017).
- [S8] L. Cao, S. Krönke, O. Vendrell, and P. Schmelcher, J. Chem. Phys. **139**, 134103 (2013).
- [S9] R. Horodecki, P. Horodecki, M. Horodecki, and K. Horodecki, Rev. Mod. Phys. **81**, 865 (2009).
- [S10] G. C. Katsimiga, G. M. Koutentakis, S. I. Mistakidis, P. G. Kevrekidis, and P. Schmelcher, New J. Phys. **19**, 073004 (2017).
- [S11] S. I. Mistakidis, G. C. Katsimiga, P. G. Kevrekidis, and P. Schmelcher, New J. Phys. **20**, 043052 (2018).
- [S12] S. I. Mistakidis, A. G. Volosniev, N. T. Zinner, and P. Schmelcher, arXiv:**1809.01889** (2018).
- [S13] M. Roncaglia, A. Montorsi, and M. Genovese, Phys. Rev. A **90**, 062303 (2014).
- [S14] G. M. Koutentakis, S. I. Mistakidis, and P. Schmelcher, arXiv:**1804.07199** (2018).
- [S15] S. I. Mistakidis, G. C. Katsimiga, G. M. Koutentakis, and P. Schmelcher, arXiv:**1808.00040** (2018).
- [S16] J. Erdmann, S. I. Mistakidis, and P. Schmelcher, Phys. Rev. A **99**, 013605 (2019).
- [S17] J. Frenkel, in *Wave Mechanics* 1st ed. (Clarendon Press, Oxford, 1934), pp. 423-428.
- [S18] P. A. Dirac, Proc. Camb. Phil. Soc., **26**, 376, Cambridge University Press (1930).
- [S19] L. P. Pitaevskii and S. Stringari, *Bose-Einstein Condensation*, Oxford University Press (Oxford, 2003).
- [S20] P. G. Kevrekidis, D. J. Frantzeskakis, and R. Carretero-González, *The Defocusing Nonlinear Schrödinger Equation*, SIAM (Philadelphia, 2015).
- [S21] M. Naraschewski, and R. J. Glauber, Phys. Rev. A **59**, 4595 (1999).
- [S22] E. J. Mueller, T. L. Ho, M. Ueda, and G. Baym, Phys. Rev. A **74**, 33612 (2006).
- [S23] O. Penrose, and L. Onsager, Phys. Rev. **104**, 576 (1956).
- [S24] P. Jain and M. Boninsegni, Phys. Rev. A **83**, 023602 (2011).
- [S25] S. Bandyopadhyay, A. Roy, and D. Angom, Phys. Rev. A **96**, 043603, (2017).

4.2.3 Many-body quantum dynamics and induced correlations of Bose polarons

PAPER • OPEN ACCESS

Many-body quantum dynamics and induced correlations of Bose polarons

To cite this article: S I Mistakidis *et al* 2020 *New J. Phys.* **22** 043007

View the [article online](#) for updates and enhancements.

Recent citations

- [Pump-probe spectroscopy of Bose polarons: Dynamical formation and coherence](#)
S. I. Mistakidis *et al*
- [Many-body effects on second-order phase transitions in spinor Bose-Einstein condensates and breathing dynamics](#)
K. M. Mittal *et al*
- [Correlated dynamics of fermionic impurities induced by the counterflow of an ensemble of fermions](#)
J. Kwasniok *et al*



PAPER

Many-body quantum dynamics and induced correlations of Bose polarons

OPEN ACCESS

RECEIVED

5 November 2019

REVISED

4 February 2020

ACCEPTED FOR PUBLICATION

12 February 2020

PUBLISHED

7 April 2020

Original content from this work may be used under the terms of the [Creative Commons Attribution 4.0 licence](https://creativecommons.org/licenses/by/4.0/).

Any further distribution of this work must maintain attribution to the author(s) and the title of the work, journal citation and DOI.

S I Mistakidis¹ , G M Koutentakis^{1,2}, G C Katsimiga¹, Th Busch³ and P Schmelcher^{1,2} ¹ Center for Optical Quantum Technologies, Department of Physics, University of Hamburg, Luruper Chaussee 149, D-22761 Hamburg Germany² The Hamburg Centre for Ultrafast Imaging, Universität Hamburg, Luruper Chaussee 149, D-22761 Hamburg, Germany³ OIST Graduate University, Onna, Okinawa 904-0495, JapanE-mail: smistaki@physnet.uni-hamburg.de**Keywords:** Bose polarons, ultracold atomic mixtures, induced interactions, quench dynamics, correlated dynamics

Abstract

We study the ground state properties and non-equilibrium dynamics of two spinor bosonic impurities immersed in a one-dimensional bosonic gas upon applying an interspecies interaction quench. For the ground state of two non-interacting impurities we reveal signatures of attractive induced interactions in both cases of attractive or repulsive interspecies interactions, while a weak impurity–impurity repulsion forces the impurities to stay apart. Turning to the quench dynamics we inspect the time-evolution of the contrast unveiling the existence, dynamical deformation and the orthogonality catastrophe of Bose polarons. We find that for an increasing postquench repulsion the impurities reside in a superposition of two distinct two-body configurations while at strong repulsions their corresponding two-body correlation patterns show a spatially delocalized behavior evincing the involvement of higher excited states. For attractive interspecies couplings, the impurities exhibit a tendency to localize at the origin and remarkably for strong attractions they experience a mutual attraction on the two-body level that is imprinted as a density hump on the bosonic bath.

1. Introduction

Mobile impurities immersed in a quantum many-body (MB) environment become dressed by the excitations of the latter. This gives rise to the concept of quasiparticles, e.g. the polarons [1, 2], which were originally introduced by Landau [3–5]. This dressing mechanism can strongly modify the elementary properties of the impurity atoms and lead to concepts such as effective mass and energy [6, 7], induced interactions [8, 9] and attractively bound bipolaron states [1, 2, 10, 11]. Polaron states have been recently realized in ultracold atom experiments [12–14], which exhibit an unprecedented degree of controllability and, in particular, allow to adjust the interaction between the impurities and the medium with the aid of Feshbach resonances [15, 16]. The spectrum of the quasiparticle excitations can be characterized in terms of radiofrequency and Ramsey spectroscopy [12, 17–19] and the trajectories of the impurities can be monitored via *in situ* measurements [20, 21]. Experimentally Bose [20–24] and Fermi [12, 13, 17] polarons have been observed and these experiments confirmed the importance of higher-order correlations for the description of the polaronic properties. The experiments in turn have spurred additional several theoretical investigations which have aimed at describing different polaronic aspects [25, 26] by operating e.g. within the Fröhlich model [27–31], effective Hamiltonian approximations [8, 32–34], variational approaches [7, 9, 22, 35–37], renormalization group methods [25, 38, 39] and the path integral formalism [40, 41].

The focus of the majority of the above-mentioned theoretical studies have been the stationary properties of the emergent quasiparticle states for single impurities in homogeneous systems. However, the non-equilibrium dynamics of impurities is far less explored and is expected to be dominated by correlation effects which build up in the course of the evolution [34–36, 39, 42–45]. Existing examples include the observation of self-trapping phenomena [46, 47], formation of dark-bright solitons [6, 42], impurity transport in optical lattices [48–51],

orthogonality catastrophe events [35, 52], injection of a moving impurity into a gas of Tonks–Girardeau bosons [53–60] and the relaxation dynamics of impurities [45, 61, 62]. Besides these investigations, which have enabled a basic description of the quasiparticle states in different interaction regimes, a number of important questions remain open and a full theoretical understanding of the dynamics specifically of Bose polarons is still far from complete.

A system of particular interest consists of two impurity atoms immersed in a Bose–Einstein condensate (BEC), where the underlying interactions between the impurities come into play. In such a system impurity–impurity correlations [10, 63, 64] can be induced by the BEC, even in the case where no direct interaction between the impurities is present. However, the competition between direct and induced interactions can also be expected to lead to interesting effects. It is therefore natural to investigate the dynamical response of the impurities with varying interspecies interactions (attractive or repulsive) and to identify in which regimes robustly propagating Bose polaron states exist [25, 39, 43]. In addition it is interesting to study the existence of bound states between the impurities [1, 10], the effect of strong correlation between the impurities on the orthogonality catastrophe [35, 52], phase separation between the two atomic species [65–67] and energy exchange processes [68, 69]. Comparing the effects in systems with single and multiple impurities is an interesting task, as well as their theoretical interpretation in terms of the spin polarization (alias the contrast) which has not yet been analyzed in the case of two impurities and involves more energy channels compared to the case of a single impurity. For these reasons, we study in this work an interspecies interaction quench for two bosonic impurities overlapping with a harmonically trapped BEC. To address the correlated quantum dynamics of the bosonic multicomponent system we use the multi-layer multi-configuration time-dependent Hartree method for atomic mixtures (ML-MCTDHX) [70–72], which is a non-perturbative variational method that enables us to comprehensively capture interparticle correlations.

In this work we start by studying the ground state of two non-interacting impurities in a bosonic gas and show that for an increasing attraction or repulsion they feature attractive induced interactions, a result that persists also for small bath sizes and heavy impurities [8]. However, two weakly repulsively interacting impurities can experience a net repulsion for repulsive interspecies interactions.

When quenching the multicomponent system, we monitor the time-evolution of the contrast and its spectrum [19, 25] for varying postquench interactions. We show that the polaron excitation spectrum depends strongly on the postquench interspecies interaction strength and the number of impurities while it is almost insensitive to the direct impurity–impurity interaction for the weak couplings considered herein. Additionally, a breathing motion of the impurities can be excited [73, 74] for weak postquench interspecies repulsions, while for stronger ones a splitting of their single-particle density occurs. In this latter case a strong attenuation of the impurities motion results in the accumulation of their density at the edges of the bosonic gas and they mainly reside in a superposition of two distinct two-body configurations: the impurities either bunch on the same or on separate sides of the BEC, while the bath exhibits an overall breathing motion. For attractive interspecies couplings, the impurities exhibit a breathing motion characterized by a beating pattern. The latter stems from the values of the impurities’ center-of-mass and relative coordinate breathing modes, whose frequency difference originates from the presence of attractive induced interactions. Additionally, the impurities possess a tendency to localize at the trap center, a behavior that becomes more pronounced for stronger attractions [75]. Strikingly, for strong attractive interspecies interactions we show that during the dynamics the impurities experience a mutual attraction on the two-body level and the density of the bosonic bath develops a small amplitude hump at the trap center. We find that a similar dynamical response also takes place for two weakly repulsively interacting impurities but the involved time-scales are different. To interpret the observed dynamics of the impurities we invoke an effective potential picture that applies for weak couplings [35, 36, 73, 75].

Our work is structured as follows. Section 2 presents our setup and introduces the correlation measures that are used to monitor the dynamics. In section 3 we address the ground state properties of the impurities for a wide range of interspecies interaction strengths. The emergent non-equilibrium dynamics triggered by an interspecies interaction quench is analyzed in detail in section 4. In particular, we present the time-evolution of the contrast and the system’s spectrum (sections 4.1–4.3) and study the full dynamics of the single-particle and two-body reduced density matrices for repulsive (section 4.4) and attractive (section 4.5) postquench interactions. We summarize and discuss future perspectives in section 5. Finally, appendix details our numerical simulation method and demonstrates the convergence properties.

2. Theoretical framework

2.1. Hamiltonian and quench protocol

We consider a highly particle number imbalanced Bose–Bose mixture composed of $N_I = 2$ bosonic impurities (I) possessing an additional pseudospin-1/2 degree of freedom [76], which are immersed in a bosonic gas of

$N_B = 100$ structureless bosons (B). Moreover, the mixture is assumed to be mass-balanced, namely $m_B = m_I \equiv m$ and each species is confined in the same one-dimensional external harmonic oscillator potential of frequency $\omega_B = \omega_I = \omega$. Such a system can be experimentally realized by considering e.g. a ^{87}Rb BEC where the majority species resides in the hyperfine state $|F = 2, m_F = 1\rangle$ and the pseudospin degree of freedom of the impurities refers for instance to the internal states $|\uparrow\rangle \equiv |F = 1, m_F = 1\rangle$ and $|\downarrow\rangle \equiv |F = 1, m_F = -1\rangle$ [77, 78]. Alternatively, it can be realized to a good approximation by a mixture of isotopes of ^{87}Rb for the bosonic gas and two hyperfine states of ^{85}Rb for the impurities. The underlying MB Hamiltonian of this system reads

$$\hat{H} = \hat{H}_B^0 + \sum_{a=\uparrow,\downarrow} \hat{H}_a^0 + \sum_{a=\uparrow,\downarrow} \hat{H}_{aa}^{\text{int}} + \hat{H}_{\uparrow\downarrow}^{\text{int}} + \hat{H}_{BB}^{\text{int}} + \hat{H}_{BI}^{\text{int}}. \quad (1)$$

The non-interacting Hamiltonian of the bosonic gas is $\hat{H}_B^0 = \int dx \hat{\Psi}_B^\dagger(x) \left(-\frac{\hbar^2}{2m} \frac{d^2}{dx^2} + \frac{1}{2} m \omega^2 x^2 \right) \hat{\Psi}_B(x)$, while for the impurities it reads $\hat{H}_a^0 = \int dx \hat{\Psi}_a^\dagger(x) \left(-\frac{\hbar^2}{2m} \frac{d^2}{dx^2} + \frac{1}{2} m \omega^2 x^2 \right) \hat{\Psi}_a(x)$ with $a = \{\uparrow, \downarrow\}$ being the indices of the spin components. Here $\hat{\Psi}_\sigma(x)$ refers to the bosonic field-operator of either the bosonic gas ($\sigma = B$) or the impurity ($\sigma = a = \{\uparrow, \downarrow\}$) atoms. Furthermore, we operate in the ultracold regime where s -wave scattering is the dominant interaction process. Therefore both the intra- and the intercomponent interactions can be adequately modeled by contact ones. The contact intraspecies interaction of the BEC component is modeled by $\hat{H}_{BB}^{\text{int}} = g_{BB} \int dx \hat{\Psi}_B^\dagger(x) \hat{\Psi}_B^\dagger(x) \hat{\Psi}_B(x) \hat{\Psi}_B(x)$ and between the impurities via $\hat{H}_{aa'}^{\text{int}} = g_{aa'} \int dx \hat{\Psi}_a^\dagger(x) \hat{\Psi}_{a'}^\dagger(x) \hat{\Psi}_a(x) \hat{\Psi}_{a'}(x)$ where either $a = a' = \uparrow, \downarrow$ or $a = \uparrow, a' = \downarrow$. Note also that we assume $g_{\uparrow\uparrow} = g_{\downarrow\downarrow} \equiv g_{II}$. Most importantly, we consider that only the pseudospin- \uparrow component of the impurities interacts with the bosonic gas while the pseudospin- \downarrow is non-interacting. The resulting intercomponent interaction is $\hat{H}_{BI}^{\text{int}} = g_{BI} \int dx \hat{\Psi}_B^\dagger(x) \hat{\Psi}_\uparrow^\dagger(x) \hat{\Psi}_\uparrow(x) \hat{\Psi}_B(x)$, where $g_{BI} \equiv g_{B\uparrow}$ and $g_{B\downarrow} = 0$.

In all of the above-mentioned cases, the effective one-dimensional coupling strength [79] is given by $g_{\sigma\sigma'} = \frac{2\hbar^2 a_{\sigma\sigma'}^s}{\mu a_\perp^2} (1 - |\zeta(1/2)| a_{\sigma\sigma'}^s / \sqrt{2} a_\perp)^{-1}$, where $\sigma, \sigma' = B, \uparrow, \downarrow$ and $\mu = \frac{m}{2}$ is the reduced mass. The transversal length scale is $a_\perp = \sqrt{\hbar / \mu \omega_\perp}$ with ω_\perp being the transversal confinement frequency and $a_{\sigma\sigma'}^s$ denotes the three-dimensional s -wave scattering length within ($\sigma = \sigma'$) or between ($\sigma \neq \sigma'$) the components. In a corresponding experiment, $g_{\sigma\sigma'}$ can be tuned either via $a_{\sigma\sigma'}^s$ with the aid of Feshbach resonances [15, 16] or by adjusting ω_\perp using confinement-induced resonances [79]. In the following, the MB Hamiltonian of equation (1) is rescaled with respect to $\hbar\omega$. As a consequence, length, time, and interaction strengths are given in units of $\sqrt{\frac{\hbar}{m\omega}}$, ω^{-1} and $\sqrt{\frac{\hbar^3\omega}{m}}$ respectively.

To study the quench dynamics, the above-described multicomponent system is initially prepared in its ground state configuration for fixed $g_{BB} = 0.5$ and $g_{BI} = 0$ and either $g_{II} = 0$ or $g_{II} = 0.2$. In this way, the case of two non-interacting and that of weakly interacting impurities are investigated. This initial (ground) state emulates a system prepared in the $|1, -1\rangle = |\downarrow\rangle_1 \otimes |\downarrow\rangle_2$ configuration for the spin degree of freedom i.e. where the impurity-BEC interaction is zero. Note that the spinor part of the wavefunction is expressed in the basis of the total spin i.e. $|S, S_z\rangle$ [80]. Accordingly, the spatial part $|\Psi_{BI}^0\rangle$ of the ground state of the system obeys the following eigenvalue equation $(\hat{H} - \hat{H}_{BI})|\Psi_{BI}^0\rangle |1, -1\rangle = E_0 |\Psi_{BI}^0\rangle |1, -1\rangle$, with E_0 being the corresponding eigenenergy and $\hat{H}_{BI}|\Psi_{BI}^0\rangle |1, -1\rangle = 0$. To trigger the dynamics we carry out an interspecies interaction quench from $g_{BI} = 0$ to a finite positive or negative value of g_{BI} at $t = 0$ and monitor the subsequent time-evolution. In a corresponding experiment, this quench protocol can be implemented by using a radiofrequency $\pi/2$ pulse with an exposure time much smaller than ω^{-1} [19]. The pulse acts upon the spin degree of freedom of the impurity, which maps the pseudospin- \downarrow impurities to the superposition state $|\psi_S\rangle_i \equiv \frac{|\uparrow\rangle_i + |\downarrow\rangle_i}{\sqrt{2}}$ with $i = 1, 2$ [18]. The corresponding MB wavefunction of the system, $|\Psi(t)\rangle = e^{-i\hat{H}t/\hbar} [|\Psi_{BI}^0\rangle (|\psi_S\rangle_1 \otimes |\psi_S\rangle_2)]$, is then given by

$$|\Psi(t)\rangle = \frac{1}{\sqrt{2}} e^{-i\hat{H}t/\hbar} [|\Psi_{BI}^0\rangle |1, 0\rangle] + \frac{1}{2} (e^{-iE_0 t/\hbar} |\Psi_{BI}^0\rangle |1, -1\rangle + e^{-i\hat{H}t/\hbar} |\Psi_{BI}^0\rangle |1, 1\rangle). \quad (2)$$

The setup and processes addressed in our work can be experimentally realized utilizing radiofrequency spectroscopy [9, 18, 22, 23, 43] and Ramsey interferometry [18].

2.2. MB wavefunction ansatz

To calculate the stationary properties and to track the MB non-equilibrium quantum dynamics of the multicomponent bosonic system discussed above we employ the ML-MCTDHX method [70–72]. This is an *ab initio* variational method for solving the time-dependent MB Schrödinger equation of atomic mixtures and it is based on the expansion of the total MB wavefunction with respect to a time-dependent and variationally optimized basis tailored to capture both the intra- and the interspecies correlations of a multicomponent system [35, 65, 81, 82].

To include the interspecies correlations, the MB wavefunction ($|\Psi(t)\rangle$) is first expanded in terms of D distinct species functions, $|\Psi_i^\sigma(t)\rangle$, for each component $\sigma = B, I$, and then expressed according to a truncated Schmidt decomposition [83] of rank D , namely

$$|\Psi(t)\rangle = \sum_{k=1}^D \sqrt{\lambda_k(t)} |\Psi_k^B(t)\rangle |\Psi_k^I(t)\rangle. \quad (3)$$

Here the time-dependent expansion coefficients $\lambda_k(t)$ are the Schmidt weights and will be referred to in the following as the natural populations of the k th species function. Evidently, the system is entangled [84] or interspecies correlated when at least two different $\lambda_k(t)$ possess a non-zero value. If this is not the case, i.e. for $\lambda_1(t) = 1, \lambda_{k>1}(t) = 0$, the wavefunction is a direct product of two states.

Therefore, in order to account for intraspecies correlations, each of the above-mentioned species functions is expressed as a linear superposition of time-dependent number-states, $|\vec{n}(t)\rangle^\sigma$, with time-dependent coefficients $A_{i;\vec{n}}^\sigma(t)$ as

$$|\Psi_i^\sigma(t)\rangle = \sum_{\vec{n}} A_{i;\vec{n}}^\sigma(t) |\vec{n}(t)\rangle^\sigma. \quad (4)$$

Each number state $|\vec{n}(t)\rangle^\sigma$ is a permanent building upon d^σ time-dependent variationally optimized single-particle functions (SPFs) $|\phi_l^\sigma(t)\rangle, l = 1, 2, \dots, d^\sigma$ with occupation numbers $\vec{n} = (n_1, \dots, n_{d^\sigma})$. Consecutively, the SPFs are expanded on a time-independent primitive basis. The latter refers to an \mathcal{M} dimensional discrete variable representation (DVR) for the majority species and it is denoted by $\{|k\rangle\}$. For the impurities this corresponds to the tensor product $\{|k, s\rangle\}$ of the DVR basis for the spatial degrees of freedom and the two-dimensional pseudospin-1/2 basis $\{|\uparrow\rangle, |\downarrow\rangle\}$. Accordingly, each SPF of the impurities is a spinor wavefunction of the form

$$|\phi_j^I(t)\rangle = \sum_{k=1}^{\mathcal{M}} (B_{jk\uparrow}^I(t) |k\rangle |\uparrow\rangle + B_{jk\downarrow}^I(t) |k\rangle |\downarrow\rangle), \quad (5)$$

with $B_{jk\uparrow}^I(t)$ [$B_{jk\downarrow}^I(t)$] being the time-dependent expansion coefficients of the pseudospin- \uparrow [\downarrow] (see also [35, 82] for a more detailed discussion).

The time-evolution of the $(N_B + N_I)$ -body wavefunction $|\Psi(t)\rangle$ governed by the Hamiltonian of equation (1) is obtained via solving the so-called ML-MCTDHX equations of motion [70]. The latter are determined by utilizing e.g. the Dirac–Frenkel [85, 86] variational principle for the generalized ansatz introduced in equations (3)–(5). This procedure results in a set of D^2 linear differential equations of motion for the $\lambda_k(t)$ coefficients which are coupled to $D \left(\frac{(N_B + d^B - 1)!}{N_B!(d^B - 1)!} + \frac{(N_I + d^I - 1)!}{N_I!(d^I - 1)!} \right)$ nonlinear integrodifferential equations for the species functions and $d^B + d^I$ nonlinear integrodifferential equations for the SPFs.

A main aspect of the ansatz outlined above is the expansion of the system's MB wavefunction with respect to a time-dependent and variationally optimized basis. The latter allows to efficiently take into account the intra- and intercomponent correlations of the system using a computationally feasible basis size. In the present case the Bose gas consists of a large number of weakly interacting particles and therefore its intracomponent correlations are suppressed. As a consequence they can be adequately captured by employing a small number of orbitals, $d^B < 4$. Additionally, the number of impurities, $N_I < 3$, is small giving rise to a small number of integrodifferential equations allowing us to employ many orbitals, d_I , and thus account for strong impurity–impurity and impurity–BEC correlations. Therefore, the number of the resulting equations of motion that need to be solved is numerically tractable. Since our method is variational, its validity is determined upon examining its convergence. For details on the precision of our simulations see [appendix](#).

2.3. Correlation measures

To study the quench-induced dynamics of each species at the single-particle level we calculate the one-body reduced density matrix for each species [87, 88]

$$\rho_\sigma^{(1)}(x, x'; t) = \langle \Psi(t) | \hat{\Psi}_\sigma^\dagger(x) \hat{\Psi}_\sigma(x') | \Psi(t) \rangle. \quad (6)$$

Here, $\hat{\Psi}_\sigma(x)$ is the σ -species bosonic field operator acting at position x and satisfying the standard bosonic commutation relations [89]. For simplicity, we will use in the following the one-body densities for each species i.e. $\rho_\sigma^{(1)}(x; t) \equiv \rho_\sigma^{(1)}(x, x' = x; t)$, which is a quantity that is experimentally accessible via averaging over a sample of single-shot images [65, 90, 91]. We remark that the eigenfunctions and eigenvalues of $\rho_\sigma^{(1)}(x, x'; t)$ are termed natural orbitals $\varphi_i^\sigma(x; t)$ and natural populations $n_i^\sigma(t)$ [65, 70] respectively. In this sense, each bosonic subsystem is called intraspecies correlated if more than a single natural population possess a non-zero contribution. Otherwise, i.e. for $n_1^\sigma(t) = 1$ and $n_{i>1}^\sigma(t) = 0$, the corresponding subsystem is said to be fully coherent and the MB wavefunction (equations (3), (5)) reduces to a mean-field product ansatz [92, 93].

To unveil the role of impurity–impurity correlations following the interspecies interaction quench we calculate the time-evolution of the corresponding diagonal of the two-body reduced density matrix

$$\rho_{aa}^{(2)}(x_1, x_2; t) = \langle \Psi(t) | \hat{\Psi}_a^\dagger(x_1) \hat{\Psi}_{a'}^\dagger(x_2) \hat{\Psi}_{a'}(x_2) \hat{\Psi}_a(x_1) | \Psi(t) \rangle, \quad (7)$$

where $a, a' = \uparrow, \downarrow$. The two-body reduced density matrix refers to the probability of finding simultaneously one pseudospin- a boson at x_1 and a pseudospin- a' boson at x_2 [65, 66]. Moreover, it provides insights into the spatially resolved dynamics of the two impurities with respect to one another. Indeed, the impurities are dressed by the excitations of the bosonic gas forming quasiparticles which in turn can move independently or interact, and possibly form a bound state [8, 10, 42, 94].

To capture the emerging effective interactions between the two bosonic impurities we monitor their relative distance [9, 42] given by

$$\langle r_{aa}(t) \rangle = \frac{\int dx_1 dx_2 |x_1 - x_2| \rho_{aa}^{(2)}(x_1, x_2; t)}{\langle \Psi(t) | \hat{N}_a (\hat{N}_a - 1) | \Psi(t) \rangle}. \quad (8)$$

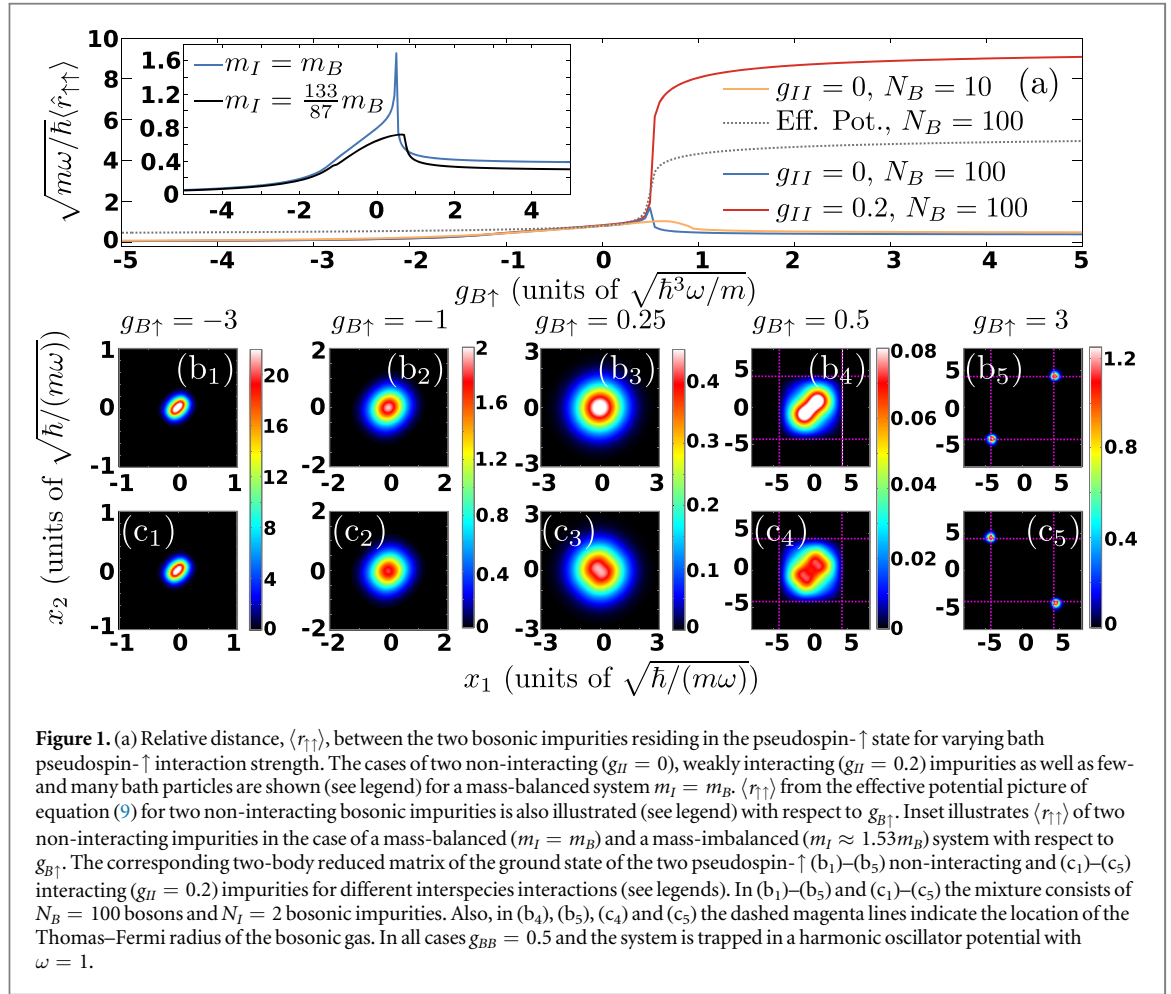
Here, \hat{N}_a with $a = \uparrow, \downarrow$ is the number operator that measures the number of bosons in the spin- a state. Experimentally, $\langle r_{aa}(t) \rangle$ can be probed via *in situ* spin-resolved single-shot measurements on the spin- a state [91]. More precisely, each image gives an estimate of $\langle r_{aa}(t) \rangle$ between the bosonic impurities if their position uncertainty is assured to be adequately small [91]. Subsequently, $\langle r_{aa}(t) \rangle$ is obtained by averaging over several such images.

3. Induced interactions in the ground state of two bosonic impurities

Before investigating the non-equilibrium dynamics of the two bosonic impurities immersed in a BEC it is instructive to first analyze the ground state of two impurities interacting with the bosonic medium for varying interspecies interactions $g_{B\uparrow}$ ranging from attractive to repulsive. Note that such a configuration corresponds in our case to two impurities residing in the pseudospin- \uparrow state since only this state is interacting with the bath (see also equation (1)). The aim of this study is to reveal the presence of induced impurity-impurity interactions mediated by the bath. As discussed in section 2.1, the mass-balanced multicomponent bosonic system consists of two impurities $N_I = 2$ immersed in a MB bath of $N_B = 100$ atoms with $g_{BB} = 0.5$ and it is externally confined in a harmonic oscillator potential of frequency $\omega = 1$. Later on, also the mass-imbalanced and the few-body ($N_B = 10$) sceneria will be investigated. Below we consider either two non-interacting ($g_{II} = 0$) or two weakly interacting impurities ($g_{II} = 0.2$). To obtain the interacting ground state of the system as described by the Hamiltonian of equation (1) we employ either imaginary time propagation or improved relaxation [70, 71] within ML-MCTDHX.

The relative distance (equation (8)) between the two impurities as well as their two-body reduced density matrix (equation (7)) for different values of $g_{B\uparrow}$ are shown in figure 1. Focusing on the case of two non-interacting impurities, $g_{II} = 0$, we see that for larger attractions the relative distance between the impurities decreases (see figure 1(a)) and converges towards a constant value i.e. $\langle r_{\uparrow\uparrow} \rangle \approx 0.1$ for $g_{B\uparrow} < -2$. The decrease in $\langle r_{\uparrow\uparrow} \rangle$ for $-2 < g_{B\uparrow} < 0$ implies that the impurities effectively experience an attraction with respect to one another. This attraction is a manifestation of the attractive induced interactions mediated by the bosonic gas since $g_{II} = 0$ [8]. The impurities reside together in the vicinity of the trap center since $\rho_{\uparrow\uparrow}^{(2)}(-1 < x_1 < 1, -1 < x_2 < 1)$ is predominantly populated (see figure 1(b₂)). Additionally, for $g_{B\uparrow} < -2$, where $\langle r_{\uparrow\uparrow} \rangle$ become approximately constant, the impurities come very close with respect to one another. Here, the corresponding $\rho_{\uparrow\uparrow}^{(2)}(x_1, x_2)$ shrinks along its anti-diagonal and its diagonal becomes elongated (see figure 1(b₁)), which is indicative of a bound state having formed between the impurities known as a bipolaron state [8, 10, 94].

Turning to weak interspecies repulsions $0 < g_{B\uparrow} < 0.5$ we find that $\langle r_{\uparrow\uparrow} \rangle$ slightly increases (see figure 1(a)) while the two impurities reside close to the trap center (see figure 1(b₃)). It is important to mention that this increase in $\langle r_{\uparrow\uparrow} \rangle$ does not directly imply that the impurities experience a weak repulsion mediated by the bosonic bath. Indeed, by neglecting all correlations between the impurities, i.e. by substituting $\rho_{\uparrow\uparrow}^{(2)}(x_1, x_2) = \rho_{\uparrow}^{(1)}(x_1) \rho_{\uparrow}^{(1)}(x_2) / 2$ into $\langle r_{\uparrow\uparrow} \rangle$ we find the same tendency of $\langle r_{\uparrow\uparrow} \rangle$ with even slightly larger values (see also the discussion below). Since in the limit of the non-correlated case there are no induced interactions, the fact that $\langle r_{\uparrow\uparrow} \rangle$ is smaller when correlations are taken into account means that the impurities still feel an effective attractive force. Note that for the other interaction regimes presented herein such an unexpected behavior of $\langle r_{\uparrow\uparrow} \rangle$ does not occur as it can also be deduced by the corresponding two-body spatial configurations building upon $\rho_{\uparrow\uparrow}^{(2)}(x_1, x_2)$ (see below). Furthermore, it can be seen that at $g_{B\uparrow} = g_{BB} = 0.5$, where the miscibility/immiscibility transition between the impurity and the BEC takes place [65, 67], the behavior of $\langle r_{\uparrow\uparrow} \rangle$ is suddenly altered. Indeed for $g_{B\uparrow} \geq 0.5$, $\langle r_{\uparrow\uparrow} \rangle$ shows a decreasing tendency which indicates the presence of attractive induced interactions between the impurities. In particular, for $0.5 \leq g_{B\uparrow} < 1.1$, $\langle r_{\uparrow\uparrow} \rangle$ reduces and the impurities tend to bunch



together at the same location. This can be confirmed by the fact that $\rho_{\uparrow\uparrow}^{(2)}(x_1, x_2)$ shows a populated elongated diagonal as depicted in figure 1(b₄) for $g_{B\uparrow} = 0.5$. Moreover for stronger repulsions $g_{B\uparrow} > 1.1$, $\langle r_{\uparrow\uparrow} \rangle$ remains almost constant. Especially so for $g_{B\uparrow} > 1.5$, where the two impurities residing either on the left or the right edge of the Thomas–Fermi profile of the BEC. The latter can be evidenced in figure 1(b₅) by the two strongly populated spots appearing at $x_1 \approx x_2 \approx \pm R_{TF}$ with R_{TF} denoting the Thomas–Fermi radius.

In view of the results of [35] it is tempting to interpret our above findings in terms of an effective potential, $V_{\text{eff}}(x; g_{BI})$. A valid candidate for such a potential can be constructed as

$$V_{\text{eff}}(x; g_{BI}) = \frac{1}{2}m_I\omega^2x^2 + g_{BI}\rho_B^{(1)}(x; g_{BI} = 0), \quad (9)$$

where $\rho_B^{(1)}(x; g_{BI} = 0)$ refers to the equilibrium density of the BEC for $g_{BI} = 0$. Equation (9) implies that $\rho_B^{(1)}(x; g_{BI} = 0)$ acts on the impurities just as an additional repulsive ($g_{BI} > 0$) or attractive ($g_{BI} < 0$) potential on top of the externally imposed parabolic trap. It is noteworthy that the simplification of the impurity problem provided by equation (9) neglects several phenomena that might be important for the description of the ground state of the impurity system. First, the renormalization of the impurity's mass, $m_I \rightarrow m_I^{\text{eff}}$ by the coupling with its environment is neglected and, most importantly, the possible emergence of induced interactions is not contained in equation (9), due to the absence of two-body terms. The latter are extremely important for the description of $\rho_{\uparrow\uparrow}^{(2)}(x_1, x_2)$. Indeed, within $V_{\text{eff}}(x; g_{BI})$ no deformations can appear in the antidiagonal of the two-body density of the impurities which dictates their relative distance. This result is in contrast to the one obtained within the full MB Hamiltonian (equation (1)) shown in figures 1(b₁)–(b₅).

To provide an estimate of the quantitative error obtained by the approximation of equation (9) we include in figure 1(a), also the results for $\langle r_{\uparrow\uparrow} \rangle$ within the effective potential picture. It is evident that when using $V_{\text{eff}}(x; g_{BI})$, $\langle r_{\uparrow\uparrow} \rangle$ is always larger than the corresponding full MB result for $g_{BI} \neq 0$. This effect is particularly pronounced for $g_{BI} > 0.5$ where $\langle r_{\uparrow\uparrow} \rangle$ within equation (9) exhibits an increasing tendency instead of a decreasing one with g_{BI} . Such an effect can be attributed to the vanishing off-diagonal elements of $\rho_{\uparrow\uparrow}^{(2)}(x_1, x_2)$ which cannot be captured within $V_{\text{eff}}(x; g_{BI})$, as in the latter case $\rho_{\uparrow\uparrow}^{(2)}(x_1, x_2) = \rho_{\uparrow}^{(1)}(x_1)\rho_{\uparrow}^{(1)}(x_2)/2$. Indeed, the large impurity–impurity interactions within this regime render the effective potential incapable of describing the ground state of the bath

impurity system within this interaction regime. Similarly, for $g_{BI} < -2$, $\langle r_{\uparrow\uparrow} \rangle$ using the effective potential is significantly larger than the corresponding MB result, which can be attributed to the prominent role of induced interactions in the formation of the bipolaron state [10].

Considering a smaller bath consisting of $N_B = 10$ atoms does not significantly alter the ground state properties of the two non-interacting bosonic impurities. Here, $\langle r_{\uparrow\uparrow} \rangle$ (figure 1(a)) exhibits a similar behavior as for $N_B = 100$ atoms, with the most notable difference occurring in the region of $g_{B\uparrow} \approx g_{BB}$ where a smoother decrease occurs when compared to the $N_B = 100$ case. The value for which the distance becomes constant is also shifted to larger values when $N_B = 10$. These differences can be qualitatively understood within a corresponding effective potential picture which we will discuss in section 4.4.1, see equation (15) and the remark⁴.

A similar to the above-described overall phenomenology of the two non-interacting bosonic impurities for a varying $g_{B\uparrow}$ is also observed for the case of heavier impurities as can be seen in the inset of figure 1(a). Here we consider a ^{87}Rb bosonic gas and two ^{133}Cs impurities prepared e.g. in the hyperfine states $|F = 1, m_F = 0\rangle$ and $|F = 3, m_F = 2\rangle$ respectively and being both confined in the same external harmonic oscillator [95, 96]. Compared to the mass-balanced scenario the behavior of $\langle r_{\uparrow\uparrow} \rangle$ around $g_{B\uparrow} \approx g_{BB}$ becomes somewhat smoother and the maximum value is also slightly shifted to larger interaction strengths. Another conclusion that can be drawn, is that heavier impurities prefer to remain closer to each other compared to the lighter ones, since $\langle r_{\uparrow\uparrow} \rangle$ has smaller values in the former than in the latter case. As a consequence we can infer that heavy impurities experience stronger attractive induced interactions than light ones. These differences can also be explained in terms of the effective potential picture which will be introduced in section 4.4.1, see also remark⁵.

When a weak intraspecies repulsion among the impurities is introduced, $g_{II} = 0.2$, see figure 1(a), the ground state properties remain the same for attractive $g_{B\uparrow}$ but change fundamentally in the repulsive regime. Indeed $\langle r_{\uparrow\uparrow} \rangle$ decreases for an increasing interspecies attraction, signifying an induced attraction between the impurities despite their repulsive mutual interaction, until it becomes constant for $g_{B\uparrow} < -2$. More specifically, for $-2 < g_{B\uparrow} < 0$ the impurities are likely to remain close to the trap center (see figure 1(c₂)) where $\rho_{\uparrow\uparrow}^{(2)}(-1 < x_1 < 1, -1 < x_2 < 1)$ is predominantly populated. Furthermore, for $g_{B\uparrow} < -2$ the impurities bunch together at a fixed distance (figure 1(a)) and the two-body reduced density matrix becomes elongated along its diagonal (see figure 1(c₁)), suggesting the formation of a bound state similar to the $g_{II} = 0$ case. However, for $g_{B\uparrow} > 0$, $\langle r_{\uparrow\uparrow} \rangle$ exhibits an overall increasing tendency, which indicates that the two impurities are located mainly symmetrically around the trap center. This latter behavior can be directly deduced by the relatively wide distribution of the anti-diagonal of their two-body reduced density matrix (see figures 1(c₃) and (c₄) for $0 < g_{B\uparrow} < 1$). Moreover, and in sharp contrast to the $g_{II} = 0$ case, for $g_{B\uparrow} > 1$ the impurities acquire a large fixed distance and in particular can be found to reside one at the left and the other at the right edge of the BEC. This configuration of the impurities can be seen from the fact that solely off-diagonal elements of $\rho_{\uparrow\uparrow}^{(2)}(x_1, x_2)$ exist in figure 1(c₅) for $g_{B\uparrow} = 3$. Finally, it is worth mentioning that for two weakly repulsive impurities the induced effective attraction can never overcome their direct s -wave interaction for $g_{B\uparrow} > 0$.

To further support the existence of attractive induced interactions between the two impurities we study the ground state energy of the system for varying $g_{B\uparrow}$. In particular, we calculate the expected position of the polaronic resonances [9] namely $\Delta_+^{N_I}(g_{B\uparrow}) = [E(N_I, g_{B\uparrow}) - E(N_I, g_{B\uparrow} = 0)]/N_I$, where $E(N_I, g_{B\uparrow})$ is the energy of the system for N_I impurities at interaction $g_{B\uparrow}$ (figure 2(a)). As it can be seen, for both, $N_I = 1$ and $N_I = 2$, the resonance position $\Delta_+^{N_I}(g_{B\uparrow})$ increases for a larger $g_{B\uparrow}$ and it takes negative and positive values for attractive and repulsive interactions, respectively. Moreover, in the $N_I = 2$ scenario $\Delta_+^{N_I}(g_{B\uparrow})$ is found to be negatively shifted when compared to the corresponding $N_I = 1$ case for $g_{II} \neq 0$. This behavior indicates the presence of attractive induced interactions for both attractive and repulsive Bose polarons [8, 10, 63]. Focusing on $g_{II} = 0.2$ and $g_{B\uparrow} < 0$ a small decrease of $\Delta_+^{N_I}(g_{B\uparrow})$ occurs when compared to the $g_{II} = 0$ case showing that attractive induced interactions become more pronounced when direct s -wave impurity–impurity repulsions are involved. However, for repulsive polarons i.e. $g_{B\uparrow} > 0$ the presence of s -wave impurity–impurity interactions counteracts the effect of attractive induced interactions and accordingly $\Delta_+^{N_I}(g_{B\uparrow})$ is almost the same for $N_I = 2, g_{II} = 0.2$ and $N_I = 1$, see the inset of figure 2(a).

The underlying mechanism behind the above-mentioned impurity–impurity induced interactions can be qualitatively understood as follows. For attractive $g_{B\uparrow}$ the presence of impurities gives rise to a small density enhancement of the BEC in the vicinity of their spatial position. This effect is captured by the deformation of the

⁴Note that for $g_{B\uparrow} > g_{BB} = 0.5$ the effective potential of equation (15) possesses a double-well structure as shown in figure 6(e). The width of its central barrier is determined by R_{TF} which substantially decreases for smaller N_B . This decreasing tendency leads to a much more prominent overlap of the impurity wavefunction among the wells which in our case implies a smoother behavior of $\langle r_{\uparrow\uparrow} \rangle$.

⁵Within the effective potential picture of equation (15) the miscibility/immiscibility transition is imprinted as a change in the shape of $\mathcal{V}_I^{\text{eff}}(x)$ from parabolic (figure 6(a)) to a double-well (figure 6(e)) potential. This transition occurs at $g_{B\uparrow} = \frac{m_I}{m_B}g_{BB}$ and therefore for $m_I > m_B$ is shifted to larger values of $g_{B\uparrow}$ than for $m_I = m_B$, a behavior that explains the shift of $\langle r_{\uparrow\uparrow} \rangle$ for heavy impurities.

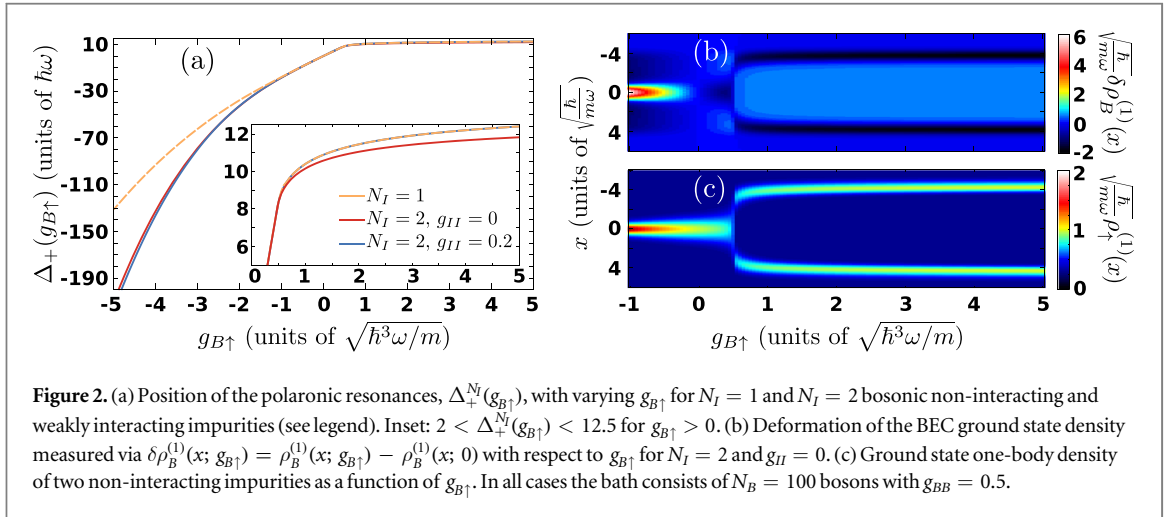


Figure 2. (a) Position of the polaronic resonances, $\Delta_+^{N_I}(g_{B\uparrow})$, with varying $g_{B\uparrow}$ for $N_I = 1$ and $N_I = 2$ bosonic non-interacting and weakly interacting impurities (see legend). Inset: $2 < \Delta_+^{N_I}(g_{B\uparrow}) < 12.5$ for $g_{B\uparrow} > 0$. (b) Deformation of the BEC ground state density measured via $\delta\rho_B^{(1)}(x; g_{B\uparrow}) = \rho_B^{(1)}(x; g_{B\uparrow}) - \rho_B^{(1)}(x; 0)$ with respect to $g_{B\uparrow}$ for $N_I = 2$ and $g_{II} = 0$. (c) Ground state one-body density of two non-interacting impurities as a function of $g_{B\uparrow}$. In all cases the bath consists of $N_B = 100$ bosons with $g_{BB} = 0.5$.

BEC density quantified by $\delta\rho_B^{(1)}(x; g_{B\uparrow}) = \rho_B^{(1)}(x; g_{B\uparrow}) - \rho_B^{(1)}(x; 0)$ and shown in figure 2(b) with respect to $g_{B\uparrow}$. Indeed $\delta\rho_B^{(1)}(x; g_{B\uparrow} < 0) > 0$ (figure 2(b)) in the vicinity of $\rho_B^{(1)}(x; g_{B\uparrow} < 0)$ (figure 2(c)). This density enhancement of the BEC forces the impurities to approach each other leading to the emergence of attractive impurity–impurity induced interactions. Similarly for $g_{B\uparrow} < 0$ the impurities tend to reside in regions of lower bath density causing a density depletion of the BEC characterized by $\delta\rho_B^{(1)}(x; g_{B\uparrow} > 0) < 0$ (figure 2(b)). The above-described density depletion of the bath gives rise to the attractive induced interactions analogously to $g_{B\uparrow} < 0$. It is also worth commenting that for $g_{B\uparrow} > 0.5$ $\rho_B^{(1)}(x; g_{B\uparrow} > 0.5)$ splits into two branches lying at the Thomas–Fermi edges $\pm R_{TF}$ of the BEC (see also figure 1 (b_5)). At these values of $g_{B\uparrow}$ $\Delta_+^{N_I}(g_{B\uparrow})$ tends to saturate indicating the impurity–BEC phase separation transition.

4. Quench induced dynamics

Next, we study the interspecies interaction quenched dynamics for the mass-balanced multicomponent system which is initially prepared in its ground state and characterized by $g_{BB} = 0.5$ and $g_{B\uparrow} = 0$. In this case the Thomas–Fermi radius of the BEC is $R_{TF} \approx 4.2$ and the impurities are in a superposition of their spin components described by equation (2). We mainly analyze the case of two non-interacting ($g_{II} = 0$) impurities and briefly discuss the scenario of two weakly interacting impurity atoms in order to expose the effect of their mutual interaction in the dynamics.

To induce the non-equilibrium dynamics we perform at $t = 0$ a sudden change from $g_{B\uparrow} = 0$ to either attractive (section 4.5) or repulsive (section 4.4) finite values of $g_{B\uparrow}$. To examine the emergent dynamics we first discuss the time-evolution of the spin polarization (alias contrast) and its spectrum. Consequently we discuss the dynamical response of the impurities in terms of their single-particle densities and the corresponding two-body reduced density matrix. An effective potential picture for the impurities is constructed in order to provide an intuitive understanding of the quench dynamics.

4.1. Interpretation of the contrast of two impurities

To examine the quench-induced dynamics of the two spinor bosonic impurities we first determine the time-evolution of the total spin polarization (contrast) $|\langle \hat{S}(t) \rangle| = \sqrt{\langle \hat{S}_x(t) \rangle^2 + \langle \hat{S}_y(t) \rangle^2}$ which enables us to infer the dressing of the impurities during the dynamics [18]. Note that $\langle \hat{S}_z(t) \rangle = \langle \hat{S}_z(t=0) \rangle = 0$ since $[\hat{S}_z, \hat{H}] = 0$ and the spin operator in the k th direction ($k = x, y, z$) is given by $\hat{S}_k = (1/N_I) \int dx \sum_{ab} \hat{\Psi}_a^\dagger(x) \sigma_{ab}^k \hat{\Psi}_b(x)$, with σ_{ab}^k denoting the Pauli matrices. The contrast for a single impurity has been extensively studied [25, 39, 43, 97] and it is related to the so-called Ramsey response [18] and therefore the structure factor. The time-dependent overlap between the interacting and the non-interacting states is given by

$$|\langle \hat{S}(t) \rangle|^2 = |\langle \tilde{\Psi}_{BI}^0 | e^{i\tilde{E}_0 t/\hbar} e^{-i\hat{H}t/\hbar} | \tilde{\Psi}_{BI}^0 \rangle|^2 \equiv |S_1(t)|^2, \quad (10)$$

where $|\tilde{\Psi}_{BI}^0\rangle$ is the spatial part of the MB ground state wavefunction of a single impurity with energy \tilde{E}_0 when $g_{BI} = 0$. $\hat{H} = \hat{P}\hat{H}\hat{P}$ with \hat{P} being the projector operator to the spin- \uparrow configuration, and \hat{H} denotes the postquench Hamiltonian (equation (1)). Note also that the contrast is chosen here to take values in the interval $[0, 1]$. From equation (10) zero contrast implies that the overlap between the interacting and the non-interacting states vanishes signifying an orthogonality catastrophe phenomenon [52, 97]. On the other hand, if

$|\langle \hat{S}(t) \rangle|^2 = 1$ then the non-interacting and the interacting states coincide and no quasiparticle is formed. Therefore only in the case that $0 < |\langle \hat{S}(t) \rangle|^2 < 1$ we can infer the dressing of the impurity and the formation of a quasiparticle.

When increasing the number of impurity atoms to $N_I > 1$, $|\langle \hat{S}(t) \rangle|^2$ is more complex since additional spin states contribute to the MB wavefunction (see equation (2)). To understand the interpretation of $|\langle \hat{S}(t) \rangle|^2$ during the dynamics we therefore first discuss it for the case of two impurities. The contrast of two pseudospin-1/2 bosonic impurities reads

$$|\langle \hat{S}(t) \rangle|^2 = \frac{1}{4} |A(|1, 0\rangle; |1, -1\rangle) + A^*(|1, 0\rangle; |1, 1\rangle)|^2, \quad (11)$$

where the spatial overlap between two different spin configurations namely $|S, S_z\rangle$ and $|S', S'_z\rangle$ is defined as [80]

$$\begin{aligned} A(|S, S_z\rangle; |S', S'_z\rangle) &\equiv \langle S, S_z | \langle \Psi_{BI}^0 | e^{i\hat{H}t/\hbar} | S, S_z \rangle \langle S', S'_z | e^{-i\hat{H}t/\hbar} [| \Psi_{BI}^0 \rangle | S', S'_z \rangle] \\ &= \int dx^{N_B} dx^{N_I} \Psi_{S,S_z}^*(\vec{x}^B, \vec{x}^I; t) \Psi_{S',S'_z}(\vec{x}^B, \vec{x}^I; t), \end{aligned} \quad (12)$$

with $\Psi_{S,S_z}(\vec{x}^B, \vec{x}^I; t) = \frac{\langle \vec{x}^B, \vec{x}^I | \langle S, S_z | \Psi(t) \rangle}{\| \langle S, S_z | \Psi(0) \rangle \|^2}$ referring to the spatial wavefunction corresponding to the spin configuration $|S, S_z\rangle$ and $| \Psi_{BI}^0 \rangle$ being the spatial part of the initial MB state for two impurities. Also, $\vec{x}^B = (x_1^B, \dots, x_{N_B}^B)$ and $\vec{x}^I = (x_1^I, \dots, x_{N_I}^I)$ refer to the coordinates of each bath and impurity particle, respectively. In particular in our case we consider two pseudospin-1/2 bosons where $|1, 1\rangle \equiv |\uparrow\rangle_1 \otimes |\uparrow\rangle_2$, $|1, -1\rangle \equiv |\downarrow\rangle_1 \otimes |\downarrow\rangle_2$, $|1, 0\rangle \equiv \frac{|\uparrow\rangle_1 \otimes |\downarrow\rangle_2 + |\downarrow\rangle_1 \otimes |\uparrow\rangle_2}{\sqrt{2}}$. The relevant overlaps read $A(|1, 0\rangle; |1, -1\rangle) = e^{-iE_0 t/\hbar} \int dx^{N_B} dx^{N_I} d^{N_I} \vec{x}^I \Psi_{1,0}^*(\vec{x}^B, \vec{x}^I; t) \Psi_{1,0}(\vec{x}^B, \vec{x}^I; 0)$ and $A(|1, 0\rangle; |1, 1\rangle) = \int dx^{N_B} dx^{N_I} d^{N_I} \vec{x}^I \Psi_{1,0}^*(\vec{x}^B, \vec{x}^I; t) \Psi_{1,1}(\vec{x}^B, \vec{x}^I; t)$. Recall that a quasiparticle is a free particle that is dressed by the excitations of a bosonic bath via their mutual interactions. As a consequence, $\Psi_{BI}^0(\vec{x}^B, \vec{x}^I)$ refers to the wavefunction where no polaron quasiparticle exists since it is the ground state wavefunction of the system with $g_{B\uparrow} = 0$. Moreover, $\Psi_{1,0}(\vec{x}^B, \vec{x}^I)$ and $\Psi_{1,1}(\vec{x}^B, \vec{x}^I)$ denote the wavefunctions where a single and two impurities respectively interact with the bosonic gas and therefore describe the formation of a single and two polarons, respectively. Accordingly, $A(|1, 0\rangle; |1, -1\rangle)$ provides the overlap between the state of a single and no impurities interacting with the bath, while $A(|1, 0\rangle; |1, 1\rangle)$ is the overlap between a single and two impurities interacting with the bath.

As a result, $|\langle \hat{S}(t) \rangle|^2 = 1$ means that $A(|1, 0\rangle; |1, -1\rangle) = A(|1, 0\rangle; |1, 1\rangle) = e^{i\varphi}$ where φ is a phase factor. The fact that $|A(|1, 0\rangle; |1, -1\rangle)| = 1$ implies that the spatial state of a single impurity interacting with the bath is the same as the non-interacting one, except for a possible phase factor, and therefore a quasiparticle is not formed. Moreover since also $|A(|1, 0\rangle; |1, 1\rangle)| = 1$ it holds that the state of a single pseudospin- \uparrow interacting impurity coincides with the state of two pseudospin- \uparrow impurities interacting with the bath and as a consequence with a bare particle due to $|A(|1, 0\rangle; |1, -1\rangle)| = 1$. Thus, $|\langle \hat{S}(t) \rangle|^2 = 1$ implies that there is no quasiparticle formation. On the contrary for $|\langle \hat{S}(t) \rangle|^2 = 0$ either $A(|1, 0\rangle; |1, -1\rangle) = A(|1, 0\rangle; |1, 1\rangle) = 0$ or $A(|1, 0\rangle; |1, -1\rangle) = -A^*(|1, 0\rangle; |1, 1\rangle)$ should be satisfied. In the former case we can deduce the occurrence of an orthogonality catastrophe phenomenon as in the single impurity case while the latter scenario is given by the destructive interference of the $A(|1, 0\rangle; |1, -1\rangle)$ and $A(|1, 0\rangle; |1, 1\rangle)$ terms. However, for $0 < |\langle \hat{S}(t) \rangle|^2 < 1$ the corresponding overlaps acquire finite values and a quasiparticle can be formed.

Notice also that in the special case of $g_{\uparrow\downarrow} = 0$ and $g_{\downarrow\downarrow} = 0$ (but $g_{\uparrow\uparrow}$ arbitrary) it can be shown that $A(|1, 0\rangle; |1, -1\rangle) = \langle \tilde{\Psi}_{BI}^0 | e^{i\hat{P}_0 \hat{H} \hat{P}_0 t/\hbar} e^{i\tilde{E}_0 t/\hbar} | \tilde{\Psi}_{BI}^0 \rangle \equiv S_1(t)$, where \hat{P}_0 refers to the projection operator to the spin state $|1, 0\rangle$. The latter is exactly the contrast or the structure factor of a single impurity (equation (10)). Indeed $| \Psi_{BI}^0 \rangle = | \tilde{\Psi}_{BI}^0 \rangle \otimes | \psi_I^0 \rangle$ for $g_{\downarrow\downarrow} = 0$ holds where $| \psi_I^0 \rangle$ is the single-particle ground state of the impurity while $| \tilde{\Psi}_{BI}^0 \rangle$ and $| \Psi_{BI}^0 \rangle$ refer to the spatial part of the MB ground state wavefunction of a single (energy \tilde{E}_0) and two impurities (energy E_0), respectively. Additionally \hat{H} is the postquench Hamiltonian given by equation (1). Consequently, the contrast in this special case acquires the simplified form

$$|\langle \hat{S}(t) \rangle|^2 = \frac{1}{4} |S_1(t) + A^*(|1, 0\rangle; |1, 1\rangle)|^2. \quad (13)$$

Evidently, here $|\langle \hat{S}(t) \rangle|$ depends explicitly on the structure factor $S_1(t)$ of a single impurity allowing for a direct interpretation of the dynamical dressing of the two impurities with respect to the single impurity case discussed in [35]. In the following, $g_{\uparrow\uparrow} = g_{\downarrow\downarrow} = g_{\uparrow\downarrow} \equiv g_{II}$ and as a consequence $g_{\uparrow\downarrow} = 0$, $g_{\downarrow\downarrow} = 0$ is encountered for $g_{II} = 0$ while the general case of equation (12) applies for the case of $g_{II} = 0.2$ analyzed below.

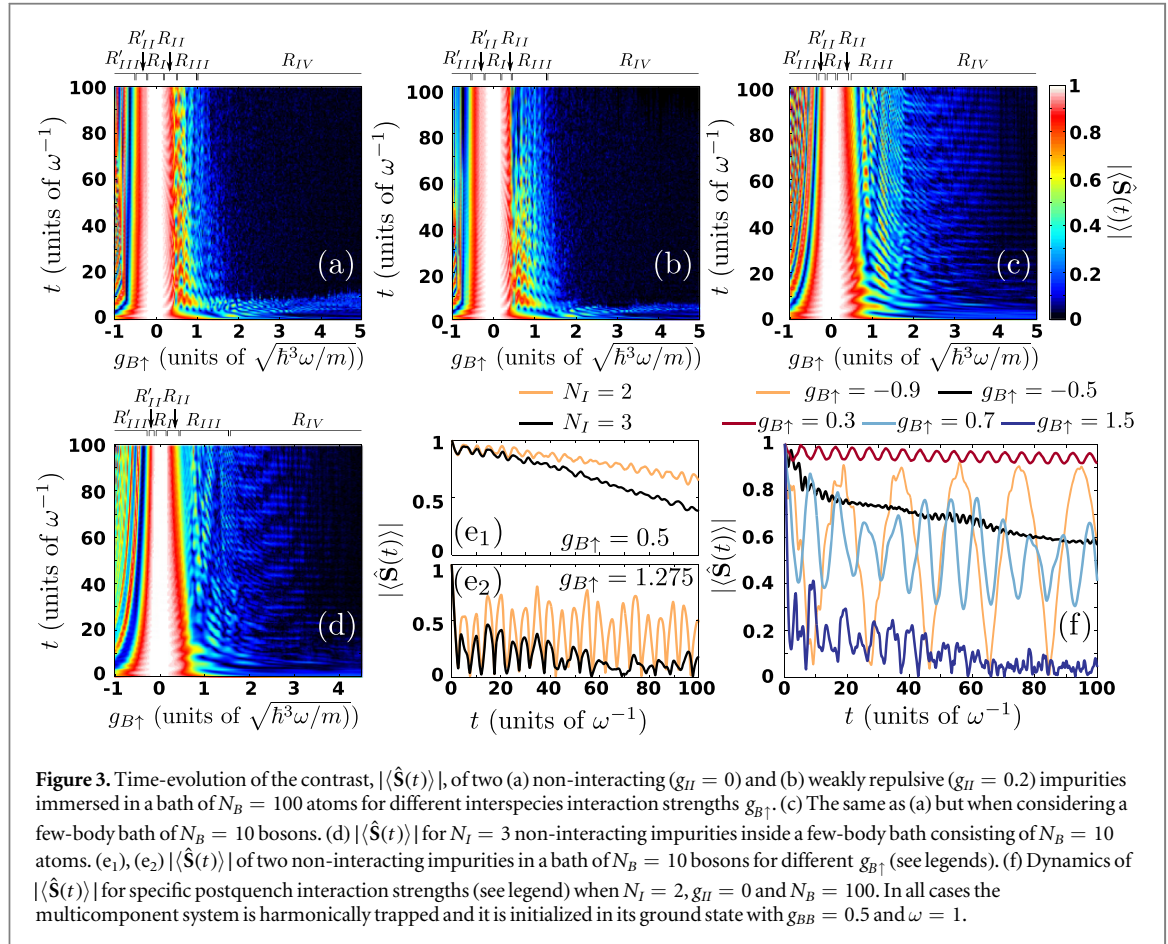


Figure 3. Time-evolution of the contrast, $|\langle \hat{S}(t) \rangle|$, of two (a) non-interacting ($g_{II} = 0$) and (b) weakly repulsive ($g_{II} = 0.2$) impurities immersed in a bath of $N_B = 100$ atoms for different interspecies interaction strengths $g_{B\uparrow}$. (c) The same as (a) but when considering a few-body bath of $N_B = 10$ bosons. (d) $|\langle \hat{S}(t) \rangle|$ for $N_I = 3$ non-interacting impurities inside a few-body bath consisting of $N_B = 10$ atoms. (e₁), (e₂) $|\langle \hat{S}(t) \rangle|$ of two non-interacting impurities in a bath of $N_B = 10$ bosons for different $g_{B\uparrow}$ (see legends). (f) Dynamics of $|\langle \hat{S}(t) \rangle|$ for specific postquench interaction strengths (see legend) when $N_I = 2$, $g_{II} = 0$ and $N_B = 100$. In all cases the multicomponent system is harmonically trapped and it is initialized in its ground state with $g_{BB} = 0.5$ and $\omega = 1$.

4.2. Evolution of the contrast

The dynamics of the two particle contrast $|\langle \hat{S}(t) \rangle|$ is presented in figures 3(a)–(c) for both attractive and repulsive postquench interspecies interactions $g_{B\uparrow}$. In particular, $|\langle \hat{S}(t) \rangle|$ is shown for either two non-interacting (figure 3(a)) or interacting (figure 3(b)) impurities and $N_B = 100$ as well as for a few-body bosonic gas with $N_B = 10$ and $g_{II} = 0$ (figure 3(c)). In all cases, six different dynamical regions with respect to $g_{B\uparrow}$ can be identified marked as R_I , R_{II} , R_{III} , R_{IV} , R'_{II} and R'_{III} . Focusing on the system with $N_B = 100$ and $g_{II} = 0$ these regions correspond to $-0.2 \leq g_{B\uparrow}^{R_I} < 0.2$, $0.2 \leq g_{B\uparrow}^{R_{II}} < 0.4$, $0.4 \leq g_{B\uparrow}^{R_{III}} < 1$, $1 \leq g_{B\uparrow}^{R_{IV}} < 5$,

$-0.5 \leq g_{B\uparrow}^{R'_{II}} < -0.2$ and $-1 \leq g_{B\uparrow}^{R'_{III}} < -0.5$ respectively (figure 3(a)). Specifically, within the very weakly interacting region R_I the contrast is essentially unperturbed remaining unity in the course of the time-evolution and therefore there is no quasiparticle formation. For postquench interactions lying within R_{II} or R'_{II} the contrast performs small and constant amplitude oscillations, weakly deviating from $|\langle \hat{S}(t=0) \rangle| = 1$ (figure 3(f)). This behavior indicates the generation of two long-lived coherent quasiparticles (see also section 4.3). Entering the intermediate repulsive interaction region R_{III} , $|\langle \hat{S}(t) \rangle|$ exhibits large amplitude ($0 < |\langle \hat{S}(t) \rangle| < 1$) multifrequency temporal oscillations (figure 3(f)). The latter signifies the dynamical formation of two Bose polarons which are coupled with higher-order excitations of the bosonic bath when compared to regions R_{II} and R'_{II} as we shall expose in section 4.4.1. For intermediate attractive interactions (region R'_{III}) $|\langle \hat{S}(t) \rangle|$ undergoes large amplitude oscillations taking values in the interval $0 < |\langle \hat{S}(t) \rangle| < 1$ (figure 3(f)). This response of $|\langle \hat{S}(t) \rangle|$ again signals quasiparticle formation. However, in addition to this dynamical dressing the destructive ($|\langle \hat{S}(t) \rangle| = 0$) and the constructive ($|\langle \hat{S}(t) \rangle| \approx 1$) interference between the states of a single and two Bose polarons can be seen (see also equation (11) and its interpretation in section 4.1).

For strong repulsive interactions lying within R_{IV} the contrast shows a fastly decaying amplitude at short evolution times ($0 < t < 2$) and subsequently fluctuates around zero (figure 3(f)). This latter behavior of $|\langle \hat{S}(t) \rangle| \rightarrow 0$ is a manifestation of an orthogonality catastrophe phenomenon of the spontaneously generated short-lived ($0 < t < 2$) Bose polarons. It is a consequence of the spatial phase separation between the impurity and the bosonic bath (see also figure 5(h) and the discussion in section 4.4.1), where the impurity prefers to reside at the edges of the BEC background, see also figure 2(c). Note that this behavior is also supported by the effective potential of the impurities, see equation (9). Most importantly this process results in an energy transfer

from the impurity to the BEC, which prohibits the revival of the dynamical state of the impurity to its initial one, implying $|\langle \hat{S}(t) \rangle| \ll 1$. Such a mechanism has been also identified to occur for the case of a single impurity, see [35].

The emergence of the different dynamical regions in the evolution of the contrast holds equally when the size of the bath decreases to $N_B = 10$ (figure 3(c)). For such a few-body scenario region R_{II} , where coherently long-lived quasiparticles are formed, becomes slightly wider, i.e. $0.2 \leq g_{B\uparrow}^{R_{II}} < 0.6$, compared to the $N_B = 100$ case. The most notable difference between the few and the many particle bath takes place in the intermediate interaction region R_{III} . The latter, occurs now at $0.6 \leq g_{B\uparrow}^{R_{III}} < 1.8$, with $|\langle \hat{S}(t) \rangle|$ performing large amplitude multifrequency oscillations implying in turn the formation of highly excited polaronic states. Note that the amplitude of the oscillations of $|\langle \hat{S}(t) \rangle|$ here is larger than in the $N_B = 100$ case (figure 3(a)). Additionally, we observe that $|\langle \hat{S}(t) \rangle|$ decreases smoothly as $g_{B\uparrow}$ increases, which is in sharp contrast to the $N_B = 100$ case. Recall that such a smooth behavior occurring in the few-body scenario has already been identified in our discussion of the ground state properties and in particular when inspecting the relative distance between the impurities. Also, the oscillations of $|\langle \hat{S}(t) \rangle|$ ($0 < |\langle \hat{S}(t) \rangle| < 1$) for intermediate attractive interactions (region R'_{III}) being a consequence of the destructive ($|\langle \hat{S}(t) \rangle| = 0$) and constructive ($|\langle \hat{S}(t) \rangle| \approx 1$) interference between the states of a single and two Bose polarons are much more prevalent and regular for $N_B = 10$ as compared to the $N_B = 100$ case. Concluding, we can infer that the overall phenomenology of the dynamical formation of quasiparticles as imprinted in the contrast is similar for $N_B = 10$ and $N_B = 100$.

To test the effect of the number of impurities on the interaction intervals of quasiparticle formation we also consider the case of $N_I = 3$ non-interacting, $g_{II} = 0$, bosons immersed in a few-body bath of $N_B = 10$ atoms. The dynamics of the corresponding contrast for this system following a quench from $g_{B\uparrow} = 0$ to a finite either attractive or repulsive $g_{B\uparrow}$ is illustrated in figure 3(d). As it can be seen, $|\langle \hat{S}(t) \rangle|$ shows a similar behavior to the case of two impurities (figure 3(c)) but the regions of finite contrast become narrower. Particularly, the intermediate repulsive interaction region here occurs for $0.5 \leq g_{B\uparrow}^{R_{III}} < 1.5$ instead of $0.6 \leq g_{B\uparrow}^{R_{III}} < 1.8$ for $N_I = 2$. Additionally, $|\langle \hat{S}(t) \rangle|$ acquires lower values within the regions R_{III} and R'_{III} for more impurities. Moreover, for $N_I = 3$ within R'_{III} we observe a pronounced dephasing of the contrast which is absent for the $N_I = 2$ case, see figures 3(e₁), (e₂). As a consequence, we can deduce that the basic characteristics of the regions of dynamical polaron formation do not significantly change for a larger number of impurities in the regime $N_I \ll N_B$.

Finally, we discuss $|\langle \hat{S}(t) \rangle|$ for weakly interacting impurities. Comparing the temporal evolution of $|\langle \hat{S}(t) \rangle|$ for $g_{II} = 0.2$ (figure 3(b)) to the one for $g_{II} = 0$ (figure 3(a)) we observe that the extent of the above-described dynamical regions (R_I , R_{II} , R_{III} , R_{IV} , R'_{II} and R'_{III}) can be tuned via g_{II} . For instance, region R_{II} occurs at $0.2 \leq g_{B\uparrow}^{R_{II}} < 0.4$ for $g_{II} = 0.2$ instead of $0.2 \leq g_{B\uparrow}^{R_{II}} < 0.5$ when $g_{II} = 0$, while region R_{III} takes place at $0.4 \leq g_{B\uparrow}^{R_{III}} < 1.3$ if $g_{II} = 0.2$ and within $0.5 \leq g_{B\uparrow}^{R_{III}} < 1$ in the non-interacting scenario. Also region R_{IV} where the orthogonality catastrophe takes place is shifted to slightly larger interactions for $g_{II} = 0.2$ compared to the $g_{II} = 0$ case. Interestingly we observe that the contrast within R_{III} and R'_{III} exhibits a decaying tendency for long evolution times $t > 50$ in the presence of weak impurity–impurity interactions, a behavior which is absent when $g_{II} = 0$.

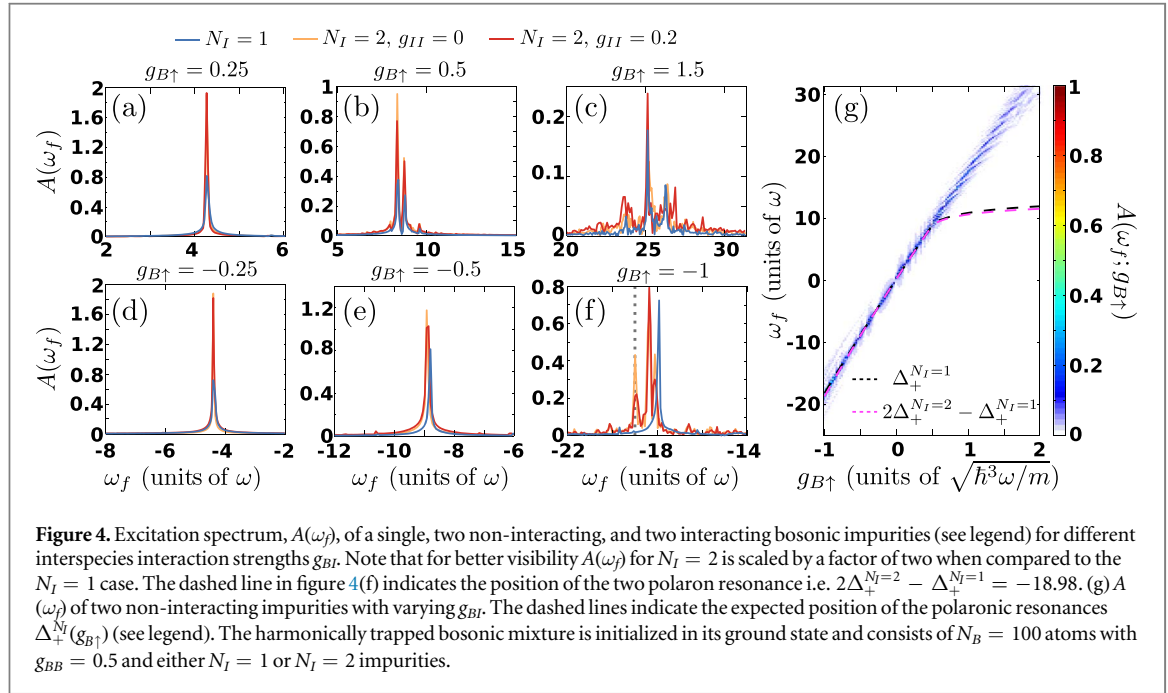
4.3. Spectrum of the contrast

To quantify the excitation spectrum of the impurity we calculate the spectrum of the contrast, namely

$$A(\omega_f) = \frac{1}{\pi} \left| \int_0^\infty dt e^{i\omega_f t} |\langle \hat{S}(t) \rangle| e^{i \tan^{-1} \frac{\langle \hat{S}_y(t) \rangle}{\langle \hat{S}_x(t) \rangle}} \right|. \quad (14)$$

Recall that at low impurity densities and weak interspecies interactions it has been shown that $|\langle \hat{S}(t) \rangle|$ is proportional to the so-called spectral function of quasiparticles [18, 97, 98]. Figure 4 presents $A(\omega_f)$ in the case of a single and two either non-interacting ($g_{II} = 0$) or weakly interacting ($g_{II} = 0.2$) impurities when $N_B = 100$ for different interspecies couplings of either sign. Evidently, for weak $g_{B\uparrow}$ belonging either to region R_{II} with $g_{B\uparrow} = 0.25$ (figure 4(a)) or R'_{II} with $g_{B\uparrow} = -0.25$ (figure 4(d)) we observe a single peak in $A(\omega_f)$ located at $\omega_f \approx 4.27$ and $\omega_f \approx -4.39$ respectively. This single peak occurs independently of the number of impurities and their intraspecies interactions. Therefore, this peak at small $g_{B\uparrow} = \pm 0.25$ corresponds to the long-time evolution of a well-defined repulsive or attractive Bose polaron respectively. Within region R_{III} e.g. at $g_{B\uparrow} = 0.5$ two dominant peaks occur in $A(\omega_f)$ (figure 4(b)) at frequencies $\omega_f \approx 8.42$ and $\omega_f \approx 8.79$ for both the $N_I = 1$ and $N_I = 2$ cases. Accordingly, these two peaks suggest the formation of a quasiparticle dressed, for higher frequencies, by higher-order excitations of the BEC background.

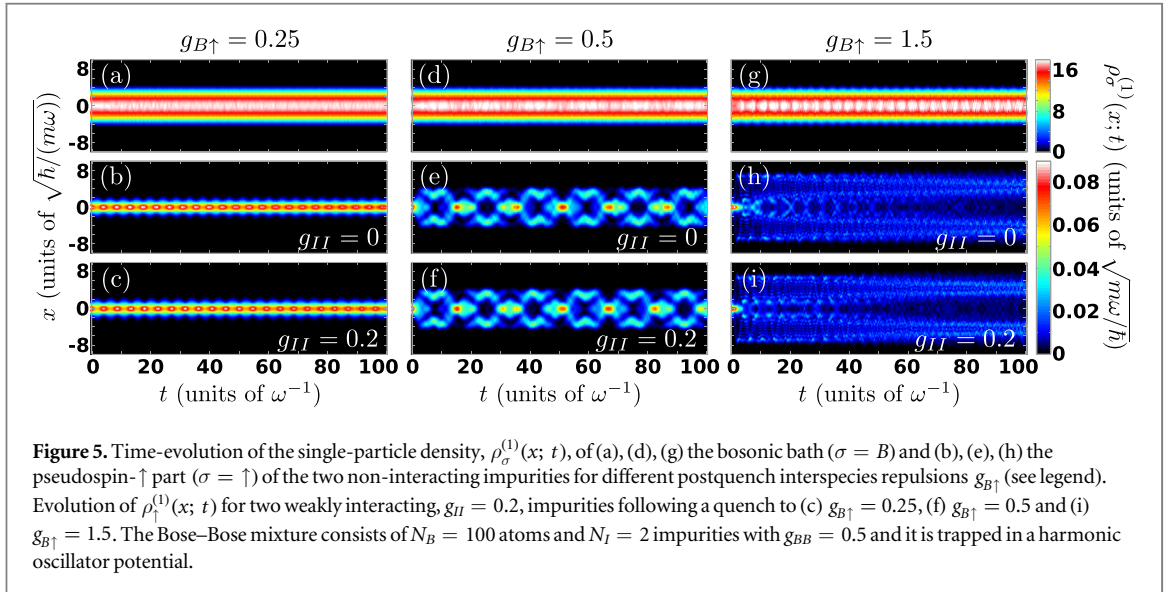
Entering the strongly interspecies repulsive region R_{IV} a multitude of frequencies are imprinted in the impurity's excitation spectrum e.g. at $g_{B\uparrow} = 1.5$, see figure 4(c). The number of the emerging frequencies is



larger for the two compared to the single impurity but does not significantly depend on g_{II} for $N_I = 2$. For instance, when $N_I = 1$ mainly three predominant peaks centered at $\omega_f \approx 23.75$, $\omega_f \approx 25.13$, and $\omega_f \approx 26.26$ appear in $A(\omega_f)$ whilst for $N_I = 2$ and $g_{II} = 0$ five dominantly contributing frequencies located at $\omega_f \approx 22.31$, $\omega_f \approx 23.81$, $\omega_f \approx 25.2$, $\omega_f \approx 26.39$ and $\omega_f \approx 27.52$ occur. These frequency peaks correspond to even higher excited states of the quasiparticle than the ones within the region R_{III} . We note that for values of $g_{B\uparrow}$ deeper in R_{IV} a variety of low amplitude but large valued frequency peaks occur in $A(\omega_f)$. This fact indicates that the impurities tend to populate a multitude of states indicating the manifestation of the polaron orthogonality catastrophe as discussed in [35, 75] (results not shown here).

Turning to intermediate attractive interactions lying within R'_{III} such as $g_{B\uparrow} = -0.5$ a single frequency peak can be seen in $A(\omega_f)$ whose frequency is shifted towards more negative values for $N_I = 2$ compared to $N_I = 1$ and also for increasing g_{II} (figure 4(e)). Specifically, when $N_I = 1$ the aforementioned peak occurs at $\omega_f \approx -8.79$ while for $N_I = 2$ and $g_{II} = 0$ [$g_{II} = 0.2$] it lies at $\omega_f \approx -8.92$ [$\omega_f \approx -8.86$]. This peak indicates the generation of an attractive Bose polaron. A further increase of the attraction, e.g. $g_{B\uparrow} = -1$, leads to the appearance of three quasiparticle peaks in $A(\omega_f)$ when $N_I = 2$ and either $g_{II} = 0$ or $g_{II} = 0.2$, centered at $\omega_f \approx -18.1$, $\omega_f \approx -18.35$ and $\omega_f \approx -18.98$, but only one for $N_I = 1$ with $\omega_f \approx -17.91$, as shown in figure 4(f). This change of $A(\omega_f)$ for increasing N_I within the regions R'_{II} and R'_{III} demonstrates the prominent role of induced interactions for attractive interspecies ones. More specifically for $N_I = 2$, $A(\omega_f)$ possesses additional quasiparticle peaks as compared to the $N_I = 1$ case. Indeed, according to equation (11) we can predict at least two peaks at positions $\omega_f = \Delta_+^{N_I=1} = -17.96$ and $\omega_f = 2\Delta_+^{N_I=2} - \Delta_+^{N_I=1} = -18.98$ explaining two of the above identified peaks. The third dominant peak at $\omega_f = 18.35$ appearing in the spectrum is attributed to the occupation of an excited state with $S_z = 1$ (see also equation (2)) according to equation (11). Recall that the $|1, 1\rangle$ spin state in the time-evolved wavefunction (equation (2)) corresponds to the two polaron case while $|1, 0\rangle$ contains only one polaron and the $|1, -1\rangle$ describes impurities that do not interact with the bath and thus no polarons. The aforementioned population of the additional polaronic states for $N_I = 2$ is a clear evidence of impurity–impurity induced interactions.

The overall behavior of the excitation spectrum $A(\omega_f; g_{B\uparrow})$ for $N_I = 2$ and $g_{II} = 0$ is shown in figure 4(g) with varying $g_{B\uparrow}$. Evidently, the position of the dominant quasiparticle peak in terms of ω_f increases almost linearly for larger $g_{B\uparrow}$. This behavior essentially reflects the linear increase of the energy of the initial state $|\Psi(0)\rangle$ (equation (2)) directly after the quench. Moreover, comparing the position of the dominant quasiparticle peak with $\Delta_+^{N_I=1}$ reveals that for $g_{B\uparrow} > 0.5$, while the latter saturates, the former increases and additional peaks appear in the spectrum $A(\omega_f; g_{B\uparrow})$. These peaks correspond to excited states of the system and already for $g_{B\uparrow} > 1$ the ground states corresponding to $\Delta_+^{N_I}$ cease to be populated during the dynamics. In a similar fashion, such additional quasiparticle peaks occur also for attractive interactions, see figure 4(g) for $g_{B\uparrow} < -0.5$. In this case the additional quasiparticle peaks stem from the induced interactions resulting in the presence of a peak at $\omega_f = 2\Delta_+^{N_I=2} - \Delta_+^{N_I=1} \neq \Delta_+^{N_I=1}$ and other ones which correspond to the occupation of higher-lying excited



polaronic states with $S_z = 1$ (equation (2)). Note that such an almost linear behavior of the polaronic spectrum is reminiscent of the corresponding three-dimensional scenario but away from the Feshbach resonance regime. The latter corresponds in one-dimension to an interspecies Tonks–Girardeau interaction regime which is not addressed in the present work. We remark that in one-dimension there is no molecular bound state occurring for repulsive interactions.

Summarizing, we can infer that the quasiparticle excitation spectrum depends strongly on the value of the postquench interspecies interaction strength and also on the number of impurities outside the weakly attractive and repulsive coupling regimes [98]. However, this behavior is also slightly altered when going from two non-interacting to two weakly interacting impurities. For a relevant discussion on the lifetime of the above-described spectral features we refer the interested reader to [99]. It is also important to mention that in the weakly interacting impurity–BEC regime where the contrast is finite in the course of the evolution the spectral function $A(\omega_j)$ corresponds to the injection spectrum in the framework of the reverse rf spectroscopy [2, 26].

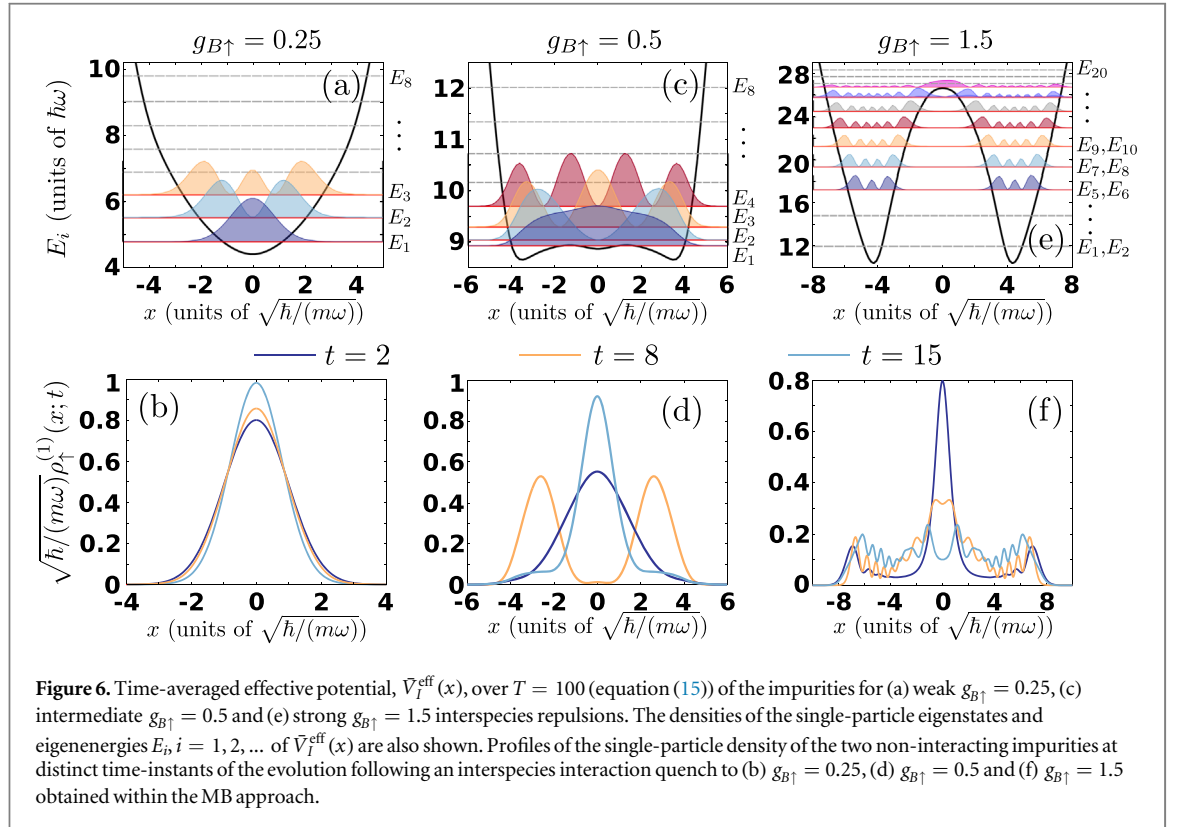
4.4. Quench to repulsive interactions

Below we further analyze the dynamical response of the multicomponent system, and especially of the impurities, following an interspecies interaction quench from $g_{B\uparrow} = 0$ to $g_{B\uparrow} > 0$ within the above identified dynamical regions of the contrast. In particular, we explore the dynamics of the system on both the single- and the two-body level and further develop an effective potential picture to provide a more concrete interpretation of the emergent phenomena. We mainly focus on the nonequilibrium dynamics of two non-interacting impurities ($g_{II} = 0$) and subsequently discuss whether possible alterations might occur for weakly interacting ($g_{II} = 0.2$) impurities. Also, in the following, only the temporal-evolution of the pseudospin- \uparrow part of the impurities is discussed since the pseudospin- \downarrow component does not interact with the bosonic medium.

4.4.1. Density evolution and effective potential

To visualize the spatially resolved dynamics of the system on the single-particle level we first inspect the time-evolution of the σ -species single-particle density $\rho_{\sigma}^{(1)}(x; t)$ (equation (6)) illustrated in figure 5. For weak postquench interspecies repulsions lying within the region R_{II} e.g. $g_{B\uparrow} = 0.25$, such that $g_{B\uparrow} < g_{BB}$, the impurities (see figure 5(b)) exhibit a breathing motion of frequency $\omega_{br}^I \approx 1.44$ inside the bosonic medium [73, 74]. Moreover, at initial evolution times ($t < 60$) the amplitude of the breathing is almost constant whilst later on ($t > 60$) it shows a slightly decaying tendency, see for instance the smaller height of the density peak at $t = 70$ compared to $t = 20$ in figure 5(b). This decaying amplitude can be attributed to the build up of impurity–impurity correlations in the course of the evolution [42] due to the presence of induced interactions discussed later on, see also figure 7(a). The breathing motion of the impurities is directly captured by the periodic contraction and expansion in the shape of the instantaneous density profiles of $\rho_{\uparrow}^{(1)}(x; t)$ depicted in figure 6(b). On the other hand, the bosonic gas remains essentially unperturbed (figure 5(a)) throughout the dynamics, showing only tiny distortions from its original Thomas–Fermi cloud due to its interaction with the impurity.

An intuitive understanding of the observed dynamics of the impurities is provided with the aid of an effective potential picture. Indeed, the impurity–BEC interactions can be taken into account, to a very good approximation, by employing a modified external potential for the impurities. The latter corresponds to the



time-averaged effective potential created by the harmonic oscillator and the density of the bosonic gas [35, 51, 73, 75] namely

$$\bar{V}_I^{\text{eff}}(x) = \frac{1}{2}m\omega^2x^2 + \frac{g_{BI}}{T} \int_0^T dt \rho_B^{(1)}(x; t). \quad (15)$$

The averaging process aims to eliminate the emergent very weak distortions on the instantaneous density of the BEC $\rho_B^{(1)}(x; t)$, and it is performed herein over $T = 100$. These distortions being a consequence of the motion of the impurities within the BEC are imprinted as a slow and very weak amplitude breathing motion of $\rho_B^{(1)}(x; t)$ with $\omega_{\text{br}}^B \approx 1.82$, hardly visible in figure 5(a). They are canceled out in our case for $T > 20$. Note that $\omega_{\text{br}}^B < 2$ is attributed to the repulsive character of the BEC background which negatively shifts its breathing frequency from the corresponding non-interacting value [100]. At $g_{B\uparrow} = 0.25$ this $\bar{V}_I^{\text{eff}}(x)$ takes the form of a modified harmonic oscillator potential illustrated in figure 6(a) together with the densities of its first few single-particle eigenstates. Furthermore, assuming the Thomas–Fermi approximation for $\rho_B^{(1)}(x, t)$ the effective trapping frequency of the impurities corresponds to $\omega_{\text{eff}} = \omega \sqrt{1 - \frac{g_{B\uparrow}}{g_{BB}}}$. Therefore their expected effective breathing frequency would be $\omega_{\text{br}}^{\text{eff}, I} = 2\omega_{\text{eff}} \approx 1.41$ which is indeed in a very good agreement with the numerically obtained ω_{br}^I . The discrepancy between the prediction of the effective potential and the MB approach is attributed to the approximate character of the effective potential which does not account for possible correlation induced shifts to the breathing frequency. Moreover, in the present case the impurities which undergo a breathing motion within $\bar{V}_I^{\text{eff}}(x)$ reside predominantly in its energetically lowest-lying state E_1 , see figure 6(a). It is also important to mention that this effective potential approximation is adequate only for weak interspecies interactions where the impurity–BEC entanglement is small [35, 75]. Note also that the inclusion of the Thomas–Fermi approximation in the effective potential of equation (15) can not adequately describe the impurities dynamics when they reach the edges of the bosonic cloud, see [36] for more details. However in this case $\rho_B^{(1)}(x; t)$ lies within $\rho_B^{(1)}(x; t)$ throughout the evolution indicating the miscible character of the dynamics for $g_{B\uparrow} < g_{BB}$ [35, 65]. Furthermore, for these weak postquench interspecies repulsions a similar to the above-described dynamics takes place also for two weakly ($g_{II} = 0.2$) repulsively interacting impurities as shown in figure 5(c). The impurities undergo a breathing motion within the bosonic medium in the course of the time-evolution exhibiting a slightly larger oscillation frequency than for the $g_{II} = 0$ case but with the same amplitude (hardly visible by comparing figures 5(b) and (c)).

For larger postquench interaction strengths $g_{B\uparrow} = 0.5$ (region R_{III}), i.e. close to the intraspecies interaction of the bosonic bath g_{BB} , the impurities show a more complex dynamics compared to the weak interspecies repulsive case (figure 5(e)). Also, the BEC medium performs a larger amplitude breathing motion (figure 5(d))

compared to the $g_{B\uparrow} = 0.25$ scenario but again with a frequency $\omega_{br}^B \approx 1.82$. Focusing on the impurities motion, we observe that at short evolution times ($0 < t < 5$) after the quench $\rho_{\uparrow}^{(1)}(x; t)$ expands and then splits into two counterpropagating density branches with finite momenta that travel towards the edges of the bosonic cloud, see figure 5(e) and the profiles shown in figure 6(d). The appearance of these counterpropagating density branches is a consequence of the interaction quench which imports energy into the system. Reaching the edges of $\rho_{\uparrow}^{(1)}(x; t)$ the density humps of $\rho_{\uparrow}^{(1)}(x; t)$ are reflected back towards the trap center ($x = 0$) where they collide around $t \approx 15$ forming a single density peak (figure 6(d)). The aforementioned impurity motion repeats itself in a periodic manner for all evolution times (figure 5(e)). Here, the underlying time-averaged effective potential (equation (15)) corresponds to a highly deformed harmonic oscillator possessing an almost square-well like profile as illustrated in figure 6(c). Moreover, a direct comparison of the densities of the lower-lying single-particle eigenstates of $\bar{V}_I^{\text{eff}}(x)$ (figure 6(c)) with the density profile snapshots of $\rho_{\uparrow}^{(1)}(x; t)$ of the MB dynamics (figure 6(d)) reveals that the impurities predominantly reside in a superposition of the two lower-lying excited states (E_1 and E_2) of $\bar{V}_I^{\text{eff}}(x)$. Additionally in the case of two weakly repulsively interacting impurities, shown in figure 5(f), the impurities' motion remains qualitatively the same. However, due to the inclusion of intraspecies repulsion the impurities possess a slightly larger overall oscillation frequency and the collisional patterns at the trap center appear to be modified as compared to the $g_{II} = 0$ case.

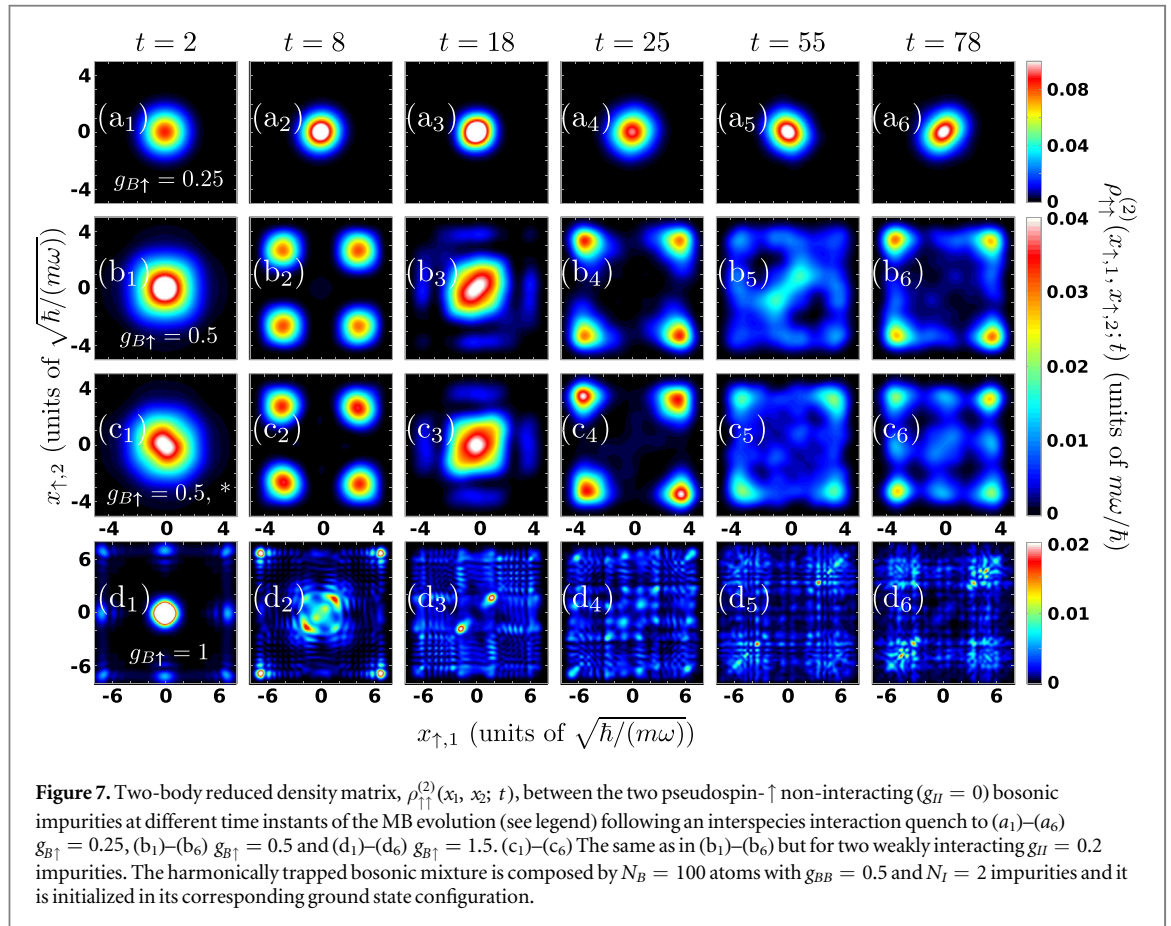
Turning to strong postquench repulsions, i.e. $g_{B\uparrow} = 1.5 \gg g_{BB}$ which belongs to R_{IV} , the dynamical response of the impurities is greatly altered and the bosonic gas exhibits an enhanced breathing dynamics as compared to the weak and intermediate interspecies repulsions discussed above. Initially $\rho_{\uparrow}^{(1)}(x; t = 0)$ consists of a density hump located at the trap center which, following the interaction quench, breaks into two density fragments, as illustrated in figure 5(h), each of them exhibiting a multihump structure (see also figure 6(f)). Note that the density hump at the trap center remains the dominant contribution of $\rho_{\uparrow}^{(1)}(x; t)$ until it eventually fades out for $t > 5$, see figure 5(h). This multihump structure building upon $\rho_{\uparrow}^{(1)}(x; t)$ is clearly captured in the instantaneous density profiles depicted in figure 6(f). Remarkably, the emergent impurity density fragments that are symmetrically placed around the trap center ($x = 0$) perform a damped oscillatory motion in time around the edges of the Thomas–Fermi radius of the bosonic gas, see in particular figures 5(g), (h).

The emergent dynamics of the impurities can also be interpreted to lowest order approximation (i.e. excluding correlation effects) by invoking the corresponding effective potential which for these strong interspecies repulsions has the form of the double-well potential shown in figure 6(e). Comparing the shape of the densities of the eigenstates of $\bar{V}_I^{\text{eff}}(x)$ (figure 6(e)) with the density profiles $\rho_{\uparrow}^{(1)}(x; t)$ (figure 6(f)) obtained within the MB dynamics simulations it becomes evident that the impurities reside in a superposition of higher-lying states of the effective potential. Furthermore the double-well structure of $\bar{V}_I^{\text{eff}}(x)$ suggests that each of the observed density fragments of the impurities is essentially trapped in each of the corresponding two sites of $\bar{V}_I^{\text{eff}}(x)$. Of course, as already mentioned above, for these strong interactions $\bar{V}_I^{\text{eff}}(x)$ provides only a crude description of the impurity dynamics since it does not account for both intra- and interspecies correlations that occur during the MB dynamics. However $\bar{V}_I^{\text{eff}}(x)$ enables the following intuitive picture for the impurity dynamics. Namely, the damped oscillations of $\rho_{\uparrow}^{(1)}(x; t)$ designate that the pseudospin- \uparrow impurities at initial times are in a superposition state of a multitude of highly excited states (see e.g. figure 6(f) at $t = 8$) while for later times they reside in a superposition of lower excited states (see e.g. figure 6(f) at $t = 15$). We should also remark that a similar overall dynamical behavior on the single-particle level has been reported in the case of a single spinor impurity and has been also related to an enhanced energy transfer from the impurity to the bosonic bath [35, 68, 69, 75]. Such an energy transfer process takes place also in the present case (results not shown here). Another important feature of the observed dynamical response of the impurities is the fact that they are not significantly affected by the presence of weak intraspecies interactions. This can be seen by inspecting figure 5(i) which shows the time-evolution of $\rho_{\uparrow}^{(1)}(x; t)$ for $g_{II} = 0.2$. Here, the most noticeable difference when compared to the $g_{II} = 0$ scenario is that the splitting of $\rho_{\uparrow}^{(1)}(x; t)$ into two branches occurs at shorter time scales (compare figures 5(h), (i)) due to the additional intraspecies repulsion.

4.4.2. Dynamics of the two-body reduced density matrix

To investigate the development of impurity–impurity correlations during the quench dynamics we next resort to the time-evolution of the pseudospin- \uparrow impurity intraspecies two-body reduced matrix $\rho_{\uparrow\uparrow}^{(2)}(x_1, x_2; t)$ (equation (7)). Recall that $\rho_{\uparrow\uparrow}^{(2)}(x_1, x_2; t)$ provides the probability of finding at time t a pseudospin- \uparrow boson at location x_1 and a second one at x_2 [65, 66]. Most importantly, it allows us to monitor the two-body spatially resolved dynamics of the impurities and infer whether they move independently or correlate with each other [8, 10, 42].

Figure 7 shows $\rho_{\uparrow\uparrow}^{(2)}(x_1, x_2; t)$ at specific time-instants of the evolution of two non-interacting (figures 7 (a₁)–(b₆) and (d₁)–(d₆)) as well as weakly interacting (figures 7(c₁)–(c₆)) impurities for different postquench



interspecies repulsions. To reveal the role of induced impurity–impurity correlations via the bath we mainly focus on two initially non-interacting impurities where $\rho_{\uparrow\uparrow}^{(2)}(x_1, x_2; t = 0) = \rho_{\uparrow}^{(1)}(x_1, t = 0)\rho_{\uparrow}^{(1)}(x_2, t = 0)/2$ since $g_{II} = 0$ and initially $g_{B\uparrow} = 0$. As already discussed in section 4.4.1 for weak interspecies postquench repulsions, namely $g_{B\uparrow} = 0.25$ (region R_{II}), the impurities perform a breathing motion on the single-particle level (figure 5(b)) exhibiting a decaying amplitude for large evolution times. Accordingly, inspecting $\rho_{\uparrow\uparrow}^{(2)}(x_1, x_2; t)$ (figures 7(a₁)–(a₆)) we observe that the impurities are likely to reside together close to the trap center since $\rho_{\uparrow\uparrow}^{(2)}(-2 < x_1 < 2, -2 < x_2 < 2; t)$ is mainly populated throughout the evolution. In particular, at initial times $\rho_{\uparrow\uparrow}^{(2)}(-2 < x_1 < 2, -2 < x_2 < 2; t)$ shows a Gaussian-like distribution which contracts (figure 7(a₂)) and expands (figures 7(a₃), (a₄)) during the dynamics as a consequence of the aforementioned breathing motion. Deeper in the evolution $\rho_{\uparrow}^{(1)}(x; t)$ decays and $\rho_{\uparrow\uparrow}^{(2)}(x_1, x_2; t)$ is deformed along its diagonal (figures 7(a₄), (a₆)) or its anti-diagonal (figure 7(a₅)) indicating that the impurities tend to be slightly apart or at the same location respectively. This is indicative of the admittedly weak induced interactions as the breathing mode along the anti-diagonal of $\rho_{\uparrow\uparrow}^{(2)}(x_1, x_2; t)$ (relative coordinate breathing mode) does not possess exactly the same frequency as the breathing along the diagonal (center-of-mass breathing mode).

For larger interspecies repulsions e.g. for $g_{B\uparrow} = 0.5$ (region R_{III}) the two-body dynamics of the impurities is significantly altered, see figures 7(b₁)–(b₆). At the initial stages of the dynamics the impurities reside together in the vicinity of the trap center as $\rho_{\uparrow\uparrow}^{(2)}(-3 < x_1 < 3, -3 < x_2 < 3; t)$ is predominantly populated. However for later times two different correlation patterns appear in $\rho_{\uparrow\uparrow}^{(2)}(x_1, x_2; t)$ in a periodic manner. Recall that for these interactions $\rho_{\uparrow}^{(1)}(x; t)$ splits into two counterpropagating density branches traveling towards the edges of the bosonic bath and then are reflected back to the trap center where they collide (figure 5(e)). Consequently, when the two density fragments appear in $\rho_{\uparrow}^{(1)}(x; t)$ the impurities reside in two different two-body configurations (figures 7(b₂), (b₄) and (b₆)). Namely the bosonic impurities either lie together at a certain density branch (see the diagonal elements of $\rho_{\uparrow\uparrow}^{(2)}(x_1, x_2; t)$) or they remain spatially separated with one of them residing in the left and the other in the right density branch (see the anti-diagonal elements of $\rho_{\uparrow\uparrow}^{(2)}(x_1, x_2; t)$). Moreover, during their collision at $x = 0$ the impurities are very close to each other as it is evident by the enhanced two-body probability in the neighborhood of $x_1 = x_2 = 0$ (figures 7(b₃), (b₅)). The dynamics of two weakly repulsive ($g_{II} = 0.2$) impurities shows similar two-body correlation patterns to the non-interacting ones, as it can be seen by comparing figures 7(b₁)–(b₆) to (c₁)–(c₆). This behavior complements the similarities already found at the

single-particle level (see section 4.4.1). The major difference on the two-body level between the $g_{II} = 0.2$ and $g_{II} = 0$ scenario is that in the former case $\rho_{\uparrow\uparrow}^{(2)}(x_1, x_2; t)$ is more elongated along its anti-diagonal when the impurities collide at $x = 0$ (figures 7(c₁), (c₃)). Therefore weakly interacting impurities tend to be further apart compared to the $g_{II} = 0$ case, a result that reflects their direct repulsion. Other differences observed at the same time-instant in $\rho_{\uparrow\uparrow}^{(2)}(x_1, x_2; t)$ between the interacting and the non-interacting cases are due to the repulsive s -wave interaction that directly competes with the attractive induced interactions emanating in the system. For instance, shortly after a collision point e.g. at $t = 55$, shown in figures 7(b₅) and (c₅), we observe that due to the repulsive s -wave interactions the attractive contribution between the impurities, see the diagonal of $\rho_{\uparrow\uparrow}^{(2)}(-2 < x_1 < 2, -2 < x_2 < 2; t)$ in figure 7(b₅) disappears (figure 7(c₅)).

Turning to very strong repulsions, e.g. for $g_{B\uparrow} = 1.5$ lying in region R_{IV} , the correlation patterns of the two non-interacting impurities (figures 7(d₁)–(d₆)) show completely different characteristics compared to the $g_{B\uparrow} \leq g_{BB}$ regime. Note here that in the dynamics of $\rho_{\uparrow}^{(1)}(x; t)$ the initially formed density hump breaks into two density fragments (figure 5(h)) possessing a multihump shape (see also figure 6(f)). Subsequently, the fragments lying symmetrically with respect to $x = 0$ perform a damped oscillatory motion in time residing around the edges of the Thomas–Fermi radius of the bosonic gas. The corresponding two-body reduced density matrix shows a pronounced probability peak around $x_1 = x_2 = 0$ (figure 7(d₁)) indicating that at the initial stages of the dynamics the impurities are mainly placed together in this location. As time evolves, the impurities predominantly move as a pair towards the edge of the Thomas–Fermi background, see in particular the diagonal of $\rho_{\uparrow\uparrow}^{(2)}(x_1, x_2; t)$ in figures 7(d₂), (d₃), and simultaneously they start to exhibit a delocalized behavior as can be deduced by the small values of the off-diagonal elements of $\rho_{\uparrow\uparrow}^{(2)}(x_1, x_2 \neq x_1; t)$. Entering deeper in the evolution the aforementioned delocalization of the impurities becomes more enhanced since $\rho_{\uparrow\uparrow}^{(2)}(x_1, x_2; t)$ disperses as illustrated in figures 7(d₄)–(d₆). This dispersive behavior of $\rho_{\uparrow\uparrow}^{(2)}(x_1, x_2; t)$ is inherently related to the multihump structure of $\rho_{\uparrow}^{(1)}(x; t)$ and suggests from a two-body perspective the involvement of several excited states during the impurity dynamics. It is also worth mentioning that at specific time instants the diagonal of $\rho_{\uparrow\uparrow}^{(2)}(x_1, x_2; t)$ is predominantly populated (figures 7(d₂), (d₃), (d₅)) which is indicative of the presence of induced interactions.

4.4.3. Two-body dynamics within the effective potential picture

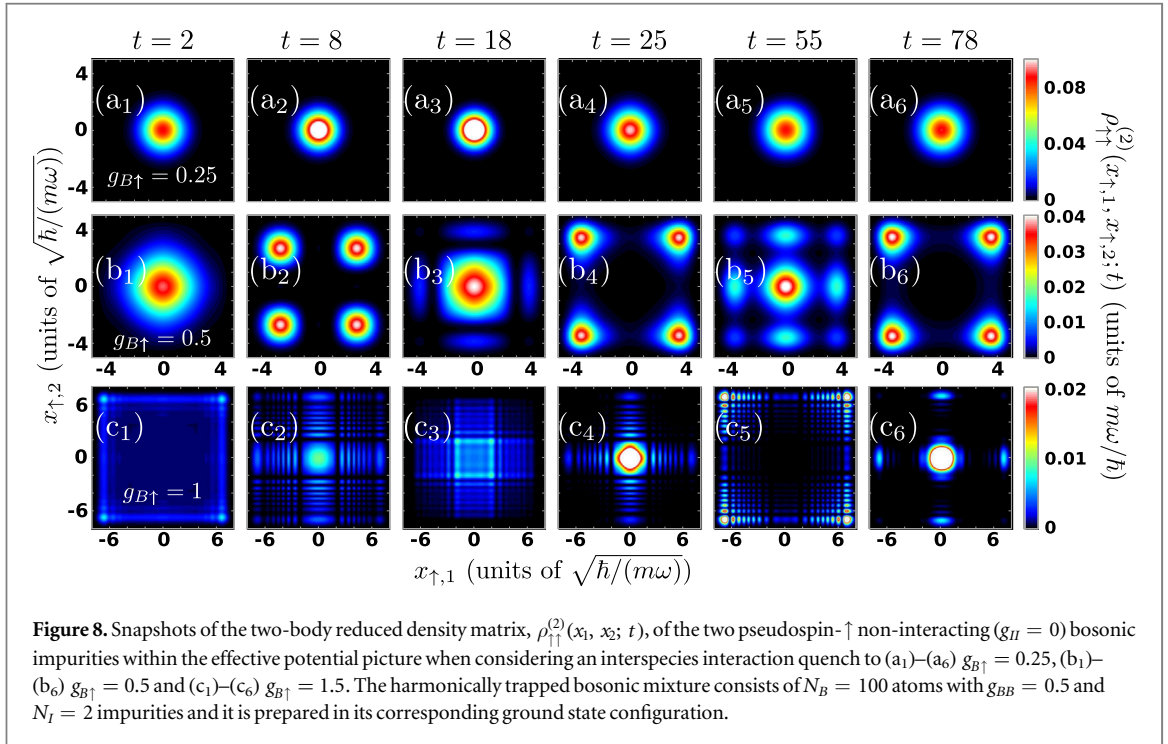
To further expose the necessity of taking into account the intra- and the interspecies correlations of the system in order to accurately describe the MB dynamics of the impurities we next solve the time-dependent Schrödinger equation that governs the system's dynamics relying on the previously introduced effective potential picture (equation (15)) via exact diagonalization⁶. Thus our main aim here is to test the validity of $\bar{V}_I^{\text{eff}}(x)$ at least to qualitatively capture the basic features of the emergent non-equilibrium dynamics of the two impurities. We emphasize again that \bar{V}_I^{eff} does not include any interspecies correlation effects that arise in the course of the temporal-evolution of the impurities. Within this approximation the effective Hamiltonian that captures the quench-induced dynamics of the impurities reads

$$H^{\text{eff}} = \int dx \hat{\Psi}_{\uparrow}^{\dagger}(x) \left(-\frac{\hbar^2}{2m} \frac{d^2}{dx^2} + \bar{V}_I^{\text{eff}} \right) \hat{\Psi}_{\uparrow}(x) + g_{\uparrow\uparrow} \int dx \hat{\Psi}_{\uparrow}^{\dagger}(x) \hat{\Psi}_{\uparrow}^{\dagger}(x) \hat{\Psi}_{\uparrow}(x) \hat{\Psi}_{\uparrow}(x), \quad (16)$$

where $\hat{\Psi}_{\uparrow}(x)$ is the bosonic field-operator of the pseudospin- \uparrow impurity and $g_{\uparrow\uparrow}$ denotes the intraspecies interactions between the two pseudospin- \uparrow impurity atoms. Recall that the intercomponent contact interaction of strength $g_{B\uparrow}$ and the intraspecies interaction between the bath atoms are inherently embedded into \bar{V}_I^{eff} (equation (15)). In particular, within \bar{V}_I^{eff} we account for the correlated Thomas–Fermi profile of the BEC since $\rho_B^{(1)}(x; t)$ is determined from the MB approach. Below, we exemplarily study the dynamics of two non-interacting impurities and therefore we set $g_{\uparrow\uparrow} = 0$ in equation (16). Moreover, in order to trigger the non-equilibrium dynamics we consider an interspecies interaction quench from $g_{B\uparrow} = 0$ ($t = 0$) to a finite repulsive value of $g_{B\uparrow}$. Such a sudden change is essentially taken into account via a deformation of \bar{V}_I^{eff} (equation (15)).

The corresponding instantaneous two-body reduced density matrix of the impurities within H^{eff} is depicted in figure 8 for distinct values of $g_{B\uparrow}$. Focusing on weak postquench interactions, e.g. $g_{B\uparrow} = 0.25$, we observe that at the initial times the two-body dynamics of the impurities is adequately described within H^{eff} (compare figures 7(a₁)–(a₃) to figures 8(a₁)–(a₃)). Indeed, in this time-interval only some minor deviations between the heights of the peaks of $\rho_{\uparrow\uparrow}^{(2)}(x_1, x_2; t)$ obtained within the MB and the H^{eff} approach are observed. However, for longer times H^{eff} (figures 8(a₄)–(a₆)) fails to capture the correct shape of $\rho_{\uparrow\uparrow}^{(2)}(x_1, x_2; t)$ and more precisely its deformations occurring along its diagonal or anti-diagonal (see figures 8(a₄)–(a₆)) which stem from the build up of higher-order correlations during the dynamics.

⁶ Notice that the exact diagonalization simulations are performed within the two-body number state basis constructed by the single-particle states of a sine DVR consisting of 600 grid points, see also [appendix](#).



Increasing the repulsion such that $g_{B\uparrow} = 0.5$, deviations between the effective potential approximation and the correlated approach become more severe. For instance, at the initial times the sharp two-body probability peak of $\rho_{\uparrow\uparrow}^{(2)}(x_1, x_2; t)$ in the vicinity of $x_1 = x_2 = 0$ arising in the MB dynamics (figure 7(b₁)) becomes smoother within H^{eff} (figure 8(b₁)) although the overall shape of $\rho_{\uparrow\uparrow}^{(2)}(x_1, x_2; t)$ remains qualitatively similar. Moreover, the observed elongations along the diagonal of $\rho_{\uparrow\uparrow}^{(2)}(x_1, x_2; t)$ exhibited due to the presence of correlations are not captured in the effective picture, e.g. compare figures 7(b₃), (b₅) with figures 8(b₃), (b₅). Remarkably, the two-body superposition identified in $\rho_{\uparrow\uparrow}^{(2)}(x_1, x_2; t)$ of two different two-body configurations occurring at specific time-instants is also predicted at least qualitatively via H^{eff} , see figures 8 (b₂), (b₄) and (b₆). We remark that the differences in the patterns of $\rho_{\uparrow\uparrow}^{(2)}(x_1, x_2; t)$ between H^{eff} and the correlated approach are even more pronounced when $g_{II} = 0.2$ (results not shown).

Strikingly for strongly repulsive interactions, $g_{B\uparrow} = 1.5$, H^{eff} completely fails to capture the two-body dynamics of the impurities. This fact can be directly inferred by comparing $\rho_{\uparrow\uparrow}^{(2)}(x_1, x_2; t)$ within the two approaches, see figures 7(c₁)–(c₆) and figures 8(c₁)–(c₆). Even at the initial stages of the dynamics the effective potential cannot adequately reproduce the correct shape of $\rho_{\uparrow\uparrow}^{(2)}(x_1, x_2; t)$, compare figure 8(c₁) with figure 7(d₁). Note, for instance, the absence of the central two-body probability peak in the region $-2 < x_1, x_2 < 2$ within H^{eff} which demonstrates the correlated character of the dynamics. More precisely, $\rho_{\uparrow\uparrow}^{(2)}(x_1, x_2; t)$ obtained via H^{eff} shows predominantly the development of two different two-body configurations. The first pattern suggests that the impurities either reside together at the same edge of the BEC background or each one is located at a distinct edge of the Thomas–Fermi profile, see e.g. figures 8(c₁), (c₅). However, at different time-instants $\rho_{\uparrow\uparrow}^{(2)}(x_1, x_2; t)$ indicates that the impurities lie in the vicinity of the trap center as illustrated e.g. in figures 8(c₂), (c₄) and (c₆), an event that never occurs for $t > 5$ in the MB dynamics (see figure 5(h)). It is also worth mentioning that the observed dispersive character of $\rho_{\uparrow\uparrow}^{(2)}(x_1, x_2; t)$ in the MB dynamics (see e.g. figures 7 (d₄)–(d₆)) is a pure correlation effect and a consequence of the participation of a multitude of excited states in the impurity dynamics which is never captured within H^{eff} .

4.5. Quench to attractive interactions

Next we discuss the dynamical behavior of both the BEC medium and the bosonic impurities on both the one- and the two-body level after an interspecies interaction quench from $g_{B\uparrow} = 0$ to the attractive regime of $g_{B\uparrow} < 0$. To explain basic characteristics of the dynamics of the impurities an effective potential picture is also employed. As in the previous section we first examine the emergent time-evolution of two non-interacting impurities ($g_{II} = 0$) and then compare our findings to that of two weakly interacting ($g_{II} = 0.2$) ones.

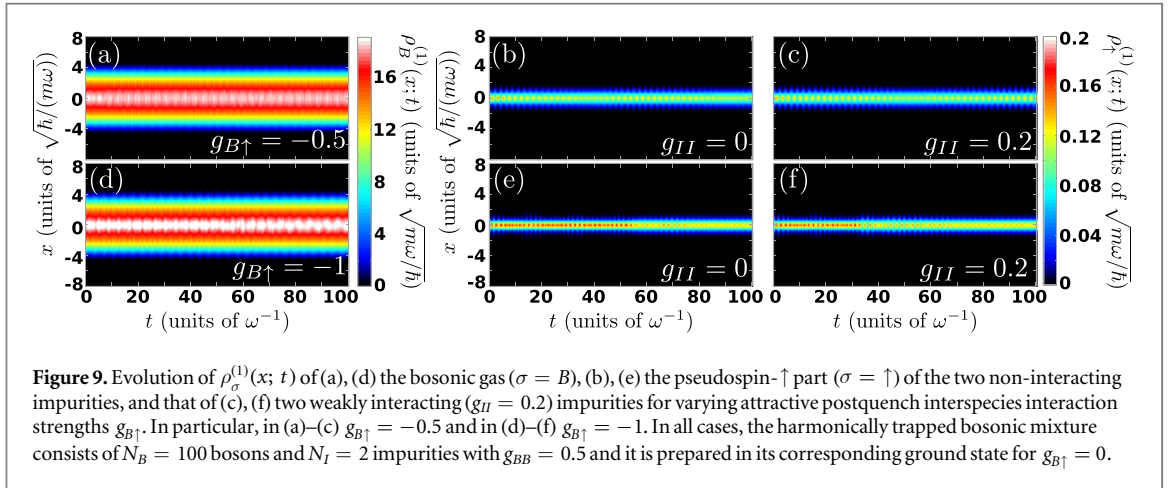


Figure 9. Evolution of $\rho_\sigma^{(1)}(x; t)$ of (a), (d) the bosonic gas ($\sigma = B$), (b), (e) the pseudospin- \uparrow part ($\sigma = \uparrow$) of the two non-interacting impurities, and that of (c), (f) two weakly interacting ($g_{II} = 0.2$) impurities for varying attractive postquench interspecies interaction strengths $g_{B\uparrow}$. In particular, in (a)–(c) $g_{B\uparrow} = -0.5$ and in (d)–(f) $g_{B\uparrow} = -1$. In all cases, the harmonically trapped bosonic mixture consists of $N_B = 100$ bosons and $N_I = 2$ impurities with $g_{BB} = 0.5$ and it is prepared in its corresponding ground state for $g_{B\uparrow} = 0$.

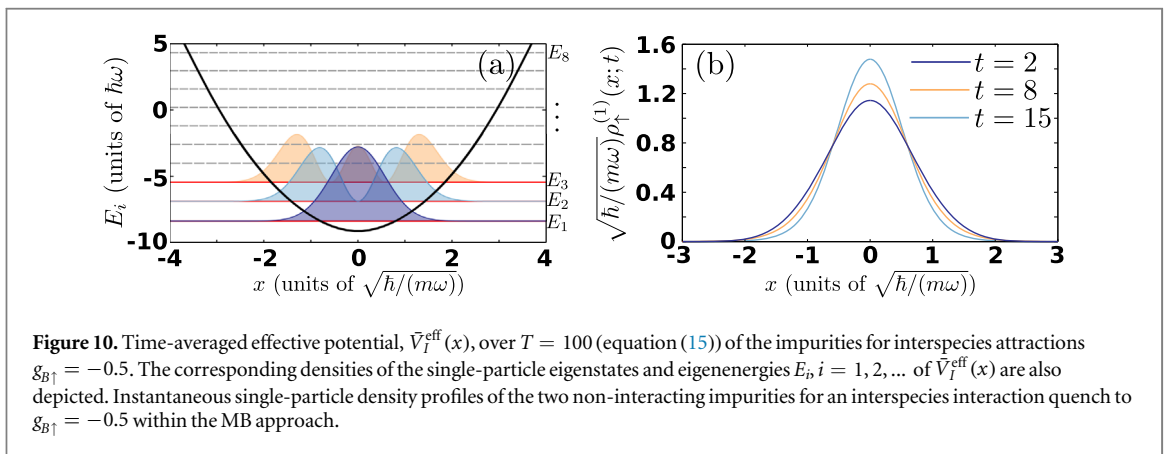


Figure 10. Time-averaged effective potential, $\bar{V}_I^{\text{eff}}(x)$, over $T = 100$ (equation (15)) of the impurities for interspecies attractions $g_{B\uparrow} = -0.5$. The corresponding densities of the single-particle eigenstates and eigenenergies $E_i, i = 1, 2, \dots$ of $\bar{V}_I^{\text{eff}}(x)$ are also depicted. Instantaneous single-particle density profiles of the two non-interacting impurities for an interspecies interaction quench to $g_{B\uparrow} = -0.5$ within the MB approach.

4.5.1. Single-particle dynamics and effective potential

To investigate the spatially resolved dynamics of the multicomponent system after an interaction quench from $g_{B\uparrow} = 0$ to $g_{B\uparrow} < 0$, we first analyze the spatio-temporal evolution of the σ -species single-particle density $\rho_\sigma^{(1)}(x; t)$. The dynamical response of $\rho_\sigma^{(1)}(x; t)$ triggered by the quench is presented in figure 9 for postquench interspecies attractions $g_{B\uparrow} = -0.5$ (figures 9(a)–(c)) and $g_{B\uparrow} = -1$ (figures 9(d)–(f)).

Inspecting the dynamics of two non-interacting impurities at $g_{B\uparrow} = -0.5$ (region R'_{III}), shown in figures 9(a), (b), we deduce that $\rho_\uparrow^{(1)}(x; t)$ undergoes a breathing motion inside $\rho_B^{(1)}(x; t)$ characterized by a predominant frequency $\omega_{br}^I \approx 2.76$ and a secondary one $\omega_{br}^{II} \approx 2.88$ thus producing a beating pattern. These two distinct frequencies stem from the center-of-mass and relative coordinate breathing modes of the impurities, whose existence originates from the presence of attractive induced interactions in the system. We remark that the breathing frequency of the center-of-mass can be estimated in terms of the corresponding effective potential of the impurities, see also equation (17). In particular for $g_{B\uparrow} = -0.5$, $\omega_{br}^I = 2\sqrt{2.06} \approx 2.87$ (see also the comment in⁷) which is in very good agreement with ω_{br}^{II} . The relevant contraction of $\rho_\uparrow^{(1)}(x; t)$ can be inferred by its increasing amplitude that takes place from the very early stages of the non-equilibrium dynamics (figure 10(b)). The beating pattern can be readily identified e.g. by comparing the maximum height of $\rho_\uparrow^{(1)}(x; t)$ during its contraction at initial and later stages of the dynamics, see e.g. $\rho_\uparrow^{(1)}(x; t)$ at $t = 10$ and $t = 40$ in figure 9(b). Moreover, as a consequence of the motion of the impurity and the relatively weak interspecies attraction, i.e. $g_{B\uparrow} = -0.5$, the Thomas–Fermi cloud of the bosonic gas becomes slightly distorted. In particular, a low amplitude density hump is imprinted on $\rho_B^{(1)}(x; t)$ exactly at the position of $\rho_\uparrow^{(1)}(x; t)$ as shown by the white colored region in figure 9(a) in the vicinity of $x = 0$ [75]. An almost similar effect to the above-mentioned breathing dynamics is present also for the case of two weakly interacting impurities (figure 9(c)). Here, the

⁷ Notice here that the time-resolved form of the effective potential $V_I^{\text{eff}}(x, t) = V(x) - |g_{B\uparrow}| \rho_B^{(1)}(x; t)$ corresponds to a deformed attractive harmonic oscillator potential exhibiting a faint additional dip around $x \approx 0$ resulting from the appearance of the density hump of $\rho_B^{(1)}(x; t)$ [75]. However in the averaged form of the effective potential this density dip contributes just as a shift of the frequency of the resulting parabolic potential. As an example at $g_{B\uparrow} = -0.5$ the effective trapping frequency $\omega^{\text{eff}} \approx \sqrt{2.06}$ within $\bar{V}_I^{\text{eff}}(x)$ while $\omega^{\text{eff}} = \sqrt{2}$ within $V_I^{\text{eff}}(x, t = 0)$.

secondary frequency manifests itself at later evolution times resulting in turn in a slower beating of $\rho_{\uparrow}^{(1)}(x; t)$ compared to the $g_{II} = 0$ scenario (hardly visible in figure 9(c)). This delayed occurrence is attributed to the presence of intraspecies repulsion which competes with the attractive induced interactions.

For a larger negatively valued interspecies coupling, e.g. for $g_{BI} = -1$ within region R'_{III} , $\rho_{\uparrow}^{(1)}(x; t)$ becomes more spatially localized and again performs a decaying amplitude breathing motion, the so-called beating identified above, but with a larger major frequency, $\omega_{br}^{\uparrow} \approx 3.2$, compared to the $g_{B\uparrow} = -0.5$ case (figure 9(e)). Notice that the observed beating motion of the impurities persists while being more dramatic for this stronger attraction (compare figures 9(b) and (e)). This enhanced attenuation of the breathing amplitude together with the strong localization of the impurities is a direct effect of the dominant presence of interspecies attractions between the impurity and the bath, see also [75]. Also, due to the stronger $g_{B\uparrow}$ and the increased spatial localization of $\rho_{\uparrow}^{(1)}(x; t)$, the density hump building upon $\rho_B^{(1)}(x; t)$ at the instantaneous position of the impurities is much more pronounced than that found for $g_{B\uparrow} = -0.5$ (figure 9(d)). Note that the density hump appearing in $\rho_B^{(1)}(x; t)$ is essentially an imprint of the impurities presence and motion within the bosonic medium. Indeed, $\rho_{\uparrow}^{(1)}(x; t)$ exhibits a sech-like form tending to be more localized for a larger interspecies attractions $g_{B\uparrow}$, see e.g. $\rho_{\uparrow}^{(1)}(x; t)$ at a fixed time-instant for $g_{B\uparrow} = -0.5$ and $g_{B\uparrow} = -1$ in figures 9(b) and (e) respectively, a behavior that also holds for the consequent density hump in $\rho_B^{(1)}(x; t)$ (figures 9(a), (d)). We should remark that for large negative $g_{B\uparrow}$ the system becomes strongly correlated and the BEC is highly excited. The latter is manifested by the development of an overall weak amplitude breathing motion of the bosonic gas, see figure 9(d). Furthermore, the inclusion of weak intraspecies repulsions between the impurities does not significantly alter their dynamics (figure 9(f)). Indeed, a faint increase of their expansion magnitude takes place and the corresponding amplitude of the beating decays faster (compare figures 9(d) and (f)).

The above-mentioned dynamics can also be qualitatively explained in terms of a corresponding effective potential approximation [35, 73, 75]. Yet again, the effective potential experienced by the impurities consists of the external harmonic oscillator $V(x)$ and the single-particle density of the BEC background. Importantly, since $\rho_B^{(1)}(x; t)$ is greatly distorted from its original Thomas–Fermi profile due to the motion of the impurities, we invoke a time-averaged effective potential. Consequently, the effective potential of the impurity reads

$$\bar{V}_I^{\text{eff}}(x) = V(x) - \frac{|g_{BI}|}{T} \int_0^T dt \rho_B^{(1)}(x; t), \quad (17)$$

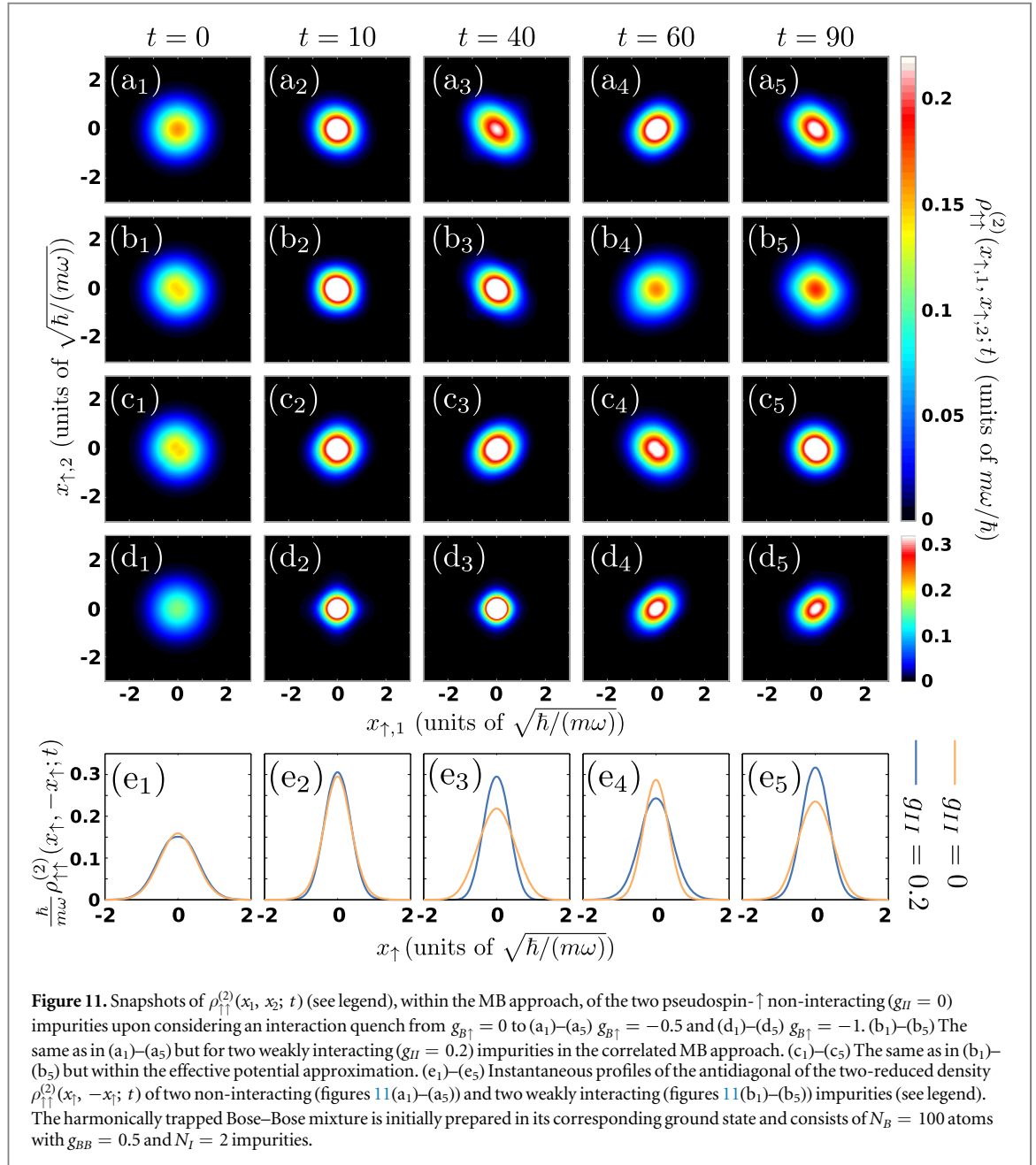
where $T = 100$ denotes the corresponding total propagation time. We remark that for the considered negative values of $g_{B\uparrow}$ the shape of $\bar{V}_I^{\text{eff}}(x)$ does not significantly change after averaging over $T = 60$. A schematic illustration of $\bar{V}_I^{\text{eff}}(x)$ and the densities of its first few single-particle eigenstates at $g_{B\uparrow} = -1$ is presented in figure 10(a), see also remark (see footnote 7). The observed localization tendency of $\rho_{\uparrow}^{(1)}(x; t)$ around the aforementioned potential minimum is essentially determined by the strongly attractive behavior of $\bar{V}_I^{\text{eff}}(x)$. Remarkably, the distinct dynamical features of the impurities for an increasing interspecies attraction can be partly understood with the aid of $\bar{V}_I^{\text{eff}}(x)$. Indeed, for increasing $|g_{BI}|$ the effective frequency of $\bar{V}_I^{\text{eff}}(x)$ is larger and $\bar{V}_I^{\text{eff}}(x)$ becomes more attractive. The former property of $\bar{V}_I^{\text{eff}}(x)$ accounts for the increasing breathing frequency of the impurity wavepacket for larger $|g_{BI}|$. Additionally, the increasing attractiveness of $\bar{V}_I^{\text{eff}}(x)$ is responsible for the reduced width of $\rho_{\uparrow}^{(1)}(x; t)$ for a larger $|g_{BI}|$ and thus its increasing localization tendency.

4.5.2. Two-body correlation dynamics and comparison to the effective potential approximation

Having described the time-evolution of the impurities on the single-particle level, we next analyze the dynamical response of the pseudospin- \uparrow component by invoking the corresponding two-body reduced density matrix $\rho_{\uparrow\uparrow}^{(2)}(x_1, x_2; t)$ (see also equation (7)).

The time-evolution of $\rho_{\uparrow\uparrow}^{(2)}(x_1, x_2; t)$ is depicted in figures 11(a₁)–(a₅) for two non-interacting ($g_{II} = 0$) impurities following an interspecies interaction quench from $g_{B\uparrow} = 0$ to $g_{B\uparrow} = -0.5$ (region R'_{III}). Before the quench the impurities lie together in the vicinity of the trap center since $\rho_{\uparrow\uparrow}^{(2)}(x_1 = 0, x_2 = 0; t = 0)$ shows a high probability peak (figure 11(a₁)). However as time evolves the two bosons start to occupy a relatively smaller spatial region as can be deduced by the shrinking of the central two-body probability peak across the diagonal at $t = 10$ in figure 11(a₂). Then they move either opposite to each other (see the elongated anti-diagonal in figures 11(a₃), (a₅)) or tend to bunch together at the same location (see the pronounced diagonal of $\rho_{\uparrow\uparrow}^{(2)}(x_1, x_2 = x_1; t = 60)$ in figure 11(a₄)). This latter behavior of the impurities is the two-body analog of their wavepacket periodic expansion and contraction (relative coordinate breathing motion) discussed previously on the single-particle level (figure 9(b)).

The dynamics of two weakly repulsively interacting ($g_{II} = 0.2$) impurities (figures 11 (b₁)–(b₅)) shows similar characteristics to the above-described non-interacting scenario. Indeed, initially (figure 11(b₁)) and at



short times (figure 11(b₂)) the impurities reside close to the trap center while later on they repel (see e.g. figure 11(b₃)) or attract (figure 11(b₄)) each other as a result of their breathing dynamics (see also figure 9(c)). The major difference between the weakly interacting and the non-interacting impurities is that their distance which is given by the anti-diagonal distribution of their two-body reduced density matrix is slightly different, see figures 11(e₁)–(e₅). For instance at $t = 40$ the non-interacting impurities are further apart from each other as compared to the case of interacting impurities, while this situation is reversed at $t = 90$. The aforementioned difference owes its existence to the distinct relative coordinate breathing frequencies. This can be directly inferred from the fact that $\rho_{\uparrow\uparrow}^{(2)}(x_1, x_2; t)$ possesses a larger spatial distribution when $g_{II} = 0.2$ and it is attributed to their underlying mutual repulsion. For instance, even initially $\rho_{\uparrow\uparrow}^{(2)}(x_1, x_2; t = 0)$ for $g_{II} = 0.2$ (figure 11(b₁)) is slightly deformed towards its anti-diagonal compared to the $g_{II} = 0$ case (figure 11(a₁)). This behavior persists also during the evolution independently of the expansion or the contraction of the impurity cloud, as can be seen by comparing figures 11(b₄) to (a₄) and figures 11(b₅) to (a₅).

To reveal the importance of both intra- and interspecies correlations for the impurity dynamics we then utilize the effective potential, $\bar{V}_I^{\text{eff}}(x)$, introduced in equation (17) and solve numerically the time-dependent Schrödinger equation of the impurities via exact diagonalization. We remark once more that \bar{V}_I^{eff} neglects the interspecies correlations of the multicomponent system but includes the density profile of the BEC determined by the MB approach. In particular, we construct the effective Hamiltonian H^{eff} of equation (16) but using the

$\bar{V}_I^{\text{eff}}(x)$ of equation (17). For brevity we focus on the case of $g_{\uparrow\uparrow} = 0.2$ and analyze the dynamics after an interspecies interaction quench from $g_{B\uparrow} = 0$ ($t = 0$) to $g_{B\uparrow} = -0.5$. As explained in section 4.4.3 within the effective potential picture this quench scenario accounts for the deformation of \bar{V}_I^{eff} . Snapshots of $\rho_{\uparrow\uparrow}^{(2)}(x_1, x_2; t)$ when $g_{II} = 0.2$ and $g_{B\uparrow} = -0.5$ obtained within H^{eff} are illustrated in figures 11(c₁)–(c₅). As it can be seen by comparing $\rho_{\uparrow\uparrow}^{(2)}(x_1, x_2; t)$ for the MB approach (figures 11(b₁)–(b₅)) and H^{eff} (figures 11(c₁)–(c₅)) significant deviations occur between the two methods. Indeed, during the time-evolution the correlation patterns visible in $\rho_{\uparrow\uparrow}^{(2)}(x_1, x_2; t)$ calculated via H^{eff} exhibit similar overall characteristics to the ones taking place in the correlated approach but at completely different time-scales. In fact, $\rho_{\uparrow\uparrow}^{(2)}(x_1, x_2; t)$ shows elongated shapes along its diagonal (figure 11(c₃)) or anti-diagonal (figure 11(c₄)) implying that the impurities tend to be relatively close or apart from one another respectively. The latter is again a manifestation of the breathing motion of the impurities at the two-body level. However H^{eff} fails in general to adequately capture the correct spatial shape of $\rho_{\uparrow\uparrow}^{(2)}(x_1, x_2; t)$, since e.g. it predicts a repulsion of the impurities (figure 11(c₄)) when in the presence of correlations they attract each other (figure 11(b₄)) and vice versa (compare figures 11(c₃) and (b₃)). This difference is caused by the failure of the effective potential to account for induced interactions emanating within the MB setting.

Finally, turning to strong postquench attractions within R'_{III} , e.g. for $g_{B\uparrow} = -1$ presented in figures 11(d₁)–(d₅), we observe that the two-body dynamics of the impurities is drastically altered with respect to the weakly attractive case $g_{B\uparrow} = -0.5$ described above. Initially, at $t = 0$, the two bosons bunch together in the vicinity of the trap center since $\rho_{\uparrow\uparrow}^{(2)}(-1 < x_1 < 1, -1 < x_2 < 1; t = 0)$ is predominantly populated (figure 11(d₁)). Subsequently the two-body distribution of $\rho_{\uparrow\uparrow}^{(2)}(x_1, x_2; t)$ spatially shrinks exhibiting a highly intense peaked structure around $-0.2 < x_1, x_2 < 0.2$ as shown in figures 11(d₂), (d₃). For longer evolution times $\rho_{\uparrow\uparrow}^{(2)}(x_1, x_2; t)$ deforms possessing an elongated shape across its diagonal (see figures 11(d₄), (d₅)) which indicates that the impurities experience a mutual attraction. This latter behavior suggests the appearance of attractive induced interactions between the impurities mediated by the bosonic gas.

5. Summary and conclusions

We have investigated the ground state properties and the interspecies interaction quench quantum dynamics of two spinor bosonic impurities immersed in a harmonically trapped bosonic gas from zero to finite repulsive and attractive couplings. For two non-interacting impurities, we have shown that for an increasing attraction or repulsion their overall distance decreases indicating the presence of attractive induced interactions. Moreover, at strong attractions or repulsions the impurities acquire a fixed distance and bunch together either at the trap center or at the edge of the Thomas–Fermi profile of the bosonic gas respectively. For two weakly repulsive impurities we find that their ground state properties remain qualitatively the same for attractive couplings, but for repulsive interactions they move apart being located symmetrically with respect to the trap center. A similar to the above-described overall phenomenology takes place for smaller system sizes and heavier impurities.

Regarding the quench dynamics of the multicomponent system we have analyzed the time-evolution of the contrast and its spectrum. We have revealed the emergence of six different dynamical response regions for varying postquench interaction strength which signify the existence, dynamical deformation and the orthogonality catastrophe of Bose polarons. We have also shown that the extent of these regions can be tuned via the intraspecies repulsion between the impurities, the impurity concentration and the size of the bath. Moreover, we have found that the polaron excitation spectrum depends strongly on the postquench interspecies interaction strength and the number of impurities but it is almost insensitive on the impurity–impurity interaction for the weak couplings.

Focusing on weak postquench interspecies repulsions the non-interacting impurities perform a breathing motion manifested as a periodic expansion and contraction of their density on both the one- and two-body level. For an increasing repulsion the impurities single-particle density splits into two counterpropagating density branches that travel to the edges of the BEC medium where they are reflected back towards the trap center and subsequently collide, repeating this motion in a periodic manner. Here the impurities mainly reside in a superposition of two distinct two-body configurations, namely they either reside together or each one lies at a specific density branch, while during their collision they tend to remain very close to each other. In the strong repulsive regime we have observed that the density of the impurities shortly after the quench breaks into two fragments which are symmetric with respect to the origin and which exhibit a multihump structure and perform a damped oscillatory motion close to the Thomas–Fermi radius of the bosonic gas. This multihump structure leads to a spatially delocalized behavior of the corresponding two-body correlation patterns and suggests the involvement of higher excited states. In all cases the bosonic gas exhibits a breathing motion whose amplitude becomes more pronounced for an increasing repulsion.

Turning to attractive interspecies couplings, the impurities show a beating breathing motion and experience a spatial localization tendency at the trap center on both the one- and two-body level, a behavior that becomes more pronounced for larger attractions. Strikingly, for strong attractive interactions we unveil that gradually the impurities experience a mutual attraction on the two-body level. This effect demonstrates the pronounced presence of induced interactions for attractive interspecies ones. As a result of the impurities motion the density of the bosonic bath deforms, developing a low amplitude density hump located at the origin. The occurrence of this hump is a direct consequence of the presence of induced interactions.

In all cases investigated in the present work, an intuitive understanding of the dynamics of the impurities is provided via an effective potential picture which is shown to be an adequate approximation for weak couplings where correlations are negligible. However, for increasing interaction strengths this effective model largely fails to adequately describe the dynamics on both the one- and two-body level due to the presence of both induced attraction and higher-order correlations. Finally, in all of the above-mentioned cases we showcase that a similar dynamical response takes place for two weakly repulsive impurities but the corresponding time-scales are slightly altered due to the competition between their mutual repulsion and the developed attractive induced interactions.

There is a multitude of fruitful possible extensions of the present effort that can be addressed in future works. A intriguing aspect would be to examine whether thermalization of the impurities dynamics takes place for strong repulsions in the framework of the eigenstate thermalization hypothesis [101]. An imperative prospect is to study the robustness of the emergent quasiparticle picture in the current setting in the presence of temperature effects [102, 103]. Moreover, the study of induced interactions of two bosonic impurities immersed in a Fermi sea would be an interesting prospect especially in order to expose their dependence on the different statistics of the medium. Additionally, the generalization of the present results to higher-dimensional settings would be highly desirable. Another interesting direction would be to investigate the collisional dynamics of subsonically or supersonically moving impurities in a lattice trapped bosonic gas. Here, one could unravel the properties of the emergent quasiparticles, such as their lifetime, residue, effective mass and induced interactions with respect to the interspecies interaction strength.

Acknowledgments

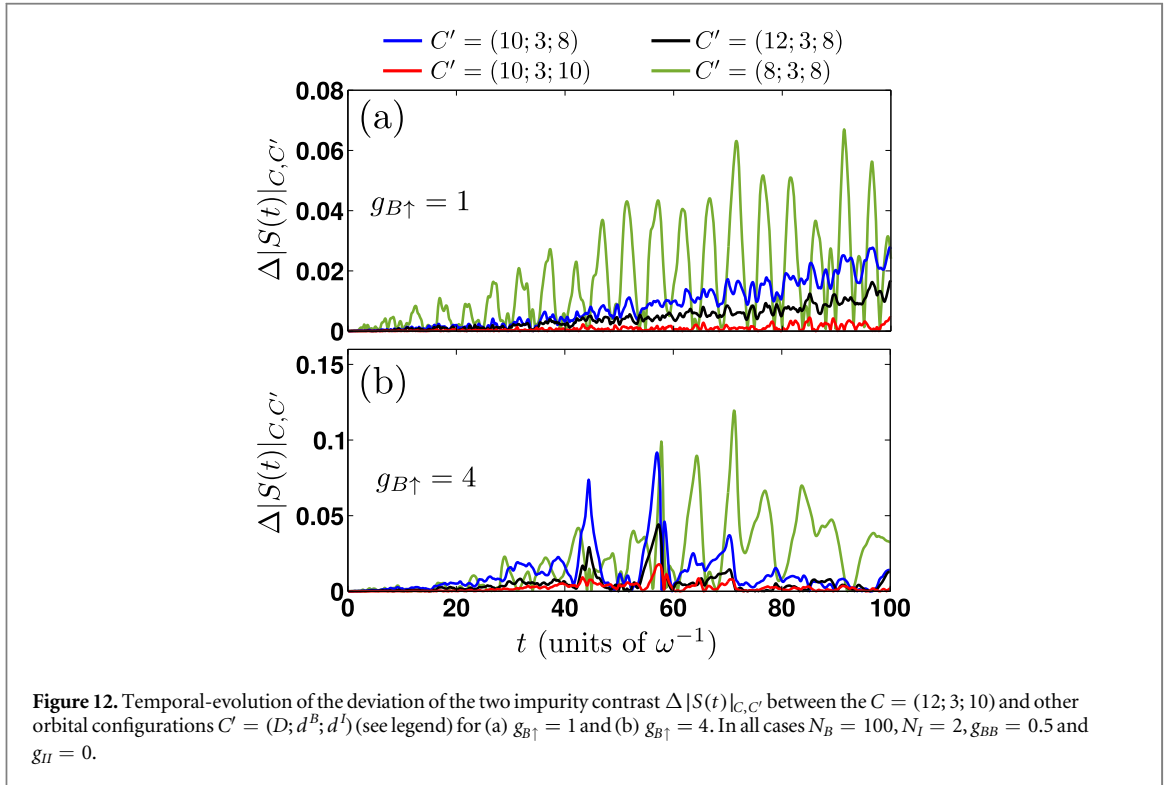
SIM and PS gratefully acknowledge financial support by the Deutsche Forschungsgemeinschaft (DFG) in the framework of the SFB 925 ‘Light induced dynamics and control of correlated quantum systems’. S I M gratefully acknowledges financial support in the framework of the Lenz-Ising Award of the University of Hamburg. TB has been supported by the Okinawa Institute of Science and Technology Graduate University.

Appendix. Remarks on the MB simulations

To solve the underlying time-dependent MB Schrödinger equation of the considered multicomponent system we invoke the ML-MCTDHX [70, 71]. As discussed in section 2.2 it constitutes a variational approach for calculating the stationary and most importantly the non-equilibrium quantum dynamics of bosonic and fermionic multicomponent mixtures [35, 36, 65] including spin degrees of freedom [9, 35, 82]. A key advantage of the method is that it assumes the expansion of the total MB wavefunction in terms of a time-dependent and variationally optimized basis. Such a treatment enables us to capture both the intra- and intercomponent correlation effects by employing a computationally feasible basis size. The latter flexibility allows to span the relevant subspace of the Hilbert space efficiently for each time-instant which is in contrast to numerical methods relying on a time-independent basis.

The used Hilbert space truncation can be deduced from the employed orbital configuration space, denoted by $C = (D; d^B, d^I)$ with $D = D^B = D_I$ and d^B, d^I being the number of species and SPFs of each species respectively (equations (3)–(5)). Additionally, within our implementation a sine discrete variable representation (sine-DVR) is utilized as the primitive basis for the spatial part of the SPFs with $\mathcal{M} = 600$ grid points. The latter intrinsically introduces hard-wall boundary conditions at both edges of the numerical grid imposed herein at $x_{\pm} = \pm 50$. We have ensured that the position of the hard-walls does not affect the presented results by assuring that no appreciable density occurs beyond $x_{\pm} = \pm 20$. The eigenstates of the composite MB system are obtained by means of the so-called improved relaxation method [70, 71] implemented in ML-MCTDHX. In order to simulate the non-equilibrium dynamics we propagate in time the wavefunction (equation (3)) utilizing the appropriate Hamiltonian within the ML-MCTDHX equations of motion.

To infer the convergence of our MB simulations we ensure that all observables of interest, e.g. $|\langle \hat{S}(t) \rangle|$, $\rho_{\uparrow}^{(1)}(x; t)$, become to a certain degree insensitive upon varying the employed orbital configuration space chosen



herein to be $C = (D; d^B; d^I) = (12; 3; 10)$. Below, we exemplarily showcase the convergence behavior of the contrast during evolution for a system composed of $N_B = 100$ bosons with $g_{BB} = 0.5$ and $N_I = 2$ non-interacting ($g_{II} = 0$) impurities. More precisely, we investigate its absolute deviation between the $C = (10; 3; 10)$ and other orbital configurations $C' = (D; d^B; d^I)$ during the non-equilibrium dynamics, namely

$$\Delta |S(t)|_{C,C'} = \frac{||\langle \hat{S}(t) \rangle|_C - |\langle \hat{S}(t) \rangle|_{C'}|}{|\langle \hat{S}(t) \rangle|_C}. \quad (\text{A.1})$$

The time-evolution of $\Delta |S(t)|_{C,C'}$ is illustrated in figure 12 after an interspecies interaction quench from $g_{B\uparrow} = 0$ to intermediate repulsions e.g. $g_{B\uparrow} = 1$ (figure 12(a)) and strong ones such as $g_{B\uparrow} = 4$ (figure 12(b)). As it can be readily seen by inspecting $\Delta |S(t)|_{C,C'}$, a systematic convergence of $|\langle \hat{S}(t) \rangle|$ can be achieved in both cases. At intermediate postquench repulsions, e.g. $g_{B\uparrow} = 1$, $\Delta |S(t)|_{C,C'}$ e.g. between the $C = (12; 3; 10)$ and $C' = (10; 3; 8)$ [$C' = (8; 3; 8)$] orbital configurations acquires a maximum value of the order of 3% [7%] at large propagation times as shown in figure 12(a). As expected, an increasing $g_{B\uparrow}$ yields a larger relative error (figure 12(b)) but still remaining at an adequately small degree. Indeed, turning to strong repulsions such as $g_{B\uparrow} = 4$ we observe that the deviation $\Delta |S(t)|_{C,C'}$ with $C = (12; 3; 10)$ and $C' = (12; 3; 8)$ [$C' = (10; 3; 8)$] lies below 5% [9%] throughout the evolution, see figure 12(b). Finally, we should mention that a similar analysis has been performed for all other interspecies interaction strengths and observables discussed in the main text and found to be adequately converged (results not shown here for brevity).

ORCID iDs

S I Mistakidis  <https://orcid.org/0000-0002-5118-5792>

P Schmelcher  <https://orcid.org/0000-0002-2637-0937>

References

- [1] Massignan P, Zaccanti M and Bruun G M 2014 *Rep. Prog. Phys.* **77** 034401
- [2] Schmidt R, Knap M, Ivanov D A, You J S, Cetina M and Demler E 2018 *Rep. Prog. Phys.* **81** 024401
- [3] Landau L D 1933 *Phys. Z. Sowjetunion* **3** 644
- [4] Pekar S I 1946 *Zh. Eksp. Teor. Fiz.* **16** 335
- [5] Pekar S I 1946 *Zh. Eksp. Teor. Fiz.* **16** 341
- [6] Grusdt F, Astrakharchik G E and Demler E 2017 *New J. Phys.* **19** 103035
- [7] Ardila L P and Giorgini S 2015 *Phys. Rev. A* **92** 033612

- [8] Dehkharghani A S, Volosniev A G and Zinner N T 2018 *Phys. Rev. Lett.* **121** 080405
- [9] Mistakidis SI, Katsimiga G C, Koutentakis G M and Schmelcher P 2019 *New J. Phys.* **21** 043032
- [10] Camacho-Guardian A, Ardila L P, Pohl T and Bruun G M 2018 *Phys. Rev. Lett.* **121** 013401
- [11] Keiler K, Krönke S and Schmelcher P 2018 *New J. Phys.* **20** 033030
- [12] Kohstall C, Zaccanti M, Jag M, Trenkwalder A, Massignan P, Bruun G M, Schreck F and Grimm R 2012 *Nature* **485** 615
- [13] Scazza F, Valtolina G, Massignan P, Recati A, Amico A, Burchianti A, Fort C, Inguscio M, Zaccanti M and Roati G 2017 *Phys. Rev. Lett.* **118** 083602
- [14] Schirotzek A, Wu C-H, Sommer A and Zwierlein M W 2009 *Phys. Rev. Lett.* **102** 230402
- [15] Chin C, Grimm R, Julienne P and Tiesinga E 2010 *Rev. Mod. Phys.* **82** 1225
- [16] Köhler T, Góral K and Julienne P S 2006 *Rev. Mod. Phys.* **78** 1311
- [17] Koschorreck M, Pertot D, Vogt E, Fröhlich B, Feld M and Köhl M 2012 *Nature* **485** 619
- [18] Cetina M, Jag M, Lous R S, Walraven J T, Grimm R, Christensen R S and Bruun G M 2015 *Phys. Rev. Lett.* **115** 135302
- [19] Cetina M et al 2016 *Science* **354** 96
- [20] Fukuhara T et al 2013 *Nat. Phys.* **9** 235
- [21] Catani J, Barontini G, Lompre S, Rabatti F, Thalhammer G, Minardi F, Stringari S and Inguscio M 2009 *Phys. Rev. Lett.* **103** 140401
- [22] Jørgensen N B, Wacker L, Skalmstang K T, Parish M M, Levinson J, Christensen R S, Bruun G M and Arlt J J 2016 *Phys. Rev. Lett.* **117** 055302
- [23] Hu M-G, Van de Graaff M J, Kedar D, Corson J P, Cornell E A and Jin D S 2016 *Phys. Rev. Lett.* **117** 055301
- [24] Yan Z Z, Ni Y, Robens C and Zwierlein M W 2019 arXiv:1904.02685
- [25] Grusdt F and Demler E 2015 New theoretical approaches to Bose polarons *Quantum Matter at Ultralow Temperatures* (Amsterdam: IOS Press) pp 325–411
- [26] Rath S P and Schmidt R 2013 *Phys. Rev. A* **88** 053632
- [27] Bruderer M, Klein A, Clark S R and Jaksch D 2007 *Phys. Rev. A* **76** 011605(R)
- [28] Privitera A and Hofstetter W 2010 *Phys. Rev. A* **82** 063614
- [29] Casteels W, Tempere J and Devreese J T 2012 *Phys. Rev. A* **86** 043614
- [30] Casteels W, Tempere J and Devreese J T 2013 *Phys. Rev. A* **88** 013613
- [31] Kain B and Ling H Y 2016 *Phys. Rev. A* **94** 013621
- [32] Volosniev A G and Hammer H W 2017 *Phys. Rev. A* **96** 031601
- [33] Dehkharghani A S, Volosniev A G and Zinner N T 2015 *Phys. Rev. A* **92** 031601
- [34] Volosniev A G, Hammer H W and Zinner N T 2015 *Phys. Rev. A* **92** 023623
- [35] Mistakidis SI, Katsimiga G C, Koutentakis G M, Busch T and Schmelcher P 2019 *Phys. Rev. Lett.* **122** 183001
- [36] Mistakidis SI, Volosniev A G, Zinner N T and Schmelcher P 2019 *Phys. Rev. A* **100** 013619
- [37] Ardila L P, Jørgensen N B, Pohl T, Giorgini S, Bruun G M and Arlt J J 2019 *Phys. Rev. A* **99** 063607
- [38] Grusdt F, Schmidt R, Shchadilova Y E and Demler E 2017 *Phys. Rev. A* **96** 013607
- [39] Grusdt F, Seetharam K, Shchadilova Y and Demler E 2018 *Phys. Rev. A* **97** 033612
- [40] Tempere J, Casteels W, Oberthaler M K, Knoop S, Timmermans E and Devreese J T 2009 *Phys. Rev. B* **80** 184504
- [41] Ichmoukamedov T and Tempere J 2019 *Phys. Rev. A* **100** 043605
- [42] Mistakidis SI, Hilbig L and Schmelcher P 2019 *Phys. Rev. A* **100** 023620
- [43] Shchadilova Y E, Schmidt R, Grusdt F and Demler E 2016 *Phys. Rev. Lett.* **117** 113002
- [44] Kamar N A, Kantian A and Giamarchi T 2019 *Phys. Rev. A* **100** 023614
- [45] Boyanovsky D, Jasnow D, Wu X L and Coalson R C 2019 *Phys. Rev. A* **100** 043617
- [46] Cucchiatti F M and Timmermans E 2006 *Phys. Rev. Lett.* **96** 210401
- [47] Schechter M, Gangardt D M and Kamenev A 2016 *New J. Phys.* **18** 065002
- [48] Cai Z, Wang L, Xie X C and Wang Y 2010 *Phys. Rev. A* **81** 043602
- [49] Johnson T H, Clark S R, Bruderer M and Jaksch D 2011 *Phys. Rev. A* **84** 023617
- [50] Siegl P, Mistakidis SI and Schmelcher P 2018 *Phys. Rev. A* **97** 053626
- [51] Theel F, Keiler K, Mistakidis SI and Schmelcher P 2020 *New J. Phys.* **22** 023027
- [52] Goold J, Fogarty T, Gullo N L, Paternostro M and Busch Th 2011 *Phys. Rev. A* **84** 063632
- [53] Rutherford L, Goold J, Busch Th and McCann J F 2011 *Phys. Rev. A* **83** 055601
- [54] Burovski E, Cheianov V, Gamayun O and Lychkovskiy O 2014 *Phys. Rev. A* **89** 041601
- [55] Lychkovskiy O 2015 *Phys. Rev. A* **91** 040101
- [56] Lychkovskiy O, Gamayun O and Cheianov V 2018 *Phys. Rev. B* **98** 024307
- [57] Gamayun O, Lychkovskiy O, Burovski E, Malcomson M, Cheianov V V and Zvonarev M B 2018 *Phys. Rev. Lett.* **120** 220605
- [58] Meinert F, Knap M, Kirilov E, Jag-Lauber K, Zvonarev M B, Demler E and Nägerl H C 2017 *Science* **356** 945
- [59] Mathy C J, Zvonarev M B and Demler E 2012 *Nat. Phys.* **8** 881
- [60] Knap M, Mathy C J, Ganahl M, Zvonarev M B and Demler E 2014 *Phys. Rev. Lett.* **112** 015302
- [61] Lausch T, Widera A and Fleischhauer M 2018 *Phys. Rev. A* **97** 033620
- [62] Lausch T, Widera A and Fleischhauer M 2018 *Phys. Rev. A* **97** 023621
- [63] Huber D, Hammer H W and Volosniev A G 2019 *Phys. Rev. Res.* **1** 033177
- [64] Mistakidis SI, Volosniev A G and Schmelcher P 2019 arXiv:1911.05353
- [65] Mistakidis SI, Katsimiga G C, Kevrekidis P G and Schmelcher P 2018 *New J. Phys.* **20** 043052
- [66] Erdmann J, Mistakidis SI and Schmelcher P 2019 *Phys. Rev. A* **99** 013605
- [67] Ao P and Chui S T 1998 *Phys. Rev. A* **58** 4836
- [68] Lampo A, Lim S H, Garcia-March M A and Lewenstein M 2017 *Quantum* **1** 30
- [69] Nielsen K K, Ardila L A P, Bruun G M and Pohl T 2019 *New J. Phys.* **21** 043014
- [70] Cao L, Bolsinger V, Mistakidis SI, Koutentakis G M, Krönke S, Schurer J M and Schmelcher P 2017 *J. Chem. Phys.* **147** 044106
- [71] Cao L, Krönke S, Vendrell O and Schmelcher P 2013 *J. Chem. Phys.* **139** 134103
- [72] Krönke S, Cao L, Vendrell O and Schmelcher P 2013 *New J. Phys.* **15** 063018
- [73] Kiehn H, Mistakidis SI, Katsimiga G C and Schmelcher P 2019 *Phys. Rev. A* **100** 023613
- [74] Sartori A and Recati A 2013 *Eur. Phys. J. D* **67** 260
- [75] Mistakidis SI, Grusdt F, Koutentakis G M and Schmelcher P 2019 *New J. Phys.* **21** 103026
- [76] Kasamatsu K, Tsubota M and Ueda M 2005 *Int. J. Mod. Phys. B* **19** 1835
- [77] Egorov M, Opanchuk B, Drummond P, Hall B V, Hannaford P and Sidorov A I 2013 *Phys. Rev. A* **87** 053614

- [78] Álvarez A, Cuevas J, Romero F R, Hamner C, Chang J J, Engels P, Kevrekidis P G and Frantzeskakis D J 2013 *J. Phys. B: At. Mol. Opt. Phys.* **46** 065302
- [79] Olshanii M 1998 *Phys. Rev. Lett.* **81** 938
- [80] Cohen-Tannoudji C, Diu B, Laloe F and Dui B 2006 *Quantum Mechanics* vol 2 (New York: Wiley)
- [81] Katsimiga G C, Koutentakis G M, Mistakidis S I, Kevrekidis P G and Schmelcher P 2017 *New J. Phys.* **19** 073004
- [82] Koutentakis G M, Mistakidis S I and Schmelcher P 2019 *New J. Phys.* **21** 053005
- [83] Horodecki R, Horodecki P, Horodecki M and Horodecki K 2009 *Rev. Mod. Phys.* **81** 865
- [84] Roncaglia M, Montorsi A and Genovese M 2014 *Phys. Rev. A* **90** 062303
- [85] Frenkel J 1934 *Wave Mechanics* 1st edn (Oxford: Clarendon) pp 423–8
- [86] Dirac P A 1930 *Proc. Camb. Phil. Soc.* **26** 376
- [87] Naraschewski M and Glauber R J 1999 *Phys. Rev. A* **59** 4595
- [88] Sakmann K, Streltsov A I, Alon O E and Cederbaum L S 2008 *Phys. Rev. A* **78** 023615
- [89] Pethick C J and Smith H 2002 *Bose–Einstein Condensation in Dilute Gases* (Cambridge: Cambridge University Press)
- [90] Bloch I, Dalibard J and Zwerger W 2008 *Rev. Mod. Phys.* **80** 885
- [91] Bergschneider A, Klinkhamer V M, Becher J H, Klemt R, Zürn G, Preiss P M and Jochim S 2018 *Phys. Rev. A* **97** 063613
- [92] Pitaevskii L P and Stringari S 2003 *Bose–Einstein Condensation* (Oxford: Oxford University Press)
- [93] Kevrekidis P G, Frantzeskakis D J and Carretero-González R (ed) 2007 *Emergent Nonlinear Phenomena in Bose–Einstein Condensates. Theory and Experiment* vol 45 (Berlin: Springer)
- [94] Klein A and Fleischhauer M 2005 *Phys. Rev. A* **71** 033605
- [95] Hohmann M, Kindermann F, Gänger B, Lausch T, Mayer D, Schmidt F and Widera A 2015 *EPJ Quantum Technol.* **2** 23
- [96] Spethmann N, Kindermann F, John S, Weber C, Meschede D and Widera A 2012 *Phys. Rev. Lett.* **109** 235301
- [97] Knap M, Shashi A, Nishida Y, Imambekov A, Abanin D A and Demler E 2012 Time-dependent impurity in ultracold fermions: orthogonality catastrophe and beyond *Phys. Rev. X* **2** 041020
- [98] Parish M M and Levinsen J 2016 *Phys. Rev. B* **94** 184303
- [99] Mistakidis S I, Katsimiga G C, Koutentakis G M, Busch T and Schmelcher P 2020 arXiv:00260.2020
- [100] Schmitz R, Krönke S, Cao L and Schmelcher P 2013 *Phys. Rev. A* **88** 043601
- [101] Rigol M, Dunjko V and Olshanii M 2008 *Nature* **452** 854
- [102] Tajima H and Uchino S 2018 *New J. Phys.* **20** 073048
- [103] Liu W E, Levinsen J and Parish M M 2019 *Phys. Rev. Lett.* **122** 205301

4.2.4 Pump Probe Spectroscopy of Polarons and Evidence for Thermalization

Pump-probe spectroscopy of Bose polarons: Dynamical formation and coherence

S. I. Mistakidis¹, G. C. Katsimiga¹, G. M. Koutentakis^{1,2}, Th. Busch³, and P. Schmelcher^{1,2}

¹Center for Optical Quantum Technologies, Department of Physics, University of Hamburg, 22761 Hamburg Germany

²The Hamburg Center for Ultrafast Imaging, University of Hamburg, 22761 Hamburg, Germany

³OIST Graduate University, Onna, Okinawa 904-0495, Japan



(Received 1 January 2020; revised 4 August 2020; accepted 7 August 2020; published 9 September 2020)

We propose and investigate a pump-probe spectroscopy scheme to unveil the time-resolved dynamics of fermionic or bosonic impurities immersed in a harmonically trapped Bose-Einstein condensate. In this scheme a pump pulse initially transfers the impurities from a noninteracting to a resonantly interacting spin state and, after a finite time in which the system evolves freely, the probe pulse reverses this transition. This directly allows us to monitor the nonequilibrium dynamics of the impurities as the dynamical formation of coherent attractive or repulsive Bose polarons and signatures of their induced interactions are imprinted in the probe spectra. We show that for interspecies repulsions exceeding the intraspecies ones a temporal orthogonality catastrophe occurs, followed by enhanced energy redistribution processes, independently of the impurity's flavor. This phenomenon takes place over the characteristic trap timescales. For much longer timescales a steady state is reached characterized by substantial losses of coherence of the impurities. This steady state is related to eigenstate thermalization and it is demonstrated to be independent of the system's characteristics.

DOI: [10.1103/PhysRevResearch.2.033380](https://doi.org/10.1103/PhysRevResearch.2.033380)

I. INTRODUCTION

Time-resolved spectroscopy is an established technique for the characterization of the dynamical response of a wide range of physical systems [1]. The general idea underlying a pump-probe spectroscopy (PPS) scheme is that a pump pulse prepares a nonstationary state of the system under consideration, which is then *interrogated* by a time-delayed probe pulse. This allows for simultaneous spectral and temporal resolution of the induced dynamical processes, exposing the energy redistribution of the selectively triggered excitations [2,3], in sharp contrast to time-independent spectroscopic techniques like injection spectroscopy [4–7]. Applications of the PPS protocol range from two- and three-level atomic systems [8–14] to the ultrafast dynamics of photoexcited quantum materials [15–22]. Such a time-domain analysis has been proven to be a powerful tool for resolving the ultrafast molecular dynamics allowing, for instance, for a coherent control of bound excited-state dimers over long timescales [23,24]. PPS has also been utilized for studying the pair-correlation dynamics of ultracold Bose gases [25], offering a potential connection between ultrafast and ultracold physics [24,26].

Operating in the ultracold regime, in this work we propose a PPS scheme as a toolkit for investigating in a time-resolved manner the *impurity problem* and the related formation of

and interactions between quasiparticles [27–64]. Understanding the physics of quasiparticles is important beyond cold atom settings in semiconducting [65] and superconducting devices [66]. Additionally, interactions among quasiparticles in liquid helium mixtures [67,68] and cuprates [69,70] are considered to be responsible for conventional and high- T_c superconductivity [71–77]. Here we consider a Bose-Einstein condensate (BEC) with one or two impurities of either bosonic or fermionic nature immersed into it and track the emergent Bose polaron formation [42–61] with a PPS radiofrequency protocol analogous to the one used in the experiment of Ref. [78]. This allows us to probe and control the coherence properties of the quasiparticles. Our results pave the way for transferring the knowledge regarding the ultrafast dynamics of condensed matter systems [79–82] to the ultracold atomic realm.

In our investigation, an intense pump pulse transfers the initially free bosonic or fermionic impurities to an attractively or repulsively interacting state with the environment. After a variable dark time, during which the system evolves freely, a probe pulse of weaker intensity is applied, which deexcites the impurities. As the formation of well-defined attractive and repulsive Bose polarons in this many-body (MB) system is captured in the probe spectrum, this process allows us to monitor the dynamics. In systems where the interaction strength between the impurity and the background is not larger than the interaction strength within the background gas, polaronic excitations can have long lifetimes. However, beyond that limit substantial losses of coherence occur with a temporal orthogonality catastrophe (TOC) [59–61,83] being imprinted in the probe spectrum. The TOC emerges due to the relaxation of the quasiparticles into energetically lower-lying, phase-separated states. This process is independent of the number of

Published by the American Physical Society under the terms of the [Creative Commons Attribution 4.0 International license](https://creativecommons.org/licenses/by/4.0/). Further distribution of this work must maintain attribution to the author(s) and the published article's title, journal citation, and DOI.

the impurities or their statistics. Remarkably, for timescales longer than the characteristic confinement one, the probe spectrum unveils evidence toward eigenstate thermalization [84–87], where the impurities reside in an incoherent state characterized by a large effective temperature. This relaxation dynamics [88,89] is found to be independent of the size of the bath, the number and nature of the impurities, and their interaction strengths and mass.

Our work is structured as follows. Section II introduces the setup under consideration and briefly comments on the employed variational approach to tackle the nonequilibrium dynamics of Bose polarons. In Sec. III we discuss the utilized PPS scheme and demonstrate the resulting Bose polaron spectrum for short and long evolution times with a particular focus on the impurity-impurity-induced interactions, coherence properties, and thermalization processes. In Sec. IV we elaborate on the emergent energy redistribution processes, while in order to gain further insights into the spectroscopically observed relaxation dynamics we invoke in Sec. V the eigenstate thermalization hypothesis (ETH). We summarize our results and provide an outlook including future perspectives in Sec. VI. Appendix A presents in detail the used radiofrequency spectroscopy scheme and Appendix B explicates briefly the predictions of a Ramsey protocol for strong impurity-medium interactions. The dimensional reduction of our MB Hamiltonian from three to one dimension (3D to 1D) is showcased in Appendix C. Finally, Appendix D deals with the variational method employed herein so as to simulate the PPS protocol and Appendix E delineates the convergence of the presented results.

II. MODEL SETUP

Our model is a highly particle imbalanced mixture. It consists of $N_I = 1, 2$ bosonic or fermionic impurities (I) having a spin-1/2 degree of freedom [90] being immersed in a bosonic bath of $N_B = 100$ structureless bosons (B). The mixture is assumed to be mass balanced, $m_B = m_I \equiv m$ (unless stated otherwise), while both species are harmonically confined in the same one-dimensional potential. Details of the dimensional reduction of our system are discussed in Appendix C. The MB Hamiltonian reads

$$\hat{H} = \hat{H}_B^0 + \hat{H}_{BB} + \sum_{a=\uparrow,\downarrow} (\hat{H}_a^0 + \hat{H}_{aa}) + \hat{H}_{\uparrow\downarrow} + \hat{H}_{BI} + \hat{H}_S^\beta. \quad (1)$$

Here $\hat{H}_B^0 = \int dx \hat{\Psi}_B^\dagger(x) (-\frac{\hbar^2}{2m_B} \frac{d^2}{dx^2} + \frac{1}{2} m_B \omega^2 x^2) \hat{\Psi}_B(x)$, and $\hat{H}_a^0 = \int dx \hat{\Psi}_a^\dagger(x) (-\frac{\hbar^2}{2m_I} \frac{d^2}{dx^2} + \frac{1}{2} m_I \omega^2 x^2) \hat{\Psi}_a(x)$ denote the noninteracting Hamiltonian of the BEC and the impurities, respectively, while $a \in \{\uparrow, \downarrow\}$. Additionally, $\hat{\Psi}_B(x)$ [$\hat{\Psi}_a(x)$] is the field operator of the BEC (spin- a impurities). We further consider that the dominant interaction is an s -wave one since we operate in the ultracold regime. As such both intra- (g_{BB} , g_{II}) and interspecies (g_{BI}) interactions are adequately described by a contact potential [91], see also Appendix C. Furthermore, $\hat{H}_{BB} = (g_{BB}/2) \int dx \hat{\Psi}_B^\dagger(x) \hat{\Psi}_B^\dagger(x) \hat{\Psi}_B(x) \hat{\Psi}_B(x)$ and $\hat{H}_{aa'} = g_{II} \int dx \hat{\Psi}_a^\dagger(x) \hat{\Psi}_a^\dagger(x) \hat{\Psi}_a(x) \hat{\Psi}_a(x)$, with $a, a' \in \{\uparrow, \downarrow\}$, correspond to the contact intraspecies interaction terms of the bosonic bath and the impurities, respectively. Note that only the spin- \uparrow component of the impurities

interacts with the BEC while the spin- \downarrow one is noninteracting. The relevant interspecies interaction term reads $\hat{H}_{BI} = g_{BI} \int dx \hat{\Psi}_B^\dagger(x) \hat{\Psi}_\uparrow^\dagger(x) \hat{\Psi}_\uparrow(x) \hat{\Psi}_B(x)$. Finally, $\hat{H}_S^\beta = \frac{\hbar \Omega_{R0}^\beta}{2} \hat{S}_x - \frac{\hbar \Delta^\beta}{2} \hat{S}_z$, with Ω_{R0}^β and $\Delta^\beta = \nu^\beta - \nu_0$ referring to the bare Rabi frequency and the detuning of the radiofrequency pulse when the bosonic bath is absent, see Appendix A for further details. Here $\beta \in \{\text{pump, probe, dark}\}$. Moreover, the total spin operators are given by $\hat{S}_i = \int dx \sum_{ab} \hat{\Psi}_a(x) \sigma_{ab}^i \hat{\Psi}_b(x)$, with σ_{ab}^i denoting the Pauli matrix $i \in \{x, y, z\}$.

It is worth mentioning at this point that the one-dimensional description adopted holds under the conditions $\frac{k_B T}{\hbar \omega} \ll \frac{\hbar^2}{m} [\rho_B^{(1)}(x=0)]^2 \approx \frac{3^{4/3}}{16} (\frac{\alpha_\perp^2 N_B^2}{a_{BB} \alpha})^{2/3}$ and $\frac{N_B a_{BB} \alpha_\perp}{\alpha^2} \ll 1$ [92,93]. In these expressions, a_{BB} is the three-dimensional s -wave scattering length between the particles of the medium, and $\alpha = \sqrt{\hbar/(m\omega)}$ and $\alpha_\perp = \sqrt{\hbar/(m\omega_\perp)}$ correspond to the axial and transversal length scales. $\rho_B^{(1)}(x=0)$ is the initial one-body density of the environment at $x=0$, k_B is the Boltzmann constant, and T refers to the temperature of the bosonic bath. To provide a concrete example, assuming $\omega \approx 2\pi \times 100$ Hz and considering a ^{87}Rb gas with $g_{BB} = 0.5 \sqrt{(\hbar^3 \omega)/(m)} \approx 3.55 \times 10^{-38}$ Jm our 1D setting can be realized for transverse frequencies $\omega_\perp \approx 2\pi \times 5.1$ kHz. Accordingly, the 1D treatment is valid since $N_B a_{BB} \alpha_\perp / \alpha^2 \approx 0.07 \ll 1$ and temperature effects are negligible for $k_B T \ll 316 \hbar \omega \approx 1.5 \mu\text{K}$.

To access the time-resolved spectral response of bosonic and fermionic impurities immersed in the BEC bath the multilayer multiconfiguration time-dependent Hartree method for atomic mixtures is utilized [94–96]. The latter is a nonperturbative approach that uses a variationally optimized time-dependent basis which spans the optimal subspace of the Hilbert space at each time instant and allows for tackling all interatomic correlations [59]. In particular, the MB wave function is expressed as a truncated Schmidt decomposition using D species functions for each component [Eq. (D1) in Appendix D]. Next, each of these species functions is expanded in a basis of d^B and d^I single-particle functions for the BEC background and the impurities, respectively [Eq. (D2)]. These single-particle functions utilize a time-independent primitive basis that is a tensor product of basis states regarding the spatial and the spin degrees of freedom [Eq. (D3)]. Then, by following a variational principle, we arrive at a set of coupled nonlinear integrodifferential equations of motion [94–96]. A detailed description of our MB variational approach and the ingredients of our numerical simulations are provided in Appendices D and E, respectively.

III. PUMP-PROBE SPECTROSCOPY SCHEME

We prepare the multicomponent system in its ground state with fixed g_{BB} and $g_{II} = 0$. The impurities are in their spin- \downarrow state and thus $\langle \hat{H}_{BI} \rangle = 0$. To trigger the dynamics, an intense, $\Omega_{R0}^{\text{pump}} = 10\omega \gg \omega$, rectangular pump pulse drives the noninteracting spin- \downarrow impurities to their interacting with the bath spin- \uparrow state for $-t_e < t < 0$ (where t_e denotes the exposure time) [Fig. 1(a)]. The condition $\Omega_{R0}^{\text{pump}} \gg \omega$ ensures that the duration of the pump pulse is much smaller than the time interval in which the polarons form. Accordingly, the

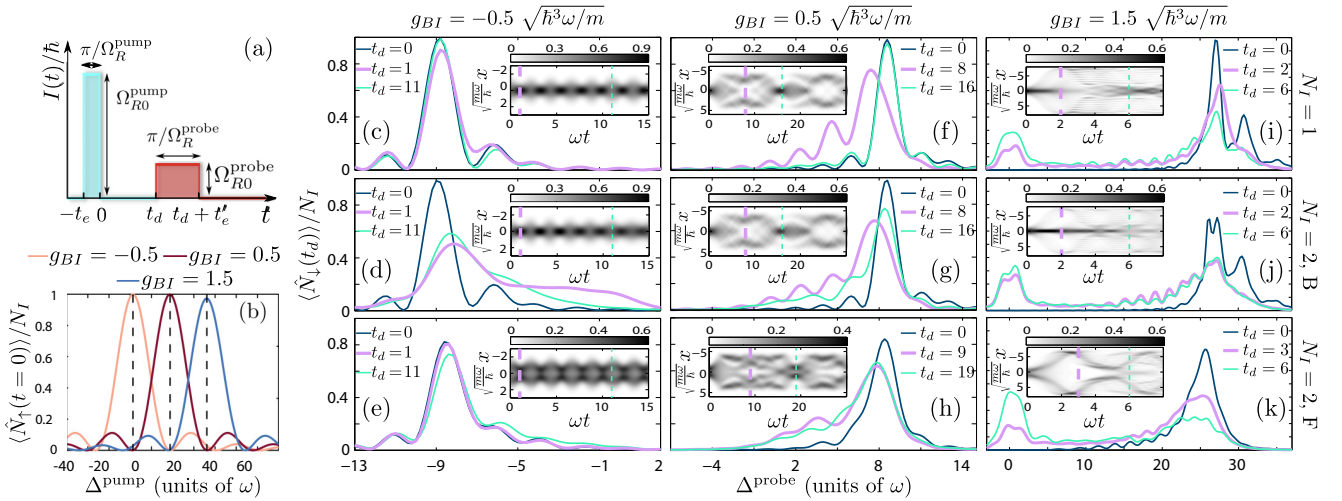


FIG. 1. (a) Schematic illustration of the PPS pulse sequences used. (b) Spectral response of the pump pulse $\langle \hat{N}_\uparrow(t=0) \rangle / N_I$ versus its detuning Δ^{pump} for $g_{BB} = 0.5\sqrt{\hbar^3\omega/m}$, $N_B = 100$, $N_I = 1$ and varying g_{BI} . Vertical dashed lines indicate the resonant detunings Δ_+ . [(c)–(k)] Time-resolved probe spectra at different g_{BI} , bosonic (B) or fermionic (F) impurity numbers $N_I = 1, 2$ with $g_{II} = 0$, and for various short dark times, t_d (see legend). In all cases insets illustrate the spatiotemporal evolution of the impurity’s one-body density and dashed lines mark the instants for which the probe spectrum is provided.

polaron formation can only occur after the termination of the pump pulse and therefore it can be captured by the subsequent probe pulse. To ensure the resonance condition of the pump pulse, namely $\Delta^{\text{pump}} = \Delta_+$, and to optimize $t_e = \pi/\Omega_R^{\text{pump}}$, the fraction of impurity atoms that have been successfully transferred to the spin- \uparrow state, $\langle \hat{N}_\uparrow(t=0) \rangle / N_I$, is monitored for variable Δ^{pump} . The resulting pump spectrum features a coherent atomic resonance [34,36,39,57,78] at $\Delta^{\text{pump}} = \Delta_+$. The latter, for $N_I = 1$ and $g_{BI} = \pm 0.5, 1.5\sqrt{\hbar^3\omega/m}$, is clearly visible in Fig. 1(b). Notice also that secondary peaks possessing an intensity of the order of 12% with respect to the dominant ones also emerge due to the rectangular shape of the pump pulse (see also Appendix A).

After the initial pump sequence the remaining population of the spin- \downarrow state is annihilated by employing an optical blast that projects the impurities to the $|\uparrow\rangle$ state (as described in Appendix A) and subsequently the spin- \uparrow atoms are left to evolve for fixed g_{BI} and $\Omega_{RO}^{\text{dark}} = 0$ but variable dark time t_d . The polaronic states can form within $0 \leq t \leq t_d$ while at $t = t_d$ a probe pulse is applied. This pulse is characterized by $\Omega_{RO}^{\text{probe}} = \omega \ll \Omega_{RO}^{\text{pump}}$ so as to enhance the spectral resolution of the signal obtained by the fraction of impurity atoms transferred to the spin- \downarrow state, $\langle \hat{N}_\downarrow(t_d) \rangle / N_I$ for variable Δ^{probe} . For the same reason the duration of the probe pulse is fixed to $t'_e = \pi/\Omega_R^{\text{probe}}$, where Ω_R^{probe} is the resonant Rabi frequency of the probe pulse at $\Delta^{\text{probe}} = \Delta_+$, $t_d = 0$, and $N_I = 1$.

Concluding within the PPS scheme, polaronic states can be identified in the probe spectrum as well-defined peaks with amplitude $\langle \hat{N}_\downarrow(t_d) \rangle / N_I < 1$. For our purposes (accounting for the finite fidelity resulting after the probe pulse) we employ the criterion $\langle \hat{N}_\downarrow(t_d) \rangle / N_I < 0.96$ in order to identify the polaronic resonances. Interestingly, a peak with $\langle \hat{N}_\downarrow(t_d) \rangle / N_I \approx 1$ does not correspond to a polaron as it implies that the accessed MB state is equivalent to a noninteracting state. Accordingly, the peaks exactly at $t_d = 0$ and $\langle \hat{N}_\downarrow(t_d) \rangle / N_I \approx 1$, that will appear later, do not indicate the formation of polarons. No-

tice that polaronic peaks with $\langle \hat{N}_\downarrow(t_d) \rangle / N_I < 1$ can occur for strong impurity-BEC interactions $g_{BI} > g_{BB}$, even for $t_d = 0$, demonstrating fast energy transfer to the polaronic states for $t_d < (\Omega_{RO}^{\text{probe}})^{-1}$.

A. Short-time dynamics of Bose polarons

The short-time ($t \sim \omega^{-1}$) dynamics of few, $N_I = 1, 2$, fermionic or bosonic impurities with $g_{II} = 0$ immersed in a BEC bath of $N_B = 100$ atoms is captured by the probe spectra for distinct attractive [Figs. 1(c)–1(e)] and repulsive [Figs. 1(f)–1(k)] interspecies interactions g_{BI} . Focusing on the attractive side, a well-defined polaron at $t_d = 0$ with central peak location at $\Delta_+ = -8.7\omega$ [Fig. 1(c)], $\Delta_{+,B} = -8.9\omega$ [Fig. 1(d)], and $\Delta_{+,F} = -8.6\omega$ [Fig. 1(e)] is identified in the cases of $N_I = 1$ and $N_I = 2$ bosonic and fermionic impurities respectively. These polarons show a nonsizable shift for all the different evolution times t_d as long as $N_I = 1$. However, a clear shift can be inferred for $N_I = 2$ [Fig. 1(d)]. This shift, being of about 10%, is a consequence of the energy redistribution between the bosonic impurities and the BEC as demonstrated in Ref. [57] and it is further related to the fact that for $g_{BI} < 0$ attractive induced interactions are significantly enhanced [57]. Additionally, due to the pronounced induced interactions a collisional broadening [97] of the spectral line is clearly observed for $t_d = 1, 11\omega^{-1}$. Indeed, since the two-body state of the impurities evolves rapidly during the probe sequence the spectral resolution of the measurement decreases, giving rise to a wide background in the PPS spectrum for $-10 < \Delta^{\text{probe}}/\omega < 2$. The imprint of induced interactions in the spatiotemporal evolution of the one-body density is the dephasing of the breathing oscillations [hardly visible in the inset of Fig. 1(d)] within the time interval $10 < \omega t_d < 15$, which is absent for the single impurity [see the inset in Fig. 1(c)]. In contrast to the above dynamics, the time-resolved evolution of fermionic impurities closely

resembles the single impurity one with the two fermions undergoing at short times a coherent breathing motion, as is evident in the inset of Fig. 1(e). This latter result can be easily understood by the fact that attractive induced-interactions between fermionic impurities are known to be suppressed, providing in turn a nonsizeable shift of the respective atomic peak resonance captured by the probe spectra [36,39].

Switching to repulsive interactions, the dynamical evolution of the system changes dramatically. Independently of flavor and concentration the motion of the impurities, as detected by the one-body density evolution for $g_{BI} = 0.5\sqrt{\hbar^3\omega/m}$, is apparently qualitatively similar [insets in Figs. 1(f)–1(h)]. From the very early stages of the nonequilibrium dynamics the density filamentizes with recurrences of an almost central density peak occurring at the collision points, i.e., around $t_d \approx 16\omega^{-1}$ and $t_d \approx 19\omega^{-1}$ for the bosonic and fermionic impurities, respectively [Fig. 1(g) and Fig. 1(h)]. However, in all three cases a clean quasiparticle peak is monitored in the respective probe spectra indicating the existence of well-defined polarons for $t \sim \omega^{-1}$. The dominant peak location appears to be shifted for $t_d \neq 0$ when compared to Δ_+ , while an overall broadening of the spectrum is also inferred. The observed shift depends strongly on the impurity's nature and it is measured to be of about 10% for bosonic but dropping down to almost 5% for fermionic impurities [Figs. 1(g) and 1(h)]. Interestingly, the difference in the spectrum between the $N_I = 1$ and the $N_I = 2$ bosonic case [compare Figs. 1(f) and 1(g)] is negligible, suggesting that attractive induced interactions cannot be directly unveiled by the observed shift. A result that complements earlier predictions indicating that attractive induced interactions are suppressed in the repulsive regime [60,98]. Indeed, for $g_{BI} > 0$ the density of the BEC is less distorted compared to $g_{BI} < 0$ [60,61]. Accordingly, the impurities are less attracted to these distortions and consequently to each other. In turn, by inspecting the oscillatory tail of the probe spectra for $g_{BI} > 0$ interference phenomena associated with the filamentation process can be identified. Indeed, already from the single impurity [Fig. 1(f)] the amplitude, $A(\Delta^{\text{probe}})$, of the secondary peak appearing in the spectra, e.g., at $t_d = 8\omega^{-1}$, $A(\Delta^{\text{probe}} \approx 4.6\omega) = 0.352$ is comparable with the dominant one $A(\Delta^{\text{probe}} \approx 7.5\omega) = 0.755$. Notice that the intensity ratio of the secondary to the dominant peak is larger than 12% and thus cannot be attributed to the rectangular shape of the probe pulse. The latter, directly reflects the coherence between the filaments formed in the one-body density (see Discussion). However, as the number of impurities increases significant losses of coherence take place. Indeed, the secondary peak at $t_d = 8\omega^{-1}$ [$t_d = 9\omega^{-1}$] has $A(\Delta^{\text{probe}} \approx 4.6\omega) = 0.266$ [$A(\Delta^{\text{probe}} \approx 3.6\omega) = 0.245$] for $N_I = 2$ bosonic (fermionic) impurities while is drastically reduced at later t_d [Figs. 1(g) and 1(h)]. These losses of coherence are an indirect manifestation of the presence of weak attractive induced interactions which we cannot probe via the shift of the spectral peaks.

Our PPS data demonstrate that well-defined quasiparticles cease to exist for $g_{BI} \gtrsim 1.5\sqrt{\hbar^3\omega/m}$ signaling their TOC [Figs. 1(i)–1(k)] [57]. Evidently, at $t_d = 0$ a predominant peak centered at $\Delta_+ = 26.7\omega$ can be discerned in the single impurity probe spectrum [Fig. 1(i)], giving its place to a double humped structure with averaged location at $\Delta_{+,B} = 26.8\omega$ for

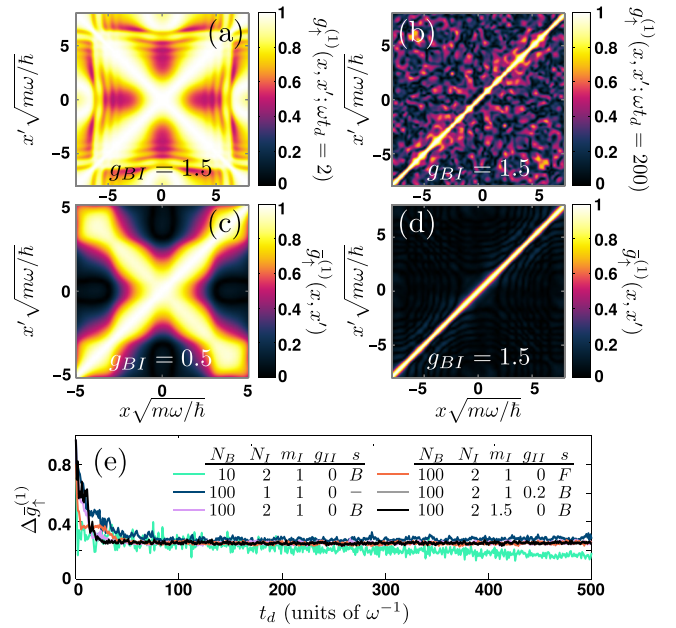


FIG. 2. [(a) and (b)] One-body coherence $g_{\uparrow}^{(1)}(x, x'; t_d)$ at different times t_d (see legend). [(c) and (d)] Time-averaged one-body coherence $\bar{g}_{\uparrow}^{(1)}(x, x')$ at distinct g_{BI} . (e) Temporal evolution of the variance $\Delta \bar{g}_{\uparrow}^{(1)}$ for different settings (see legend).

the two bosonic impurities [Fig. 1(j)] and to a slightly shifted but significantly broadened peak at $\Delta_{+,F} = 25.6\omega$ for the fermionic ones [Fig. 1(k)]. The latter broadening is attributed to the fermion statistics. Indeed, fermionic impurities occupy higher momenta and as such couple stronger to the BEC excitations. However, at $t_d = 2\omega$ deformation of the central peak is present and a highly oscillatory tail is seen in all cases. To appreciate the aforementioned degree of coherence already indicated by the probe spectra we next invoke the spatial first-order coherence function,

$$g_{\sigma}^{(1)}(x, x'; t) = \frac{\rho_{\sigma}^{(1)}(x, x'; t)}{\sqrt{\rho_{\sigma}^{(1)}(x; t)\rho_{\sigma}^{(1)}(x'; t)}}. \quad (2)$$

Here $\rho_{\sigma}^{(1)}(x, x'; t) = \langle \Psi(t) | \hat{\Psi}_{\sigma}^{\dagger}(x) \hat{\Psi}_{\sigma}(x') | \Psi(t) \rangle$ is the σ -species ($\sigma = B, \uparrow, \downarrow$) one-body reduced density matrix, $|\Psi(t)\rangle$ is the MB wave function, and $\rho_{\sigma}^{(1)}(x; t)$ is the one-body density, see also Appendix D. Importantly, $|g_{\sigma}^{(1)}(x, x'; t)| \in [0, 1]$ indicates the spatially resolved deviation of a MB wave function from a corresponding product state. Specifically, if $|g_{\sigma}^{(1)}(x, x'; t)| = 1$, then the system is termed fully coherent; otherwise, coherence losses occur, signifying the buildup of correlations [60,99]. Indeed, the instantaneous $|g_{\uparrow}^{(1)}(x, x'; t_d = 2\omega)|$ for $g_{BI} = 1.5\sqrt{\hbar^3\omega/m}$ clearly dictates that the quasiparticle remains adequately coherent since, e.g., $|g_{\uparrow}^{(1)}(x = -5\sqrt{\hbar/m\omega}, x' = 5\sqrt{\hbar/m\omega}; t_d = 2\omega)| \approx 0.96$ [Fig. 2(a)]. Finally, notice that for $t_d > 6\omega$ any quasiparticle notion is lost as detected by the probe spectra. This outcome, being consistent with recent works [39,57], is also supported by the diffusive behavior of the corresponding one-body density evolution [insets in Figs. 1(i)–1(k)]. In contrast, a peak corresponding to free parti-

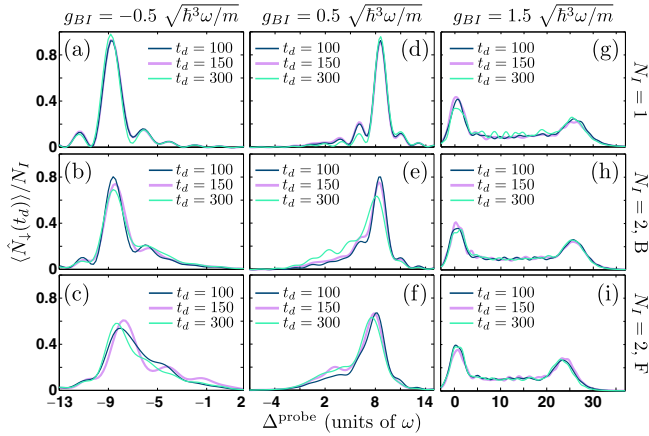


FIG. 3. [(a)–(i)] Probe spectra for different g_{BI} , N_I , and impurity flavors at various dark times t_d deep in the evolution (see legend). The remaining system parameters are the same as in Fig. 1.

cles $\Delta^{\text{probe}} = 0$ emanates in the PPS spectrum, referring to a phase separation between the impurity and the BEC. It is also worth mentioning that by employing a corresponding Ramsey scheme (see the discussion in Appendix B) it is not possible to conclude the emergence of the TOC within the same time interval since the structure factor is still finite and drops close to zero for substantially longer evolution times.

B. Long-time Bose polaron dynamics

Next let us study the evolution of the system at longer times, $100 < \omega t_d < 300$. Note that for a typical axial confinement $\omega \approx 2\pi \times 100$ Hz, the interval $100 < t_d < 300$ corresponds to $0.16 < t_d < 0.48$ s. As time evolves one expects that significant losses of coherence signaling the buildup of correlations will take place in the MB evolution of the system [Fig. 2(b)]. A powerful asset of exposing the latter is the temporal average

$$\bar{g}_{\uparrow}^{(1)}(x, x') = \lim_{T \rightarrow \infty} \frac{1}{T} \int_0^T dt g_{\uparrow}^{(1)}(x, x'; t), \quad (3)$$

which depends solely on the eigenstate properties of the interacting system [100]. This allows us to infer the relaxation tendency of the impurities in the framework of the ETH [84,86], see also the discussion in Sec. V. Evidently, $\bar{g}_{\uparrow}^{(1)}(x, x')$ reveals that for $g_{BI} = 0.5\sqrt{\hbar^3\omega/m}$ the impurity is largely coherent [Fig. 2(c)] while at $g_{BI} = 1.5\sqrt{\hbar^3\omega/m}$ any coherence property is lost [Fig. 2(d)]. This outcome is further supported by the time-resolved probe spectra illustrated for longer times in Figs. 3(a)–3(i). A strong suppression of the interaction shift with respect to Δ_+ is found to persist at long times, which, together with the weakly fluctuating amplitude $A(\Delta^{\text{probe}} \approx \Delta_+)$ observed in the course of time, verifies the longevity of coherent single and two polarons irrespectively of their flavor and for both attractive and moderate repulsive $g_{BI} = \pm 0.5\sqrt{\hbar^3\omega/m}$ [Figs. 3(a)–3(f)]. Alterations come into play for $g_{BI} > g_{BB}$, where, as per our discussion above, losses of coherence, as captured by $g_{\uparrow}^{(1)}(x, x'; t_d)$, become significant and the polaron picture breaks down. Here a two-humped distribution appears in our probe spectra independently of

the number of the impurities and their nature. The most pronounced feature of Figs. 3(g)–3(i) is the peak located at $\Delta^{\text{probe}} = 0$. The latter findings suggest that a relaxed state is reached characterized by incoherent impurities being unpredicted so far.

Indeed, by fitting $\bar{g}_{\uparrow}^{(1)}(x, x')$ to the corresponding prediction of the N_I -particle Gibbs ensemble we obtain large effective temperatures. These refer to $k_B T_{\text{eff}} = 8.45\hbar\omega$ for $N_I = 1$ and $k_B T_{\text{eff}} = 8.58\hbar\omega$ ($k_B T_{\text{eff}} = 5.89\hbar\omega$) in the case of two bosons (fermions) showcasing their tendency to approach an incoherent thermalized state, see also our detailed discussion in Secs. V and IV. Notice that the initial state of fermions involves higher momenta than bosons, while the critical velocity of the BEC is the same [101–103]. Therefore, fermions couple stronger to the BEC excitations losing a larger portion of their energy, implying a smaller T_{eff} . Further evidences supporting the observed thermalization [88,89] are provided by the temporal evolution of the variance,

$$\Delta \bar{g}_{\uparrow}^{(1)} = \frac{1}{TS} \int_S dx dx' \int dt [g_{\uparrow}^{(1)}(x, x'; t) - \bar{g}_{\uparrow}^{(1)}(x, x')]^2, \quad (4)$$

with S denoting the relevant spatial region in which the impurities reside and $\Delta \bar{g}_{\uparrow}^{(1)} \in (0, 1)$. Remarkably a tendency toward thermalization is seen [Fig. 2(e)], with $\Delta \bar{g}_{\uparrow}^{(1)}$ saturating at long times irrespectively of the size of the BEC cloud and whether one or two, noninteracting or interacting, impurities are present and what their nature is.

IV. IMPURITY-MEDIUM INTERACTION ENERGY

To further support the thermalization tendency of the multicomponent system for strong impurity-BEC interactions at longer times of the nonequilibrium dynamics, we next inspect the behavior of the interspecies interaction energy. The latter quantity is defined as $\langle \hat{H}_{BI}(t) \rangle \equiv \langle \Psi(t) | \hat{H}_{BI} | \Psi(t) \rangle$, where the operator of the interspecies interactions is $\hat{H}_{BI} = g_{BI} \int dx \hat{\Psi}_B^\dagger(x) \hat{\Psi}_\uparrow^\dagger(x) \hat{\Psi}_\uparrow(x) \hat{\Psi}_B(x)$. Also, $\hat{\Psi}_\sigma(x)$ and $\hat{\Psi}_\sigma^\dagger(x)$ denote the σ -species field operator that annihilates and creates, respectively, a σ -species particle at position x .

The time evolution of $\langle \hat{H}_{BI}(t) \rangle / N_I$ is illustrated in Fig. 4 upon considering a pumping that drives the atoms to the spin- \uparrow state with $g_{BI} = 1.5\sqrt{\hbar^3\omega/m}$. Specifically, we consider different settings consisting of $N_I = 1$, $N_I = 2$ spin-polarized bosons or fermions as well as a few-body system containing $N_B = 10$ bosons and $N_I = 2$ noninteracting impurities. In all cases we observe that $\langle \hat{H}_{BI}(t) \rangle / N_I$ decreases up to $t = 100\omega^{-1}$ while for later times, and in particular for $t > 200\omega^{-1}$, it shows a saturation trend to a certain value depending on both N_I and N_B . Recall that this saturation effect allowed for the derivation of Eq. (11) within the ETH scheme. Notice also that the saturation value of $\langle \hat{H}_{BI}(t) \rangle / N_I$ is smaller for the few-body system ($N_B = 10$, $N_I = 2$) while for the $N_B = 100$ setups $\langle \hat{H}_{BI}(t) \rangle / N_I$ acquires its smaller value for two fermionic impurities and takes almost the same value for $N_I = 1$ and $N_I = 2$ noninteracting bosonic impurities. Finally, let us note that the overall decreasing behavior of $\langle \hat{H}_{BI}(t) \rangle / N_I$ suggests a transfer of energy from the impurities to the bosonic gas as it has been also demonstrated in Refs. [59,61]. This energy transfer process, identified by the decreasing rate

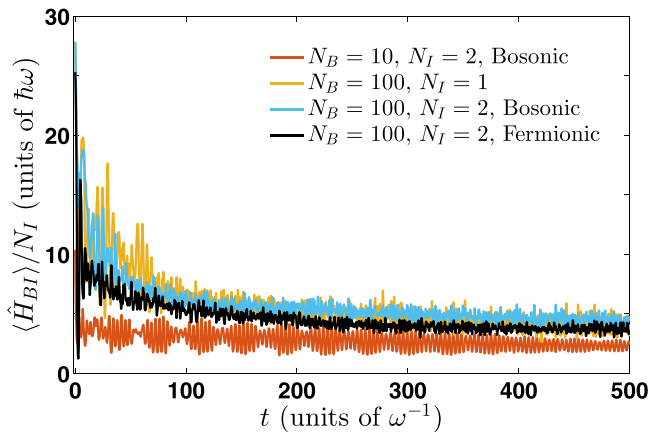


FIG. 4. Evolution of the impurity-BEC interaction energy per impurity particle applying a pump pulse to drive the impurities to the spin- \uparrow state with $g_{BI} = 1.5\sqrt{\hbar^3\omega/m}$ for a single ($N_I = 1$) and two ($N_I = 2$) bosonic or fermionic impurities and also for a few-body bath consisting of $N_B = 10$ particles (see legend). In all cases $g_{BB} = 0.5\sqrt{\hbar^3\omega/m}$ and $g_{II} = 0$.

of $\langle \hat{H}_{BI}(t) \rangle / N_I$, seems to be enhanced for $N_B = 10$ while for the $N_B = 100$ case it is more pronounced for the fermionic impurities. We remark that a saturation trend at long timescales being in turn suggestive of the thermalization tendency of the system occurs also for other observables. These include, for instance, the dynamical structure factor (Appendix B) as well as entropic measures [104, 105] such as the von-Neumann entropy [61, 99, 106] quantifying the degree of entanglement (results not shown for brevity).

V. CHARACTERIZATION OF THE RELAXATION DYNAMICS

We next explicate our method for characterizing the relaxation dynamics occurring in our setup during the hold time t_d . To achieve this, we employ the ETH [84, 86]. Within this framework it is assumed that after a quench, the finite subsystems of a larger extended system relax to a steady state reminiscent of thermal equilibrium. Here, by fitting the time-averaged one-body density of the impurities to a thermal equilibrium one, we show that this thermalization process explains the relaxed state of the impurities emanating for long times after the orthogonality catastrophe of the polarons.

The relaxation of an isolated (closed) system is understood in terms of the principle of local equivalence [107]. Within this framework as the thermodynamical limit is approached, i.e., the system size tends to infinity, the reduced density matrices of the involved few-particle subsystems at long times can be calculated in terms of the density matrix of a (generalized) Gibbs ensemble at thermal equilibrium. Indeed, if the only conserved quantity of the Hamiltonian is the total energy, then it can be shown that these reduced density matrices can be calculated in terms of the equilibrium density matrix within the Gibbs ensemble

$$\hat{\rho}_{\text{Gibbs}} = \frac{1}{Z} e^{-\frac{\hat{H}}{k_B T_{\text{eff}}}}. \quad (5)$$

In Eq. (5) Z is the partition function stemming from the normalization of the density matrix, i.e., $\text{Tr}[\hat{\rho}_{\text{Gibbs}}] = 1$. \hat{H} refers to the MB Hamiltonian and T_{eff}, k_B correspond to the effective temperature and the Boltzmann constant, respectively. Of course, our setup exhibits also other conserved quantities than the total energy. Below we resort to the approximation of no further symmetries as it is the only case that explicit results showing the relaxation dynamics of the system are available within ETH [107]. As we shall show later on, the aforementioned choice leads to an excellent agreement between our numerical findings and the relevant estimates provided by applying Eq. (5). Within this approximation the effective temperature, T_{eff} , is fixed by the conserved value of the energy per particle in the thermodynamic limit (TL),

$$\lim_{\text{BEC} \rightarrow \text{TL}} \frac{\text{Tr}[|\Psi(0)\rangle\langle\Psi(0)|\hat{H}]}{N_B} = \lim_{\text{BEC} \rightarrow \text{TL}} \frac{\text{Tr}[\hat{\rho}_{\text{Gibbs}}\hat{H}]}{N_B}. \quad (6)$$

Here $\text{BEC} \rightarrow \text{TL}$ is defined as the limit where $N_B \rightarrow \infty$, $g_{BB} \rightarrow 0$, $N_B g_{BB} = \text{const}$, and $g_{BI}/g_{BB} = \text{const}$. Notice, however, that Eqs. (5) and (6), are impractical for calculations since the eigenvalues and eigenstates of the full interacting Hamiltonian, \hat{H} , are required for the evaluation of the Gibbs ensemble of the $(N_B + N_I)$ MB ensemble which are difficult if not impossible to obtain. For this reason, we simplify the above-mentioned set of equations so as to obtain explicit results which can be subsequently compared with those obtained by the time evolution of the $(N_B + N_I)$ MB system within the multilayer multiconfiguration time-dependent Hartree (ML-MCTDHX) approach.

Since we intend to employ the thermodynamic limit where the MF Gross-Pitaevskii treatment of the BEC is exact in the weak interaction limit [92], it is reasonable to assume that the corresponding density operator of the Gibbs ensemble acquires the product form $\hat{\rho}_{\text{Gibbs}} = \hat{\rho}_{B;\text{Gibbs}}^{(N_B)} \otimes \hat{\rho}_{\uparrow;\text{Gibbs}}^{(N_I)}$. Recall that during the dark time all of the impurities are in their spin- \uparrow state. In this case, the form of $\hat{\rho}_{\uparrow;\text{Gibbs}}$ is similar to Eq. (5), namely

$$\hat{\rho}_{\uparrow;\text{Gibbs}}^{(N_I)} = \frac{1}{Z_{\uparrow}} e^{-\frac{\hat{H}_{\uparrow}^{\text{eff}}}{k_B T_{\text{eff}}}}, \quad (7)$$

where $H_{\uparrow}^{\text{eff}}$ is an effective Hamiltonian that acts only on the impurity. Equation (7) greatly simplifies the description of our system, since the density matrix of the impurity depends only on the eigenvectors and eigenvalues of an N_I -body effective Hamiltonian. To proceed further we specify the form of $\hat{H}_{\uparrow}^{\text{eff}}$. Within a zeroth-order approximation we assume that the BEC acts solely as a potential barrier for the impurities, and as consequence their effective Hamiltonian reads

$$\hat{H}_{\uparrow}^{\text{eff}}(t) = - \sum_{i=1}^{N_I} \frac{\hbar^2}{2m_I} \frac{d^2}{dx_i^2} + \frac{1}{2} m_I \omega^2 x_i^2 + g_{BI} \rho_B^{(1)}(x_i; t). \quad (8)$$

Notice that this approximation for the effective potential is a simplification of the impurity problem. First, it neglects, among others, the renormalization of the impurity's mass, $m_I \rightarrow m_I^{\text{eff}}$, due to the presence of the BEC [59]. Second, the presence of induced interactions between the impurities cannot be captured [60].

The time dependence of the Hamiltonian of Eq. (8) implies a nonstationary state for the impurities. However,

it is well known that following an interaction quench the density of the BEC is only slightly perturbed by the motion of the impurities [59–61]. The latter justifies the substitution of the effective Hamiltonian by its time-averaged value $\hat{H}_\uparrow^{\text{eff}} = \lim_{T \rightarrow \infty} \frac{1}{T} \int dt \hat{H}_\uparrow^{\text{eff}}(t)$, since $\rho_B^{(1)}(x_i; t) \approx \lim_{T \rightarrow \infty} \frac{1}{T} \int_0^T dt \rho_B^{(1)}(x_i; t)$ for the density of the bath. By incorporating the above-mentioned approximations we obtain explicit forms for the one-body density of the impurity within the Gibbs ensemble, namely

$$\rho_{\uparrow; \text{Gibbs}}^{(1)}(x, x'; T_{\text{eff}}) = \sum_{i=1}^{\infty} n_i(T_{\text{eff}}) \phi_i(x) \phi_i^*(x'). \quad (9)$$

Here $n_i(T_{\text{eff}})$ is the distribution function of the N_I particles and ϕ_i refers to the eigenstates of $\hat{H}_\uparrow^{\text{eff}}$. Due to the small number of impurities considered herein ($N_I = 1, 2$) both the fermionic and the bosonic impurities do not follow the appropriate, for $N_I \rightarrow \infty$, Fermi-Dirac or Bose-Einstein distributions. Instead, it can be shown that the relevant distribution in the case of a single particle or two bosons is the Boltzmann distribution,

$$n_i(T_{\text{eff}}) = Z(1)^{-1} \exp\left(-\frac{\epsilon_i}{k_B T_{\text{eff}}}\right), \quad (10)$$

with ϵ_i being the eigenvalues of $\hat{H}_\uparrow^{\text{eff}}$ and $Z(1) = \sum_{i=1}^{\infty} \exp(-\frac{\epsilon_i}{k_B T_{\text{eff}}})$. For two fermions the corresponding distribution reads

$$n_i(T_{\text{eff}}) = \left[\frac{Z(2) - e^{-\frac{\epsilon_i}{k_B T_{\text{eff}}}} (Z(1) - e^{-\frac{\epsilon_i}{k_B T_{\text{eff}}}})}{Z(1) - e^{-\frac{\epsilon_i}{k_B T_{\text{eff}}}}} e^{\frac{\epsilon_i}{k_B T_{\text{eff}}}} + 1 \right]^{-1}, \quad (11)$$

where $Z(2) = \sum_{i=1}^{\infty} e^{-\frac{\epsilon_i}{k_B T_{\text{eff}}}} [Z(1) - e^{-\frac{\epsilon_i}{k_B T_{\text{eff}}}}]$. Note also that the one-body density of the impurity, Eq. (9), depends only on a single parameter, namely the effective temperature, T_{eff} .

As shown earlier, the one-body density matrix of the impurities, $\rho_\uparrow^{(1)}(x, x'; t)$, saturates to its time-averaged value, i.e., $\rho_\uparrow^{(1)}(x, x'; t \rightarrow \infty) \approx \bar{\rho}_\uparrow^{(1)}(x, x') = \lim_{T \rightarrow \infty} \frac{1}{T} \int_0^T dt \rho_\uparrow^{(1)}(x, x'; t)$, for long hold times, as it is evident in the relaxation dynamics of $\Delta \bar{g}^{(1)}$ [see also Fig. 2(e)]. In order to facilitate the comparison of our results to the ETH prediction [Eq. (9)] we fit the averaged one-body density matrix, $\bar{\rho}_\uparrow^{(1)}(x, x')$, obtained within ML-MCTDHX to the corresponding Gibbs ensemble, $\rho_{\uparrow; \text{Gibbs}}^{(1)}(x, x'; T_{\text{eff}})$, and extract the value of T_{eff} . Our results for the best-fitted parameters are shown in Fig. 5. We remark that the fitting is performed on the level of $\bar{\rho}_\uparrow^{(1)}(x, x')$, while only the diagonal $\bar{\rho}_\uparrow^{(1)}(x) \equiv \bar{\rho}_\uparrow^{(1)}(x, x)$ is presented in Fig. 5 in order to enhance the visibility of the obtained results. By comparing the time-averaged one-body density and the fitted Gibbs ensemble prediction a very good agreement is observed for both one [Fig. 5(a)] and two impurities of either bosonic [Fig. 5(b)] or fermionic [Fig. 5(c)] nature. This result holds equally also in the case of mass-imbalanced mixtures composed, for instance, of heavy bosonic impurities, $m_I = 133/78 m_B$ [see, e.g., Fig. 5(d)]. The above findings indicate that despite the employed approximations the ETH scheme is able to capture the main features exhibited by the relaxed state of the impurities within our correlated MB system.

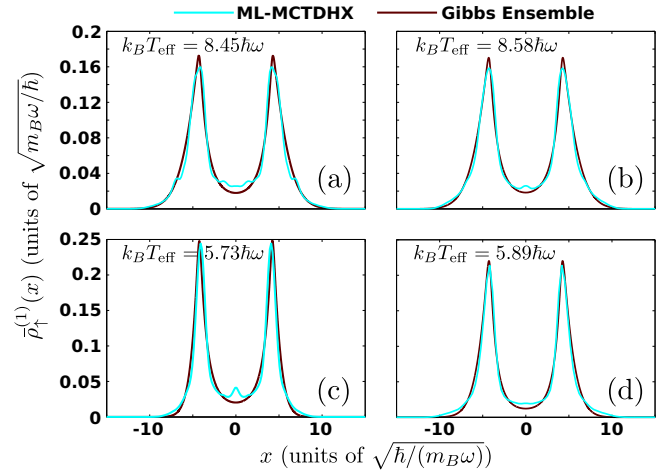


FIG. 5. The time-averaged one-body density, $\bar{\rho}_\uparrow^{(1)}(x)$, within the MB approach (light blue lines) compared to the best fit of the ETH model, $\rho_{\uparrow; \text{Gibbs}}^{(1)}(x; T_{\text{eff}})$ (dark red lines). Our results refer to (a) $N_I = 1$, (b) $N_I = 2$ bosonic, and (c) $N_I = 2$ fermionic mass-balanced, $m_I = m_B$ impurities. (d) Corresponds to the case of $N_I = 2$ heavy, $m_I = (133/78)m_B$, bosonic impurities.

Regarding the effective temperature we find rather large values of T_{eff} for one and two bosonic impurities that is of the order of $T_{\text{eff}} \approx 8\hbar\omega/k_B$. While for two fermions and two heavier bosonic impurities the temperature is slightly smaller, possessing values of the order of $T_{\text{eff}} \approx 6\hbar\omega/k_B$. These large values of the effective temperature are indicative of the incoherent character of the impurities after the probe pulse [see also Fig. 2(d)]. To advance further the correspondence between the ETH model and the correlated MB results we estimate the effective temperature of the relaxed state by expressing Eq. (6) only in terms of the impurity's degrees of freedom. Notice that the energy of the impurity is not conserved during the MB evolution of our system due to the presence of energy exchange processes between the impurity and the bath. However, as evidenced in Fig. 4, the energy of the impurities saturates for large times (see also Sec. IV). Indeed, by taking advantage of this observation we can cast Eq. (6) in the form

$$\begin{aligned} \bar{E}_\uparrow &= \lim_{T \rightarrow \infty} \frac{1}{T} \int_0^T dt \langle \Psi(t) | \hat{H} - \hat{H}_B^0 - \hat{H}_{BB} | \Psi(t) \rangle \\ &= \text{Tr}[\bar{\rho}_{\uparrow; \text{Gibbs}}^{(N_I)} \hat{H}_\uparrow^{\text{eff}}], \end{aligned} \quad (12)$$

where \bar{E}_\uparrow is the time-averaged impurity energy. In the case of a single impurity, Eq. (12) gives an estimation for the effective temperature of $T_{\text{eff}} = 8.56\hbar\omega/k_B$ which is in good agreement with the effective temperature obtained by fitting $T_{\text{eff}} = 8.45\hbar\omega/k_B$. Note also here that the effective Hamiltonian of Eq. (8) is known to overestimate the zero-point energy of the impurity since it neglects its dressing by the excitations of the BEC [59]. This in turn explains the higher T_{eff} obtained via Eq. (12). In contrast, in the case of two impurities the related estimates for T_{eff} are much higher than the ones obtained by the fitting of $\bar{\rho}_\uparrow^{(1)}(x, x')$. Specifically, Eq. (12) yields $T_{\text{eff}} = 10.28\hbar\omega/k_B$ and $T_{\text{eff}} = 6.89\hbar\omega/k_B$ for the two bosonic and the two fermionic impurities, respec-

tively. The observed discrepancy is attributed to the presence of induced interactions between the impurities that are more prevalent in the case of bosonic impurities than fermionic ones [60]. However, their effect is neglected within the effective Hamiltonian of Eq. (8).

VI. CONCLUSIONS

We have developed a PPS scheme to study the time-resolved dynamics of fermionic and bosonic impurities immersed in a harmonically confined BEC. Coherence properties and induced interactions are encoded in the probe spectra for both attractive and repulsive interactions. Moreover, long-lived attractive and repulsive polarons exist up to $g_{BI} \approx g_{BB}$. For $g_{BI} > g_{BB}$, with the dynamics being dominated by energy redistribution processes, a rather rapid temporal orthogonality catastrophe occurs. To explicitly showcase that energy redistribution processes take place we have discussed the behavior of the corresponding interspecies interaction energy which decreases for short evolution times and thus captures the energy transfer from the impurities to the environment. Furthermore, it shows a saturation tendency for large evolution times, a behavior that is indicative of a relaxation process of the impurities. Indeed, at longer times ($t_d > 100\omega^{-1}$), where any coherence information is lost, a thermalized state is reached. To further characterize the aforementioned relaxation dynamics we have resorted to an effective ETH model which has enabled us to identify that for strong interspecies couplings and long evolution times the impurities acquire an effective temperature. This effective temperature is found to be smaller for the fermionic impurities than the bosonic ones. Importantly, we have found that the thermalization process is independent of the size of the bath and the impurity concentration, the interacting nature of the impurities as well as their flavor and mass.

It would be intriguing to utilize PPS at finite temperature [108,109] and also in higher dimensions to explore the time-resolved formation of quasiparticles. As further perspectives, PPS could be exploited to unravel recondensation dynamics [110,111] in excited bands of optical lattices and the dynamics of vibrational states of ultra-long-range Rydberg molecules [112,113] to infer their lifetime.

ACKNOWLEDGMENTS

This work is funded by the Cluster of Excellence ‘‘The Hamburg Centre for Ultrafast Imaging’’ of the Deutsche Forschungsgemeinschaft (DFG)- EXC 2056 - project ID 390715994. G.C.K. gratefully acknowledges financial support by the DFG in the framework of the SFB 925 ‘‘Light induced dynamics and control of correlated quantum systems.’’ S.I.M. gratefully acknowledges financial support in the framework of the Lenz-Ising Award of the University of Hamburg. T.B. has been supported by the Okinawa Institute of Science and Technology Graduate University.

G.C.K., S.I.M., and G.M.K. contributed equally to this work.

APPENDIX A: DETAILS OF THE REVERSE RADIOFREQUENCY SPECTROSCOPY

Let us elaborate on the model that allows for the simulation of the MB dynamics under the influence of radiofrequency fields [5,36]. This model has been employed in the main text for the characterization of the coherence properties of polaronic quasiparticles in the context of PPS.

In our case few atomic impurities are immersed in a BEC environment close to an interspecies magnetic Feshbach resonance [114]. The case of bosonic impurities possessing equal mass to the BEC atoms can be realized by employing different hyperfine states of a particular isotope, e.g., ^{85}Rb or ^{87}Rb . For fermionic impurities the equal-mass scenario occurs approximately, e.g., for ^{173}Yb impurities immersed in a ^{174}Yb BEC with mass ratio of $m_B/m_I \approx 1.006$. Different masses for the impurities and the BEC atoms can be realized by invoking different atomic species, e.g., considering ^{87}Rb and ^{133}Cs [115]. Typically broad Feshbach resonances occur at magnetic fields of the order of 800G [114], referring to a regime where the atoms experience a sizable Zeeman shift. This sizable Zeeman shift allows us to address selectively the distinct m_F transitions provided that the intensity of the radiofrequency pulse results in a Rabi frequency Ω_R much smaller than the Zeeman splitting of the involved hyperfine levels. The latter is typically of the order of a few tenths of MHz. This large splitting of the different m_F levels implies that magnetic phenomena such as spin-exchange interactions can be safely neglected for these values of the magnetic field, see also Appendix C.

In this work we consider two hyperfine levels of the impurity atoms, denoted as $|\uparrow\rangle$ and $|\downarrow\rangle$. These states can be identified and resonantly coupled for a frequency ν_0 , corresponding to the Zeeman splitting between the two levels, when a BEC environment is absent. Due to the harmonic confinement of the atoms each of the hyperfine levels is further divided into states of different atomic motion. The average spacing between these sublevels is of the order of the harmonic trap frequency, $\hbar\omega$ lying within the range of a few tenths of $h \times \text{Hz}$ to a few $h \times \text{kHz}$ in typical ultracold atom experiments [78,117]. In the vicinity of a Feshbach resonance the energy of these sublevels strongly depends on the interspecies interaction strength, g_{BI} , between the impurity atoms in the resonantly interacting hyperfine state and their BEC environment. Accordingly, the energy of each motional state shifts by $\Delta_+(g_{BI})$ from the corresponding noninteracting one. As is also made obvious within the main text [see Fig. 1(b)] this shift is of the order of ω to $\sim 10\omega$. Therefore, due to the separation of the different involved energy scales it suffices to treat the impurities as two-level atoms. Furthermore, even for $\Omega_{R0}^\beta \gtrsim \Delta_+ \sim \text{kHz}$ where the regime of strong intense pulses is accessed, $\Omega_{R0}^\beta \ll \nu_0 \sim 10 \text{ MHz}$, allowing us to invoke the rotating wave approximation. Notice here that $\beta \in \{\text{pump, probe, dark}\}$. Within this approximation and in the interaction picture of the $|\uparrow\rangle \leftrightarrow |\downarrow\rangle$ transition, the Hamiltonian for the internal state of the impurities reads $\hat{H}_S = -\frac{\hbar\Delta^\beta}{2}\hat{S}_z + \frac{\hbar\Omega_{R0}^\beta}{2}\hat{S}_x$, which is exactly the form employed in Eq. (1) of the main text. Ω_{R0}^β and $\Delta^\beta = \nu^\beta - \nu_0^\beta$ refer respectively to the (bare) Rabi frequency and the detuning

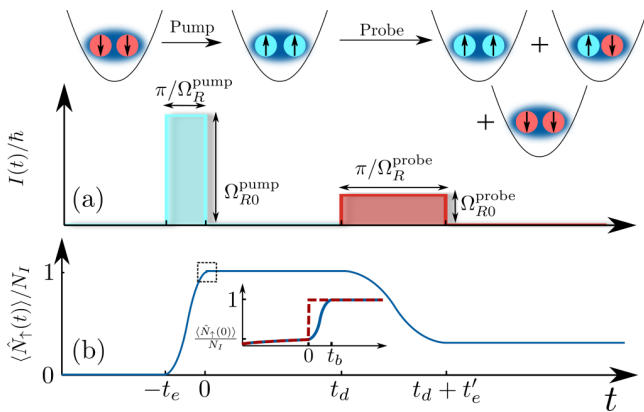


FIG. 6. (a) Schematic illustration of the employed PPS pulse sequences. The involved spin configuration at each state of the dynamics is also provided. (b) Expected time evolution of the population of spin- \uparrow atoms during the PPS sequence. The inset depicts the evolution of $\langle \hat{N}_\uparrow(t) \rangle / N_I$ during the application of the optical burst pulse (blue line) and the approximation of employing the projection operator \hat{P} at $t = 0$ (dark red line).

with respect to the resonance of the $|\uparrow\rangle \leftrightarrow |\downarrow\rangle$ transition at $g_{BI} = 0$. We remark that the $|\uparrow\rangle$ and $|\downarrow\rangle$ states in the Schrödinger and interaction pictures are equivalent, so our conclusions are invariant under this frame transformation [118].

To populate the polaronic states we employ a pump pulse of rectangular shape as depicted in Fig. 6(a). The system is initialized in the noninteracting ground state where the impurity atoms are spin polarized in their $|\downarrow\rangle$ state. The pump pulse is characterized by frequency ν^{pump} , and a detuning Δ^{pump} is employed. This pulse is further characterized by an exposure time t_e and a bare Rabi-frequency $\Omega_{R0}^{\text{pump}}$. Different realizations utilize different detunings Δ^{pump} and exposure times t_e but the same $\Omega_{R0}^{\text{pump}}$. In the duration of the pulse the system undergoes Rabi oscillations which for strong-enough pulses $\Omega_{R0}^{\text{pump}} \gg \omega$ are well characterized by a Rabi frequency $\Omega_R(\Delta^{\text{pump}}) = \sqrt{(\Omega_{R+}^{\text{pump}})^2 + (\Delta^{\text{pump}} - \Delta_+)^2}$, where $\Omega_{R+}^{\text{pump}}$ and Δ_+ are the corresponding resonance values. By fitting the spectroscopic signal, which is the fraction of atoms transferred to the $|\uparrow\rangle$ hyperfine state, to the theoretical line shape for rectangular pulses reading

$$\frac{\langle \hat{N}_\uparrow(t) \rangle}{N_I} = \left[\frac{\Omega_{R+}^{\text{pump}}}{\Omega_R^{\text{pump}}(\Delta^{\text{pump}})} \right]^2 \sin^2 \left[\frac{\Omega_R^{\text{pump}}(\Delta^{\text{pump}})t_e}{2} \right], \quad (\text{A1})$$

these resonance values of $\Omega_{R+}^{\text{pump}}$ and Δ_+ can be obtained. Note here that the line shape [Eq. (A1)] exhibits an infinite sequence of peaks at the locations, Δ_n^{pump} , $n = 0, \pm 1, \dots$, given by the solutions of

$$\frac{\Omega_R^{\text{pump}}(\Delta^{\text{pump}})t_e}{2} = \tan \left[\frac{\Omega_R^{\text{pump}}(\Delta^{\text{pump}})t_e}{2} \right] \quad (\text{A2})$$

for Δ^{pump} . Solving numerically Eq. (A2) we can identify the location of the three first peaks at positions $\Delta_0^{\text{pump}} = \Delta_+$ and $\Delta_{\pm 1}^{\text{pump}} \approx \Delta_+ \pm \Omega_{R+}^{\text{pump}} \sqrt{\left(\frac{8.9868}{\Omega_{R+}^{\text{pump}} t_e}\right)^2 - 1}$. Their corresponding amplitudes read $A_0 = \sin^2\left(\frac{1}{2}\Omega_{R+}^{\text{pump}} t_e\right)$ and $A_{\pm 1} \approx$

$0.01179(\Omega_{R+}^{\text{pump}} t_e)^2$. In order to achieve a high spectroscopic signal, $\langle \hat{N}_\uparrow(t_d) \rangle / N_I$, we set the exposure time to $t_e = \pi / \Omega_{R+}^{\text{pump}}$ (to the obtained fitting accuracy) ensuring that $A_0 \approx 1$. This choice implies that the peaks at $\Delta_{\pm 1}^{\text{pump}}$ are clearly imprinted in the obtained spectrum possessing an amplitude $A_{\pm 1} \approx 0.116438$. Indeed, these side peaks can be clearly identified in Fig. 1(b).

To infer about the coherence properties of the polaronic states we employ PPS, see Fig. 6(a). Initially, we prepare the system in the same noninteracting ground state as in the previously examined protocol and apply a rectangular π pulse, with $\Omega_{R0}^{\text{pump}} = 10\omega$ and $t_e = \pi / \Omega_{R+}^{\text{pump}}$ on a polaronic resonance where we have identified the resonant $\Omega_{R+}^{\text{pump}}$ and Δ_+^{pump} as explained above. This sequence transfers the atoms from the ground state to the polaronic state in a very efficient manner, see Fig. 6(b). Then the impurity atoms are projected to the spin- \uparrow state by employing an optical burst transition on the lowest hyperfine state $|\downarrow\rangle$ to an available P electronic level at $t = 0$ which essentially ejects all the spin- \downarrow atoms from the trap. This procedure has been simulated by the application of the operator $\hat{H}_P = -i\hbar\Gamma \int dx \hat{\Psi}_\uparrow^\dagger(x)\hat{\Psi}_\downarrow(x)$ over a short time interval t_b . We can numerically verify that for large $\Gamma > 100\omega$ and small $t_b \ll \omega^{-1}$ (corresponding to the experimentally relevant values) the action of \hat{H}_P to the state after the pump pulse is equivalent to the projection of the impurity to the spin- \uparrow configuration. For this reason and for computational simplicity we employ the state $|\Psi(t=0^+)\rangle = \frac{\hat{P}|\Psi(t=0^-)\rangle}{\|\hat{P}|\Psi(t=0^-)\rangle\|}$ as an initial state for the subsequent time evolution $t > 0$. Note that this sequence for $\Omega_{R0}^{\text{pump}} \ll \omega$ is approximately equivalent to an interaction quench, as the pump-pulse has almost no spectral selectivity due to the pronounced power broadening of the radiofrequency transition, as $\Omega_{R0}^{\text{pump}} \sim \Delta_+^{\text{pump}}$ and the fact that the out-of-equilibrium dynamics is effectively frozen due to the small timescale $t_e = \pi / \Omega_{R+}^{\text{pump}} \ll \omega^{-1}$. Indeed, these properties of the pump-pulse have been verified numerically for the selected parameters $\Omega_{R0}^{\text{pump}}$ and Δ_+^{pump} as the MB state after this pulse is found to possess a fidelity in excess of 90% to the initial one.

After the pump sequence is completed we let the system evolve in the absence of radiofrequency fields, $\Omega_{R0}^{\text{dark}} = 0$, for a dark time, t_d . Finally, we apply a second probe π pulse with a smaller $\Omega_{R0}^{\text{probe}} = 1\omega$ to the first one and varying Δ_+^{probe} to transfer the atoms from the polaronic to the initial ground state. The employed spectroscopic signal is the fraction of atoms that have been deexcited by the probe pulse (recall that within our scheme all of the particles are at t_d in the spin- \uparrow state) divided by the total number of impurities, $\frac{N_I(t_d)}{N_I}$. Note that a smaller $\Omega_{R0}^{\text{probe}}$, when compared to $\Omega_{R0}^{\text{pump}}$, is employed in order to reduce the power broadening during the probe sequence and subsequently increase the resolution in terms of detuning. However, this value cannot be arbitrarily lowered since for decreasing probe intensities the frequency resolution is increased at the expense of lower temporal resolution. For such low intensities the motional state of the spin- \uparrow impurities is significantly altered during the application of the probe pulse. As a heuristic argument the relation $\delta\nu\delta t \approx 1$ that connects the temporal (δt) and spectral ($\delta\nu$) resolution is commonly employed [119]. The value of $\Omega_{R0}^{\text{probe}} = 1\omega$ is selected within this work as it consists an adequate trade-off

between the spectral and the temporal resolution. Finally, due to the rectangular shape of the probe pulse the exhibited line shape of $\frac{\langle \hat{N}_I(t_d) \rangle}{N_I}$ is given by Eq. (A1) as long as the impurity is coherent, i.e., $|g^{(1)}(x, x'; t_d)| \approx 1$. Accordingly, in our analysis we attribute all fringes appearing in the spectra to the line shape of a single resonance if the ratio of the amplitude of two neighboring peaks satisfies $\frac{A_{n+1}}{A_n} < 0.12$.

APPENDIX B: COMPARISON WITH RAMSEY SPECTROSCOPY

Next we demonstrate the advantage of utilizing the PPS scheme in comparison to Ramsey spectroscopy. In particular, we explicitly showcase the differences between the predictions of the PPS and the Ramsey schemes for intriguing phenomena exhibited by our system including the TOC and the thermalization process. To achieve this comparison we have simulated the Ramsey response of our system following the scheme described in Refs. [59,60]. The main facet of this Ramsey protocol is that by applying an intense radiofrequency pulse to the initially noninteracting with the bath spin- \downarrow impurities we transfer them into a superposition state $\frac{|\uparrow\rangle + |\downarrow\rangle}{\sqrt{2}}$, where the state $|\uparrow\rangle$ interacts with the bosonic medium. Thus, the time-evolved MB wave function, e.g., of a single impurity is given by $|\Psi(t)\rangle = (1/\sqrt{2})e^{-i\hat{H}_R t/\hbar} |\Psi_{BI}^0\rangle |\uparrow\rangle + (1/\sqrt{2})e^{-iE_0 t/\hbar} |\Psi_{BI}^0\rangle |\downarrow\rangle$. Here $\hat{H}_R = \hat{H}_B + \hat{H}_{BB} + \hat{H}_\uparrow^0 + \hat{H}_\downarrow^0 + \hat{H}_{BI}$ as introduced in Sec. II, $|\Psi_{BI}^0\rangle$ is the spatial part of the initial MB wave function (see also Appendix D), and E_0 refers to the corresponding eigenenergy. In this protocol the structure factor, $|S(t)| = |\langle \Psi_{BI}^0 | e^{iE_0 t/\hbar} e^{-i\hat{H}_R t/\hbar} | \Psi_{BI}^0 \rangle|$, of the system is monitored by inspecting the magnitude of the impurity's spin $|\langle \hat{S}(t) \rangle|$.

According to our discussion in Sec. III it becomes apparent that time-dependent phenomena such as the TOC and the consecutive thermalization of the impurities can be clearly tracked in an experimentally relevant fashion via employing the temporarily resolved PPS scheme. Indeed, Figs. 1(i)–1(k) in the main text reveal that TOC takes place already for $t_d = 2\omega^{-1}$, with the presence of quasifree impurities at $\Delta^{\text{probe}} \approx 0$ being also readily imprinted in the probe spectrum. On the contrary, the only information that Ramsey spectroscopy conveys is the value of the structure factor, $|S(t)|$. Importantly, it does not deliver any further insights about the physical origin of its decreasing tendency and thus the underlying physical processes, see in particular Figs. 7(a) and 7(b). Indeed, for $t < 10\omega^{-1}$ $|S(t)|$ oscillates having a minimum value of 0.4 when $g_{BI} = 1.5\sqrt{\hbar^3\omega/m}$ and thus does not provide any clear signature for the emergence of the TOC identified using PPS. Along the same lines for $g_{BI} = 1.5\sqrt{\hbar^3\omega/m} > g_{BB}$, namely after the TOC manifests itself, a thermalization tendency is clearly imprinted in the probe spectrum [see Figs. 3(g)–3(i)] with a predominant peak appearing at $\Delta^{\text{probe}} \approx 0$. In other words, the dynamics after the decay of the strongly ($g_{BI} > g_{BB}$) repulsive Bose polarons leads to a quasistationary state of the MB system with respect to the energy redistribution among the different dynamical modes, providing this way strong evidences toward a thermalized state. This mechanism cannot be even suggested by invoking the contrast com-

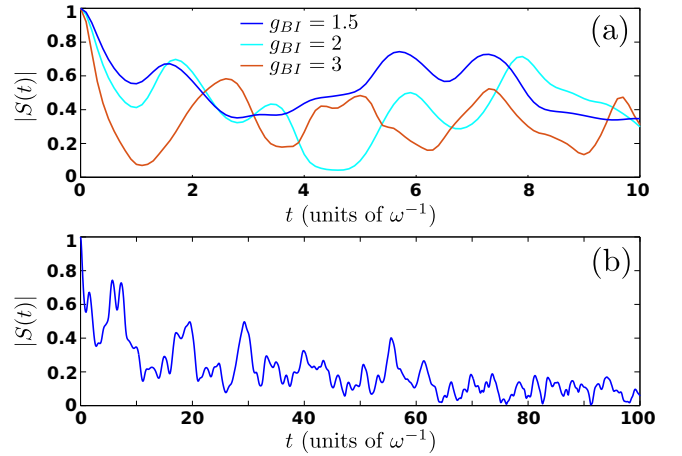


FIG. 7. (a) Time evolution of the structure factor of one impurity at different impurity-BEC interaction strengths (see legend). (b) Dynamics of the structure factor depicted in (a) of one impurity for $g_{BI} = 1.5\sqrt{\hbar^3\omega/m}$ over a longer timescale. The bosonic bath contains $N_B = 100$ bosons. The system is initialized in its ground state with $g_{BI} = 0$.

puted within the above-discussed Ramsey scheme. Indeed, the Ramsey scheme only indicates the tendency toward thermalization due to the decreasing behavior of the structure factor which, however, fluctuates within the depicted time interval.

APPENDIX C: DIMENSIONAL REDUCTION OF THE MANY-BODY HAMILTONIAN FROM THREE TO ONE DIMENSIONS

We consider an ensemble of confined ultracold atoms in three different hyperfine states, denoted as B , \uparrow , and \downarrow . State B is occupied by bosonic bath particles and the \uparrow and \downarrow states constitute a pseudo-spin-1/2 subsystem. We assume that state B belongs to a different manifold of hyperfine states with respect to the total angular-momentum quantum number, F , than the other two pseudospin states. The system is optically trapped and therefore all of the above hyperfine states experience the same confinement.

The *ab initio* Hamiltonian of this multicomponent system reads $\hat{H} = \hat{H}_0 + \hat{H}_{SD} + \hat{H}_I$. The spin-independent part \hat{H}_0 is given by

$$\hat{H}_0 = \int d^3r \sum_{\sigma \in \{B, \uparrow, \downarrow\}} \hat{\psi}_\sigma^\dagger(\mathbf{r}) \left[-\frac{\hbar^2}{2m} \nabla^2 + V_0(\mathbf{r}) \right] \hat{\psi}_\sigma(\mathbf{r}), \quad (\text{C1})$$

where m is the mass of the chemical element and $V_0(\mathbf{r})$ refers to the confining potential.

By imposing a homogeneous magnetic field, along the z -direction, the energy of the magnetic sublevels characterized by different m_F shift due to the Zeeman effect. Accordingly, the state-dependent part of the Hamiltonian is expressed as

$$\begin{aligned} \hat{H}_{SD} = & E_B \hat{N}_B + \frac{E_\uparrow + E_\downarrow}{2} \hat{N}_I \\ & + \frac{E_\uparrow - E_\downarrow}{2} \sum_{\alpha, \beta \in \{\uparrow, \downarrow\}} \int d^3r \hat{\psi}_\alpha^\dagger(\mathbf{r}) \sigma_{\alpha\beta}^z \hat{\psi}_\beta(\mathbf{r}). \end{aligned} \quad (\text{C2})$$

where $\sigma_{\alpha\beta}^z$ corresponds to the spin- z Pauli matrix and E_σ is the energy of the atomic state of species $\sigma \in \{B, \uparrow, \downarrow\}$. The typical energy difference between hyperfine levels possessing different F is of the order of several $h \times \text{GHz}$. In particular, for ^{87}Rb the hyperfine splitting between the two lowest hyperfine manifolds $F = 1$ and $F = 2$ is $E_{F=2} - E_{F=1} \approx h \times 6.83 \text{ GHz}$ [116]. Additionally, the amplitude of the Zeeman energy shifts is also of the order of $h \times \text{MHz/G}$. For instance, in ^{87}Rb this amplitude is of the order of $\sim 0.7 h \times \text{MHz/G}$ [116]. Furthermore, in the same species quadratic Zeeman shifts that lead to a nonequidistant distribution of magnetic sublevels possessing an amplitude of several $h \times \text{MHz}$ can be observed already for magnetic fields of the order of $\sim 10 \text{ G}$ [116]. Typical ultracold atom experiments involve interaction energies ranging from hundreds of $h \times \text{Hz}$ to a few $h \times \text{kHz}$ generating this way interaction energy shifts and spin-exchange processes characterized by energies of the same order of magnitude. Therefore, except for the case where the magnetic field applied is of the order of few Gauss, the spin-exchanging collisions are strongly suppressed [120].

Operating in the ultracold limit dominated by s -wave scattering [92] the interaction Hamiltonian can be expressed as [121]

$$\hat{H}_I = \sum_{\sigma, \sigma'} \frac{4\pi \hbar^2 a_{\sigma\sigma'}}{m} \int d^3r \hat{\psi}_\sigma^\dagger(\mathbf{r}) \hat{\psi}_{\sigma'}^\dagger(\mathbf{r}) \hat{\psi}_{\sigma'}(\mathbf{r}) \hat{\psi}_\sigma(\mathbf{r}). \quad (\text{C3})$$

The scattering lengths $a_{\sigma\sigma'}$, with $\sigma' \in \{B, \uparrow, \downarrow\}$, can be tuned via a Fano-Feshbach resonance between two distinct hyperfine levels [114].

In order to effectively reduce the dimensionality of the above system from 3D to 1D a strong confinement along the two perpendicular spatial directions is usually employed [93]. Then the confining potential reads

$$V_0(\mathbf{r}) = \frac{1}{2} m \omega^2 x^2 + \frac{1}{2} m \omega_\perp^2 (y^2 + z^2), \quad (\text{C4})$$

where $\omega_\perp \gg \omega$ holds for the transverse and longitudinal trapping frequencies. Note that the potential of Eq. (C4) can be realized either by a single optical dipole trap [120] or by applying a deep two-dimensional optical lattice potential [42,122]. To access the 1D regime, the frequency of the transverse confinement ω_\perp has to be selected such that the excited states of the harmonic trap along the transverse directions (y, z) are not populated. The condition for a 1D BEC is well known [93] and reads $N_B a_{BB} \alpha_\perp / \alpha^2 \ll 1$, where $\alpha_\perp = \sqrt{\hbar/m\omega_\perp}$ and $\alpha = \sqrt{\hbar/m\omega}$. In the few atom case, referring to the impurity species, a sufficient condition for accessing the 1D limit is $\omega_\perp \gg N\omega$ [123]. Indeed, under this assumption it is known that even in the strong interaction limit the system behaves as a Tonks-Girardeau gas of hard-core bosons sharing some characteristics with a gas of free fermions of the same particle number [124,125]. Properties of such fermionized 1D bosons have been probed experimentally in Refs. [126,127].

Accordingly, the corresponding 3D field operators can be expressed in terms of 1D ones as follows:

$$\hat{\psi}_\sigma^\dagger(\mathbf{r}) = \sqrt{\frac{m\omega_\perp}{\pi \hbar}} e^{-\frac{m\omega_\perp}{2\hbar}(y^2+z^2)} \hat{\psi}_\sigma^\dagger(x). \quad (\text{C5})$$

By employing Eq. (C5) we can then evaluate straightforwardly the reduced 1D effective Hamiltonian for $\hat{H}_0 + \hat{H}_{\text{SD}}$

which takes the form

$$\hat{H}_0 + \hat{H}_{\text{SD}} = \frac{E_\uparrow - E_\downarrow}{\hbar} \hat{S}_z + \sum_{\sigma \in \{B, \uparrow, \downarrow\}} \int dx \hat{\psi}_\sigma^\dagger(x) \times \left(-\frac{\hbar^2}{2m} \frac{d^2}{dx^2} + \frac{1}{2} m \omega^2 x^2 \right) \hat{\psi}_\sigma(x). \quad (\text{C6})$$

Here all terms contributing to the total energy shift for constant N_I and N_B are dropped while the \hat{S}_z operator reads

$$\hat{S}_z = \frac{\hbar}{2} \int dx [\hat{\psi}_\uparrow^\dagger(x) \hat{\psi}_\uparrow(x) - \hat{\psi}_\downarrow^\dagger(x) \hat{\psi}_\downarrow(x)]. \quad (\text{C7})$$

The dimensional reduction of \hat{H}_I is, however, more complicated. In particular, the phenomenon of the confinement induced resonance [91,128] occurs when $\alpha_\perp = \sqrt{\hbar/(m\omega_\perp)}$ is comparable to $a_{\sigma\sigma'}$. This implies that the actual 1D coupling constant deviates from $g_{\sigma\sigma'}^{\text{MF}} = \frac{2\hbar^2 a_{\sigma\sigma'}}{m\alpha_\perp^2}$ [93], which is obtained by evaluating the integrals appearing in Eq. (C3) along the transverse (y, z) directions. Detailed theoretical and experimental investigations [91,128] reveal that the 1D coupling strength $g_{\sigma\sigma'}$ possesses a simple analytical form, i.e., $g_{\sigma\sigma'} = g_{\sigma\sigma'}^{\text{MF}} (1 - \frac{|\zeta(1/2)| a_{\sigma\sigma'}}{\sqrt{2} \alpha_\perp})^{-1}$, and the effective 1D interaction Hamiltonian simplifies to

$$\hat{H}_I = \sum_{\sigma, \sigma'} g_{\sigma\sigma'} \int dx \hat{\psi}_\sigma^\dagger(x) \hat{\psi}_{\sigma'}^\dagger(x) \hat{\psi}_{\sigma'}(x) \hat{\psi}_\sigma(x). \quad (\text{C8})$$

Note here that due to the double counting for intraspecies interaction terms in Eq. (C8), the parameter g_{BB} appearing in the latter is two times larger than the corresponding one that is involved in Eq. (1).

According to the above discussion, for the experimental implementation of the setup described in the main text the interaction parameters, g_{BB} , g_{BI} , and g_{II} , used herein are related to the corresponding 3D scattering lengths as follows:

$$a_{\sigma\sigma'} = \alpha_\perp \frac{2\tilde{g}_{\sigma\sigma'}}{\sqrt{2}|\zeta(1/2)|\tilde{g}_{\sigma\sigma'} + 8\eta}. \quad (\text{C9})$$

Here $\tilde{g}_{\sigma\sigma'} = g_{\sigma\sigma'} / \sqrt{\hbar^3 \omega / m}$ refers to the dimensionless interaction strength and $\eta = \alpha / \alpha_\perp = \sqrt{\omega_\perp / \omega}$ is the aspect ratio. Furthermore, BECs involving particle numbers of the order of $N_B \sim 100$ are already accessible by current state-of-the-art experimental settings, e.g., in optical lattice experiments [42,122]. Finally, it is worth commenting that three-body recombination processes are highly suppressed for alkali ultracold atomic vapors, as the one considered herein. For instance, for a ^{87}Rb BEC and in the presence of three-body recombination a lifetime of 14.8 s has been reported [129]. Note also that the rate of three-body recombination scales with the cube of the density and, as a consequence, this effect is negligible for the mesoscopic system under consideration which involves low densities.

APPENDIX D: THE MANY-BODY VARIATIONAL METHODOLOGY: ML-MCTDHX

To track the stationary properties and, most importantly, the MB quantum dynamics of the multicomponent system addressed in the main text, we resort to the ML-MCTDHX

[94–96]. It constitutes an *ab initio* variational method for solving the time-dependent MB Schrödinger equation of atomic mixtures possessing either bosonic [57,99,130] or fermionic [39,106,118,131] spinor components. A major advantage of this approach is the expansion of the total MB wave function with respect to a time-dependent and variationally optimized basis (see below). This allows us to capture all the relevant inter- and intraspecies correlations of a multicomponent system in an efficient manner at each time instant by utilizing a reduced number of basis states when compared to expansions relying on a time-independent basis.

The system considered in the main text consists of a bosonic bath (B) with $N_B = 100$ atoms and either one ($N_I = 1$) or two ($N_I = 2$) impurity (I) atoms. Most importantly, the impurities being either bosons or fermions possess an internal pseudospin-1/2 degree of freedom [59,90]. To account for interspecies correlations, the MB wave function $|\Psi(t)\rangle$ is expressed according to a truncated Schmidt decomposition [99,130,132] in terms of D different species functions, i.e., $|\Psi_k^\sigma(t)\rangle$, for each component $\sigma = B, I$. We remark that the time-dependent species functions $|\Psi_k^\sigma(t)\rangle$ form an orthonormal N_σ -body wave function set within a subspace of the σ -species Hilbert space \mathcal{H}^σ [94]. Then the MB wave function $|\Psi(t)\rangle$ ansatz reads

$$|\Psi(t)\rangle = \sum_{k=1}^D \sqrt{\lambda_k(t)} |\Psi_k^B(t)\rangle |\Psi_k^I(t)\rangle, \quad (\text{D1})$$

where the time-dependent Schmidt weights $\lambda_k(t)$ are also known as the natural species populations of the k th species function and provide information about the degree of entanglement between the individual subsystems. For instance, if two different $\lambda_k(t)$ are nonzero, then $|\Psi(t)\rangle$ is a linear superposition of two states and therefore the system is entangled [132,133] or interspecies correlated. On the other hand, in the case of $\lambda_1(t) = 1$, $\lambda_{k>1}(t) = 0$, the wave function is a direct product of two states and the system is nonentangled.

Next, in order to include intraspecies correlations into our MB wave function ansatz, each species function $|\Psi_k^\sigma(t)\rangle$ is further expanded on a time-dependent number-state basis set $|\vec{n}(t)\rangle^\sigma$. Namely

$$|\Psi_k^\sigma(t)\rangle = \sum_{\vec{n}} A_{k;\vec{n}}^\sigma(t) |\vec{n}(t)\rangle^\sigma, \quad (\text{D2})$$

where $A_{k;\vec{n}}^\sigma(t)$ denote the underlying time-dependent expansion coefficients. Moreover, each number state $|\vec{n}(t)\rangle^\sigma$ corresponds to a permanent for bosons or a determinant for fermions building on d^σ time-dependent variationally optimized single-particle functions (SPFs), i.e., $|\phi_l^\sigma(t)\rangle$, with $l = 1, 2, \dots, d^\sigma$, being characterized by occupation numbers $\vec{n} = (n_1, \dots, n_{d^\sigma})$. Additionally, the SPFs are expanded with respect to a time-independent primitive basis. For the majority species, this primitive basis corresponds to an \mathcal{M} dimensional discrete variable representation denoted in the following by $\{|q\rangle\}$. However, for the impurities the primitive basis refers to the tensor product $\{|q, s\rangle\}$ of the discrete variable representation basis regarding the spatial degrees of freedom and the two-dimensional pseudospin-1/2 basis $\{|\uparrow\rangle, |\downarrow\rangle\}$. Consequently, each SPF of the impurities acquires the following

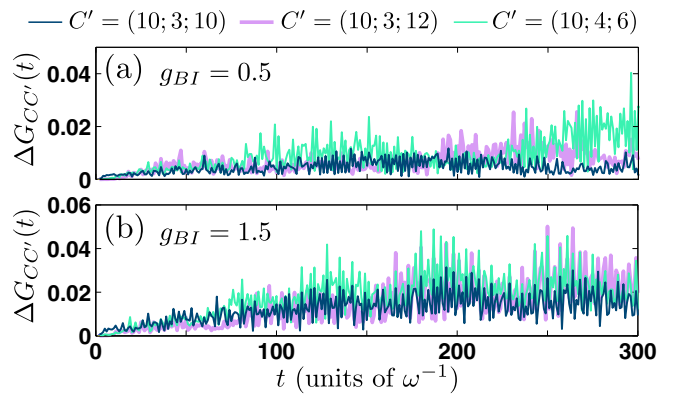


FIG. 8. Evolution of the one-body coherence absolute deviation $\Delta G_{C,C'}(t)$ between the $C = (10; 3; 8)$ and other orbital configurations $C' = (D; d^B; d^I)$ (see legend) for (a) $g_{BI} = 0.5\sqrt{\hbar^3\omega/m}$ and (b) $g_{BI} = 1.5\sqrt{\hbar^3\omega/m}$. In all cases $N_B = 100$, $N_I = 2$ with $g_{BB} = 0.5\sqrt{\hbar^3\omega/m}$ and $g_{II} = 0$ while initially $g_{BI} = 0$.

spinor wave function form:

$$|\phi_j^I(t)\rangle = \sum_{q=1}^{\mathcal{M}} (B_{jq\uparrow}^I(t) |q\rangle |\uparrow\rangle + B_{jq\downarrow}^I(t) |q\rangle |\downarrow\rangle). \quad (\text{D3})$$

Here $B_{jq\uparrow}^I(t)$ [$B_{jq\downarrow}^I(t)$] are the time-dependent expansion coefficients of the pseudospin- \uparrow and \downarrow respectively, see also Refs. [59,118].

Having exemplified the MB wave-function ansatz and in order to address the time evolution of the $(N_B + N_I)$ -body wave function $|\Psi(t)\rangle$ obeying the Hamiltonian of Eq. (1) provided in the main text we then numerically solve the so-called ML-MCTDHX equations of motion [94]. These equations are determined by following the Dirac-Frenkel [134,135] variational principle for the generalized ansatz of Eqs. (D1), (D2), and (D3). In this way, we obtain a set of D^2 linear differential equations of motion for the $\lambda_k(t)$ coefficients coupled to $D \left(\frac{(N_B + d^B - 1)!}{N_B! (d^B - 1)!} + \frac{(N_I + d^I - 1)!}{N_I! (d^I - 1)!} \right)$ nonlinear integrodifferential equations for the species functions and $d^B + d^I$ nonlinear integrodifferential equations for the SPFs.

APPENDIX E: CONVERGENCE OF THE MANY-BODY SIMULATIONS

The Hilbert space truncation within the ML-MCTDHX method is determined by the considered orbital configuration space, i.e., $C = (D; d^B; d^I)$. In this notation, $D = D^B = D^I$ and d^B and d^I denote the number of species functions and SPFs respectively for each species [Eqs. (D1) and (D2)]. Moreover, within our numerical calculations we employ a primitive basis based on a sine discrete variable representation for the spatial part of the SPFs with $\mathcal{M} = 600$ grid points. This sine discrete variable representation intrinsically introduces hard-wall boundary conditions at both edges of the numerical grid which in our case are located at $x_{\pm} = \pm 50\sqrt{\hbar/m\omega}$. We assured that the location of the hard-wall boundaries does not impact our findings since no significant density portion occurs beyond $x_{\pm} = \pm 20\sqrt{\hbar/m\omega}$. The eigenstates of the multicomponent system are obtained by utilizing

the so-called improved relaxation method [94–96] within ML-MCTDHX. To address the corresponding nonequilibrium dynamics, we numerically solve the ML-MCTDHX equations of motion using the MB wave function [Eq. (D1)] under the influence of the Hamiltonian (1) of the main text.

To testify the convergence of the MB results we ensured that all observables of interest are to a certain level of accuracy insensitive for a varying orbital configuration space, $C = (D; d^B; d^I)$. Note that for the MB simulations discussed in the main text we relied on the orbital configuration $C = (10; 3; 8)$. To infer the convergence of our results we exemplarily showcase below the behavior of the spatially integrated one-body coherence function, $g^{(1)}(x, x'; t)$, for different number of species and SPFs in the course of time. In particular we calculate its normalized absolute deviation between the $C = (10; 3; 8)$ and other orbital configurations $C' = (D; d^B; d^I)$, namely

$$\Delta G_{C,C'}(t) = \frac{\int dx dx' |g_C^{(1)}(x, x'; t) - g_{C'}^{(1)}(x, x'; t)|}{\int dx dx' g_C^{(1)}(x, x'; t)}. \quad (\text{E1})$$

The dynamics of $\Delta G_{C,C'}(t)$ is illustrated in Fig. 8 for the multicomponent bosonic system consisting of $N_B = 100$ atoms and $N_I = 2$ noninteracting impurities upon considering the pump spectroscopic sequence introduced in Sec. A from $g_{BI} = 0$ either to $g_{BI} = 0.5\sqrt{\hbar^3\omega/m}$ [Fig. 8(a)] or toward $g_{BI} = 1.5\sqrt{\hbar^3\omega/m}$ [Fig. 8(b)]. Evidently, a systematic convergence of $\Delta G_{C,C'}(t)$ is achieved in both cases. Indeed, closely inspecting $\Delta G_{C,C'}(t)$ for $g_{BI} = 0.5\sqrt{\hbar^3\omega/m}$ we observe that the deviation between the $C = (10; 3; 8)$ and $C' = (10; 4; 6)$ [$C' = (10; 3; 10)$] orbital configurations remains below 3.8% (1.2%) in the entire time evolution [Fig. 8(a)]. On the other hand, for increasing g_{BI} , $\Delta G_{C,C'}(t)$ takes larger values as shown in Fig. 8(b). For instance, at $g_{BI} = 1.5\sqrt{\hbar^3\omega/m}$ the relative error $\Delta G_{C,C'}(t)$ with $C = (10; 3; 8)$ and $C' = (10; 4; 6)$ [$C' = (10; 3; 10)$] becomes at most of the order of 5.2% [3%] at long evolution times $t > 150\omega^{-1}$. It is also worth mentioning at this point that for all other observables and interspecies interaction strengths discussed in the main text a similar degree of convergence takes place (results not shown here for brevity).

-
- [1] W. Demtröder, *Laser Spectroscopy: Basic Concepts and Instrumentation* (Springer Science & Business Media, New York, 2013).
- [2] A. S. Disa, M. Fechner, T. F. Nova, B. Liu, M. Först, D. Prabhakaran, P. G. Radaelli, and A. Cavalleri, [arXiv:2001.00540](https://arxiv.org/abs/2001.00540) (2020).
- [3] M. Lara-Astiaso, M. Galli, A. Trabattoni, A. Palacios, D. Ayuso, F. Frassetto, L. Poletto, S. De Camillis, J. Greenwood, P. Decleva, and I. Tavernelli, *J. Phys. Chem. Lett.* **9**, 4570 (2018).
- [4] M. Levenson, *Introduction to Nonlinear Laser Spectroscopy*, 2nd ed. (Elsevier, Amsterdam, 2012).
- [5] C. Kohstall, M. Zaccanti, M. Jag, A. Trenkwalder, P. Massignan, G. M. Bruun, F. Schreck, and R. Grimm, *Nature* **485**, 615 (2012).
- [6] M. Koschorreck, D. Pertot, E. Vogt, B. Fröhlich, M. Feld, and M. Köhl, *Nature* **485**, 619 (2012).
- [7] M. Cetina, M. Jag, R. S. Lous, I. Fritsche, J. T. M. Walraven, R. Grimm, J. Levinsen, M. M. Parish, R. Schmidt, M. Knap, and E. Demler, *Science* **354**, 96 (2016).
- [8] B. R. Mollow, *Phys. Rev. A* **5**, 2217 (1972).
- [9] C. Wei, A. S. Windsor, and N. B. Manson, *J. Phys. B: Atom. Mol. Opt. Phys.* **30**, 4877 (1997).
- [10] P. R. Berman and B. Dubetsky, *Phys. Rev. A* **62**, 053412 (2000).
- [11] F. Y. Wu, S. Ezekiel, M. Ducloy, and B. R. Mollow, *Phys. Rev. Lett.* **38**, 1077 (1977).
- [12] A. K. Mills and D. S. Elliott, *Phys. Rev. A* **86**, 063819 (2012).
- [13] A. V. Gorshkov, L. Jiang, M. Greiner, P. Zoller, and M. D. Lukin, *Phys. Rev. Lett.* **100**, 093005 (2008).
- [14] H. Li, V. A. Sautenkov, M. M. Kash, A. V. Sokolov, G. R. Welch, Y. V. Rostovtsev, M. S. Zubairy, and M. O. Scully, *Phys. Rev. A* **78**, 013803 (2008).
- [15] G. Stock and W. Domcke, *Phys. Rev. A* **45**, 3032 (1992).
- [16] Y.-Ch. Wu, B. Zhao, and S.-Y. Lee, *J. Chem. Phys.* **144**, 054104 (2016).
- [17] F. Sotier, T. Thomay, T. Hanke, J. Korger, S. Mahapatra, A. Frey, K. Brunner, R. Bratschitsch, and A. Leitenstorfer, *Nat. Phys.* **5**, 352 (2009).
- [18] M. Eisele, T. L. Cocker, M. A. Huber, M. Plankl, L. Viti, D. Ercolani, L. Sorba, M. S. Vitiello, and R. Huber, *Nat. Photon.* **8**, 841 (2014).
- [19] N. Takei, C. Sommer, C. Genes, G. Pupillo, H. Goto, K. Koyasu, H. Chiba, M. Weidemüller, and K. Ohmori, *Nat. Commun.* **7**, 1 (2016).
- [20] M. Kolarczik, C. Ulbrich, P. Geiregat, Y. Zhu, L. K. Sagar, A. Singh, B. Herzog, A. W. Achtstein, X. Li, D. Van Thourhout, and Z. Hens, *APL Photon.* **3**, 016101 (2018).
- [21] M. Buzzi, M. Först, R. Mankowsky, and A. Cavalleri, *Nat. Rev. Mat.* **3**, 299 (2018).
- [22] M. Mitrano, A. Cantaluppi, D. Nicoletti, S. Kaiser, A. Perucchi, S. Lupi, P. Di Pietro, D. Pontiroli, M. Riccò, S. R. Clark, and D. Jaksch, *Nature* **530**, 461 (2016).
- [23] M. Machholm, A. Giusti-Suzor, and F. H. Mies, *Phys. Rev. A* **50**, 5025 (1994).
- [24] D. J. McCabe, D. G. England, H. E. L. Martay, M. E. Friedman, J. Petrovic, E. Dimova, B. Chatel, and I. A. Walmsley, *Phys. Rev. A* **80**, 033404 (2009).
- [25] C. P. Koch and R. Kosloff, *Phys. Rev. Lett.* **103**, 260401 (2009).
- [26] W. Salzmann, T. Mullins, J. Eng, M. Albert, R. Wester, M. Weidemüller, A. Merli, S. M. Weber, F. Sauer, M. Plewicki, F. Weise, L. Woste, and A. Lindinger, *Phys. Rev. Lett.* **100**, 233003 (2008).
- [27] A. Schirotzek, C.-H. Wu, A. Sommer, and M. W. Zwierlein, *Phys. Rev. Lett.* **102**, 230402 (2009).
- [28] S. Nascimbène, N. Navon, K. J. Jiang, L. Tarruell, M. Teichmann, J. McKeever, F. Chevy, and C. Salomon, *Phys. Rev. Lett.* **103**, 170402 (2009).

- [29] F. Chevy and C. Mora, *Rep. Prog. Phys.* **73**, 112401 (2010).
- [30] S. Pilati, G. Bertaina, S. Giorgini, and M. Troyer, *Phys. Rev. Lett.* **105**, 030405 (2010).
- [31] P. Massignan and G. Bruun, *Eur. Phys. J. D* **65**, 83 (2011).
- [32] R. Schmidt, T. Enss, V. Pietilä, and E. Demler, *Phys. Rev. A* **85**, 021602(R) (2012).
- [33] P. Massignan, Z. Yu, and G. M. Bruun, *Phys. Rev. Lett.* **110**, 230401 (2013).
- [34] P. Massignan, M. Zaccanti, and G. M. Bruun, *Rep. Prog. Phys.* **77**, 034401 (2014).
- [35] E. Burovski, V. Cheianov, O. Gamayun, and O. Lychkovskiy, *Phys. Rev. A* **89**, 041601(R) (2014).
- [36] F. Scazza, G. Valtolina, P. Massignan, A. Recati, A. Amico, A. Burchianti, C. Fort, M. Inguscio, M. Zaccanti, and G. Roati, *Phys. Rev. Lett.* **118**, 083602 (2017).
- [37] R. Schmidt, M. Knap, D. A. Ivanov, J.-S. You, M. Cetina, and E. Demler, *Rep. Prog. Phys.* **81**, 024401 (2018).
- [38] O. Gamayun, O. Lychkovskiy, E. Burovski, M. Malcomson, V. V. Cheianov, and M. B. Zvonarev, *Phys. Rev. Lett.* **120**, 220605 (2018).
- [39] S. I. Mistakidis, G. C. Katsimiga, G. M. Koutentakis, and P. Schmelcher, *New J. Phys.* **21**, 043032 (2019).
- [40] M. Knap, A. Shashi, Y. Nishida, A. Imambekov, D. A. Abanin, and E. Demler, *Phys. Rev. X* **2**, 041020 (2012)..
- [41] J. Sous, H. R. Sadeghpour, T. C. Killian, E. Demler, and R. Schmidt, *Phys. Rev. Res.* **2**, 023021 (2020).
- [42] J. Catani, G. Lamporesi, D. Naik, M. Gring, M. Inguscio, F. Minardi, A. Kantian, and T. Giamarchi, *Phys. Rev. A* **85**, 023623 (2012).
- [43] T. Fukuhara, A. Kantian, M. Endres, M. Cheneau, P. Schauss, S. Hild, D. Bellem, U. Schollwöck, T. Giamarchi, C. Gross, I. Bloch, and S. Kuhr, *Nat. Phys.* **9**, 235 (2013).
- [44] Z. Z. Yan, Y. Ni, C. Robens, and M. W. Zwierlein, *Science* **368**, 190 (2020).
- [45] R. Scelle, T. Rentrop, A. Trautmann, T. Schuster, and M. K. Oberthaler, *Phys. Rev. Lett.* **111**, 070401 (2013).
- [46] R. Schmidt, H. R. Sadeghpour, and E. Demler, *Phys. Rev. Lett.* **116**, 105302 (2016).
- [47] L. A. Peña Ardila, and S. Giorgini, *Phys. Rev. A* **94**, 063640 (2016).
- [48] A. G. Volosniev and H.-W. Hammer, *Phys. Rev. A* **96**, 031601(R) (2017).
- [49] N. E. Guenther, P. Massignan, M. Lewenstein, and G. M. Bruun, *Phys. Rev. Lett.* **120**, 050405 (2018).
- [50] D. Mayer, F. Schmidt, D. Adam, S. Haupt, J. Koch, T. Lausch, J. Nettersheim, Q. Bouton, and A. Widera, *J. Phys. B: At. Mol. Opt. Phys.* **52**, 015301 (2018).
- [51] N. B. Jørgensen, L. Wacker, K. T. Skalmstang, M. M. Parish, J. Levinsen, R. S. Christensen, G. M. Bruun, and J. J. Arlt, *Phys. Rev. Lett.* **117**, 055302 (2016).
- [52] M.-G. Hu, M. J. Van de Graaff, D. Kedar, J. P. Corson, E. A. Cornell, and D. S. Jin, *Phys. Rev. Lett.* **117**, 055301 (2016).
- [53] Y. E. Shchadilova, R. Schmidt, F. Grusdt, and E. Demler, *Phys. Rev. Lett.* **117**, 113002 (2016).
- [54] J. Levinsen, M. M. Parish, and G. M. Bruun, *Phys. Rev. Lett.* **115**, 125302 (2015).
- [55] R. S. Christensen, J. Levinsen, and G. M. Bruun, *Phys. Rev. Lett.* **115**, 160401 (2015).
- [56] F. Grusdt, K. Seetharam, Y. Shchadilova, and E. Demler, *Phys. Rev. A* **97**, 033612 (2018).
- [57] S. I. Mistakidis, A. G. Volosniev, N. T. Zinner, and P. Schmelcher, *Phys. Rev. A* **100**, 013619 (2019).
- [58] M. Drescher, M. Salmhofer, and T. Enss, *Phys. Rev. A* **99**, 023601 (2019).
- [59] S. I. Mistakidis, G. C. Katsimiga, G. M. Koutentakis, Th. Busch, and P. Schmelcher, *Phys. Rev. Lett.* **122**, 183001 (2019).
- [60] S. I. Mistakidis, G. M. Koutentakis, G. C. Katsimiga, Th. Busch, and P. Schmelcher, *New J. Phys.* **22**, 043007 (2019).
- [61] S. I. Mistakidis, F. Grusdt, and G. M. Koutentakis, and P. Schmelcher, *New J. Phys.* **21**, 103026 (2019).
- [62] A. Camacho-Guardian, L. A. Peña Ardila, T. Pohl, and G. M. Bruun, *Phys. Rev. Lett.* **121**, 013401 (2018).
- [63] A. Camacho-Guardian and G. M. Bruun, *Phys. Rev. X* **8**, 031042 (2018).
- [64] L. A. Peña Ardila, N. B. Jørgensen, T. Pohl, S. Giorgini, G. M. Bruun, and J. J. Arlt, *Phys. Rev. A* **99**, 063607 (2019).
- [65] M. E. Gershenson, V. Podzorov, and A. F. Morpurgo, *Rev. Mod. Phys.* **78**, 973 (2006).
- [66] S. T. Ruggiero and D. A. Rudman (Eds.), *Superconducting Devices* (Academic Press, Boston, 1990).
- [67] J. Bardeen, G. Baym, and D. Pines, *Phys. Rev.* **156**, 207 (1967).
- [68] G. Baym and C. Pethick, *Landau Fermi-Liquid Theory: Concepts and Applications* (Wiley-VCH, New York, 1991).
- [69] D. J. Scalapino, *Phys. Rep.* **250**, 329 (1995).
- [70] J. Sous, M. Chakraborty, R. V. Krems, and M. Berciu, *Phys. Rev. Lett.* **121**, 247001 (2018).
- [71] L. N. Cooper, *Phys. Rev.* **104**, 1189 (1956).
- [72] J. R. Schrieffer, *Theory of Superconductivity*, Advanced Book Program Series (Avalon, New York, 1983).
- [73] A. S. Alexandrov and A. B. Krebs, *Sov. Phys. Usp.* **35**, 345 (1992).
- [74] N. F. Mott, *J. Phys.: Condens. Matter* **5**, 3487 (1993).
- [75] A. S. Alexandrov and N. F. Mott, *Rep. Prog. Phys.* **57**, 1197 (1994).
- [76] E. K. Salje, A. S. Alexandrov, and W. Y. Liang, *Polarons and Bipolarons in High-Tc Superconductors and Related Materials* (Cambridge University Press, Cambridge, UK, 2005).
- [77] M. Berciu, I. Elfmov, and G. A. Sawatzky, *Phys. Rev. B* **79**, 214507 (2009).
- [78] A. Amico, F. Scazza, G. Valtolina, P. E. S. Tavares, W. Ketterle, M. Inguscio, G. Roati, and M. Zaccanti, *Phys. Rev. Lett.* **121**, 253602 (2018).
- [79] N. Takemura, S. Trebaol, M. Wouters, M. T. Portella-Oberli, and B. Deveaud, *Nat. Phys.* **10**, 500 (2014).
- [80] M. Navadeh-Toupchi, N. Takemura, M. D. Anderson, D. Y. Oberli, and M. T. Portella-Oberli, *Phys. Rev. Lett.* **122**, 047402 (2019).
- [81] J. Orenstein, *Phys. Today* **65**(9), 44 (2012).
- [82] C. Giannetti, M. Capone, D. Fausti, M. Fabrizio, F. Parmigiani, and D. Mihailovic, *Adv. Phys.* **65**, 58 (2016).
- [83] J. Goold, T. Fogarty, N. Lo Gullo, M. Paternostro, and T. Busch, *Phys. Rev. A* **84**, 063632 (2011).
- [84] M. Rigol, V. Dunjko, and M. Olshanii, *Nat.* **452**, 854 (2008).
- [85] M. Rigol, *Phys. Rev. Lett.* **103**, 100403 (2009).
- [86] M. Rigol and M. Srednicki, *Phys. Rev. Lett.* **108**, 110601 (2012).
- [87] D. Jansen, J. Stolpp, L. Vidmar, and F. Heidrich-Meisner, *Phys. Rev. B* **99**, 155130 (2019).

- [88] T. Lausch, A. Widera, and M. Fleischhauer, *Phys. Rev. A* **97**, 033620 (2018).
- [89] T. Lausch, A. Widera, and M. Fleischhauer, *Phys. Rev. A* **97**, 023621 (2018).
- [90] K. Kasamatsu, M. Tsubota, and M. Ueda, *Int. J. Mod. Phys. B* **19**, 1835 (2005).
- [91] M. Olshanii, *Phys. Rev. Lett.* **81**, 938 (1998).
- [92] C. J. Pethick and H. Smith, *Bose-Einstein Condensation in Dilute Gases* (Cambridge University Press, Cambridge, UK, 2008).
- [93] L. Pitaevskii and S. Stringari, *Bose-Einstein Condensation and Superfluidity* (Oxford University Press, Oxford, 2016).
- [94] L. Cao, V. Bolsinger, S. I. Mistakidis, G. M. Koutentakis, S. Krönke, J. M. Schurer, and P. Schmelcher, *J. Chem. Phys.* **147**, 044106 (2017).
- [95] L. Cao, S. Krönke, O. Vendrell, and P. Schmelcher, *J. Chem. Phys.* **139**, 134103 (2013).
- [96] S. Krönke, L. Cao, O. Vendrell, and P. Schmelcher, *New J. Phys.* **15**, 063018 (2013).
- [97] M. O. Scully and M. S. Zubairy, *Quantum Optics* (Cambridge University Press, Cambridge, UK, 1997).
- [98] S. I. Mistakidis, A. G. Volosniev, and P. Schmelcher, *Phys. Rev. Res.* **2**, 023154 (2020).
- [99] S. I. Mistakidis, G. C. Katsimiga, P. G. Kevrekidis, and P. Schmelcher, *New J. Phys.* **20**, 043052 (2018).
- [100] S. I. Mistakidis, L. Cao, and P. Schmelcher, *J. Phys. B: At. Mol. Opt. Phys.* **47**, 225303 (2014).
- [101] V. Hakim, *Phys. Rev. E* **55**, 2835 (1997).
- [102] G. C. Katsimiga, S. I. Mistakidis, G. M. Koutentakis, P. G. Kevrekidis, and P. Schmelcher, *Phys. Rev. A* **98**, 013632 (2018).
- [103] P. Engels and C. Atherton, *Phys. Rev. Lett.* **99**, 160405 (2007).
- [104] S. Bera, B. Chakrabarti, A. Gammal, M. C. Tsatsos, M. L. Lekala, B. Chatterjee, C. Lévesque, and A. U. J. Lode, *Sci. Rep.* **9**, 1 (2019).
- [105] R. Roy, A. Gammal, M. C. Tsatsos, B. Chatterjee, B. Chakrabarti, and A. U. J. Lode, *Phys. Rev. A* **97**, 043625 (2018).
- [106] J. Erdmann, S. I. Mistakidis, and P. Schmelcher, *Phys. Rev. A* **99**, 013605 (2019).
- [107] F. H. L. Essler and M. Fagotti, *J. Stat. Mech.* (2016) 064002.
- [108] J. Levinsen, M. M. Parish, R. S. Christensen, J. J. Arlt, and G. M. Bruun, *Phys. Rev. A* **96**, 063622 (2017).
- [109] B. Field, J. Levinsen, and M. M. Parish, *Phys. Rev. A* **101**, 013623 (2020).
- [110] T. Kock, C. Hippler, A. Ewerbeck, and A. Hemmerich, *J. Phys. B: At. Mol. Opt. Phys.* **49**, 042001 (2016).
- [111] G. Q. Luo, A. Hemmerich, and Z. F. Xu, *Phys. Rev. A* **98**, 053617 (2018).
- [112] F. Engel, T. Dieterle, F. Hummel, C. Fey, P. Schmelcher, R. Löw, T. Pfau, and F. Meinert, *Phys. Rev. Lett.* **123**, 073003 (2019).
- [113] B. Butscher, V. Bendkowsky, J. Nipper, J. B. Balewski, L. Kukota, R. Löw, T. Pfau, W. Li, T. Pohl, and J. M. Rost, *J. Phys. B: At. Mol. Opt. Phys.* **44**, 184004 (2011).
- [114] C. Chin, R. Grimm, P. Julienne, and E. Tiesinga, *Rev. Mod. Phys.* **82**, 1225 (2010).
- [115] M. Hohmann, F. Kindermann, B. Gänger, T. Lausch, D. Mayer, F. Schmidt, and A. Widera, *EPJ Quant. Technol.* **2**, 23 (2015).
- [116] D. A. Steck, Rubidium 85 D Line Data, <http://steck.us/alkalidata> (2013).
- [117] M. A. Hofer, J. J. Chang, C. Hamner, and P. Engels, *Phys. Rev. A* **84**, 041605(R) (2011).
- [118] G. M. Koutentakis, S. I. Mistakidis, and P. Schmelcher, *New J. Phys.* **21**, 053005 (2019).
- [119] J. J. Sakurai, *Advanced Quantum Mechanics* (Pearson Education, MA, United States, 1967).
- [120] T. M. Bersano, V. Gokhroo, M. A. Khamelchi, J. D'Ambrise, D. J. Frantzeskakis, P. Engels, and P. G. Kevrekidis, *Phys. Rev. Lett.* **120**, 063202 (2018).
- [121] K. Huang and C. N. Yang, *Phys. Rev.* **105**, 767 (1957).
- [122] F. Meinert, M. Knap, E. Kirilov, K. Jag-Lauber, M. B. Zvonarev, E. Demler, and H.-C. Nägerl, *Science* **356**, 945 (2017).
- [123] Z. Idziaszek and T. Calarco, *Phys. Rev. A* **74**, 022712 (2006).
- [124] M. Girardeau, *J. Math. Phys. (NY)* **1**, 516 (1960).
- [125] E. H. Lieb and W. Liniger, *Phys. Rev.* **130**, 1605 (1963).
- [126] B. Paredes, A. Widera, V. Murg, O. Mandel, S. Fölling, I. Cirac, G. V. Shlyapnikov, T. W. Hänsch, and I. Bloch, *Nature* **429**, 277 (2004).
- [127] T. Kinoshita, T. Wenger, and D. S. Weiss, *Science* **305**, 1125 (2004).
- [128] E. Haller, M. J. Mark, R. Hart, J. G. Danzl, L. Reichsöllner, V. Melezhik, P. Schmelcher, and H.-C. Nägerl, *Phys. Rev. Lett.* **104**, 153203 (2010).
- [129] J. Söding, D. Guéry-Odelin, P. Desbiolles, F. Chevy, H. Inamori, and J. Dalibard, *Appl. Phys. B* **69**, 257 (1999).
- [130] G. C. Katsimiga, G. M. Koutentakis, S. I. Mistakidis, P. G. Kevrekidis, and P. Schmelcher, *New J. Phys.* **19**, 073004 (2017).
- [131] P. Siegl, S. I. Mistakidis, and P. Schmelcher, *Phys. Rev. A* **97**, 053626 (2018).
- [132] R. Horodecki, P. Horodecki, M. Horodecki, and K. Horodecki, *Rev. Mod. Phys.* **81**, 865 (2009).
- [133] M. Roncaglia, A. Montorsi, and M. Genovese, *Phys. Rev. A* **90**, 062303 (2014).
- [134] J. Frenkel, *Wave Mechanics: Advanced General Theory* 1st ed. (Oxford University Press, Oxford, 1934), pp. 423–428.
- [135] P. A. Dirac, *Proc. Camb. Phil. Soc.* **26**, 376 (1930).

SCIENTIFIC CONTRIBUTIONS

Chapter 5

Conclusions and Outlook

In this cumulative dissertation we have investigated the dynamics of spinor ultracold atoms that are either isolated or interact with a more extensive Fermi or Bose gas. In particular, by exploiting the spin-degrees of freedom, inherent in these setups, we have analyzed the magnetic properties of one dimensional few-body spinor Fermi gases [K1,K2] and the dynamical formation of Fermi [98,116,144,145] and Bose [91,182,183] polarons when the spinor atoms are immersed in a fermionic or bosonic environment respectively [K3–K6]. In all of these cases we have demonstrated that the spin of these systems allows us to access information regarding the nature and development of correlations during their dynamics, which is difficult to obtain both experimentally, as well as, theoretically in the spinless case. In this final section we summarize our key findings regarding the physics of the above mentioned systems and provide intriguing perspectives for future studies.

Regarding the study of the dynamics, emanating in confined spin-1/2 fermions, we have unraveled the stability properties of states, regarded within the framework of the Stoner instability [104] as ferromagnetic, when correlations are fully taken into account [K1,K2]. Those states appear within the Stoner model for repulsive interactions exceeding a threshold value of the interaction strength. Particularly, they refer to configurations exhibiting phase separated spin-components or a non-zero spin-polarization of the ensemble. The spin-symmetries of the system play a crucial role in [K1,K2]. Indeed, in the absence of additional fields, the total-spin and its projections commute with the total Hamiltonian of the spinor Fermi gas and therefore, the total Hilbert space can be decomposed in different manifolds, according to these conserved quantities. It is evident that breaking these symmetries crucially alters the stability properties of the initial state. The systematic study of such systems with broken symmetries unveils the magnetic mechanisms that either protect the initial state or drive the system to a different spin-manifold. The role of the external confinement within our investigations is twofold. First, it allows for experimentally feasible setups and detection schemes. Second, it enables the creation of reduced effective models, as the many-body state of the spinor fermions can be expanded on the different participating energetic channels of the system.

CONCLUSIONS AND OUTLOOK

In order to study the stability of the fully polarized state we have employed a parabolically confined few-fermion spin-1/2 Fermi gas, whose spin-components are Rabi coupled by an inhomogeneous field [K1]. This inhomogeneous field breaks both the total-spin and the spin- z symmetry. During the dynamics we have observed that the magnitude of the spin vector fluctuates for all interaction strengths, showing that the corresponding polarized state is dynamically unstable. In contrast, there is an interaction regime where the spin-spin correlations are stable throughout the dynamics. These results point towards the presence of ferromagnetic spin-spin interactions stabilizing the spin-spin correlations [139–141], while the magnetization remains unstable. An effective XXZ model, being a generalized version of the one introduced in [135] is shown to be able to reproduce to a large extent the magnetization dynamics in the weak and intermediate interaction regimes, indicating that the magnetic processes in the system deviate from the framework of the Stoner model.

However, the origin of these magnetic mechanisms became clear only when we have considered the fate of the system initialized in a state with phase separated spin-components [K2]. More specifically, we have initialized the system in a phase separated state consisting of all spin- \uparrow particles occupying one well and all of the spin- \downarrow particles occupying the other well [97]. This implies that the spin-spin correlations within each individual well are ferromagnetic. The coupling among the wells is the only process that can disrupt the magnetic order of the particles. In particular, it is found that the inter-well interactions, stemming from the particle tunnelling, are of antiferromagnetic character, in accordance also to the Anderson antiferromagnetic exchange interaction [142]. The interplay between the ferromagnetic intra-well interactions and the antiferromagnetic intersite ones can be characterized within an effective spin-chain model that stems from the weak-coupling expansion of the interaction Hamiltonian corresponding to a Fermi gas, see Eq. (2.47).

The model we have put forward, constitutes a tJU model, incorporating effects stemming from tunnelling among the wells of the double-well (t), ferromagnetic exchange interactions (J) within each well and on-site interactions (U), stemming from the double occupation of a particular single-particle level by two anti-oriented spins. The explanation of the itinerant ferromagnetic processes, emanating in 1D systems by this model extends the well-established Stoner model of ferromagnetism [104]. As already discussed, the concept of Stoner instability relies on the competition of kinetic and interaction energies. Our approach considers a more fundamental interplay, on the level of competing spin-spin interactions. Particularly, the spin-spin interaction attributed to the kinetic energy, being expressed in terms of the tunnelling of fermions in the double-well structure is antiferromagnetic and corresponds exactly to the Anderson exchange interaction [142]. Simultaneously, the system also incorporates ferromagnetic interactions due to the density-density repulsion of anti-oriented spins, residing in distinct single-particle states. The latter interaction mechanism is also well-known and refers to the so-called Hund interaction [139–141]. This simultaneous presence of both ferromagnetic and antiferromagnetic interactions is a particularly important feature, since it promotes the development of states possessing non-trivial spin-spin correla-

tions. All in all, the above demonstrate that itinerant ferromagnetism is a particularly involved phenomenon even within the simplest context of an 1D system. Nevertheless, such systems provide the insight that, when correlations are explicitly and fully taken into account, the itinerant ferromagnetism seems to occur due to inter-band interactions rather than the energetics within a single-band.

There are mainly two paths for the extension of the above mentioned findings in future endeavors. The first refers to the systematic generalization of the above mentioned findings in higher dimensions. One key element, inherent in multidimensional setups, that 1D ensembles lack, is the concept of degeneracy of single-particle levels [247]. This degeneracy is usually associated with the symmetry properties of multidimensional potentials. A typical example is the invariance of central potentials under rotations that induces degeneracies in the single-particle spectrum, connected with the conservation of the third projection of the particles angular momentum. Importantly, there is also the case of accidental degeneracies that are not connected to any apparent symmetries of the system. Therefore, a fruitful extension of our work is the study of the impact of single-particle degeneracies of either kind to the magnetic properties of fermions. Such studies might allow for a direct comparison of our findings to multidimensional ensembles consisting of a macroscopic number of particles, as in the experiments [94, 96–98, 100, 101]. Indeed, in the latter case a large density of states is involved at the Fermi level, implying a high degree of degeneracy. It is worth investigating whether this macroscopic degeneracy dominates the magnetic properties of such systems and how the weak-coupling expansion of Eq. (2.47) needs to be modified, in order to theoretically track such systems in the level of approximation which we have proposed in this thesis.

The second extension refers to the study of multi-well systems and networks thereof. In particular, the studies [K1, K2] have revealed that the spin-spin interactions among unpaired fermions in different bands are inherently ferromagnetic, while the corresponding interactions among different sites are of antiferromagnetic character. The study of multi-well setups also allows for examining the range of the magnetic order, resulting from the above mentioned spin-spin interactions. An important prospect for such investigations is to study the robustness of ferromagnetic intrawell order for different number of vacancies (holes) in the excited band. The presence of holes can affect the interplay of the Hund [139–141] and the Anderson [142] exchange interaction thus possibly leading to modifications of the magnetic properties and dynamics. A crucial question here is whether the magnetic order that is anticipated in view of [K2] is perturbed only locally, in the vicinity of the hole, or globally, within the whole system [62]. This investigation is also relevant in view of the spin-charge separation, which was recently experimentally identified in 1D single-band systems [61]. More specifically, the multi-band tJU Hamiltonian, despite being derived in 1D, represents a two-dimensional ladder model. It is therefore, interesting to understand whether spin-charge separation is exhibited within the 1D systems, involving multiple bands, or whether their effective description in terms of a ladder model prevails, resulting to effective interactions of the charge and spin degrees-of-freedom. Furthermore, exploiting the magnetic properties

CONCLUSIONS AND OUTLOOK

of multi-band systems to control the behaviour of Fermi gases, or even design novel quantum materials, is an intriguing prospective for further study. For example, this interplay between the different magnetic orderings implies that systems with valence band holes, coexisting with unpaired conduction band fermions, possess particularly interesting magnetic properties. It is therefore intriguing to examine whether effects attributed to the weak-coupling tJU model emerge in such systems and whether there are possible connections with exciton physics [107, 154].

Finally, it is worthwhile to explore the impact of the higher band excitations possibly appearing in contemporary experiments and whether recently reported discrepancies with theoretical models can be explained due to their presence. In particular, recently there are several experimental and theoretical advances in the study of spin-order emerging in fermionic Mott insulators [57–60, 62]. These systems consist of spin-1/2 fermions, occupying the lowest band of an optical lattice with an almost one-particle-per-site filling. In this case, the spatial degrees-of-freedom of these systems are almost fixed, due to a large on-site interaction that exceeds the kinetic energy expressed in terms of the tunnelling rate [57]. In such a configuration the spin-degrees-of-freedom are able to order according to the Anderson kinetic exchange interaction, leading to a largely antiferromagnetic state. The presence of holes in doped fermionic Mott insulators [59, 60, 62] gives rise to novel structures, the so-called magnetic polarons [174], which are connected to effects such as high-temperature superconductivity [174, 392]. Here the presence of impurity fermions in some excited band of the lattice might have a significant effect on the magnetic ordering of the lowest-band fermions. More specifically, such excitations would be much more mobile than their lowest band counterparts and due to their ferromagnetic Hund interactions (predicted within the low-coupling expansion [K1, K2]) they might scramble the magnetic order of the lowest band states, smearing out effects that stem from the Anderson interaction. Such effects might be particularly important in state-of-the-art experiments since the latter involve inhomogeneous parabolic trapping, on top of the optical lattice potential and relatively high-temperatures [62] that favour higher band excitations.

In addition to the above, the analysis of spinor setups enables the development of powerful techniques in order to characterize a wide variety of ultracold atomic systems. In this thesis we have provided an example of this utility of spinor systems by exploring the properties and dynamics of Fermi [98, 116, 144, 145] and Bose [91, 182, 183] polarons, based on spectroscopic techniques, such as injection, Ramsey and pump-probe spectroscopy [143]. In particular, the specific attributes of polarons enable the realization of powerful experimentally relevant protocols for their characterization. An important aspect is that, owing to their quasiparticle character, polaronic states possess a large similarity, in terms of wavefunction overlap, with the eigenstates of a non-interacting system. This allows the implementation of setups, where the spin of the impurities acts as a switch of their interaction with their host, by properly selecting the hyperfine states involved in the experiment. In this case the polaronic features of impurities interacting with their environment can be probed by employing a transition between the involved spin states via an radiofrequency field [143, 219]. Our studies provide sev-

eral key insights into the dynamics and stability of polaronic states revealing the effect of well-known non-linear phenomena, such as phase separation [202–206] and pattern formation [200, 207–210, 386, 388], as we will summarize below.

In the case of a fermionic environment in 1D [K3], we reveal that the impurities interacting with their host, form Fermi polarons characterized by a finite quasi-particle residue, Z , and a large lifetime. This fact is quite counter-intuitive, given that the Anderson orthogonality catastrophe [190–192] dictates that the polaron does not exist within the thermodynamic limit of 1D ensembles. Nevertheless, as it has also been demonstrated experimentally [185], several aspects regarding the 1D extensive Fermi sea can be extracted from few-body systems. We advance this claim by demonstrating spectroscopically the existence of 1D Fermi polarons. In particular, to probe the quasi-particle residue we employ injection or reverse radiofrequency spectroscopy [143], while the lifetime is extracted via a Ramsey sequence [145]. In the case of two impurities we unravel several interfering pathways by which different Fermi polaron states can be excited. Importantly, for strong interactions multiple peaks appear in the injection spectrum. Among these peaks only one involves a state where both impurities are simultaneously interacting with their environment, realizing two polarons. The remainder of the peaks correspond to distinct single polaron resonances, where either the bath or the impurity are motionally excited. By examining the location of the two-polaron resonance for varying interaction strength we unveil that it is hardly shifted from the corresponding resonance of a single Fermi polaron, found in the case of one impurity. The absence of such a shift is in agreement to recent experiments [98]. Nevertheless, significant impurity-impurity induced interactions, mediated via the fermionic environment, are present in the two-polaron state. We demonstrate that in order to probe them an alternative measure is required. An example of such a quantity is the relative distance between two impurities, which constitutes an experimentally relevant quantity [306]. We observe that the relative distance of the two polarons decreases as the bath-impurity interactions increase, demonstrating that Fermi polarons experience a significant effective attraction.

We next turn our attention to the case of Bose polarons [K4–K6]. In the literature Bose polarons are expected to be quite robust [179, 180]. Here, we demonstrate that non-linear effects under certain conditions can lead to their dynamical decay, realizing a phenomenon that we dub “temporal orthogonality catastrophe” [K4]. To characterize this and related effects we employ quench-like spectroscopic protocols where the transition of the spin of the impurity is induced by a strong pulse (within the diabatic regime of spin-transfer, see Sec. 2.5.1B). This is approximately equivalent to an abrupt increase of the interaction strength, which notably is also possible in ultracold atoms [393–396]. Our main tool for characterizing the dynamics of Bose polarons relies on Ramsey spectroscopy [145], allowing for tracking the dynamical structure factor of the composite bath-impurity system. In addition, several elusive features of the 1D Bose polaron dynamics can be understood by employing the pump-probe technique [K6], especially regarding the stability properties of the polaron. Below we provide a short summary of the features of Bose polaron dynamics as they were unveiled in Ref. [K4–K6].

CONCLUSIONS AND OUTLOOK

Focussing on the repulsive Bose polaron, three regimes of impurity dynamics are observed [K4]. The first, refers to the impurity-medium weak interaction regime where the polaron is largely stable and, as the structure factor reveals, possesses a large overlap with the corresponding non-interacting configuration. The second regime corresponds to large fluctuations of the dynamical structure factor, indicating a stable Bose polaron, but possessing a significantly altered state from the non-interacting one. Finally, for strong repulsions the temporal orthogonality catastrophe emerges. Here, after a brief oscillatory behaviour, the structure factor decays to a value proximal to zero.

In this characterization, the effective potential created by the inhomogeneous bath density which affects the impurity, provides an intuitive picture (see also Ref. [211, 212]). The shape of this effective potential is altered from a harmonic trap, for small interactions, to a square-well like form and, finally for large interactions, it attains a double-well structure. The change of the effective potential with increasing interaction strength explains the increase of the amplitude of the structure factor oscillations. In particular, the interacting portion of the impurity density avoids the trap center, where it was initially placed, due to the large density-density interaction that experiences in this region. In addition, by considering the effective potential in conjunction to well-known nonlinear mechanisms occurring in BEC systems [200, 207–210, 386, 388], a simple-mechanism explaining the emergence of temporal orthogonality catastrophe is captured. More specifically, the double-well form of the effective potential, for repulsive interactions exceeding the bath intraspecies ones, forces the impurity to accelerate towards the periphery of the bosonic environment. If the velocity of the impurity exceeds a critical value, the BEC is excited, in agreement to the Landau criterion for superfluidity [201]. These excitations lead to an energy transfer from the impurity to its environment, leading to an attenuating motion. Finally, the impurity localizes in the periphery of its host, realizing this way a phase separated state [202–206]. The above clearly indicate the importance of non-linear effects in the dynamics of Bose polarons.

Turning our attention to attractive bath-impurity interactions we observe a similar response as in the weakly-repulsive impurity case, associated with the oscillatory behaviour of the Ramsey contrast, due to the presence of the attractive Bose polaron [K5]. However, in this case, depending also on the magnitude of the attractive interaction, the bosonic environment is prominently deformed. In particular, due to the attractive nature of the impurity-bath interactions, the impurities effectively experience a stronger effective confinement potential, leading to their increased localization at the trap center. Subsequently, the bath atoms are attracted to this density increase of impurity particles, leading also to the development of a density peak of the BEC in the vicinity of the impurities. These result to prominent fluctuations of the Ramsey contrast, indicating the strong suppression of the dynamical structure factor during the dynamics, as a result of the strong excitation of the bosonic environment.

The question of impurity-impurity interactions was also addressed within our Bose polaron studies [K5]. Similarly, to the Fermi polaron case [K3] the difference in the Bose polaron energy between a two-polaron state and a single polaron one, hardly reveals the presence of induced polaron-polaron interactions, except for the case of strong

impurity-bath attractions. As we demonstrate, the relative distance of the impurities is a valuable quantity to characterize the polaron-polaron interactions. More specifically, it reveals that, within their equilibrium state, two impurities that are interacting with a bosonic environment tend to lie closer together than a model of uncoupled polarons would predict, demonstrating the presence of an effective attraction. However, these mediated interactions are found to be quite weak, as, even a small s -wave repulsion, largely counteracts their imprint on the relative distance. Unsurprisingly, the relative distance indicates that these effective interactions become more pronounced for larger attractions [365], where also a substantial deviation between the single and two polaron energies is observed. The fact that effective interactions are much more prominent for attractive impurity-medium strengths can be attributed to the dramatic modification of the density of the bosonic host. In particular, strongly interacting attractive Bose polarons realize a bipolaron [162, 164, 166, 365], where two-polarons bind to form a composite structure, due to their strong effective attraction. Pump-probe spectroscopy allows for further probes of the induced impurity-impurity interactions [K6]. In particular, features attributed to induced interaction have been identified in the pump-probe spectrum for attractive, moderate and strong repulsive bath-impurity interactions and for two bosonic, or fermionic impurities. In conclusion, impurity-impurity interactions of confined Bose polarons are quite weak, but they are expected to be observable by employing appropriate detection schemes.

Our analysis in [K4–K6] explicated the importance of the effective potential in the dynamics of Bose polarons and the related emergence of the orthogonality catastrophe phenomenon. When pondering on the generalization of the results presented in this thesis, there are several avenues of further study that become evident. The first such direction regards the manipulation of the effective potential. As we have demonstrated, see Sec. 2.4.4, the effective potential is an inescapable consequence for trapped systems that alters their behaviour from homogeneous ones. Therefore, the first path for extension of our work, presented within this thesis, relies on the utilization of this effective potential. As we have seen, for mass-balanced particles the effective potential changes from a parabolic to a double-well form when the interspecies interactions exceed the intraspecies ones, precluding, therefore, access to the strongly correlated regime, by favoring phase separation [K4]. The form of the effective potential can be manipulated by tuning the mass, or modifying the imposed harmonic confinement of the impurity atoms. Such manipulations might lead to the realization of strongly coupled and stable, towards temporal orthogonality catastrophe, impurity-bath states and allow for the separate study of the effects stemming from the imposed confinement and the mobility of impurity atoms. Notice, that novel experimental techniques, see also Sec. 2.1.2, allow for the hyperfine state-selective modification of the atomic potential, allowing for the independent manipulation of confining frequencies, even in the case of homonuclear mixtures. In addition, the case of a Bose gas, experiencing a box-like confinement [29–32], is particularly interesting. Notice that such setups have been proposed recently as a solution for isolating trap effects from impurity mobility ones. In this case there is also an effective potential emanating in the system stemming from the

CONCLUSIONS AND OUTLOOK

inhomogeneous density of the bath, close to the walls of the box. Understanding the importance of such an effective potential might prove crucial for future experiments.

The extension to multidimensional setups is also highly desirable, especially regarding the phenomenon of orthogonality catastrophe. More specifically, the temporal orthogonality catastrophe is connected with the effective potential, possessing a double-well form for strong bath-impurity repulsions and forcing the impurity particles, initially placed at the trap center, to accelerate towards the periphery of the bath cloud [K4,K6]. This acceleration consequently causes the impurities to reach a velocity larger than the critical one of the BEC, resulting in the excitation of their Bose environment and, consequently, in the manifestation of orthogonality catastrophe. However, due to the nature of the ultracold collisions at different spatial dimensions, we expect that this phenomenon might be significantly altered in higher dimensions. In particular, two elastically colliding atoms in 1D, can only back-scatter by exchanging their momentum. Accordingly we expect that, generally, when a 1D quantum-gas expands within a different quantum gas, then there will be a ballistically expanding portion, referring to the particles that have not experienced collisions and a diffusively expanding portion, stemming from the particles that have scattered with their host. In the case that there is a sizable potential that favors the ballistically expanding gas, as is the case of a double-well effective potential [K4], we expect that the diffusive portion will be negligible. However, this is not the case in multiple dimensions. More specifically, for $d > 2$ dimensions the elastic collision of two particles changes the direction of their momenta [247]. Therefore, for the expansion dynamics of impurities embedded within a Bose gas we expect a Brownian-type dynamics [397], with a pronounced diffusive character. In this case, the acceleration of the impurities in the Mexican-hat shaped effective potential might be counteracted by their diffusive dynamics, leading to a reduced amount of induced excitations of the bosonic host and the absence of the temporal orthogonality catastrophe.

A third-extension of our work regards the effect of temperature in the impurity dynamics [398–400]. In particular, the small impurity number involved in the experiment might render the impurities vulnerable to thermal fluctuations of the more extensive BEC, they are embedded in. Notice also, that the tendency of impurities to escape the spatial extent of the BEC and to accumulate in its periphery, for strong inter-species interactions, might promote the influence of such thermal effects, since the thermal fraction of a Bose gas tends to be larger in the region directly outside of the Thomas-Fermi radius [22,23]. Understanding the interplay of thermal fluctuations and temporal orthogonality catastrophe might, indeed, be important for the experimental identification of this mechanism.

Acknowledgements

First and foremost, I would like to thank my supervisor, Professor Peter Schmelcher, for introducing me into the field of ultracold atoms, his support and guidance in my doctoral research. Second, I would like to thank Dr. Simeon Mistakidis for easing my transition into the field, and for the numerous collaborations and “fights” we have given together. Much of the projects success is owed to him, but also to the essential contribution of Dr. Garyfallia Katsimiga whom I also cordially thank. In addition, I am indebted to Professor Panagiotis (Peter) Lambropoulos and Dr. Evangelos Karamatskos for their recommendation to join Peter’s group which enabled me to be embedded in this productive and friendly environment, as well as, for their support especially on the initial stages of my PhD studies. I would like to express my gratitude to Professor Panagiotis Kevrekidis, Professor Thomas Busch, Professor Hossein Sadeghpour, Dr. Fabian Grusdt, and Dr. Julliete Simonet for several discussions and the fruitful collaborations we have shared.

It has also been a great pleasure to work and interact scientifically with all the members of Professor Schmelcher’s group, including Simos, Garyfallia, Giorgos, Christian, Alexandra, Antonio, Fabian, Kevin, Frederic, Maxim, Malte, Lushuai, Johannes, Valentin, Sven, Markus, Aritra, Thomas, Andrea, Jie, Dan, Jan, Alejandro, Christian and Ansgar. Furthermore, I am indebted to Simos Mistakidis, Alexandra Zampetaki, Christian Morfonios, Garyfallia Katsimiga, and Kevin Keiler for proof-reading this thesis. I am heartfully thankful to my friends and colleagues Simos, Garyfallia, Giorgos, Christian, Alexandra and Panos for many extended and insightful discussions and their support. I have been also privileged to collaborate with the incredible graduate students Tobias Klafka, Alexander Illin, Julius Seeger and recently Judith Becker. Many thanks to all of them for their work and scientific exchanges.

Outside of my direct scientific environment I had the pleasure to meet many people of different walks of life that in their unique way have assisted me. I would have liked to thank each one of them individually if not for the limited space I have here. However, it would be a huge omission if I would not thank my new friends, Maria Kokkinidou, Eleni Ntomari, Evangelos Karamatskos, Eleftheria Fillipaki, Monica Ott, as well as the young Sonja and Elina, for their support during my studies. Of course, when you make new friends is important to not forget the old ones! Therefore, I owe my heartfelt thanks to Nikos Angelinos, Natalia Pinirtzi, Didi Atanasova, Thanos Lampronikos, and Christos Mourikis for supporting me throughout my academic journeys and offer my

ACKNOWLEDGMENTS

best wishes for their careers in science and beyond. Finally, with sincere respect I would like to thank Fr. Georgios Manos for his aid to me and more generally to the people of Hamburg.

I am grateful for generous financial support from the Center of Ultrafast imaging via the Cluster of Excellence “Advanced Imaging of Matter” of the Deutsche Forschungsgemeinschaft (DFG). I would also like to extend my thanks to all the members of the cluster for the assistance and the joyous moments we have shared during the numerous cluster events. I am especially thankful to Dr. Antonio Negretti and Dr. Johannes Schürer for their assistance.

Last but not least, there is an immense debt I owe to my parents, Maria and Michail, and my brother, Aristidis, that have assisted me immeasurable times all these years and despite being ≈ 2300 km away continue to stand by me and my decisions. I want to also give thanks to my soon-to-be spouse Alexandra, and her family, especially her parents Vassilis and Maria for their support and for providing me a second place to call home.

Bibliography

- [1] M. H. Anderson, J. R. Ensher, M. R. Matthews, C. E. Wieman, and E. A. Cornell, “Observation of Bose-Einstein Condensation in a Dilute Atomic Vapor”, *Science* **269**, 198 (1995).
- [2] K. B. Davis, M. O. Mewes, M. R. Andrews, N. J. van Druten, D. S. Durfee, D. M. Kurn, and W. Ketterle, “Bose-Einstein Condensation in a Gas of Sodium Atoms”, *Phys. Rev. Lett.* **75**, 3969 (1995).
- [3] A. G. Truscott, K. E. Strecker, W. I. McAlexander, G. B. Partridge, and R. G. Hulet, “Observation of Fermi Pressure in a Gas of Trapped Atoms”, *Science* **291**, 2570 (2001).
- [4] G. Roati, F. Riboli, G. Modugno, and M. Inguscio, “Fermi-Bose Quantum Degenerate ^{40}K – ^{87}Rb Mixture with Attractive Interaction”, *Phys. Rev. Lett.* **89**, 150403 (2002).
- [5] Z. Hadzibabic, S. Gupta, C. A. Stan, C. H. Schunck, M. W. Zwierlein, K. Dieckmann, and W. Ketterle, “Fiftyfold Improvement in the Number of Quantum Degenerate Fermionic Atoms”, *Phys. Rev. Lett.* **91**, 160401 (2003).
- [6] G. Modugno, G. Roati, and M. Inguscio, “Quantum degenerate potassium-rubidium mixtures”, *Fortschritte der Phys.* **51**, 396 (2003).
- [7] C. Silber, S. Günther, C. Marzok, B. Deh, P. W. Courteille, and C. Zimmermann, “Quantum-Degenerate Mixture of Fermionic Lithium and Bosonic Rubidium Gases”, *Phys. Rev. Lett.* **95**, 170408 (2005).
- [8] M. Taglieber, A.-C. Voigt, T. Aoki, T. W. Hänsch, and K. Dieckmann, “Quantum Degenerate Two-Species Fermi-Fermi Mixture Coexisting with a Bose-Einstein Condensate”, *Phys. Rev. Lett.* **100**, 010401 (2008).
- [9] N. Spethmann, F. Kindermann, S. John, C. Weber, D. Meschede, and A. Widera, “Dynamics of Single Neutral Impurity Atoms Immersed in an Ultracold Gas”, *Phys. Rev. Lett.* **109**, 235301 (2012).
- [10] A. Khramov, A. Hansen, W. Dowd, R. J. Roy, C. Makrides, A. Petrov, S. Kotochigova, and S. Gupta, “Ultracold Heteronuclear Mixture of Ground and Excited State Atoms”, *Phys. Rev. Lett.* **112**, 033201 (2014).
- [11] C. J. Myatt, E. A. Burt, R. W. Ghrist, E. A. Cornell, and C. E. Wieman, “Production of Two Overlapping Bose-Einstein Condensates by Sympathetic Cooling”, *Phys. Rev. Lett.* **78**, 586 (1997).
- [12] D. S. Hall, M. R. Matthews, C. E. Wieman, and E. A. Cornell, “Measurements of Relative Phase in Two-Component Bose-Einstein Condensates”, *Phys. Rev. Lett.* **81**, 1543 (1998).

BIBLIOGRAPHY

- [13] D. S. Hall, M. R. Matthews, J. R. Ensher, C. E. Wieman, and E. A. Cornell, “Dynamics of Component Separation in a Binary Mixture of Bose-Einstein Condensates”, *Phys. Rev. Lett.* **81**, 1539 (1998).
- [14] D. M. Stamper-Kurn, M. R. Andrews, A. P. Chikkatur, S. Inouye, H.-J. Miesner, J. Stenger, and W. Ketterle, “Optical Confinement of a Bose-Einstein Condensate”, *Phys. Rev. Lett.* **80**, 2027 (1998).
- [15] W. Dowd, R. J. Roy, R. K. Shrestha, A. Petrov, C. Makrides, S. Kotochigova, and S. Gupta, “Magnetic field dependent interactions in an ultracold Li–Yb(3P2) mixture”, *New J. Phys.* **17**, 055007 (2015).
- [16] R. Roy, R. Shrestha, A. Green, S. Gupta, M. Li, S. Kotochigova, A. Petrov, and C. H. Yuen, “Photoassociative production of ultracold heteronuclear YbLi* molecules”, *Phys. Rev. A* **94**, 033413 (2016).
- [17] M. D. Barrett, J. A. Sauer, and M. S. Chapman, “All-Optical Formation of an Atomic Bose-Einstein Condensate”, *Phys. Rev. Lett.* **87**, 010404 (2001).
- [18] H. Schmaljohann, M. Erhard, J. Kronjäger, M. Kottke, S. van Staa, L. Cacciapuoti, J. J. Arlt, K. Bongs, and K. Sengstock, “Dynamics of $F = 2$ Spinor Bose-Einstein Condensates”, *Phys. Rev. Lett.* **92**, 040402 (2004).
- [19] A. Görlitz, T. L. Gustavson, A. E. Leanhardt, R. Löw, A. P. Chikkatur, S. Gupta, S. Inouye, D. E. Pritchard, and W. Ketterle, “Sodium Bose-Einstein Condensates in the $F = 2$ State in a Large-Volume Optical Trap”, *Phys. Rev. Lett.* **90**, 090401 (2003).
- [20] K. M. O’Hara, S. L. Hemmer, M. E. Gehm, S. R. Granade, and J. E. Thomas, “Observation of a Strongly Interacting Degenerate Fermi Gas of Atoms”, *Science* **298**, 2179 (2002).
- [21] T. Bourdel, J. Cubizolles, L. Khaykovich, K. M. F. Magalhães, S. J. J. M. F. Kokkelmans, G. V. Shlyapnikov, and C. Salomon, “Measurement of the Interaction Energy near a Feshbach Resonance in a ${}^6\text{Li}$ Fermi Gas”, *Phys. Rev. Lett.* **91**, 020402 (2003).
- [22] C. J. Pethick and H. Smith, *Bose-Einstein Condensation in Dilute Gases*, (Cambridge University Press, Cambridge, 2008), 2 edition.
- [23] L. Pitaevskii and S. Stringari, *Bose-Einstein condensation and superfluidity*, International series of monographs on physics, (Oxford University Press, Oxford, 2016).
- [24] S. Giorgini, L. P. Pitaevskii, and S. Stringari, “Theory of ultracold atomic Fermi gases”, *Rev. Mod. Phys.* **80**, 1215 (2008).
- [25] J. A. Sauer, M. D. Barrett, and M. S. Chapman, “Storage Ring for Neutral Atoms”, *Phys. Rev. Lett.* **87**, 270401 (2001).

- [26] I. Lesanovsky and W. von Klitzing, “Time-Averaged Adiabatic Potentials: Versatile Matter-Wave Guides and Atom Traps”, *Phys. Rev. Lett.* **99**, 083001 (2007).
- [27] S. Beattie, S. Moulder, R. J. Fletcher, and Z. Hadzibabic, “Persistent Currents in Spinor Condensates”, *Phys. Rev. Lett.* **110**, 025301 (2013).
- [28] T. A. Bell, J. A. P. Glidden, L. Humbert, M. W. J. Bromley, S. A. Haine, M. J. Davis, T. W. Neely, M. A. Baker, and H. Rubinsztein-Dunlop, “Bose–Einstein condensation in large time-averaged optical ring potentials”, *New J. Phys.* **18**, 035003 (2016).
- [29] A. L. Gaunt, T. F. Schmidutz, I. Gotlibovych, R. P. Smith, and Z. Hadzibabic, “Bose-Einstein Condensation of Atoms in a Uniform Potential”, *Phys. Rev. Lett.* **110**, 200406 (2013).
- [30] L. Corman, L. Chomaz, T. Bienaimé, R. Desbuquois, C. Weitenberg, S. Nascimbène, J. Dalibard, and J. Beugnon, “Quench-Induced Supercurrents in an Annular Bose Gas”, *Phys. Rev. Lett.* **113**, 135302 (2014).
- [31] B. Mukherjee, Z. Yan, P. B. Patel, Z. Hadzibabic, T. Yefsah, J. Struck, and M. W. Zwierlein, “Homogeneous Atomic Fermi Gases”, *Phys. Rev. Lett.* **118**, 123401 (2017).
- [32] K. Hueck, N. Luick, L. Sobirey, J. Siegl, T. Lompe, and H. Moritz, “Two-Dimensional Homogeneous Fermi Gases”, *Phys. Rev. Lett.* **120**, 060402 (2018).
- [33] A. Görlitz, J. M. Vogels, A. E. Leanhardt, C. Raman, T. L. Gustavson, J. R. Abo-Shaeer, A. P. Chikkatur, S. Gupta, S. Inouye, T. Rosenband, and W. Ketterle, “Realization of Bose-Einstein Condensates in Lower Dimensions”, *Phys. Rev. Lett.* **87**, 130402 (2001).
- [34] M. Greiner, I. Bloch, O. Mandel, T. W. Hänsch, and T. Esslinger, “Exploring Phase Coherence in a 2D Lattice of Bose-Einstein Condensates”, *Phys. Rev. Lett.* **87**, 160405 (2001).
- [35] H. Moritz, T. Stöferle, M. Köhl, and T. Esslinger, “Exciting Collective Oscillations in a Trapped 1D Gas”, *Phys. Rev. Lett.* **91**, 250402 (2003).
- [36] M. A. Cazalilla, R. Citro, T. Giamarchi, E. Orignac, and M. Rigol, “One dimensional bosons: From condensed matter systems to ultracold gases”, *Rev. Mod. Phys.* **83**, 1405 (2011).
- [37] I. Bloch, J. Dalibard, and W. Zwerger, “Many-body physics with ultracold gases”, *Rev. Mod. Phys.* **80**, 885 (2008).
- [38] P. Soltan-Panahi, J. Struck, P. Hauke, A. Bick, W. Plenkers, G. Meineke, C. Becker, P. Windpassinger, M. Lewenstein, and K. Sengstock, “Multi-component quantum gases in spin-dependent hexagonal lattices”, *Nat. Phys.* **7**, 434 (2011).

BIBLIOGRAPHY

- [39] P. Soltan-Panahi, D.-S. Lühmann, J. Struck, P. Windpassinger, and K. Sengstock, “Quantum phase transition to unconventional multi-orbital superfluidity in optical lattices”, *Nat. Phys.* **8**, 71 (2012).
- [40] D.-S. Lühmann, O. Jürgensen, M. Weinberg, J. Simonet, P. Soltan-Panahi, and K. Sengstock, “Quantum phases in tunable state-dependent hexagonal optical lattices”, *Phys. Rev. A* **90**, 013614 (2014).
- [41] S. Taie, H. Ozawa, T. Ichinose, T. Nishio, S. Nakajima, and Y. Takahashi, “Coherent driving and freezing of bosonic matter wave in an optical Lieb lattice”, *Sci. Adv.* **1** (2015).
- [42] B. Paredes, A. Widera, V. Murg, O. Mandel, S. Fölling, I. Cirac, G. V. Shlyapnikov, T. W. Hänsch, and I. Bloch, “Tonks-Girardeau gas of ultracold atoms in an optical lattice”, *Nature* **429**, 277 (2004).
- [43] A. H. van Amerongen, J. J. P. van Es, P. Wicke, K. V. Kheruntsyan, and N. J. van Druten, “Yang-Yang Thermodynamics on an Atom Chip”, *Phys. Rev. Lett.* **100**, 090402 (2008).
- [44] S. Hofferberth, I. Lesanovsky, T. Schumm, A. Imambekov, V. Gritsev, E. Demler, and J. Schmiedmayer, “Probing quantum and thermal noise in an interacting many-body system”, *Nat. Phys.* **4**, 489 (2008).
- [45] E. Haller, R. Hart, M. J. Mark, J. G. Danzl, L. Reichsöllner, M. Gustavsson, M. Dalmonte, G. Pupillo, and H.-C. Nägerl, “Pinning quantum phase transition for a Luttinger liquid of strongly interacting bosons”, *Nature* **466**, 597 (2010).
- [46] B. Yang, Y.-Y. Chen, Y.-G. Zheng, H. Sun, H.-N. Dai, X.-W. Guan, Z.-S. Yuan, and J.-W. Pan, “Quantum criticality and the Tomonaga-Luttinger liquid in one-dimensional Bose gases”, *Phys. Rev. Lett.* **119**, 165701 (2017).
- [47] T. L. Yang, P. Grišins, Y. T. Chang, Z. H. Zhao, C. Y. Shih, T. Giamarchi, and R. G. Hulet, “Measurement of the Dynamical Structure Factor of a 1D Interacting Fermi Gas”, *Phys. Rev. Lett.* **121**, 103001 (2018).
- [48] F. S. Cataliotti, S. Burger, C. Fort, P. Maddaloni, F. Minardi, A. Trombettoni, A. Smerzi, and M. Inguscio, “Josephson Junction Arrays with Bose-Einstein Condensates”, *Science* **293**, 843 (2001).
- [49] M. Albiez, R. Gati, J. Fölling, S. Hunsmann, M. Cristiani, and M. K. Oberthaler, “Direct Observation of Tunneling and Nonlinear Self-Trapping in a Single Bosonic Josephson Junction”, *Phys. Rev. Lett.* **95**, 010402 (2005).
- [50] G. Valtolina, A. Burchianti, A. Amico, E. Neri, K. Xhani, J. A. Seman, A. Trombettoni, A. Smerzi, M. Zaccanti, M. Inguscio, and G. Roati, “Josephson effect in fermionic superfluids across the BEC-BCS crossover”, *Science* **350**, 1505 (2015).

- [51] M. Pigneur, T. Berrada, M. Bonneau, T. Schumm, E. Demler, and J. Schmiedmayer, “Relaxation to a Phase-Locked Equilibrium State in a One-Dimensional Bosonic Josephson Junction”, *Phys. Rev. Lett.* **120**, 173601 (2018).
- [52] M. Greiner, O. Mandel, T. Esslinger, T. W. Hänsch, and I. Bloch, “Quantum phase transition from a superfluid to a Mott insulator in a gas of ultracold atoms”, *Nature* **415**, 39 (2002).
- [53] T. Stöferle, H. Moritz, C. Schori, M. Köhl, and T. Esslinger, “Transition from a Strongly Interacting 1D Superfluid to a Mott Insulator”, *Phys. Rev. Lett.* **92**, 130403 (2004).
- [54] I. B. Spielman, W. D. Phillips, and J. V. Porto, “Mott-Insulator Transition in a Two-Dimensional Atomic Bose Gas”, *Phys. Rev. Lett.* **98**, 080404 (2007).
- [55] I. B. Spielman, W. D. Phillips, and J. V. Porto, “Condensate Fraction in a 2D Bose Gas Measured across the Mott-Insulator Transition”, *Phys. Rev. Lett.* **100**, 120402 (2008).
- [56] M. Köhl, H. Moritz, T. Stöferle, K. Günter, and T. Esslinger, “Fermionic Atoms in a Three Dimensional Optical Lattice: Observing Fermi Surfaces, Dynamics, and Interactions”, *Phys. Rev. Lett.* **94**, 080403 (2005).
- [57] R. Jördens, N. Strohmaier, K. Günter, H. Moritz, and T. Esslinger, “A Mott insulator of fermionic atoms in an optical lattice”, *Nature* **455**, 204 (2008).
- [58] A. Mazurenko, C. S. Chiu, G. Ji, M. F. Parsons, M. Kanász-Nagy, R. Schmidt, F. Grusdt, E. Demler, D. Greif, and M. Greiner, “A cold-atom Fermi-Hubbard antiferromagnet”, *Nature* **545**, 462 (2017).
- [59] C. S. Chiu, G. Ji, A. Bohrdt, M. Xu, M. Knap, E. Demler, F. Grusdt, M. Greiner, and D. Greif, “String patterns in the doped Hubbard model”, *Science* **365**, 251 (2019).
- [60] J. Koepsell, J. Vijayan, P. Sompet, F. Grusdt, T. A. Hilker, E. Demler, G. Salomon, I. Bloch, and C. Gross, “Imaging magnetic polarons in the doped Fermi-Hubbard model”, *Nature* **572**, 358 (2019).
- [61] J. Vijayan, P. Sompet, G. Salomon, J. Koepsell, S. Hirthe, A. Bohrdt, F. Grusdt, I. Bloch, and C. Gross, “Time-resolved observation of spin-charge deconfinement in fermionic Hubbard chains”, *Science* **367**, 186 (2020).
- [62] J. Koepsell, D. Bourgund, P. Sompet, S. Hirthe, A. Bohrdt, Y. Wang, F. Grusdt, E. Demler, G. Salomon, C. Gross, and I. Bloch, “Microscopic evolution of doped Mott insulators from polaronic metal to Fermi liquid”, arXiv: **2009.04440** (2020).
- [63] X.-J. Liu, K. T. Law, T. K. Ng, and P. A. Lee, “Detecting Topological Phases in Cold Atoms”, *Phys. Rev. Lett.* **111**, 120402 (2013).

BIBLIOGRAPHY

- [64] M. Atala, M. Aidelsburger, J. T. Barreiro, D. Abanin, T. Kitagawa, E. Demler, and I. Bloch, “Direct measurement of the Zak phase in topological Bloch bands”, *Nat. Phys.* **9**, 795 (2013).
- [65] M. Atala, M. Aidelsburger, M. Lohse, J. T. Barreiro, B. Paredes, and I. Bloch, “Observation of chiral currents with ultracold atoms in bosonic ladders”, *Nat. Phys.* **10**, 588 (2014).
- [66] G. Jotzu, M. Messer, R. Desbuquois, M. Lebrat, T. Uehlinger, D. Greif, and T. Esslinger, “Experimental realization of the topological Haldane model with ultracold fermions”, *Nature* **515**, 237 (2014).
- [67] M. Aidelsburger, M. Lohse, C. Schweizer, M. Atala, J. T. Barreiro, S. Nascimbène, N. Â. R. Cooper, I. Bloch, and N. Goldman, “Measuring the Chern number of Hofstadter bands with ultracold bosonic atoms”, *Nat. Phys.* **11**, 162 (2015).
- [68] L. Duca, T. Li, M. Reitter, I. Bloch, M. Schleier-Smith, and U. Schneider, “An Aharonov-Bohm interferometer for determining Bloch band topology”, *Science* **347**, 288 (2015).
- [69] M. Mancini, G. Pagano, G. Cappellini, L. Livi, M. Rider, J. Catani, C. Sias, P. Zoller, M. Inguscio, M. Dalmonte, and L. Fallani, “Observation of chiral edge states with neutral fermions in synthetic Hall ribbons”, *Science* **349**, 1510 (2015).
- [70] B. K. Stuhl, H.-I. Lu, L. M. Ayccock, D. Genkina, and I. B. Spielman, “Visualizing edge states with an atomic Bose gas in the quantum Hall regime”, *Science* **349**, 1514 (2015).
- [71] N. Fläschner, B. S. Rem, M. Tarnowski, D. Vogel, D.-S. Lühmann, K. Sengstock, and C. Weitenberg, “Experimental reconstruction of the Berry curvature in a Floquet Bloch band”, *Science* **352**, 1091 (2016).
- [72] T. Li, L. Duca, M. Reitter, F. Grusdt, E. Demler, M. Endres, M. Schleier-Smith, I. Bloch, and U. Schneider, “Bloch state tomography using Wilson lines”, *Science* **352**, 1094 (2016).
- [73] Z. Wu, L. Zhang, W. Sun, X.-T. Xu, B.-Z. Wang, S.-C. Ji, Y. Deng, S. Chen, X.-J. Liu, and J.-W. Pan, “Realization of two-dimensional spin-orbit coupling for Bose-Einstein condensates”, *Science* **354**, 83 (2016).
- [74] M. Leder, C. Grossert, L. Sitta, M. Genske, A. Rosch, and M. Weitz, “Real-space imaging of a topologically protected edge state with ultracold atoms in an amplitude-chirped optical lattice”, *Nat. Com.* **7**, 13112 (2016).
- [75] E. J. Meier, F. A. An, and B. Gadway, “Observation of the topological soliton state in the Su-Schrieffer-Heeger model”, *Nat. Com.* **7**, 13986 (2016).

- [76] B. Song, L. Zhang, C. He, T. F. J. Poon, E. Hajiyev, S. Zhang, X.-J. Liu, and G.-B. Jo, “Observation of symmetry-protected topological band with ultracold fermions”, *Sci. Adv.* **4** (2018).
- [77] C. Chin, R. Grimm, P. Julienne, and E. Tiesinga, “Feshbach resonances in ultracold gases”, *Rev. Mod. Phys.* **82**, 1225 (2010).
- [78] R. P. Feynman, “Simulating physics with computers”, *Int. J. Theor. Phys.* **21**, 467 (1982).
- [79] I. M. Georgescu, S. Ashhab, and F. Nori, “Quantum simulation”, *Rev. Mod. Phys.* **86**, 153 (2014).
- [80] C. Gross and I. Bloch, “Quantum simulations with ultracold atoms in optical lattices”, *Science* **357**, 995 (2017).
- [81] M. Boninsegni and N. V. Prokof’ev, “Colloquium: Supersolids: What and where are they?”, *Rev. Mod. Phys.* **84**, 759 (2012).
- [82] L. Tanzi, E. Lucioni, F. Famà, J. Catani, A. Fioretti, C. Gabbanini, R. N. Bisset, L. Santos, and G. Modugno, “Observation of a Dipolar Quantum Gas with Metastable Supersolid Properties”, *Phys. Rev. Lett.* **122**, 130405 (2019).
- [83] F. Böttcher, J.-N. Schmidt, M. Wenzel, J. Hertkorn, M. Guo, T. Langen, and T. Pfau, “Transient Supersolid Properties in an Array of Dipolar Quantum Droplets”, *Phys. Rev. X* **9**, 011051 (2019).
- [84] G. Natale, R. M. W. van Bijnen, A. Patscheider, D. Petter, M. J. Mark, L. Chomaz, and F. Ferlaino, “Excitation Spectrum of a Trapped Dipolar Supersolid and Its Experimental Evidence”, *Phys. Rev. Lett.* **123**, 050402 (2019).
- [85] L. Chomaz, D. Petter, P. Ilzhöfer, G. Natale, A. Trautmann, C. Politi, G. Durastante, R. M. W. van Bijnen, A. Patscheider, M. Sohmen, M. J. Mark, and F. Ferlaino, “Long-Lived and Transient Supersolid Behaviors in Dipolar Quantum Gases”, *Phys. Rev. X* **9**, 021012 (2019).
- [86] M. Tomza, K. Jachymski, R. Gerritsma, A. Negretti, T. Calarco, Z. Idziaszek, and P. S. Julienne, “Cold hybrid ion-atom systems”, *Rev. Mod. Phys.* **91**, 035001 (2019).
- [87] Y. Kawaguchi and M. Ueda, “Spinor Bose–Einstein condensates”, *Phys. Rep.* **520**, 253 (2012).
- [88] D. M. Stamper-Kurn and M. Ueda, “Spinor Bose gases: Symmetries, magnetism, and quantum dynamics”, *Rev. Mod. Phys.* **85**, 1191 (2013).
- [89] J. Catani, G. Lamporesi, D. Naik, M. Gring, M. Inguscio, F. Minardi, A. Kantian, and T. Giamarchi, “Quantum dynamics of impurities in a one-dimensional Bose gas”, *Phys. Rev. A* **85**, 023623 (2012).

BIBLIOGRAPHY

- [90] G. Zürn, T. Lompe, A. N. Wenz, S. Jochim, P. S. Julienne, and J. M. Hutson, “Precise Characterization of ${}^6\text{Li}$ Feshbach Resonances Using Trap-Sideband-Resolved RF Spectroscopy of Weakly Bound Molecules”, *Phys. Rev. Lett.* **110**, 135301 (2013).
- [91] N. B. Jørgensen, L. Wacker, K. T. Skalmstang, M. M. Parish, J. Levinsen, R. S. Christensen, G. M. Bruun, and J. J. Arlt, “Observation of Attractive and Repulsive Polarons in a Bose-Einstein Condensate”, *Phys. Rev. Lett.* **117**, 055302 (2016).
- [92] R. Schmidt, M. Knap, D. A. Ivanov, J.-S. You, M. Cetina, and E. Demler, “Universal many-body response of heavy impurities coupled to a Fermi sea: a review of recent progress”, *Rep. Prog. Phys.* **81**, 024401 (2018).
- [93] Q. Bouton, J. Nettersheim, D. Adam, F. Schmidt, D. Mayer, T. Lausch, E. Tiemann, and A. Widera, “Single-Atom Quantum Probes for Ultracold Gases Boosted by Nonequilibrium Spin Dynamics”, *Phys. Rev. X* **10**, 011018 (2020).
- [94] G.-B. Jo, Y.-R. Lee, J.-H. Choi, C. A. Christensen, T. H. Kim, J. H. Thywissen, D. E. Pritchard, and W. Ketterle, “Itinerant Ferromagnetism in a Fermi Gas of Ultracold Atoms”, *Science* **325**, 1521 (2009).
- [95] D. Pekker, M. Babadi, R. Sensarma, N. Zinner, L. Pollet, M. W. Zwierlein, and E. Demler, “Competition between Pairing and Ferromagnetic Instabilities in Ultracold Fermi Gases near Feshbach Resonances”, *Phys. Rev. Lett.* **106**, 050402 (2011).
- [96] C. Sanner, E. J. Su, W. Huang, A. Keshet, J. Gillen, and W. Ketterle, “Correlations and Pair Formation in a Repulsively Interacting Fermi Gas”, *Phys. Rev. Lett.* **108**, 240404 (2012).
- [97] G. Valtolina, F. Scazza, A. Amico, A. Burchianti, A. Recati, T. Enss, M. Inguscio, M. Zaccanti, and G. Roati, “Exploring the ferromagnetic behaviour of a repulsive Fermi gas through spin dynamics”, *Nat. Phys.* **13**, 704 (2017).
- [98] F. Scazza, G. Valtolina, P. Massignan, A. Recati, A. Amico, A. Burchianti, C. Fort, M. Inguscio, M. Zaccanti, and G. Roati, “Repulsive Fermi Polarons in a Resonant Mixture of Ultracold ${}^6\text{Li}$ Atoms”, *Phys. Rev. Lett.* **118**, 083602 (2017).
- [99] W. Li and X. Cui, “Repulsive Fermi polarons with negative effective mass”, *Phys. Rev. A* **96**, 053609 (2017).
- [100] A. Amico, F. Scazza, G. Valtolina, P. E. S. Tavares, W. Ketterle, M. Inguscio, G. Roati, and M. Zaccanti, “Time-Resolved Observation of Competing Attractive and Repulsive Short-Range Correlations in Strongly Interacting Fermi Gases”, *Phys. Rev. Lett.* **121**, 253602 (2018).
- [101] F. Scazza, G. Valtolina, A. Amico, P. E. S. Tavares, M. Inguscio, W. Ketterle, G. Roati, and M. Zaccanti, “Exploring emergent heterogeneous phases in strongly repulsive Fermi gases”, *Phys. Rev. A* **101**, 013603 (2020).

- [102] D. Vollhardt, N. Blümer, K. Held, and M. Kollar, *Metallic Ferromagnetism - An Electronic Correlation Phenomenon*, volume 580, p. 191 (2001).
- [103] M. Brando, D. Belitz, F. M. Grosche, and T. R. Kirkpatrick, “Metallic quantum ferromagnets”, *Rev. Mod. Phys.* **88**, 025006 (2016).
- [104] E. C. Stoner, “LXXX. Atomic moments in ferromagnetic metals and alloys with non-ferromagnetic elements”, *London, Edinburgh, Dublin Philos. Mag. J. Sci.* **15**, 1018 (1933).
- [105] F. Bloch, “Bemerkung zur Elektronentheorie des Ferromagnetismus und der elektrischen Leitfähigkeit”, *Z. Phys.* **57**, 545 (1929).
- [106] M. S. Hossain, T. Zhao, S. Pu, M. A. Mueed, M. K. Ma, K. A. Villegas Rosales, Y. J. Chung, L. N. Pfeiffer, K. W. West, K. W. Baldwin, J. K. Jain, and M. Shayegan, “Bloch ferromagnetism of composite fermions”, *Nat. Phys.* **17**, 48 (2021).
- [107] H. Ibach and H. Lüth, *Solid-State Physics: An Introduction to Principles of Materials Science ; with 100 Problems*, Advanced texts in physics, (Springer, Berlin Heidelberg, 2003).
- [108] J. C. Slater, “The Theory of Ferromagnetism: Lowest Energy Levels”, *Phys. Rev.* **52**, 198 (1937).
- [109] C. Herring and C. Kittel, “On the Theory of Spin Waves in Ferromagnetic Media”, *Phys. Rev.* **81**, 869 (1951).
- [110] E. Lieb and D. Mattis, “Theory of Ferromagnetism and the Ordering of Electronic Energy Levels”, *Phys. Rev.* **125**, 164 (1962).
- [111] N. D. Mermin and H. Wagner, “Absence of Ferromagnetism or Antiferromagnetism in One- or Two-Dimensional Isotropic Heisenberg Models”, *Phys. Rev. Lett.* **17**, 1133 (1966).
- [112] E. H. Lieb, “Two theorems on the Hubbard model”, *Phys. Rev. Lett.* **62**, 1201 (1989).
- [113] E. Langmann and M. Wallin, “Mean Field Magnetic Phase Diagrams for the Two Dimensional $t - t' - U$ Hubbard Model”, *J. Stat. Phys.* **127**, 825 (2007).
- [114] E. Nielsen and R. N. Bhatt, “Search for ferromagnetism in doped semiconductors in the absence of transition metal ions”, *Phys. Rev. B* **82**, 195117 (2010).
- [115] V. B. Shenoy and T.-L. Ho, “Nature and Properties of a Repulsive Fermi Gas in the Upper Branch of the Energy Spectrum”, *Phys. Rev. Lett.* **107**, 210401 (2011).

BIBLIOGRAPHY

- [116] C. Kohstall, M. Zaccanti, M. Jag, A. Trenkwalder, P. Massignan, G. M. Bruun, F. Schreck, and R. Grimm, “Metastability and coherence of repulsive polarons in a strongly interacting Fermi mixture”, *Nature* **485**, 615 (2012).
- [117] P. Massignan, M. Zaccanti, and G. M. Bruun, “Polarons, dressed molecules and itinerant ferromagnetism in ultracold Fermi gases”, *Rep. Prog. Phys.* **77**, 034401 (2014).
- [118] P. O. Fedichev, M. W. Reynolds, and G. V. Shlyapnikov, “Three-Body Recombination of Ultracold Atoms to a Weakly Bound s Level”, *Phys. Rev. Lett.* **77**, 2921 (1996).
- [119] E. Nielsen and J. H. Macek, “Low-Energy Recombination of Identical Bosons by Three-Body Collisions”, *Phys. Rev. Lett.* **83**, 1566 (1999).
- [120] B. D. Esry, C. H. Greene, and J. P. Burke, “Recombination of Three Atoms in the Ultracold Limit”, *Phys. Rev. Lett.* **83**, 1751 (1999).
- [121] P. F. Bedaque, E. Braaten, and H.-W. Hammer, “Three-body Recombination in Bose Gases with Large Scattering Length”, *Phys. Rev. Lett.* **85**, 908 (2000).
- [122] I. Zintchenko, L. Wang, and M. Troyer, “Ferromagnetism of the repulsive atomic Fermi gas: three-body recombination and domain formation”, *Eur. Phys. J. B* **89**, 180 (2016).
- [123] T. Roscilde and J. I. Cirac, “Quantum Emulsion: A Glassy Phase of Bosonic Mixtures in Optical Lattices”, *Phys. Rev. Lett.* **98**, 190402 (2007).
- [124] L. Sanchez-Palencia and M. Lewenstein, “Disordered quantum gases under control”, *Nat. Phys.* **6**, 87 (2010).
- [125] F. Serwane, G. Zürn, T. Lompe, T. B. Ottenstein, A. N. Wenz, and S. Jochim, “Deterministic Preparation of a Tunable Few-Fermion System”, *Science* **332**, 336 (2011).
- [126] S. Murmann, F. Deuretzbacher, G. Zürn, J. Bjerlin, S. M. Reimann, L. Santos, T. Lompe, and S. Jochim, “Antiferromagnetic Heisenberg Spin Chain of a Few Cold Atoms in a One-Dimensional Trap”, *Phys. Rev. Lett.* **115**, 215301 (2015).
- [127] R. Grimm, M. Weidemüller, and Y. B. Ovchinnikov, “Optical Dipole Traps for Neutral Atoms”, volume 42 of *Adv. At., Mol., Opt. Phys.*, pp. 95 – 170, (Academic Press 2000).
- [128] A. G. Volosniev, D. V. Fedorov, A. S. Jensen, M. Valiente, and N. T. Zinner, “Strongly interacting confined quantum systems in one dimension”, *Nat. Com.* **5**, 5300 (2014).

- [129] F. Deuretzbacher, D. Becker, J. Bjerlin, S. M. Reimann, and L. Santos, “Quantum magnetism without lattices in strongly interacting one-dimensional spinor gases”, *Phys. Rev. A* **90**, 013611 (2014).
- [130] X. Cui and T.-L. Ho, “Spin-orbit-coupled one-dimensional Fermi gases with infinite repulsion”, *Phys. Rev. A* **89**, 013629 (2014).
- [131] L. Yang, L. Guan, and H. Pu, “Strongly interacting quantum gases in one-dimensional traps”, *Phys. Rev. A* **91**, 043634 (2015).
- [132] J. Levinsen, P. Massignan, G. M. Bruun, and M. M. Parish, “Strong-coupling ansatz for the one-dimensional Fermi gas in a harmonic potential”, *Sci. Adv.* **1** (2015).
- [133] C. Yannouleas, B. B. Brandt, and U. Landman, “Ultracold few fermionic atoms in needle-shaped double wells: spin chains and resonating spin clusters from microscopic Hamiltonians emulated via antiferromagnetic Heisenberg and t - J models”, *New J. Phys.* **18**, 073018 (2016).
- [134] A. P. Koller, J. Mundinger, M. L. Wall, and A. M. Rey, “Demagnetization dynamics of noninteracting trapped fermions”, *Phys. Rev. A* **92**, 033608 (2015).
- [135] A. P. Koller, M. L. Wall, J. Mundinger, and A. M. Rey, “Dynamics of Interacting Fermions in Spin-Dependent Potentials”, *Phys. Rev. Lett.* **117**, 195302 (2016).
- [136] A. S. Dehkharghani, A. G. Volosniev, and N. T. Zinner, “Impenetrable mass-imbalanced particles in one-dimensional harmonic traps”, *J. Phys. B: At., Mol. Opt. Phys.* **49**, 085301 (2016).
- [137] J. Erdmann, S. I. Mistakidis, and P. Schmelcher, “Phase-separation dynamics induced by an interaction quench of a correlated Fermi-Fermi mixture in a double well”, *Phys. Rev. A* **99**, 013605 (2019).
- [138] J. Kwasniok, S. I. Mistakidis, and P. Schmelcher, “Correlated dynamics of fermionic impurities induced by the counterflow of an ensemble of fermions”, *Phys. Rev. A* **101**, 053619 (2020).
- [139] K. Haule and G. Kotliar, “Coherence-incoherence crossover in the normal state of iron oxypnictides and importance of Hund’s rule coupling”, *New J. Phys.* **11**, 025021 (2009).
- [140] J. Hu, “Iron-Based Superconductors as Odd-Parity Superconductors”, *Phys. Rev. X* **3**, 031004 (2013).
- [141] A. Georges, L. d. Medici, and J. Mravlje, “Strong Correlations from Hund’s Coupling”, *Annu. Rev. Condens. Matter Phys.* **4**, 137 (2013).
- [142] P. W. Anderson, “New Approach to the Theory of Superexchange Interactions”, *Phys. Rev.* **115**, 2 (1959).

BIBLIOGRAPHY

- [143] W. Demtröder, *Laser spectroscopy: basic concepts and instrumentation*, (Springer Science & Business Media, Berlin Heidelberg, 2003).
- [144] A. Schirotzek, C.-H. Wu, A. Sommer, and M. W. Zwierlein, “Observation of Fermi Polarons in a Tunable Fermi Liquid of Ultracold Atoms”, *Phys. Rev. Lett.* **102**, 230402 (2009).
- [145] M. Cetina, M. Jag, R. S. Lous, I. Fritsche, J. T. M. Walraven, R. Grimm, J. Levinsen, M. M. Parish, R. Schmidt, M. Knap, and E. Demler, “Ultrafast many-body interferometry of impurities coupled to a Fermi sea”, *Science* **354**, 96 (2016).
- [146] D. J. Thouless, *The Quantum Mechanics of Many-Body Systems*, volume 11 of *Pure and Applied Physics*, (Elsevier, London, 1961).
- [147] M. Knap, A. Shashi, Y. Nishida, A. Imambekov, D. A. Abanin, and E. Demler, “Time-Dependent Impurity in Ultracold Fermions: Orthogonality Catastrophe and Beyond”, *Phys. Rev. X* **2**, 041020 (2012).
- [148] L. D. Landau, “The Theory of a Fermi Liquid”, *Sov. Phys. JETP* **3**, 920 (1957).
- [149] S. I. Pekar, “Autolocalization of the electron in an inertially polarizable dielectric medium”, *Zh. Eksp. Teor. Fiz.* **16**, 335 (1946).
- [150] S. I. Pekar, “Theory of Colored Crystals”, *Zh. Eksp. Teor. Fiz.* **17**, 868 (1947).
- [151] L. D. Landau and S. I. Pekar, “Effective mass of a polaron”, *Zh. Eksp. Teor. Fiz.* **18**, 419 (1948).
- [152] H. Fröhlich, “Electrons in lattice fields”, *Adv. Phys.* **3**, 325 (1954).
- [153] L. D. Landau, “On the motion of electrons in a crystal lattice”, *Phys. Z. Sowjetunion* **3**, 664 (1933).
- [154] J. T. Devreese and F. Peeters, *Polarons and excitons in polar semiconductors and ionic crystals*, volume 108, (Springer, New York, 1984).
- [155] V. M. Kenkre, “Finite-bandwidth calculations for charge carrier mobility in organic crystals”, *Phys. Lett. A* **305**, 443 (2002).
- [156] S. Fratini and S. Ciuchi, “Bandlike Motion and Mobility Saturation in Organic Molecular Semiconductors”, *Phys. Rev. Lett.* **103**, 266601 (2009).
- [157] J. H. Fetherolf, D. Golež, and T. C. Berkelbach, “A Unification of the Holstein Polaron and Dynamic Disorder Pictures of Charge Transport in Organic Crystals”, *Phys. Rev. X* **10**, 021062 (2020).
- [158] S. Moser, L. Moreschini, J. Jaćimović, O. S. Barišić, H. Berger, A. Magrez, Y. J. Chang, K. S. Kim, A. Bostwick, E. Rotenberg, L. Forró, and M. Grioni, “Tunable Polaronic Conduction in Anatase TiO₂”, *Phys. Rev. Lett.* **110**, 196403 (2013).

-
- [159] C. Verdi, F. Caruso, and F. Giustino, “Origin of the crossover from polarons to Fermi liquids in transition metal oxides”, *Nat. Commun.* **8**, 15769 (2017).
- [160] R. P. Feynman, “Slow Electrons in a Polar Crystal”, *Phys. Rev.* **97**, 660 (1955).
- [161] A. S. Alexandrov and J. T. Devreese, *Advances in Polaron Physics*, (Springer, Berlin Heidelberg, 2010).
- [162] A. Alexandrov and J. Ranninger, “Theory of bipolarons and bipolaronic bands”, *Phys. Rev. B* **23**, 1796 (1981).
- [163] J. L. Bredas and G. B. Street, “Polarons, bipolarons, and solitons in conducting polymers”, *Acc. Chem. Res.* **18**, 309 (1985).
- [164] M. R. Mahani, A. Mirsakiyeva, and A. Delin, “Breakdown of Polarons in Conducting Polymers at Device Field Strengths”, *J. Phys. Chem. C* **121**, 10317 (2017).
- [165] P. A. Bobbert, T. D. Nguyen, F. W. A. van Oost, B. Koopmans, and M. Wohlgenannt, “Bipolaron Mechanism for Organic Magnetoresistance”, *Phys. Rev. Lett.* **99**, 216801 (2007).
- [166] N. Mott, “Polaron models of high-temperature superconductivity”, *Physica C* **205**, 191 (1993).
- [167] A. S. Alexandrov and N. F. Mott, *High Temperature Superconductors And Other Superfluids*, (CRC Press, London, 1994).
- [168] A. S. Alexandrov, V. V. Kabanov, and N. F. Mott, “Coherent *ab* and *c* Transport Theory of High- T_c Cuprates”, *Phys. Rev. Lett.* **77**, 4796 (1996).
- [169] V. Lakhno, “Superconducting properties of a nonideal bipolaron gas”, *Physica C* **561**, 1 (2019).
- [170] B. K. Chakraverty, J. Ranninger, and D. Feinberg, “Experimental and Theoretical Constraints of Bipolaronic Superconductivity in High T_c Materials: An Impossibility”, *Phys. Rev. Lett.* **81**, 433 (1998).
- [171] J. Sous, M. Chakraborty, R. V. Krems, and M. Berciu, “Light Bipolarons Stabilized by Peierls Electron-Phonon Coupling”, *Phys. Rev. Lett.* **121**, 247001 (2018).
- [172] T. Holstein, “Studies of polaron motion: Part I. The molecular-crystal model”, *Ann. Phys.* **8**, 325 (1959).
- [173] T. Holstein, “Studies of polaron motion: Part II. The “small” polaron”, *Ann. Phys.* **8**, 343 (1959).
- [174] E. Dagotto, “Correlated electrons in high-temperature superconductors”, *Rev. Mod. Phys.* **66**, 763 (1994).

BIBLIOGRAPHY

- [175] A. R. Srimath Kandada and C. Silva, “Exciton Polarons in Two-Dimensional Hybrid Metal-Halide Perovskites”, *J. Phys. Chem. Lett.* **11**, 3173 (2020).
- [176] J. Bardeen, G. Baym, and D. Pines, “Effective Interaction of He^3 Atoms in Dilute Solutions of He^3 in He^4 at Low Temperatures”, *Phys. Rev.* **156**, 207 (1967).
- [177] A. Davydov, “The theory of contraction of proteins under their excitation”, *J. Theor. Biol.* **38**, 559 (1973).
- [178] F. Grusdt and E. Demler, *New theoretical approaches to Bose polarons*, volume 191, pp. 325 – 411, (IOS Press Amsterdam, Amsterdam2015).
- [179] J. Tempere, W. Casteels, M. K. Oberthaler, S. Knoop, E. Timmermans, and J. T. Devreese, “Feynman path-integral treatment of the BEC-impurity polaron”, *Phys. Rev. B* **80**, 184504 (2009).
- [180] W. Casteels, T. Van Cauteren, J. Tempere, and J. T. Devreese, “Strong coupling treatment of the polaronic system consisting of an impurity in a condensate”, *Laser Phys.* **21**, 1480 (2011).
- [181] F. Chevy and C. Mora, “Ultra-cold polarized Fermi gases”, *Rep. Prog. Phys.* **73**, 112401 (2010).
- [182] M.-G. Hu, M. J. Van de Graaff, D. Kedar, J. P. Corson, E. A. Cornell, and D. S. Jin, “Bose Polarons in the Strongly Interacting Regime”, *Phys. Rev. Lett.* **117**, 055301 (2016).
- [183] Z. Z. Yan, Y. Ni, C. Robens, and M. W. Zwierlein, “Bose polarons near quantum criticality”, *Science* **368**, 190 (2020).
- [184] M. Koschorreck, D. Pertot, E. Vogt, B. Fröhlich, M. Feld, and M. Köhl, “Attractive and repulsive Fermi polarons in two dimensions”, *Nature* **485**, 619 (2012).
- [185] A. N. Wenz, G. Zürn, S. Murmann, I. Brouzos, T. Lompe, and S. Jochim, “From Few to Many: Observing the Formation of a Fermi Sea One Atom at a Time”, *Science* **342**, 457 (2013).
- [186] J. Vlietinck, J. Ryckebusch, and K. Van Houcke, “Quasiparticle properties of an impurity in a Fermi gas”, *Phys. Rev. B* **87**, 115133 (2013).
- [187] F. Grusdt, Y. E. Shchadilova, A. N. Rubtsov, and E. Demler, “Renormalization group approach to the Fröhlich polaron model: application to impurity-BEC problem”, *Sci. Rep.* **5**, 12124 (2015).
- [188] Y. E. Shchadilova, F. Grusdt, A. N. Rubtsov, and E. Demler, “Polaronic mass renormalization of impurities in Bose-Einstein condensates: Correlated Gaussian-wave-function approach”, *Phys. Rev. A* **93**, 043606 (2016).

- [189] L. A. Peña Ardila, G. E. Astrakharchik, and S. Giorgini, “Strong coupling Bose polarons in a two-dimensional gas”, *Phys. Rev. Research* **2**, 023405 (2020).
- [190] P. W. Anderson, “Infrared Catastrophe in Fermi Gases with Local Scattering Potentials”, *Phys. Rev. Lett.* **18**, 1049 (1967).
- [191] A. Rosch and T. Kopp, “Heavy Particle in a d-Dimensional Fermionic Bath: A Strong Coupling Approach”, *Phys. Rev. Lett.* **75**, 1988 (1995).
- [192] H. Castella, “Effect of finite impurity mass on the Anderson orthogonality catastrophe in one dimension”, *Phys. Rev. B* **54**, 17422 (1996).
- [193] T. Frisch, Y. Pomeau, and S. Rica, “Transition to dissipation in a model of superflow”, *Phys. Rev. Lett.* **69**, 1644 (1992).
- [194] T. Winiecki, J. F. McCann, and C. S. Adams, “Pressure Drag in Linear and Nonlinear Quantum Fluids”, *Phys. Rev. Lett.* **82**, 5186 (1999).
- [195] G. E. Astrakharchik and L. P. Pitaevskii, “Motion of a heavy impurity through a Bose-Einstein condensate”, *Phys. Rev. A* **70**, 013608 (2004).
- [196] V. Hakim, “Nonlinear Schrödinger flow past an obstacle in one dimension”, *Phys. Rev. E* **55**, 2835 (1997).
- [197] Z. Dutton, M. Budde, C. Slowe, and L. V. Hau, “Observation of Quantum Shock Waves Created with Ultra- Compressed Slow Light Pulses in a Bose-Einstein Condensate”, *Science* **293**, 663 (2001).
- [198] N. Pavloff, “Breakdown of superfluidity of an atom laser past an obstacle”, *Phys. Rev. A* **66**, 013610 (2002).
- [199] P. Engels and C. Atherton, “Stationary and Nonstationary Fluid Flow of a Bose-Einstein Condensate Through a Penetrable Barrier”, *Phys. Rev. Lett.* **99**, 160405 (2007).
- [200] G. C. Katsimiga, S. I. Mistakidis, G. M. Koutentakis, P. G. Kevrekidis, and P. Schmelcher, “Many-body dissipative flow of a confined scalar Bose-Einstein condensate driven by a Gaussian impurity”, *Phys. Rev. A* **98**, 013632 (2018).
- [201] L. D. Landau, “Two-fluid model of liquid helium II”, *J. Phys. (Moscow)* **5**, 71 (1941).
- [202] J. Stenger, S. Inouye, D. M. Stamper-Kurn, H.-J. Miesner, A. P. Chikkatur, and W. Ketterle, “Spin domains in ground-state Bose-Einstein condensates”, *Nature* **396**, 345 (1998).
- [203] K. M. Mertes, J. W. Merrill, R. Carretero-González, D. J. Frantzeskakis, P. G. Kevrekidis, and D. S. Hall, “Nonequilibrium Dynamics and Superfluid Ring Excitations in Binary Bose-Einstein Condensates”, *Phys. Rev. Lett.* **99**, 190402 (2007).

BIBLIOGRAPHY

- [204] S. B. Papp, J. M. Pino, and C. E. Wieman, “Tunable Miscibility in a Dual-Species Bose-Einstein Condensate”, *Phys. Rev. Lett.* **101**, 040402 (2008).
- [205] R. P. Anderson, C. Ticknor, A. I. Sidorov, and B. V. Hall, “Spatially inhomogeneous phase evolution of a two-component Bose-Einstein condensate”, *Phys. Rev. A* **80**, 023603 (2009).
- [206] S. Tojo, Y. Taguchi, Y. Masuyama, T. Hayashi, H. Saito, and T. Hirano, “Controlling phase separation of binary Bose-Einstein condensates via mixed-spin-channel Feshbach resonance”, *Phys. Rev. A* **82**, 033609 (2010).
- [207] P. Ao and S. T. Chui, “Binary Bose-Einstein condensate mixtures in weakly and strongly segregated phases”, *Phys. Rev. A* **58**, 4836 (1998).
- [208] S. Campbell, M. A. García-March, T. Fogarty, and Th. Busch, “Quenching small quantum gases: Genesis of the orthogonality catastrophe”, *Phys. Rev. A* **90**, 013617 (2014).
- [209] Y. Eto, M. Takahashi, M. Kunimi, H. Saito, and T. Hirano, “Nonequilibrium dynamics induced by miscible–immiscible transition in binary Bose–Einstein condensates”, *New J. Phys.* **18**, 073029 (2016).
- [210] S. I. Mistakidis, G. C. Katsimiga, P. G. Kevrekidis, and P. Schmelcher, “Correlation effects in the quench-induced phase separation dynamics of a two species ultracold quantum gas”, *New J. Phys.* **20**, 043052 (2018).
- [211] T. H. Johnson, M. Bruderer, Y. Cai, S. R. Clark, W. Bao, and D. Jaksch, “Breathing oscillations of a trapped impurity in a Bose gas”, *Europhys. Lett.* **98**, 26001 (2012).
- [212] A. Boudjemâa, N. Guebli, M. Sekmane, and S. Khelifa-Karfa, “Breathing modes of repulsive polarons in Bose–Bose mixtures”, *J. Phys.: Cond. Mat.* **32**, 415401 (2020).
- [213] M. Rigol, V. Dunjko, and M. Olshanii, “Thermalization and its mechanism for generic isolated quantum systems”, *Nature* **452**, 854 (2008).
- [214] M. Rigol, “Breakdown of Thermalization in Finite One-Dimensional Systems”, *Phys. Rev. Lett.* **103**, 100403 (2009).
- [215] M. Rigol and M. Srednicki, “Alternatives to Eigenstate Thermalization”, *Phys. Rev. Lett.* **108**, 110601 (2012).
- [216] D. Jansen, J. Stolpp, L. Vidmar, and F. Heidrich-Meisner, “Eigenstate thermalization and quantum chaos in the Holstein polaron model”, *Phys. Rev. B* **99**, 155130 (2019).
- [217] E. Feenberg, *Theory of Quantum Fluids*, Pure and applied physics ; a series of monographs and textbooks, (Academic Press, New York and London, 1969).

- [218] A. Bramati and M. Modugno, *Physics of quantum fluids: new trends and hot topics in atomic and polariton condensates*, Springer Series in Solid-State Sciences, (Springer, Heidelberg, 2013).
- [219] M. Born, *Atomic Physics: 8th Edition*, Dover Books on Physics, (Dover Publications, New York, 2013).
- [220] C. Cohen-Tannoudji and D. Guéry-Odelin, *Advances in Atomic Physics*, (World Scientific, Hackensack, 2011).
- [221] T. F. Gallagher, *Rydberg Atoms*, Cambridge Monographs on Atomic, Molecular and Chemical Physics, (Cambridge University Press, Cambridge, 1994).
- [222] R. Schmidt, H. R. Sadeghpour, and E. Demler, “Mesoscopic Rydberg Impurity in an Atomic Quantum Gas”, *Phys. Rev. Lett.* **116**, 105302 (2016).
- [223] F. Camargo, R. Schmidt, J. D. Whalen, R. Ding, G. Woehl, S. Yoshida, J. Burgdörfer, F. B. Dunning, H. R. Sadeghpour, E. Demler, and T. C. Killian, “Creation of Rydberg Polarons in a Bose Gas”, *Phys. Rev. Lett.* **120**, 083401 (2018).
- [224] R. Schmidt, J. D. Whalen, R. Ding, F. Camargo, G. Woehl, S. Yoshida, J. Burgdörfer, F. B. Dunning, E. Demler, H. R. Sadeghpour, and T. C. Killian, “Theory of excitation of Rydberg polarons in an atomic quantum gas”, *Phys. Rev. A* **97**, 022707 (2018).
- [225] Y. Wang and B. D. Esry, “Efimov Trimer Formation via Ultracold Four-Body Recombination”, *Phys. Rev. Lett.* **102**, 133201 (2009).
- [226] J. von Stecher, J. P. D’Incao, and C. H. Greene, “Signatures of universal four-body phenomena and their relation to the Efimov effect”, *Nat. Phys.* **5**, 417 (2009).
- [227] D. Guéry-Odelin, J. Söding, P. Desbiolles, and J. Dalibard, “Is Bose-Einstein condensation of atomic cesium possible?”, *Europhysics Letters (EPL)* **44**, 25 (1998).
- [228] J. Söding, D. Guéry-Odelin, P. Desbiolles, G. Ferrari, and J. Dalibard, “Giant Spin Relaxation of an Ultracold Cesium Gas”, *Phys. Rev. Lett.* **80**, 1869 (1998).
- [229] T. Weber, J. Herbig, M. Mark, H.-C. Nägerl, and R. Grimm, “Bose-Einstein Condensation of Cesium”, *Science* **299**, 232 (2003).
- [230] M. Arndt, M. Ben Dahan, D. Guéry-Odelin, M. W. Reynolds, and J. Dalibard, “Observation of a Zero-Energy Resonance in Cs-Cs Collisions”, *Phys. Rev. Lett.* **79**, 625 (1997).
- [231] S. J. J. M. F. Kokkelmans, B. J. Verhaar, and K. Gibble, “Prospects for Bose-Einstein Condensation in Cesium”, *Phys. Rev. Lett.* **81**, 951 (1998).

BIBLIOGRAPHY

- [232] T. Weber, J. Herbig, M. Mark, H.-C. Nägerl, and R. Grimm, “Three-Body Recombination at Large Scattering Lengths in an Ultracold Atomic Gas”, *Phys. Rev. Lett.* **91**, 123201 (2003).
- [233] T. Weber, *Bose-Einstein Condensation of Optically Trapped Cesium*, Ph.D. thesis, Leopold-Franzens-Universität Innsbruck, Innsbruck, Austria (2003).
- [234] V. Efimov, “WEAKLY-BOUND STATES OF 3 RESONANTLY-INTERACTING PARTICLES”, *Sov. J. Nucl. Phys.* **12**, 589 (1971).
- [235] V. Efimov, “Energy levels of three resonantly interacting particles”, *Nucl. Phys. A* **210**, 157 (1973).
- [236] T. Kraemer, M. Mark, P. Waldburger, J. G. Danzl, C. Chin, B. Engeser, A. D. Lange, K. Pilch, A. Jaakkola, H.-C. Nägerl, and R. Grimm, “Evidence for Efimov quantum states in an ultracold gas of caesium atoms”, *Nature* **440**, 315 (2006).
- [237] S. Earnshaw, “On the Nature of the Molecular Forces which Regulate the Constitution of the Luminiferous Ether”, *Trans. Camb. Phil. Soc.* **7**, 97 (1848).
- [238] W. Braunebeck, “Freischwebende Körper im elektrischen und magnetischen Feld”, *Z. Phys.* **112**, 753 (1939).
- [239] S. Murmann, A. Bergschneider, V. M. Klinkhamer, G. Zürn, T. Lompe, and S. Jochim, “Two Fermions in a Double Well: Exploring a Fundamental Building Block of the Hubbard Model”, *Phys. Rev. Lett.* **114**, 080402 (2015).
- [240] L. J. LeBlanc and J. H. Thywissen, “Species-specific optical lattices”, *Phys. Rev. A* **75**, 053612 (2007).
- [241] J. Catani, G. Barontini, G. Lamporesi, F. Rabatti, G. Thalhammer, F. Minardi, S. Stringari, and M. Inguscio, “Entropy Exchange in a Mixture of Ultracold Atoms”, *Phys. Rev. Lett.* **103**, 140401 (2009).
- [242] W. F. Holmgren, R. Trubko, I. Hromada, and A. D. Cronin, “Measurement of a Wavelength of Light for Which the Energy Shift for an Atom Vanishes”, *Phys. Rev. Lett.* **109**, 243004 (2012).
- [243] D. C. McKay, C. Meldgin, D. Chen, and B. DeMarco, “Slow Thermalization between a Lattice and Free Bose Gas”, *Phys. Rev. Lett.* **111**, 063002 (2013).
- [244] R. H. Leonard, A. J. Fallon, C. A. Sackett, and M. S. Safronova, “High-precision measurements of the $^{87}\text{Rb}D$ -line tune-out wavelength”, *Phys. Rev. A* **92**, 052501 (2015).
- [245] F. Schmidt, D. Mayer, M. Hohmann, T. Lausch, F. Kindermann, and A. Widera, “Precision measurement of the ^{87}Rb tune-out wavelength in the hyperfine ground state $F = 1$ at 790 nm”, *Phys. Rev. A* **93**, 022507 (2016).

-
- [246] T. M. Bersano, V. Gokhroo, M. A. Khomehchi, J. D'Ambrose, D. J. Frantzeskakis, P. Engels, and P. G. Kevrekidis, "Three-Component Soliton States in Spinor $F = 1$ Bose-Einstein Condensates", *Phys. Rev. Lett.* **120**, 063202 (2018).
- [247] A. Messiah, *Quantum Mechanics*, (Elsevier Science, Amsterdam, 1981).
- [248] M. Olshanii, "Atomic Scattering in the Presence of an External Confinement and a Gas of Impenetrable Bosons", *Phys. Rev. Lett.* **81**, 938 (1998).
- [249] E. Haller, M. Gustavsson, M. J. Mark, J. G. Danzl, R. Hart, G. Pupillo, and H.-C. Nägerl, "Realization of an Excited, Strongly Correlated Quantum Gas Phase", *Science* **325**, 1224 (2009).
- [250] E. Haller, M. J. Mark, R. Hart, J. G. Danzl, L. Reichsöllner, V. Melezhik, P. Schmelcher, and H.-C. Nägerl, "Confinement-Induced Resonances in Low-Dimensional Quantum Systems", *Phys. Rev. Lett.* **104**, 153203 (2010).
- [251] C.-H. Wu, J. W. Park, P. Ahmadi, S. Will, and M. W. Zwierlein, "Ultracold Fermionic Feshbach Molecules of $^{23}\text{Na}^{40}\text{K}$ ", *Phys. Rev. Lett.* **109**, 085301 (2012).
- [252] E. Tiesinga, C. J. Williams, F. H. Mies, and P. S. Julienne, "Interacting atoms under strong quantum confinement", *Phys. Rev. A* **61**, 063416 (2000).
- [253] T. Bergeman, M. G. Moore, and M. Olshanii, "Atom-Atom Scattering under Cylindrical Harmonic Confinement: Numerical and Analytic Studies of the Confinement Induced Resonance", *Phys. Rev. Lett.* **91**, 163201 (2003).
- [254] J. I. Kim, J. Schmiedmayer, and P. Schmelcher, "Quantum scattering in quasi-one-dimensional cylindrical confinement", *Phys. Rev. A* **72**, 042711 (2005).
- [255] K. Günter, T. Stöferle, H. Moritz, M. Köhl, and T. Esslinger, " p -Wave Interactions in Low-Dimensional Fermionic Gases", *Phys. Rev. Lett.* **95**, 230401 (2005).
- [256] P. Giannakeas, F. K. Diakonov, and P. Schmelcher, "Coupled ℓ -wave confinement-induced resonances in cylindrically symmetric waveguides", *Phys. Rev. A* **86**, 042703 (2012).
- [257] T. Koch, T. Lahaye, J. Metz, B. Fröhlich, A. Griesmaier, and T. Pfau, "Stabilization of a purely dipolar quantum gas against collapse", *Nat. Phys.* **4**, 218 (2008).
- [258] H. Kadau, M. Schmitt, M. Wenzel, C. Wink, T. Maier, I. Ferrier-Barbut, and T. Pfau, "Observing the Rosensweig instability of a quantum ferrofluid", *Nature* **530**, 194 (2016).
- [259] C. Ticknor, C. A. Regal, D. S. Jin, and J. L. Bohn, "Multiplet structure of Feshbach resonances in nonzero partial waves", *Phys. Rev. A* **69**, 042712 (2004).

BIBLIOGRAPHY

- [260] J. Zhang, E. G. M. van Kempen, T. Bourdel, L. Khaykovich, J. Cubizolles, F. Chevy, M. Teichmann, L. Tarruell, S. J. J. M. F. Kokkelmans, and C. Salomon, “*P*-wave Feshbach resonances of ultracold ${}^6\text{Li}$ ”, *Phys. Rev. A* **70**, 030702 (2004).
- [261] M. Gerken, B. Tran, S. Häfner, E. Tiemann, B. Zhu, and M. Weidemüller, “Observation of dipolar splittings in high-resolution atom-loss spectroscopy of ${}^6\text{Li}$ *p*-wave Feshbach resonances”, *Phys. Rev. A* **100**, 050701 (2019).
- [262] J. M. Schurer, A. Negretti, and P. Schmelcher, “Unraveling the Structure of Ultracold Mesoscopic Collinear Molecular Ions”, *Phys. Rev. Lett.* **119**, 063001 (2017).
- [263] D. J. Bosworth, M. Pyzh, and P. Schmelcher, “Spectral properties of a three body atom-ion hybrid system”, arXiv: **2101.08716** (2021).
- [264] A. Ashkin, “Acceleration and Trapping of Particles by Radiation Pressure”, *Phys. Rev. Lett.* **24**, 156 (1970).
- [265] A. Ashkin, J. M. Dziedzic, J. E. Bjorkholm, and S. Chu, “Observation of a single-beam gradient force optical trap for dielectric particles”, *Opt. Lett.* **11**, 288 (1986).
- [266] L. Anderegg, L. W. Cheuk, Y. Bao, S. Burchesky, W. Ketterle, K.-K. Ni, and J. M. Doyle, “An optical tweezer array of ultracold molecules”, *Science* **365**, 1156 (2019).
- [267] K. Schakenraad, A. S. Biebricher, M. Sebregts, B. ten Bonsel, E. J. G. Peterman, G. J. L. Wuite, I. Heller, C. Storm, and P. van der Schoot, “Hyperstretching DNA”, *Nat. Comm.* **8**, 2197 (2017).
- [268] L. Mitchem and J. P. Reid, “Optical manipulation and characterisation of aerosol particles using a single-beam gradient force optical trap”, *Chem. Soc. Rev.* **37**, 756 (2008).
- [269] J. B. Wills, K. J. Knox, and J. P. Reid, “Optical control and characterisation of aerosol”, *Chem. Phys. Lett.* **481**, 153 (2009).
- [270] M. Karski, L. Förster, J.-M. Choi, A. Steffen, W. Alt, D. Meschede, and A. Widera, “Quantum Walk in Position Space with Single Optically Trapped Atoms”, *Science* **325**, 174 (2009).
- [271] K. Jiménez-García, L. J. LeBlanc, R. A. Williams, M. C. Beeler, A. R. Perry, and I. B. Spielman, “Peierls Substitution in an Engineered Lattice Potential”, *Phys. Rev. Lett.* **108**, 225303 (2012).
- [272] K. Huang and C. N. Yang, “Quantum-Mechanical Many-Body Problem with Hard-Sphere Interaction”, *Phys. Rev.* **105**, 767 (1957).
- [273] Z. Idziaszek and T. Calarco, “Analytical solutions for the dynamics of two trapped interacting ultracold atoms”, *Phys. Rev. A* **74**, 022712 (2006).

- [274] D. A. Steck, “Rubidium 87 D line data”, available online at <http://steck.us/alkalidata> (revision 2.1.4, 23 December 2010).
- [275] D. R. Hartree, “The Wave Mechanics of an Atom with a Non-Coulomb Central Field. Part I. Theory and Methods”, *Math. Proc. Cambridge* **24**, 89–110 (1928).
- [276] V. Fock, “Näherungsmethode zur Lösung des quantenmechanischen Mehrkörperproblems”, *Z. Physik* **61**, 126 (1930).
- [277] N. N. Bogolyubov, *The dynamical theory in statistical physics*, (Hindustan, Delhi, 1965).
- [278] M. Born and H. S. Green, “A general kinetic theory of liquids. IV. Quantum mechanics of fluids”, *Proc. R. Soc. London A* **191**, 168 (1947).
- [279] J. G. Kirkwood, “The Statistical Mechanical Theory of Transport Processes I. General Theory”, *J. Chem. Phys.* **14**, 180 (1946).
- [280] J. Yvon, “Une méthode d’étude des corrélations dans les fluides quantiques en équilibre”, *Nucl. Phys.* **4**, 1 (1957).
- [281] L. Landau and E. Lifshitz, “Statistical Physics”, , (Butterworth-Heinemann, Oxford, 1980), third edition edition.
- [282] P. Debye and E. Hückel, “The theory of electrolytes I. The lowering of the freezing point and related occurrences”, *Phys. Z.* **24**, 185 (1923).
- [283] J. Hubbard and B. H. Flowers, “Electron correlations in narrow energy bands”, *Proc. R. Soc. London A* **276**, 238 (1963).
- [284] M. C. Gutzwiller, “Effect of Correlation on the Ferromagnetism of Transition Metals”, *Phys. Rev. Lett.* **10**, 159 (1963).
- [285] J. Kanamori, “Electron Correlation and Ferromagnetism of Transition Metals”, *Prog. Theor. Phys.* **30**, 275 (1963).
- [286] J. Hubbard and B. H. Flowers, “Electron correlations in narrow energy bands III. An improved solution”, *Proc. R. Soc. London A* **281**, 401 (1964).
- [287] O. Gunnarsson, “Band model for magnetism of transition metals in the spin-density-functional formalism”, *J. Phys. F: Metal Physics* **6**, 587 (1976).
- [288] M. B. Walker and T. W. Ruijgrok, “Absence of Magnetic Ordering in One and Two Dimensions in a Many-Band Model for Interacting Electrons in a Metal”, *Phys. Rev.* **171**, 513 (1968).
- [289] D. K. Ghosh, “Nonexistence of Magnetic Ordering in the One- and Two-Dimensional Hubbard Model”, *Phys. Rev. Lett.* **27**, 1584 (1971).

BIBLIOGRAPHY

- [290] T. Koma and H. Tasaki, “Decay of superconducting and magnetic correlations in one- and two-dimensional Hubbard models”, *Phys. Rev. Lett.* **68**, 3248 (1992).
- [291] A. Mielke, “Ferromagnetic ground states for the Hubbard model on line graphs”, *J. Phys. A* **24**, L73 (1991).
- [292] H. Tasaki, “Ferromagnetism in the Hubbard models with degenerate single-electron ground states”, *Phys. Rev. Lett.* **69**, 1608 (1992).
- [293] N. A. Spaldin, *Magnetic materials : fundamentals and applications*, (Cambridge University Press, Cambridge; New York, 2011).
- [294] Y. Nagaoka, “Ferromagnetism in a Narrow, Almost Half-Filled s Band”, *Phys. Rev.* **147**, 392 (1966).
- [295] A. Barbieri, J. A. Riera, and A. P. Young, “Stability of the saturated ferromagnetic state in the one-band Hubbard model”, *Phys. Rev. B* **41**, 11697 (1990).
- [296] G. M. Pastor, R. Hirsch, and B. Mühlischlegel, “Electron correlations, magnetism, and structure of small clusters”, *Phys. Rev. Lett.* **72**, 3879 (1994).
- [297] X.-J. Liu, H. Hu, and P. D. Drummond, “Three attractively interacting fermions in a harmonic trap: Exact solution, ferromagnetism, and high-temperature thermodynamics”, *Phys. Rev. A* **82**, 023619 (2010).
- [298] A. Tichai, R. Wirth, J. Ripoche, and T. Duguet, “Symmetry reduction of tensor networks in many-body theory”, *Eur. Phys. J. A* **56**, 272 (2020).
- [299] J. G. Cosme, C. Weiss, and J. Brand, “Center-of-mass motion as a sensitive convergence test for variational multimode quantum dynamics”, *Phys. Rev. A* **94**, 043603 (2016).
- [300] T. Grining, M. Tomza, M. Lesiuk, M. Przybytek, M. Musiał, P. Massignan, M. Lewenstein, and R. Moszynski, “Many interacting fermions in a one-dimensional harmonic trap: a quantum-chemical treatment”, *New J. Phys.* **17**, 115001 (2015).
- [301] M. Girardeau, “Relationship between Systems of Impenetrable Bosons and Fermions in One Dimension”, *J. Math. Phys.* **1**, 516 (1960).
- [302] M. D. Girardeau and A. Minguzzi, “Soluble Models of Strongly Interacting Ultracold Gas Mixtures in Tight Waveguides”, *Phys. Rev. Lett.* **99**, 230402 (2007).
- [303] H. Bethe, R. Peierls, and D. R. Hartree, “Quantum theory of the dipton”, *Proc. R. Soc. A* **148**, 146 (1935).
- [304] K. Sakmann and M. Kasevich, “Single-shot simulations of dynamic quantum many-body systems”, *Nat. Phys.* **12**, 451 (2016).

- [305] A. U. J. Lode and C. Bruder, “Fragmented Superradiance of a Bose-Einstein Condensate in an Optical Cavity”, *Phys. Rev. Lett.* **118**, 013603 (2017).
- [306] A. Bergschneider, V. M. Klinkhamer, J. H. Becher, R. Klemt, G. Zürn, P. M. Preiss, and S. Jochim, “Spin-resolved single-atom imaging of ${}^6\text{Li}$ in free space”, *Phys. Rev. A* **97**, 063613 (2018).
- [307] A. Bergschneider, V. M. Klinkhamer, J. H. Becher, R. Klemt, L. Palm, G. Zürn, S. Jochim, and P. M. Preiss, “Experimental characterization of two-particle entanglement through position and momentum correlations”, *Nat. Phys.* **15**, 640 (2019).
- [308] J. H. Becher, E. Sindici, R. Klemt, S. Jochim, A. J. Daley, and P. M. Preiss, “Measurement of Identical Particle Entanglement and the Influence of Antisymmetrization”, *Phys. Rev. Lett.* **125**, 180402 (2020).
- [309] M. Ogata and H. Shiba, “Bethe-ansatz wave function, momentum distribution, and spin correlation in the one-dimensional strongly correlated Hubbard model”, *Phys. Rev. B* **41**, 2326 (1990).
- [310] K. A. Matveev, “Conductance of a quantum wire at low electron density”, *Phys. Rev. B* **70**, 245319 (2004).
- [311] W. Becker, B. Gerlach, and H. Schliffke, “Monte Carlo calculation of the ground-state energy of an optical polaron”, *Phys. Rev. B* **28**, 5735 (1983).
- [312] F. M. Peeters and J. T. Devreese, “Comment on “Monte Carlo calculation of the ground-state energy of an optical polaron””, *Phys. Rev. B* **31**, 6826 (1985).
- [313] N. V. Prokof’ev and B. V. Svistunov, “Polaron Problem by Diagrammatic Quantum Monte Carlo”, *Phys. Rev. Lett.* **81**, 2514 (1998).
- [314] A. S. Mishchenko, N. V. Prokof’ev, A. Sakamoto, and B. V. Svistunov, “Diagrammatic quantum Monte Carlo study of the Fröhlich polaron”, *Phys. Rev. B* **62**, 6317 (2000).
- [315] I. Biaggio, R. W. Hellwarth, and J. P. Partanen, “Band Mobility of Photoexcited Electrons in $\text{Bi}_{12}\text{SiO}_{20}$ ”, *Phys. Rev. Lett.* **78**, 891 (1997).
- [316] E. Hendry, F. Wang, J. Shan, T. F. Heinz, and M. Bonn, “Electron transport in TiO_2 probed by THz time-domain spectroscopy”, *Phys. Rev. B* **69**, 081101 (2004).
- [317] W. Kohn, “Density-functional theory for excited states in a quasi-local-density approximation”, *Phys. Rev. A* **34**, 737 (1986).
- [318] P. Hohenberg and W. Kohn, “Inhomogeneous electron gas”, *Phys. Rev.* **136**, B864 (1964).
- [319] W. Kohn and L. J. Sham, “Self-consistent equations including exchange and correlation effects”, *Phys. Rev.* **140**, A1133 (1965).

BIBLIOGRAPHY

- [320] T.-D. Lee and D. Pines, “The Motion of Slow Electrons in Polar Crystals”, *Phys. Rev.* **88**, 960 (1952).
- [321] M. Gurari, “XXXVI. Self energy of slow electrons in polar materials”, London, Edinburgh, Dublin Philos. Mag. J. Sci. **44**, 329 (1953).
- [322] T. D. Lee, F. E. Low, and D. Pines, “The Motion of Slow Electrons in a Polar Crystal”, *Phys. Rev.* **90**, 297 (1953).
- [323] F. Grusdt and M. Fleischhauer, “Tunable Polarons of Slow-Light Polaritons in a Two-Dimensional Bose-Einstein Condensate”, *Phys. Rev. Lett.* **116**, 053602 (2016).
- [324] T. Ameri, G. Dennler, C. Lungenschmied, and C. J. Brabec, “Organic tandem solar cells: A review”, *Energy Environ. Sci.* **2**, 347 (2009).
- [325] P. Fulde and R. A. Ferrell, “Superconductivity in a Strong Spin-Exchange Field”, *Phys. Rev.* **135**, A550 (1964).
- [326] A. I. Larkin and Y. N. Ovchinnikov, “Nonuniform state of superconductors”, *Zh. Eksp. Teor. Fiz.* **47**, 1136 (1964).
- [327] C. J. M. Mathy, M. M. Parish, and D. A. Huse, “Trimers, Molecules, and Polarons in Mass-Imbalanced Atomic Fermi Gases”, *Phys. Rev. Lett.* **106**, 166404 (2011).
- [328] R. Casalbuoni and G. Nardulli, “Inhomogeneous superconductivity in condensed matter and QCD”, *Rev. Mod. Phys.* **76**, 263 (2004).
- [329] F. Chevy, “Universal phase diagram of a strongly interacting Fermi gas with unbalanced spin populations”, *Phys. Rev. A* **74**, 063628 (2006).
- [330] R. Combescot, A. Recati, C. Lobo, and F. Chevy, “Normal State of Highly Polarized Fermi Gases: Simple Many-Body Approaches”, *Phys. Rev. Lett.* **98**, 180402 (2007).
- [331] P. Massignan and G. M. Bruun, “Repulsive polarons and itinerant ferromagnetism in strongly polarized Fermi gases”, *Eur. Phys. J. D* **65**, 83 (2011).
- [332] R. Combescot and S. Giraud, “Normal State of Highly Polarized Fermi Gases: Full Many-Body Treatment”, *Phys. Rev. Lett.* **101**, 050404 (2008).
- [333] S. Pilati, G. Bertainia, S. Giorgini, and M. Troyer, “Itinerant Ferromagnetism of a Repulsive Atomic Fermi Gas: A Quantum Monte Carlo Study”, *Phys. Rev. Lett.* **105**, 030405 (2010).
- [334] S. Nascimbène, N. Navon, K. J. Jiang, L. Tarruell, M. Teichmann, J. McKeever, F. Chevy, and C. Salomon, “Collective Oscillations of an Imbalanced Fermi Gas: Axial Compression Modes and Polaron Effective Mass”, *Phys. Rev. Lett.* **103**, 170402 (2009).

- [335] N. Navon, S. Nascimbène, F. Chevy, and C. Salomon, “The Equation of State of a Low-Temperature Fermi Gas with Tunable Interactions”, *Science* **328**, 729 (2010).
- [336] N. Prokof’ev and B. Svistunov, “Fermi-polaron problem: Diagrammatic Monte Carlo method for divergent sign-alternating series”, *Phys. Rev. B* **77**, 020408 (2008).
- [337] E. Müller-Hartmann, T. V. Ramakrishnan, and G. Toulouse, “Localized Dynamic Perturbations in Metals”, *Phys. Rev. B* **3**, 1102 (1971).
- [338] T. Kopp, A. E. Ruckenstein, and S. Schmitt-Rink, “Single spin flip in the Nagaoka state: Problems with the Gutzwiller wave function”, *Phys. Rev. B* **42**, 6850 (1990).
- [339] J. B. McGuire, “Interacting Fermions in One Dimension. I. Repulsive Potential”, *J. Math. Phys.* **6**, 432 (1965).
- [340] J. B. McGuire, “Interacting Fermions in One Dimension. II. Attractive Potential”, *J. Math. Phys.* **7**, 123 (1966).
- [341] S. Mistakidis, G. Koutentakis, F. Grusdt, H. R. Sadeghpour, and P. Schmelcher, “Radiofrequency spectroscopy of one-dimensional trapped Bose polarons: crossover from the adiabatic to the diabatic regime”, *New J. Phys.* (in press).
- [342] F. M. Cucchietti and E. Timmermans, “Strong-Coupling Polarons in Dilute Gas Bose-Einstein Condensates”, *Phys. Rev. Lett.* **96**, 210401 (2006).
- [343] M. Schechter, D. M. Gangardt, and A. Kamenev, “Quantum impurities: from mobile Josephson junctions to depletions”, *New J. Phys.* **18**, 065002 (2016).
- [344] Y. E. Shchadilova, R. Schmidt, F. Grusdt, and E. Demler, “Quantum Dynamics of Ultracold Bose Polarons”, *Phys. Rev. Lett.* **117**, 113002 (2016).
- [345] S. I. Mistakidis, F. Grusdt, G. M. Koutentakis, and P. Schmelcher, “Dissipative correlated dynamics of a moving impurity immersed in a Bose–Einstein condensate”, *New J. Phys.* **21**, 103026 (2019).
- [346] S. I. Mistakidis, L. Hilbig, and P. Schmelcher, “Correlated quantum dynamics of two quenched fermionic impurities immersed in a Bose-Einstein condensate”, *Phys. Rev. A* **100**, 023620 (2019).
- [347] G. Bougas, S. I. Mistakidis, and P. Schmelcher, “Pattern formation of correlated impurities subjected to an impurity-medium interaction pulse”, *Phys. Rev. A* **103**, 023313 (2021).
- [348] G. Stock and W. Domcke, “Detection of ultrafast molecular-excited-state dynamics with time- and frequency-resolved pump-probe spectroscopy”, *Phys. Rev. A* **45**, 3032 (1992).

BIBLIOGRAPHY

- [349] F. Sotier, T. Thomay, T. Hanke, J. Korger, S. Mahapatra, A. Frey, K. Brunner, R. Bratschitsch, and A. Leitenstorfer, “Femtosecond few-fermion dynamics and deterministic single-photon gain in a quantum dot”, *Nat. Phys.* **5**, 352 (2009).
- [350] M. Eisele, T. L. Cocker, M. A. Huber, M. Plankl, L. Viti, D. Ercolani, L. Sorba, M. S. Vitiello, and R. Huber, “Ultrafast multi-terahertz nano-spectroscopy with sub-cycle temporal resolution”, *Nat. Photonics* **8**, 841 (2014).
- [351] Y.-C. Wu, B. Zhao, and S.-Y. Lee, “Time-dependent wave packet averaged vibrational frequencies from femtosecond stimulated Raman spectra”, *J. Chem. Phys.* **144**, 054104 (2016).
- [352] N. Takei, C. Sommer, C. Genes, G. Pupillo, H. Goto, K. Koyasu, H. Chiba, M. Weidemüller, and K. Ohmori, “Direct observation of ultrafast many-body electron dynamics in an ultracold Rydberg gas”, *Nat. Com.* **7**, 13449 (2016).
- [353] M. Mitrano, A. Cantaluppi, D. Nicoletti, S. Kaiser, A. Perucchi, S. Lupi, P. Di Pietro, D. Pontiroli, M. Riccò, S. R. Clark, D. Jaksch, and A. Cavalleri, “Possible light-induced superconductivity in K3C60 at high temperature”, *Nature* **530**, 461 (2016).
- [354] M. Kolarczik, C. Ulbrich, P. Geiregat, Y. Zhu, L. K. Sagar, A. Singh, B. Herzog, A. W. Achtstein, X. Li, D. van Thourhout, Z. Hens, N. Owschimikow, and U. Woggon, “Sideband pump-probe technique resolves nonlinear modulation response of PbS/CdS quantum dots on a silicon nitride waveguide”, *APL Photonics* **3**, 016101 (2018).
- [355] M. Buzzi, M. Först, R. Mankowsky, and A. Cavalleri, “Probing dynamics in quantum materials with femtosecond X-rays”, *Nat. Rev. Mater.* **3**, 299 (2018).
- [356] T. Sowiński, T. Grass, O. Dutta, and M. Lewenstein, “Few interacting fermions in a one-dimensional harmonic trap”, *Phys. Rev. A* **88**, 033607 (2013).
- [357] S. R. White, “Strongly correlated electron systems and the density matrix renormalization group”, *Phys. Rep.* **301**, 187 (1998).
- [358] U. Schollwöck, “The density-matrix renormalization group”, *Rev. Mod. Phys.* **77**, 259 (2005).
- [359] J. J. García-Ripoll, “Time evolution of Matrix Product States”, *New J. Phys.* **8**, 305 (2006).
- [360] I. P. McCulloch, “From density-matrix renormalization group to matrix product states”, *J. Stat. Mech.: Theory Exp.* **2007**, P10014 (2007).
- [361] F. Verstraete, V. Murg, and J. Cirac, “Matrix product states, projected entangled pair states, and variational renormalization group methods for quantum spin systems”, *Adv. Phys.* **57**, 143 (2008).

- [362] U. Schollwöck, “The density-matrix renormalization group in the age of matrix product states”, *Ann. Phys.* **326**, 96 (2011).
- [363] N. V. Prokof’ev, B. V. Svistunov, and I. S. Tupitsyn, “Exact, complete, and universal continuous-time worldline Monte Carlo approach to the statistics of discrete quantum systems”, *J. Exp. Theor. Phys.* **87**, 310 (1998).
- [364] L. A. Peña Ardila and S. Giorgini, “Impurity in a Bose-Einstein condensate: Study of the attractive and repulsive branch using quantum Monte Carlo methods”, *Phys. Rev. A* **92**, 033612 (2015).
- [365] A. Camacho-Guardian, L. A. Peña Ardila, T. Pohl, and G. M. Bruun, “Bipolarons in a Bose-Einstein Condensate”, *Phys. Rev. Lett.* **121**, 013401 (2018).
- [366] L. Cao, V. Bolsinger, S. I. Mistakidis, G. M. Koutentakis, S. Krönke, J. M. Schurer, and P. Schmelcher, “A unified ab initio approach to the correlated quantum dynamics of ultracold fermionic and bosonic mixtures”, *J. Chem. Phys.* **147**, 044106 (2017).
- [367] S. Krönke, L. Cao, O. Vendrell, and P. Schmelcher, “Non-equilibrium quantum dynamics of ultra-cold atomic mixtures: the multi-layer multi-configuration time-dependent Hartree method for bosons”, *New J. Phys.* **15**, 063018 (2013).
- [368] L. Cao, S. Krönke, O. Vendrell, and P. Schmelcher, “The multi-layer multi-configuration time-dependent Hartree method for bosons: Theory, implementation, and applications”, *J. Chem. Phys.* **139**, 134103 (2013).
- [369] H.-D. Meyer, U. Manthe, and L. Cederbaum, “The multi-configurational time-dependent Hartree approach”, *Chem. Phys. Lett.* **165**, 73 (1990).
- [370] M. Beck, A. Jäckle, G. Worth, and H.-D. Meyer, “The multiconfiguration time-dependent Hartree (MCTDH) method: a highly efficient algorithm for propagating wavepackets”, *Phys. Rep.* **324**, 1 (2000).
- [371] M. Nest, T. Klamroth, and P. Saalfrank, “The multiconfiguration time-dependent Hartree–Fock method for quantum chemical calculations”, *J. Chem. Phys.* **122**, 124102 (2005).
- [372] T. Kato and H. Kono, “Time-dependent multiconfiguration theory for electronic dynamics of molecules in an intense laser field”, *Chem. Phys. Lett.* **392**, 533 (2004).
- [373] A. I. Streltsov, O. E. Alon, and L. S. Cederbaum, “Role of Excited States in the Splitting of a Trapped Interacting Bose-Einstein Condensate by a Time-Dependent Barrier”, *Phys. Rev. Lett.* **99**, 030402 (2007).
- [374] O. E. Alon, A. I. Streltsov, and L. S. Cederbaum, “Multiconfigurational time-dependent Hartree method for bosons: Many-body dynamics of bosonic systems”, *Phys. Rev. A* **77**, 033613 (2008).

BIBLIOGRAPHY

- [375] O. E. Alon, A. I. Streltsov, and L. S. Cederbaum, “Unified view on multiconfigurational time propagation for systems consisting of identical particles”, *J. Chem. Phys.* **127**, 154103 (2007).
- [376] H. Wang and M. Thoss, “Multilayer formulation of the multiconfiguration time-dependent Hartree theory”, *J. Chem. Phys.* **119**, 1289 (2003).
- [377] U. Manthe, “A multilayer multiconfigurational time-dependent Hartree approach for quantum dynamics on general potential energy surfaces”, *J. Chem. Phys.* **128**, 164116 (2008).
- [378] O. Vendrell and H.-D. Meyer, “Multilayer multiconfiguration time-dependent Hartree method: Implementation and applications to a Henon–Heiles Hamiltonian and to pyrazine”, *J. Chem. Phys.* **134**, 044135 (2011).
- [379] R. Horodecki, P. Horodecki, M. Horodecki, and K. Horodecki, “Quantum entanglement”, *Rev. Mod. Phys.* **81**, 865 (2009).
- [380] P. A. M. Dirac, “Note on Exchange Phenomena in the Thomas Atom”, *Proc. Cambridge Phil. Soc.* **26**, 376–385 (1930).
- [381] I. A. I. Frenkel, *Wave mechanics; advanced general theory*, (Clarendon Press, Oxford 1934).
- [382] J. Broeckhove, L. Lathouwers, E. Kesteloot, and P. Van Leuven, “On the equivalence of time-dependent variational principles”, *Chem. Phys. Lett.* **149**, 547 (1988).
- [383] E. P. Gross, “Hydrodynamics of a Superfluid Condensate”, *J. Math. Phys.* **4**, 195 (1963).
- [384] L. Pitaevskii, “Vortex Lines in an Imperfect Bose Gas”, *Sov. Phys. JETP* **13**, 451 (1960).
- [385] S. Krönke, J. Knörzer, and P. Schmelcher, “Correlated quantum dynamics of a single atom collisionally coupled to an ultracold finite bosonic ensemble”, *New J. Phys.* **17**, 053001 (2015).
- [386] G. C. Katsimiga, G. M. Koutentakis, S. I. Mistakidis, P. G. Kevrekidis, and P. Schmelcher, “Dark–bright soliton dynamics beyond the mean-field approximation”, *New J. Phys.* **19**, 073004 (2017).
- [387] O. E. Alon, A. I. Streltsov, and L. S. Cederbaum, “Multiconfigurational time-dependent Hartree method for mixtures consisting of two types of identical particles”, *Phys. Rev. A* **76**, 062501 (2007).
- [388] G. C. Katsimiga, S. I. Mistakidis, G. M. Koutentakis, P. G. Kevrekidis, and P. Schmelcher, “Many-body quantum dynamics in the decay of bent dark solitons of Bose–Einstein condensates”, *New J. Phys.* **19**, 123012 (2017).

- [389] V. Penna and L. Salasnich, “Itinerant ferromagnetism of two-dimensional repulsive fermions with Rabi coupling”, *New J. Phys.* **19**, 043018 (2017).
- [390] V. Penna and L. Salasnich, “Polarization in a three-dimensional Fermi gas with Rabi coupling”, *J. Phys. B: At., Mol. Opt. Phys.* **52**, 035301 (2019).
- [391] Néel, M. Louis, “Propriétés magnétiques des ferrites ; ferrimagnétisme et antiferromagnétisme”, *Ann. Phys.* **12**, 137 (1948).
- [392] B. Keimer, S. A. Kivelson, M. R. Norman, S. Uchida, and J. Zaanen, “From quantum matter to high-temperature superconductivity in copper oxides”, *Nature* **518**, 179 (2015).
- [393] S. I. Mistakidis, L. Cao, and P. Schmelcher, “Interaction quench induced multi-mode dynamics of finite atomic ensembles”, *J. Phys. B: At., Mol. and Opt. Phys.* **47**, 225303 (2014).
- [394] S. I. Mistakidis, L. Cao, and P. Schmelcher, “Negative-quench-induced excitation dynamics for ultracold bosons in one-dimensional lattices”, *Phys. Rev. A* **91**, 033611 (2015).
- [395] J. Neuhaus-Steinmetz, S. I. Mistakidis, and P. Schmelcher, “Quantum dynamical response of ultracold few-boson ensembles in finite optical lattices to multiple interaction quenches”, *Phys. Rev. A* **95**, 053610 (2017).
- [396] S. Mistakidis, G. Koutentakis, and P. Schmelcher, “Bosonic quantum dynamics following a linear interaction quench in finite optical lattices of unit filling”, *Chem. Phys.* **509**, 106 (2018).
- [397] R. P. Feynman, R. B. Leighton, and M. Sands, “The Feynman lectures on physics; vol. i”, *Am. J. Phys.* **33**, 750 (1965).
- [398] J. Levinsen, M. M. Parish, R. S. Christensen, J. J. Arlt, and G. M. Bruun, “Finite-temperature behavior of the Bose polaron”, *Phys. Rev. A* **96**, 063622 (2017).
- [399] N.-E. Guenther, P. Massignan, M. Lewenstein, and G. M. Bruun, “Bose Polarons at Finite Temperature and Strong Coupling”, *Phys. Rev. Lett.* **120**, 050405 (2018).
- [400] B. Field, J. Levinsen, and M. M. Parish, “Fate of the Bose polaron at finite temperature”, *Phys. Rev. A* **101**, 013623 (2020).

Eidesstattliche Versicherung / Declaration on oath

Hiermit versichere ich an Eides statt, die vorliegende Dissertationsschrift selbst verfasst und keine anderen als die angegebenen Hilfsmittel und Quellen benutzt zu haben.

Die eingereichte schriftliche Fassung entspricht der auf dem elektronischen Speichermedium.

Die Dissertation wurde in der vorgelegten oder einer ähnlichen Form nicht schon einmal in einem früheren Promotionsverfahren angenommen oder als ungenügend beurteilt.

Hamburg, den xx.xx.20xx

Unterschrift der Doktorandin / des Doktoranden